research report

Direct Strength Prediction of Cold-Formed Steel Beam-Columns

RESEARCH REPORT RP16-3

October 2016

American Iron and Steel Institute

The material contained herein has been developed by researchers based on their research findings. The material has also been reviewed by the American Iron and Steel Institute Committee on Specifications for the Design of Cold-Formed Steel Structural Members. The Committee acknowledges and is grateful for the contributions of such researchers.

The material herein is for general information only. The information in it should not be used without first securing competent advice with respect to its suitability for any given application. The publication of the information is not intended as a representation or warranty on the part of the American Iron and Steel Institute, or of any other person named herein, that the information is suitable for any general or particular use or of freedom from infringement of any patent or patents. Anyone making use of the information assumes all liability arising from such use.

![Johns Hopkins University logo]

Johns Hopkins
U N I V E R S I T Y

Department of Civil Engineering
Latrobe Hall 205
Baltimore, MD 21218

Final Report

Direct Strength Prediction of Cold-Formed Steel Beam-Columns

Committee on Specifications for the Design of Cold-Formed Steel
Structural Members

American Iron and Steel Institute
October 2016

Direct Strength Prediction of Cold-Formed Steel Beam-Columns

Research completed by:
Shahabeddin Torabian,
Baofeng Zheng, Yared Shifferaw, and Benjamin W. Schafer

American Iron and Steel Institute
October 2016

Abstract

The Direct Strength Method (DSM) of cold-formed steel member design employs local, distortional, and global cross-section elastic buckling analysis with empirically derived "direct" expressions to predict member strength. DSM is an accepted design method in national design specifications (e.g., AISI-S100-16) and enables a unified, robust, and flexible design approach. However, for beam-columns DSM in current design specifications employs simplified linear interaction expressions based on combining the isolated axial and bending elastic buckling and strength response. Today, local, distortional, and global elastic buckling under any combination of axial load and bending moments may be found using elastic buckling analysis tools such as the finite strip method (e.g., CUFSM). Thus, stability may be assessed under the combined actions, but new DSM expressions are needed to utilize this explicit stability information in determining beam-column strength. In this report, new strength expressions for each limit state are developed. In addition, the results of beam-column tests performed by the authors and those available in the literature are used to validate the performance of the new proposed DSM for beam-columns. The development of DSM for beam-columns has the potential to provide a more mechanically sound solution to the strength of cold-formed steel beam-columns, eliminate excessive conservativeness, and at the same time encourage the next generation of optimized, high strength, cold-formed steel shapes. This report covers: a new formulation for DSM that can account for stability and strength under multiple actions; targeted testing under P-M-M loadings to explore the beam-column stability space explicitly and find capacities; nonlinear FEA analysis to expand the studies and flesh out issues in the final design methods; and technology transfer to ease the use of the develop method and its related tools.

Table of Contents

List of Figures

xi

xiv

List of Tables

Chapter 1 - Introduction

This project develops a new Direct Strength Method (DSM) – based design method for cold-formed steel (CFS) beam-columns that explicitly and directly considers the applied actions, including axial loads and biaxial bending, in uniquely determining the stability and strength of a CFS member under those actions. This report covers: (1) a new formulation for DSM that can account for stability and strength under multiple actions; (2) targeted testing under axial, major-axis and minor-axis bending (P-M-M) loadings to explore the beam-column stability space explicitly and find capacities; (3) nonlinear finite element analysis (FEA) analysis to expand the studies and flesh out issues in the final design methods; and (4) technology transfer to ease the use of the develop method and its related tools.

The project deliverables and progress are provided in a year-by-year format in the following sections, to document the efforts and the research methodology implemented to achieve the goals.

1.1 Year 1 summary

The first year of the project was devoted to conducting preliminarily studies on beam-column related subjects such as beam-column applications, an industry survey, identifying targeted CFS beam-columns for testing; and designing and manufacturing a new test rig to perform experimental studies on the targeted beam-columns. Resulting from year 1 a number of research reports were provided on the project website: www.ce.jhu.edu/bschafer/dsmbeamcol. A summary of the released reports and a discussion on the experimental program in Year 1 is provided here and followed by reviewing the overall work plan.

The first report (TWG-RR01-12) entitled "Cold-formed steel beam-column applications in residential and commercial midrise buildings and design method comparisons." was prepared in the Thin-walled Structures Group at Johns Hopkins University by Y. Shifferaw in July 2012. This "survey of the industry" report summarizes the use of beam-columns in common cold-formed steel applications. The cold-formed systems emphasized are trusses and load bearing framing as typically used in residential and commercial cold-formed steel buildings and secondary cold-formed steel systems (purlins, girts, etc.) as typically used in metal building systems. Case studies are employed to illustrate typical scenarios. The survey identified a number of unusual beam-column sections in common use including deep leg hat sections in CFS trusses and eave struts in CFS metal buildings. Most members are either axial, or bending dominant, and designers attempt to enforce these assumptions wherever possible; however, a number of cases with high compression and bending (including biaxial demand) are found. Boundary conditions are often simplified in a manner to ignore or simplify beam-column behavior – efficiencies in design may be possible for the myriad of partially rigid connections in use – resulting in far more members needing to be treated as beam-columns. Comprehensive case studies, on archetype buildings, for all possible load cases, utilizing software to identify the beam-column demands, could be performed in the future to further identify the importance and prevalence of cold-formed steel beam-columns. (Such analysis is typically conducted for metal buildings, but not in cold-formed steel framing).

The second report (TWG-RR02-12) entitled "Towards optimization of CFS beam-column industry sections." was prepared in Thin-walled Structures Group at Johns Hopkins University by Y. Shifferaw in July 2012. This brief report was produced independently, but motivated from the current project. In particular, the research looks at the use of optimization

and preliminary DSM beam-column formulations to create optimal CFS beam-columns. The report demonstrates that Σ- and S-shaped CFS members have the potential to improve greatly upon the performance of lipped C-shaped members in common use.

The third report (TWG-RR03-12) "Identifying targeted CFS beam-columns for testing." was written by Y. Shifferaw in July 2012. This report studies local, distortional, and yielding limit states of cold-formed steel sections, with an emphasis on lipped channels to try to determine the best subset of sections for testing as beam-columns. 600S162 and 800S200 sections are identified as covering all three studied limit states under compression and major-axis bending. In addition, these same members have independent tests as beams (performed in previous works) and a subset are utilized in the archetype building for the CFS-NEES project. These two sections are proposed to be pursued in testing program.

A letter report entitled "Development of DSM Direct Design Formulas for Beam-Columns (Year 1 Proposed)." was prepared in Thin-walled Structures Group at Johns Hopkins University by B. W. Schafer in July 2012. This letter report summarizes the development of a proposed set of Direct Strength Method beam-column formulas that, for the first time, provides a direct method that includes axial and bi-axial bending (P-M-M), and incorporates inelastic bending, and members with holes. The proposed expressions provide the first fully conceived Direct Strength Method (DSM) beam-column formulation. This proposed method is going to be compared against testing and nonlinear finite element analysis with small modifications made as necessary.

Based on the expressions developed in this letter report a small custom-built MATLAB program was written that performs the necessary stability and strength analysis across the complete P-M-M space and provides the predicted strength results. The results were to be

compared with testing and nonlinear collapse finite element models. The comparison to nonlinear collapse finite element models was started.

In the first year of the project the proposed testing schedule was not completely accomplished. Design, procurement, and construction of the modifications for the existing testing rig (Big-Blue-Baby: BBB) took considerably longer than anticipated. However, at the end of Year 1 the new testing rig modifications were designed and installed. See Figure 1-1 for a picture of the new fixtures in the testing rig. Axial load is applied from the top, bending is applied from the side (in tension), and the members may be oriented at an angle away from the vertical to create bi-axial bending. The member is explicitly pinned about the axis of bending.

Specimen. Two specimens are placed In the rig to provide the potential to Remove torsional buckling modes.

Bottom of test fixture, pin can be rotated so that axis of bending is at an angle, creating biaxial bending in specimens.
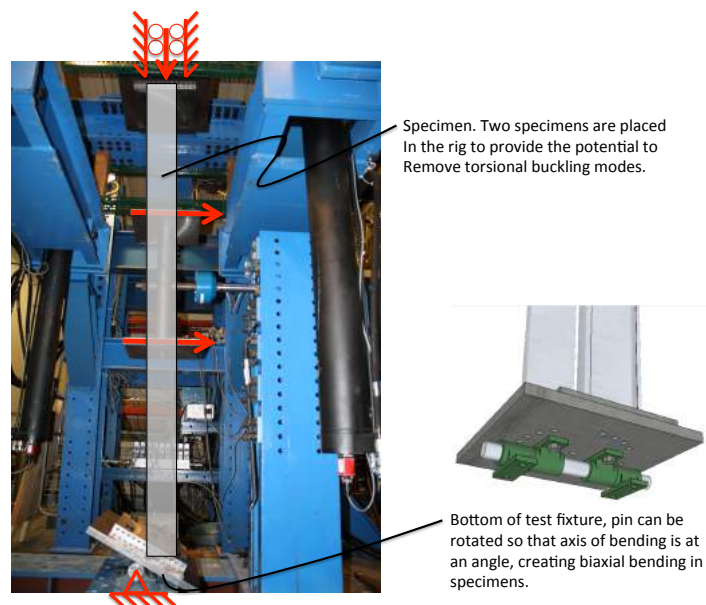
Figure 1-1:Beam-column testing rig at JHU, ready for shakedown tests (30 July 2012)

1.2 Year 2 summary

By completion of the test rig modifications, a shakedown test was performed on two connected beam-columns to study the performance of the rest rig and to start the experimental program. Shakedown test results, constructive feedback from the AISI committee in an AISI

meeting, and re-thinking about the load path of the test rig convinced the PI that the design test rig would not fulfill all testing objectives and a modification on the test rig or testing method was required (see Figure 1-2). The main issues about the test rig were: (1) an inevitable relatively large distance between the shear-center and the loading point resulting in large torsional moments; (2) behaving like built-up sections due to shear flow caused by the test rig elements; (3) probable failure modes under concentrated point loads.

Scuttled August 2012 after feedback

Bottom of test fixture, pin can be rotated so that axis of bending is at an angle, creating biaxial bending in specimens.
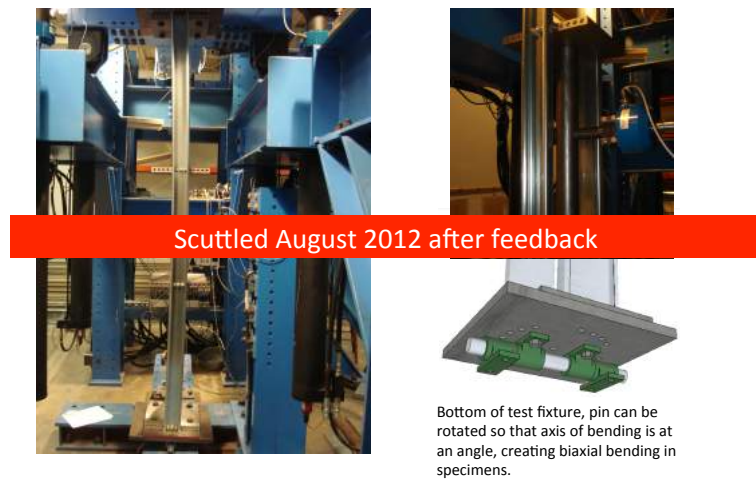
Figure 1-2: Beam-column testing: shakedown test
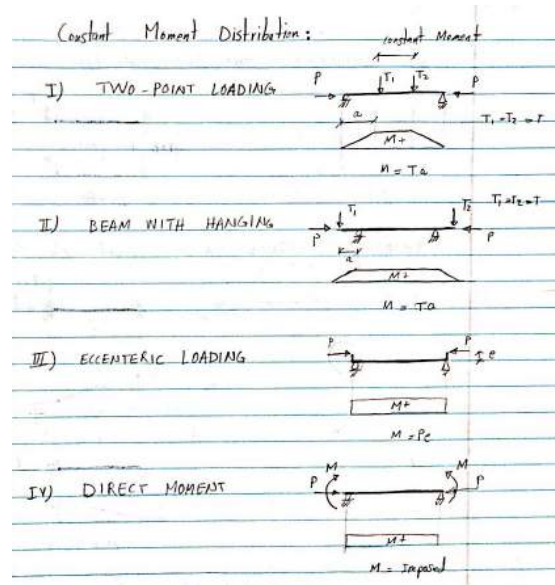
Figure 1-3: Basic schematic of the different ways for providing uniform moment in a beam-column

5

Consequently, the research group endeavored to come up with new ideas on testing beam-columns and a completely different way of thinking to continue the experimental testing program. As shown in Figure 1-3, several ways are available to provide uniform moment in a beam-column member. However, applying eccentric loading appeared to be the simplest and the most practical way to test a beam-column. Therefore, a new test rig was designed for performing experiments within a uniaxial MTS loading machine that was available in the Thin-walled Structures Lab at JHU. Switching from the old rig to the new one required a mandatory change in the project work plan and delayed the testing program. However, the project team aimed to speedup the design and construction process. As the test specimens in the new rig needed to have two welded end plates for clamping, a new issue for specimen preparation and manufacturing came into the design. All the test rig elements including loading plates and all other items needed for mounting instrumentation were prepared at JHU, but welding of the specimens was done in a welding shop off campus to save time and facilitate the preparation process.
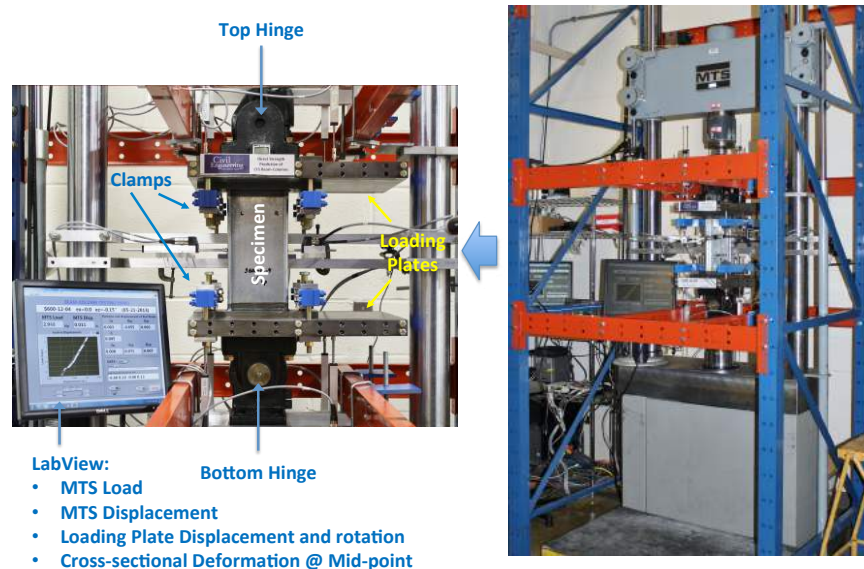
Figure 1-4: Test setup configuration for the beam-column experiments

Figure 1-4 shows the new test setup configuration including the test rig and the MTS loading machine during one of the tests on the short (stub column) specimens. The test setup consists of two loading plates connected to swivel joints at the top and bottom, clamps for connecting the test specimen, a uniaxial MTS loading machine, a supporting frame around the loading machine, instrumentation, and a data acquisition system.

According to test matrix proposed in the second year of the project (see Chapter 2), a total of 37 specimens including short (L=12 inches) and long specimens (L=48 inches) were initially considered for testing and then another 18 test specimens (L=24 inches) were added. At the end of Year 2 of the project, all short specimens and almost one-third of long specimens (total 23 specimens) were tested. The remaining specimens were welded and prepared for testing. The remaining specimens were tested in the Year 3 (see Chapter 3 for complete experimental results).

Other than preparing and performing the experiments, both analytical and numerical aspects of the project had notable progress in Year 2 of the project. A custom built MATLAB program has been written that performs an integrated stability and strength analyses and utilizes the results in the newly proposed DSM direct design formulas for beam-columns. The program determines elastic buckling loads, yield and plastic surfaces of cold-formed sections, and predicts the strength surface of the section in accordance with the new DSM method. Several methods are proposed to determine the plastic surface of cold-formed steel sections based on a fiber element based approach. The results of DSM prediction of strength are compared to the test results to make further improvements to the formulations, as explained in Chapter 4. The strength surface of a 12 in. long lipped C-channel 600S137-54 is shown in Figure 1-5 and compared to the beam-column strength surface in the current AISI specifications. It is shown that the newly proposed

DSM method for beam-columns provides a more realistic platform for prediction of beam-column strength.
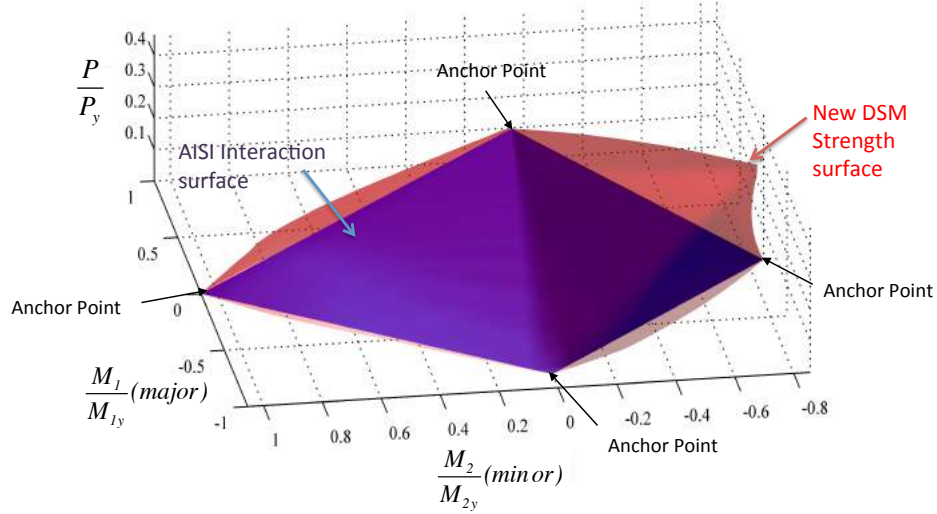
Figure 1-5: Comparison of the new proposed DSM for beam-columns to the current AISI interaction surface

On the numerical side of the project, parametric input files for performing collapse analysis in ABAQUS were prepared for performing both validation analyses against the tested specimens, and parametric studies on other cold-formed steel lipped channels with different dimensions and therefore different slenderness in the local, distortional, and global buckling modes. Several modeling parameters including material σ–ε behavior, residual stresses and strains from cold-forming, and geometric imperfections; as well as, basic member properties including cross-section dimensions, member length, and boundary conditions were all considered in the study.

To validate the FEM models against the experimental results in terms of the failure strength, initial stiffness, and failure modes; the member lengths and boundary conditions employed in the beam-column models are selected consistent with the test setup assumptions and

configurations as shown in Figure 1-6. Chapter 5 has summarized results of the numerical studies on the tested lipped channel beam-columns.
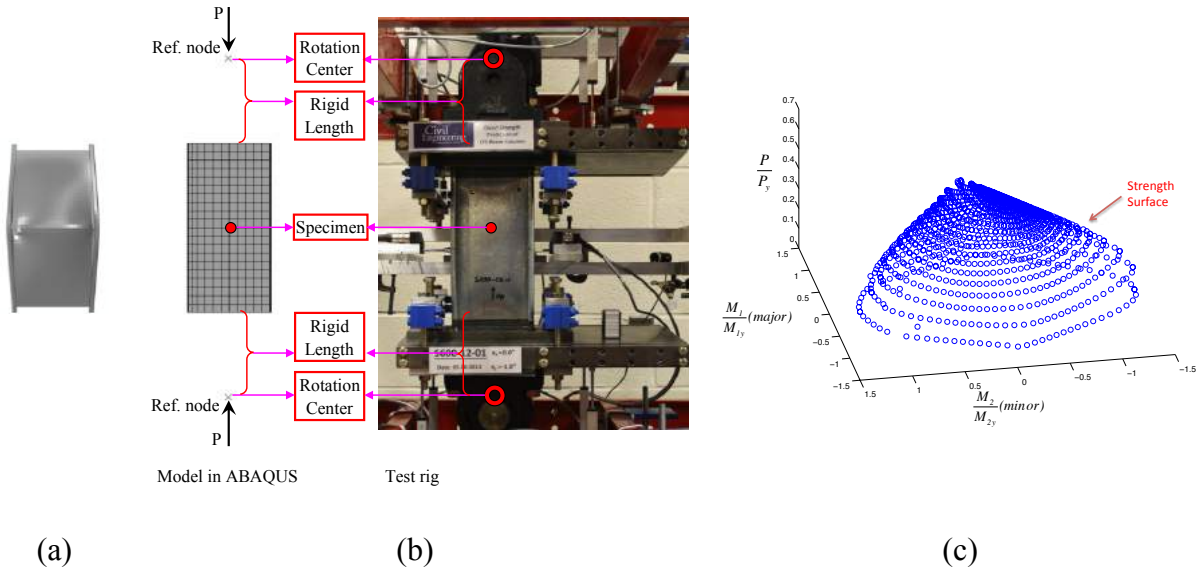
Figure 1-6: (a): a squashed specimen in FEM analysis; (b) geometrical modeling assumptions; (c) strength surface resulted from FEM collapse analyses

In addition to providing solutions for the strength of beam-columns under specific actions (axial load, P, and major-axis, M_1, and minor-axis, M_2, bending moments) the modeling provides a means to develop the complete strength surface in P-M-M space. This surface is compared with current, and newly proposed Direct Strength Method (DSM) design methods for cold-formed steel, and potential for improvements in the newly proposed DSM design method is discussed.

Resulting from year 2, a progress report was uploaded to the project website: http://www.ce.jhu.edu/bschafer/dsmbeamcol/Report_09_24_2013_Final.pdf.

1.3 Year 3 summary

In the third year of the project, the testing on lipped channels was completely done. Moreover, both analytical and numerical aspects of the project have been completed and the proposed method was completely developed and verified for the tested lipped channel, as well as

a wide variety of lipped channel beam-column via parametric finite element method (FEM) analyses.

The experimental program included 17 short specimens (12 inches), 20 intermediate specimens (24 inches), and 18 long specimens (48 inches); for a total of 55 lipped channel specimens. All experimental results on lipped channel beam columns are provided in Chapter 3. All post-processing and data reductions has been completed and the results are compared against both current AISI specifications and the new beam column DSM, as discussed in Chapter 4 of the report. Utilizing the experimental results, the reliability of the current AISI design method and the new beam column DSM are also evaluated.

In chapter 5, FEM models have been verified against all 55 experimental testing results and the most relevant modeling assumptions are considered as a modeling protocol for the parametric studies. The FEM predictions have been used to extend the experimental results to the complete P-M-M space (all loading conditions) and to evaluate the current and the proposed method over the space.

As discussed in chapter 6, the parametric study consists of collapse analysis of numerous lipped channel sections under combined axial load and bending moments (bi-axial bending). In total, 75 lipped channel cross-sections out of 364 cross-sections in the SFIA product catalog have been chosen and 127 combination of axial force and bi-axial moments used to perform collapse analyses. This results in a total of 19050 nonlinear FEM collapse analyses, that have been used to evaluate the prediction methods and determine the reliability of the new beam column DSM.

1.4 Year 4 summary

In the last year of the project, a testing matrix for the extension of the experimental testing was prepared to evaluate the proposed method for a more complex cross-sectional shape.

After consulting with the industry about the most favorable cross-section for additional testing, Zee-sections that are popular mostly in industrial frames as girts and purlins have been chosen and 22 short (L=12 in.) and 21 long (L=48 in.) Zee-section beam columns were tested. Further, the proposed beam-column DSM has been implemented to predict the strength of the tested Zee-shaped specimens. Chapter 3 has provided the summary of the testing program on the Zee-shaped beam-columns.

The most practical outcome of the project is a technology transfer to ease the use of the developed method and its related tools. Accordingly, a beam-column stability and plastic analysis tool is added to CUFSM (http://www.ce.jhu.edu/bschafer/cufsm/) that enables a universal and stand-alone tool to perform required stability and plastic analyses required for beam-columns in accordance to the proposed DSM method. In the provided tool, it is possible to load a general section and perform elastic buckling analysis, and plastic section analysis in the P-M-M space directly.
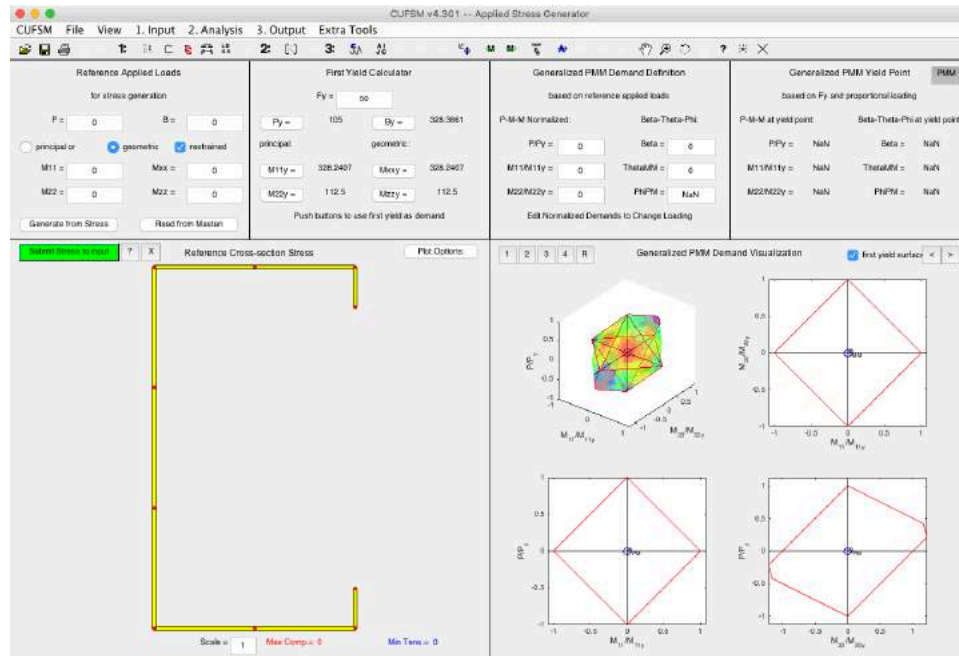
Figure 1-7: Beam-column stability analysis and first yield surface tool in CUFSM 4.301
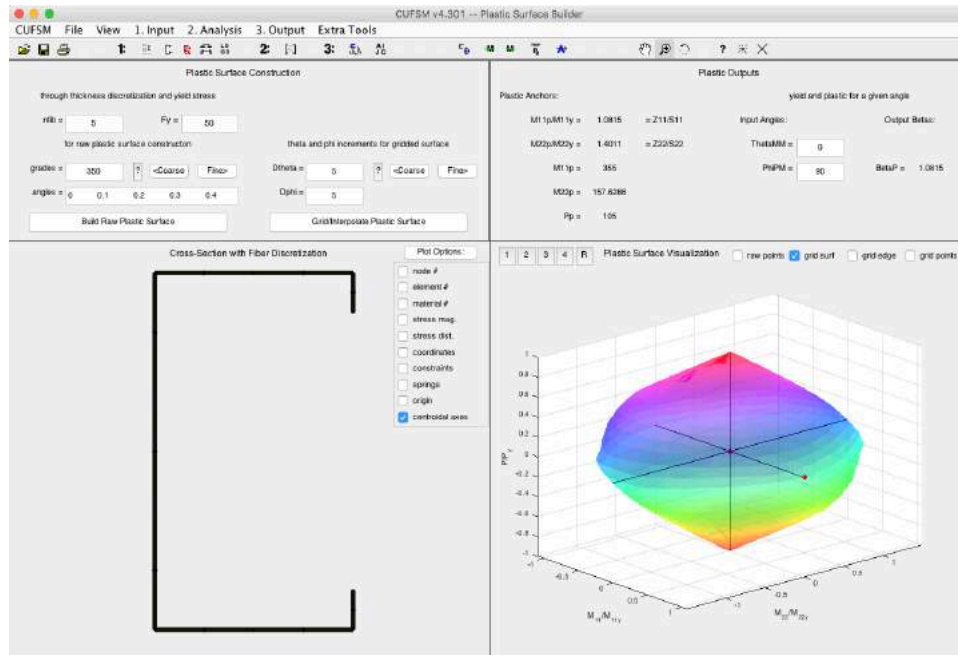
Figure 1-8: Beam-column plastic analysis/surface tool (fiber model) in CUFSM 4.301

The following achievements are provided by the end of this project:

- improved and increased capacity predictions for the next version of AISI-S100,

- improved understanding of stability and collapse behavior under multiple actions,

- enable a uniform design method for CFS member under multiple actions, and

- enable accurate CFS member and system collapse analysis in beam element programs (MASTAN, SAP, STAAD, etc.) through stress resultant yield and plastic surfaces.

1.5 Project Publications

1.5.1 Journal Articles (Torabian et al. 2015b, 2016b):

Torabian, S., Fratamico, D.C., Schafer, B.W. (2016) "Experimental response of cold-formed steel Zee-section beam-columns." *Thin-walled Structures* 98 496-517 (DOI: 10.1016/j.tws.2015.10.016).

Torabian, S., Zheng, B., Schafer, B.W. (2015). "Experimental response of cold-formed steel lipped channel beam-columns." Elsevier, *Thin-walled Structures,* 89 152-168 (DOI: 10.1016/j.tws.2014.12.003)

Forthcoming paper on DSM design method based on Chapter 4 of this report.

Forthcoming paper on Numerical modeling of beam-columns based on Chapter 5/6 of this report.

1.5.2 Conference Papers (Torabian et al. 2014a; b, 2015a, 2016a)

Torabian S., Amouzegar H., Tootkaboni M. and Schafer B.W. (2016). "Finite element modeling protocols and parametric analyses for short cold-formed steel zee-section beam-columns". *Structural Stability Research Council Annual Stability Conference 2015, SSRC 2015*, Orlando, Florida, April 12-15, 2016.

Torabian, S., Fratamico, D.C. and Schafer, B.W. (2015). "Experiments on cold-formed steel Zee-shaped stub beam-columns", *Structural Stability Research Council Annual Stability Conference 2015, SSRC 2015*, Nashville, TN. pp. 571-588.

Torabian, S., Zheng, B., Schafer, B.W. (2014). "Development of a New Beam-Column Design Method for Cold-Formed Steel Lipped Channel Members." *Proc. of the 22nd[t] Int'l. Spec. Conf. on Cold-Formed Steel Structures*, 5-6 November 2014, St. Louis, MO, 359-376.

Torabian, S., Zheng, B., Schafer, B.W. (2014). "Experimental Study and Modeling of Cold-Formed Steel Lipped Channel Stub Beam-Columns." Proceedings of the Annual Stability Conference - Structural Stability Research Council, Toronto, ON, March 25-28, 366-387.

Related Conference Papers During Development of Proposal (Shifferaw and Schafer 2010, 2011):

Shifferaw, Y., Schafer, B.W. (2011) "Towards a cold-formed steel beam-column design by the Direct Strength Method." *Proceedings of Eurosteel 2011: 6th European Conference on Steel and Composite Structures*, Budapest, Hungary. 31 August – 2 September 2011. 1785-1790.

Shifferaw[†], Y., Schafer, B.W. (2010). "Towards a direct strength method for cold-formed steel beam-columns." *Proceedings of the Structural Stability Research Council - Annual Stability Conference*, Orlando, FL. 613-630.

1.5.3 Reports

Torabian, S., Zheng, B., Schafer, B.W. (2016). "Direct Strength Prediction of Cold-Formed Steel Beam-Columns." Final Report to the American Iron and Steel Institute, Washington, DC. [This document]

Torabian, S., Zheng, B., Schafer, B.W. (2013). "Direct Strength Prediction of Cold-Formed Steel Beam-Columns." Year 2 Interim Report to the American Iron and Steel Institute, Washington, DC. [access at www.ce.jhu.edu/bschafer/dsmbeamcol]

Schafer, B.W., Shiferaw, Y. (2012). "Direct Strength Prediction of Cold-Formed Steel Beam-Columns." Year 1 Interim Report to the American Iron and Steel Institute, Washington, DC. [access at www.ce.jhu.edu/bschafer/dsmbeamcol]

Chapter 2 - Identifying CFS beam-columns for testing program

As discussed in Section 1.1, based on the Year 1 studies two groups of sections were initially identified for the testing program: lipped channel sections, 600S162 and 800S200. However, in accordance with the new test rig designed in Year 2, the selected beam-column cross-sections were again reviewed and revised to select the best possible section. Accordingly, a cross-section, close to the Year 1 suggested sections, was selected, and a complete test matrix identifying the precise details of the test specimens was provided. The studies concluded that a 600S137-54 (F_y=50 ksi) can provide enough diversity in failure mode, including all local, local-global and distortional modes, and was thus selected.

In the following section, the decision-making process for finding the targeted CFS beam-column cross-section utilized in the testing program is detailed.

2.1 Requirements for desired beam-column cross-sections

To identify the beam-column cross-section a series of requirements and limitations are considered for selection as follows,

- The selected section should be a common and practical column section

  Lipped C-channels do not explore all beam-column possibilities, but the most important baseline. It is recommended to select a section close to 600S162 or 800S200 identified in Year 1 studies.

- Distinct local and distortional buckling

  The selected section should provide distinct local and distortional buckling capacities to enable the use of experimental data to readily evaluate new DSM formulas for

15

beam-columns. Using different lengths of the section other coupled buckling issues like local-global interaction, can be mobilized. Notably, adding battens can increase the distortional capacity of the member fairly easily and the global capacity can be increased with bracing or end conditions.

- Avoid highly inelastic buckling, try to explore primarily buckling induced limit states

- Perform enough tests to reliably reproduce the P-M-M interaction surface

  Building the P-M-M interaction surface requires many tests and given the limited number of the specimens likely just one cross-section can be tested under various P-M-M loading conditions.

- Consider MTS machine limitations: 100 kips (450 KN) capacity, 6 in. (150 mm) stroke movement, and 8 ft. (2.4 m) space between the crosshead and the actuator including all joint and loading plates.

- Consider loading plate limitations: 12 inches × 20 inches loading plate can accommodate limited cross-sections due to the space required for clamping the end plates and providing the eccentricity.

- Limited number of test specimens (~50 specimens), due to time and financial constraints.

2.2 Evaluating Lipped C-channel data base to find section
2.2.1 Evaluation Method

Based on the issues discussed in the previous section, a number of lipped C-channel sections ranging from 362S137-t to 800S200-t with various thicknesses, t, ranging from 33 mil to 97 mil were selected for studying the local and distortional interaction curves in principal axes in accordance to AISI-S100-12 (NAS 2012) .

The interaction curves can help determine which mode of failure, local or distortional is predicted to happen first. It is desired that the local buckling does not happen prior to distortional buckling. Actually, when the section fails in local buckling, there is no easy physical way to force the failure mode to any other kind of failure, e.g. distortional. Further, in this case when the specimen becomes more slender in global buckling, local-global interaction makes the situation worse. On the other hand, when the distortional failure mode is governing, there are possibilities to capture other modes of failures such as local buckling. Increasing the length of the beam-column member can result in mobilizing a local-global failure mode that can govern the member capacity. Furthermore, the flanges of the member can be battened to help prevent the distortional mode of failure, if needed. In case of global buckling modifications are also possible to shift the failure modes to other desired modes, e.g. bracing.

Accordingly, utilizing AISI-S100-12 (NAS 2012) interaction equations are developed for several lipped C-channels assuming: no p-δ effect, the Direct Strength Method of Appendix 1 for calculating the nominal flexural and compressive strengths, utilizing CUFSM to calculate elastic buckling load factors in local and distortional buckling, assuming no global buckling or a braced condition, and no inelastic reserve in bending.

As mentioned, the CUFSM 4.05 finite strip program was used to determine elastic buckling load factors. Accordingly, the proposed "FSM@cFSM-L_{cr}" method was used to automatically identify local and distortional buckling in conventional FSM models. Using this method avoids the problems of non-unique minima in conventional finite strip models (Li and Schafer 2010). "FSM@cFSM-L_{cr}" stands for the result of the finite strip method at half-wave length (L_{cr}) determined by the constrained-finite strip method.

It should be briefly noted that in "FSM@cFSM-L_{cr}" straight-line cross-section definition should be used to perform a constrained finite strip method (cFSM) analysis to determine local and distortional buckling loads and the corresponding half-wave lengths (L_{cr}). Notably, cFSM cannot meaningfully identify the modes in models including rounded-corners. Given L_{cr} is known for both local and distortional buckling, FSM can be utilized to determine the signature curve of the rounded-corner model. Local and distortional buckling loads at the associated L_{cr} are determined from the signature curve. The method is illustrated in Figure 2-2 for a hypothetical beam section. For more details see (Li and Schafer 2010). The estimated buckling loads are required for predicting the design strength in accordance with DSM in Appendix 1 of AISI-S100-12 (NAS 2012).
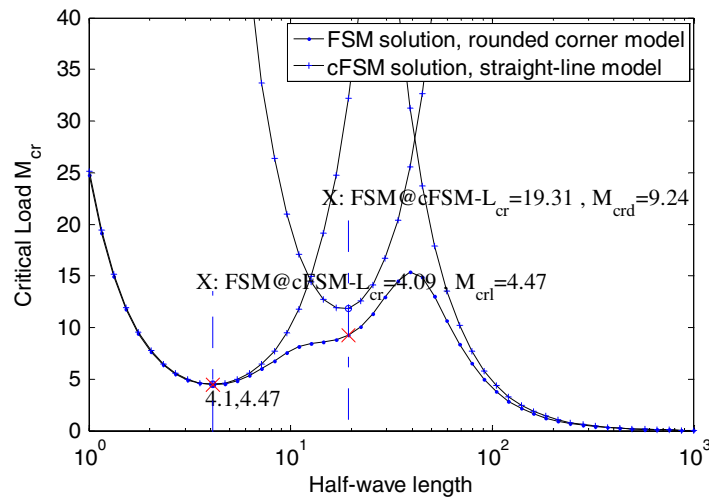
Figure 2-1: FSM@cFSM-L_{cr} method (Li and Schafer 2010)

2.2.2 Interaction surface in principal axes

The interaction surfaces (axial force (P) and both minor and major axes moments, M_{major} and M_{minor}) calculated based on the assumptions discussed in the previous section are shown in the following figures.

P-M$_{major}$ P-M$_{minor (Lips in Tension)}$ P-M$_{minor (Lips in Compression)}$
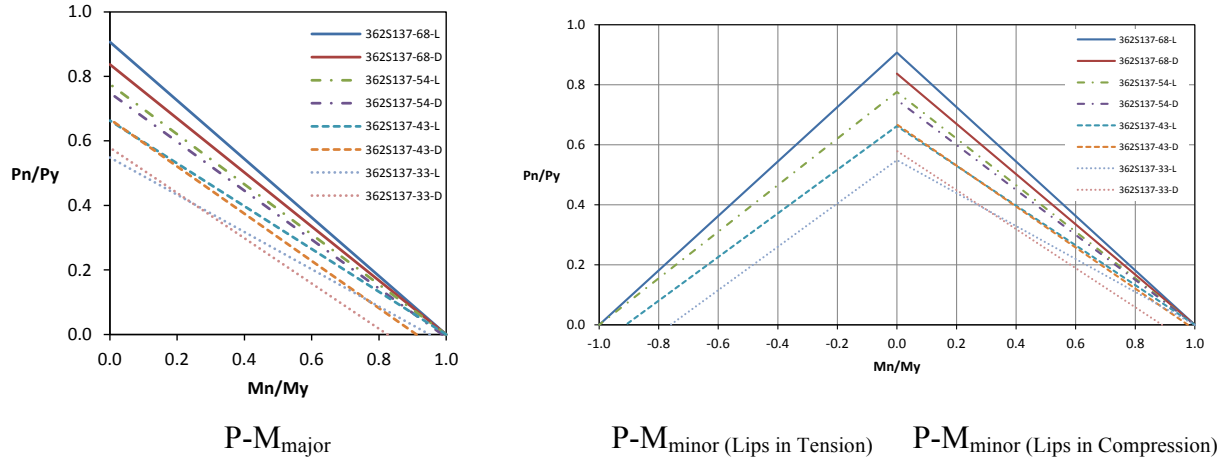
Figure 2-2: Interaction Surface in principal axes: 362S137-t. "-L" and "-D" stand for Local and Distortional, respectively.

P-M$_{major}$ P-M$_{minor (Lips in Tension)}$ P-M$_{minor (Lips in Compression)}$
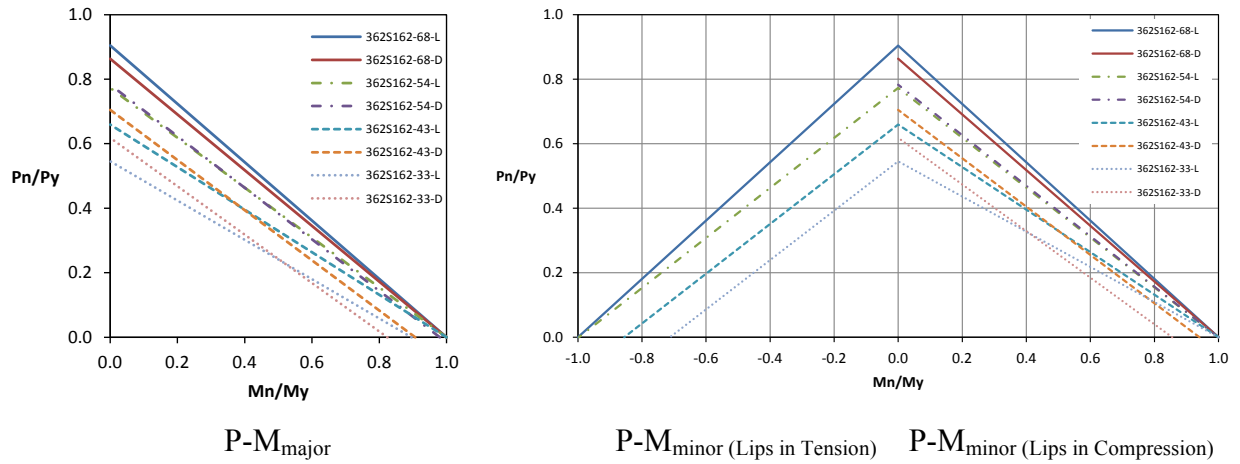
Figure 2-3: Interaction Surface in principal axes: 362S162-t

Interaction curves of the 362S137 and 362S168 sections are presented in Figure 2-2 and Figure 2-3, respectively. The results show that local buckling is typically initiating prior to distortional buckling. However, in a few cases distortional buckling initiates, e.g. 362S137-68 and 362S168-68, but in these cases inelastic buckling dominates.

Interaction curves of the 400S137 sections are shown in Figure 2-4. This section also cannot provide distinct local/distortional buckling except for thick members where the buckling is highly inelastic.

19

P-M$_{major}$ P-M$_{minor}$ (Lips in Tension)   P-M$_{minor}$ (Lips in Compression)
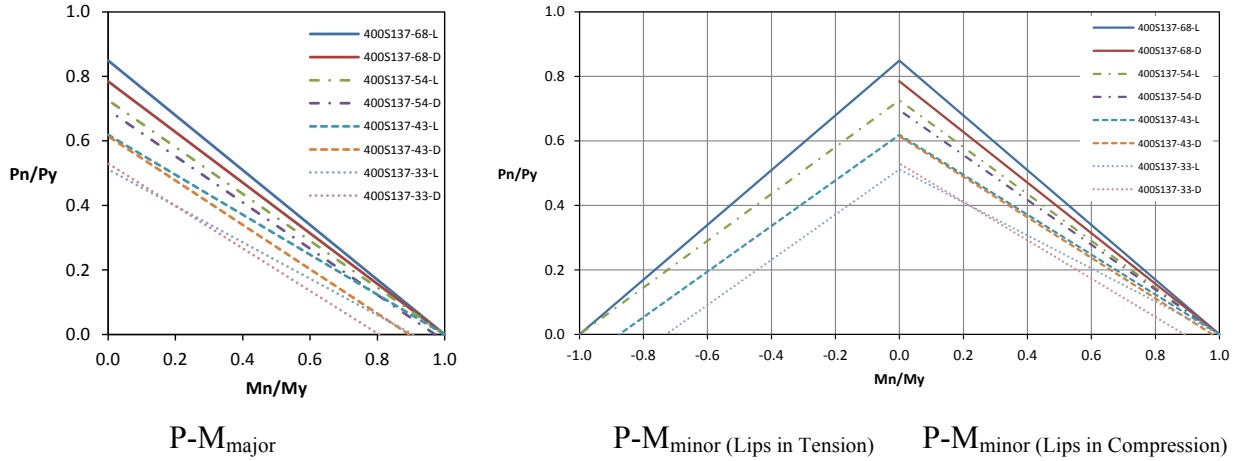
Figure 2-4: Interaction Surface in principal axes: 400S137-t

P-M$_{major}$ P-M$_{minor}$ (Lips in Tension)   P-M$_{minor}$ (Lips in Compression)
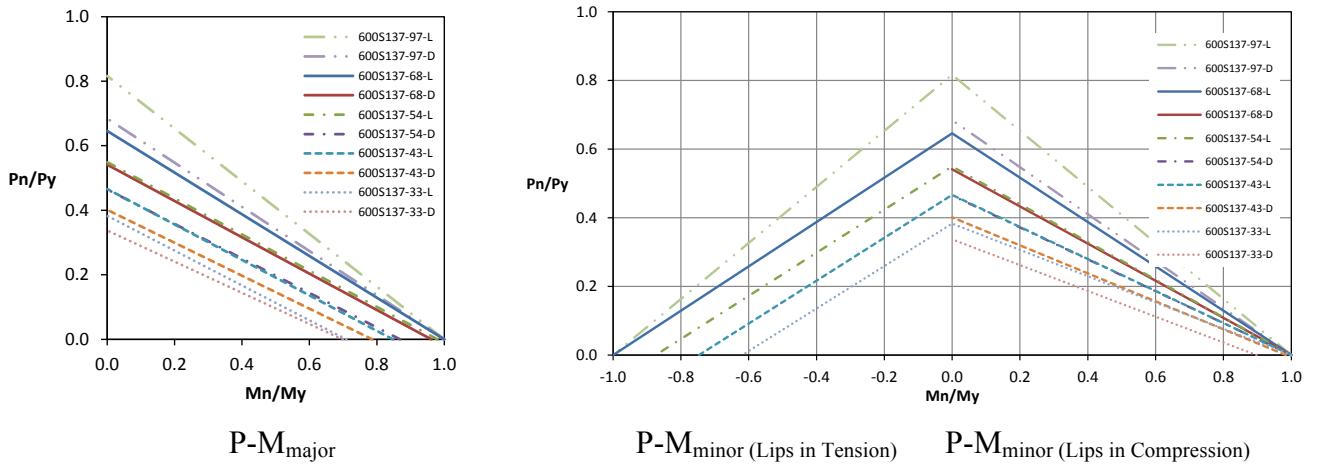
Figure 2-5: Interaction Surface in principal axes: 600S137-t

Moving on to deeper sections, the 600S137 is examined as shown in Figure 2-5. Unlike the other sections, a distinct local and distortional buckling strength is seen in this section. It seems that for almost all kinds of the 600S137 cross-section, the distortional failure initiates prior to local buckling. Although the 600S137-97 definitely has inelastic buckling, other sections such as the 600S137-54 and 68 have no highly inelastic failures. As shown in Figure 2-6, the 600S168 is also studied. This section is similar to the 600S137, but local/distortional distinction in 600S137 is more pronounced.

P-M_major   P-M_minor (Lips in Tension)   P-M_minor (Lips in Compression)
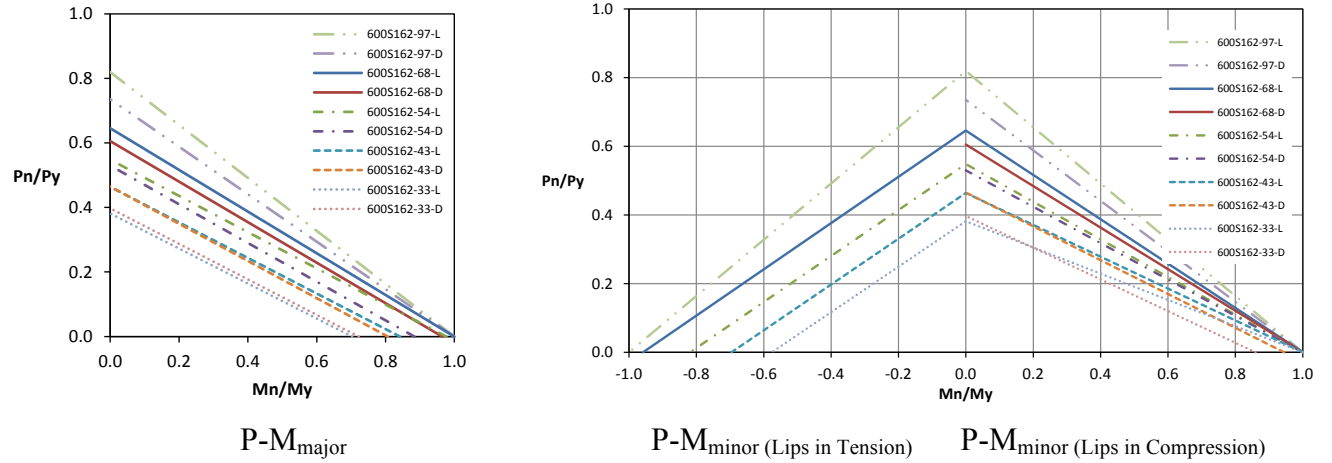
Figure 2-6: Interaction Surface in principal axes: 600S162-t

P-M_major   P-M_minor (Lips in Tension)   P-M_minor (Lips in Compression)
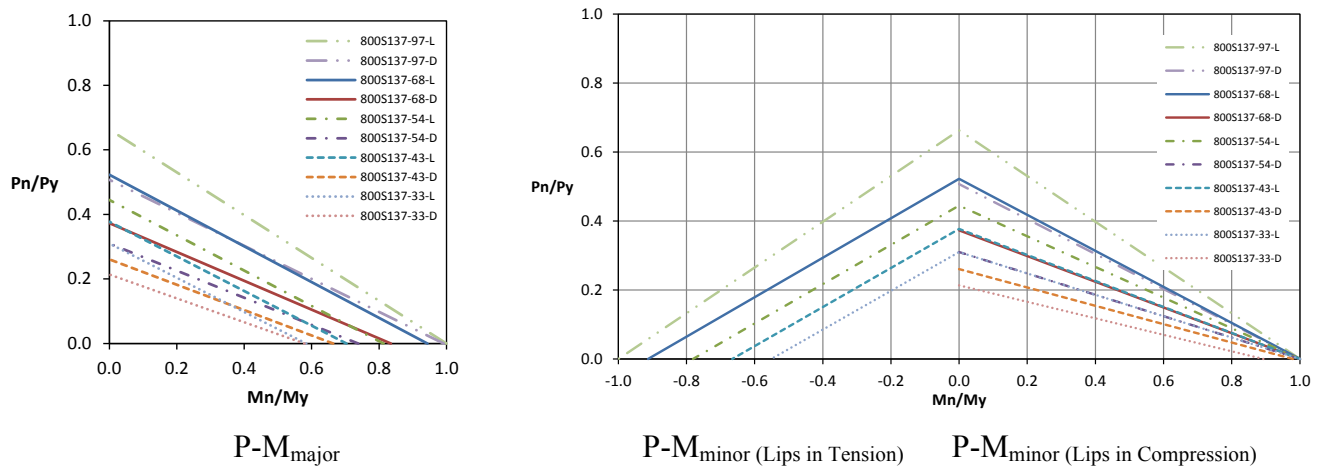
Figure 2-7: Interaction Surface in principal axes: 800S137-t

800S137 interaction curves are shown in Figure 2-7. Although the section seems to be acceptable in terms of both local/distortional buckling distinction and the no-highly-inelastic buckling criterion, the 800S137 cannot be accepted as a column as the section mostly serves as a beam section in structural design. The other similar section, 800S200 is also studied as shown in Figure 2-8. The section has relatively distinct buckling modes for t=68 and 97 mils, and t=68 mils provides more elastic failure modes.

P-M$_{major}$	P-M$_{minor}$ (Lips in Tension) P-M$_{minor}$ (Lips in Compression)
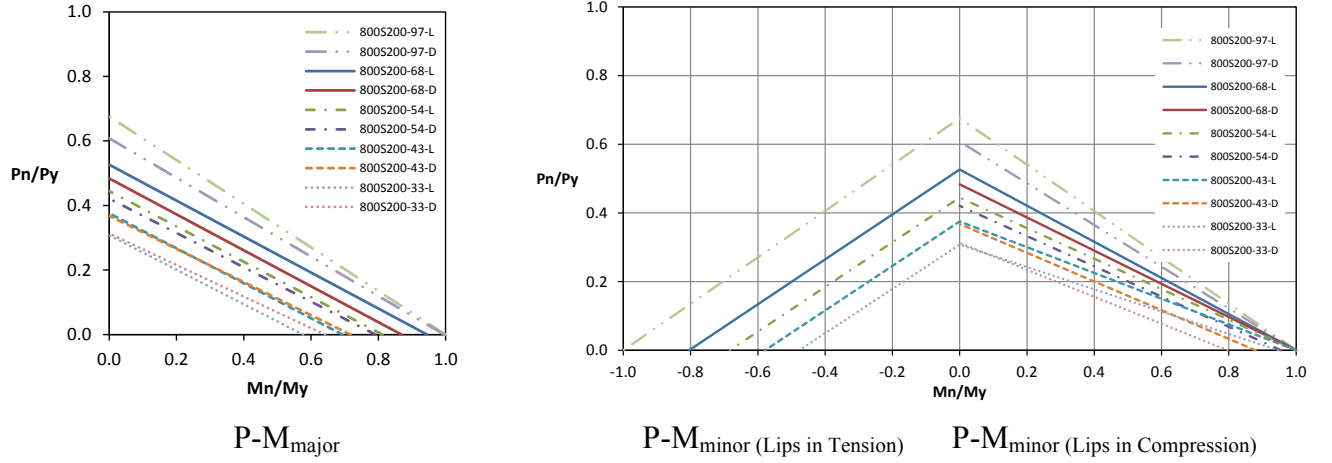
Figure 2-8: Interaction Surface in principal axes: 800S200-t

2.2.3 Discussion and selection of the test specimen

According to the studies and discussions in the previous section, the cross-section alternatives are narrowed: 600S137, 600S168 and/or 800S200. Given the limited number of test specimens (~50 specimens) to be tested, it is deemed most reasonable to test a single cross-section under several combinations of axial load and bending moment to provide enough observations to fully realize the 3D P-M-M interaction/strength surfaces.

As an eccentric loading condition is adopted in the beam-column experiments (see Section 3.1), larger cross-sections require larger eccentricities for some marginal points in 3D P-M-M space. Therefore, in the same situations, sections with lower structural capacities are preferred to higher capacity members. Accordingly, it is decided to use the 600S section rather than 800S sections in the experimental program.

To select the final section between the 600S137 and the 600S168, a correction is made on the distortional buckling interaction curve to address the actual boundary conditions in the test rig. As the specimens are welded to end plates so that they may be clamped in the test rig (see Section 3.1.1), the end boundary condition of the specimen in both the local and distortional

buckling is theoretically clamped. The clamped boundary condition can increase both the local and distortional elastic buckling loads. However, the increase in local buckling critical load is negligible. However, for distortional buckling in short members this increase may be large, particularly when the distortional buckling half-wave length (L_{crd}) is comparable to the length of the element. To account for this phenomenon, an empirical increase had been developed for boosting up the distortional buckling critical load (Moen 2008).

$$D_{boost} = 1 + \frac{1}{2}(\frac{L_{crd}}{L})^2 \tag{2.1}$$

$$\text{P-M}_{major} \qquad\qquad \text{P-M}_{minor \ (Lips \ in \ Tension)} \qquad \text{P-M}_{minor \ (Lips \ in \ Compression)}$$
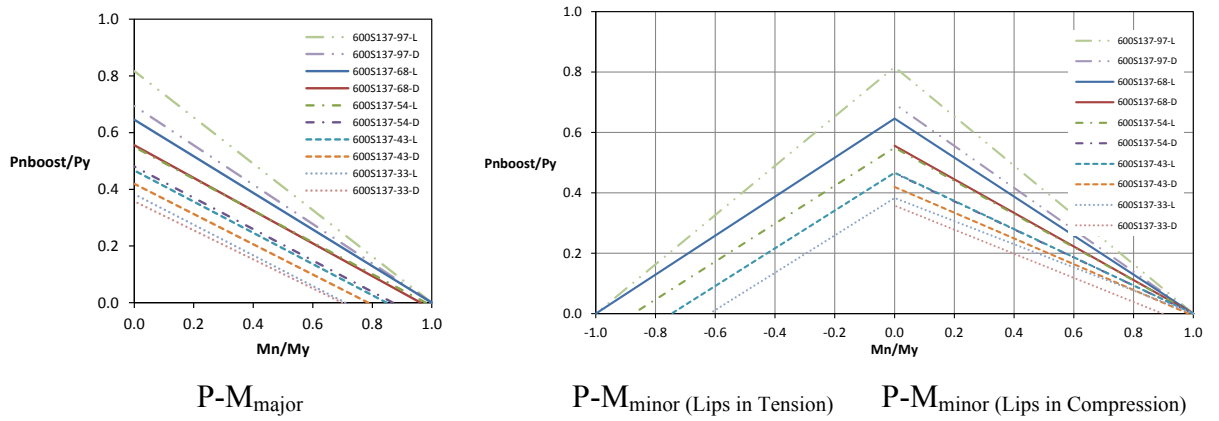
Figure 2-9: Interaction Surface in principal axes: 600S137-t (Boosted distortional buckling)

Applying the boosting factor to account for end conditions to the 600S137 and 600S168 strength interaction curves, shows that the distortional mode is very close to local mode in the 600S168 and this section is no longer suitable in terms of local/distortional distinction (see Figure 2-9 and Figure 2-10). Therefore, the 600S137 cross-section is selected for beam-column experiments in Phase 1. The selected section has a wide web for local, narrow flange for distortional, and the global mode can be mobilized by choosing longer specimens. It is worth mentioning that this section was also used in a comprehensive cyclic testing program on cold-

formed steel sections to study energy dissipation characteristics of the thin-walled cold-formed steel members (Padilla-Llano et al. 2012; Padilla et al. 2012a; b).
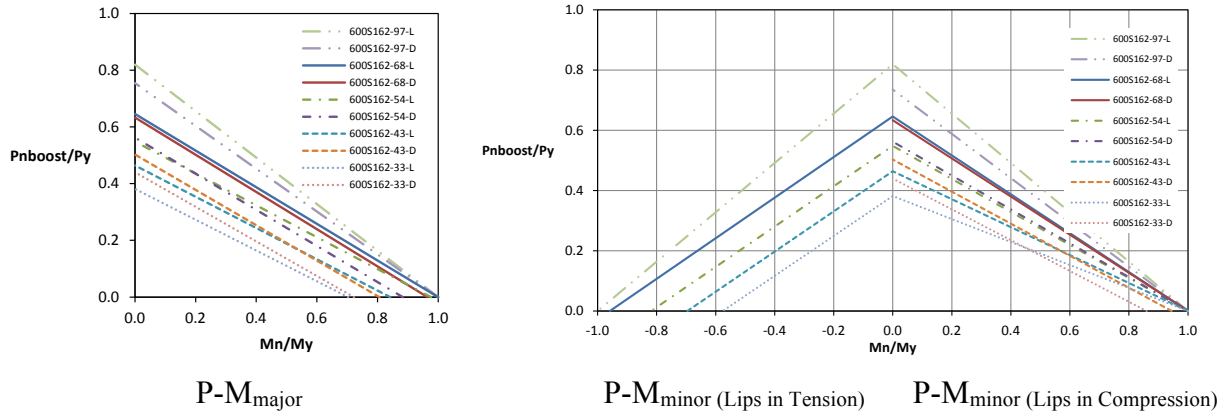
Figure 2-10: Interaction Surface in principal axes: 600S162-t (Boosted distortional buckling)

With the cross-section identified, two other parameters still need to be finalized, the thickness and the length of the specimen. To determine the thickness, more detailed buckling analyses using the general boundary condition capability in CUFSM was performed to determine the local and distortional critical loads. As mentioned, according to the specimen details (see Section 3) that include two end plates, the test specimens are end-clamped in the local and distortional buckling modes. By using general boundary conditions, there is no need to use the approximate boosting coefficient (Eq. 2.1) and more accurate results may be achieved. The elastic buckling analysis for both 600S137-54 and 600S137-68 cross-sections are summarized in Appendix A. The elastic buckling results are used in the Direct Strength Method to calculate the member strength. Accordingly, the interaction curves for both selected sections are shown in Figure 2-11 and Figure 2-12; and as before, local-global buckling is not considered (i.e. the member is assumed globally braced). The results show that using the 600S137-54 can provide more distinct local/distortional buckling modes and may result in more interpretable test data.
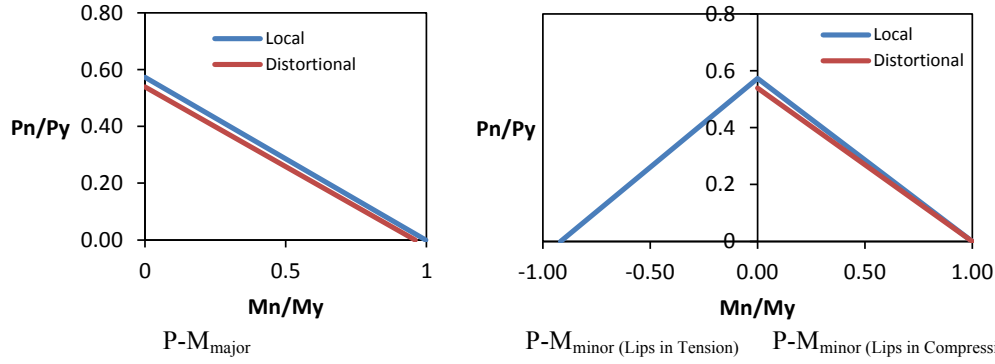
Figure 2-11: Interaction Surface in principal axes: 600S137-54 (Clapmed-Clamped in local and distortional buckling, CUFSM-General boundary condition)
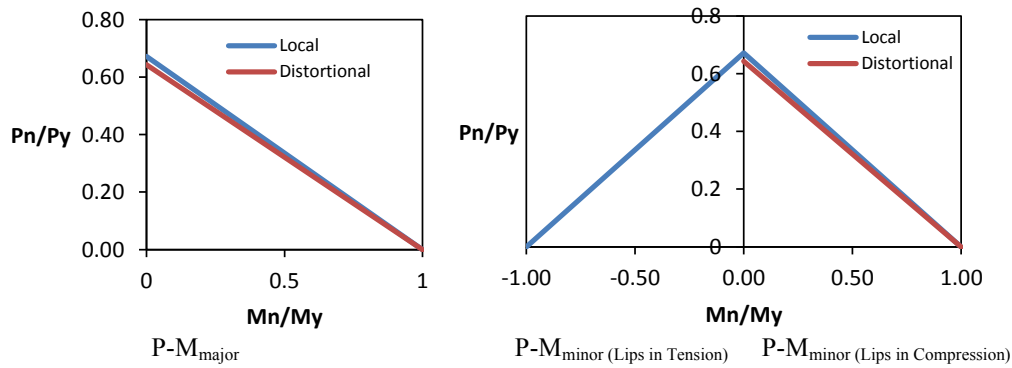
Figure 2-12: Interaction Surface in principal axes: 600S137-68 (Clapmed-Clamped in local and distortional buckling, CUFSM-General boundary condition)

Given the 600S137-54 as the cross-section for the beam-column testing program, the length effect on failure modes are studied using the CUTWP program to calculate the elastic global critical load and DSM to predict the local-global strength interaction. It should be noted that in DSM distortional-global interaction is assumed to be negligible. The elastic buckling analysis of 600S137-54 including all local, distortional and global modes are summarized in Table 2-1c(see Appendix A) and implied in DSM to determine the interaction curves.

The lengths are selected based on both desired structural behavior and the test rig limitations. From the structural point of view, the shortest possible length should be used to eliminate local-global interaction and prevent local buckling to happen prior to distortional buckling (see Figure 2-11). On the other hand, distortional buckling critical load might be

boosted due to the short length of the member as expressed in Eq. 2.1. Therefore, the member capacity will be the result of several mode capacities and interactions especially in shorter members.

Table 2-1: Summary of the critical loads (local, distortional, global) for 600S137-54 and 600S137-68

Section	B.C.	Length	Compression (kips)				Bending (kips-in)									
							Major				Minor					
											Lips in tension			Lips in compression		
			P_y	P_{crl}	P_{crd}	P_{cre}	M_y	M_{crl}	M_{crd}	M_{cre}	M_y	M_{crl}	M_{cre}	M_{crl}	M_{crd}	M_{cre}
600S137-54	C-C	12″	25.7	8.2	12.3	212.2	42.0	69.3	80.0	1111.1	4.9	6.2	36458.0	52.9	21.8	811.4
600S137-54	C-C	48″	25.7	7.2	10.6	13.3	42.0	65.0	60.0	70.0	4.9	5.4	2279.0	48.9	14.3	51.5
600S137-54	S.S/FSM@cFSM	-	25.7	7.3	9.1	-	42.0	65.3	57.5	-	4.9	5.4	-	49.1	13.7	-
600S137-54	S.S/boosted	12"	25.7	7.3	14.2	212.2	42.0	65.3	75.6	1111.1	4.9	5.4	36458.0	49.1	18.0	811.4
600S137-54	S.S/boosted	48"	25.7	7.3	9.4	13.3	42.0	65.3	58.6	70.0	4.9	5.4	2279.0	49.1	13.9	51.5
600S137-68	C-C	12″	32.0	16.0	22.3	263.1	51.5	128.7	123.7	1320.0	5.9	11.9	45097.0	105.7	32.5	953.0
600S137-68	C-C	48″	32.0	13.8	18.9	15.8	51.5	121.3	99.4	83.6	5.9	10.9	2820.0	97.1	23.0	61.2
600S137-68	S.S/FSM@cFSM	-	32.0	14.3	15.4	-	51.5	127.0	98.4	-	5.9	10.4	-	97.5	22.4	-
600S137-68	S.S/boosted	12"	32.0	14.3	21.9	263.1	51.5	127.0	129.2	1320.0	5.9	10.4	45097.0	97.5	28.0	953.0
600S137-68	S.S/boosted	48"	32.0	14.3	15.8	15.8	51.5	127.0	100.3	83.6	5.9	10.4	2820.0	97.5	22.8	61.2

To study the effect of global buckling on both the local and distortional strengths more explicitly, the global phenomenon may be mobilized via increasing the length of the beam-column member. Increasing the length not only can trigger local-global interaction but also remove length-related end condition boosting effects in distortional buckling.

P-M_{major} P-$M_{minor\ (Lips\ in\ Tension)}$ P-$M_{minor\ (Lips\ in\ Compression)}$
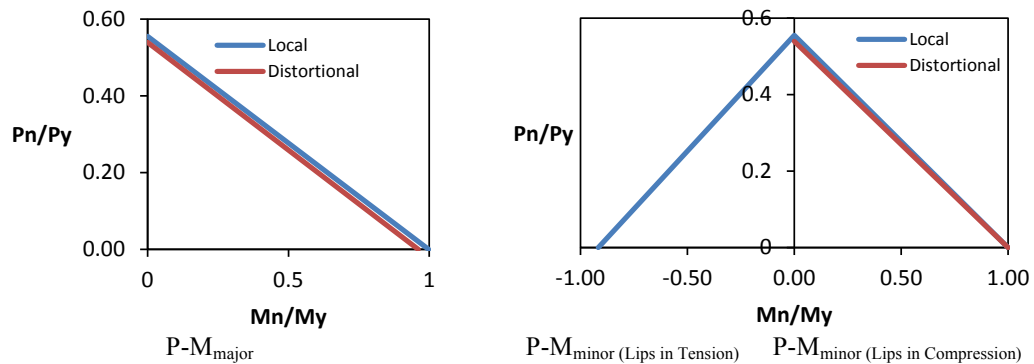
Figure 2-13: Interaction Surface in principal axes: 600S137-54, L=12 inches (C-C in Local and distortional buckling, CUFSM-General B.C.; S-S in flexural buckling and C-C in torsional buckling, CUTWP)

The shortest possible practical specimen for the testing rig is 12 inches long. Measuring beams, end clamps, position transducers, and the space required to set the specimen in the rig governs this length. Therefore, the first selected length is set to the shortest length: 12 inches. The interaction surface in the principal axes of a 12 in. long-600S137-54 beam-column specimen is shown in Figure 2-13 (see Table 2-1 for critical loads). The specimen is supposed to be end clamped in local/distortional buckling (performed via CUFSM), simple-simple in the flexural buckling, and clamped-clamped in the torsional buckling (performed in CUTWP). The results show that distortional buckling still happens prior to local buckling. It should be noted that test results always opens new windows to understand the structural behavior and the predicted behavior might not happen. Though, generally speaking, each cross-section from the SSMA /SFIA structural cross-section database is a possibility for testing, it is attempted here to find the most diverse section in terms of distinct failure modes.

As a small finding, comparison of the boosted results and the exact FSM results by CUFSM shows the boosting factor is somewhat conservative and the distortional buckling load might be more than the predicted values. However, the accuracy of the boosting factor seems to be great enough for design purposes.

P-M$_{major}$ P-M$_{minor \, (Lips \, in \, Tension)}$ P-M$_{minor \, (Lips \, in \, Compression)}$
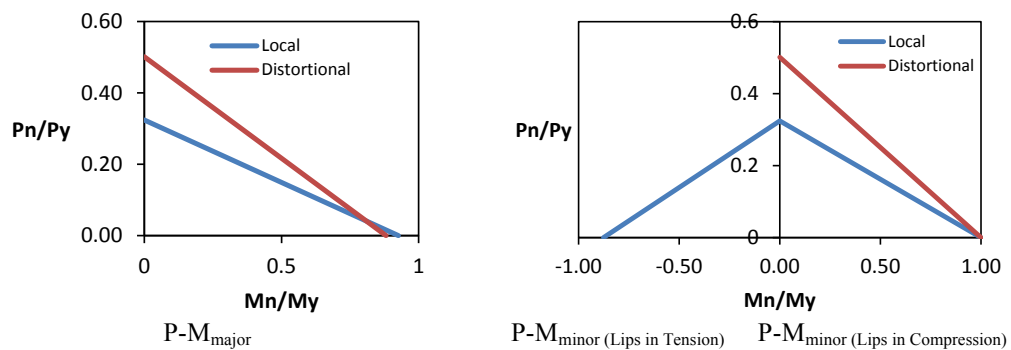
Figure 2-14: Interaction Surface in principal axes: 600S137-54, L=48 inches (C-C in local and distortional buckling ,CUFSM-General B.C.; S-S in flexural buckling and C-C in torsional buckling, CUTWP)

To cover all buckling modes including local, distortional, and global modes, one-third of the specimens (about 17 specimens) are set aside for local/distortional buckling modes via 12 in. long specimens and the rest of them are considered for local-global and distortional modes. The longest specimen that can be tested in the test rig and the existing MTS loading machine is around 50 in. long (see Section 3.1.1 for the test setup details). To provide a real local-global interaction phenomenon, the longest possible length is adopted to mobilize global, local-global and potentially distortional modes. Accordingly, the length of these specimens is assumed to be 48 inches. The interaction surfaces of 48 in. long-600S137-54 beam-column specimens are shown in Figure 2-14 (see Table 2-1 for critical loads). Clamped ends in local/distortional buckling (performed via CUFSM), simple-simple in the flexural buckling, and clamped-clamped in the torsional buckling (performed in CUTWP) are assumed. As shown in Figure 2-14, local-global interaction can effectively decrease the member strength in local buckling and a failure mode switch happens compared to short specimens, which are mostly distortional buckling dominant.

To study the length effect more precisely, and also to provide more data to investigate local-global and possibly distortional-global interaction, an intermediate length is also considered in the testing program. The intermediate specimens are assumed to be 24 in. long 600S137-54 lipped channels, which are to be tested similar to the short (12 in.) and long (48 in.) specimens.

2.3 Test specimens and Test Matrix

The selected cross-section is the 600S137-54 (50 ksi), the lengths of the specimens are considered to be 12 in., 24 in., and 48 in. thus covering local, distortional, local-global, and potentially local-distortional, and distortional-global interactions.

To define the test matrix, a normalized P-M-M space is defined as following (also see Figure 2-15),

$$x = \frac{M_1}{M_{y1}}$$ (2.2)

$$y = \frac{M_2}{M_{y2}}$$ (2.3)

$$z = \frac{P}{P_y}$$ (2.4)

where, M_1 and M_2 are two orthogonal (principal) axes of the cross section and the denominators are the corresponding yield moments (force) about those axes.
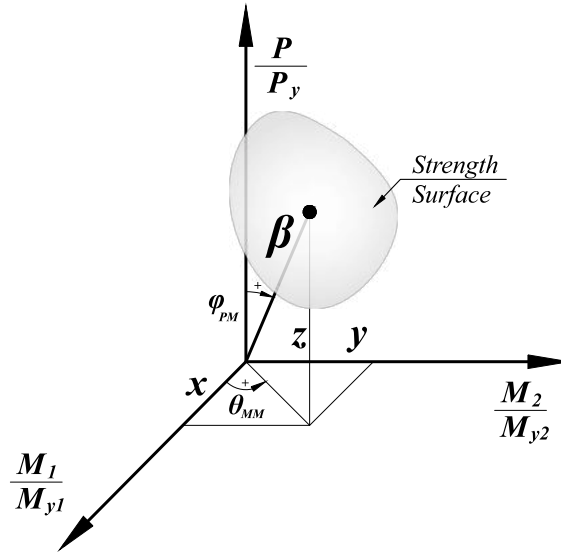
Figure 2-15: Normalized P-M_1-M_2 Space

In this report, axis 1 (axis x in Figure 2-15) is assumed to be the major axis of the lipped channel section ("axis z" in the physical tests detailed in Chapter 3); and axis 2 (axis y in Figure 2-15) is assumed to be the minor axis of the lipped channel section ("axis x" in the physical tests detailed in Chapter 3). A point in the P-M-M space may be defined by x,y,z or the angles θ_{MM} and ϕ_{PM} and radius β , which are defined as below:

$$\theta_{MM} = \tan^{-1}\left(y/x\right) \tag{2.5}$$

$$\phi_{PM} = \cos^{-1}(z/\beta) \tag{2.6}$$

$$\beta = \sqrt{x^2 + y^2 + z^2} \tag{2.7}$$

Based on the defined dimensionless parameters, 17 uniformly distributed (in the P-M-M space) tests are considered for each of the short and long specimens. Different loading conditions are considered for testing the specimens as shown in Figure 2-16. 9 specimens are considered for principal axes including minor axis when lip is in tension (θ_{MM}=270°), minor axis when lip is in compression (θ_{MM}=90°), and major axis (θ_{MM}=0°). Moreover, 8 other specimens are considered in four other non-principal axes that are for bi-axial bending and axial force (θ_{MM}=30°, 60°, 300°, 330°) as tabulated in Table 2-2 to Table 2-4.

For both intermediate (24 in. long) and long (48 in. long) specimens which global buckling matters, pure compression tests (ϕ_{PM}=0°) are also included in the text matrix.

The equivalent physical eccentricities are also tabulated in the test matrix tables and illustrated in Figure 2-18 to Figure 2-22, also see Figure 2-17 for axis definition and the naming notation.

no bending
(Pure Compression)

Minor axis bending
(lip in compression)

Major axis bending

Minor axis bending
(lip in tension)

Biaxial bending
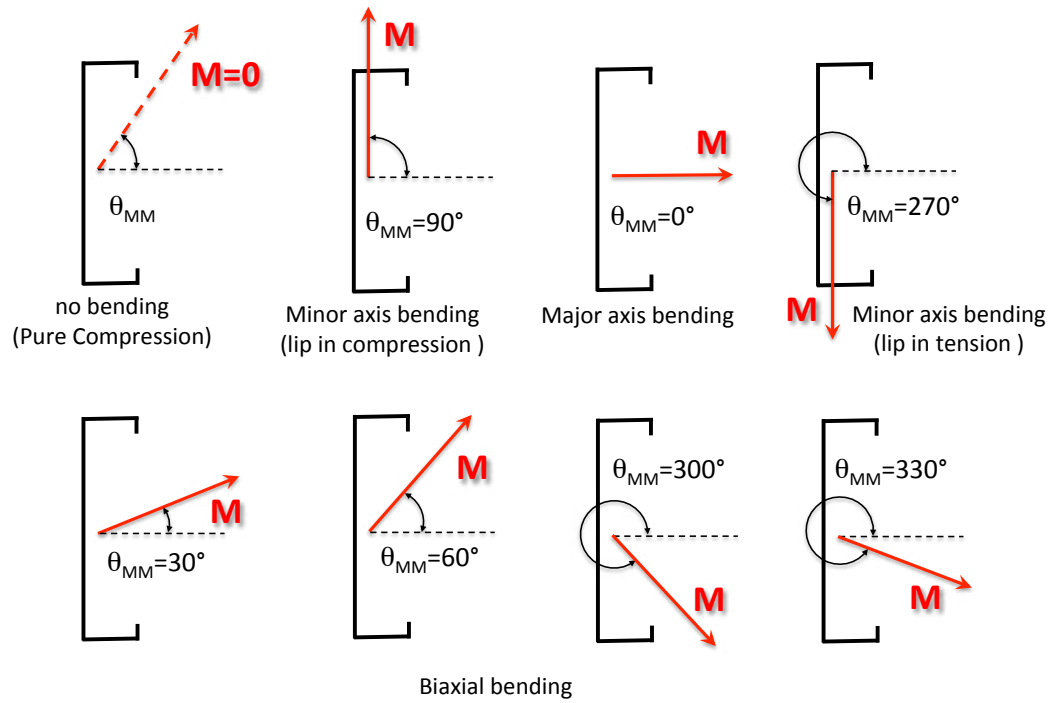
Figure 2-16: Loading conditions

a

b

Loading plate

e_x

e_z

X

Z

S600-12-ex(-1.5)-ez(-1.0)

Depth of the
Lipped channel Section
(600S137-54 herein)
(10^{-2}inches)

Length of
the specimen
(between the end-plates)
(inches)

Eccentricity in
x-direction
(inches)

Eccentricity in
z-direction
(inches)
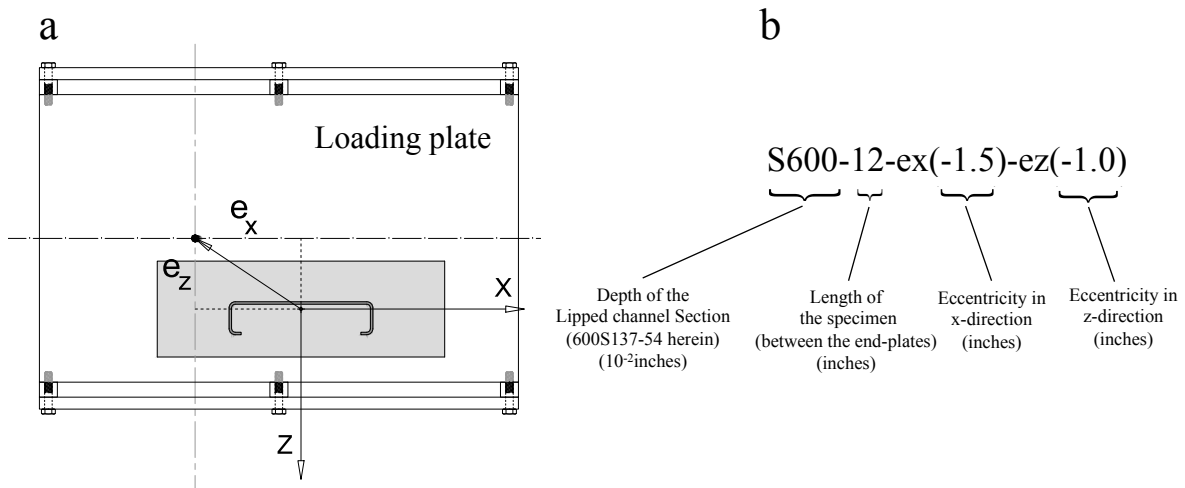
Figure 2-17: (a) Definition of x- and z-axis; (b) test specimen naming notation

Table 2-2: Test matrix of short specimens (600S137-54, L=12 inches)

			Target			
			Eccentricities		**Angles**	
			e_x	e_z	θ_{MM}	ϕ_{PM}
		Speccimen	(in.)	(in.)	(deg.)	(deg.)
1		S600-12-ex(0)-ez(-1.0)	0.00	-1.00	270	79
2		S600-12-ex(0)-ez(-0.5)	0.00	-0.50	270	69
3	Minor	S600-12-ex(0)-ez(-0.15)	0.00	-0.15	270	38
4		S600-12-ex(0)-ez(+0.15)	0.00	0.15	90	38
5		S600-12-ex(0)-ez(+0.35)	0.00	0.35	90	61
6		S600-12-ex(0)ez(+1.0)	0.00	1.00	90	79
7		S600-12-ex(-1.0)-ez(0)	-1.00	0.00	0	31
8	Major	S600-12-ex(-3.5)-ez(0)	-3.50	0.00	0	65
9		S600-12-ex(-7.5)-ez(0)	-7.50	0.00	0	78
10		S600-12-ex(-1.5)ez(+0.1)	-1.50	0.1019	30	47
11		S600-12-ex(-5.0)-ez(+0.34)	-5	0.3397	30	74
12		S600-12-ex(-0.8)-ez(+0.17)	-0.813	0.1656	60	45
13	Bi-Axial	S600-12-ex(-3.0)-ez(+0.6)	-3	0.6115	60	75
14		S600-12-ex(-0.8)-ez(-0.17)	-0.813	-0.1656	300	45
15		S600-12-ex(-3.0)-ez(-0.6)	-3	-0.6115	300	75
16		S600-12-ex(-1.5)ez(-0.1)	-1.5	-0.1019	330	47
17		S600-12-ex(-5.0)-ez(-0.34)	-5	-0.3397	330	74

Table 2-3: Test matrix of intermediate specimens (600S137-54, L=24 inches)

			Target			
			Eccentricities		**Angles**	
			e_x	e_z	θ_{MM}	ϕ_{PM}
		Speccimen	(in.)	(in.)	(deg.)	(deg.)
1		S600-24-ex(0)-ez(-1.25)	0.00	-1.25	270	81
2		S600-24-ex(0)-ez(-0.6)	0.00	-0.60	270	72
3	Minor	S600-24-ex(0)-ez(-0.15)	0.00	-0.15	270	38
4		S600-24-ex(0)-ez(0.15)	0.00	0.15	90	38
5		S600-24-ex(0)-ez(0.6)	0.00	0.60	90	72
6		S600-24-ex(0)-ez(1.25)	0.00	1.25	90	81
7		S600-24-ex(-0.85)-ez(0)	-0.85	0.00	0	27
8	Major	S600-24-ex(-3.0)-ez(0)	-3.00	0.00	0	61
9		S600-24-ex(-6.5)-ez(0)	-6.50	0.00	0	76
10		S600-24-ex(-1.25)-ez(0.09)	-1.25	0.09	30	41
11		S600-24-ex(-4.5)-ez(0.3)	-4.50	0.31	30	73
12		S600-24-ex(-0.75)-ez(0.15)	-0.75	0.15	60	43
13	Bi-Axial	S600-24-ex(-2.75)-ez(0.56)	-2.75	0.56	60	73
14		S600-24-ex(-0.75)-ez(-0.15)	-0.75	-0.15	300	43
15		S600-24-ex(-2.75)-ez(-0.56)	-2.75	-0.56	300	73
16		S600-24-ex(-1.25)-ez(-0.08)	-1.25	-0.08	330	41
17		S600-24-ex(-4.5)-ez(-0.3)	-4.50	-0.31	330	73
18	Column	S600-24-ex(0.0)-ez(0.0)	0.0	0.00	**0**	**0**
19	Major	S600-24-ex(0.0)-ez(0.0)	-6.50	0.00	**0**	**76**
20	Column	S600-24-ex(0.0)-ez(0.0)	0.0	0.00	**0**	**0**

Table 2-4: Test matrix of long specimens (600S137-54, L=48 inches)

		Speccimen	Target			
			Eccentricities		Angles	
			e_x	e_z	θ_{MM}	ϕ_{PM}
			(in.)	(in.)	(deg.)	(deg.)
1		S600-48-ex(0)-ez(-1.5)	0.00	-1.50	270	83
2		S600-48-ex(0)-ez(-0.65)	0.00	-0.65	270	74
3	Minor	S600-48-ex(0)-ez(-0.2)	0.00	-0.20	270	46
4		S600-48-ex(0)-ez(0.2)	0.00	0.30	90	57
5		S600-48-ex(0)-ez(0.65)	0.00	0.65	90	74
6		S600-48-ex(0)-ez(1.5)	0.00	1.50	90	83
7		S600-48-ex(-0.6)-ez(0)	-0.60	0.00	0	20
8	Major	S600-48-ex(-2.0)-ez(0)	-2.00	0.00	0	51
9		S600-48-ex(-5.5)-ez(0)	-5.50	0.00	0	73
10		S600-48-ex(-1.0)-ez(0.07)	-1.00	0.07	30	35
11		S600-48-ex(-4.0)-ez(0.27)	-4.00	0.27	30	71
12		S600-48-ex(-0.7)-ez(0.14)	-0.7	0.14	60	41
13	Bi-Axial	S600-48-ex(-2.5)-ez(0.5)	-2.5	0.51	60	72
14		S600-48-ex(-0.7)-ez(-0.14)	-0.7	-0.14	300	41
15		S600-48-ex(-2.5)-ez(-0.5)	-2.5	-0.51	300	72
16		S600-48-ex(-1.0)-ez(-0.07)	-1.0	-0.07	330	35
17		S600-48-ex(-4.0)-ez(-0.27)	-4.0	-0.27	330	71
18	Column	S600-48-ex(0.0)-ez(0.0)	0.0	0.00	0	0
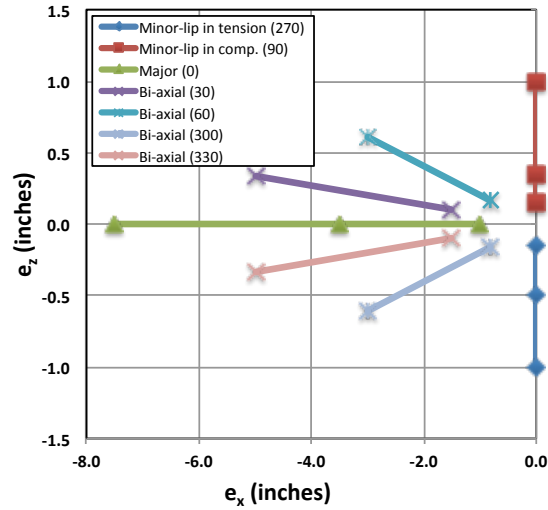
Figure 2-18: Axial load eccentricities of short specimens (600S137-54, L=12 inches)
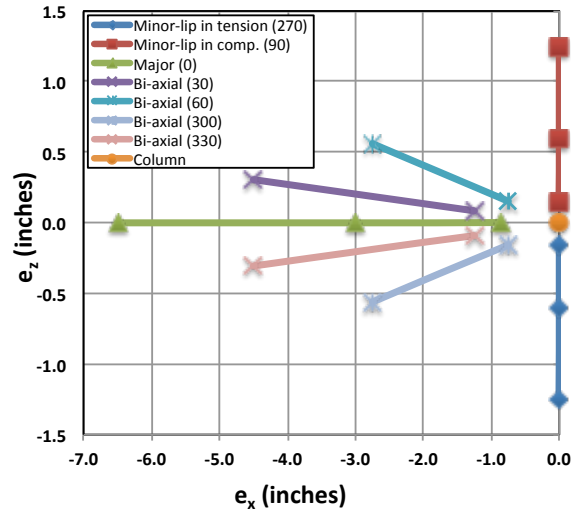
Figure 2-19: Axial load eccentricities of intermediate specimens (600S137-54, L=24 inches)
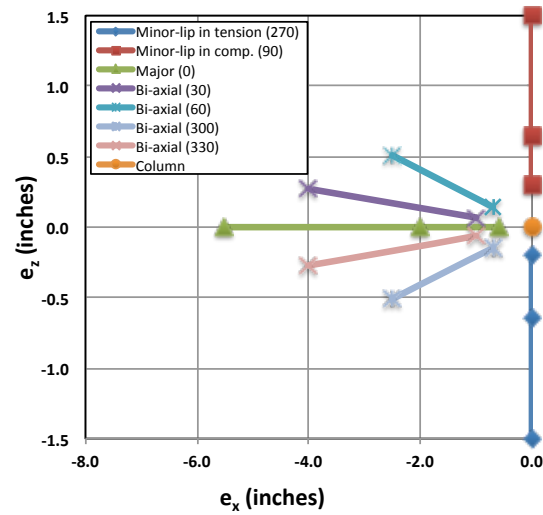
Figure 2-20: Axial load eccentricities of short specimens (600S137-54, L=48 inches)
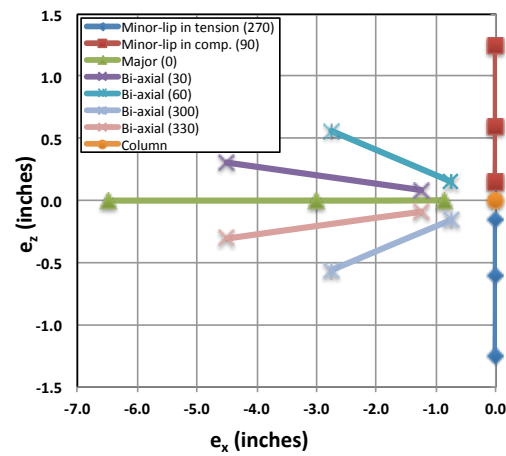
Figure 2-21: Axial load eccentricities of intermediate specimens (600S137-54, L=24 inches)
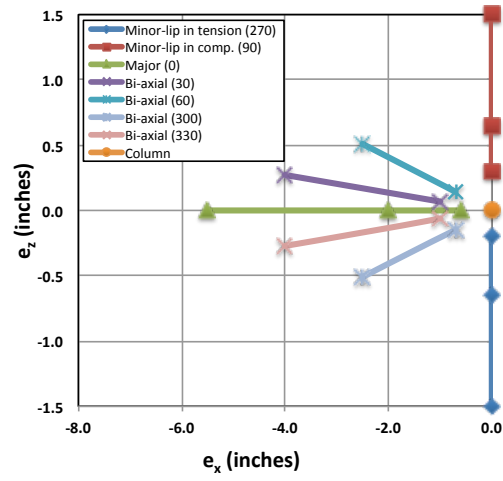
Figure 2-22: Axial load eccentricities of short specimens (600S137-54, L=48 inches)

Chapter 3 - Experiments on lipped channel cold-formed steel beam-columns

In this chapter, all details of the experimental program on lipped channel cold-formed steel beam-columns are discussed. Design and preparation of the test setup and loading rig, instrumentation and data acquisition system, preparing test specimens, installation and testing procedures, and material testing are all provided. Moreover, test results including member load-displacement response and local responses such as end rotations and section deformations are presented and the results are compared to the predicted values via current AISI Specifications.

3.1 Testing Program

3.1.1 Test setup and loading rig

The test setup in every experimental program is designed to provide all means required to simulate the desired behavior, perform the physical test, and record the instrumented results in a safe way.
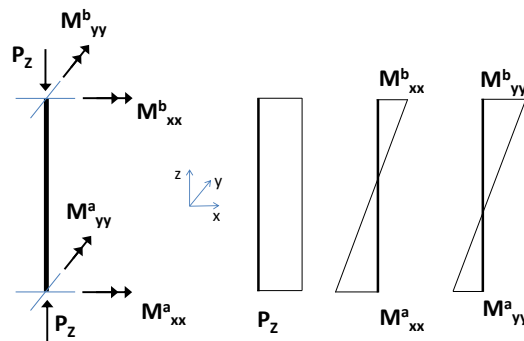
Figure 3-1: Beam-column: Axial force and bi-axial bending

In a general definition, beam-columns are members under combined actions of axial force and bi-axial bending moments as shown in Figure 3-1.

Theoretically, every loading conditions that results in a combined axial force and bending moment in the beam-column member can be used to build up a test setup for beam-column testing. End moments, transverse distributed and/or point loading, shear force, and eccentric loading are just a few examples of loading that can provide combined axial force and bending moments in the members. Figure 3-2 shows a general example of beam-columns with/without joint translation (sideway) under end moments and transverse loading.
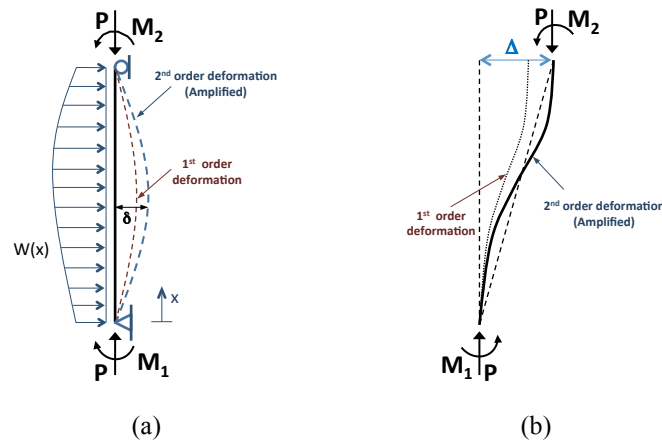
Figure 3-2: Beam-column: (a) Beam-Columns restrained against joint
translation; (b) Beam-Columns with joint translation (sideway)

Presence of both axial force and moments on a member (beam-column) raises a couple of new issues in the analysis and design of these members. Axial force affects the internal moments and deformation of the member, i.e. the so-called 2nd order effects, as shown in Figure 3-2. Moreover, combined actions and resulting applied stress distributions on the cross-section affects the elastic critical loads (local, distortional, global) as well as the yield and plastic surfaces.

Current codes are dealing with this multi-parameter problem by scaling down the problem to a combination of more simple problems. The AISI-S100-12 interaction equation for combined compressive axial load and bending (Eq. 3.1) asserts that the combined capacity of the member may be assumed to be a simple linear combination of the distinct actions in the principal

axes of the member (i.e. major and minor bending) and axial force. The method ignores any nonlinear interaction between the aforementioned parameters and is expressed as follows:

$$\frac{\overline{P}}{\phi_c P_n} + \frac{C_{mx}\overline{M}_x}{\phi_b M_{nx}\alpha_x} + \frac{C_{my}\overline{M}_y}{\phi_b M_{ny}\alpha_y} \leq 1.0$$

(3.1)

Second-order effects, and the effect of end-restraints and the moment distribution are considered by $\alpha_{x,y}$ and $C_{mx,y}$ coefficients, respectively. Where $\alpha_{x,y}$ provides an approximate solution for increasing first-order moments, and $C_{mx,y}$ approximately accounts for any moment distribution and end-restraints other than the case shown in Figure 3-3, which is combined compressive axial load and uniform moment (single curvature).
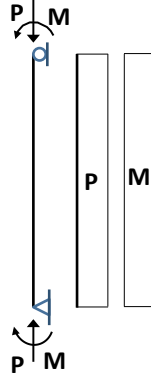
Figure 3-3:Combined compressive axial load and uniform moment (single curvature)

Therefore, combined compressive axial load and constant moment distribution can be considered as a baseline for the beam-column element. While, both axial load and bending moment are constant all along the length, the stress distribution on the cross-section would also be constant. Uniform stress distribution on the cross-section element such as web and flanges makes the problem more consistent to theoretical solutions of plate stability problems and basic assumptions of the finite strip method (FSM). FSM is often utilized to investigate the elastic stability issues of the cold-formed steel members, including local and distortional buckling.

38
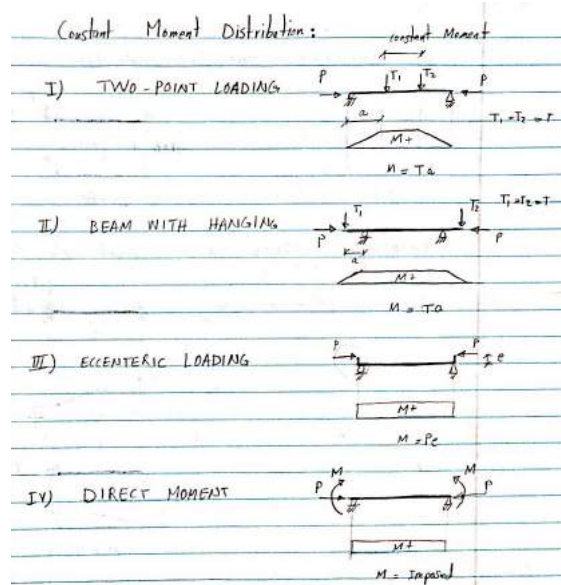
Figure 3-4:Basic schematic of the different ways for providing uniform moment in a beam-column (repeated figure)

Figure 3-4 shows basic schematics of the different ways for providing constant moment distribution moment in a beam-column element. The first one, two equal transverse point loads, is a very common way, which was also tried in Year 1 of this project. However, applying eccentric loading is simpler and found to be the most practical approach. Following this idea, the desired test rig should have the following characteristics:

- o applying "Axial force";
- o applying "Bi-axial bending moment";
- o providing "Uniform bending moment";
- o providing warping restraint for the ends;
- o pin-pin boundary condition;
- o exploring all local, distortional and global instabilities; and
- o adjustability and repeatability.

To fulfill the required characteristics, a new test rig is designed for performing beam-column test within an available uniaxial MTS loading frame. The test setup and the test rig are

39

shown in Figure 3-5 for short specimens (12 in.). However, no considerable change other than the length of the specimen is considered for the intermediate (24 in.) and long (48 in.) specimens.

As shown in Figure 3-5, the loading rig consists of two top and bottom MTS standard swivel joints for applying compressive force and providing pin-pin end-restraints for the beam-column specimen, two loading plates to accommodate eccentricity in both axes, and required clamps (see Appendix B for more details on loading plates). Welded plates at the ends of the specimens provide warping fixed restraints and enable the specimen to be adjusted in the rig and clamped to the loading plates via sliders. The clamps provide sufficient compressive bearing stress between the end plates and the loading plate to prevent uplift and detachment. The clamping mechanism enables the test rig to be used several times for all beam-column specimens in the project.

To adjust the top and bottom loading plate, hanging bolts and sitting bolts, which are connected to the external Frazier rack frame, are considered. These bolts are removed before testing so as not to be involved in the load path of the test rig. As shown in Figure 3-6, the Frazier rack frame (frame with blue columns and orange beams) is a supporting frame placed around the MTS loading frame to provide support for the loading plates and instrumentations.

Test setup configuration including the test rig and the MTS loading machine during a test on a short specimen is shown in Figure 3-6. The test setup consists of two loading plates connected to swivel joints at top and bottom, required clamps for connecting the test specimen, a uniaxial MTS loading machine (100 kips), a supporting frame around the loading machine, instrumentation, and a data acquisition system.

Figure 3-5: Test setup configuration of beam-column testing program (a short specimen is illustrated)
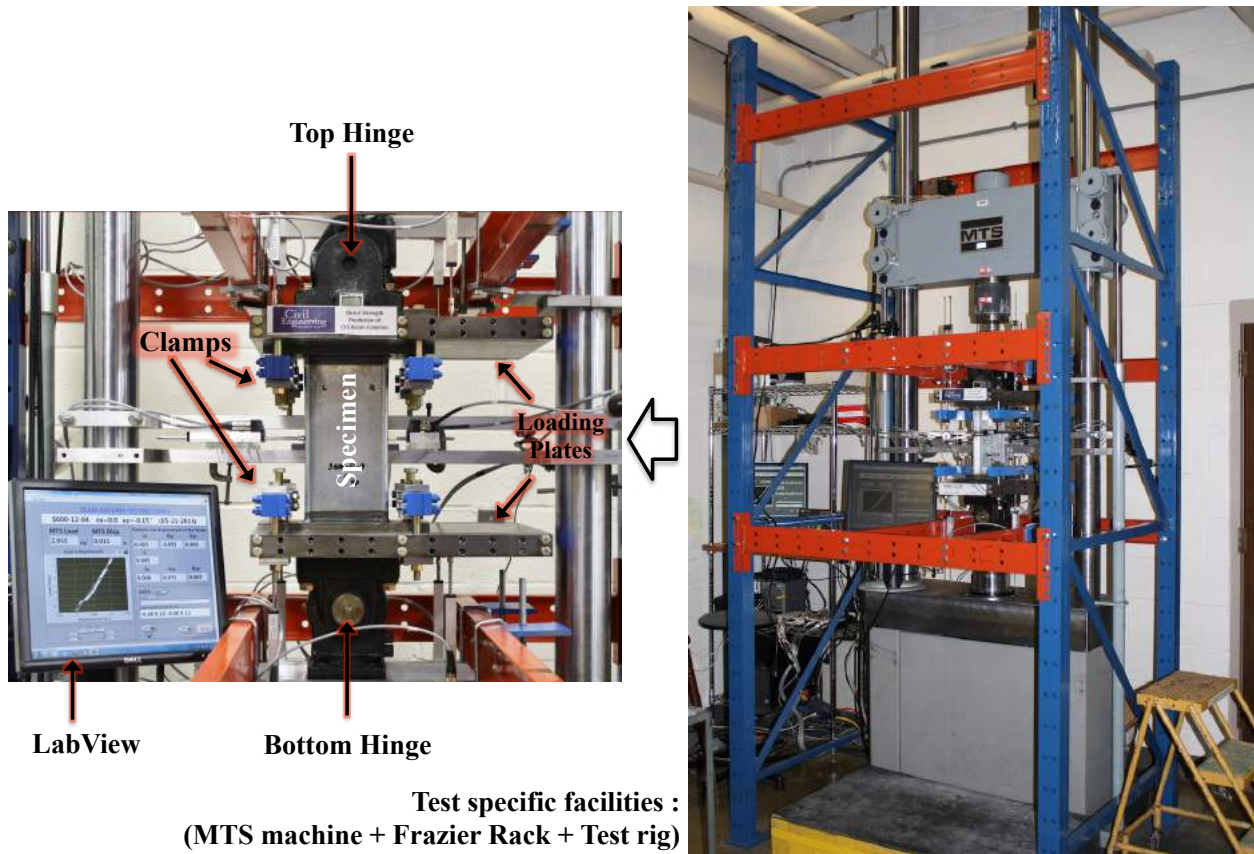
Figure 3-6: Annotated test setup of the beam-column experimental program

3.1.2 Instrumentation

The beam-column test setup is equipped with a series of position transducers (PTs) to record the displacements and rotations of the end plates and the specimen throughout the experiments. All position transducers are routed to a NI-6024 PCI card for reading and monitoring of the results via LabView.

An MTS407 controller drives the actuator displacements and records the applied displacement via an internal LVDT installed in the actuator; and the force via a load cell connected to the crosshead. Both force and displacement transducers are routed to the PCI card via the MTS407 and monitored in LabView.
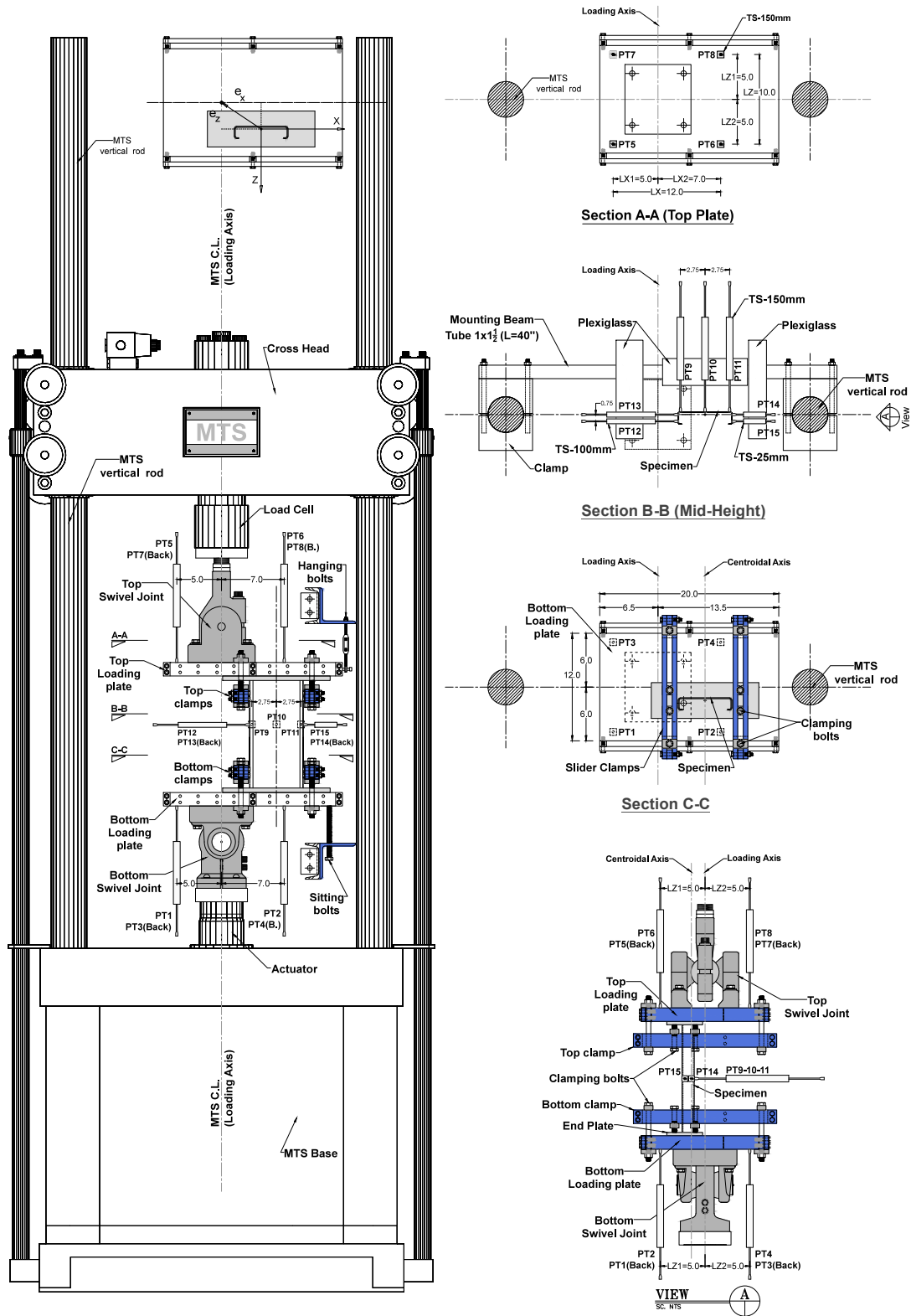
Figure 3-7: Instrumentation for beam-column experiments (a short specimen is illustrated; PT: Position Transducer)

All mounted instrumentations are illustrated in Figure 3-7. As shown in the figure, four position transducers (PT1 to PT4) are utilized to record bottom plate rotations and displacements (see Figure 3-8(a)) and four other PTs (PT5 to PT8) are utilized to capture the rotations and displacements of the bottom plate (see Figure 3-8(b)).

| (a) | (b) |
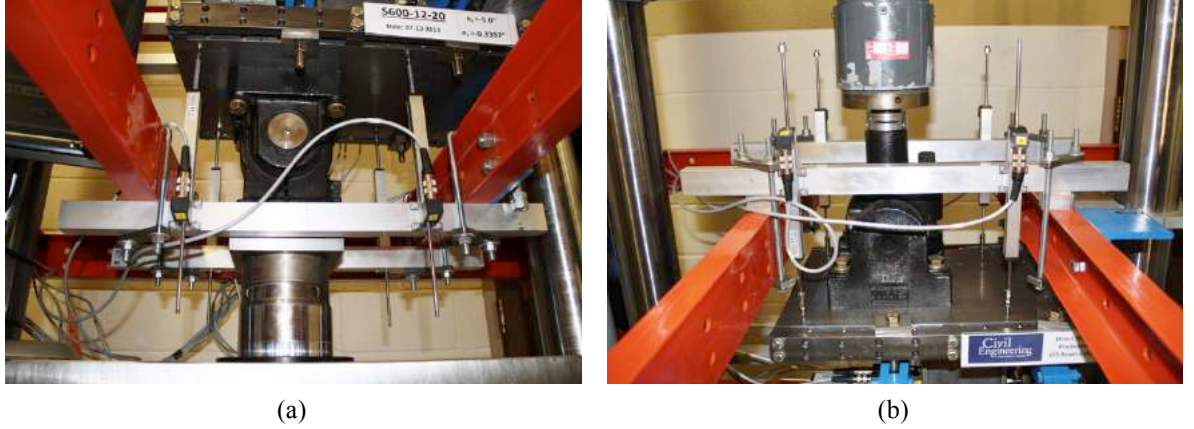
Figure 3-8: (a) Position Transducers (PT1-4) of the bottom plate; (a) Position Transducers (PT5-8) of the top plate;

The plate displacement and rotations can be calculated as follows,

$$\delta_B = \frac{d_1 + d_3}{2} \frac{L_{X2}}{L_X} + \frac{d_2 + d_4}{2} \frac{L_{X1}}{L_X} \tag{3.2}$$

$$\delta_T = \frac{d_5 + d_7}{2} \frac{L_{X2}}{L_X} + \frac{d_6 + d_8}{2} \frac{L_{X1}}{L_X} \tag{3.3}$$

$$\delta = |\delta_B| - |\delta_T| \tag{3.4}$$

$$\theta_{XB} = \frac{1}{L_Z} \left[\frac{d_1 + d_2}{2} - \frac{d_3 + d_4}{2} \right] \tag{3.5}$$

$$\theta_{ZB} = \frac{1}{L_X} \left[\frac{d_1 + d_3}{2} - \frac{d_2 + d_4}{2} \right] \tag{3.6}$$

$$\theta_{XT} = \frac{1}{L_Z} \left[\frac{d_7 + d_8}{2} - \frac{d_5 + d_6}{2} \right] \tag{3.7}$$

44

$$\theta_{XT} = \frac{1}{L_X}\left[\frac{d_6 + d_8}{2} - \frac{d_5 + d_7}{2}\right]$$

where, d_i is the displacement at the ith PT, δ_T and δ_B are the top and the bottom plate vertical displacement, and δ is the specimen shortening. L_{X1} is the distance to the left PTs from the centerline, L_{X2} is the distance to the Right PTs, $L_X = L_{X1} + L_{X2}$, and L_Z is the distance between the front and back PTs (in z direction). θ_{XT}, θ_{ZT}, θ_{XB}, and θ_{ZB} are top and bottom plate rotations around x and z axes, as defined in Figure 3-9.

(a) Front view   (b) Side-view
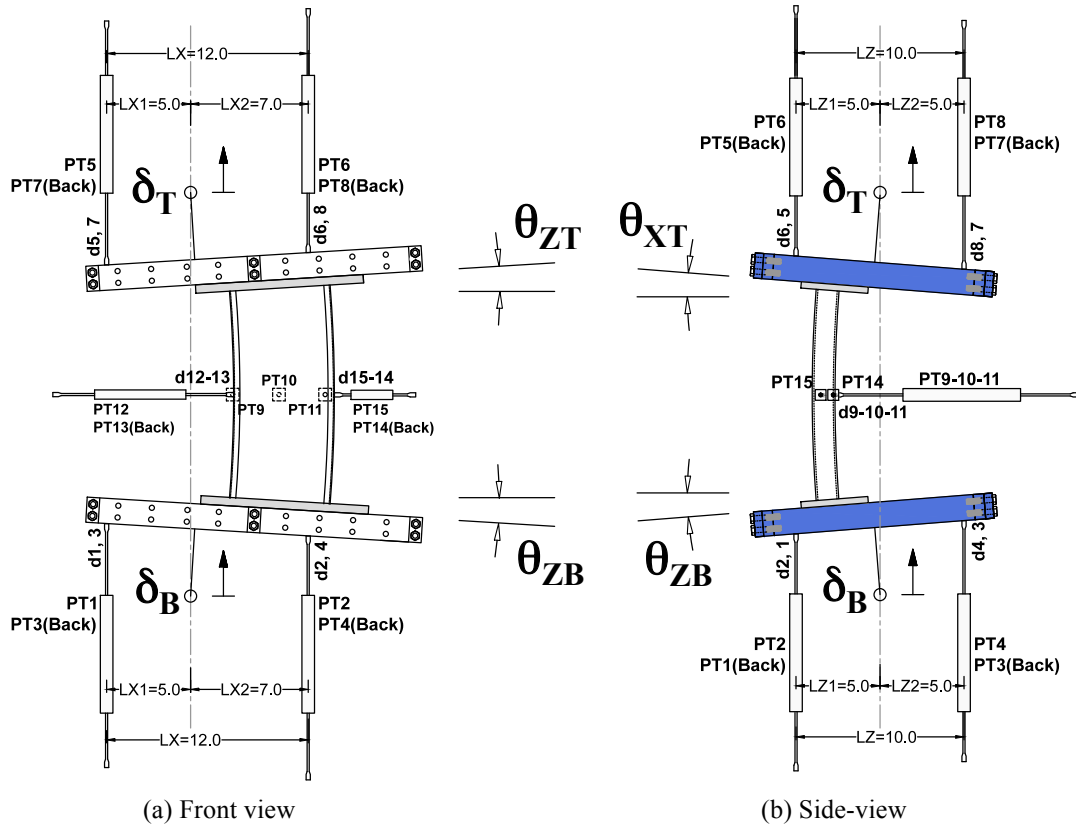
Figure 3-9: Top and bottom plate movements and rotations

45

Other than the PTs utilized on the top and the bottom loading plates, 7 other PTs are mounted to record the movements and deformations of the specimen at the mid-height as shown in Figure 3-10. These PTs measure the cross-section movements at 7 points including both flanges and the web. The results can be used to calculate several parameters such as mid-height displacements in x and z axes, rigid-body rotation of the specimen, flange local rotations in distortional buckling, and web local buckling.
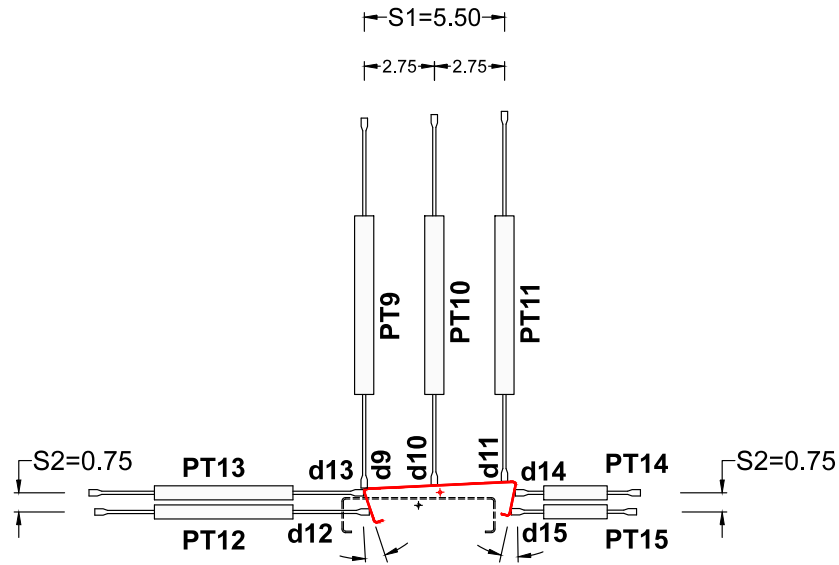
Figure 3-10: Deformations at the mid-height of the specimen

(a)   (b)   (c)
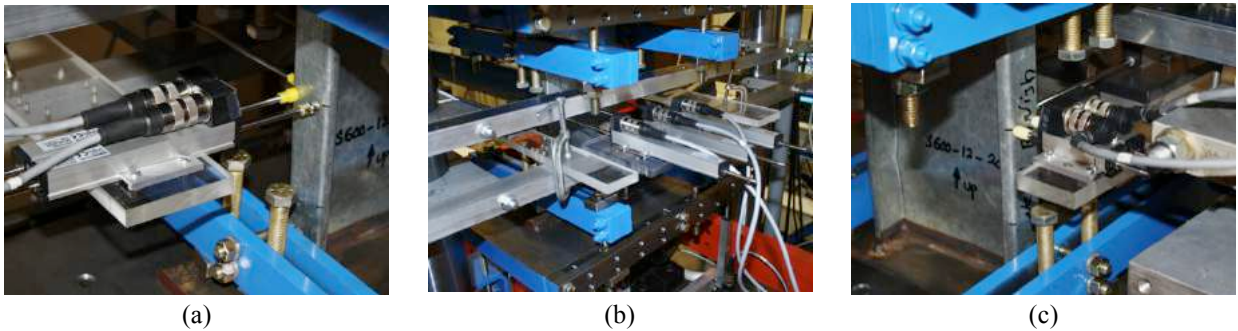
Figure 3-11: (a) Left flange's PTs (PT12-13); (b) Web's PTs (PT9-11); (c) Right flange's PTs (PT14-15);

The configuration of the PTs installed on the specimen at the mid-height is shown in Figure 3-11. To provide enough flexibility in mounting, PTs are connected on the Plexiglas sheets and clamped to the mounting beam; and then routed to the data acquisition systems.
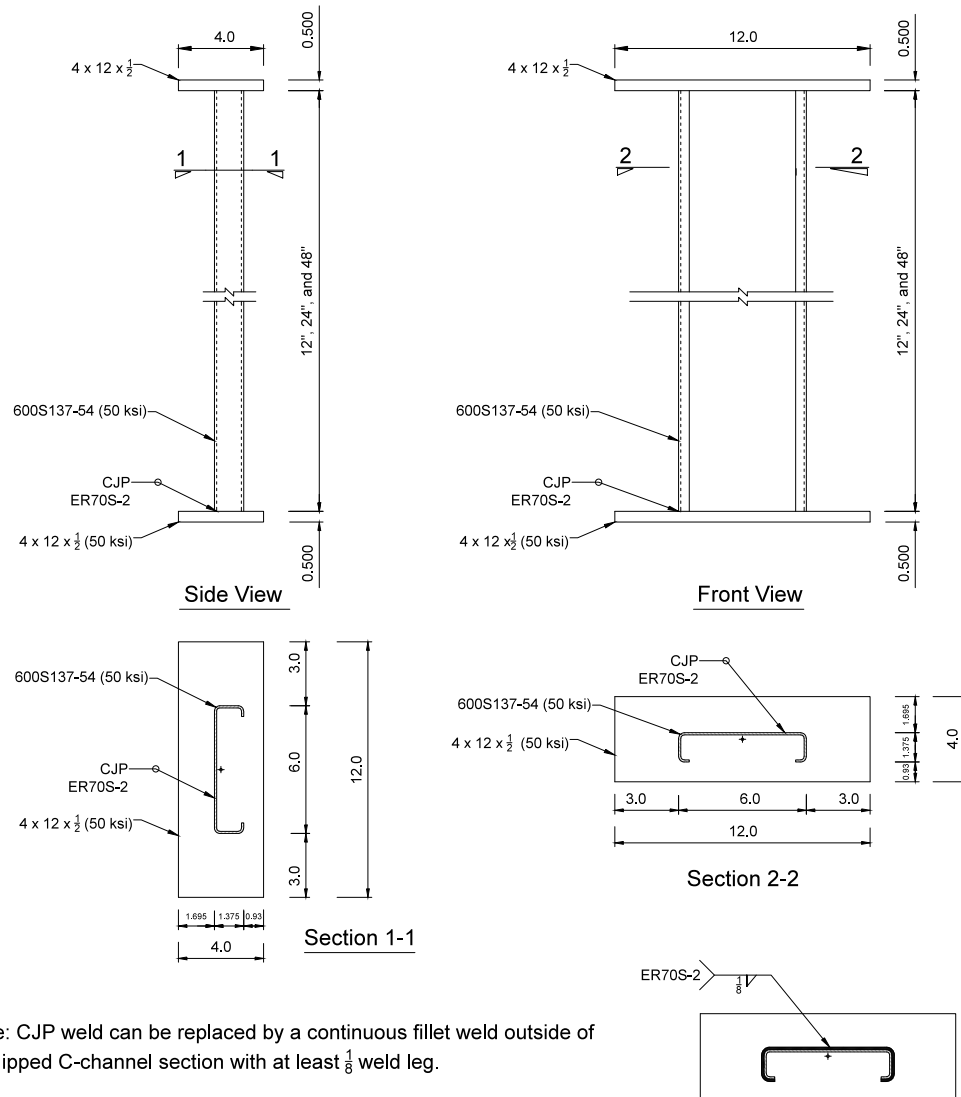
Figure 3-12: Test specimens: 600S137-54 (L=12, 24, and 48 inches)

3.1.1 Specimen preparation

All details of the beam-column test specimens are shown in Figure 3-12. Test specimens consist of a lipped channel section welded to end plates. To prepare the specimens, a series of

preliminary activities are needed before welding such as material testing, dimension measurements, and stripping the zinc-coating off the ends.

All the specimens were ordered in accordance to the required length. Accordingly, the end preparation including cutting and grinding were not necessary. However, short specimens (L=12 in.) were grinded at the ends to ensure flatness. As, the specimens are welded to end plates, the effect of the end conditions on the results is assumed to be relatively small.

| (a) 600S137-54 (L=12 inches) | (b) 600S137-54 (L=24 inches) | (c) 600S137-54 (L=48 inches) |
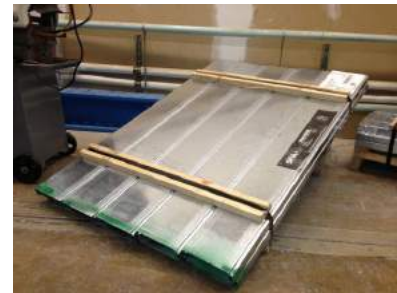
Figure 3-13: Lipped channel specimens

3.1.1.1 Material properties

To determine the material properties of the test specimens, 21 coupon samples taken from both un-rolled plates and lipped channel specimens were tested. Un-rolled plates and the studs were requested to be from the same coil.

The tension test specimens were selected from both flanges and web of all types of the beam-column specimens. The sampling detail for material testing is tabulated in Table 3-1. The dimensions of the tension test specimens were determined in accordance with ASTM E8-11 as shown in Figure 3-14 (See Appendix C for more details).

To study the effect of zinc coating on the tensile strength and behavior of galvanized steel, three coupons were tested without zinc coating. The rest of the coupons were tested with coating, but the coating at the ends of the coupons was stripped to determine the zinc coating thickness (see Figure 3-15).

Table 3-1: Tension test specimens

Specimen (Sample)	Designation	Coupons	Coating
Un-rolled Plate-1	PL1-	3	Coated
Un-rolled Plate-2	PL1-	3	Un-Coated
Un-rolled Plate-1	PL2-	3	coated
600-12-1	600-12-1-	2 (1 Web+ 1 Flange)	Coated
600-12-2	600-12-2-	2 (1 Web+ 1 Flange)	Coated
600-24-1	600-24-1-	2 (1 Web+ 1 Flange)	Coated
600-24-2	600-24-2-	2 (1 Web+ 1 Flange)	Coated
600-48-1	600-48-1-	2 (1 Web+ 1 Flange)	Coated
600-48-2	600-48-1-	2 (1 Web+ 1 Flange)	Coated
Total		**21**	

600 - **24** - **1** - **F** - **(L)**

Depth of section (Typically stands for 600S137-54-50 ksi) | Lenght of specimen (12",24",48") | Randomlly selected specimen (1st=1, 2nd=2) | Flange (F) or Web(W) | Left flange (L) or Right flange (R)
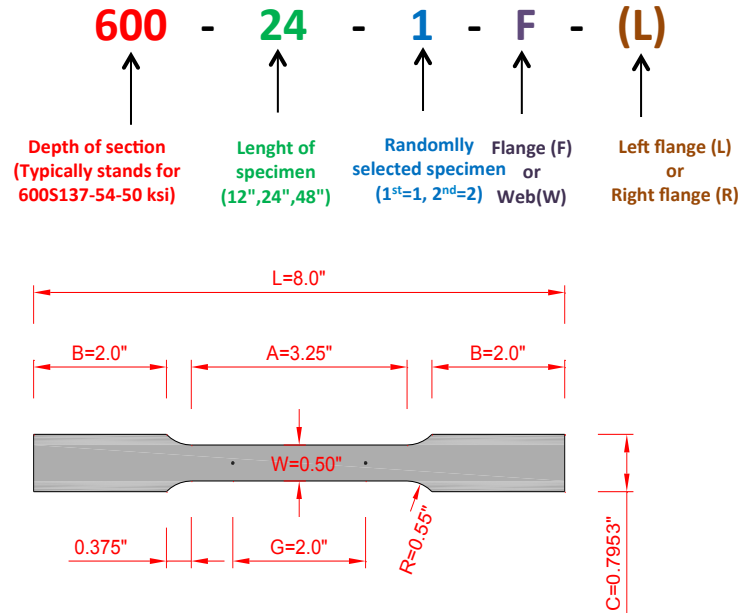
Figure 3-14: Coupon dimensions
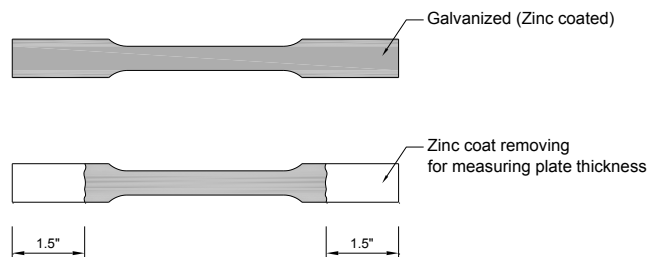
Figure 3-15: Coupon preparation: removing the zinc coating at the ends

The preparation process of the tension test specimens is illustrated in Figure 3-16. As mentioned, the sampling was from both un-rolled plates and the lipped channel studs. The rough-cut samples were taken from the central parts of the plates, the channel web and the flange. CNC cutting was utilized for machining out the desired shape of the test specimens per Figure 3-14. The zinc coating of the specimens was stripped by putting the specimen in Hydrochloride acid (HCL-1N) for about 30 min as shown in see Figure 3-16(e).

| (a) Sampling unrolled sheet | (b) Sampling specimens | (c) Rough-cut coupons |
| (d) CNC cut coupons | (e) Un-coating by acid | (f) Un-coated and tested specimens |
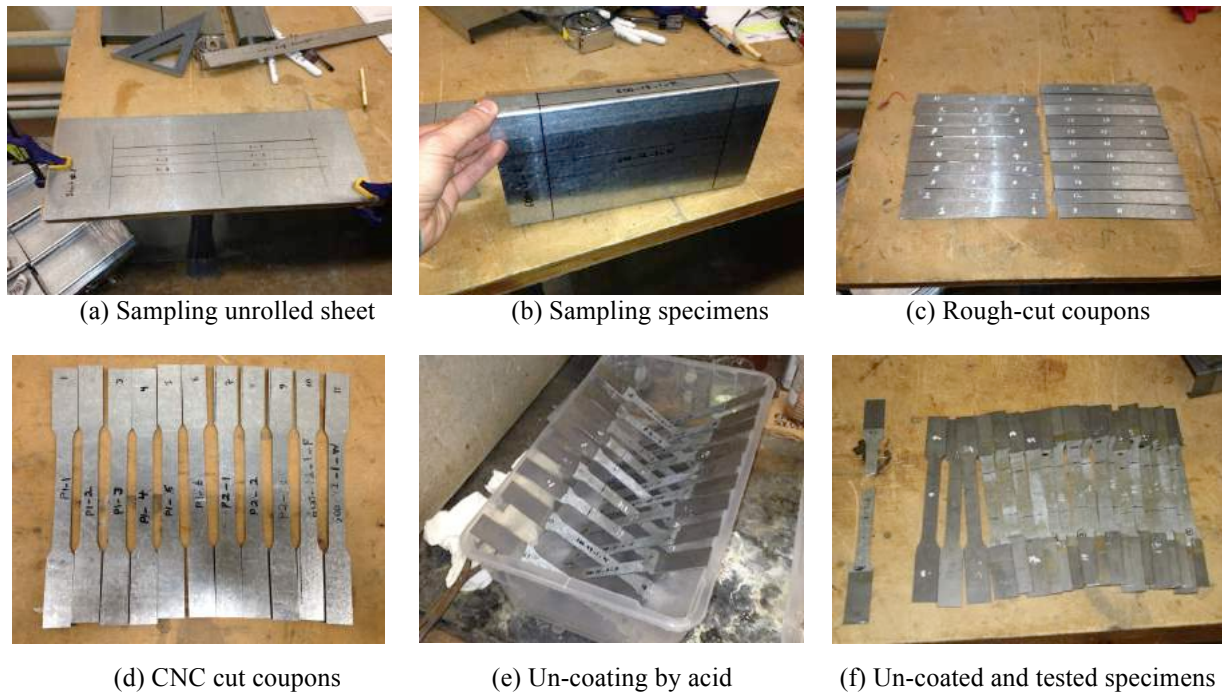
Figure 3-16: Coupon preparation for material testing

Before testing, the width and the thickness of the tension test specimens within the gauge length were measured. The thickness of the specimens at the ends was also measured to determine the thickness of the zinc-coating. The measured dimensions are used to calculated the plate cross-sectional area that is necessary for determine the engineering stress-strain curves of the specimens throughout the tension test. Table 3-2 summarizes the measured dimensions of the test coupons.

Table 3-2: Dimension measurement of the test coupons (plate thickness, zinc-coating thickness, and width)

No.	Specimen	Average coated thickness (in.X10⁻³)		Average uncoated thickness (in.X10⁻³)		Average thickness of zinc coating (in.X10⁻³)		Width within the gauge length (in.)			
		t	C.O.V	$t_{uc\text{-}ave.}$	C.O.V	$t_{z\text{-}ave}$	C.O.V	$W_{ave.}$	C.O.V.	W_{min}	$W_{min}/W_{ave.}$
1	PL1-1	55.93	0.23%	55.57	0.17%	0.37	38%	0.4994	0.08%	0.4990	0.999
2	PL1-2	56.17	0.14%	55.73	0.21%	0.45	19%	0.4996	0.04%	0.4995	1.000
3	PL1-3	56.29	0.13%	55.72	0.22%	0.59	26%	0.4999	0.04%	0.4995	0.999
4	PL1-4	56.03	0.32%	55.44	0.15%	0.62	27%	0.4999	0.04%	0.4995	0.999
5	PL1-5	56.16	0.15%	55.45	0.19%	0.71	15%	0.4997	0.09%	0.4990	0.999
6	PL1-6	56.33	0.16%	55.66	0.18%	0.68	16%	0.4998	0.05%	0.4995	0.999
7	PL2-1	56.19	0.27%	55.55	0.19%	0.62	37%	0.5001	0.18%	0.4990	0.998
8	PL2-2	56.05	0.18%	55.49	0.13%	0.53	20%	0.4992	0.05%	0.4990	1.000
9	PL2-3	56.07	0.21%	55.44	0.19%	0.60	33%	0.4995	0.07%	0.4990	0.999
10	600-12-1-F (L)	56.45	0.13%	55.60	0.17%	0.85	14%	0.4990	0.00%	0.4990	1.000
11	600-12-1-W	55.81	0.19%	55.19	0.20%	0.62	32%	0.4988	0.05%	0.4985	0.999
12	600-12-2-F (R)	55.98	0.22%	54.95	0.18%	1.02	17%	0.4998	0.11%	0.4990	0.998
13	600-12-2-W	56.30	0.19%	55.73	0.15%	0.61	18%	0.4996	0.11%	0.4990	0.999
14	600-24-1-F (R)	55.93	0.31%	55.03	0.21%	0.84	25%	0.4992	0.05%	0.4990	1.000
15	600-24-1-W	56.27	0.32%	55.67	0.19%	0.62	35%	0.4988	0.09%	0.4980	0.998
16	600-24-2-F (L)	56.56	0.34%	55.91	0.27%	0.68	23%	0.4989	0.04%	0.4985	0.999
17	600-24-2-W	55.95	0.23%	55.39	0.22%	0.59	33%	0.4996	0.13%	0.4990	0.999
18	600-48-1-F (R)	55.51	0.38%	54.68	0.24%	0.88	31%	0.4993	0.11%	0.4985	0.998
19	600-48-1-W	55.78	0.26%	55.36	0.13%	0.43	25%	0.4997	0.13%	0.4990	0.999
20	600-48-2-F (L)	56.55	0.31%	55.84	0.19%	0.68	33%	0.4991	0.04%	0.4990	1.000
21	600-48-2-W	56.00	0.39%	55.42	0.24%	0.62	35%	0.4986	0.08%	0.4980	0.999
Total		56.11	0.46%	55.47	0.55%	0.65	24%	0.4994	0.08%	0.4989	0.999

The tension tests were performed in a 10-kips ATS loading frame. Specimens were installed in the loading grips aligned with the actuator and loaded at a rate of 0.05 in./min for around 80% of the yielding force. Then, the loading rate was gradually decreased to 0.005 in./min within the yielding plateau and a part of the strain-hardening region. The loading rate was again gradually increased to 0.05 in/min and kept at this value until failure. Figure 3-17 shows the test setup and the testing equipment. Notably, an extensometer was installed on the coupons within the gauge length to precisely measure the engineering strains.

| (a) Test setup | (b) Extensometer on the gauge length | (c) Ruptured specimen |
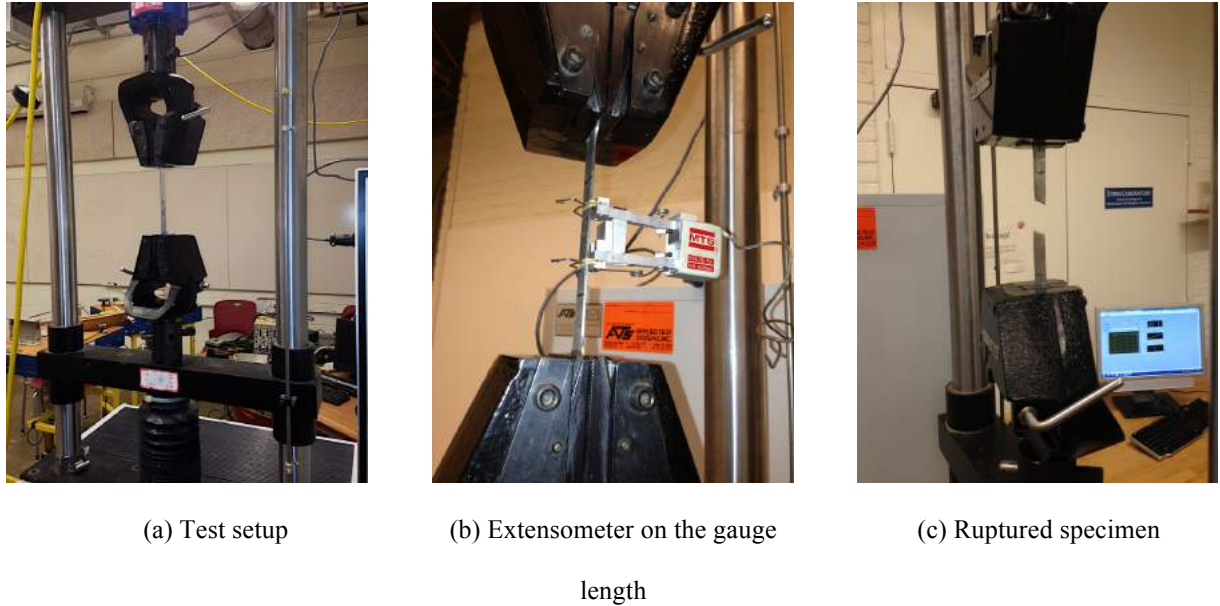
Figure 3-17: Tension test

The test results of all tension test specimens are reported in Appendix C. However, the average test results for each group of similar coupons are also shown in Figure 3-18. The yielding stress calculated by two different methods (0.2% offset and autographic method) and ultimate strength of the material are also reposted on each curve. Comparison of rolled vs. un-rolled specimens and also coated vs. un-coated specimens reveals that both rolling and zinc-coating effects on yield and ultimate strengths are not remarkable. Accordingly, an averaged engineering stress-strain curve is provided in Figure 3-19 along with the averaged yield and ultimate strength of the material. To enable using the material testing results in the numerical analyses, a 23-point material model is adopted and converted to true-stress strain results. Moreover, all results of tension testing are summarized in Table 3-3.

The table includes the results of elongation at rupture, upper yield point, yield strength (0.2% offset), yield strength (ave. 0.4% to 0.8% ELU), yield point elongation, strain at tensile strength, rupture point location and area reduction at rupture.

Un−rolled Coated plate−1 (3 Coupons)

mean+STDV ↓

↑ mean−STDV

F_y (0.2% offset)=52.4 ksi

F_y (Autographic method)=52.3 ksi

F_u=66.5 ksi

Axial Tensile Stress (ksi)

Engineering Strain,(in./in.)

Un−rolled Uncoated plate−1 (3 Coupons)

mean+STDV ↓

↑ mean−STDV

F_y (0.2% offset)=52.4 ksi

F_y (Autographic method)=52.3 ksi

F_u=66.5 ksi

Axial Tensile Stress (ksi)

Engineering Strain,(in./in.)

Un−rolled un−coated plate−2 (3 Coupons)

mean+STDV ↓

↑ mean−STDV

F_y (0.2% offset)=52.6 ksi

F_y (Autographic method)=52.9 ksi

F_u=66.8 ksi

Axial Tensile Stress (ksi)

Engineering Strain,(in./in.)

600S137−53 specimens (Length=12") (4 Coupons)

mean+STDV ↓

↑ mean−STDV

F_y (0.2% offset)=52.8 ksi

F_y (Autographic method)=52.9 ksi

F_u=66.6 ksi

Axial Tensile Stress (ksi)

Engineering Strain,(in./in.)

600S137−53 specimens (Length=24") (4 Coupons)

mean+STDV ↓

↑ mean−STDV

F_y (0.2% offset)=53.1 ksi

F_y (Autographic method)=53.2 ksi

F_u=66 ksi

Axial Tensile Stress (ksi)

Engineering Strain,(in./in.)

600S137−53 specimens (Length=48") (4 Coupons)

mean+STDV ↓

↑ mean−STDV

F_y (0.2% offset)=53.5 ksi

F_y (Autographic method)=53.5 ksi

F_u=67.3 ksi

Axial Tensile Stress (ksi)

Engineering Strain,(in./in.)

Figure 3-18: Tensile test results: Tensile Stress vs. Engineering Strain
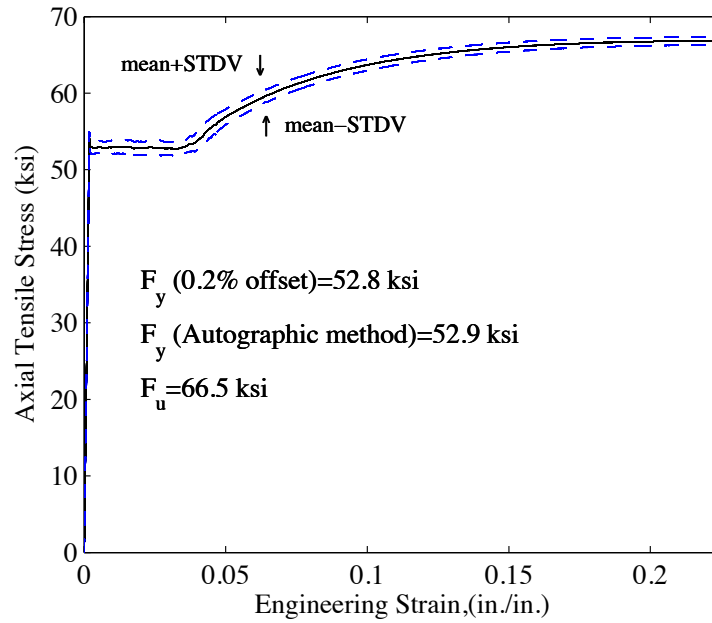
Figure 3-19: Averaged results: Tensile Stress vs. Engineering Strain
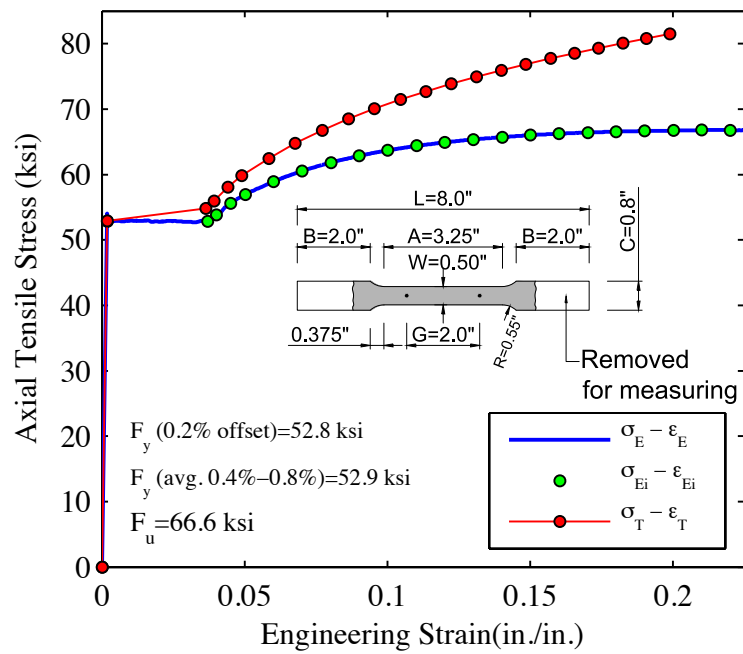
Figure 3-20: Idealized Stress-Strain Curve (σ_E-ε_E); and idealized True Stress-Strain Curve (σ_{Ei}-ε_{Ei})

Table 3-3: Tensile test results

No.	Specimen	Uncoated thickness t_{uc} (in.x10^{-3})	Width W (in.)	Elongation (2 in. gage length) $e_{(2\,in.\,gage)}$ (%)	Upper Yield strength F_{UYS} (ksi)	Yield strength (0.2% offset) $F_{y\,(0.2\%\,offset)}$ (ksi)	Yield strength (ave. 0.4% to 0.8% ELU) $F_{y\,(0.4\,to\,0.8\%\,ELU)}$ (ksi)	Yield point elongation YPE (in./in.)	Tensile strength F_u (ksi)	Strain at Tensile strength ε_u (in./in.)	Rupture point to the center x_r (in.)	Width at the point of rupture W_r (in.)	Thickness at the point of rupture t_r (in.x10^{-3})	Area reduction at rupture $A_{reduction}$ (%)
1	PL1-1	55.57	0.4994	35.4%	53.05	51.98	51.85	0.0302	66.41	>0.225	0.58	0.383	34.8	52.0%
2	PL1-2	55.73	0.4996	35.1%	53.14	52.64	52.08	0.0286	66.65	>0.225	0.863	0.353	34.6	56.1%
3	PL1-3	55.72	0.4999	35.3%	54.34	53.33	52.97	0.0388	67.23	>0.225	0.71	0.381	36.1	50.6%
4	PL1-4	55.42	0.4999	36.7%	52.96	51.64	51.72	0.0338	66.12	>0.225	0.65	0.378	38.6	47.3%
5	PL1-5	55.40	0.4997	35.0%	53.09	51.73	51.84	0.0299	66.23	>0.225	0.63	0.382	34.9	51.8%
6	PL1-6	55.64	0.4998	35.1%	54.43	52.74	52.53	0.0400	66.38	>0.225	0.45	0.385	35.6	50.7%
7	PL2-1	55.55	0.5001	37.5%	54.14	52.77	53.00	0.0304	66.84	>0.225	0.25	0.362	36	53.1%
8	PL2-2	55.49	0.4992	35.8%	53.76	52.54	52.75	0.0370	66.89	>0.225	1.12	0.374	36.8	50.3%
9	PL2-3	55.44	0.4995	36.5%	53.69	52.63	52.81	0.0373	66.56	>0.225	0.08	0.374	36	51.4%
10	600-12-1-F (L)	55.60	0.4990	31.9%	54.65	53.73	53.76	0.0403	66.78	>0.225	0.728	0.38	37.6	48.5%
11	600-12-1-W	55.19	0.4988	36.1%	53.30	52.26	52.32	0.0370	66.34	>0.225	1.32	0.376	36.6	50.0%
12	600-12-2-F (R)	54.95	0.4998	37.0%	53.87	53.20	53.22	0.0379	66.85	>0.225	0.47	0.383	36.1	49.7%
13	600-12-2-W	55.73	0.4996	36.0%	52.61	52.02	52.17	0.0449	66.29	>0.225	0.738	0.361	36.6	52.5%
14	600-24-1-F (R)	55.03	0.4992	30.5%	53.86	52.79	53.37	0.0427	66.73	>0.225	0.1	0.375	38.7	47.2%
15	600-24-1-W	55.67	0.4988	35.3%	53.98	52.28	52.28	0.0397	66.52	>0.225	1.19	0.378	37.3	49.2%
16	600-24-2-F (L)	55.91	0.4989	31.5%	55.32	54.21	54.11	0.0349	67.63	>0.225	0.26	0.374	37.1	50.3%
17	600-24-2-W	55.39	0.4996	36.9%	54.70	52.95	53.23	0.0358	N.A.	N.A.	0.44	0.375	37.2	49.6%
18	600-48-1-F (R)	54.68	0.4993	35.8%	55.62	52.90	52.68	0.0391	66.63	>0.225	1.11	0.381	36.5	49.1%
19	600-48-1-W	55.36	0.4997	34.7%	54.10	53.07	53.04	0.0331	67.01	>0.225	0.36	0.375	36	51.2%
20	600-48-2-F (L)	55.84	0.4991	32.5%	55.54	54.45	54.60	0.0382	67.95	>0.225	0.61	0.381	36.9	49.6%
21	600-48-2-W	55.42	0.4986	36.4%	55.08	53.76	53.82	0.0344	67.50	>0.225	1.03	0.366	36.1	52.2%
Total	Mean			35.1%	54.06	52.84	52.87	0.0364	66.78					50.6%
	STDV			1.9%	0.87	0.76	0.78	0.0043	0.49					2.0%
	C.O.V			5.4%	1.6%	1.4%	1.5%	11.9%	0.7%					4.0%

55

3.1.1.2 Geometric Dimension measurements

To estimate the realistic shape of the test specimens, the cross-section dimensions such as depth (H), flange width (B), lip width (d) and the corner angles and radii were measured before welding. The measurment were performed on a measuring table using several measuring tools such as calipers, micrometers, inclinometers, radius gauges, measuring tapes, and required clamps and plates as shown in Figure 3-21.

Figure 3-21: Measuring table

The measured parameters and the measuring method are illustrated in Figure 3-23. As shown all the parameters were measured from the outside of the section.
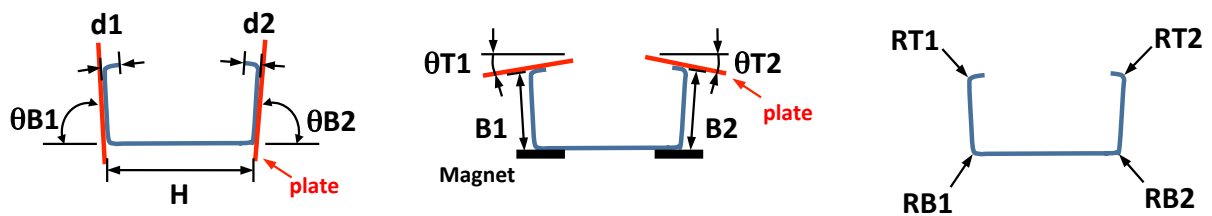
Figure 3-22: Measured parameters

(b) Lip (angles)   (c) Flange (angles)
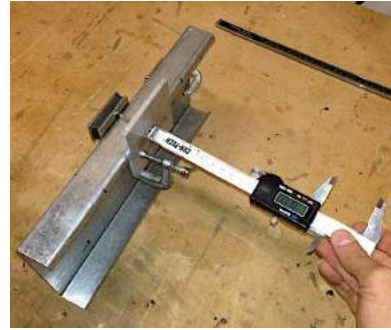
(c) Depth   (d) Flange width
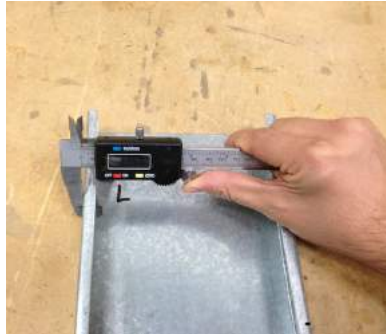
(e) Lip (width) (plates are used for measurments)   (f) Thickness

Figure 3-23: Dimension measurement procedure

The same measuring method was adopted to measure the cross-sectional dimensions for all specimens. Accordingly, an illustrative dimension measurement procedure is provided in Figure 3-23.

The results of the measurements at the mid-height of the specimens are summarized in Table 3-4, Table 3-5, and Table 3-6 for short, intermediate and long specimens, respectively. For

the short and the intermediate specimens, only the measuring data at the mid-length is reported, but for the long specimens, three measuring points near the middle are averaged and reported.

The tabulated results are presented in AISI-S200 adopted format to enable comparisons to the nominal cross-sectional dimensions. Measurements at all recorded points are provided in Appendix D. It should be noted that all measurements were done before welding the end plates.

Table 3-4: Dimension Measurements: 600S137-54 (L=12 inches)

Specimen	H	B1	B2	D1	D2	RT1	RT2	RB1	RB2	θT1	θT2	θB1	θB2	t (avg.)	L (avg.)
	in.	in.	in.	in.	in.	in.	in.	in.	in.	deg.	deg.	deg.	deg.	10^{-4} in.	in.
S600-12-1	6.015	1.395	1.362	0.368	0.409	0.156	0.203	0.141	0.141	1.62	3.03	89.4	85.7	559	11.75
S600-12-2	6.002	1.414	1.316	0.390	0.390	0.156	0.203	0.141	0.125	2.57	5.44	-88.6	-89.9	563	12.03
S600-12-3	5.994	1.403	1.340	0.387	0.409	0.156	0.203	0.156	0.141	1.82	2.12	-89.9	86.6	563	11.75
S600-12-4	5.996	1.420	1.310	0.364	0.408	0.156	0.203	0.141	0.141	-0.79	9.01	89.3	89.0	559	11.69
S600-12-5	6.009	1.425	1.306	0.364	0.402	0.156	0.188	0.141	0.141	3.38	7.67	89.3	89.6	561	11.70
S600-12-6	6.017	1.391	1.354	0.372	0.400	0.156	0.203	0.141	0.141	-0.97	7.80	88.9	87.0	563	11.75
S600-12-7	5.981	1.421	1.310	0.378	0.396	0.156	0.188	0.141	0.125	-1.05	6.49	-89.4	-89.9	560	12.04
S600-12-8	5.990	1.417	1.360	0.382	0.402	0.141	0.203	0.125	0.141	2.56	1.20	-89.3	-86.8	554	11.62
S600-12-9	5.989	1.398	1.344	0.377	0.407	0.156	0.219	0.141	0.141	-0.37	4.01	-88.9	-86.6	553	11.65
S600-12-10	6.021	1.401	1.345	0.356	0.399	0.156	0.188	0.125	0.141	-0.13	1.55	-89.1	-86.7	553	11.60
S600-12-11	6.001	1.430	1.331	0.381	0.380	0.156	0.172	0.156	0.125	1.27	4.96	-88.5	89.6	561	12.06
S600-12-12	6.004	1.393	1.363	0.373	0.401	0.156	0.188	0.156	0.156	-1.80	0.42	-90.0	-86.3	563	11.64
S600-12-13	6.001	1.452	1.305	0.380	0.396	0.156	0.172	0.141	0.125	-1.03	6.45	-88.7	-89.5	562	12.07
S600-12-14	5.999	1.440	1.308	0.384	0.388	0.156	0.188	0.156	0.141	-0.13	6.69	-88.4	-89.9	561	11.64
S600-12-15	6.006	1.417	1.314	0.355	0.406	0.156	0.203	0.156	0.141	2.26	1.00	89.7	88.8	563	11.75
S600-12-16	5.995	1.443	1.303	0.386	0.393	0.156	0.188	0.141	0.125	-1.27	7.00	-89.4	-89.8	553	11.68
S600-12-17	6.014	1.408	1.312	0.365	0.394	0.156	0.188	0.156	0.141	1.39	6.83	89.2	89.3	563	11.72
S600-12-18	5.989	1.386	1.380	0.359	0.405	0.156	0.203	0.141	0.156	1.37	0.29	89.8	-86.6	562	12.12
S600-12-19	6.006	1.413	1.392	0.370	0.404	0.156	0.203	0.156	0.141	-0.36	2.82	89.5	-86.2	564	12.06
S600-12-20	6.019	1.427	1.304	0.363	0.393	0.156	0.188	0.156	0.141	0.45	8.54	-89.30	89.20	561	11.60

Table 3-5: Dimension Measurements: 600S137-54 (L=24 inches)

Specimen	H	B1	B2	D1	D2	RT1	RT2	RB1	RB2	θT1	θT2	θB1	θB2	t (avg.)	L (avg.)
	in.	in.	in.	in.	in.	in.	in.	in.	in.	deg.	deg.	deg.	deg.	10^{-4} in.	in.
S600-24-1	6.005	1.425	1.327	0.358	0.404	0.156	0.203	0.125	0.141	-0.86	2.64	89.5	-88.7	561	24.16
S600-24-2	6.007	1.423	1.315	0.357	0.399	0.156	0.203	0.141	0.141	-1.03	6.49	89.8	-88.8	562	24.08
S600-24-3	6.013	1.420	1.340	0.362	0.391	0.156	0.203	0.141	0.156	-1.26	4.25	89.8	-88.7	562	23.72
S600-24-4	5.985	1.434	1.318	0.374	0.396	0.156	0.203	0.141	0.125	-0.79	3.92	90.0	89.8	562	23.65
S600-24-5	5.996	1.425	1.329	0.365	0.391	0.156	0.203	0.125	0.125	-0.04	1.18	-89.4	90.0	562	24.06
S600-24-6	5.993	1.428	1.323	0.373	0.388	0.156	0.203	0.141	0.141	-0.56	4.91	-89.1	89.9	839	24.16
S600-24-7	5.992	1.416	1.330	0.364	0.398	0.156	0.203	0.125	0.125	-0.48	3.61	-89.3	90.0	561	23.66
S600-24-8	5.997	1.422	1.332	0.369	0.390	0.156	0.203	0.125	0.141	0.57	2.51	-89.5	-89.4	561	24.09
S600-24-9	6.009	1.436	1.321	0.360	0.398	0.156	0.203	0.141	0.141	-0.90	4.97	89.5	-88.5	561	23.69
S600-24-10	6.005	1.418	1.335	0.358	0.401	0.156	0.203	0.141	0.141	0.42	2.81	89.7	-89.0	562	23.65
S600-24-11	5.996	1.433	1.328	0.369	0.417	0.156	0.203	0.141	0.141	-1.86	5.81	89.9	-90.0	564	24.21
S600-24-12	6.016	1.443	1.327	0.354	0.400	0.156	0.203	0.141	0.141	-0.97	5.43	89.8	-88.7	565	24.21
S600-24-13	6.018	1.430	1.322	0.354	0.402	0.156	0.203	0.125	0.141	0.59	6.02	89.9	-89.1	562	23.71
S600-24-14	6.003	1.419	1.342	0.350	0.410	0.156	0.203	0.125	0.141	-1.84	5.02	-89.5	-89.9	562	23.66
S600-24-15	5.986	1.430	1.302	0.372	0.388	0.156	0.203	0.125	0.125	-1.03	5.31	89.9	89.9	563	24.09
S600-24-16	6.006	1.433	1.326	0.356	0.403	0.156	0.203	0.125	0.141	-0.56	5.81	89.5	-88.8	563	23.71
S600-24-17	6.002	1.422	1.321	0.349	0.400	0.156	0.203	0.125	0.141	-1.02	6.71	89.9	-88.9	561	23.68
S600-24-18	5.992	1.452	1.315	0.364	0.394	0.156	0.203	0.141	0.141	-1.66	3.94	-89.2	-89.7	563	24.09
S600-24-19	5.991	1.433	1.316	0.368	0.393	0.156	0.203	0.141	0.125	0.03	5.19	90.0	89.7	561	24.14
S600-24-20	6.004	1.430	1.340	0.362	0.392	0.156	0.203	0.125	0.141	-0.40	5.13	89.7	-88.4	563	23.71

Table 3-6: Dimension Measurements: 600S137-54 (L=48 inches)

Specimen	H	B1	B2	D1	D2	RT1	RT2	RB1	RB2	θT1	θT2	θB1	θB2	t (avg.)	L (avg.)
	in.	in.	in.	in.	in.	in.	in.	in.	in.	deg.	deg.	deg.	deg.	10⁻⁴in.	in.
S600-48-1	6.009	1.423	1.337	0.360	0.395	0.156	0.188	0.141	0.156	0.20	6.16	89.3	89.1	565	48.02
S600-48-2	6.010	1.426	1.328	0.360	0.401	0.156	0.203	0.141	0.156	0.43	6.34	89.5	89.5	563	48.05
S600-48-3	6.008	1.427	1.326	0.366	0.394	0.156	0.203	0.156	0.156	0.68	5.22	89.1	89.7	564	47.83
S600-48-4	6.009	1.414	1.325	0.360	0.402	0.156	0.203	0.141	0.156	-2.13	8.59	89.5	89.4	564	48.05
S600-48-5	6.008	1.429	1.323	0.358	0.398	0.156	0.203	0.141	0.156	-0.53	3.90	89.5	89.5	565	47.75
S600-48-6	6.005	1.425	1.325	0.355	0.401	0.156	0.188	0.156	0.141	-1.61	5.26	89.5	89.2	561	48.25
S600-48-7	6.007	1.418	1.314	0.356	0.403	0.156	0.203	0.141	0.172	0.89	6.27	89.4	89.4	561	47.78
S600-48-8	6.018	1.417	1.319	0.357	0.399	0.156	0.203	0.141	0.156	0.72	4.31	89.8	89.4	564	47.78
S600-48-9	6.010	1.414	1.320	0.366	0.395	0.156	0.203	0.141	0.156	1.25	5.45	89.6	89.6	563	48.05
S600-48-10	6.007	1.412	1.320	0.358	0.399	0.156	0.203	0.141	0.156	0.87	5.09	89.4	89.6	564	48.05
S600-48-11	6.002	1.417	1.319	0.360	0.401	0.156	0.203	0.141	0.141	-0.25	5.71	89.3	89.5	561	48.04
S600-48-12	6.008	1.414	1.325	0.358	0.397	0.141	0.203	0.141	0.141	0.39	4.79	89.4	89.7	561	47.78
S600-48-13	6.005	1.426	1.312	0.361	0.403	0.141	0.203	0.125	0.141	0.98	5.93	89.3	89.2	563	48.00
S600-48-14	6.008	1.417	1.318	0.355	0.403	0.141	0.203	0.125	0.141	0.46	5.68	89.4	89.5	564	47.74
S600-48-15	6.008	1.418	1.315	0.360	0.399	0.156	0.203	0.125	0.141	-1.03	6.30	89.4	89.3	563	48.05
S600-48-16	6.008	1.423	1.313	0.363	0.397	0.156	0.203	0.125	0.141	-0.23	6.88	89.3	89.5	564	47.78
S600-48-17	6.007	1.427	1.342	0.362	0.401	0.156	0.203	0.125	0.141	-0.37	3.66	89.1	89.7	563	48.05
S600-48-18	6.005	1.419	1.334	0.356	0.400	0.141	0.203	0.125	0.141	0.25	6.69	89.4	89.9	561	47.75

3.1.1.3 Stripping zinc coating

To ensure the welding quality and also to avoid poisonous gas produced during welding of the galvanized steel, the zinc coating of the test specimens was stripped by Hydrochloric (HCL-1N) acid. The specimens were immersed partly in the acid bath for about 30 min. and them removed and dried to avoid premature rusting (see Figure 3-24). It should be noted that working with acid has strict safety requirements. Accordingly, a detailed procedure for using acid to remove zinc coating is provided in Appendix E.
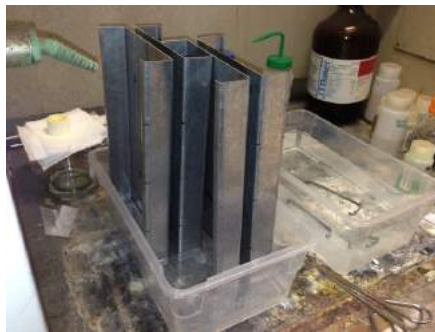
(a) Short specimens in acid bath   (b) Stripped zinc-coating

Figure 3-24: Stripping zinc coating by acid

3.1.1.4 Welding

As explained in Section 3.1.1, it is required to weld the specimens to the end plates to provide the desired end boundary condition and as a means to clamp the specimen to the loading plates. To ensure the welding quality and perpendicularity of the specimen to the end plates, a welding rig was designed and fabricated as shown in Figure 3-25(a). The specimen was clamped to the welding rig during the welding of one end and turned over to weld the other end.

| (a) Welding rig | (b) Welded specimen | (c) Lip welding |
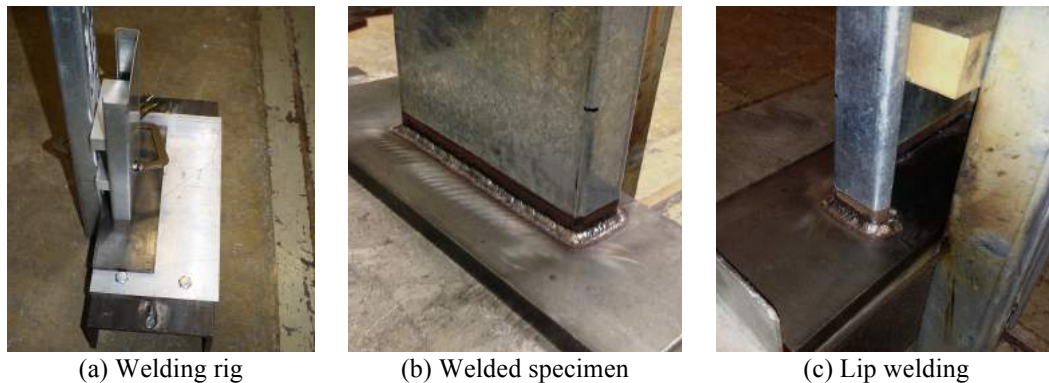
Figure 3-25: Welding process

The welding quality was examined via visual tests and weld dimensions were measured and inspected by a weld gauge; and the required repairs were made. Welding of the lips were especially inspected to ensure the complete and sound welded connection between the specimen and the end plate. The welding electrode was ER70S-2 (70ksi) and a TIG welding system using GTAW welding process (Argon shield gas) was utilized to weld the specimens. To avoid the end plate thermal bending during the welding, the weld leg size was kept at a minimum as depicted in Figure 3-12.

3.1.2 Setting the specimen in the test rig

Setting the specimens in the test rig is the most important part of the testing program that can directly affect the test results. The main purpose of the setting procedure is to place the

specimen at the targeted eccentricity considered for each specimen per Section 2.3. Each specimen should be place at a particular distance to the load point along both X- and Z-axis. To precisely measure the position of the specimen, two precise reference (measuring) beams are provided in the test rig as illustrated in Figure 3-27.

The reference beams consist of two clamps connected to the MTS vertical rods and a horizontal roller connected to a rectangular tube mounted on the clamps. The reference beam provides a precise and fixed datum parallel to the MTS machine to measure the position of the specimens directly. Using two reference beams and doing two measurements against each one ensures the rotation angle of the specimen and the vertical alignment of the specimen to the loading axis of the MTS machine. The measurements in the Z-direction were performed by caliper as shown in Figure 3-26 and the roller on the reference beam measured the position in the X-direction. The required measurement precision in the Z-direction that causes minor axis eccentricity on the cross-section is much more than the required precision along the X-axis, which results in major axis eccentricity. Accordingly, caliper measurement to the precision of 0.0005 in. was made in Z-direction and roller measurement to the precision of 0.015 in. was considered for the X-direction.
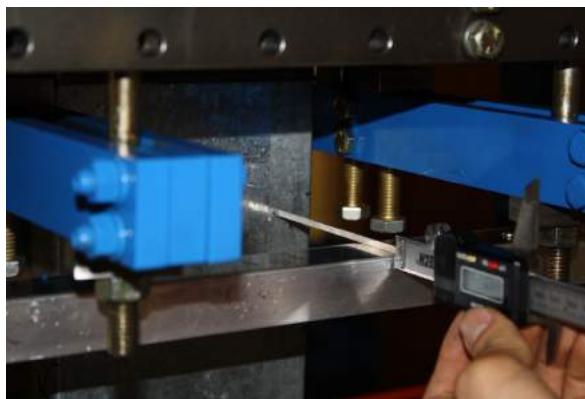
Figure 3-26: Measuring position of the specimens inside the test rig
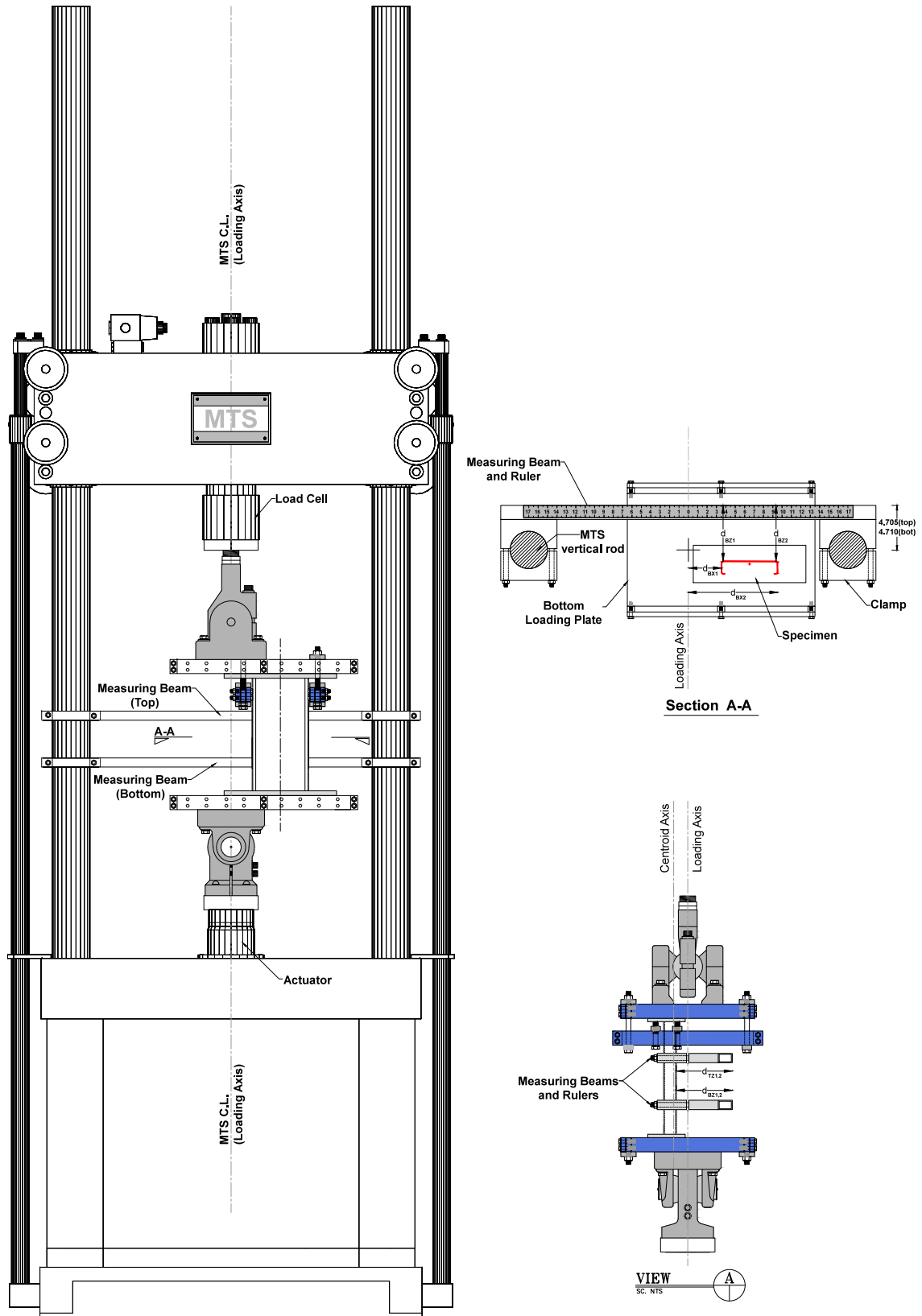
Figure 3-27: Setting the specimens in the test rig

It should be noted that in most of the cases the specimens are not perfectly perpendicularly welded to the end plates. In these cases, the rotational capability of the swivel joints can accommodate the initial end angles. Direct measuring of the eccentricities to an external reference, ensures the accuracy of the load position on the cross-section as illustrated in Figure 3-28.
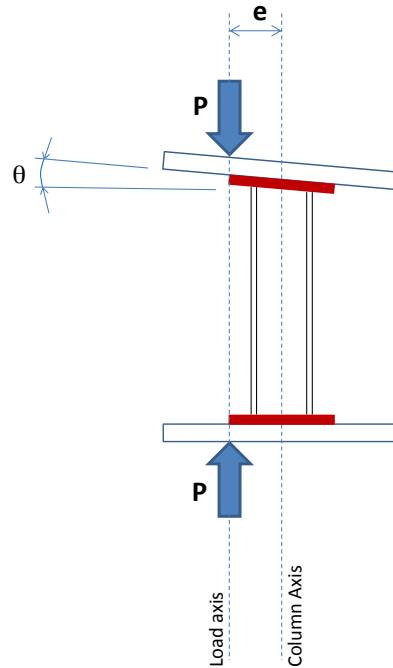
Figure 3-28: Using loading plate to place the specimen at the desired eccentricity

3.1.3 Test procedure and data acquisition

The MTS 407 controller directs the movements of the MTS actuator. All tests are done in displacement control with a proper (pseudo static) loading rate. The controller provides manual movements for setting the specimen and connecting the bottom loading plate to the bottom end plate of the specimens. Moreover, the controller is programmable to apply a ramped shape movement with a selected loading rate. The controller itself does not have a data acquisition system, and therefore the controller and all position transducers are routed to a National

Instruments PCI card and all data monitored via Labview as shown in Figure 3-29. The prepared LabView program provides live data reductions and visualizations throughout the tests.
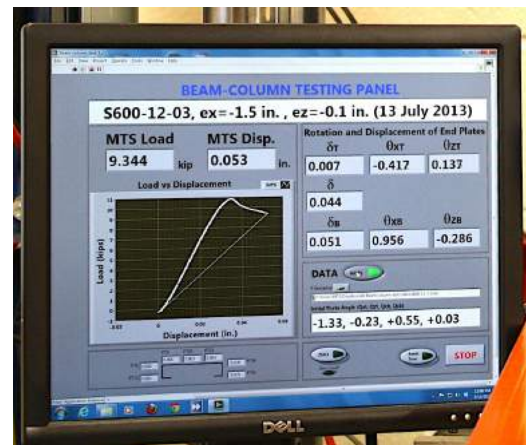
| (a) MTS 407 controller | (b) Beam-column testing panel in LabView |

Figure 3-29: Controlling and data acquisition

3.2 Experiment results

The experimental results consist of observations, load-displacement results, and instrumentation results. In Phase 1 of the experimental program 55 lipped channel specimens have been tested including: 17 short specimens (600S137-54, L=12 in.), 20 intermediate specimens (600S137-54, L=24 in.), and 18 long specimens (600S137-54, L=48 in.). All test results are provided in Appendix F, this includes all test observations, load-displacement results, and instrumentation results. Only main figures, tabular results, and discussions are provided in this chapter.

The experimental results, such as load-displacement curves, end plate rotations, and the applied force at the failure point are used in the following chapters to verify the proposed beam-column Direct Strength Method and FEM models. In the following sections, a summary of the test results is provided to identify the failure modes and structural behavior of the tested beam-columns.

3.2.1 Test results and observations of the short specimens (S600-12)

3.2.1.1 Force-Displacement (P-δ) and Moment-Rotation (M-θ) results

Figure 3-30 shows axial force-displacement curves for 17 short specimens. Figure 3-30 (a) shows the results of the specimens with axial force and bending moment about the principal axes including both minor and major axes and Figure 3-30 (b) depicts the results of the rest of the specimens that are under axial force and bi-axial moments. As shown, the member ductility (i.e., energy or area under the deformation curve) is significantly dependent on the axial force level. High axial forces resulted in low member ductility in most of the specimens. It can be seen that the member behavior is typically more ductile in minor axis bending than major axis bending. Since the larger eccentricities result in larger bending moment and also smaller axial force on the specimens, the specimens with larger eccentricities showed more ductile member behavior. The larger the eccentricities the more the member behavior is similar to "beams"; and the smaller the eccentricities the closer the specimens are to "columns". The results show the high sensitivity of the behavior to the magnitude and the position of the eccentric load.

(a) Principal axis bending (minor and major)   (b) Bi-axial bending
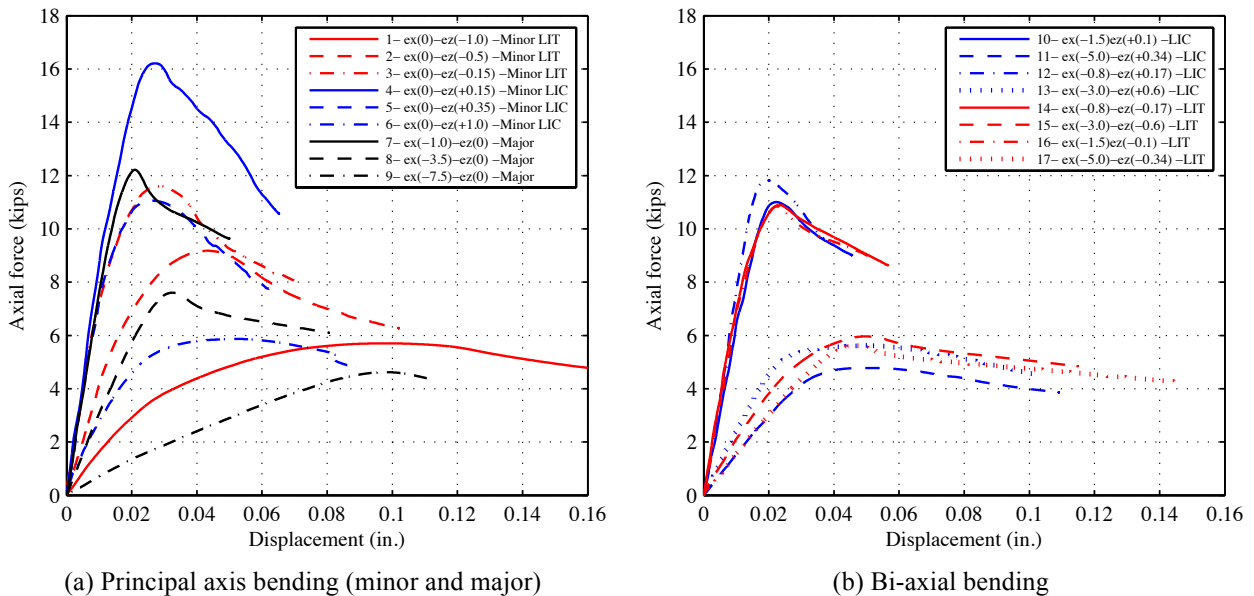
Figure 3-30: Load-displacement results for short specimens (S600-12); LIC: lip in compression, LIT: lip in tension

Figure 3-31 (a) summarizes the moment-rotation curves for 6 specimens under axial force and minor axis bending, and 6 specimens under axial force and major axis bending. The left side of the figure is considered for the rotation around the "z" axis, that is the major axis of the specimen, and the right side of the figure shows the rotation around the "x" axis, that is the minor axis of the specimen. The vertical axis of the figure is the normalized moment of the specimen around either the "x" or "z" axes and the horizontal axis is the absolute average value of the top and the bottom plate rotations. Accordingly, both left and right sides of the figure show positive rotation values, but about different axes. Figure 3-31 (a) reveals that the principal axes have had almost decoupled behaviors.

All of the first six specimens respond just in the θ_x space and no rotation about major axis is observed. This means that the minor axis eccentricity result in a pure minor axis rotation, while the small major axis eccentricity and high stiffness of the major axis prevents the specimen from deforming in the major axis. All minor axis moment-rotation curves typically show ductile member behavior. However, specimens with positive eccentricities (lip in compression and web in tension) provided less post-buckling strength degradation. The larger eccentricities resulted in larger rotation magnitude in both minor and major axis bending. Higher end moments and higher rotation capacities are positively correlated in minor axis bending.

Specimen behavior in major axis bending is typically a less ductile at the member level, and rapid post-peak strength deterioration occurs. The total rotation capacity in the major axis is about 4 or 5 times smaller than the rotation capacity in the minor axis. Higher failure moments and higher rotation capacities are positively correlated in major axis bending.

Figure 3-31 (b) shows the moment-rotation curves of the specimens under axial force and bi-axial bending. Compared to Figure 3-31 (a), each specimen had rotation in both "x" and "z"

66

axis and clearly show the presence of bi-axial bending in the specimens. The results show that the specimen behavior in minor axis bending experiences larger deformations than the behavior in major axis bending. Notably, the behavior of the specimen is a resultant of both minor and major axis bending behavior, in presence of the axial load. Like both pure minor and major axis bending cases, higher end moments and higher sustained end rotations are positively correlated.

(a) Principal axis bending (minor and major)   (b) Bi-axial bending
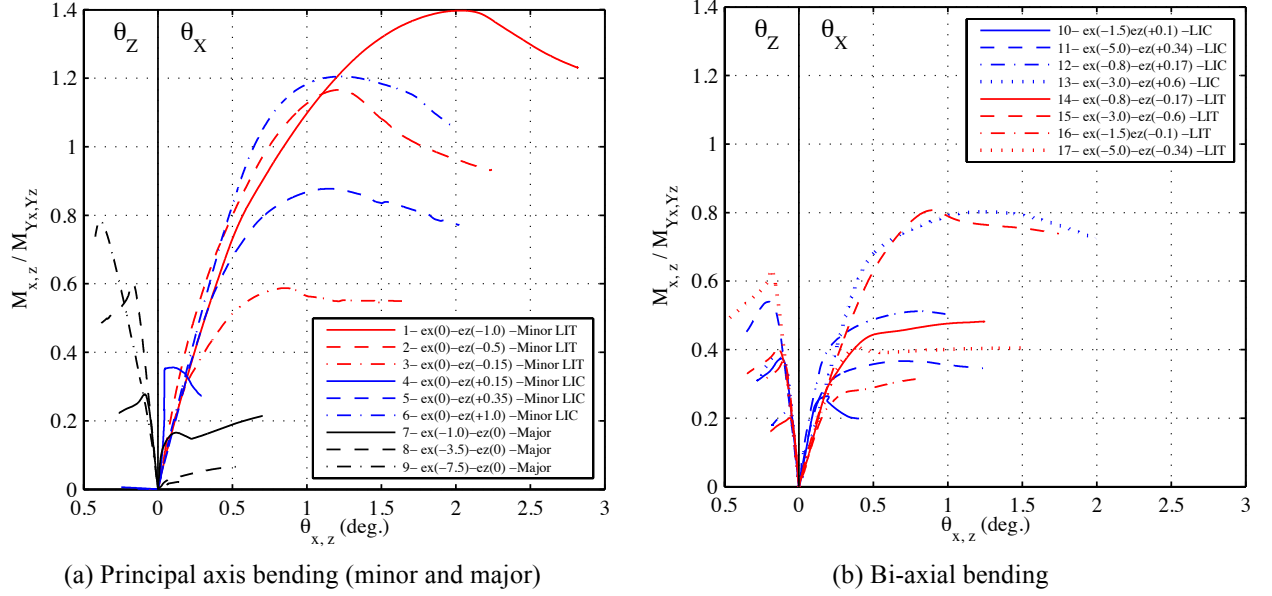
Figure 3-31: Moment-rotation results for short specimens (S600-12); LIC: lip in compression, LIT: lip in tension

3.2.1.2 Axial load and Minor axis bending observations

Based on the test matrix provided in Chapter 2, six test specimens were tested under axial load and minor axis bending. Different behaviors are expected when the lips are in tension or compression due to the bending. Three specimens were tested with negative eccentricities in minor axis to provide tension on the lips and three other specimens were tested with positive eccentricities to apply compression on the lips.

Table 3-7: Beam-columns under axial load and Minor axis bending (lips in tension): $\theta_{MM}=270^{o}$
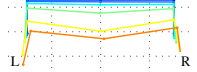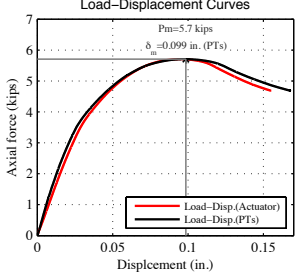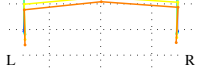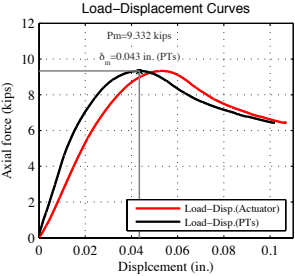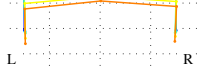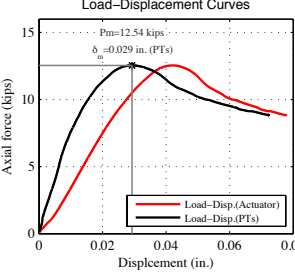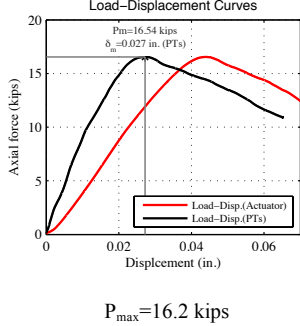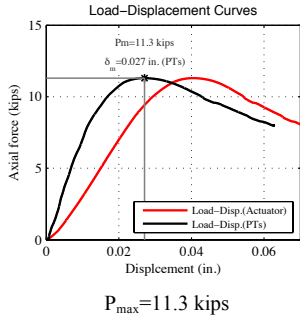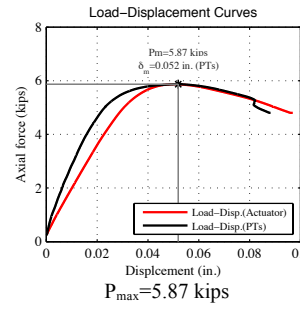
Descriptions	Deformation @ peak	Load-Displcement curves	Observations
1-S600-12-e$_x$(0)-e$_z$(-1.0) Test specimen: S600-12-1 Axial force and Minor axis bending (lip in tension) ecc. in x-dir (e$_x$): ~0.0 (in.) ecc. in z-dir (e$_z$)-Top: -1.077 (in.) ecc in z-dir (e$_z$)-Bot: -1.073 (in.)		Load–Displacement Curves P_{max}=5.706 kips	Symmetric web local buckling (one big half wave) along with consistent flange deformations. Failure mode: WLB
2-S600-12-e$_x$(0)-e$_z$(-0.50) Test specimen: S600-12-19 Axial force and Minor axis bending (lip in tension) ecc. in x-dir (e$_x$): ~0.0 (in.) ecc. in z-dir (e$_z$)-Top: -0.538 (in.) ecc in z-dir (e$_z$)-Bot: -0.543 (in.)		Load–Displacement Curves P_{max}=9.3 kips	Web local buckling (1 big half wave). Very small flange deformations. Specimen squashed at the bottom. Failure mode: WLB
3-S600-12-e$_x$(0)-e$_z$(-0.15) Test specimen: S600-12-4 Axial force and Minor axis bending (lip in tension) ecc. in x-dir (e$_x$): ~0.0 (in.) ecc. in z-dir (e$_z$)-Top: -0.178 (in.) ecc in z-dir (e$_z$)-Bot: -0.191 (in.)		Load–Displacement Curves P_{max}=12.5 kips	Web local buckling (3 half waves). Specimen squashed at the bottom. Failure mode: WLB

Table 3-7 shows the test results of beam-columns under minor axis bending, where the lips were in tension. In all three tested specimens, the characteristic observed failure mode was web local buckling (WLB) followed by consistent flange deformations in the final post-peak stages. Flange deformations were relatively small and happened late compared to the web deformations.

The observed behavior was in agreement with the expected behavior. While, axial load and minor axis bending with negative eccentricity applies compressive stresses on the web and tensile stresses on the flanges and the lips, it is expected that the web buckling dominates, while the lips are stabilized under tensile stresses. As shown in the results, the web local buckling waves were the first visible instability mode of the specimens, and as the buckling shape and the magnitude of the out-of-plane deformations increased, both flanges deformed to provide consistency with the buckled web. Accordingly, the observed flange deformations were either inward (Specimen 1) or outward (Specimen 2,3) based on the web deformed shape and the initial imperfections. It should be noted that the selected cross-section (600S137-54) has typically a slender web and a relatively compact flange in local buckling. Accordingly, the local buckling is primarily expected in the web and the distortional buckling can be seen in the flanges.

Table 3-8 summarizes the results of the cases with positive minor axis eccentricities, which result in higher compressive stresses on the flanges and the lips. As expected, the compressive stress caused flange distortional buckling (FDB) in almost all cases as shown in the table. Following the flange buckling, a consistent web deformation was observed in all three tests. The specimens with smaller eccentricities behaved more like columns. Accordingly, a mixed local and distortional buckling occurred in Specimen 4 with the smallest positive eccentricity in the minor axis (z-direction). The load-displacement curve of the specimen also shows a less ductile failure compared to the other specimens with larger eccentricities. It seems that the small minor axis moment could not overcome the axial stress on the cross-section and all elements including the web and the flanges were in compression at the peak load.

Table 3-8: Beam-columns under axial load and Minor axis bending (lips in compression): $\theta_{MM}=90^{o}$

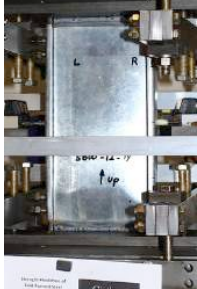| Descriptions	Deformation @ peak	Load-Displcement curves	Observations
4- S600-12-e$_x$(0)-e$_z$(+0.15) Test specimen: S600-12-5 Axial force and Minor axis bending (lip in compression) ecc. in x-dir (e$_x$): ~0.0 (in.) ecc. in z-dir (e$_z$)-Top: +0.115 (in.) ecc in z-dir (e$_z$)-Bot: +0.102 (in.)		 P$_{max}$=16.2 kips	Web local buckling (3 half waves) following by the consistent inward flange deformations. Failure mode: WLB+FDB
5- S600-12-e$_x$(0)-e$_z$(+0.35) Test specimen: S600-12-6 Axial force and Minor axis bending (lip in compression) ecc. in x-dir (e$_x$): ~0.0 (in.) ecc. in z-dir (e$_z$)-Top: +0.311 (in.) ecc in z-dir (e$_z$)-Bot: +0.304 (in.)		 P$_{max}$=11.3 kips	Flange distortional buckling (inward deformation) of both flanges followed by a consistent web deformation Failure mode: FDB
6- S600-12-e$_x$(0)-e$_z$(+1.0) Test specimen: S600-12-8 Axial force and Minor axis bending (lip in compression) ecc. in x-dir (e$_x$): ~0.0 (in.) ecc. in z-dir (e$_z$)-Top: +0.927 (in.) ecc in z-dir (e$_z$)-Bot: +0.973 (in.)		 P$_{max}$=5.87 kips	Flange distortional buckling (inward deformation) in the right flange and a little smaller deformation in the left flange followed by a consistent web deformation Failure mode: FDB

The load-displacement curves show that increasing the positive eccentricity resulted in an increase in the member ductility. It is hypothesized that the increase in the ductility can be understood by the increase of the web tensile stresses resulting from the minor axis moment.

3.2.1.3 Axial load and Major axis bending observations

Table 3-9 summarizes the results of the experiments on the beam-columns under axial loads and major axis bending. Typically the "left flange" (flange with compression from major axis moment) distortional buckling was the main characteristic failure mode of the specimens, but web buckling was also observed. Specimen 7, with the smallest eccentricity in the major axis experienced more severe web local buckling than the left flange distortional buckling. Given the relatively high level of axial load in this specimen, the tested beam-column is more like a column and the uniform axial stress on the cross-section is enough to mobilize web local buckling. However, mostly in the post-peak stage, the major axis bending of the specimen caused distortional deformations in the left flange. For larger eccentricities in the major axis (x-direction) such as Specimen 8 and 9, the (left) flange distortional buckling was observed to be the primary failure mode; while in all cases a consistent web local buckling was also observed.

According to the test results, the more the "beam-column" is close to the "beam" assumptions, the more ductility and inelastic-reserve is observed. On the other hand, when the "beam-column" is close to "column" characteristics, less ductility and more steep post-peak strength degradation is observed.

3.2.1.4 Axial load and Bi-axial bending observations (Positive eccentricity in the minor axis)

The rest of the specimens are beam-columns under axial load and bi-axial bending loading conditions. Four specimens have been tested assuming positive eccentricity in the minor axis and four other specimens were tested by providing negative eccentricity in the minor axis.

Table 3-9: Beam-columns under axial load and Major axis bending: $\theta_{MM}=0^o$
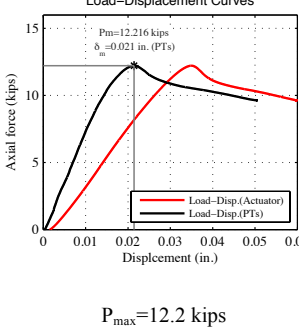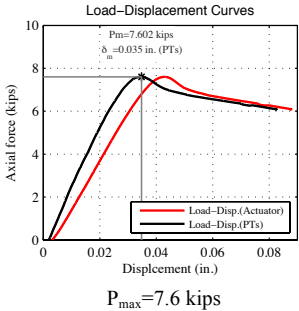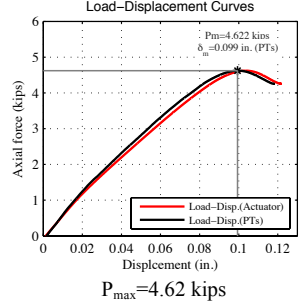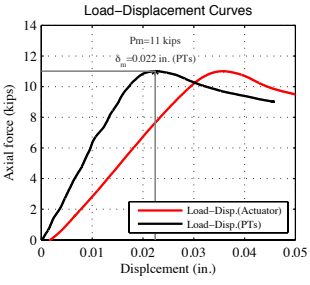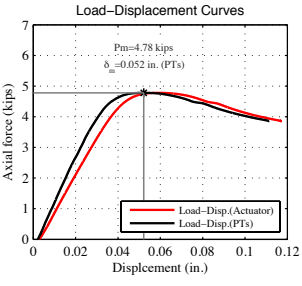
Descriptions	Deformation @ peak	Load-Displcement curves	Observations
7- S600-12-e_x(-1.0)-e_z(0) Test specimen: S600-12-9 Axial force and Major axis bending ecc. in x-dir (e_x): -1.0 (in.) ecc. in z-dir (e_z)-Top: -0.068 (in.) ecc in z-dir (e_z)-Bot: -0.017 (in.)	P_{max}=12.2 kips		Unsymmetrical (almost symmetric) web buckling (3 half waves visible at about P=8.0 kips) and a small left flange inward deformation (distortional buckling) Failure mode: WLB
8- S600-12-e_x(-3.5)-e_z(0) Test specimen: S600-12-10 Axial force and Major axis bending ecc. in x-dir (e_x): -3.5 (in.) ecc. in z-dir (e_z)-Top: -0.016 (in.) ecc in z-dir (e_z)-Bot: -0.01 (in.)		P_{max}=7.6 kips	Unsymmetrical web buckling (seemed like 3 half-waves) and left flange distortional buckling Failure mode: FDB
9- S600-12-e_x(-7.5)-e_z(0) Test specimen: S600-12-11 Axial force and Major axis bending ecc. in x-dir (e_x): -7.5 (in.) ecc. in z-dir (e_z)-Top: +0.0045 (in.) ecc in z-dir (e_z)-Bot: -0.003 (in.)		P_{max}=4.62 kips	Left flange distortional buckling (inward deformation) followed by unsymmetrical web buckling (visible at P=1.5 kips) Failure mode: FDB

Table 3-10 presents the results of two specimens at $\theta_{MM}=30^o$. Both Specimen 10 and 11 have positive eccentricity in the minor axis, which causes compressive stresses in both flanges and lips. Two sources of compressive stresses on the left flange, one from the minor axis bending and the other from the major axis bending, make the flange distortional buckling the main failure
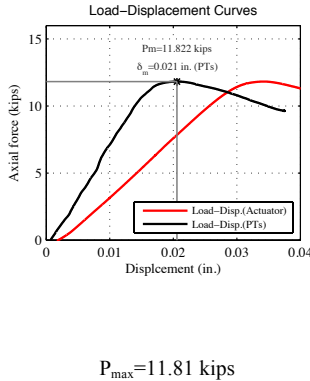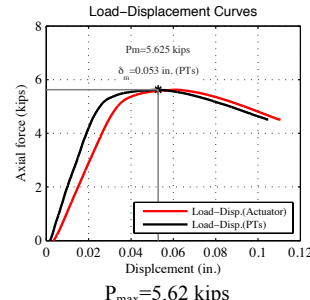
mode. However, for the specimen with the smaller eccentricity, higher axial load on the specimen mobilized web buckling as well.

Table 3-10: Beam-columns under axial load bi-axial bending (+ ecc. in minor axis): $\theta_{MM}=30^o$

Descriptions	Deformation @ peak	Load-Displcement curves	Observations
10- S600-12-e$_x$(-1.5)-e$_z$(0.10) Test specimen: S600-12-2 Axial force and bi-axial bending ecc. in x-dir (e$_x$): -1.5 (in.) ecc. in z-dir (e$_z$)-Top: +0.107 (in.) ecc in z-dir (e$_z$)-Bot: +0.107 (in.)		P_{max}=11.0 kips	Inward movement (distortional buckling) of the left flange and a very small right flange deformation (mostly in post-peak stage) followed by a web buckling (3 half waves) consistent with flange deformations Failure mode: FDB+WLB
11- S600-12-e$_x$(-5.0)-e$_z$(0.34) Test specimen: S600-12-13 Axial force and bi-axial bending ecc. in x-dir (e$_x$): -5.0 (in.) ecc. in z-dir (e$_z$)-Top: +0.3425 (in.) ecc in z-dir (e$_z$)-Bot: +0.332 (in.)		P_{max}=4.78 kips	Inward movement (distortional buckling) of the left flange and a smaller right flange movement (mostly in the post-peak stage) A web consistent deformation with the flange movements in the post peak. Failure mode: FDB

At $\theta_{MM}=60^o$ the pattern of the behavior is almost similar to the $\theta_{MM}=30^o$ (see Table 3-10). Increasing θ_{MM} implies the bending moment is greater in the minor axis. Accordingly, the behavior of the specimens at this azimuth angle is more like the specimens under axial load and pure minor axis bending. Both tested specimens (Specimen 12 and 13) showed the flange distortional buckling mode of failure. It is hypothesized that the different failure shapes of the specimens, shown in the table, may be developed due to different patterns of distortional (largely flange angle) imperfection.

73

Table 3-11: Beam-columns under axial load bi-axial bending (+ ecc. in minor axis): $\theta_{MM}=60^{o}$

Descriptions	Deformation @ peak	Load-Displcement curves	Observations
12- S600-12-e$_x$(-0.8)-e$_z$(0.17) Test specimen: S600-12-14 Axial force and bi-axial bending ecc. in x-dir (e$_x$): -0.8 (in.) ecc. in z-dir (e$_z$)-Top: +0.16 (in.) ecc in z-dir (e$_z$)-Bot: +0.172 (in.)		 P_{max}=11.81 kips	Left flange inward movement (distortional buckling) as the main failure mode of the specimen and a smaller right flange movement mostly in post-peak stage. A web consistent deformation with the flange movements in the post-peak. Failure mode: FDB
13- S600-12-e$_x$(-3.0)-e$_z$(0.6) Test specimen: S600-12-15 Axial force and bi-axial bending ecc. in x-dir (e$_x$): -3.0 (in.) ecc. in z-dir (e$_z$)-Top: +0.62 (in.) ecc in z-dir (e$_z$)-Bot: +0.637 (in.)		 P_{max}=5.62 kips	Flange distortional buckling resulted in outward movement of both flanges. Web buckling was not observed until the post-peak stage. Web deformation was consistent to the flange outward movement. Failure mode: FDB
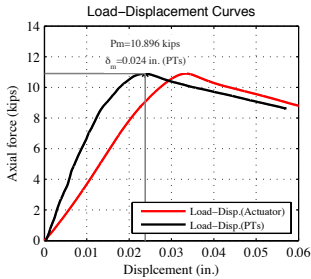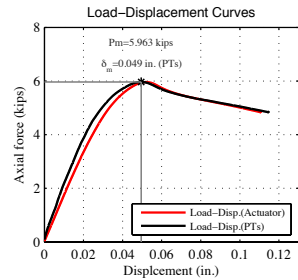
3.2.1.5 Axial load and Bi-axial bending observations (Negative eccentricity in the minor axis)

The test results for the beam-column specimens under bi-axial bending including negative eccentricity in the minor axis are presented in Table 3-12 and Table 3-13. At $\theta_{MM}=300^{o}$ the observed failure mode for both tested specimens was web local buckling and the distortion and movement of the flanges was small compared to the web buckling.

Although smaller minor axis eccentricities were applied at $\theta_{MM}=330^{o}$, the web local buckling was the first observed failure mode of the specimens. However, a flange movement was

also seen, but it seems that the flange movement (based on location and wavelength) is consistent with the web local buckling and is not assumed to be distortional buckling.

Table 3-12: Beam-columns under axial load bi-axial bending (- ecc. in minor axis): $\theta_{MM}=300^{o}$
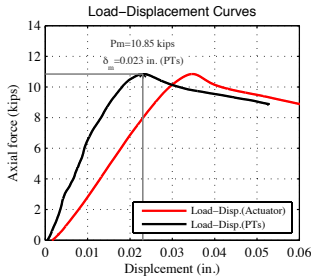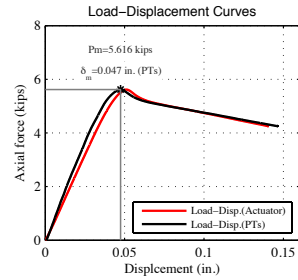
Descriptions	Deformation @ peak	Load-Displcement curves	Observations
14- S600-12-e$_x$(-0.8)-e$_z$(-0.17) Test specimen: S600-12-16 Axial force and bi-axial bending ecc. in x-dir (e$_x$): -0.8 (in.) ecc. in z-dir (e$_z$)-Top: -0.163 (in.) ecc in z-dir (e$_z$)-Bot: -0.158 (in.)		 P$_{max}$=10.8 kips	Unsymmetrical web local buckling (3 half-waves visible at about P=6.5 kips). Flange local buckling of the left flange within the post-peak stage and consistent with the web buckling Failure mode: WLB
15- S600-12-e$_x$(-3.0)-e$_z$(-0.6) Test specimen: S600-12-17 Axial force and bi-axial bending ecc. in x-dir (e$_x$): -3.0 (in.) ecc. in z-dir (e$_z$)-Top: -0.612 (in.) ecc in z-dir (e$_z$)-Bot: -0.615 (in.)		 P$_{max}$=5.96 kips	Almost symmetric web local buckling (one big half wave) and consequent flange outward movement. Flange local buckling of the left flange within the post-peak stage. Failure mode: WLB

The test results at $\theta_{MM}=300^{o}$ and $\theta_{MM}=330^{o}$ show that the slender web of the cross-section governs the failure modes of the member and even a small eccentricity causing more compression on the slender web can mobilize web local buckling. This is a surprising finding worthy of future study.

Comparing the results of the specimens with positive and negative eccentricities show that the web local buckling resulted in a less ductile failure and the specimens squashed showing

flange distortional buckling typically provided more ductile failures, also somewhat surprising given the failure mechanisms assumed to be engaged by theses buckling modes.

Table 3-13: Beam-columns under axial load bi-axial bending (- ecc. in minor axis): $\theta_{MM}=330^o$

Descriptions	Deformation @ peak	Load-Displcement curves	Observations
16- S600-12-e$_x$(-1.5)-e$_z$(-0.10) Test specimen: S600-12-3 Axial force and bi-axial bending ecc. in x-dir (e$_x$): -1.5 (in.) ecc. in z-dir (e$_z$)-Top: -0.105 (in.) ecc in z-dir (e$_z$)-Bot: -0.095 (in.)		 P$_{max}$=10.85 kips	Almost symmetric web local buckling (3 half-waves) and local buckling in the compression flange (left flange) Web buckling was visible around P=7.0 kips. Failure mode: WLB
17- S600-12-e$_x$(-5.0)-e$_z$(-0.34) Test specimen: S600-12-20 Axial force and bi-axial bending ecc. in x-dir (e$_x$): -5.0 (in.) ecc. in z-dir (e$_z$)-Top: -0.335 (in.) ecc in z-dir (e$_z$)-Bot: -0.338 (in.)		 P$_{max}$=5.61 kips	Unsymmetrical web local buckling and left flange local buckling (3-half waves). Twisting was seen after the peak load. Web buckling was visible at about P=+5.0 kips. Failure mode: WLB

3.2.2 Test results and observations of the intermediate specimens (S600-24)

3.2.2.1 Load-Displacement (P-δ) and Moment-Rotation (M-θ) results

Figure 3-32 shows axial force-displacement curves for 20 intermediate length specimens (24 in. long). Results of the specimens with axial force and bending moment about the principal axes including both minor and major axes are shown in Figure 3-32 (a), the results of the rest of the specimens that are under the axial force and bi-axial moments are depicted in Figure 3-32 (b). As shown, the member ductility and the axial force level are negatively correlated and high

axial forces resulted in low member ductility in most of the specimens. Again, the behavior appears more ductile in the (more flexible) minor axis bending compared to the (stiffer) major axis bending. Larger moments caused by larger eccentricities at the ends of the specimens result in smaller axial force on the specimens, therefore the specimens with larger eccentricities exhibit more ductile member behavior. The large eccentricity corresponds to the "beam" behavior; and the small the eccentricity corresponds to "column" behavior. Similar to short specimens, the results are highly sensitive to the magnitude and the position of the applied eccentric load.

Two specimens (Specimen 18 and 20) were tested as a column with no eccentricity. The results are shown with green lines in Figure 3-32 (a). These results are assumed to be the envelope of the "column" behavior. It can be seen that the behavior of the specimens with small eccentricities ultimately merge to the behavior of the column specimens.
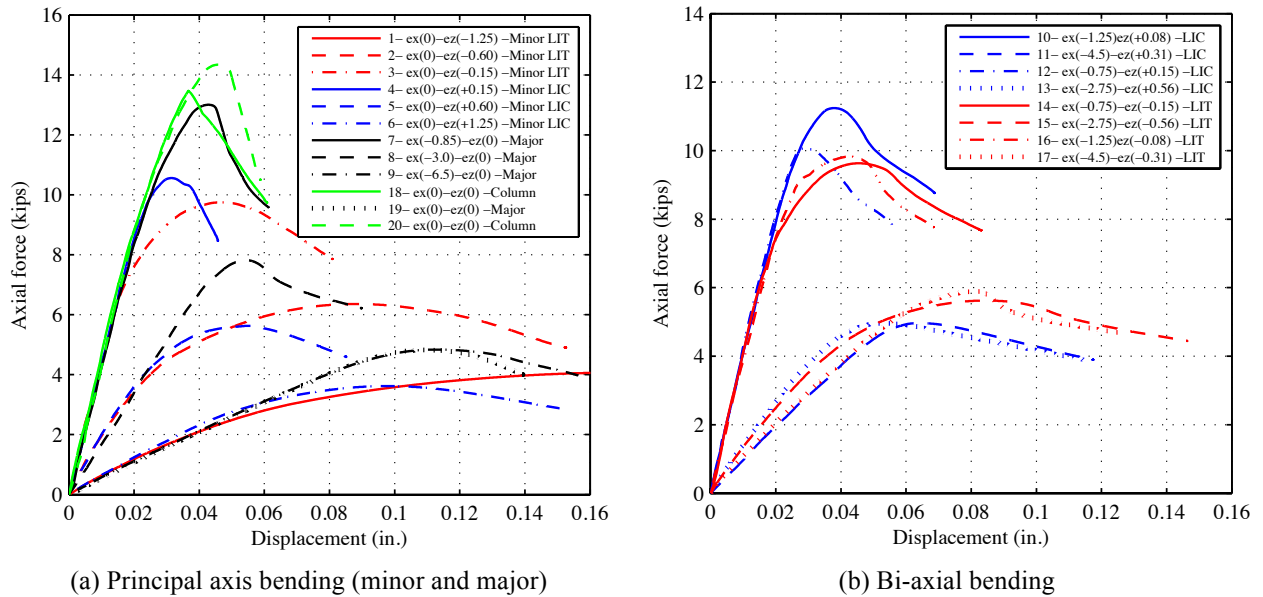
(a) Principal axis bending (minor and major)   (b) Bi-axial bending
Figure 3-32: Load-displacement results for short specimens (S600-24); LIC: lip in compression, LIT: lip in tension

Figure 3-33 summarizes the moment-rotation curves for all 20 specimens under axial force and bending moments. Similar to the short specimens, Figure 3-33 (a) shows that the principal axes have almost decoupled behaviors. All six minor axis specimens provide rotation in

θ_x but no rotation in θ_z. On the other hand, major axis specimens (Specimen 7, 8, 9, and 19) exhibit rotation in θ_z with no projection into θ_x.

All minor axis moment-rotation curves show more ductile member behavior than the major axis curves. Compared to the short specimens, the intermediate length specimens provided less ductility due to the relatively fast strength degradation after peak (load) moment.

With equal eccentricity magnitude (in minor-axis bending) but different directions of the eccentricity, specimens with negative eccentricities (lip in tension and web in compression) provided higher end moments and higher end rotations at the peak load. The post-peak degradation behavior is similar for both LIC (lip in compression) and LIT (lip in tensions) cases.
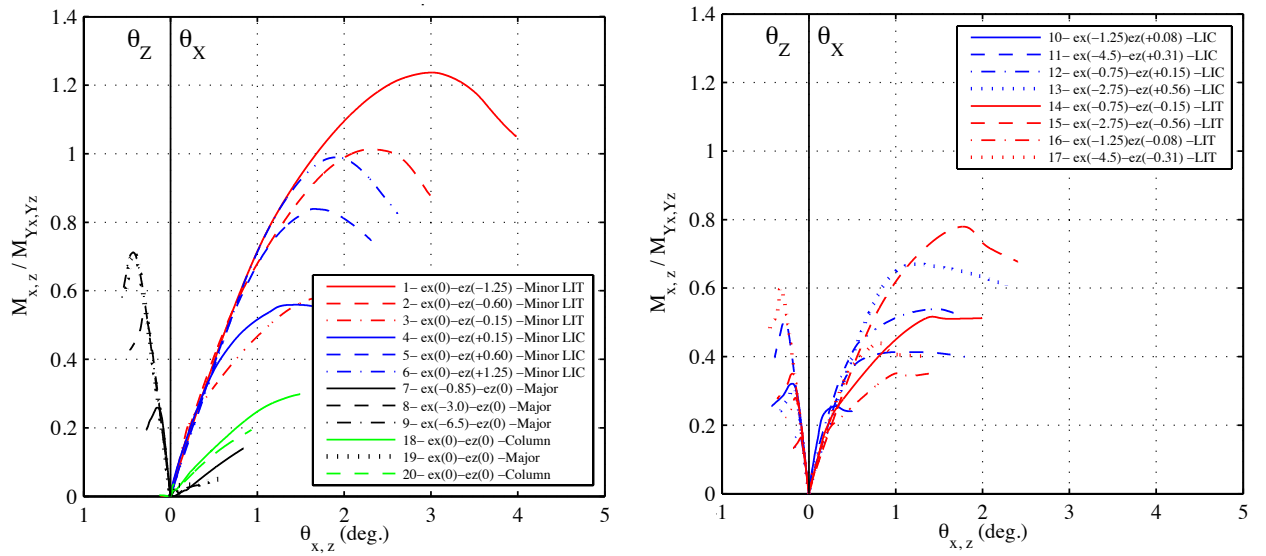
(a) Principal axis bending (minor and major)   (b) Bi-axial bending

Figure 3-33: Load-displacement results for short specimens (S600-24) ; LIC: lip in compression, LIT: lip in tension

The behavior in major axis bending is characterized by rapid strength deterioration after reaching the maximum load. The total rotation capacity in major axis bending is about 3 times smaller than minor axis rotation capacity. Similar to the short specimens, failure moments and rotation capacities are positively correlated in major axis bending.

Figure 3-33 (b) provides the moment-rotation curves of the specimens under axial force and bi-axial bending. As shown, and like the short specimens, the specimen behavior in minor axis bending is more flexible and more ductile than the behavior in major axis bending. Moreover, the specimens with positive eccentricities in z-direction (the direction that causes minor axis bending) have less strength deterioration after the peak load. Similar to all short specimens, end moment magnitude and the maximum applicable end rotations are positively correlated, due to lower axial load in presence of higher bending moments in these specimens.

3.2.2.2 Axial load and Minor axis bending observations

Six intermediate length specimens were tested under axial load and minor axis bending as shown in Table 3-14 and Table 3-15. Like the short specimens, three specimens were tested with negative eccentricities in minor axis to provide tension on the lips and three other specimens were tested with positive eccentricities to apply compression on the lips.

Table 3-14 shows the test results of the three beam-column specimens under minor axis bending, where the lips were in tension. The characteristic observed failure mode was web local buckling (WLB) typically at the mid-height that was followed by small consistent flange deformations in the final post-peak stages.

In all these three specimens, axial load and minor axis bending with negative eccentricity provides compressive stresses on the web and tensile stresses on the flanges and the lips, this leads to web buckling and stabilization of the lips. The web local buckling waves were the first observed buckling mode of the specimens. Web local buckling mostly included three buckling half-waves, one around the mid-height and to others before and after that. As the magnitude of the out-of-plane deformations and buckling shapes of the web increased both flanges deformed

to provide consistency with the buckled web. Accordingly, the observed flange deformations were mostly outward at the point of measurement, i.e. at the mid-height.

Table 3-14: Beam-columns under axial load and Minor axis bending (lips in tension): $\theta_{MM}=270^{o}$
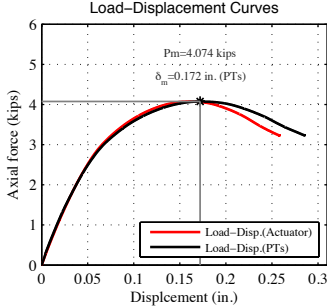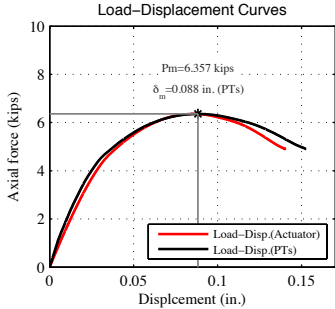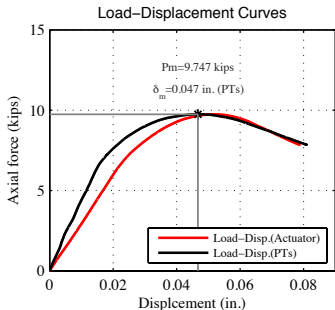
Descriptions	Deformation @ peak	Load-Displcement curves	Observations
1- S600-24-e_x(0)-e_z(-1.25) Test specimen: S600-24-1 Axial force and Minor axis bending (lip in tension) ecc. in x-dir (e_x): ~0.0 (in.) ecc. in z-dir (e_z)-Top: -1.279 (in.) ecc in z-dir (e_z)-Bot: -1.285 (in.)		 P_{max}=4.074 kips	Symmetric web local buckling along with consistent flange deformations. Specimen squashed at the middle. Visible buckling waves at P=2.7 kips Failure mode: WLB
2- S600-24-e_x(0)-e_z(-0.6) Test specimen: S600-24-2 Axial force and Minor axis bending (lip in tension) ecc. in x-dir (e_x): ~0.0 (in.) ecc. in z-dir (e_z)-Top: -0.609 (in.) ecc in z-dir (e_z)-Bot: -0.595 (in.)		 P_{max}=6.357 kips	Web local buckling (1 big half wave at the mid-height). Small flange deformations. Specimen squashed at the middle. Visible buckling waves at P=3.9 kips Failure mode: WLB
3-S600-24-e_x(0)-e_z(-0.15) Test specimen: S600-24-3 Axial force and Minor axis bending (lip in tension) ecc. in x-dir (e_x): ~0.0 (in.) ecc. in z-dir (e_z)-Top: -0.160 (in.) ecc in z-dir (e_z)-Bot: -0.139 (in.)		 P_{max}=9.747 kips	Web local buckling (3 half-waves) along with the consistent small flange deformations. Specimen squashed at the mid-height. Failure mode: WLB

Table 3-15: Beam-columns under axial load and Minor axis bending (lips in compression): $\theta_{MM}=90^{o}$
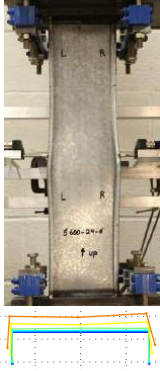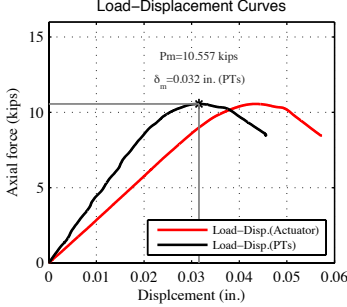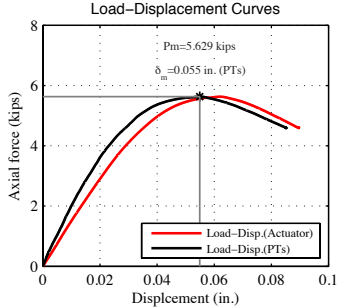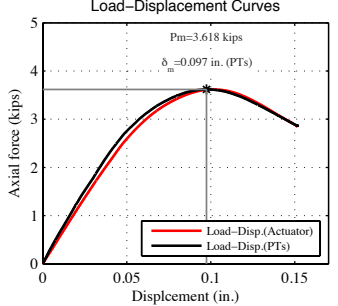
Descriptions	Deformation @ peak	Load-Displcement curves	Observations
4- S600-24-e_x(0)-e_z(+0.15) Test specimen: S600-24-6 Axial force and Minor axis bending (lip in compression) ecc. in x-dir (e_x): ~0.0 (in.) ecc. in z-dir (e_z)-Top: +0.153 (in.) ecc in z-dir (e_z)-Bot: +0.149 (in.)		 P_{max}=10.557 kips	Distortional local buckling in both flanges along with consistent web deformations. Visible distortional buckling waves at P=8.0 kips. Failure mode: FDB
5- S600-24-e_x(0)-e_z(+0.60) Test specimen: S600-24-5 Axial force and Minor axis bending (lip in compression) ecc. in x-dir (e_x): ~0.0 (in.) ecc. in z-dir (e_z)-Top: +0.614 (in.) ecc in z-dir (e_z)-Bot: +0.600 (in.)		 P_{max}=5.63 kips	Flange distortional buckling (outward deformation) of both flanges followed by a consistent small web deformation. Visible distortional buckling wave at P=4.0 first in the left flange. Failure mode: FDB
6- S600-24-e_x(0)-e_z(+1.25) Test specimen: S600-24-4 Axial force and Minor axis bending (lip in compression) ecc. in x-dir (e_x): ~0.0 (in.) ecc. in z-dir (e_z)-Top: +1.2495 (in.) ecc in z-dir (e_z)-Bot: +1.212 (in.)		 P_{max}=3.618 kips	Flange distortional buckling (outward deformation) first in the right flange and then in the left flange followed by a consistent web deformation. Failure mode: FDB

Table 3-15 shows the results of the three beam-column specimens under positive minor axis eccentricities, which result in higher compressive stresses on the flanges and the lips and lower axial stress on the web. As shown in the table, the compressive stress caused the expected flange distortional buckling (FDB) in all cases. Flange distortional buckling was followed by small, but consistent web deformations. The specimen with smaller eccentricities (e.g., Specimen
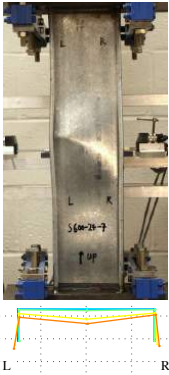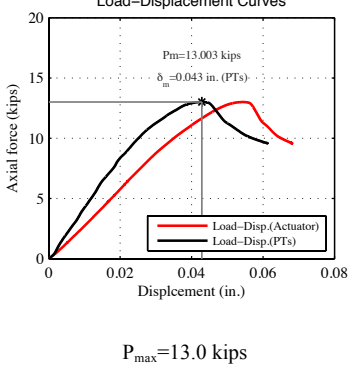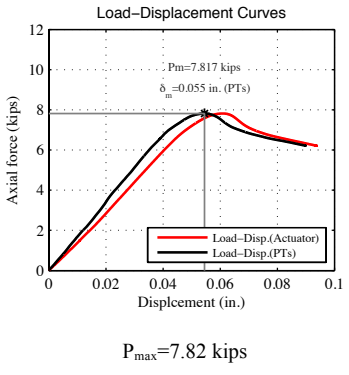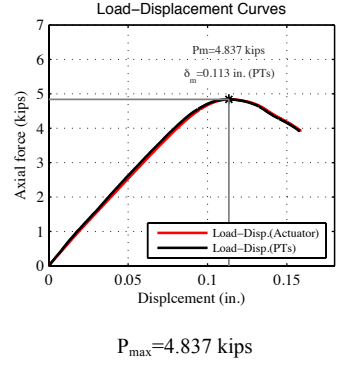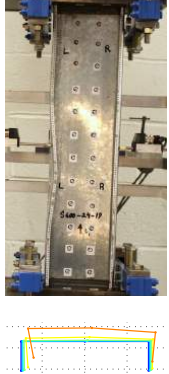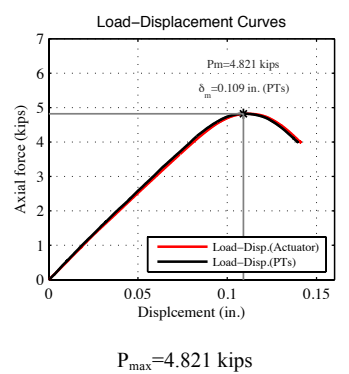
4) provided a more abrupt failure compared to the other specimens with larger eccentricities. The provided lower member ductility could be justified by the compression stress on all elements of the cross-section including the web and the flanges at the peak load.

3.2.2.3 Axial load and Major axis bending observations

The results of four experiments on the beam-columns under axial load and major axis bending were summarized in Table 3-16. Flange distortional buckling (of the left flange, with compression from the major axis moment) was identified as the main characteristic failure mode of the specimens, but web buckling/deformation was also observed. The Specimen with the smallest eccentricity in the major axis (Specimen 7) experienced more severe web local buckling than flange distortional buckling. However, the flange distortional buckling was still visible. For specimens 8-10 and 19 with larger eccentricities in x-direction, the observed primary failure mode of the specimens was mostly a single half-wave length of flange distortional buckling followed by a consistent web local buckling. The web deformation was unsymmetrical with more contraction on the left (compression) side.

As also observed in the short specimens the intermediate specimens verified that the more the beam-column is close to the "beam" characteristics, the more ductility and inelastic-reserve are provided. On the other hand, when the beam-column is close to "column" assumptions, less member ductility and more abrupt post-peak strength degradation is expected.

Table 3-16: Beam-columns under axial load and Major axis bending: $\theta_{MM}=0^o$
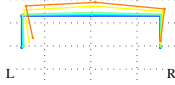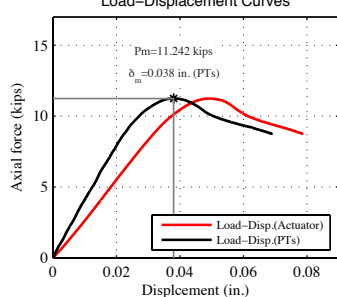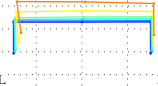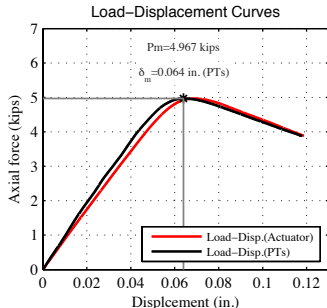
Descriptions	Deformation @ peak	Load-Displcement curves	Observations
7- S600-24-e$_x$(-0.85)-e$_z$(0) Test specimen: S600-24-7 Axial force and Major axis bending ecc. in x-dir (e$_x$): -0.87 (in.) ecc. in z-dir (e$_z$)-Top: 0.004 (in.) ecc in z-dir (e$_z$)-Bot: 0.020 (in.)	 P$_{max}$=13.0 kips		Local buckling waves in the web at P=7kips followed by flange distortional buckling of the left flange at P=10 kips and the consistent web deformations. Failure mode: WLB+FDB
8- S600-24-e$_x$(-3.0)-e$_z$(0) Test specimen: S600-24-8 Axial force and Major axis bending ecc. in x-dir (e$_x$): -3.0 (in.) ecc. in z-dir (e$_z$)-Top: 0.003 (in.) ecc in z-dir (e$_z$)-Bot: 0.003 (in.)	 P$_{max}$=7.82 kips		Unsymmetrical web buckling and Flange distortional buckling of the left flange first at P=6.8 kips followed by consistent web deformations. Maximum flange movement at one-third of the height. Failure mode: FDB
9- S600-24-e$_x$(-6.5)-e$_z$(0) Test specimen: S600-24-9 Axial force and Major axis bending ecc. in x-dir (e$_x$): -6.5 (in.) ecc. in z-dir (e$_z$)-Top: +0.006(in.) ecc in z-dir (e$_z$)-Bot: -0.012 (in.)		 P$_{max}$=4.837 kips	Left flange distortional buckling (inward deformation) followed by unsymmetrical web buckling (visible at P=3.0 kips) Failure mode: FDB
19- S600-24-e$_x$(-6.5)-e$_z$(0) Test specimen: S600-24-19 Axial force and Major axis bending ecc. in x-dir (e$_x$): -6.5 (in.) ecc. in z-dir (e$_z$)-Top: -0.031 (in.) ecc in z-dir (e$_z$)-Bot: 0.042 (in.)		 P$_{max}$=4.821 kips	Left flange distortional buckling (inward deformation) followed by unsymmetrical web buckling Failure mode: FDB

3.2.2.4 Axial load and Bi-axial bending observations (Positive eccentricity in the minor axis)

Four specimens have been tested assuming positive eccentricity in the minor axis, and four other specimens were tested providing negative eccentricity in the minor axis.
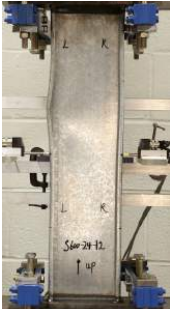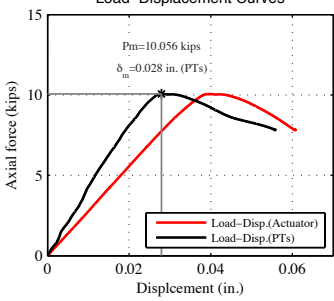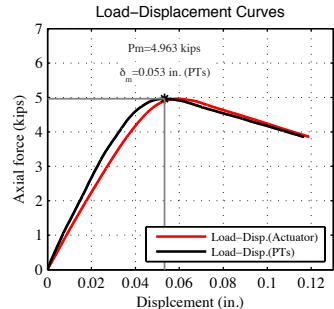
Results of two specimens (Specimen 10 and 11) with positive eccentricity at $\theta_{MM}=30^{o}$ are shown in Table 3-17. There are three sources of compressive stresses on the left flange, one from axial, a second from the minor axis bending, and the third from the major axis bending, resulting in flange distortional buckling as the main failure mode, observed as a single half wave of inward distortional buckling. However, Specimen 10 with the smaller eccentricity, and thus higher axial load on the web of the specimen, mobilized web buckling as well.

Table 3-17: Beam-columns under axial load bi-axial bending (+ ecc. in minor axis): $\theta_{MM}=30^{o}$

Descriptions	Deformation @ peak	Load-Displcement curves	Observations
10- S600-24-e$_x$(-1.25)-e$_z$(0.09) Test specimen: S600-24-10 Axial force and bi-axial bending ecc. in x-dir (e$_x$): -1.25 (in.) ecc. in z-dir (e$_z$)-Top: +0.088 (in.) ecc in z-dir (e$_z$)-Bot: +0.094 (in.)		 P_{max}=11.242 kips	Inward movement (distortional buckling) of the left flange (visible at P=7.0 kips) and a very small right flange deformation (mostly in post-peak stage) followed by a web buckling consistent with flange deformations Failure mode: FDB+WLB
11- S600-24-e$_x$(-4.5)-e$_z$(0.31) Test specimen: S600-24-11 Axial force and bi-axial bending ecc. in x-dir (e$_x$): -4.5 (in.) ecc. in z-dir (e$_z$)-Top: +0.331 (in.) ecc in z-dir (e$_z$)-Bot: +0.365 (in.)		 P_{max}=4.97 kips	Flange distortional buckling of the left flange first visible at P=4.0 kips. Outward flange buckling at two-third of the height and inward flange movement at the mid-height at the end of the test. Failure mode: FDB

As shown in Table 3-18, at $\theta_{MM}=60^{\circ}$, while positive eccentricity in the minor axis direction is still applied, the pattern of the behavior is similar to $\theta_{MM}=30^{\circ}$. Notably, increasing the azimuth to $\theta_{MM}=60^{\circ}$ leads to larger moments about the minor axis. Therefore, the behavior of the specimens are expected to be more similar to the case of beam-columns with pure minor axis moment. The failure mode of both of the tested specimens (Specimen 12 and 13) was flange distortional buckling. The different failure shapes of the tested specimens can potentially be justified by the existence of different patterns of initial imperfections.
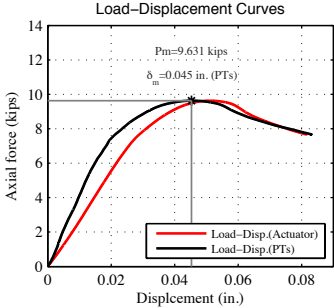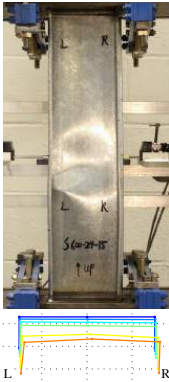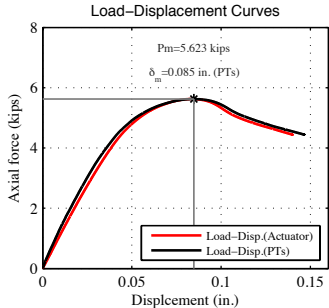
Table 3-18: Beam-columns under axial load bi-axial bending (+ ecc. in minor axis): $\theta_{MM}=60^{\circ}$

Descriptions	Deformation @ peak	Load-Displcement curves	Observations
12- S600-24-e_x(-0.75)-e_z(0.15) Test specimen: S600-24-12 Axial force and bi-axial bending ecc. in x-dir (e_x): -0.75 (in.) ecc. in z-dir (e_z)-Top: +0.169 (in.) ecc in z-dir (e_z)-Bot: +0.169 (in.)		P_{max}=10.06 kips	Left flange inward movement (distortional buckling) at the mid-height and Outward flange buckling at two-third of the height at the end of the test. A web consistent deformation with the flange movements in the post-peak. Failure mode: FDB
13- S600-24-e_x(-2.75)-e_z(0.56) Test specimen: S600-24-13 Axial force and bi-axial bending ecc. in x-dir (e_x): -2.75 (in.) ecc. in z-dir (e_z)-Top: +0.592 (in.) ecc in z-dir (e_z)-Bot: +0.572 (in.)		P_{max}=4.96 kips	Flange distortional buckling of the left flange first visible at P=4.0 kips. Outward flange buckling at one-third of the height at the end of the test. Small right flange outward movement and consistent small web deformation in the post-peak stage. Failure mode: FDB

3.2.2.5 Axial load and Bi-axial bending observations (Negative eccentricity in the minor axis)

Table 3-19 and Table 3-21 present the test results for the beam-column specimens under bi-axial bending including negative eccentricity in the minor axis. At $\theta_{MM}=300^o$ the mode of failure for both tested specimens was web local buckling and consistent distortion of the flanges was observed, but small in magnitude compared to the web buckling.

Table 3-19: Beam-columns under axial load bi-axial bending (- ecc. in minor axis): $\theta_{MM}=300^o$
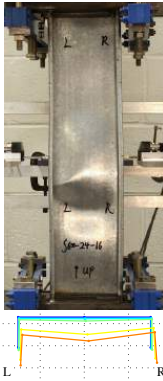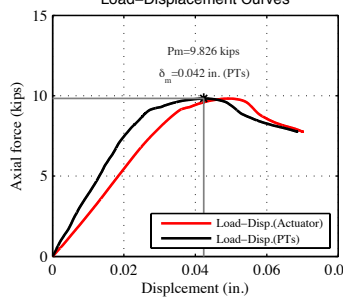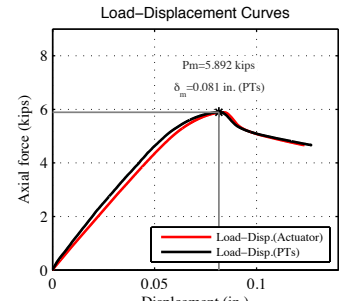
Descriptions	Deformation @ peak	Load-Displcement curves	Observations
14-S600-24-e$_x$(-0.75)-e$_z$(-0.15) Test specimen: S600-24-14 Axial force and bi-axial bending ecc. in x-dir (e$_x$): -0.75 (in.) ecc. in z-dir (e$_z$)-Top: -0.141 (in.) ecc in z-dir (e$_z$)-Bot: -0.139 (in.)		 P_{max}=9.63 kips	Web local buckling (5 half-waves visible at about P=6.0 kips). Small flange local buckling of the left flange and outward movement within the post-peak stage and consistent with the web buckling Failure mode: WLB
15-S600-24-e$_x$(-2.75)-e$_z$(-0.56) Test specimen: S600-24-15 Axial force and bi-axial bending ecc. in x-dir (e$_x$): -2.75 (in.) ecc. in z-dir (e$_z$)-Top: -0.521 (in.) ecc in z-dir (e$_z$)-Bot: -0.565 (in.)		 P_{max}=5.62 kips	Unsymmetrical web local buckling first visible at P=4.3 kips (3 half-waves) and then turned into 5 half-waves. Very small outward flange movement and flange local buckling of the left flange within the post-peak stage. Failure mode: WLB

Although smaller minor axis eccentricities were applied at $\theta_{MM}=330^o$, the web local buckling was the dominant failure mode of the specimens. However, flange movement was observed, but based on location and the short wavelength it is believed to be consistent with the web local buckling and is not assumed to be distortional buckling.

As found in the short specimens, the intermediate length test results at $\theta_{MM}=300^{o}$ and $\theta_{MM}=330^{o}$ show that the slender web of the cross-section governs the failure modes of the member and even a small eccentricity causing greater compression on the slender web can mobilize web local buckling.

As in the short specimens, for intermediate length specimens comparing the results of specimens with positive and negative eccentricities show that web local buckling resulted in a more abrupt failure than those failing in flange distortional buckling – perhaps related to the amount of axial vs. bending demand (small to large eccentricity) in the observed failures.
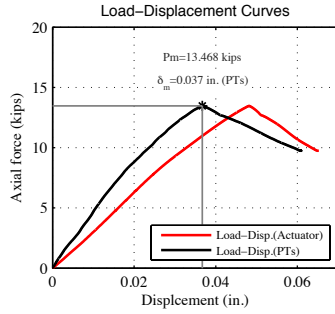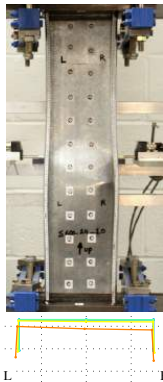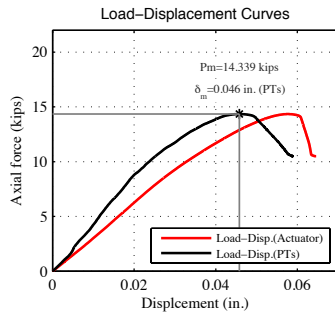
Table 3-20: Beam-columns under axial load bi-axial bending (- ecc. in minor axis): $\theta_{MM}=330^{o}$

Descriptions	Deformation @ peak	Load-Displcement curves	Observations
16-S600-24-e_x(-1.25)-e_z(-0.09) Test specimen: S600-24-16 Axial force and bi-axial bending ecc. in x-dir (e_x): -1.25 (in.) ecc. in z-dir (e_z)-Top: -0.078 (in.) ecc in z-dir (e_z)-Bot: -0.094 (in.)		 P_{max}=9.83 kips	Unsymmetrical web local buckling (5 half-waves) first visible at P=7.0 kips. Very small outward flange movement and flange local buckling of the left flange within the post-peak stage consistent with web buckling deformations. Failure mode: WLB
17-S600-24-e_x(-4.5)-e_z(-0.31) Test specimen: S600-24-17 Axial force and bi-axial bending ecc. in x-dir (e_x): -4.5 (in.) ecc. in z-dir (e_z)-Top: -0.310 (in.) ecc in z-dir (e_z)-Bot: -0.302 (in.)		 P_{max}=5.89 kips	Unsymmetrical web local buckling (3-half waves) and left flange local buckling. Very small flange movement Web buckling was visible at about P=+4.5 kips. Failure mode: WLB

3.2.2.6 Axial load and no bending (column test) observations

Two 24 in. long specimens have been tested under axial load with no eccentricity in x or z directions, as shown in Table 3-21 (Specimen 18 and 20). Failure mode for both tested specimens was web local buckling and consistent distortional movement of the flanges was also observed throughout the test. The axial strength suddenly deteriorated after reaching the peak load and the specimens moved in the positive z direction (the direction that leads to tension in the lips). Local-global buckling is the final mode of failure for these specimens.

Table 3-21: Column test (no eccentricity)

Descriptions	Deformation @ peak	Load-Displcement curves	Observations
18-S600-24-e_x(0.0)-e_z(0.0) Test specimen: S600-24-18 Axial force (Column test) ecc. in x-dir (e_x): 0.0 (in.) ecc. in z-dir (e_z)-Top: -0.020 (in.) ecc in z-dir (e_z)-Bot: 0.013 (in.)		 P_{max}=13.47 kips	Web local buckling first visible at P=7 kips (5 half-waves). Very small flange movement consistent with the web buckling. Fast strength drop at the maximum load. Failure mode: WLB
20-S600-24-e_x(0.0)-e_z(0.0) Test specimen: S600-24-20 Axial force (Column test) ecc. in x-dir (e_x): 0.0 (in.) ecc. in z-dir (e_z)-Top: -0.017 (in.) ecc in z-dir (e_z)-Bot: 0.019 (in.)		 P_{max}=14.34 kips	Web local buckling (3 half-waves). Small flange movement consistent with the web buckling. Fast strength drop at the maximum load. Failure mode: WLB

3.2.3 Test results and observations of the long specimens (S600-48)

3.2.3.1 Load-Displacement (P-δ) and Moment-Rotation (M-θ) results

Load-displacement curves for 18 long specimens (48 in. long) are shown in Figure 3-34. Similar to both short and intermediate length specimens, test results for axial force and bending moment about the principal axes and also the column test (no eccentricity) are shown in Figure 3-34 (a), and the rest of the results are depicted in Figure 3-34 (b). The specimen behavior was more ductile in minor axis bending, in comparison to major axis bending. Larger moments caused by larger eccentricities at the ends of the specimens result in smaller axial force on the specimens, therefore the specimens with larger eccentricities also showed more ductile behavior. The results are systematically consistent with the results of the short and intermediate length specimens. However, the negative correlation of axial forces and member ductility is not clear for all long length specimens, especially in the biaxial bending results.

(a) Principal axis bending (minor and major)　　　(b) Bi-axial bending
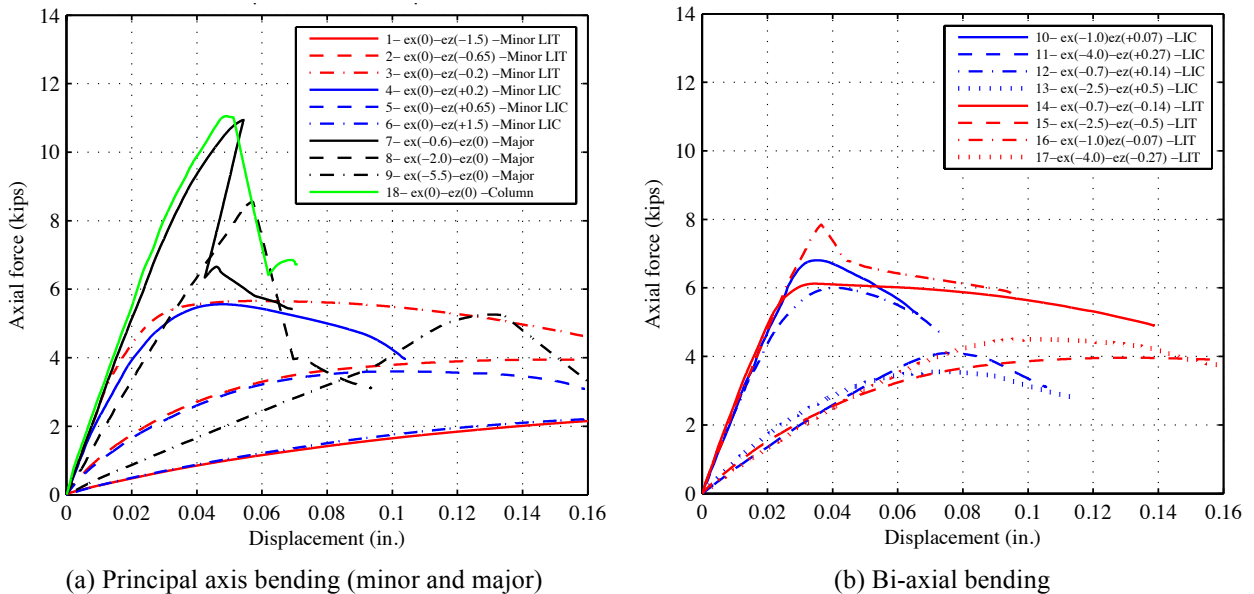
Figure 3-34: Load-displacement results for long specimens (S600-48); LIC: lip in compression, LIT: lip in tension

Specimen 18 was tested as a column with no eccentricity. The results are shown with a solid green line in Figure 3-34 (a). As shown, the behavior of the specimens with small eccentricities (Specimen 7, 8) ultimately merge to the behavior of the column specimen.

Figure 3-35 provides the moment-rotation curves for all 18 long beam-column specimens. Like the short and intermediate length specimens, Figure 3-35 (a) shows decoupled rotation about minor axis. All six minor axis specimens provide rotation in θ_x, and no rotation in θ_z. On the other hand, major axis specimens (Specimen 7, 8 and 9) show rotation in both θ_z and θ_x. The behavior in major axis bending (Specimen 7, 8) is mostly characterized by rapid strength deterioration after reaching the maximum load. According to the test observations most of the minor axis rotations happen after the peak load of the specimen, and as a result of a global buckling type of failure. Moreover, the Specimen 18, which was a column specimen, provided only minor axis rotation (θ_x) right after the peak load and global buckling about the minor axis.

All minor axis moment-rotation curves exhibit more ductile member behavior than their counterparts about the major axis. It should be noted that the stiffness about the minor axis is considerably softer than the major axis. Correspondingly, the rotation magnitude is larger but this does not mean that the provided ductility would be necessarily larger – and the preceding comments refer largely to the nature of the post-peak, not pre-peak response.

Similar to the intermediate length specimens, different directions of the eccentricity in the minor axis can affect the moment-rotation behavior. Specimens with negative eccentricities (lip in tension and web in compression) provided higher end moments and higher end rotations at the peak load. The post-peak degradation behavior is similar for both LIC (lip in compression) and LIT (lip in tensions) cases.
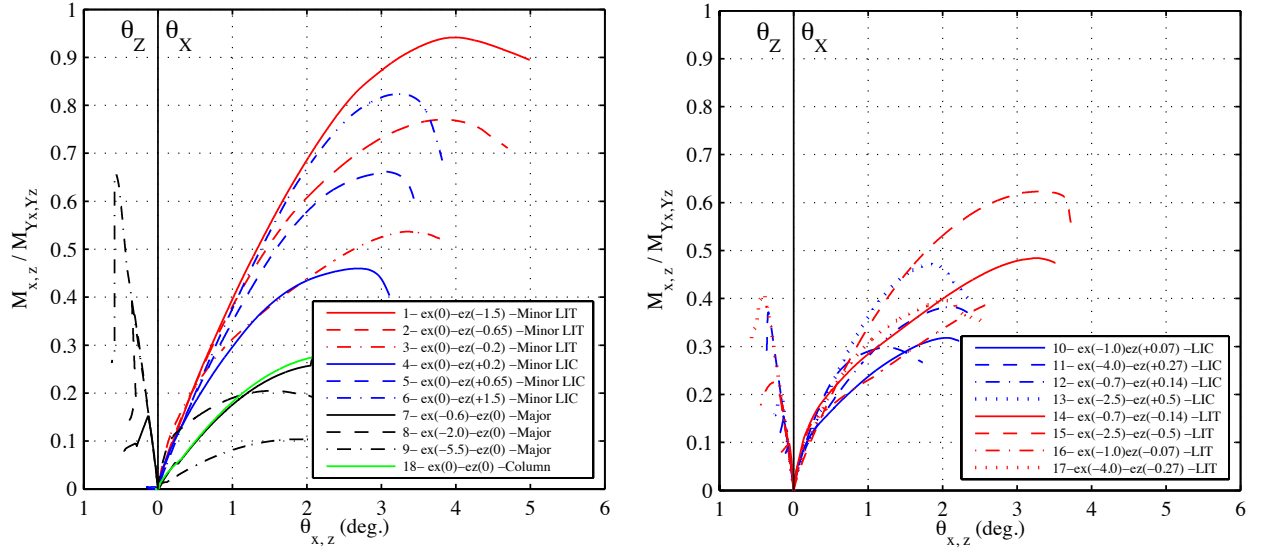
(a) Principal axis bending (minor and major) (b) Bi-axial bending

Figure 3-35: Moment-rotation results for long specimens (S600-48); LIC: lip in compression, LIT: lip in tension

The moment-rotation curves of the specimens under axial force and bi-axial bending is shown in Figure 3-35 (b). Similar to the short and intermediate length specimens, the specimen behavior in minor axis bending is more ductile than the behavior in major axis bending. However, due to global buckling, the minor axis behavior is not as ductile (not as much area under the moment-rotation curve) as the similar short and intermediate length specimens.

For long length specimens, abrupt post-peak strength deterioration is a characteristic behavior for all specimens, even under the principal axis or bi-axial bending.

3.2.3.2 Axial load and Minor axis bending observations

Six specimens were tested under axial load and minor axis bending, including lips in tension (negative eccentricity in the minor axis) and lips in compression (positive eccentricity in the minor axis).

Test results of beam-columns under minor axis bending (lips in tension) are shown in Table 3-22. The dominant failure mode of the three tested specimens was several half-waves of

web local buckling (WLB) followed by very small flange deformations, consistent with the WLB, in the final post-peak stages. A plastic mechanism was formed at the mid-height of the specimen where permanent plastic web deformations were accommodated.

Relatively small bending stiffness of the long length specimens led to large bending deformation of the specimens under end moments resulting from the eccentrically applied axial load. Accordingly, most of the specimens had large mid-height deformations at the peak load and in the post-peak stage. Large mid-height deformation creates second-order demands and related deformations in the specimen.

The test results for the specimens with positive minor axis eccentricities (lip in compression) are presented in Table 3-23. Per expectations, the compressive stress led to 5 half-waves of flange distortional buckling (FDB) in all cases. The flange distortional buckling is followed by a very small, but consistent in wavelength web deformations. Flange distortional deformation primarily consisted of an inward buckling half-wave at the mid-height and two outward and inward buckling half-waves below and above of the center.

The load-displacement curve of Specimen 4 with the smallest eccentricity shows a more abrupt failure compared to the specimens with larger eccentricities. Like the first three specimens, end moments of the specimen caused relatively large mid-height deformation in the negative z-direction, which mobilized the second order demands in the beam-column.

Comparing the load-displacement results of the specimens with positive minor axis eccentricity (lips in compression) with the specimens with negative minor axis eccentricity show that for all these specimens, the strength deteriorated right after the peak load and low member ductility is expected for longer member beam-columns under minor axis bending.

Table 3-22: Beam-columns under axial load and Minor axis bending (lips in tension): $\theta_{MM}=270^o$
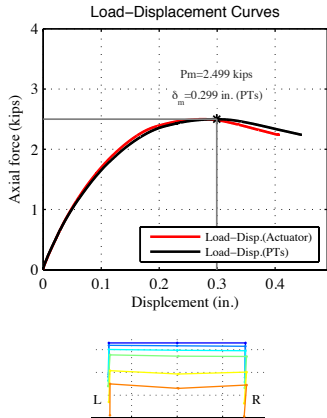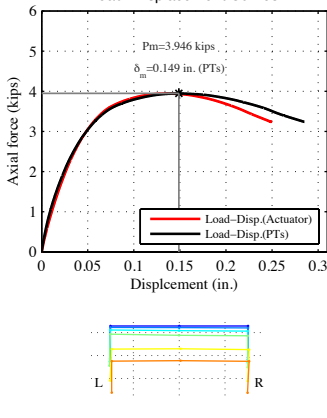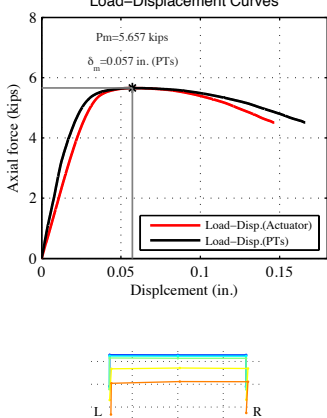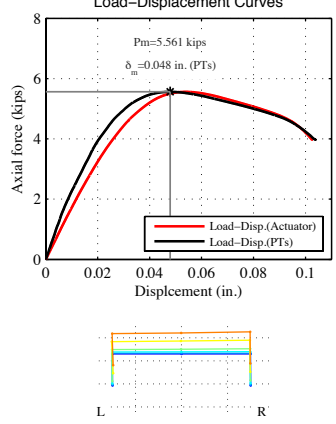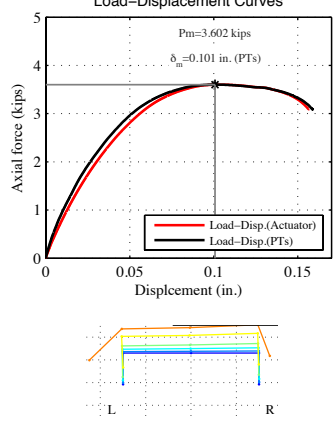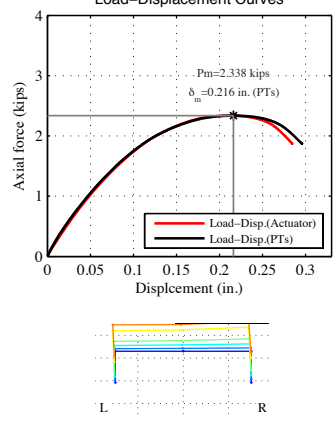
Descriptions	Deformation @ peak	Load-Displcement curves	Observations
1- S600-48-e$_x$(0)-e$_z$(-1.50) Test specimen: S600-48-1 Axial force and Minor axis bending (lip in tension) ecc. in x-dir (e$_x$): ~0.0 (in.) ecc. in z-dir (e$_z$)-Top: -1.552 (in.) ecc in z-dir (e$_z$)-Bot: -1.570 (in.)		 P$_{max}$=2.499 kips	Large local buckling half-wave at the middle at P=2.3 kips. 5 local buckling half-waves around the maximum and in the post-peak. Large global out of plane movement of the specimen in the Z-direction. Failure mode: WLB
2- S600-48-e$_x$(0)-e$_z$(-0.65) Test specimen: S600-48-2 Axial force and Minor axis bending (lip in tension) ecc. in x-dir (e$_x$): ~0.0 (in.) ecc. in z-dir (e$_z$)-Top: -0.696 (in.) ecc in z-dir (e$_z$)-Bot: -0.610 (in.)		 P$_{max}$=3.946 kips	Several local buckling half-waves along the length around P=3.5 kips. Following the pick load, web plastic deformations at mid-height of the specimen. Large global out-of-plane movement of the specimen in the Z-direction. Failure mode: WLB
3-S600-48-e$_x$(0)-e$_z$(-0.20) Test specimen: S600-48-3 Axial force and Minor axis bending (lip in tension) ecc. in x-dir (e$_x$): ~0.0 (in.) ecc. in z-dir (e$_z$)-Top: -0.196 (in.) ecc in z-dir (e$_z$)-Bot: -0.193 (in.)		 P$_{max}$=5.657 kips	Several local buckling half-waves along the length around P=5.0 kips. Following the pick load, web plastic deformations at mid-height of the specimen. Large global out-of-plane movement of the specimen in the Z-direction. Failure mode: WLB

Table 3-23: Beam-columns under axial load and Minor axis bending (lips in compression): $\theta_{MM}=90^{o}$
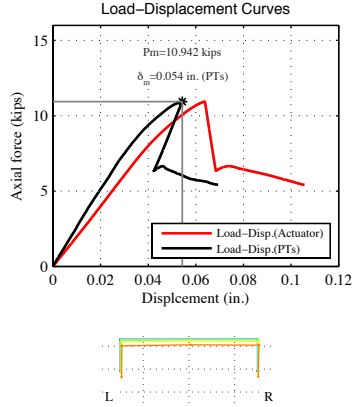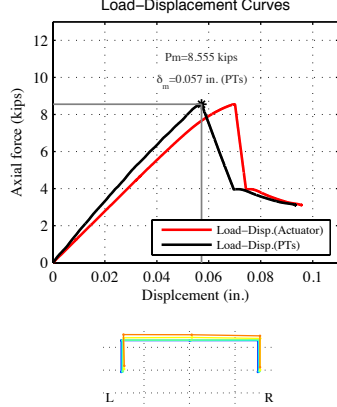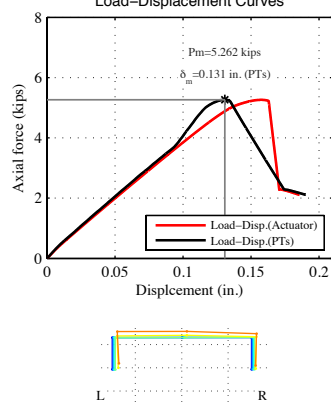
Descriptions	Deformation @ peak	Load-Displcement curves	Observations
4- S600-48-e$_x$(0)-e$_z$(+0.20) Test specimen: S600-48-4 Axial force and Minor axis bending (lip in compression) ecc. in x-dir (e$_x$): ~0.0 (in.) ecc. in z-dir (e$_z$)-Top: +0.202 (in.) ecc in z-dir (e$_z$)-Bot: +0.207 (in.)		 P$_{max}$=5.561 kips	5 distortional buckling half-waves in both flanges along with consistent web deformations. Global out-of-plane movement of the specimen in the negative Z-direction. Failure mode: FDB
5- S600-48-e$_x$(0)-e$_z$(+0.65) Test specimen: S600-48-5 Axial force and Minor axis bending (lip in compression) ecc. in x-dir (e$_x$): ~0.0 (in.) ecc. in z-dir (e$_z$)-Top: +0.650 (in.) ecc in z-dir (e$_z$)-Bot: +0.669 (in.)		 P$_{max}$=3.602 kips	5 distortional buckling half-waves in both flanges along with consistent web deformations first at around P=2.6 kips. Global out-of-plane movement of the specimen in the negative Z-direction. Failure mode: FDB
6- S600-48-e$_x$(0)-e$_z$(+1.5) Test specimen: S600-48-6 Axial force and Minor axis bending (lip in compression) ecc. in x-dir (e$_x$): ~0.0 (in.) ecc. in z-dir (e$_z$)-Top: +1.511 (in.) ecc in z-dir (e$_z$)-Bot: +1.505 (in.)		 P$_{max}$=2.338 kips	5 distortional buckling half-waves in both flanges along with consistent web deformations visible around P=2.2 kips. Large global out-of-plane movement of the specimen in the negative Z-direction. Failure mode: FDB

3.2.3.3 Axial load and Major axis bending observations

Table 3-24 shows the results of the experiments on the beam-columns under axial loads and major axis bending. For Specimen 8 and 9 with relatively large major axis eccentricity, flange distortional buckling (of the left flange under compression) along with global flexural-torsional buckling in the negative z-direction was the characteristic failure mode of the specimens, but consistent web buckling/deformation was also occurred. Both specimens buckled suddenly after reaching the peak load and then considerable strength deterioration occurred. Just before the peak load the flange distortional buckling wave was visible and right after the peak load, the specimens moved toward and twisted in the negative z-direction and the distortional buckling deformations in the left flange were intensified.

Specimen 7 with the smallest eccentricity in the major axis experienced more severe web local buckling along with global flexural buckling in the positive z-direction and relatively minor flange distortional buckling. This specimen buckled suddenly after reaching the peak with considerable strength deterioration. Web local buckling half-waves were visible before reaching the peak load and right after the peak load, the specimens moved toward the positive z-direction and the web local buckling deformations were intensified and led to a plastic mechanism at the mid-height of the specimen. This specimen behaves essentially like a "column".
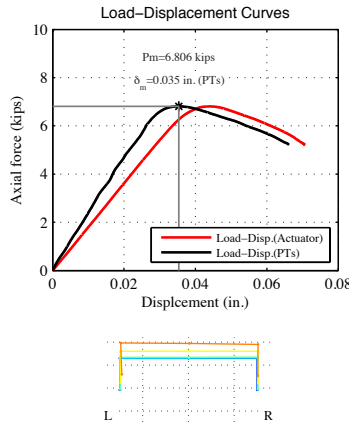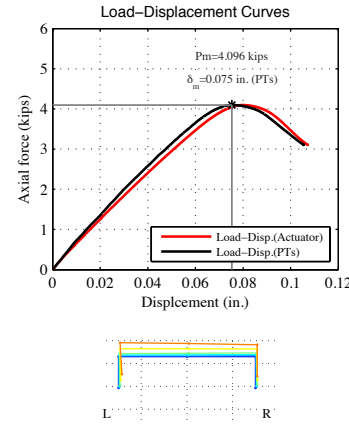
Table 3-24: Beam-columns under axial load and Major axis bending: $\theta_{MM}=0^o$

Descriptions	Deformation @ peak	Load-Displcement curves	Observations
7- S600-48-e_x(-0.60)-e_z(0) Test specimen: S600-48-7 Axial force and Major axis bending ecc. in x-dir (e_x): -0.60 (in.) ecc. in z-dir (e_z)-Top: 0.005 (in.) ecc in z-dir (e_z)-Bot: 0.001 (in.)		 P_{max}=10.942 kips	Several web buckling half-waves visible around P=7.5 kips. Flange deformations consistent with the web buckling. Sudden strength drop and global out-of-plane movement of the specimen in the Z-direction. Failure mode: WLB+FDB
8- S600-48-e_x(-2.0)-e_z(0) Test specimen: S600-48-8 Axial force and Major axis bending ecc. in x-dir (e_x): -2.0 (in.) ecc. in z-dir (e_z)-Top: 0.015 (in.) ecc in z-dir (e_z)-Bot: 0.078 (in.)		 P_{max}=8.555 kips	Flange distortional buckling half-waves in the left flange visible around P=7.0 kips. Web deformations consistent with the flange buckling. Sudden strength drop and global out-of-plane movement of the specimen in the Z-direction. Failure mode: FDB
9- S600-48-e_x(-5.5)-e_z(0) Test specimen: S600-48-9 Axial force and Major axis bending ecc. in x-dir (e_x): -5.5 (in.) ecc. in z-dir (e_z)-Top: -0.010 (in.) ecc in z-dir (e_z)-Bot: +0.014 (in.)		 P_{max}=5.262 kips	Flange distortional buckling half-waves in the left flange visible at around P=4.0 kips. Web deformations consistent with the flange buckling. Sudden strength drop and global out-of-plane movement of the specimen in the Z-direction Failure mode: FDB

3.2.3.4 Axial load and Bi-axial bending observations (Positive eccentricity in the minor axis)

Four long length beam-column specimens were tested with positive eccentricity (lips in compression) about the minor axis and four other specimens were tested with negative eccentricity (lips in tension) about the minor axis.
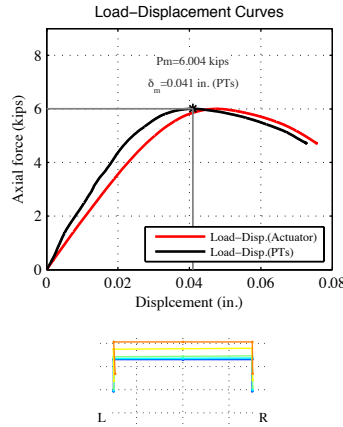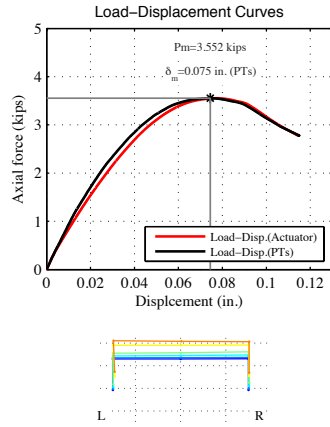
Table 3-25: Beam-columns under axial load bi-axial bending (+ ecc. in minor axis): $\theta_{MM}=30^o$

Descriptions	Deformation @ peak	Load-Displacement curves	Observations
10- S600-48-e_x(-1.0)-e_z(0.07) Test specimen: S600-48-11 Axial force and bi-axial bending ecc. in x-dir (e_x): -1.0 (in.) ecc. in z-dir (e_z)-Top: +0.079 (in.) ecc in z-dir (e_z)-Bot: +0.076 (in.)		 P_{max}=6.806 kips	Flange distortional buckling half-waves in the left flange (visible at P=4.0 kips) and a very small right flange distortional deformation (mostly in post-peak stage) followed by a web buckling consistent with flange deformations. Failure mode: FDB
11- S600-48-e_x(-4.0)-e_z(0.27) Test specimen: S600-48-10 Axial force and bi-axial bending ecc. in x-dir (e_x): -4.0 (in.) ecc. in z-dir (e_z)-Top: +0.238 (in.) ecc in z-dir (e_z)-Bot: +0.295 (in.)		 P_{max}=4.096 kips	Flange distortional buckling half-waves in the left flange visible at around P=3.0 kips. Small web deformations consistent with the flange buckling. Outward flange buckling at two-third of the height and inward flange movement at the mid-height at the end of the test. Failure mode: FDB

Given three sources of compressive stresses on the left flange, one from axial, a second from the minor axis bending, and the third from the major axis bending, the flange distortional buckling was observed to be the main failure mode for the two specimens at azimuth $\theta_{MM}=30^o$,

97

as shown in Table 3-25. Both specimens moved towards the negative z-direction and the strength deteriorated abruptly after the peak load.
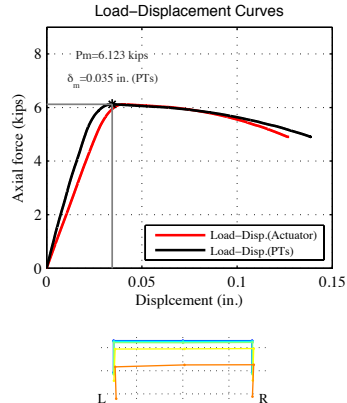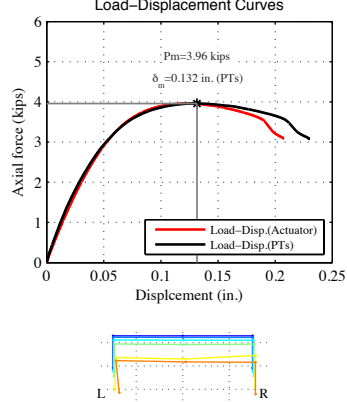
Table 3-26: Beam-columns under axial load bi-axial bending (+ ecc. in minor axis): $\theta_{MM}=60^{o}$

Descriptions	Deformation @ peak	Load-Displcement curves	Observations
12- S600-48-e$_x$(-0.70)-e$_z$(0.14) Test specimen: S600-48-12 Axial force and bi-axial bending ecc. in x-dir (e$_x$): -0.70 (in.) ecc. in z-dir (e$_z$)-Top: +0.143 (in.) ecc in z-dir (e$_z$)-Bot: +0.149 (in.)		 P$_{max}$=6.004 kips	Left flange inward movement (distortional buckling) at the mid-height and Outward flange buckling at two-third of the height at the end of the test. Visible at around P=5.0 kips. Distortional buckling in the right flange and small web deformations consistent with the flange buckling at the end of test. Failure mode: FDB
13- S600-48-e$_x$(-2.5)-e$_z$(0.51) Test specimen: S600-48-13 Axial force and bi-axial bending ecc. in x-dir (e$_x$): -2.5 (in.) ecc. in z-dir (e$_z$)-Top: +0.492 (in.) ecc in z-dir (e$_z$)-Bot: +0.523 (in.)		 P$_{max}$=3.552 kips	Flange distortional buckling half-waves in the left flange visible at around P=3.0 kips. Small web deformations consistent with the flange buckling. Outward flange buckling at two-third of the height and global movement in the Z-direction at the end of the test. Failure mode: FDB

At azimuth $\theta_{MM}=60^{o}$ the pattern of the behavior is almost similar to the $\theta_{MM}=30^{o}$ (see Table 3-26). $\theta_{MM}=60^{o}$ is much closer to $\theta_{MM}=90^{o}$ (pure minor axis bending) and therefore, the behavior of the specimens at this azimuth angle is more like the specimens under axial load and pure minor axis bending (lips in compression). Specimens 12 and 13 exhibited the flange

distortional buckling mode of failure and deformed in the negative z-direction. The strength deteriorated abruptly after peak load.

Table 3-27: Beam-columns under axial load bi-axial bending (- ecc. in minor axis): $\theta_{MM}=300^o$
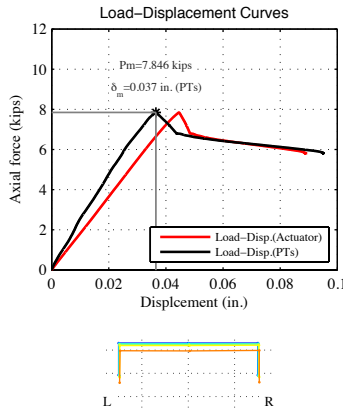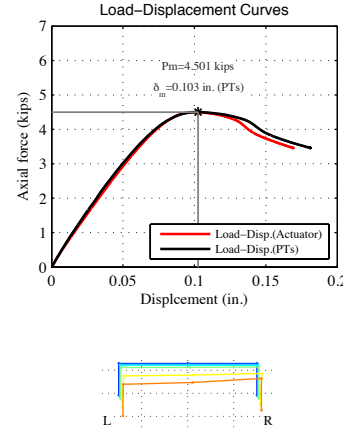
Descriptions	Deformation @ peak	Load-Displcement curves	Observations
14-S600-48-e$_x$(-0.70)-e$_z$(-0.14) Test specimen: S600-48-14 Axial force and bi-axial bending ecc. in x-dir (e$_x$): -0.70 (in.) ecc. in z-dir (e$_z$)-Top: -0.140 (in.) ecc in z-dir (e$_z$)-Bot: -0.134 (in.)		 P_{max}=6.123 kips	Several local buckling half-waves along the length (symmetric about the mid-height) at around P=3.0 kips. Following the pick load, web plastic deformations at mid-height of the specimen. Failure mode: WLB
15-S600-48-e$_x$(-2.50)-e$_z$(-0.51) Test specimen: S600-48-15 Axial force and bi-axial bending ecc. in x-dir (e$_x$): -2.50 (in.) ecc. in z-dir (e$_z$)-Top: -0.524 (in.) ecc in z-dir (e$_z$)-Bot: -0.499 (in.)		 P_{max}=3.96 kips	Several local buckling half-waves along the length (One unsymmetrical larger half-wave at the mid height) visible at around P=3.2 kips. Very small outward flange movement and flange local buckling of the left flange in the post-peak stage. Failure mode: WLB

3.2.3.5 Axial load and Bi-axial bending observations (Negative eccentricity in the minor axis)

The test results for the beam-column specimens under bi-axial bending including negative eccentricity in the minor axis (lips in tension) are presented in Table 3-27 ($\theta_{MM}=300^o$) and Table 3-28 ($\theta_{MM}=330^o$). At $\theta_{MM}=300^o$ the observed failure mode for both tested beam-column specimens was web local buckling with small distortional movement of the flanges

consistent with the web local buckling wavelength. However, web buckling patterns of the specimens were different. Specimen 14, with the smaller minor axis eccentricity, showed several symmetric local buckling half-waves along the length along with very small flange movement, while Specimen 15 experienced an unsymmetrical larger half-wave at the mid height along with larger consistent flange distortional deformation.

Table 3-28: Beam-columns under axial load bi-axial bending (- ecc. in minor axis): $\theta_{MM}=330^{o}$
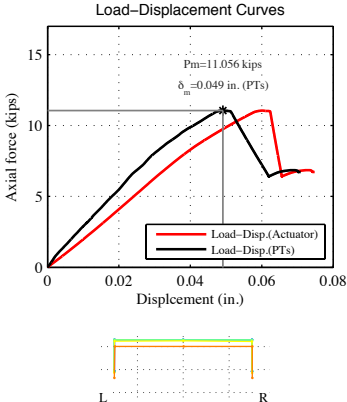
Descriptions	Deformation @ peak	Load-Displcement curves	Observations
16-S600-48-e$_x$(-1.0)-e$_z$(-0.07) Test specimen: S600-48-16 Axial force and bi-axial bending ecc. in x-dir (e$_x$): -1.0 (in.) ecc. in z-dir (e$_z$)-Top: -0.077 (in.) ecc in z-dir (e$_z$)-Bot: -0.061 (in.)		 P$_{max}$=7.846 kips	Several local buckling half-waves along the length. Small consistent flange movements. Sudden strength drop at the maximum load. Failure mode: WLB
17-S600-48-e$_x$(-4.0)-e$_z$(-0.27) Test specimen: S600-48-17 Axial force and bi-axial bending ecc. in x-dir (e$_x$): -4.0 (in.) ecc. in z-dir (e$_z$)-Top: -0.290 (in.) ecc in z-dir (e$_z$)-Bot: -0.242 (in.)		 P$_{max}$=4.501 kips	Several local buckling half-waves along the length. One larger unsymmetrical half-wave at the mid height visible at around P=4 kips. Consistent small flange movement at the end of the test Failure mode: WLB

At $\theta_{MM}=330^{o}$, the web local buckling was still the first observed failure mode of the specimens. Consistent flange distortional movement was also observed in Specimen 17;

however, the flange movement is more consistent with the web local buckling and is not assumed to be a distinct distortional buckling failure.

Comparing the results of the specimens with positive and negative eccentricities show that the more the web local buckling is included in the failure modes, the more severe is the post buckling strength degradation. Accordingly, both Specimen 14 and 16 with the small eccentricities in minor axis exhibited fast strength degradation, while Specimen 15 and 17 with larger eccentricities provided more ductile post-peak behavior.

Table 3-29: Column test (no eccentricity)

Descriptions	Deformation @ peak	Load-Displcement curves	Observations
18-S600-48-e$_x$(0.0)-e$_z$(0.0) Test specimen: S600-48-18 Axial force (Column test) ecc. in x-dir (e$_x$): 0.0 (in.) ecc. in z-dir (e$_z$)-Top: 0.006 (in.) ecc in z-dir (e$_z$)-Bot: 0.000 (in.)		 P$_{max}$=11.056 kips	Several local buckling half-waves along the length visible at around P=5 kips. Consistent flange movements along the length. Sudden Strength drop at the maximum load. Failure mode: WLB

3.2.3.6 Axial load and no bending (column test) observations

Specimen 18 was tested under axial load without any eccentricity in either x or z directions, as shown in Table 3-29. The observed failure mode for the tested specimen was primarily web local buckling and consistent small flange distortional movements were also observed throughout the test. The axial strength suddenly deteriorated after reaching the peak load and the specimens moved in the positive z direction (the direction that leads to tension in the lips). Local-global buckling is the final observed failure mode for these specimens.

3.2.4 Second-order effects

The eccentricities set in Table 2-2 and Table 2-4 are target eccentricities that are used to place the specimen in the test rig. However, the actual provided eccentricities are determined via measuring at the reference beams as described in Section 3.1.2. The measured eccentricities are tabulated in Table 3-30 to Table 3-32 for short, intermediate, and long length specimens. The provided eccentricities (e_{zT-m} and e_{zB-m}) and the corresponding angles (θ_{MM-m} and ϕ_{PM-m}) represent the normalized load points in the 3D P-M-M interaction space. In these tables, e_{x-t} and e_{z-t}, are the nominal target eccentricities, e_{zT-m} and e_{zB-m} are measured/provided eccentricities at the top and bottom plate, $e_{z-Average}$ is the average measured top and bottom eccentricities in the z direction, and θ_{MM-t}, ϕ_{PM-t}, θ_{MM-m}, and ϕ_{PM-m} are the corresponding azimuth and elevation angles.

Table 3-30: Measured eccentricities: 600S137-54 (L=12 inches)

No.		Speccimen	Specimen in testing	Target Eccentricities e_{x-t} (in.)	e_{z-t} (in.)	Angles θ_{MM-t} (deg.)	ϕ_{PM-t} (deg.)	Measured Eccentricities e_{x-m} (in.)	e_{zB-m} (in.)	e_{zT-m} (in.)	$e_{zT-Average}$ (in.)	Angles θ_{MM-m} (deg.)	ϕ_{PM-m} (deg.)
1		S600-12-ex(0)-ez(-1.0)	S600-12-1	0.00	-1.00	270	79	0.00	-1.077	-1.073	-1.075	270.0	79.8
2		S600-12-ex(0)-ez(-0.5)	S600-12-19	0.00	-0.50	270	69	0.00	-0.543	-0.538	-0.541	270.0	70.4
3	Minor axis	S600-12-ex(0)-ez(-0.15)	S600-12-4	0.00	-0.15	270	38	0.00	-0.191	-0.178	-0.185	270.0	43.8
4	bending	S600-12-ex(0)-ez(+0.15)	S600-12-5	0.00	0.15	90	38	0.00	0.102	0.115	0.109	90.0	29.4
5		S600-12-ex(0)-ez(+0.35)	S600-12-6	0.00	0.35	90	61	0.00	0.304	0.311	0.308	90.0	58.0
6		S600-12-ex(0)ez(+1.0)	S600-12-8	0.00	1.00	90	79	0.00	0.973	0.927	0.950	90.0	78.5
7		S600-12-ex(-1.0)-ez(0)	S600-12-9	-1.00	0.00	0	31	-1.00	-0.017	-0.068	-0.043	340.1	33.0
8	Major axis bending	S600-12-ex(-3.5)-ez(0)	S600-12-10	-3.50	0.00	0	65	-3.50	-0.010	-0.016	-0.013	358.2	65.0
9		S600-12-ex(-7.5)-ez(0)	S600-12-11	-7.50	0.00	0	78	-7.50	-0.003	0.005	0.001	360.0	77.7
10		S600-12-ex(-1.5)ez(+0.1)	S600-12-2	-1.50	0.1019	30	47	-1.50	0.107	0.107	0.107	31.1	47.0
11		S600-12-ex(-5.0)-ez(+0.34)	S600-12-13	-5	0.3397	30	74	-5	0.333	0.343	0.338	29.8	74.2
12		S600-12-ex(-0.8)-ez(+0.17)	S600-12-14	-0.813	0.1656	60	45	-0.813	0.172	0.160	0.166	60.1	44.9
13	Bi-axial	S600-12-ex(-3.0)-ez(+0.6)	S600-12-15	-3	0.6115	60	75	-3	0.637	0.620	0.628	60.7	75.1
14	bending	S600-12-ex(-0.8)-ez(-0.17)	S600-12-16	-0.813	-0.1656	300	45	-0.813	-0.158	-0.163	-0.161	300.8	44.2
15		S600-12-ex(-3.0)-ez(-0.6)	S600-12-17	-3	-0.6115	300	75	-3	-0.615	-0.612	-0.614	299.9	74.8
16		S600-12-ex(-1.5)ez(-0.1)	S600-12-3	-1.5	-0.1019	330	47	-1.5	-0.095	-0.105	-0.100	330.5	46.5
17		S600-12-ex(-5.0)-ez(-0.34)	S600-12-20	-5	-0.3397	330	74	-5	-0.338	-0.335	-0.337	330.2	74.2

Table 3-31: Measured eccentricities: 600S137-54 (L=24 inches)

No.		Speccimen	Specimen in the test	Target Eccentricities e_x-t (in.)	e_z-t (in.)	Target Angles θ_MM-t (deg.)	φ_PM-t (deg.)	Measured Eccentricities e_x-m (in.)	e_zB-m (in.)	e_zT-m (in.)	e_z-Average (in.)	Measured Angles θ_MM-m (deg.)	φ_PM-m (deg.)
1		S600-24-ex(0)-ez(-1.25)	S600-24-1	0.0	-1.25	270.0	81	0.00	-1.29	-1.2790	-1.2820	270.0	81.5
2		S600-24-ex(0)-ez(-0.6)	S600-24-2	0.0	-0.60	270.0	72	0.00	-0.60	-0.6090	-0.6020	270.0	72.3
3	Minor axis	S600-24-ex(0)-ez(-0.15)	S600-24-3	0.0	-0.15	270.0	38	0.00	-0.14	-0.1600	-0.1495	270.0	37.8
4	bending	S600-24-ex(0)-ez(0.15)	S600-24-6	0.0	0.15	90.0	38	0.00	0.15	0.1530	0.1510	90.0	38.1
5		S600-24-ex(0)-ez(0.6)	S600-24-5	0.0	0.60	90.0	72	0.00	0.60	0.6140	0.6070	90.0	72.4
6		S600-24-ex(0)-ez(1.25)	S600-24-4	0.0	1.25	90.0	81	0.00	1.21	1.2500	1.2310	90.0	81.1
7	Major axis	S600-24-ex(-0.85)-ez(0)	S600-24-7	-0.85	0.00	0.0	27	-0.87	0.02	0.0040	0.0120	6.7	28.2
8	bending	S600-24-ex(-3.0)-ez(0)	S600-24-8	-3.00	0.00	0.0	61	-3.00	0.00	0.0030	0.0030	0.5	61.4
9		S600-24-ex(-6.5)-ez(0)	S600-24-9	-6.50	0.00	0.0	76	-6.50	-0.01	0.0060	-0.0030	359.8	75.9
10		S600-24-ex(-1.25)-ez(0.09)	S600-24-10	-1.25	0.09	30	41	-1.25	0.09	0.0880	0.091	31.7	41.9
11		S600-24-ex(-4.5)-ez(0.3)	S600-24-11	-4.50	0.3058	30	73	-4.50	0.3650	0.3310	0.3480	33.3	73.1
12		S600-24-ex(-0.75)-ez(0.15)	S600-24-12	-0.75	0.1529	60	43	-0.75	0.1690	0.1690	0.1690	62.4	44.7
13	Bi-axial	S600-24-ex(-2.75)-ez(0.56)	S600-24-13	-2.75	0.5606	60	73	-2.75	0.5720	0.5920	0.5820	60.9	73.9
14	bending	S600-24-ex(-0.75)-ez(-0.15)	S600-24-14	-0.75	-0.1529	300	43	-0.75	-0.1390	-0.1410	-0.1400	302.2	40.7
15		S600-24-ex(-2.75)-ez(-0.56)	S600-24-15	-2.75	-0.5606	300	73	-2.75	-0.5650	-0.5210	-0.5430	300.8	73.1
16		S600-24-ex(-1.25)-ez(-0.08)	S600-24-16	-1.25	-0.0849	330	41	-1.25	-0.0940	-0.0780	-0.0860	329.7	41.5
17		S600-24-ex(-4.5)-ez(-0.3)	S600-24-17	-4.50	-0.3058	330	73	-4.50	-0.3020	-0.3100	-0.3060	330.0	72.5
18	Axial	S600-24-ex(0.0)-ez(0.0)	S600-24-18	0.00	0.0	0.0	0	0.000	0.0130	-0.0200	-0.0035	-	1.0
19	Major	S600-24-ex(-6.5)-ez(0)	S600-24-19	-6.50	0.0	0.0	76	-6.5	0.0419	-0.031	0.0055	0.414	75.9
20	Axial	S600-24-ex(0.0)-ez(0.0)	S600-24-20	0.00	0.0	0.0	0	0.000	0.0194	-0.0166	0.0014	-	0.4

Table 3-32: Measured eccentricities: 600S137-54 (L=48 inches)

No.		Speccimen	Specimen in the test	Target Eccentricities e_x-t (in.)	e_z-t (in.)	Target Angles θ_MM-t (deg.)	φ_PM-t (deg.)	Measured Eccentricities e_x-m (in.)	e_zB-m (in.)	e_zT-m (in.)	e_z-Average (in.)	Measured Angles θ_MM-m (deg.)	φ_PM-m (deg.)
1		S600-48-ex(0)-ez(-1.5)	S600-48-1	0.00	-1.50	270.0	83	0.00	-1.57	-1.5524	-1.5614	270.0	83.0
2		S600-48-ex(0)-ez(-0.65)	S600-48-2	0.00	-0.65	270.0	74	0.00	-0.61	-0.6958	-0.6531	270.0	73.6
3	Minor axis	S600-48-ex(0)-ez(-0.2)	S600-48-3	0.00	-0.20	270.0	46	0.00	-0.19	-0.1963	-0.1948	270.0	45.3
4	bending	S600-48-ex(0)-ez(0.2)	S600-48-4	0.00	0.30	90.0	57	0.03	0.21	0.2024	0.2047	89.0	46.8
5		S600-48-ex(0)-ez(0.65)	S600-48-5	0.00	0.65	90.0	74	0.00	0.67	0.6496	0.6594	90.0	73.7
6		S600-48-ex(0)-ez(1.5)	S600-48-6	0.00	1.50	90.0	83	0.00	1.51	1.5111	1.5081	90.0	82.7
7	Major axis	S600-48-ex(-0.6)-ez(0)	S600-48-7	-0.60	0.00	0.0	20	-0.60	0.00	0.0052	0.0030	2.4	20.2
8	bending	S600-48-ex(-2.0)-ez(0)	S600-48-8	-2.00	0.00	0.0	51	-2.00	0.08	0.0148	0.0463	11.1	51.3
9		S600-48-ex(-5.5)-ez(0)	S600-48-9	-5.50	0.00	0.0	73	-5.50	0.01	-0.0104	0.0016	0.1	73.4
10		S600-48-ex(-1.0)-ez(0.07)	S600-48-11	-1.00	0.07	30	35	-1.00	0.08	0.0790	0.078	33.4	36.2
11		S600-48-ex(-4.0)-ez(0.27)	S600-48-10	-4.00	0.2718	30	71	-4.00	0.2948	0.2378	0.2663	29.5	70.4
12		S600-48-ex(-0.7)-ez(0.14)	S600-48-12	-0.70	0.1427	60	41	-0.70	0.1485	0.1425	0.1455	60.5	41.0
13	Bi-axial	S600-48-ex(-2.5)-ez(0.5)	S600-48-13	-2.50	0.5096	60	72	-2.50	0.5231	0.4916	0.5074	59.9	71.8
14	bending	S600-48-ex(-0.7)-ez(-0.14)	S600-48-14	-0.70	-0.1427	300	41	-0.70	-0.1401	-0.1341	-0.1371	301.0	39.7
15		S600-48-ex(-2.5)-ez(-0.5)	S600-48-15	-2.50	-0.5096	300	72	-2.50	-0.4985	-0.5240	-0.5113	299.9	71.9
16		S600-48-ex(-1.0)-ez(-0.07)	S600-48-16	-1.00	-0.0680	330	35	-1.00	-0.0609	-0.0774	-0.0692	329.6	35.3
17		S600-48-ex(-4.0)-ez(-0.27)	S600-48-17	-4.00	-0.2718	330	71	-4.00	-0.2418	-0.2898	-0.2658	330.5	70.4
18	Axial	S600-48-ex(0.0)-ez(0.0)	S600-48-18	0	0	0	0	0.000	0.0000	0.0060	0.0030	-	0.9

The specimens were all tested under the applied measured eccentricities. As shown in Figure 3-36, the eccentricity at the ends of the specimen is changed due to the rigid end plate rotations. Accordingly, the end eccentricities need to be adjusted for the end rotation. By applying all required corrections, the eccentricities in both directions at the peak load (e_x and e_z) are summarized in Table 3-33 to Table 3-35 for all short, intermediate and long length

specimens. It should be noted that "e_z" is the average of the top and bottom end eccentricities in the z-axis.

The tables also provide the eccentricities at the mid-height of the specimen, which is the summation of the end and mid-height deformations under the applied actions.
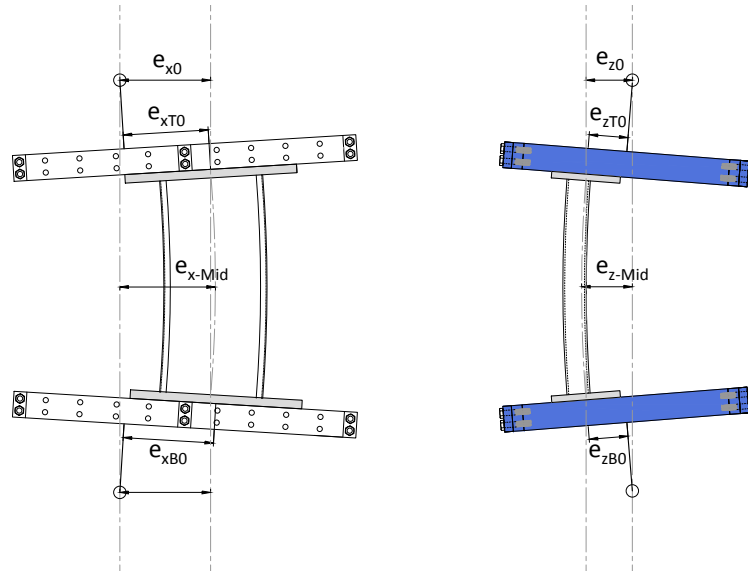
Figure 3-36: Definition of the eccentricities at the peak load

Knowing the measured eccentricities at the ends (rigid end plates), and the specimen deformation at the mid-height (via the mounted position transducers, e_{x-Mid} and e_{z-Mid}), experimental displacement amplification factors (α_{z-exp} and α_{x-exp}) for the specimen can be calculated as presented in Table 3-33 to Table 3-35.

The displacement amplification factors ($\alpha_{z-exp}=e_x/e_{x-Mid}$ and $\alpha_{x-exp}=e_z/e_{z-Mid}$) are estimating the second-order displacements caused by the second order moment of axial force "P" times the deflections at the mid point "δ", which is called "p-δ" effect. Since, no transverse load is applied, the ratio of primary moment to the moment at the point of failure, which is basically the moment amplification ratio can also be assumed to be equal to the calculated displacement amplification factor, α_{z-exp} and α_{x-exp}.

As the specimens have a lower stiffness in the minor axis bending, the second order effects resulted in average 12% increase over the 1st order analysis in short, 35% in intermediate, and 81% in long length specimens, while the second order effects in the major axis bending (max 3% in long specimens) were not remarkable due to its much higher stiffness. It should be noted that due to different axial loads and different end moment of the tested specimens, the experimental amplification factor is a case dependent quantity and calculating an average values for all specimens is just for comparison purposes.

Table 3-33: Moment amplification factors: 600S137-54 (L=12 inches)

No.		Speccimen	Specimen in the test	@ Peak load Eccentricities at the ends e_x (in.)	e_z (in.)	Eccentricities at the mid-height $e_{x\text{-Mid}}$ (in.)	$e_{z\text{-Mid}}$ (in.)	Experimental Moment amplification factor $\alpha_{z\text{-exp}}$	$\alpha_{x\text{-exp}}$	Analytical Moment amplification factor $\alpha_{z\text{-a}}$	$\alpha_{x\text{-a}}$	Comparison $\alpha_{z\text{-exp}}/\alpha_{z\text{-a}}$	$\alpha_{x\text{-exp}}/\alpha_{x\text{-a}}$
1		S600-12-ex(0)-ez(-1.0)	S600-12-1	-0.002	-1.268	-	-1.413	-	1.11	-	1.10	-	1.02
2		S600-12-ex(0)-ez(-0.5)	S600-12-19	-0.003	-0.657	-	-0.745	-	1.13	-	1.17	-	0.97
3	Minor axis	S600-12-ex(0)-ez(-0.15)	S600-12-4	0.001	-0.253	-	-0.263	-	1.04	-	1.22	-	0.85
4	bending	S600-12-ex(0)-ez(+0.15)	S600-12-5	0.001	0.113	-	0.157	-	1.38	-	1.34	-	1.04
5		S600-12-ex(0)-ez(+0.35)	S600-12-6	0.001	0.398	-	0.477	-	1.20	-	1.21	-	0.99
6		S600-12-ex(0)ez(+1.0)	S600-12-8	-0.005	1.064	-	1.128	-	1.06	-	1.10	-	0.96
7		S600-12-ex(-1.0)-ez(0)	S600-12-9	-1.009	-0.057	-1.019	-	1.01	-	1.01	-	1.00	-
8	Major axis bending	S600-12-ex(-3.5)-ez(0)	S600-12-10	-3.518	-0.020	-3.535	-	1.00	-	1.00	-	1.00	-
9		S600-12-ex(-7.5)-ez(0)	S600-12-11	-7.541	-0.006	-7.559	-	1.00	-	1.00	-	1.00	-
10		S600-12-ex(-1.5)ez(+0.1)	S600-12-2	-1.512	0.123	-1.523	0.153	1.01	1.24	1.01	1.21	1.00	1.03
11		S600-12-ex(-5.0)-ez(+0.34)	S600-12-13	-5.021	0.386	-5.033	0.428	1.00	1.11	1.00	1.08	1.00	1.03
12		S600-12-ex(-0.8)-ez(+0.17)	S600-12-14	-0.821	0.205	-0.827	0.252	1.01	1.23	1.01	1.23	1.00	1.00
13	Bi-axial	S600-12-ex(-3.0)-ez(+0.6)	S600-12-15	-3.017	0.736	-3.003	0.780	1.00	1.06	1.00	1.10	0.99	0.97
14	bending	S600-12-ex(-1.5)ez(-0.1)	S600-12-16	-0.819	-0.210	-0.823	-0.225	1.01	1.07	1.01	1.20	1.00	0.89
15		S600-12-ex(-5.0)-ez(-0.34)	S600-12-17	-3.015	-0.704	-3.022	-0.769	1.00	1.09	1.00	1.10	1.00	0.99
16		S600-12-ex(-0.8)-ez(-0.17)	S600-12-3	-1.511	-0.131	-1.519	-0.129	1.01	0.99	1.01	1.20	1.00	0.82
17		S600-12-ex(-3.0)-ez(-0.6)	S600-12-20	-5.019	-0.376	-5.031	-0.386	1.00	1.03	1.00	1.10	1.00	0.94
							Average	1.00	1.12	1.01	1.17	1.00	0.96
							Standard deviation	0.00	0.11	0.00	0.07	0.00	0.07
							C.O.V	0.4%	9.4%	0.2%	6.4%	0.3%	7.0%

As presented in Table 3-33 to Table 3-35, the moment amplification factors for all tested specimen were also calculated using a code based analytical moment amplification factors ($\alpha_{z\text{-a}}$ and $\alpha_{x\text{-a}}$) and compared to the test result. The moment amplification factor are shown in the following equations:

$$\alpha_x = 1 - \frac{P}{P_{EX}}, \quad \text{where } P_{EX} = \frac{\pi^2 E I_X}{(K_X L_X)^2} \tag{3.9}$$

$$\alpha_Z = 1 - \frac{P}{P_{EZ}}, \quad \text{where } P_{EZ} = \frac{\pi^2 E I_Z}{(K_Z L_Z)^2} \tag{3.10}$$

where, P is the axial load on the member, P_{EX} and P_{EZ} are elastic Euler buckling loads, $I_{X,Z}$ are moments of inertia, E is the Elastic modulus, $K_X L_X$ and $K_Z L_Z$ are effective lengths. Notably, elastic buckling loads are adjusted to account for 6 in. rigid links at the ends of the specimens.

Comparing the analytical moment amplification factor to experimental results shows that the current code-based moment amplification factor can successfully estimate the moment amplifications for short and intermediate specimens, where the elastic global buckling load is much more than the applied axial load.

Table 3-34: Moment amplification factors: 600S137-54 (L=24 inches)

No.		Speccimen	Specimen in the test	@ Peak load				Experimental Moment amplification factor		Analytical Moment amplification factor		Comparison	
				Eccentricities at the ends		Eccentricities at the mid-height							
				e_x	e_z	$e_{x\text{-Mid}}$	$e_{z\text{-Mid}}$	$\alpha_{z\text{-exp}}$	$\alpha_{x\text{-exp}}$	$\alpha_{z\text{-a}}$	$\alpha_{x\text{-a}}$	$\alpha_{z\text{-exp}}/\alpha_{z\text{-a}}$	$\alpha_{x\text{-exp}}/\alpha_{x\text{-a}}$
				(in.)	(in.)	(in.)	(in.)						
1		S600-24-ex(0)-ez(-1.25)	S600-24-1	0.008	-1.565	-	-1.854	-	1.18	-	1.19	-	0.99
2		S600-24-ex(0)-ez(-0.6)	S600-24-2	0.003	-0.817	-	-1.073	-	1.31	-	1.34	-	0.98
3	Minor axis	S600-24-ex(0)-ez(-0.15)	S600-24-3	0.001	-0.283	-	-0.426	-	1.51	-	1.63	-	0.92
4	bending	S600-24-ex(0)-ez(0.15)	S600-24-6	0.003	0.245	-	0.318	-	1.30	-	1.72	-	0.75
5		S600-24-ex(0)-ez(0.6)	S600-24-5	0.002	0.775	-	0.929	-	1.20	-	1.29	-	0.93
6		S600-24-ex(0)-ez(1.25)	S600-24-4	0.002	1.421	-	1.589	-	1.12	-	1.17	-	0.96
7	Major axis	S600-24-ex(-0.85)-ez(0)	S600-24-7	-0.886	-0.003	-0.895	-	1.01	-	1.02	-	0.99	-
8	bending	S600-24-ex(-3.0)-ez(0)	S600-24-8	-3.032	-0.011	-3.060	-	1.01	-	1.01	-	1.00	-
9		S600-24-ex(-6.5)-ez(0)	S600-24-9	-6.545	-0.006	-6.587	-	1.01	-	1.01	-	1.00	-
10		S600-24-ex(-1.25)-ez(0.09)	S600-24-10	-1.270	0.112	-1.292	0.182	1.02	1.62	1.02	1.81	1.00	0.90
11		S600-24-ex(-4.5)-ez(0.3)	S600-24-11	-4.529	0.417	-4.549	0.531	1.00	1.27	1.01	1.25	1.00	1.02
12		S600-24-ex(-0.75)-ez(0.15)	S600-24-12	-0.761	0.234	-0.768	0.318	1.01	1.36	1.02	1.67	0.99	0.82
13	Bi-axial	S600-24-ex(-2.75)-ez(0.56)	S600-24-13	-2.768	0.697	-2.769	0.851	1.00	1.22	1.01	1.25	0.99	0.98
14	bending	S600-24-ex(-0.75)-ez(-0.15)	S600-24-14	-0.759	-0.258	-0.767	-0.408	1.01	1.58	1.02	1.62	0.99	0.98
15		S600-24-ex(-2.75)-ez(-0.56)	S600-24-15	-2.770	-0.714	-2.793	-0.896	1.01	1.25	1.01	1.29	1.00	0.97
16		S600-24-ex(-1.25)-ez(-0.08)	S600-24-16	-1.266	-0.169	-1.317	-0.298	1.04	1.76	1.02	1.64	1.02	1.07
17		S600-24-ex(-4.5)-ez(-0.3)	S600-24-17	-4.535	-0.388	-4.568	-0.466	1.01	1.20	1.01	1.31	1.00	0.92
18	Axial	S600-24-ex(0.0)-ez(0.0)	S600-24-18	0.003	-0.028	0.007	-0.074	-	-	-	-	-	-
19	Major	S600-24-ex(-6.5)-ez(0)	S600-24-19	-6.544	0.013	-6.585	0.058	1.01	-	1.01	-	-	-
20	Axial	S600-24-ex(0.0)-ez(0.0)	S600-24-20	0.002	-0.011	0.006	-0.030	-	-	-	-	-	-
							Average	1.01	1.35	1.01	1.44	1.00	0.94
							Standard deviation	0.01	0.19	0.00	0.23	0.01	0.08
							C.O.V	1.0%	14.2%	0.5%	15.7%	0.9%	8.6%

For long specimens that are sensitive to global buckling and the applied load is close the elastic buckling load, the analytical methods provided conservative results, especially for the specimens with small eccentricities, which are more like "columns". In most long columns having small eccentricities, the denominator of Eq. 3.9 becomes small and therefore, the factor rises up quickly. Moreover, it can be concluded that moment amplification factors are not accurate near the bifurcation buckling point.

Table 3-35: Moment amplification factors: 600S137-54 (L=48 inches)

No.		Speccimen	Specimen in the test	@ Peak load				Experimental Moment amplification factor		Analytical Moment amplification		Comparison	
				Eccentricities at the ends		Eccentricities at the mid-height							
				e_x	e_z	$e_{x\text{-Mid}}$	$e_{z\text{-Mid}}$	$\alpha_{z\text{-exp}}$	$\alpha_{x\text{-exp}}$	$\alpha_{z\text{-a}}$	$\alpha_{x\text{-a}}$	$\alpha_{z\text{-exp}}/\alpha_{z\text{-a}}$	$\alpha_{x\text{-exp}}/\alpha_{x\text{-a}}$
				(in.)	(in.)	(in.)	(in.)						
1		S600-48-ex(0)-ez(-1.5)	S600-48-1	0.003	-1.950	-	-2.817	-	1.44	-	1.40	-	1.03
2		S600-48-ex(0)-ez(-0.65)	S600-48-2	-0.001	-0.974	-	-1.683	-	1.73	-	1.83	-	0.94
3	Minor axis	S600-48-ex(0)-ez(-0.2)	S600-48-3	-0.001	-0.380	-	-0.808	-	2.13	-	2.87	-	0.74
4	bending	S600-48-ex(0)-ez(0.2)	S600-48-4	0.035	0.381	-	0.772	-	2.03	-	2.78	-	0.73
5		S600-48-ex(0)-ez(0.65)	S600-48-5	0.006	0.922	-	1.464	-	1.59	-	1.71	-	0.93
6		S600-48-ex(0)-ez(1.5)	S600-48-6	0.011	1.828	-	2.496	-	1.37	-	1.37	-	1.00
7	Major axis	S600-48-ex(-0.6)-ez(0)	S600-48-7	-0.614	-0.021	-0.649	-	1.06	-	1.06	-	1.00	-
8	bending	S600-48-ex(-2.0)-ez(0)	S600-48-8	-2.037	0.070	-2.107	-	1.03	-	1.04	-	0.99	-
9		S600-48-ex(-5.5)-ez(0)	S600-48-9	-5.560	0.014	-5.707	-	1.03	-	1.03	-	1.00	-
10		S600-48-ex(-1.0)-ez(0.07)	S600-48-11	-1.014	0.169	-1.032	0.383	1.02	2.26	1.03	4.62	0.98	0.49
11		S600-48-ex(-4.0)-ez(0.27)	S600-48-10	-4.036	0.356	-4.085	0.609	1.01	1.71	1.02	1.89	0.99	0.91
12		S600-48-ex(-0.7)-ez(0.14)	S600-48-12	-0.708	0.288	-0.712	0.618	1.01	2.14	1.03	3.24	0.98	0.66
13	Bi-axial	S600-48-ex(-2.5)-ez(0.5)	S600-48-13	-2.518	0.683	-2.534	1.121	1.01	1.64	1.02	1.69	0.99	0.97
14	bending	S600-48-ex(-0.7)-ez(-0.14)	S600-48-14	-0.706	-0.241	-0.737	-0.488	1.04	2.03	1.03	3.39	1.01	0.60
15		S600-48-ex(-2.5)-ez(-0.5)	S600-48-15	-2.528	-0.782	-2.581	-1.406	1.02	1.80	1.02	1.84	1.00	0.98
16		S600-48-ex(-1.0)-ez(-0.07)	S600-48-16	-1.016	-0.097	-1.050	-0.165	1.03	1.70	1.04	-	-	-
17		S600-48-ex(-4.0)-ez(-0.27)	S600-48-17	-4.043	-0.416	-4.168	-0.756	1.03	1.82	1.02	2.07	1.01	0.88
18	Axial	S600-48-ex(-0.0)-ez(0.0)	S600-48-18	0.000	-0.011	0.003	-0.063	-	-	-	-	-	-
			Average					1.03	1.81	1.03	2.36	1.00	0.83
			Standard deviation					0.02	0.27	0.01	0.96	0.01	0.17
			C.O.V					1.5%	14.9%	1.1%	40.5%	1.1%	20.6%

3.3 Experiments on Zee-section cold-formed beam-columns (Torabian et al. 2016b)

An experimental program including forty-three Zee-section beam-columns, 700Z225-60 (F_y=80ksi) at lengths of 12 in. and 48 in., was used to evaluate current AISI-S100-12 specification predictions for beam-column strength. This testing on Zee-section beam-column specimens complements an earlier test series on lipped channel specimens (Chapter 3 of this report) and provides an exploration of the impact of the principal axis configuration and the differing location of shear center for Zee-sections as relative to their location in lipped channels. Please find the complete detail in the following paper:

Torabian, S., Fratamico, D. C., and Schafer, B. W. (2016). "Experimental response of cold-formed steel Zee-section beam-columns." *Thin-Walled Structures*, 98, 496–517.

The results has shown, the cross-sectional applied stress distribution is the most important parameter in modulating the failure mechanisms, namely local or distortional buckling. In addition, the member ductility is strongly correlated to the degree of eccentricity in the applied axial load on the member. The comparisons of the results to the current AISI-S100-12 specification predictions for both short and long members show that existing predictions, using only linear interaction expressions for the beam-column strength, can be excessively conservative. This conservatism is particularly pronounced when the applied load creates tension on the sloping lips of the Zee-section. This is true regardless of whether the Effective Width Method or the Direct Strength Method us used for determined the isolated compression and bending strengths. This testing on Zee sections, combined with previous testing on lipped channels, provides the experimental background for developing new cold-formed steel beam-column design methods that accurately account for the applied stress distribution on the stability and strength of the section.

Chapter 4 - Direct Strength Method for of cold-formed steel beam-columns

4.1 Introduction

Design under combined actions such as axial load and bending moments is required for essentially all actual loading conditions, although in practice many members are simply handled as either beams or columns. Thin-walled cold-formed steel structural members are often sensitive to instabilities at the element scale (i.e., local buckling), the cross-section scale (i.e., distortional buckling), and the member scale (i.e. global buckling). Current design specifications such as the North American Specification of the American Iron and Steel Institute (AISI-S100-16) and the Australian/New Zealand Standard (AZ/NZS) for cold-formed steel structures (AS/NZS-2005) formally provide the traditional Effective Width Method (EWM) and the Direct Strength Method (DSM) to determine the axial load and bending moment capacities (AISI 2016; Schafer 2008; Standards Australia 2005). The combined effect of the actions on the member is taken into account through a simple linear combination of the isolated pure axial or flexural design previously determined using EWM or DSM. Note, in the past, EWM was implemented under the actual stress distribution resulting from combined actions on the member and a satisfactory correlation with experimental results was observed (Loh 1985; Miller and Pekoz 1994; Pekoz 1986). However, it was concluded that the iterative approach required to obtain the results was too tedious for design purposes, and therefore a simpler and more conservative approach, including a linear interaction equation was adopted for design of cold-formed steel members under combined actions (Loh 1985). Continuing today, cold-formed steel beam-column design methods ignore any nonlinear interaction in the strength between axial load and bending (AISI 2016).

DSM-based design of cold-formed steel structural members does not require iteration. Cross-section stability may be taken into account through numerical analyses, such as the finite strip method, to determine the elastic buckling response of the member in local, distortional and/or global modes of failure, including interactions. The elastic buckling loads (or moments) drive a series of "direct" strength equations to determine both axial and bending moment capacity of cold-formed structural members. Although extensive efforts have been devoted to estimating the capacity of cold-formed steel members under pure axial or flexural actions (Hancock 2003; Macdonald et al. 2008; Rondal 2000; Schafer 2008; Young 2008), the design of structural members under explicit combined actions has seen less study in both EWM and DSM (Kalyanaraman and Jayabalan 1994; Loh 1985; Miller and Pekoz 1994; Pekoz 1986; Peterman 2012; Shifferaw 2010)

This chapter provides an extension to the DSM method where stability and strength of beam-columns are assessed under the actual applied stresses consistent with the actions on the member. The extensions to the DSM are developed such that they remain consistent with the current procedures for isolated axial or flexural actions. The beam-column DSM provisions proposed herein have in many situations the potential to realize significant strength increases above a linear interaction beam-column expression, and as shown herein follows the overall trends in the data well.

The sections of this chapter are organized as follows. The chapter begins with formal definition of the P-M_1-M_2 beam-column space. Followed by discussions of the yield and plastic surface that enable inelastic reserve capacity calculations for the cross-section. Then, the elastic stability of beam-columns under combined actions and the resulting elastic buckling surface for local and distortional buckling in the P-M_1-M_2 space is presented. This is followed by a brief

110

description on the philosophy and derivation of the new DSM for beam-columns. This chapter concludes by comparing the proposed DSM beam-column method against the results of experiment on lipped channels (e.g., see (Torabian et al. 2015b)) and Zee-sections (e.g., see (Torabian et al. 2016b)), and other available test results on beam-columns along with related reliability analysis and discussions.

4.2 Background

4.2.1 Direct Strength Method for P or M

The Direct Strength Method (DSM) for capacity prediction of thin-walled cold-formed steel members utilizes basic information on the yield limits of a member cross-section and the elastic stability of the same cross-section; including local, distortional, and global (Euler) buckling, to provide a prediction of member capacity. The method was developed for columns (Schafer 2002) and beams (Yu and Schafer 2006, 2003), has been adopted in national design specifications (AISI 2016). A complete review of DSM is available in Schafer (2008).

For a column, the DSM nominal strength prediction (P_n) for a member without holes may be expressed in a compact form emphasizing the role of slenderness, λ, as follows:

$$P_n = \min(P_{nG}, P_{nL}, P_{nD}) \tag{4.1}$$

$$\text{Global: } \frac{P_{nG}}{P_y} = \begin{Bmatrix} 0.658^{\lambda_G^2} & \lambda_G \le 1.5 \\ 0.877/\lambda_G^2 & \lambda_G > 1.5 \end{Bmatrix}, \ \lambda_G = \sqrt{P_y/P_{crG}} \tag{4.2}$$

$$\text{Local: } \frac{P_{nL}}{P_y} = \begin{Bmatrix} \dfrac{P_{nG}}{P_y} & \lambda_L \le 0.776 \\ \left(1 - 0.15\lambda_L^{-0.8}\right)\lambda_L^{-0.8}\dfrac{P_{nG}}{P_y} & \lambda_L > 0.776 \end{Bmatrix}, \ \lambda_L = \sqrt{P_{nG}/P_{crL}} \tag{4.3}$$

Distortional: $\dfrac{P_{nD}}{P_y} = \begin{cases} 1.0 & \lambda_D \leq 0.561 \\ \left(1 - 0.25\lambda_D^{-1.2}\right)\lambda_L^{-1.2} & \lambda_D > 0.561 \end{cases}$, $\lambda_D = \sqrt{P_y/P_{crD}}$ (4.4)

where the necessary inputs are the material yield limit or squash load (P_y) and the loads for global (P_{crG}), local (P_{crL}), and distortional (P_{crD}) elastic buckling. Note, the expressions (Eq. 4.2-4.4) are written as a function of slenderness λ_G, λ_L and λ_D to show the key role of slenderness in calculating nominal global (P_{nG}), local (P_{nL}), and distortional (P_{nD}) strength. Similarly for a beam, the DSM nominal strength prediction (M_n) for a member without holes, but including inelastic reserve, are as follows:

$$M_n = \min(M_{nG}, M_{nL}, M_{nD})$$ (4.5)

Global: $\dfrac{M_{nG}}{M_y} = \begin{cases} \dfrac{M_P}{M_y} - \left(\dfrac{M_P}{M_y} - 1\right)\dfrac{\lambda_G - 0.23}{0.37} & \lambda_G \leq 0.6 \\[2mm] \dfrac{10}{9}\left(1 - \dfrac{10}{36}\lambda_G^2\right) & 0.6 \leq \lambda_G \leq 1.336 \\[2mm] \dfrac{1}{\lambda_G^2} & \lambda_G > 1.5 \end{cases}$, $\lambda_G = \sqrt{M_y/M_{crG}}$ (4.6)

Local:

$\dfrac{M_{nL}}{M_y} = \begin{cases} 1 + \left(1 - 1/C_{yL}^2\right)\left(\dfrac{M_P}{M_y} - 1\right) & \lambda_L \leq 0.776 \\[2mm] \left(1 - 0.15\lambda_L^{-0.8}\right)\lambda_L^{-0.8} & \lambda_L > 0.776 \end{cases}$, $\lambda_L = \sqrt{M_y/M_{crL}}$, $M_{nG} > M_y$

$C_{yL} = \sqrt{0.776/\lambda_L} \leq 3$ (4.7)

$\dfrac{M_{nL}}{M_y} = \begin{cases} \dfrac{M_{nG}}{M_y} & \lambda_L \leq 0.776 \\[2mm] \left(1 - 0.15\lambda_L^{-0.8}\right)\lambda_L^{-0.8}\dfrac{M_{nG}}{M_y} & \lambda_L > 0.776 \end{cases}$, $\lambda_L = \sqrt{M_{nG}/M_{crL}}$, $M_{nG} \leq M_y$

Distortional: $\dfrac{M_{nD}}{M_y} = \begin{cases} 1 + \left(1 - 1/C_{yD}^2\right)\left(\dfrac{M_P}{M_y} - 1\right) & \lambda_D \leq 0.673 \\[2mm] \left(1 - 0.22\lambda_D^{-1}\right)\lambda_D^{-1} & \lambda_D > 0.673 \end{cases}$, $\lambda_D = \sqrt{M_y/M_{crD}}$

$C_{yD} = \sqrt{0.673/\lambda_D} \leq 3$ (4.8)

where the necessary inputs are the material yield limits in bending at first yield (M_y) and fully plastic (M_p) and the moments for global (M_{crG}), local (M_{crL}), and distortional (M_{crD}) elastic buckling. As for the columns, expressions (Eq. 4.5-4.8) are written as a function of slenderness λ_G, λ_L and λ_D to show the key role of slenderness in calculating nominal global (M_{nG}), local (M_{nL}), and distortional (M_{nD}) flexural strength. The DSM expressions provided in Eq.'s 4.1-4.8 are codified in AISI S100 (AISI 2016) and explicitly include the limit states of yielding, global buckling, local-global interaction buckling, and distortional buckling for isolated beams and columns. Slenderness in each of the buckling modes, i.e. a ratio between the elastic buckling and material yielding (provided either as a direct ratio or using the slenderness parameter λ), controls the predicted capacity.

4.2.2 Beam-column strength by interaction expressions

The traditional approach in steel design for determining the capacity of a member subjected to multiple actions is to employ an interaction expression, the simplest of which for a member under axial load and bending is the linear form:

$$\frac{P_r}{P_n} + \frac{M_r}{M_n} \leq 1 \tag{4.9}$$

where P_r and M_r are the required actions (or demands) and P_n and M_n are the available capacity, presented in Eq. 9 without consideration of reliability (i.e., load factors and/or resistance factors). A linear interaction expression similar to Eq. 4.9 is employed in the AISI S100 (AISI 2016) specification for strength determination of beam-columns. Interaction equations only utilize the "anchor points", that is the isolated column (P_n) and beam (M_n) capacity, for determining the capacity under any combination of applied demands (P_r, M_r). Implicit in the interaction equation approach is that the underlying mechanics for yielding and

elastic buckling, which form the basis for the strength prediction, follow the same interaction expression – in this case linear. The method developed herein foregoes the interaction expression in favor of an explicit approach that considers the yielding and buckling response under the actual applied actions. Cross-section specific interaction expressions can be re-constructed from the developed solution if desired for design convenience.

4.3 Explicit beam-column predictions and generalized action: β

If one examines the space defined by any combination of axial load P and bending M, the P-M space, then the same yielding and stability considerations made for isolated beams and columns may be extended to beam-columns, as depicted in Figure 4-1. A given demand, P_r and M_r, may be understood as existing in the P-M space at angle

$$\phi_{PM} = \tan^{-1}\left(\frac{M_r / M_y}{P_r / P_y}\right) \tag{4.10}$$

and magnitude

$$\beta_r = \sqrt{\left(\frac{P_r}{P_y}\right)^2 + \left(\frac{M_r}{M_y}\right)^2} \tag{14.11}$$

This same demand implies a stress on the cross-section of

$$\sigma_r = \frac{P_r}{A} + \frac{M_r y}{I} \tag{4.12}$$

where A is the cross-sectional area, y the perpendicular distance from the elastic neutral axis to any point in the cross-section, and I the moment of inertia about the axis of bending. The stability and yield limits under this applied stress distribution may be characterized in terms of β magnitudes along the angle ϕ_{PM}, i.e. β_y and β_p for yielding and plastic behaviour, and β_{crG}, β_{crD},

and β_{crL} for global, distortional, and local elastic buckling. The existing DSM provisions provide the column strength

$$P_n = f_p\left(P_{crG}, P_{crD}, P_{crL}, P_y\right) \tag{4.13}$$

where Eq. 4.1-4.4 provides f_P, and the beam strength

$$M_n = f_M\left(M_{crG}, M_{crD}, M_{crL}, M_y, M_p\right) \tag{4.14}$$

where Eq. 4.5-4.8 provides f_M. A generalized form of Eq. 4.1-4.8 is sought that instead provides capacity

$$\beta_n = f_\beta\left(\beta_{crG}, \beta_{crD}, \beta_{crL}, \beta_y, \beta_p\right) \tag{4.15}$$

where the expressions that define f_β are the subject of this chapter. The resulting design check, without reliability considerations would simply be $\beta_n \geq \beta_r$. This approach was first conceptualized by Schafer in 2006 (AISI 2006) and has been the subject of considerable research in recent years (Shifferaw 2010; Torabian et al. 2014c, 2015b)
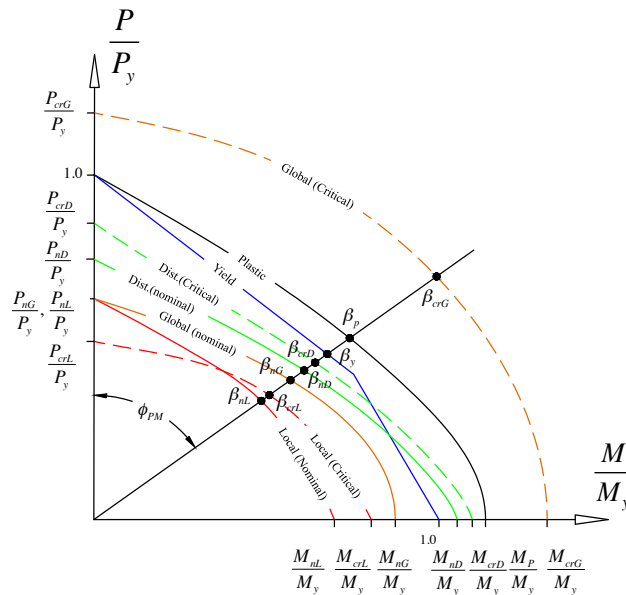
Figure 4-1: Yielding, elastic buckling, and strength curves for CFS beam-column under axial load and bending.

115

4.3.1 Generalization to P-M$_1$-M$_2$ space and β, θ$_{MM}$, φ$_{PM}$ coordinate system

In general CFS beam-columns may be unsymmetric sections and subjected to axial load and biaxial bending. Thus, the simple two-dimensional P-M space of Figure 4-1, must be generalized. A normalized P-M$_1$-M$_2$ space is utilized to define the state of the combined actions including bi-axial bending moments about principal axes (M$_1$, M$_2$) and axial load (P) normalized with respect to the corresponding first yield strength (M$_{1y}$, M$_{2y}$, and P$_y$). The coordinates in the P-M$_1$-M$_2$ space are defined as:

$$x = \frac{M_1}{M_{1y}}, \ y = \frac{M_2}{M_{2y}}, \ z = \frac{P}{P_y} \tag{4.16}$$

M$_1$ is defined as the major principal axis of bending (x in the normalized P-M$_1$-M$_2$ space), and M$_2$ as the minor principal axis of bending (y in the normalized P-M$_1$-M$_2$ space). Points in the normalized P-M$_1$-M$_2$ space are defined by an azimuth angle, θ$_{MM}$, an elevation angle, φ$_{PM}$, and a radial length β, as follows,

$$\theta_{MM} = \tan^{-1}\left(y/x\right), \ \phi_{PM} = \cos^{-1}\left(z/\beta\right), \ \beta = \sqrt{x^2 + y^2 + z^2} \tag{4.17}$$

The isolated axial load and bending moments are just points on the x, y, and z axes, and any combination of the actions can be expressed in terms of θ$_{MM}$, φ$_{PM}$, and β. θ$_{MM}$ is a measure of biaxial bending, and φ$_{PM}$ a measure of axial-bending interaction. For any θ$_{MM}$ and φ$_{PM}$, the elastic stress distribution on a given cross-section can be determined; of course β is still required to know the absolute magnitude. For example, θ$_{MM}$=0° and φ$_{PM}$=90° defines pure major (principal) axis bending, and β=1.0 implies the major axis yield moment (M$_{1y}$); θ$_{MM}$=90°, φ$_{PM}$=90°, and β=1.0 corresponds to the minor (principal) axis yield moment (M$_{2y}$); and θ$_{MM}$=[0, 2π], φ$_{PM}$=0°, and β=0.5 indicate a pure compressive stress equal to 0.5F$_y$, where F$_y$ is the material

yield stress. For a given set of demands P_r, M_{1r}, M_{2r} the angles θ_{MM} and ϕ_{PM} are set and the elastic stress on the cross-section may be determined from:

$$\sigma_r = \frac{P_r}{A} + \frac{M_{1r}y_{c2}}{I_1} + \frac{M_{2r}y_{c1}}{I_2} \tag{4.18}$$

where y_{c1} and y_{c2} are the distance to the centroidal principal axes 1 and 2, respectively; and A, I_1, and I_2 are cross-sectional area, moment of inertia about axis 1 (major principal), and moment of inertia about axis 2 (minor principal), respectively. For this stress distribution (i.e. at this angle of θ_{MM} and ϕ_{PM}) one can determine the yielding limits β_y and β_p for yielding and plastic behavior, the elastic buckling values β_{crG}, β_{crD}, and β_{crL} for global, distortional, and local elastic buckling and ultimately the strength of the section β_n as depicted in Figure 4-1 and Figure 4-2.
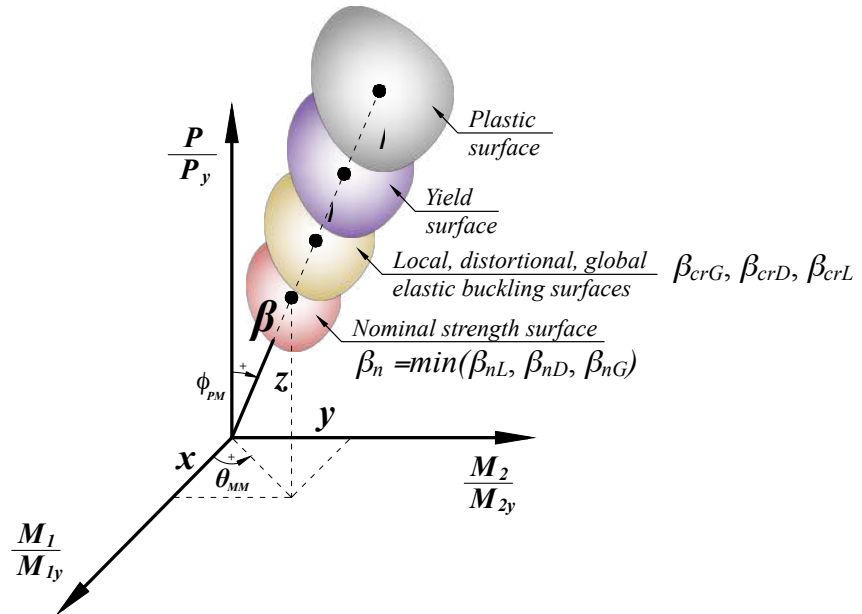
Figure 4-2: Normalized P-M_1-M_2 space and conceptual strength surfaces.

Evaluation of the strength under all combinations of θ_{MM} and ϕ_{PM} results in the strength (or interaction) surface for a given member in the three-dimensional normalized P-M_1-M_2 space.

This surface is the three-dimensional analogy to the simpler two-dimensional strength curves of Figure 4-1. This strength surface is built-up from three considerations: yielding (Section 4.3.3), cross-section stability (Section 4.3.6), and limit states-based strength determination (Section 4.4).

4.3.2 Yield and plastic response of CFS beam-columns (β_y, β_p)

4.3.3 First yield (β_y)

The state of elastic stress on the cross-section for any applied P_r, M_{1r}, M_{2r} is defined by Eq. (4.18). First yield occurs when:

$$\sigma_{r-max} = \left| \sigma_r \left(y_{c1}, y_{c2} \right) \right|_{max} = F_y \tag{4.19}$$

The β magnitude at which first yield occurs (for the specific θ_{MM} and ϕ_{PM} angle), β_y, may be found through the ratio of the maximum reference applied axial stress σ_{r-max} to F_y,

$$\alpha_y = F_y / \sigma_{r-max} \tag{4.20}$$

via:

$$\beta_y = \alpha_y \beta_r \tag{4.21}$$

where the magnitude of the applied demand, β_r, is found from Eq. 4.17. For inelastic reserve calculations, it is useful to determine the yielding strength associated with yielding in tension (t) or compression (c), separately, in this case:

$$\text{for } \sigma_r \left(y_{c1}, y_{c2} \right) \Big|_{min} < 0, \text{ then } \alpha_{yt} = -F_y / \sigma_r \left(y_{c1}, y_{c2} \right) \Big|_{min}, \text{ and } \beta_{yt} = \alpha_{yt} \beta_r \tag{4.22}$$

$$\text{for } \sigma_r \left(y_{c1}, y_{c2} \right) \Big|_{max} > 0, \text{ then } \alpha_{yc} = -F_y / \sigma_r \left(y_{c1}, y_{c2} \right) \Big|_{max}, \text{ and } \beta_{yc} = \alpha_{yc} \beta_r \tag{4.23}$$

Notably, for the cases of $\sigma_r\left(y_{c1},y_{c2}\right)\big|_{\min}\geq 0$ or $\sigma_r\left(y_{c1},y_{c2}\right)\big|_{\max}\leq 0$, the section is under tensile only or compressive only stresses, respectively.

4.3.4 Fully plastic (β_p)

The plastic capacity is an essential quantity to determine the inelastic reserve capacity of a member (Shifferaw and Schafer 2012). In beam-columns the plastic capacity of the cross-section needs to be determined at a given combination of applied axial load and bending moments. For a doubly-symmetric member the plastic neutral axis (PNA) and the elastic neutral axis (ENA) under a principal bending axis coincide and determination of plastic moments is straightforward (Figure 4-3a). However, even for a doubly symmetric member under non-principal (bi-axial) bending a more complicated plastic response occurs (Figure 4-3b).
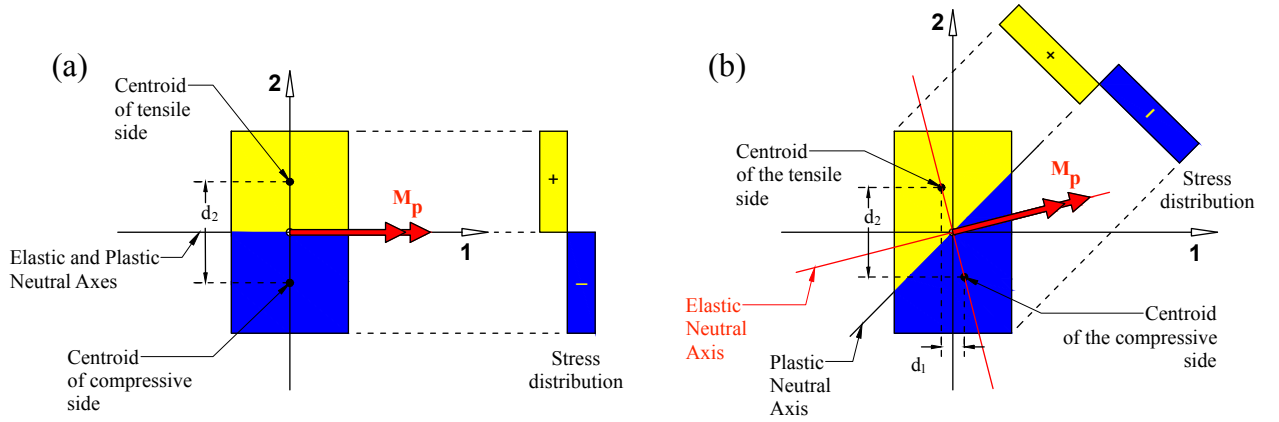
Figure 4-3: Plastic behavior of a rectangular section under, (a) major axis bending; (b) bi-axial bending. (The dark (blue) area shows yielding in compression and the grey (yellow) area shows yielding in tension)

Nonetheless, closed-form relationships for plastic surface determination is possible for doubly symmetric cross-sections such as I-sections, box-sections and tubes (Baptista 2012a; b; Baptista and Muzeau 2006, 2008); however for more general unsymmetric and complex cross-sections a numerical method for evaluating the plastic strength is inevitable (Albermani and

Kitipornchai 1990; Chan and Kitipornchait 1987; Charalampakis and Koumousis 2008; Kitipornchai et al. 1991; Papanikolaou 2012; Sfakianakis 2002).
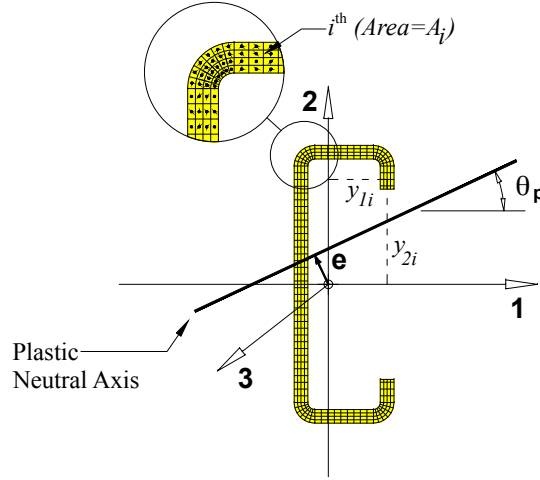
Figure 4-4: Fiber discretization of the cross-section: plastic neutral axis at angle "θ_p" and distance "e" from the centroid. (Note coordinate axes x-y have no relationship to x,y in P-M_1-M_2 space)

In this work, a relatively simple numerical procedure is implemented to determine the plastic capacity of the cross-section under combinations of P, M_1, and M_2 that cause fully plastic response in the cross-section. As shown in Figure 4-4, the cross-section to be evaluated is discretised into "fibers" both through the thickness and along the elements (strips) of the cross-section. The area of each fiber (A_i) is lumped at the center of the fiber, while the fiber cross-section location (y_{1i}, y_{2i}) is known in the principal coordinate system of the cross-section. For any arbitrary plastic neutral axis at angle θ_p ($0 \leq \theta_p \leq 2\pi$) and a perpendicular distance e from the centroid, any fiber below the neutral axis is assumed to be in compression, while the fibers above the neutral axis are in tension, and the fibers on the neutral axis have no force. These conditions can be written as follows,

$$\sigma\left(y_{1i}, y_{2i}\right) = y_{2i}\cos(\theta_p) - y_{1i}\sin(\theta_p) - e \tag{4.24}$$

$$\begin{cases} \sigma\left(y_{1i}, y_{2i}\right) > 0, & \text{then} \quad P_i = +A_i F_y \\ \sigma\left(y_{1i}, y_{2i}\right) = 0, & \text{then} \quad P_i = 0 \\ \sigma\left(y_{1i}, y_{2i}\right) < 0, & \text{then} \quad P_i = -A_i F_y \end{cases} \qquad (4.25)$$

The static equilibrium of the fiber forces implies bending moments about the principal axes (M_{1p} and M_{2p}) and axial load (P_p) that correspond to the plastic equilibrium of the section at the particular values of (θ_p and e) or (P, M_1, and M_2)

$$\begin{cases} M_{1p} = \sum_i^n P_i y_{2i} \\ M_{2p} = \sum_i^n P_i y_{1i} \\ P_p = \sum_i^n P_i \end{cases} \qquad (4.26)$$

Thus for any assumed PNA location defined by θ_p and e we find the following points on the plastic surface:

$$x_p = \frac{M_{1p}}{M_{1y}}, \ y_p = \frac{M_{2p}}{M_{2y}}, \ z_p = \frac{P_p}{P_y} \qquad (4.27)$$

$$\theta_{MM} = \tan^{-1}\left(y_p/x_p\right), \ \phi_{PM} = \cos^{-1}\left(z_p/\beta_p\right), \ \beta_p = \sqrt{x_p^2 + y_p^2 + z_p^2} \qquad (4.28)$$

Moving the neutral axis throughout the cross-section ($0 \le \theta_p \le 2\pi$) and e from 0 to the limits of the cross-section dimensions results in combinations of axial load and bending moments that correspond to the plastic surface of the cross-section. Accuracy for the plastic surface is a function of the number of fibers employed and the discretization of θ_p and e. Practically, the fiber model for plastic section determination may be based on model discretization from a finite strip model as has recently been implemented in CUFSM (Schafer and Adany 2006). It is possible to use iteration to determine β_p for a selected θ_{MM} and ϕ_{PM}, but an efficient numerical

121

procedure has not been established by the authors for this to be done directly. Instead, a grid of θ_p and e values are established and interpolation of the x_p, y_p, z_p plastic surface results is performed.

4.3.5 Examples of yield and plastic response of CFS beam-columns (β_y, β_p)

CFS members employ a relatively rich amount of different cross-sections. The first yield and fully plastic behavior (essentially β_y and β_p) of four common CFS sections: a composite back-to-back lipped channel (doubly-symmetric), a single lipped channel (singly-symmetric), zee (point-symmetric), and an eave strut (un-symmetric member) is provided in Figure 4-5. To understand the yield and plastic behaviour of these typical CFS sections slices of the developed yield surfaces are provided in the P-M_1, P-M_2, and M_1-M_2 space in Figure 4-5. The inelastic reserve between first yield and fully plastic is shaded in grey and a linear interaction expression for first yield is provided as a dashed line. Linear interaction only exists when bending is about an axis of symmetry, in all other cases even first yield requires calculation beyond a linear interaction equation. For example, a lipped channel beam-column under axial load and minor axis bending (P-M_2) has a significantly greater β_y than would be assumed by a linear interaction expression. The plastic surface can be significantly in excess of the first yield surface, particularly about the minor axis, and is nonlinear in form.
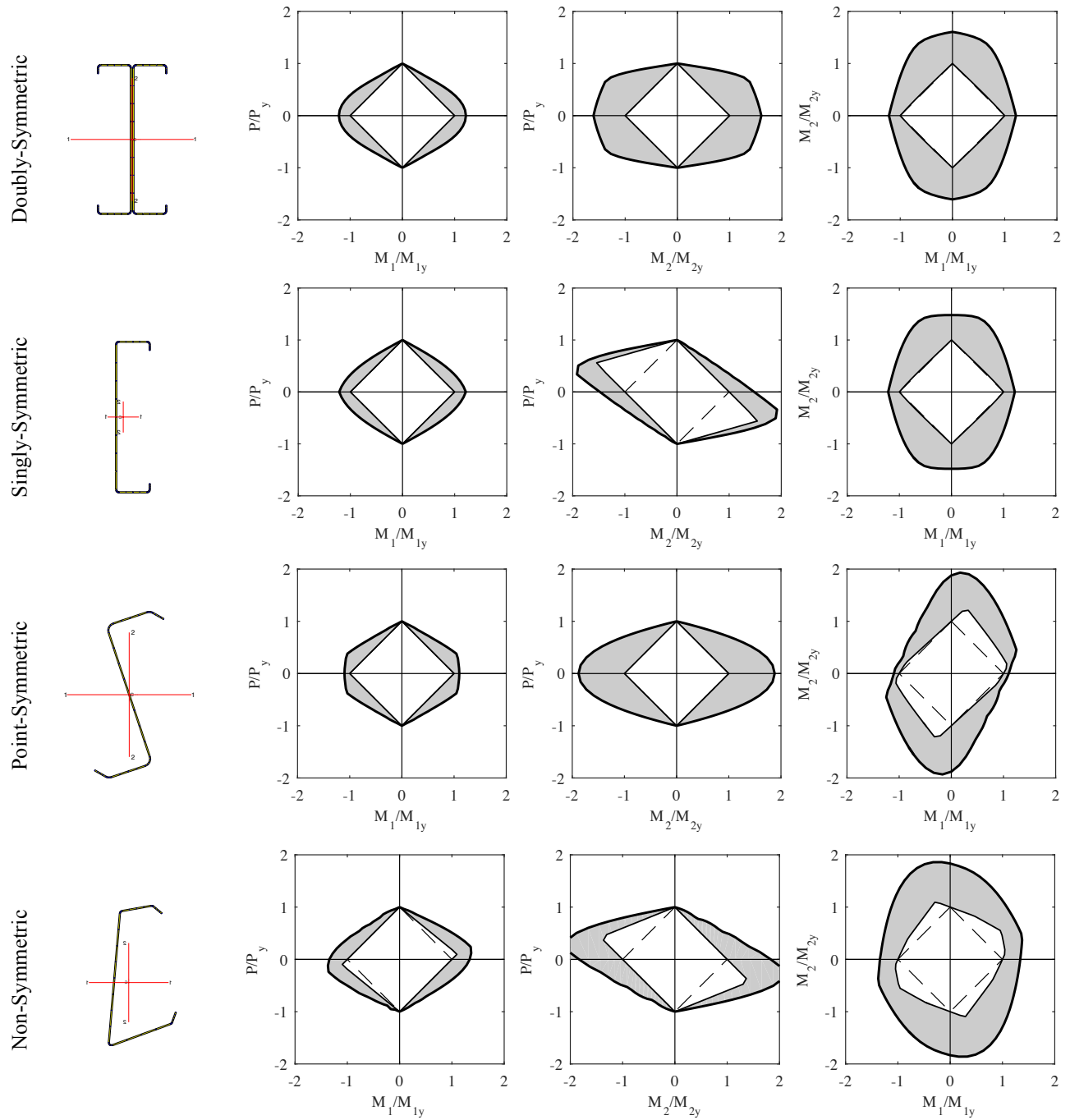
Figure 4-5: Interaction diagrams for first yield (Thin solid black line), plastic strength (solid black line) of fully effective sections, and linear interaction equation (dashed line). Shaded areas indicate the inelastic reserve between actual first yield, and the plastic surface. Calculations are performed assuming bending about principal axes. The C section has a web height of 6 in., flange width of 13.7 in., lip length of 0.5 in., and t=0.0566 in., all others drawn to scale, F_y=50 ksi.

The fully three-dimensional yield and plastic surface may also be constructed. For the lipped channel of Figure 4-5 the first yield and plastic surfaces are constructed and provided in Figure 4-6. The yield surface is a rotated pyramidion and the plastic surface is a general convex shape. These surfaces form the crucial inputs for determining the maximum capacity of a CFS member. If the member has no reductions due to local, distortional, or global buckling the plastic surface will be the capacity. Using plastic surface capacity is common in stocky hot-rolled structural steel members designed per AISC specifications. AISC seismic provisions provide width-to-thickness ratios for highly-ductile elements to enable the plastic strength and high plastic strain capacity with no strength degradation due to geometric instabilities. Nevertheless, for members with slender cross-sections the first yield surface establishes the slenderness in relation to the cross-section elastic buckling and is utilized to determined capacity. Accordingly, the nominal strength surface of the member falls inside the plastic surface and may fall even inside the first yield surface due to reductions caused by local, distortional, or global buckling, as discussed in Section 4.4.
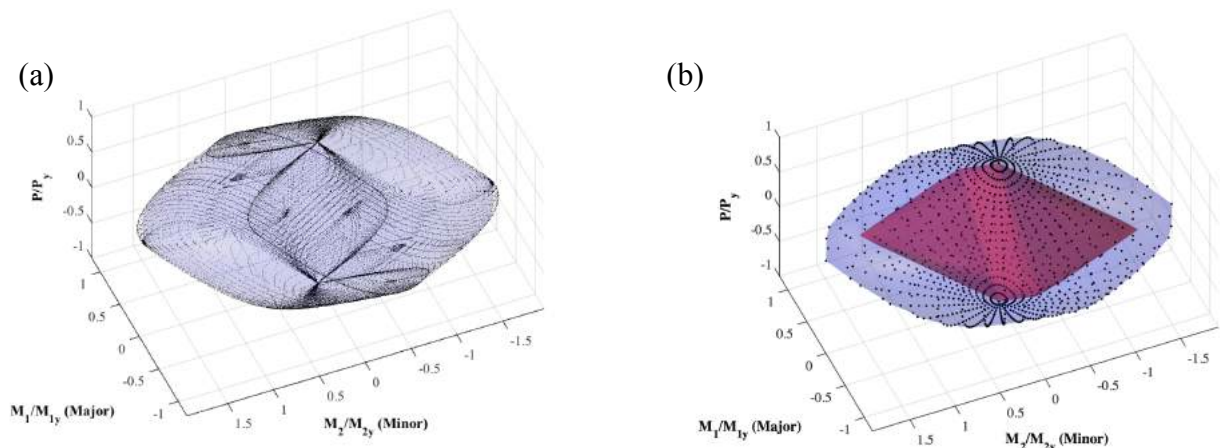
Figure 4-6: Normalized plastic surface of lipped channel section: 600S137-54. (a) Plastic point cloud; (b) plastic grid points, the plastic surface (β_p surface: blue shading), and the elastic surface (β_y surface: red shading).

4.3.6 Elastic buckling response of CFS beam-columns (β_{crL}, β_{crD}, β_{crG})

Design of thin-walled cold-formed steel members must consider local, distortional, and global (and their potential interactions) stability limits. Stability analyses pertain to the elastic critical loads of the members under a specified loading condition, but the behavior of the member is not always elastic and yielding is another key ingredient to establishing strength. The yielding limit is an upper bound strength limit that can be provided by cross-sections. Yielding also interacts with all buckling limits and results in inelastic buckling limits. DSM connects the elastic bucking limits to the strength and considers inelastic buckling and post-buckling limits via empirical expressions validated against experimental results. Accordingly, elastic buckling loads are essential inputs for DSM calculations.

Cold-formed steel members are versatile in cross-sectional shapes and providing general analytical solutions for each element of the cross-section is difficult. The effective width method is an example of a semi-analytical method that provides analytical solutions for each element based on the stress distribution and boundary conditions, but simplifying assumptions are required to handle complex cross-sections. Accordingly, numerical methods for elastic buckling loads are preferred because they work for arbitrary sections and loading conditions. Multiple numerical methods such as the Finite Element Method (FEM), Generalized Beam Theory (GBT), and Finite Strip Method (FSM) can be used to determine elastic buckling loads, but FSM and in particular the Semi-Analytical Finite Strip Method (SAFSM) and the signature curve have a foundational role in the development and represent the primary method for understanding and determining elastic buckling in CFS members.

Traditional signature curve SAFSM analysis for a column, and establishing P_{crL}, P_{crD}, and P_{crG} as would be utilized in Eq. 4.1-4.4 is provided in Figure 4-7a. Similarly, traditional signature

curve analyses for a beam, and establishing M_{crL}, M_{crD}, and M_{crG} as would be utilized in Eq 4.5-4.8 is provided in Figure 4-7b. Note that for beams and columns the results are usually provided normalized to first yield (P_y, M_{1y} or M_{2y}). This simplifies the calculation and is recommended when analysing stability under a generalized action as well.

For an arbitrary loading condition P_r, M_{1r}, and M_{2r}, one can determine the reference stress, and determine the scale factor to first yield – this is nothing more than using Eq. 4.19-4.21, i.e. scaling the reference applied stress so the maximum stress is F_y, thus resulting in β_y. Thus P_r, M_{1r}, and M_{2r} define the stress distribution and the θ_{MM} and ϕ_{PM} angles as in Section 2.4. The reference magnitude is set to first yield, β_y. Then stability analysis is conducted and β_{crL}, β_{crD}, and β_{crG} may be read directly from the results. This process has been automated in the latest version of CUFSM (Schafer and Adany 2006).

Alternatively, the stability analysis may be performed on the reference applied stress directly, in that case, cross-section stability analysis performed on σ_r (eq. 4.18) provides elastic buckling load factors for local (α_{crL}), distortional (α_{crD}), and global (α_{crG}) buckling. Using the elastic buckling load factor, elastic buckling strength under the combined actions (β_{crL}, θ_{MM}, and ϕ_{PM}) are as below:

$$\beta_{crL} = \alpha_{crL}\beta_r \tag{4.29}$$

$$\beta_{crD} = \alpha_{crD}\beta_r \tag{4.30}$$

$$\beta_{crG} = \alpha_{crG}\beta_r \tag{4.31}$$

SAFSM can have challenges with identifying buckling modes. Several methods have been proposed to resolve these challenges. The use of a surrogate constrained FSM (cFSM) model for finding the critical half-wavelength is preferred by the authors as it is shown to be

accurate and consistent with the original DSM development ("FSM@cFSM-L$_{cr}$" method as proposed after Li and Schafer 2010). cFSM curves are depicted with dashed lines in Figure 4-7 and are utilized only to find the half-wavelength at which the buckling values are determined.
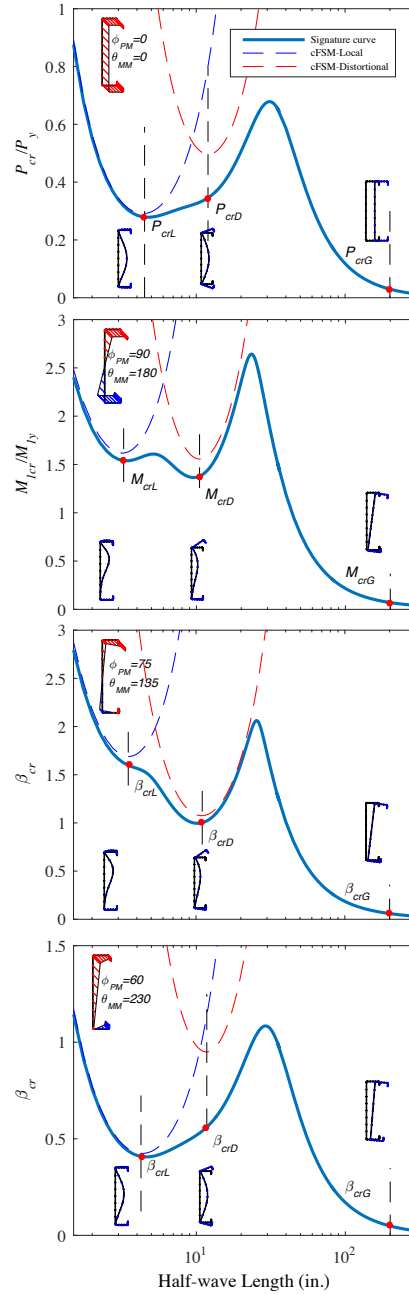
Figure 4-7: Semi-analytical finite strip method signature curves for 600S137-54 lipped channel under four different applied actions. Elastic buckling β_{crL}, β_{crD}, and β_{crG} are direct generalizations of the isolated column and beam P$_{crL}$, P$_{crD}$, and P$_{crG}$ and M$_{crL}$, M$_{crD}$, and M$_{crG}$.

Stability analyses of all possible load combinations can generate elastic buckling surfaces. θ_{MM} changes from 0° to 360° and ϕ_{PM} changes between 0° and 180°, and the stability analysis provides β_{cr} for the associated θ_{MM} and ϕ_{PM}. The examples studied for first yield and plastic capacity (see Figure 4-5) are examined here from the standpoint of cross-section stability.

Figure 4-8 shows the results of local, distortional, and global elastic stability analyses of four different cross-sections in the normalized P-M_1-M_2 space. The first yield surface is also shown as a measure of how slender the members is under any specific loading condition. Notably, the smaller the buckling load compared to the yield strength, the more slender the members are. The elastic buckling results are strongly nonlinear and not readily characterized based on their isolated compression or bending response.

Departures from linear interaction, such as the large changes possible in global buckling depending on bracing conditions, and the smaller changes for distortional buckling are possible, but not shown here. The results show the high sensitivity of the buckling loads to the stress distributions on the cross-section. For example, the distortional critical loads for a lipped channel where the lips are in tension (i.e. pure minor axis bending, where $M_2/M_{2y}>0$) is higher compared to when the lips are in compression (i.e. pure minor axis bending, where $M_2/M_{2y}<0$) (See Chapter 3 for discussion of the ramifications of this fact in testing). Similar behaviour can be seen in Zee-sections, where the minor axis bending and major axis bending counteracts each other on the lips (i.e. pure bending, where $M_1/M_{1y}>0$ and $M_2/M_{2y}>0$) is much higher compared to the case in which both minor and major axis bending impose compression on the lip (i.e. pure bending, where $M_1/M_{1y}>0$ and $M_2/M_{2y}<0$).

128
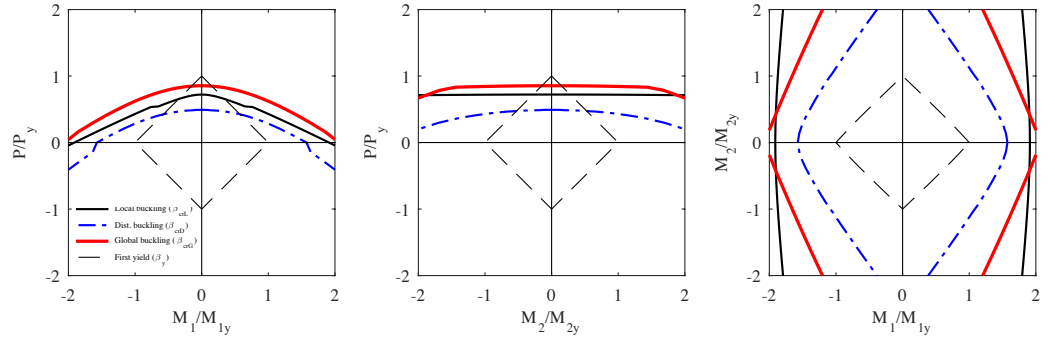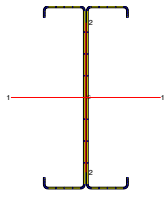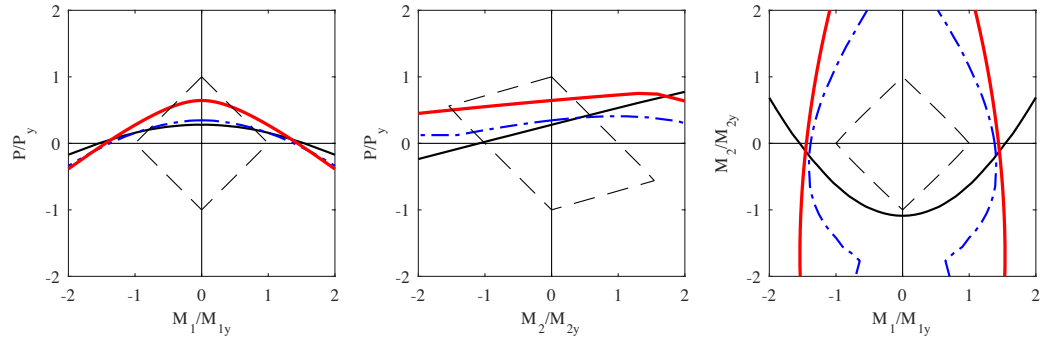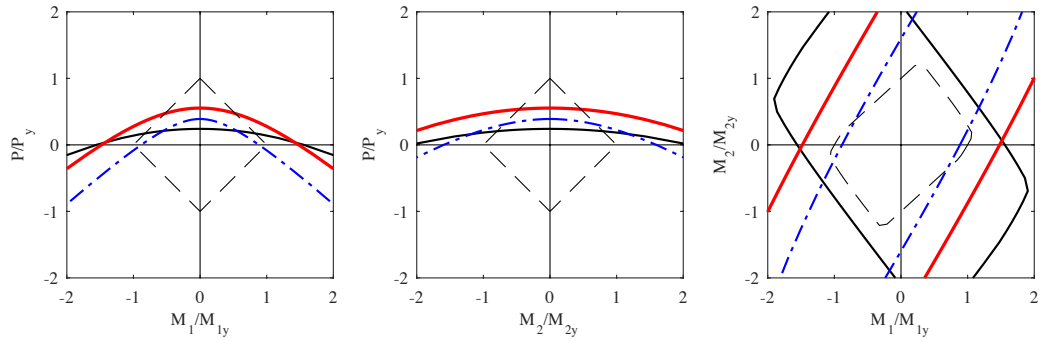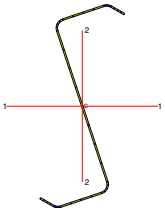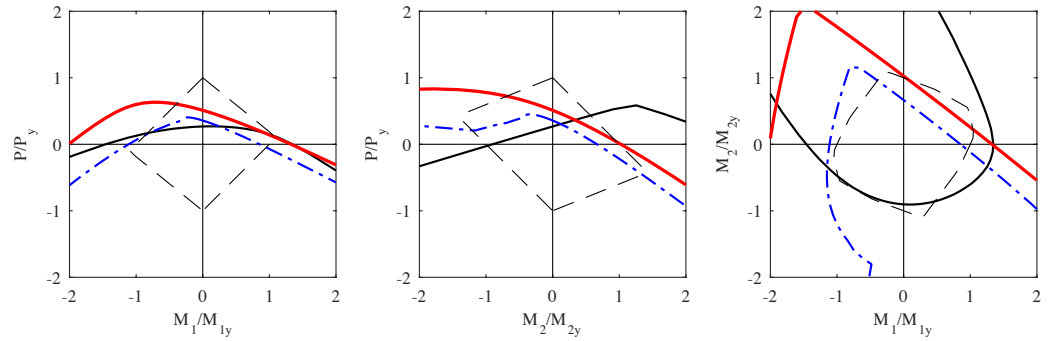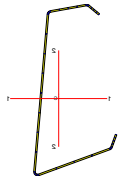
Figure 4-8: Local (thin solid line:black), distortional (dash-dot solid line:blue), global elastic buckling (L=3 ft thin solid line:red), yield (dashed thin line: black) curves for selected CFS sections. Same sections and scale as Figure 4-5.
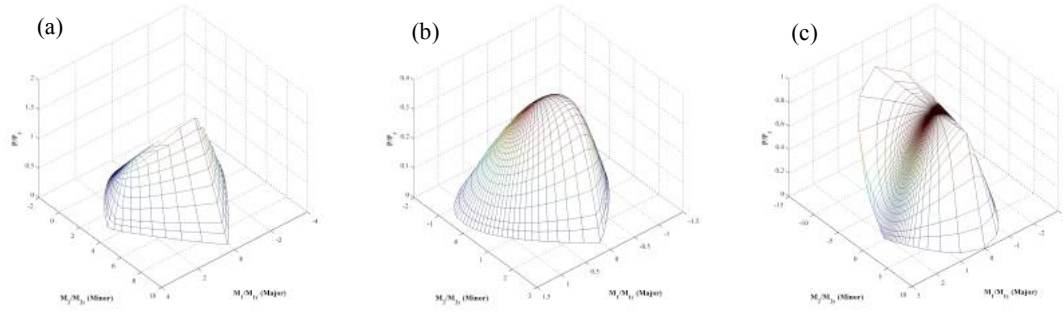
Figure 4-9: 3D elastic buckling surfaces for the same lipped channel. (a-c): Local, distortional, and global buckling (L=2 ft), respectively.

4.4 Direct strength prediction of CFS beam-columns (β_{nL}, β_{nD}, β_{nG})

The beam-column DSM formulation proposed herein is consistent with the existing DSM provisions for the design of beams and columns as provided in AISI-S100-12. The strength of isolated beams and columns may be understood as the "anchor points" in the P-M_1-M_2 space. The anchor points include pure axial compression ($\phi_{PM}=0^o$), and pure bending moments about one of the principal axes ($\phi_{PM}=90^o$; $\theta_{MM}=0^o$, 90°, 180°, 270°). In the P-M_1-M_2 space, ϕ_{PM} determines how much a given point is close to either "beam" or "column" condition and is thus used in many of the formulas in the following. All design results are represented in the β-θ_{MM}-ϕ_{PM} coordinate, where β indicates how far a loading point can be pushed along the (θ_{MM}, ϕ_{PM}) line in normalized P-M_1-M_2 space to reach a particular limit such as elastic buckling, yield, or plastic limits, as shown in Figure 4-1 and Figure 4-2.

For each loading condition such as (P-M_1-M_2) or (β-θ_{MM}-ϕ_{PM}), applied stress on the cross-section is used to determine elastic buckling loads, i.e. local (β_{crL}), distortional (β_{crD}) and global (β_{crG}) buckling loads, as explained in Section 4. The stress distribution along the (θ_{MM}, ϕ_{PM}) line is used to determine β corresponding to first yield and the plastic strength of the cross-section, β_y and β_p, respectively. As noted in Section 3, calculation of the plastic strength of the

section, β_p, may not be trivial and may need a numerical approach. The new DSM method for beam-columns provides a unified definition for members under arbitrary stress distribution and directly connects the buckling loads under applied stresses to the nominal strength of the member. Figure 4-10 schematically compares the workflow of the new DSM method to the current workflow for designing beam-columns using linear interaction equations.
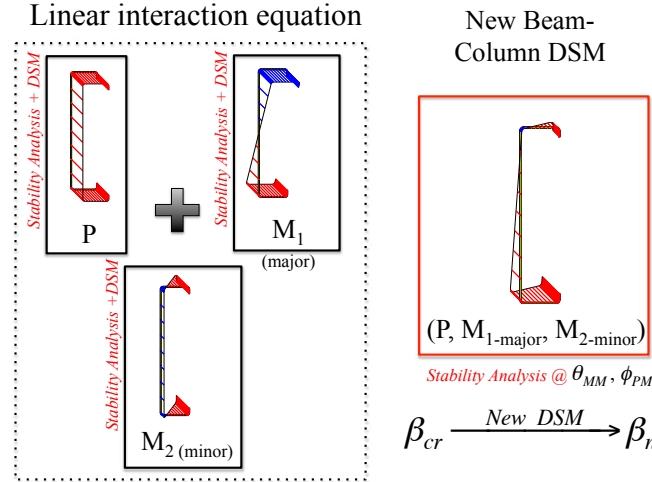
Figure 4-10: Workflow of the new DSM for beam-columns versus the

As discussed in section 2.3, a generalized form of DSM can be written as follows,

$$\beta_n = f_\beta \left(\beta_{crG}, \beta_{crD}, \beta_{crL}, \beta_y, \beta_p \right) \tag{4.32}$$

where the expressions that define f_β are directly connecting buckling (β_{crL}, β_{crD}, and β_{crG}), yield, and plastic limits to the nominal strength of the member, β_n. For the derivation here it is enforced that f_β should be consistent to the "beam" and "column" design equations (Eq. 4.1-4.8) and provide the same results at the "anchor points" in the normalized P-M_1-M_2 space (see above for definitions).

As shown in Eq.'s 4.1-4.8, the slenderness λ, the square root of the ratio between material yielding strength and the elastic buckling load, controls the predicted nominal strength. λ shows

how far buckling limits are from the yielding strength. While the slenderness at the anchor points

are $\lambda = \sqrt{P_{cr}/P_y}$ and $\lambda = \sqrt{M_{cr}/M_y}$ for beams and columns, respectively; the slenderness, for

the new beam-column DSM equations under any action in the normalized P-M$_1$-M$_2$ space is:

$$\lambda = \sqrt{\frac{\beta_y}{\beta_{cr}}}$$

(4.33)

At the anchor points, the slenderness definition in Eq. 4.33 reflects the slenderness of a

"beam" or "column", but at other loading conditions it provides a more realistic representation of

the slenderness in accordance with the existing stress distribution on the cross-section. Using the

generalized definition for beam-column nominal strength, β_n, and slenderness, λ, design

equations for each limit of buckling including global, local, and distortional buckling are

proposed in the following sections. Notably, the final form of equations including inelastic

reserve equations are provided in Section 4.7 for clarity in the following sections.

4.4.1 Global Buckling (and Yielding)

The DSM expressions for global buckling of columns (Eq. 4.2) and beams (Eq. 4.6)

establish that global slenderness can be utilized to predict strength in global buckling. If global

slenderness is generalized to:

$$\lambda_G = \sqrt{\frac{\beta_y}{\beta_{crG}}}$$

(4.34)

then the column and beam expressions can be provided in a common notation. If we

generalize the column expressions the global buckling strength equations under combined axial

load and bending can be written as follows:

Global: $\dfrac{\beta_{nG}}{\beta_y} = \begin{cases} 0.658^{\lambda_G^2} & \lambda_G \leq 1.5 \\ 0.877/\lambda_G^2 & \lambda_G > 1.5 \end{cases}$

(4.35)

and the beam expressions when generalized result in:

$$\frac{\beta_{nGM}}{\beta_y} = \begin{cases} \dfrac{\beta_P}{\beta_y} - \left(\dfrac{\beta_P}{\beta_y} - 1\right)\dfrac{\lambda_G - 0.23}{0.37} & \lambda_G \le 0.6 \\[2ex] \dfrac{10}{9}\left(1 - \dfrac{10}{36}\lambda_G^2\right) & 0.6 \le \lambda_G \le 1.336 \\[2ex] \dfrac{1}{\lambda_G^2} & \lambda_G > 1.5 \end{cases}, \; \lambda_G = \sqrt{M_y / M_{crG}} \qquad (4.36)$$

Figure 4-11 directly compares the two predictions. There is no slenderness for which the two sets of expressions provide the same capacity. For a stocky section the difference between a beam (with significant inelastic reserve) and a column (which has none) is expected, but even inelastic buckling and elastic buckling follow different strength expressions for global buckling. In part this is due to the fact that despite their general use for any global buckling (flexural, flexural-torsional, etc.) column global buckling is typically established consistent with minor-axis flexural buckling and beam global buckling is typically established from lateral-torsional buckling, so they are in a sense calibrated to different types of global buckling. However, the inclusion of a reduction for elastic buckling in the column expression, but no reduction in the beam expression reflects inconsistency in how the AISI-S100 Specification handles global buckling. Nonetheless, it is desired to keep the pure column and beam "anchor" point predictions unchanged and thus these differences must be bridged.
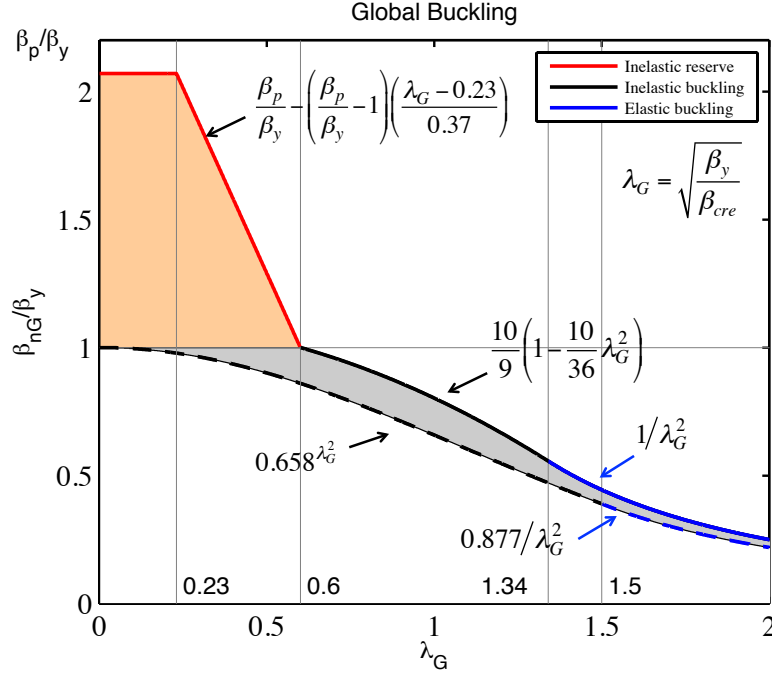
Figure 4-11: DSM for beam-columns: Global Buckling

The nominal capacity, β_{nG}, in the new beam-column DSM formulation is proposed as a function of the nominal capacity in axial compression, β_{nGP}, and the nominal flexural capacity, β_{nGM}, including inelastic reserve, as follows,

$$\beta_{nG} = \beta_{nGP} + (\beta_{nGM} - \beta_{nGP})\, \gamma(\phi_{PM}) \tag{4.37}$$

where, $\gamma\,(\phi_{PM})$ is a transfer function typically between 0 and 1 that bounds the nominal capacity between the "beam" and "column" expressions. This function must satisfy the following boundary conditions to ensure consistent results at the anchor points,

$$\begin{cases} \beta_{nG} = \beta_{nGP}, & \text{where } \gamma(0°,180°) = 0 \\ \beta_{nG} = \beta_{nGM}, & \text{where } \gamma(90°) = 1 \end{cases} \tag{4.38}$$

Accordingly, a valid transfer function of the form

$$\gamma(\phi_{PM}) = 1 - \left(1 - \sin(\phi_{PM})\right)^{i} \tag{4.39}$$

is selected, where, i is a number greater than 1. For the case of i=1 the transfer function is simply a sine function. In addition, the transfer function can be assumed to be a linear function of ϕ_{PM} (i.e. $\alpha(\phi_{PM}) = 2\phi_{PM}/\pi$). Different transfer functions are considered and evaluated versus experimental results in Section 6. The exponent i is assumed to be 1, 2, and 10 in transfer functions γ_1 to γ_3, respectively, and a linear transfer function γ_4 are considered as follows,

$$\gamma_1(\phi_{PM}) = \sin(\phi_{PM}) \tag{4.40}$$

$$\gamma_2(\phi_{PM}) = 1 - \left(1 - \sin(\phi_{PM})\right)^2 \tag{4.41}$$

$$\gamma_3(\phi_{PM}) = 1 - \left(1 - \sin(\phi_{PM})\right)^{10} \tag{4.42}$$

$$\gamma_4(\phi_{PM}) = 2\phi_{PM}/\pi \tag{4.43}$$
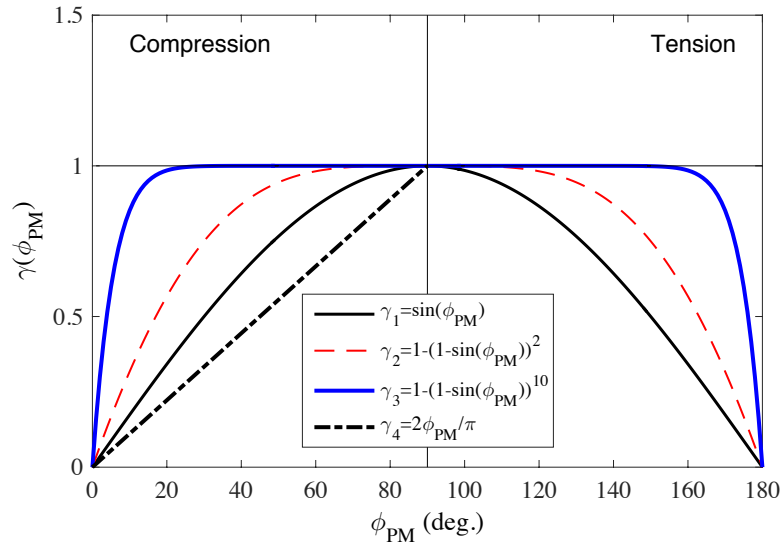
Figure 4-12: Transfer functions.

Figure 4-12 shows all transfer functions for comparison. Using higher i values results in higher transfer function values for a wider range of ϕ_{PM}, practically that means using the "beam" equations more than the "column" equations. As shown, both yield and plastic surfaces could

provide values greater than 1.0, corresponding to nominal strengths even higher than the "beam" equations.

4.4.2 Local Buckling (and Local-Global Interaction)

Consistent with the DSM method in AISI-S100, local-global interaction is adopted in the proposed beam-column DSM. The nominal capacity of beam-columns in local buckling, β_{nL}, can be determined here as a function of local slenderness λ_L, defined as follows:

$$\begin{cases} \lambda_L = \sqrt{\beta_{nG}/\beta_{crL}} & \beta_{nG} \leq \beta_y \\ \lambda_L = \sqrt{\beta_y/\beta_{crL}} & \beta_{nG} > \beta_y \end{cases} \tag{4.44}$$

As local buckling equations for "beams" and "columns" are of the same format in DSM, the new equations for beam-column DSM also provide a consistent set of equations including local-global interaction and inelastic reserve as follows (see eqs. 1.2.1-5, and 1.2.1-6 for columns and 1.2.2-7, and 1.2.2-8 for beams in AISI-S100-16 (AISI 2016)),

$$\frac{\beta_{nL}}{\beta_y} = \begin{cases} 1.0 & \lambda_L \leq 0.776 \\ \left(1 - 0.15\lambda_L^{-0.8}\right)\lambda_L^{-0.8} & \lambda_L > 0.776 \end{cases} , \lambda_L = \sqrt{\beta_y/\beta_{crL}}, \ \beta_{nG} > \beta_y$$

$$\frac{\beta_{nL}}{\beta_y} = \begin{cases} \dfrac{\beta_{nG}}{P_y} & \lambda_L \leq 0.776 \\ \left(1 - 0.15\lambda_L^{-0.8}\right)\lambda_L^{-0.8}\dfrac{\beta_{nG}}{P_y} & \lambda_L > 0.776 \end{cases} , \lambda_L = \sqrt{\beta_{nG}/\beta_{crL}}, \ \beta_{nG} \leq \beta_y \tag{4.45}$$
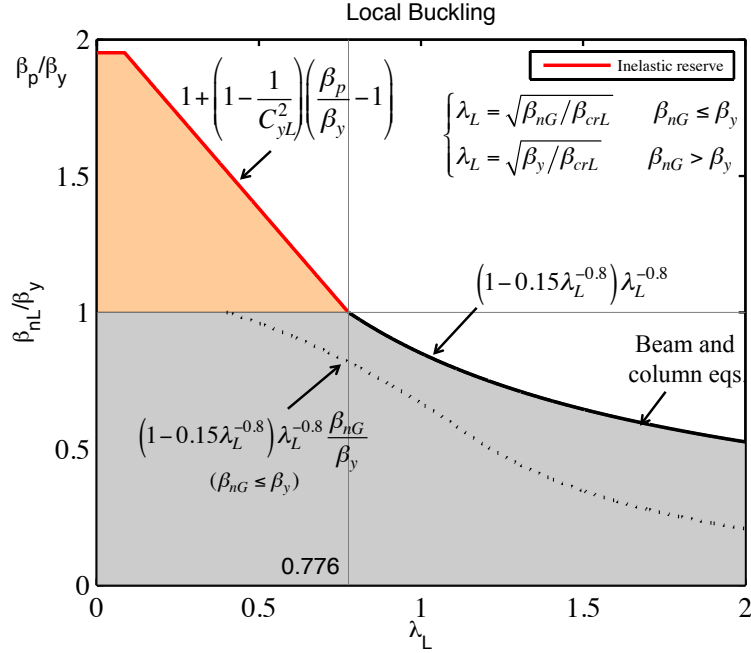
Figure 4-13: DSM for beam-columns: Local Buckling

Figure 4-13 illustrates the proposed local buckling strength equations. The inelastic reserve capacity is adopted from the inelastic reserve capacity of beams in (Shifferaw and Schafer 2012) and the details are addressed in Section 4.7.

4.4.3 Distortional Buckling

Consistent with the DSM method in AISI-S100-16, distortional-global interaction is ignored in the proposed beam-column DSM. The nominal capacity of beam-columns in distortional buckling, β_{nD}, is determined here as a function of distortional slenderness λ_D, calculated as follows:

$$\lambda_D = \sqrt{\frac{\beta_y}{\beta_{crD}}} \tag{4.46}$$

As distortional buckling equations for "beams" and "columns" are almost similar in DSM, the new equations for beam-column DSM provides a set of equations with a slenderness

limit dependent on ϕ_{PM}. The transfer function concept discussed in Section 5.2 is adopted here to determine slenderness limits and coefficients, as follows (see eqs. 1.2.1-10, and 1.2.1-11 for columns and 1.2.2-17, and 1.2.2-18 for beams in AISI-S100-16 (AISI 2016)),

$$\frac{\beta_{nD}}{\beta_y} = \begin{cases} 1.0 & \lambda_D \le 0.561 + 0.112\gamma(\phi_{PM}) \\ \left(1 - c_1\lambda_D^{c_2}\right)\lambda_L^{c_2} & \lambda_D > 0.561 + 0.112\gamma(\phi_{PM}) \end{cases}, \lambda_D = \sqrt{\beta_y/\beta_{crD}} \tag{4.47}$$

$$c_1 = 0.25 - 0.03\gamma(\phi_{PM}), c_2 = 0.2\gamma(\phi_{PM}) - 1.2 \tag{4.48}$$
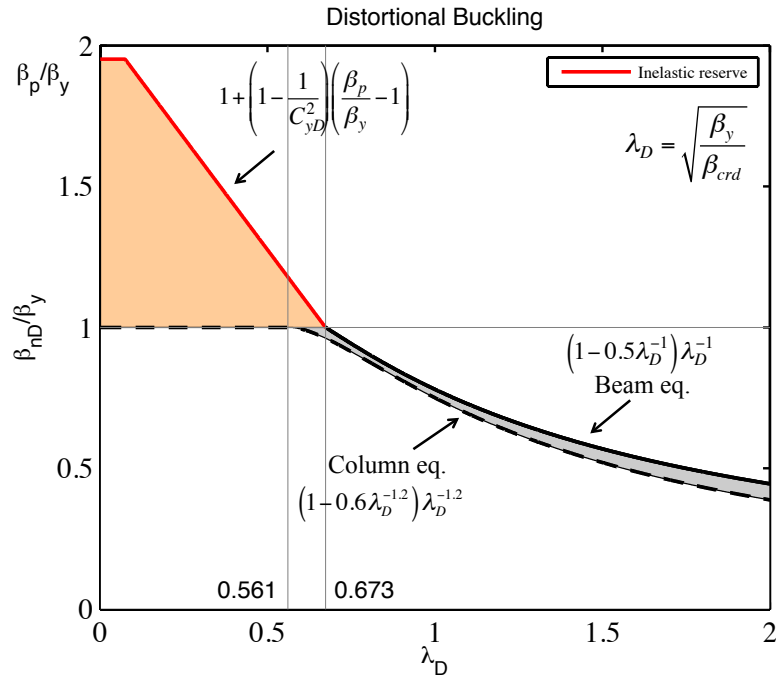
Figure 4-14: DSM for beam-columns: Distortional Buckling

shows the proposed distortional buckling strength equations versus distortional slenderness. The inelastic reserve capacity is adopted from the inelastic reserve capacity beams in (Shifferaw and Schafer 2012) and the details are provided in Section 4.7.

4.4.4 Examples of strength predictions

The examples studied for first yield and plastic capacity (see Figure 4-5) and elastic buckling analyses (see Figure 4-8) are examined here from the standpoint of nominal strength using the new DSM provided herein, using γ_1 (sine: i=1) transfer function.

Figure 4-15 shows the results of local, distortional, and global nominal strength for a doubly-symmetric (back-to-back lipped channel), singly-symmetric (lipped channel), point-symmetric (Zee-section), and non-symmetric (eave strut) cross-sections in the normalized P-M_1-M_2 space. The nominal strength of the member, the minimum of all strength limits, is shaded light grey in the figures. Comparing the nominal strength surface against the plastic surface clearly shows the effect of stability related limits on the strength and the dependency of the results on the loading conditions. In addition, the linear interaction prediction of the current AISI-S100 specifications is shown in the figures for comparison to the new DSM results and the difference is shaded grey.

For the examples studies in Section 4.3.6, the distortional nominal strength of the lip channel where the lips are in tension (i.e. pure minor axis bending, where $M_2/M_{2y} > 0$) is higher compared to when the lips are in compression (i.e. pure minor axis bending, where $M_2/M_{2y} < 0$). In the Zee-sections, counteracting minor axis bending and major axis bending (i.e. pure bending, where $M_1/M_{1y} > 0$ and $M_2/M_{2y} > 0$) results in higher strength prediction compared to the case with both minor and major axis bending imposing compression on the lip (i.e. pure bending, where $M_1/M_{1y} > 0$ and $M_2/M_{2y} < 0$). The method consistently predicts higher strengths (closer to the plastic strength surface) for all cross-sections studied here, particularly when tension on a portion of the cross-section overrides the buckling instabilities in the cross-section.
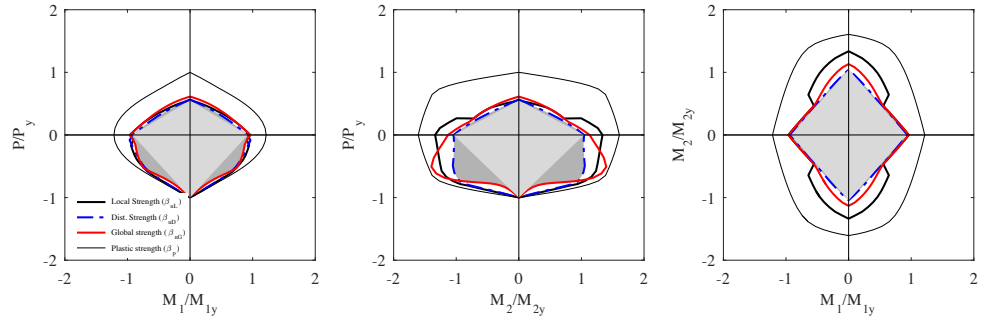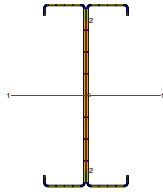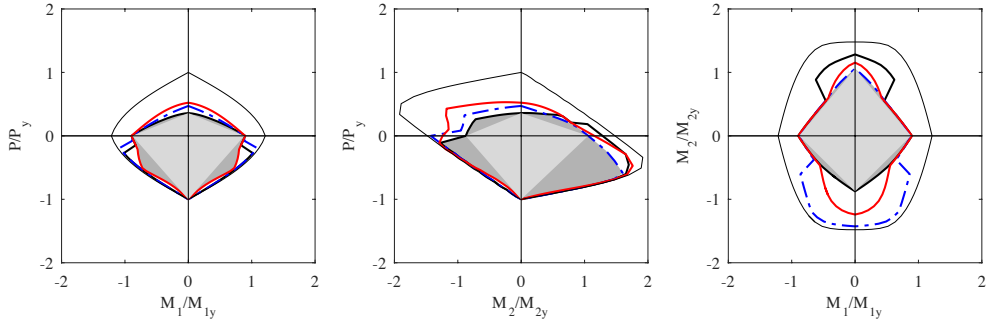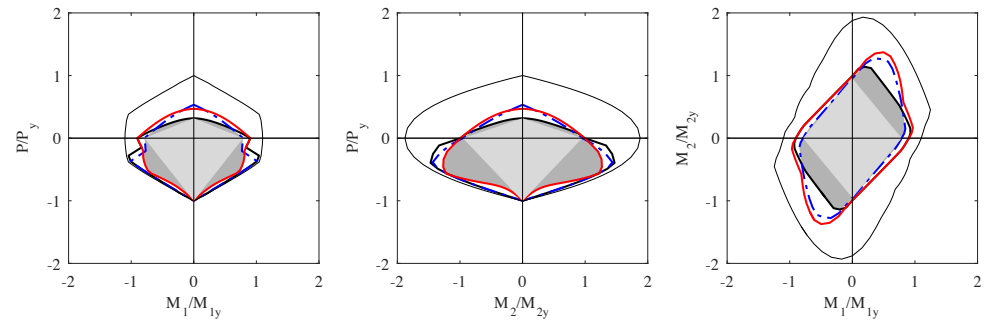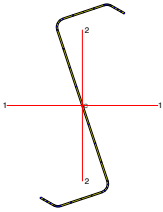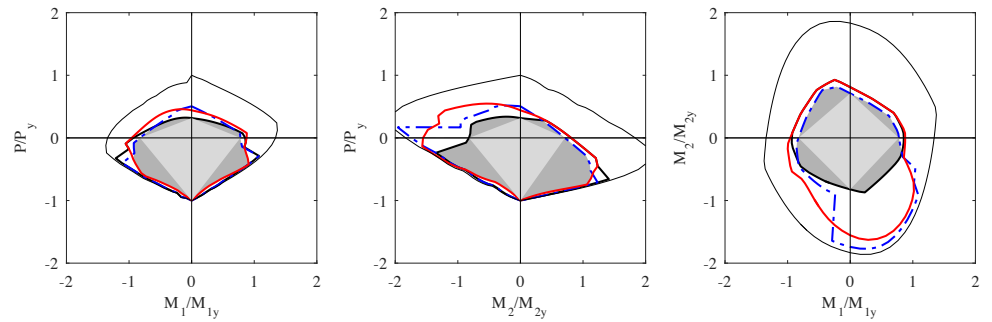
Figure 4-15: Local (solid line: black), distortional (dash-dot solid line: blue), global (L=3 ft solid line: red) nominal strength buckling, plastic (thin dashed line: black), current DSM linear interaction (light gray), and the difference between the New DSM and the linear interaction equation (dark gray) curves for selected CFS sections. Same sections and scale as Figure 4-5.

4.4.5 Design Check

The nominal capacity of a beam-column under a particular loading (θ_{MM}, ϕ_{PM}) in P-M_1-M_2 can be calculated as follows,

$$\beta_n = \min(\beta_{nL}, \beta_{nD}, \beta_{nG}) \tag{4.49}$$

For design purposes, the capacity of the member including the resistance factor ϕ in LRFD method or safety factor Ω in allowable stress design method should satisfy the following design equations,

$$\beta_r \leq \phi\beta_n \text{ or } \beta_r \leq \beta_n/\Omega \tag{4.50}$$

The resistance factor for design can be considered in either of the following two forms,

$$\phi\beta_n = \min(\phi_L\beta_{nL}, \phi_D\beta_{nD}, \phi_G\beta_{nG}), \text{ or,} \tag{4.51}$$

$$\phi\beta_n = \phi\min(\beta_{nG}, \beta_{nL}, \beta_{nD}) \tag{4.52}$$

where ϕ_L, ϕ_D, and ϕ_G are local, distortional, and global buckling resistance factors, respectively, that provides the possibility for limit state dependent ϕ's. However, using a single ϕ factor is simpler and since each mode has multiple limit states within it (yielding, inelastic buckling, elastic buckling) the use of a single ϕ factor for members is a possible simplification.

ϕ is determined using the existing resistance factors for axial forces ($\phi_P=\phi_c=0.85$, typically; or ($\phi_P=\phi_t=0.9$, typically) and bending ($\phi_P=\phi_b=0.9$, typically) and a transfer function γ as explained in Section 4.4 for LRFD design method:

$$\phi = \phi_P + \gamma(\phi_M - \phi_P) \tag{4.53}$$

and for ASD:

$$\Omega = \Omega_P + \gamma(\Omega_M - \Omega_P) \tag{4.54}$$

where $\Omega_P=\Omega_c=1.80$ (for compression, typically) and $\Omega_P=\Omega_t=1.67$ (for tension), and for bending $\Omega_P=\Omega_b=1.67$, typically.

4.5 Comparison of the new proposed DSM method against test results

4.5.1 JHU test specimens and general results

Previous experimental work by the authors characterized the failure modes and the ultimate capacity of fifty-five 600S137-54 (AISI-S200-12 nomenclature) lipped channel (Chapter 3) and forty-three 700S225-60 (similar to AISI-S200-12 nomenclature) Zee-section (Section 3.3) beam-columns under combined bi-axial bending moments and axial load (Torabian et al. 2014c, 2015b, 2016b). The lipped channel specimens were three different lengths: 12 in. (short), 24 in. (intermediate), and 48 in. (long), and the Zee-section specimens were 12 in. and 48 in. in length. As summarized in Table 6-3, comparing the experimental results to the strength predictions of both EWM and DSM in the current AISI-S100-12 demonstrates the conservatism of the current design methods in disregarding the nonlinear interaction of the applied load actions by utilizing a simple interaction equation for beam-column strength predictions,

Table 4-1: Test results on the beam-columns under combined bi-axial bending moments and axial load

| Cross-section | Designation | Length (in.) | No. of specimens | AISI-S100-12 | | | | |
| | | | | DSM | | EWM | |
				β_{Test}/β_n	C.o.V	β_{Test}/β_n	C.o.V
Lipped channel[a]	600S137-54	12	17	1.58	15.2%	1.62	10.8%
Lipped channel[a]	600S137-54	24	20	1.51	12.2%	1.45	10.0%
Lipped channel[a]	600S137-54	48	18	1.58	16.8%	1.59	17.8%
Zee-section[b]	700Z225-60	12	22	1.26	19.0%	1.21	19.0%
Zee-section[b]	700Z225-60	48	21	1.14	18.0%	1.01	21.0%

[a] see (Torabian et al. 2015b) for more details.
[b] see (Torabian et al. 2016b) for more details.

For implementing the new beam-column DSM, the elastic critical loads, yield, and plastic strength are required. The critical elastic local and distortional buckling axial load and moments were determined using SAFSM in CUFSM as explained in Section 4.4. In the buckling analyses the end boundary conditions are assumed to be clamped-clamped based on the test setup configuration in the experimental program, and the average geometric dimensions of the specimens are taken from the hand measurements. The generalized boundary condition capability in CUFSM can directly model the warping fixed end conditions (Li et al. 2011), but the results are slightly more complex to evaluate than the signature curve results. Accordingly, visual inspection of the buckling mode shapes, or using the mode classification capability of CUFSM via constrained Finite Strip Method (cFSM) may be required to identify the type of buckling. Notably, the cFSM requires sharp corner models to perform the mode classification and using round corner models may result in inaccurate results (Li and Schafer 2010). Although the clamped-clamped end conditions in the CUFSM model reasonably represents the boundary conditions for local and distortional buckling, it does not reflects the pin-pin (simple) global boundary condition. Accordingly lateral-torsional beam buckling and global elastic column buckling loads were determined using CUTWP (Sarawit 2006). For the global flexural buckling, the full length between the pins was used, but for the global flexural-torsional buckling the specimen length was used instead to consider the warping fixity at the end of the tested specimens (see (Torabian et al. 2016b) for more details).

Table 4-2(a) and (b) summarize test-to-predicted ratios and associated coefficients of variation (C.o.V), respectively, for all different test specimens and different transfer functions. The results show that the average results are not strongly correlated to the form of the transfer functions, while the average value varies between 1.159 and 1.184, and C.o.V is changing

between 15.2% and 16.3%. The closest result is provided by the simplest transfer function, $\gamma_1(\phi_{PM})=\sin(\phi_{PM})$, where the mean test-to-predicted ratio is 1.159 and the corresponding C.o.V is 16.3%. Accordingly, transfer function γ_1 seems to be simple and accurate enough to be implemented in the new beam-column DSM equations.

Table 4-2: Test-to-predicted ratio (β_{Test}/β_n) statistics of all tested specimens using different transfer functions

(a) Mean test-to-predicted ratio (β_{Test}/β_n) for different coefficients

Shape	Designation	Length (in.)	Beam equation	Column equation	Mean Test-to-predicted ratio Transfer function			
					γ_1[a]	γ_2[b]	γ_3[c]	γ_4[d]
Lipped Channel[e]	600S137-54	12	1.298	1.369	1.307	1.314	1.327	1.318
Lipped Channel[e]	600S137-54	24	1.261	1.370	1.284	1.294	1.311	1.298
Lipped Channel[e]	600S137-54	48	1.059	1.200	1.080	1.091	1.115	1.098
Zee-Section[f]	700Z225-60	12	1.188	1.217	1.197	1.201	1.206	1.202
Zee-Section[f]	700Z225-60	48	0.923	1.021	0.948	0.963	0.981	0.964
	Mean (all 98 specimens)		1.141	1.229	1.159	1.168	1.184	1.172

(b) Test-to-predicted ratio (β_{Test}/β_n) C.o.V (%) for different transfer functions

Shape	Designation	Length (in.)	Beam equation	Column equation	Test-to-predicted ratio C.o.V. Transfer function			
					γ_1[a]	γ_2[b]	γ_3[c]	γ_4[d]
Lipped Channel	600S137-54	12	12.8	12.4	12.6	12.5	12.3	12.4
Lipped Channel	600S137-54	24	9.5	8.5	9.4	9.5	9.3	9.3
Lipped Channel	600S137-54	48	12.3	9.8	12.5	12.8	12.0	12.2
Zee-Section	700Z225-60	12	12.0	11.7	11.9	11.8	11.8	11.8
Zee-Section	700Z225-60	48	10.8	12.7	12.2	12.8	12.7	12.3
	C.o.V (all 98 specimens)		16.6	15.2	16.3	16.2	15.8	16.0

[a] $\gamma_1(\phi_{PM})=\sin(\phi_{PM})$
[b] $\gamma_2(\phi_{PM})=1-(1-\sin(\phi_{PM}))^2$
[c] $\gamma_3(\phi_{PM})=1-(1-\sin(\phi_{PM}))^{10}$
[d] $\gamma_4(\phi_{PM})= 2\phi_{PM}/\pi$
[e] see (Torabian et al. 2015b) for more details.
[f] see (Torabian et al. 2016b) for more details.

Table 4-3 provides more detailed test-to-predicted ratios (β_{Test}/β_n) for all tested lipped channel and Zee-section specimens using the "sine" transfer function. The tabulated results show the distribution of the test-to-predicted ratios over the tested specimens. The loading condition of axial load and minor axis bending is underestimated by the proposed method, especially in the short specimens where the global buckling capacity is high and the behavior is controlled by

local or distortional modes. The inelastic reserve associated with the minor axis bending at the anchor points may be too conservative in the AISI design specification and the inelastic reserve which was implemented with a certain degree of built-in conservatism might need some additional modifications (Shifferaw and Schafer 2012; Shifferaw 2010; Torabian et al. 2014b) to reach better general agreement.

Table 4-3: Test-to-predicted ratio (β_{Test}/β_n) statistics for all tested specimens using "sine" transfer function

Specimen	Lipped channel (600S137-54) Length (in.)			Zee-section (700Z225-60) Length (in.)	
	12	24	48	12	48
1	1.748 [a]	1.622 [a]	1.240 [a]	1.239 [a]	1.071 [a]
2	1.448 [a]	1.334 [a]	1.067 [a]	1.378 [a]	0.866 [a]
3	1.102 [a]	1.095 [a]	0.977 [a]	1.389 [a]	1.022 [a]
4	1.471 [a]	1.276 [a]	0.828 [a]	1.192 [a]	0.957 [e]
5	1.402 [a]	1.152 [a]	0.897 [a]	1.342 [e]	0.830 [e]
6	1.388 [a]	1.197 [a]	1.022 [a]	1.318 [e]	0.868 [e]
7	1.224 [b]	1.407 [b]	1.258 [b]	1.313 [e]	1.032 [b]
8	1.143 [b]	1.190 [b]	1.207 [b]	1.295 [e]	0.851 [c]
9	1.104 [b]	1.158 [b]	1.163 [b]	1.096 [b]	0.752 [b]
10	1.322 [c]	1.432 [c]	1.071 [c]	1.043 [b]	1.077 [b]
11	1.131 [c]	1.245 [c]	1.072 [c]	0.881 [b]	0.883 [f]
12	1.372 [c]	1.347 [c]	0.905 [c]	1.080 [f]	0.799 [f]
13	1.307 [c]	1.270 [c]	0.965 [c]	0.963 [f]	1.122 [c]
14	1.196 [c]	1.209 [c]	1.034 [c]	1.158 [c]	0.964 [c]
15	1.369 [c]	1.334 [c]	1.108 [c]	1.109 [c]	1.056 [c]
16	1.273 [c]	1.263 [c]	1.318 [c]	1.344 [c]	1.109 [c]
17	1.215 [c]	1.299 [c]	1.202 [c]	1.346 [c]	0.951 [c]
18		1.305 [d]	1.110 [d]	1.243 [c]	0.874 [c]
19		1.162 [b]		1.209 [c]	0.908 [c]
20		1.384 [d]		1.188 [c]	0.808 [c]
21				1.009 [c]	1.107 [d]
22				1.197 [d]	
mean	1.307	1.284	1.080	1.197	0.948
C.o.V	12.6%	9.4%	12.5%	11.9%	12.2%
Mean (98 specimens)	1.159				
C.o.V (98 specimens)	16.3%				

[a] Minor axis bending and axial load
[b] Major axis bending and axial loads
[c] Biaxial axis bending and axial load
[d] Axial load
[e] Minor axis (geometric) bending and axial load
[f] Major axis (geometric) bending and axial load

4.5.2 Other test results in the literature

In addition to the test results recently provided by the authors on the strength of lipped channel and Zee-section CFS beam-columns, other data sets in the literature are also implemented to validate the new beam-column DSM (Loh 1982a; b, 1985; Loughlan 1979; Mulligan n.d.; Pekoz 1967; Torabian et al. 2015b, 2016b). Dividing normalized test results (β_{Test}) in the P-M_1-M_2 space by the corresponding nominal capacity (β_n), the average and the coefficient of variation (C.o.V) of test-to-predicted ratios (β_{Test}/β_n) using the "sine" transfer function are tabulated in Table 4-4. The results are provided for each data set as well as each cross-section type such as lipped channels (151 specimens), Zee-sections (43 specimens), and Hat-sections (17 specimens). The DSM predictions for lipped channel specimens are in a good agreement with the test results for almost all data sets. The predictions for Zee-sections show lower mean test-to-predicted ratios and higher C.o.V than the lipped channel specimens. Overestimating strength prediction by DSM and EWM has been also reported in Zee-section specimens by Schafer (2002). However, after Table 4-2, the selected transfer function avoids excessive overestimating of the beam-column method for Zee-sections, and provides reasonable results for all types of cross-sections. Notably, and consistent with the original DSM the proposed beam-column DSM expressions underestimate the strength of the Hat-sections (Schafer 2008).

To study the results more quantitatively, the reliability index or safety index, β_o, [note unfortunately reliability analysis also uses the greek letter β, this is not to be confused with the β in the DSM formulation and will always carry the subscript $_o$ in this report for reliability calcuations] which is a measure of the reliablity or safety of the structural member, is determined based on the available test results and the corresponding predicted results. The studied prediction

146

method is the new beam-column DSM presented herein. The reliability index is calculated using the method described in Chapter K of AISI-S100 (AISI 2016). Mean test-to-predicted ratios and the associated standard deviations for the proposed beam-column DSM are provided in Table 4-5 for all specimens.

Table 4-4: Test-to-predicted ratio (β_{Test}/β_n) of the tested beam-column in the literature

Shape	Data set	No. of tested Specimens	Test-to-predicted ratio Mean	C.o.V (%)
Lipped Channel	Torabian (2015)	55	1.244	14.0
Lipped Channel (rack)	Loh (1985)	42	1.105	11.4
Lipped Channel	Mulligan (1983)	5	1.243	11.0
Lipped Channel	Loh (1982)	23	1.155	9.4
Lipped Channel	Loughlan (1979)	26	1.003	5.2
Lipped Channels		**151**	**1.143**	**13.6**
Zee-Sections	Torabian (2016)	**43**	**1.075**	**16.7**
Hat-Section	Loh (1985)	4	1.362	6.8
Hat-Section	Pekoz (1967)	13	1.478	8.2
Hat-Sections		**17**	**1.451**	**8.5**
All		**211**	**1.154**	**15.8**

In Table 4-5, the reliability index is back-calculated for two different resistance factors; and the resistance factor is also calculated based on the target reliability of 2.5. Two resistance factors 0.85 (typical for columns) and 0.9 (typical for beams) have been investigated for the beam-column member (see more details in (Torabian et al. 2015b)).

Table 4-5: Reliability index for all tested specimens

Method	No. of specimens	Mean P_m	C.oV V_p	Reliability Index $\beta_0(\phi=0.85)$	$\beta_0(\phi=0.9)$	Resistance factor $\phi(\beta_0=2.5)$
New Beam-column Direct Strength Method	211	1.154	0.158	2.71	2.51	0.90
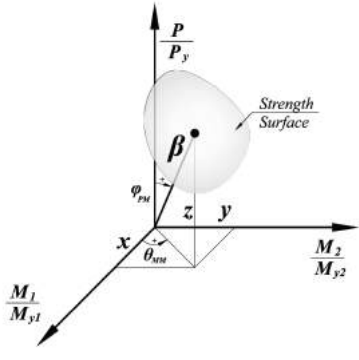
The results shows that the proposed beam-column DSM can provide the required reliability index of 2.5 as defined in Chapter K of AISI-S100-16. However, more detailed reliability analysis using a wide range of structural cross-sections via numerical models to

finalize the strength reduction factors in the design procedure is provided in Chapter 6 of this report.

4.6 Conclusions

A new design formulation that directly incorporates stability under the actual applied P-M_1-M_2 actions and inelastic reserve is proposed. The new method uses normalized P-M_1-M_2 coordinates that enables stability analysis of the cross-section under the actual stress distribution. Moreover, a unified definition of the yield and plastic surface of the cross-sections are provided in the normalized P-M_1-M_2 to be implemented in the new DSM for beam-columns. The proposed method is consistent with the current DSM method for beams and columns, but provides explicit solutions for all other loading conditions. Different sets of experimental studies have been utilized to validate the proposed method and a reasonable agreement found between beam-column DSM predictions and the experimental results. Reliability analysis of the newly proposed beam-column DSM using test results shows that the proposed method can provide a more reasonable strength prediction and meet the required reliability objectives. A set of design expressions ready for implementing in design specification is provided in Section 4.7.

4.7 Beam-Column Direct Strength Method (Compact form for specifications)

Coordinates	Coordinate transformations	
P, M_1, M_2 and $\beta, \theta_{MM}, \phi_{PM}$	$P, M_1, M_2 \rightarrow \beta, \theta_{MM}, \phi_{PM}$	$\beta, \theta_{MM}, \phi_{PM} \rightarrow P, M_1, M_2$

$$x = \frac{M_1}{M_{1y}}$$

$$y = \frac{M_2}{M_{2y}}$$

$$z = \frac{P}{P_y}$$

$$\beta = \sqrt{x^2 + y^2 + z^2}$$

$$\theta_{MM} = \tan^{-1}(y/x)$$

$$\phi_{PM} = \cos^{-1}(z/\beta)$$

$$x = \beta \cos\theta_{MM} \sin\phi_{PM}$$

$$y = \beta \sin\theta_{MM} \sin\phi_{PM}$$

$$z = \beta \cos\phi_{PM}$$

$$M_1 = xM_{1y}$$

$$M_2 = yM_{2y}$$

$$P = zP_y$$

4.7.1 Global buckling strength

Global buckling strength is determined using the global slenderness under combined action: $\lambda_G = \sqrt{\beta_y / \beta_{crG}}$

Global buckling strength, β_{nG}, is calculated using β_{nGP}, global strength using column equations, and β_{nGM}, global strength using beam equations, and combined via a sine transfer function,

$$\beta_{nG} = \beta_{nGP} + (\beta_{nGM} - \beta_{nGP}) \sin\phi_{PM} \tag{4.55}$$

4.7.1.1 Using column equation: β_{nGP}

For compressive members: $0 \leq \phi_{PM} < \pi/2$

for $\lambda_G \leq 1.5$

$$\beta_{nGP} = 0.658^{\lambda_G^2} \beta_y \tag{4.56}$$

for $\lambda_G > 1.5$

$$\beta_{nGP} = 0.877 \beta_{crG} \tag{4.57}$$

For Tensile members: $\pi/2 < \phi_{PM} \leq \pi$

$$\beta_{nGP} = \beta_y \tag{4.58}$$

4.7.1.2 Using beam equation: β_{nGM}

a) With no global inelastic reserve

for $\lambda_G \leq 0.6$

$$\beta_{nGM} = \beta_y \tag{4.59}$$

for $0.60 \leq \lambda_G \leq 1.34$

$$\beta_{nGM} = \frac{10}{9} \beta_y \left(1 - \frac{10\beta_y}{36\beta_{crG}}\right) \tag{4.60}$$

for $\lambda_G > 1.34$

$$\beta_{nGM} = \beta_{crG} \tag{4.61}$$

b) With global inelastic reserve

for $\lambda_G \leq 0.23$

$$\beta_{nGM} = \beta_p \tag{4.62}$$

for $0.23 < \lambda_G < 0.60$

$$\beta_{nGM} = \beta_p - (\beta_p - \beta_y)\frac{\lambda_G - 0.23}{0.37} \tag{4.63}$$

For $0.60 \leq \lambda_G \leq 1.34$ use section 4.7.1.1 and 4.7.1.2 (a)

4.7.2 Local buckling strength

Local buckling strength is determined using the local slenderness under combined: $\lambda_L = \sqrt{\beta_{nG}/\beta_{crL}}$

In local buckling calculations, β_{nG} is calculated with no inelastic reserve using section 4.7.1.1 and 4.7.1.2 (a), unless specified.

4.7.2.1 With no local inelastic reserve

for $\lambda_L \leq 0.776$

$$\beta_{nL} = \beta_y \qquad (4.64)$$

for $\lambda_L > 0.776$

$$\beta_{nL} = \left[1 - 0.15\left(\frac{\beta_{crL}}{\beta_{nG}}\right)^{0.4}\right]\left(\frac{\beta_{crL}}{\beta_{nG}}\right)^{0.4}\beta_{nG} \quad (4.65)$$

4.7.2.2 With local inelastic reserve

for $\lambda_L \leq 0.776$ and β_{nG} (from section 4.7.1 including inelastic reserve) $\geq \beta_y$

for sections symmetric about the axis of bending or first yield in compression

$$\beta_{nL} = \beta_y + \left(1 - 1/C_{yL}^2\right)\left(\beta_p - \beta_y\right) \qquad (4.66)$$

where, $C_{yL} = \sqrt{0.776/\lambda_L} \leq 3$ \qquad (4.67)

for sections with first yield in tension

$$\beta_{nL} = \beta_{y2c} + \left(1 - 1/C_{yL}^2\right)\left(\beta_p - \beta_{y2c}\right) \leq \beta_{yt3} \qquad (4.68)$$

$$\beta_{yt3} = \beta_y + \left(1 - 1/C_{yt}^2\right)\left(\beta_p - \beta_y\right), \ C_{yt} = 3 \qquad (4.69)$$

β_{y2c} = Strength at which yielding initiates in compression (after yielding in tension)

β_y may be used as a conservative approximation (4.70)

For $\lambda_L \leq 0.776$ use section 4.7.2.1.

4.7.3 Distortional buckling

Distortional buckling strength is determined using the distortional slenderness under combined action: $\lambda_D = \sqrt{\beta_y/\beta_{crD}}$

4.7.3.1 With no distortional inelastic reserve

$\lambda_D \leq 0.561 + 0.112\sin\phi_{PM}$

$$\beta_{nD} = \beta_y \qquad (4.71)$$

for $\lambda_D > 0.561 + 0.112\sin\phi_{PM}$

$$\beta_{nD} = \left(1 - c_1\left(\frac{\beta_{crd}}{\beta_y}\right)^{c_2}\right)\left(\frac{\beta_{crd}}{\beta_y}\right)^{c_2}\beta_y \quad (4.72)$$

where,

$$c_1 = 0.25 - 0.03\sin\phi_{PM} \qquad (4.73)$$

$$c_2 = 0.6 - 0.1\sin\phi_{PM} \qquad (4.74)$$

4.7.3.2 With distortional inelastic reserve

for $\lambda_D \leq 0.561 + 0.112\sin\phi_{PM}$ and $\beta_{nL} \geq \beta_y$

for cross-sections symmetric about the axis of bending or first yield in compression

$$\beta_{nD} = \beta_y + \left(1 - 1/C_{yD}^2\right)\left(\beta_p - \beta_y\right) \qquad (4.75)$$

where, $C_{yD} = \sqrt{\left(0.561 + 0.112\sin\phi_{PM}\right)/\lambda_{crD}} \leq 3$ \quad (4.76)

for cross-sections with first yield in tension

$$\beta_{nD} = \beta_{y2c} + \left(1 - 1/C_{yD}^2\right)\left(\beta_p - \beta_{y2c}\right) \leq \beta_{yt3} \qquad (4.77)$$

$$\beta_{yt3} = \beta_y + \left(1 - 1/C_{yt}^2\right)\left(\beta_p - \beta_y\right), \ C_{yt} = 3 \qquad (4.78)$$

β_{y2c} = Strength at which yielding initiates in compression (after yielding in tension)

β_y may be used as a conservative approximation (4.79)

For $\lambda_D > 0.561 + 0.112\sin\phi_{PM}$ use section 4.7.3.1.

4.7.4 Required actions (demands): P_r, M_{1r}, M_{2r}

$$x_r = \frac{M_{1r}}{M_{1y}}, \; y_r = \frac{M_{2r}}{M_{2y}}, z_r = \frac{P_r}{P_y} \tag{4.80}$$

$$\beta_r = \sqrt{x_r^2 + y_r^2 + z_r^2} \tag{4.81}$$

$$\theta_{MM} = \tan^{-1}\left(y_r / x_r\right) \tag{4.82}$$

$$\phi_{PM} = \cos^{-1}(z_r / \beta_r) \tag{4.83}$$

where subscript "$_r$" stands for required action that includes second order effects (P-d and P-D)

4.7.5 Cross-section Yield Strength: $\beta_y, \theta_{MM}, \phi_{PM}$

The state of stress on the cross-section can be determined as follows:

$$\sigma_r = \frac{P_r}{A} + \frac{M_{1r} y_{c2}}{I_1} + \frac{M_{2r} y_{c1}}{I_2} \tag{4.84}$$

σ_r is the required axial stress at point (y_{c1}, y_{c2}) under combined required actions P_r, M_{1r}, and M_{2r}. y_{c1} and y_{c2} are the distance to the centroidal principal axes 1 and 2, respectively; and A, I_1, and I_2 are cross-sectional area, moment of inertia about axis 1, and moment of inertia about axis 2, respectively.

Knowing the maximum required axial stress $\sigma_{r\text{-max}}$, the yielding actions ($\beta_y, \theta_{MM}, \phi_{PM}$) can be determined as follows:

$$\sigma_{r-\max} = \left|\sigma_r\left(y_{c1}, y_{c2}\right)\right|_{\max} = F_y \tag{4.85}$$

$$\alpha_y = F_y / \sigma_{r-\max} \tag{4.86}$$

$$\beta_y = \alpha_y \beta_r \tag{4.87}$$

For inelastic reserve calculations, it is required to determine the yielding strength associated with the yielding in tension or compression, separately:

for $\sigma_r(y_{c1}, y_{c2})\big|_{\min} < 0$

$$\alpha_{yt} = -F_y / \sigma_r(y_{c1}, y_{c2})\big|_{\min} \tag{4.88}$$

for $\sigma_r(y_{c1}, y_{c2})\big|_{\max} > 0$

$$\alpha_{yc} = F_y / \sigma_r(y_{c1}, y_{c2})\big|_{\max} \tag{4.89}$$

$$\beta_{yt} = \alpha_{yt} \beta_r \tag{4.90}$$

$$\beta_{yc} = \alpha_{yc} \beta_r \tag{4.91}$$

Notably, for the cases of $\sigma_r(y_{c1}, y_{c2})\big|_{\max} \leq 0$ or $\sigma_r(y_{c1}, y_{c2})\big|_{\min} \geq 0$, the section is under tensile only or compressive only stresses, respectively.

4.7.6 Cross-section Plastic Strength: $\beta_p, \theta_{MM}, \phi_{PM}$

Moving along the loading line (θ_{MM}, ϕ_{PM}) in P, M_1, M_2 will result in the full plastification of the cross-section that can be expressed as follows:

$$\beta_p = \alpha_p \beta_r \tag{4.92}$$

According to the classification mechanisms α_p will be greater than or equal to α_y and the α_p/α_y can be interpreted as the shape factor of the cross-section at θ_{MM} and ϕ_{PM} associated with the required demands. For most of the cross-sections β_p needs to be determined by numerical methods such as fiber element analysis.

4.7.7 Stability analysis under combined actions (eigen-buckling): $\beta_{cr}, \theta_{MM}, \phi_{PM}$

Cross-section stability analysis performed on σ_r provides elastic buckling load factors for local (α_{crL}), distortional (α_{crD}), and global (α_{crG}) buckling. Using the elastic buckling load factor, elastic buckling strength under the combined actions ($\beta_r, \theta_{MM}, \phi_{PM}$) are as below:

$$\beta_{crL} = \alpha_{crL} \beta_r \tag{4.93}$$
$$\beta_{crD} = \alpha_{crD} \beta_r \tag{4.94}$$
$$\beta_{crG} = \alpha_{crG} \beta_r \tag{4.95}$$

4.7.8 Nominal strength and design check

4.7.8.1 Nominal strength under combined actions

Nominal strength under combined action is the least nominal strength of the member in local, distortional and global buckling, as follows,

$$\beta_n = \min\left(\beta_{nG}, \beta_{nL}, \beta_{nD}\right) \tag{4.96}$$

4.7.8.2 Resistance factors (and safety factors)

Resistance factor, ϕ, is determined using θ_{MM} and ϕ_{PM},

for LRFD
$$\phi = \phi_P + (\phi_M - \phi_P)\sin\phi_{PM} \tag{4.97}$$
$$\tag{4.98}$$

for ASD
$$\Omega = \Omega_P + (\Omega_M - \Omega_P)\sin\phi_{PM} \tag{4.99}$$
$$\tag{4.100}$$

4.7.8.3 Design check

for LRFD
$$\beta_r \le \phi\beta_n \tag{4.101}$$
for ASD
$$\beta_r \le \beta_n/\Omega \tag{4.102}$$

Chapter 5 - Nonlinear finite element modeling of lipped channel cold-formed steel beam-columns

Commercial finite element programs using shell elements have been proven to provide a means for realistic collapse simulation of cold-formed steel structural members. Considering the labor and time consumption of experimental work, it is more efficient to expand the test database by using finite element analysis. However, attention must be paid to all the input parameters when using these programs to make sure one generates a robust and reliable model prediction.

This chapter first presents the key parameters used in the finite element modeling, and explores the sensitivity of the computational result to these parameters. Second, a comparatively simple model is employed to do Eigen buckling analysis, and the result is compared with predictions from CUFSM. The objective of this part is to make sure the Eigen buckling load from CUFSM is exact enough to be used in DSM formulae for beam-columns. Third, a nonlinear model for the collapse analysis of the members is verified by using the test results in Chapter 3. The validated model is then used to generate predictions of the load capacity of beam-columns with different eccentricities in Chapter 6, which are subsequently compared with the predictions of AISI-S100-12.

5.1 Finite element Modeling

The shell element model is built in the commercial software ABAQUS with the help of the finite strip software CUFSM [14]. CUFSM is used to generate imperfections for the finite element model. Several parameters that affect the behavior of the finite element model, such as mesh density, geometric imperfections, and residual stresses, are discussed. All these parameters are embedded in a custom MATLAB code to perform parametric study on the beam-columns as detailed in Chapter 6.

5.1.1 Geometric modeling: CUFSM to ABAQUS

Two types of geometric dimensions are used here: nominal, and actual (measured). The nominal geometric dimensions are those given by the producer of the cold-formed steel members, and the actual geometric dimensions are the average of those taken from measurements. Table 5-1 shows the cross-section dimensions with the symbols defined in Figure 5-1. It should be noted that all dimensions are measured at the mid-thickness (Mid-thickness dimensions are needed for modeling, but are not the same as commonly reported out-to-out dimensions).

Table 5-1: Cross section geometry dimensions used in finite element analysis

Parameters	Nominal dimensions	Measured dimensions		
		L=12 inches	L=24 inches	L=48 inches
H/ inches	5.943	5.946	5.943	5.952
t/ inches	0.057	0.056	0.058	0.056
B_1/ inches	1.319	1.358	1.371	1.364
B_2/ inches	1.319	1.278	1.269	1.267
D_1/ inches	0.347	0.344	0.333	0.331
D_2/ inches	0.347	0.372	0.369	0.371
R_{B1}/ inches	0.113	0.117	0.104	0.109
R_{B2}/ inches	0.113	0.110	0.109	0.121
R_{T1}/ inches	0.113	0.128	0.128	0.125
R_{T2}/ inches	0.113	0.167	0.174	0.173
θ_{B1}/deg	90.00	89.72	89.96	90.61
θ_{B2}/deg	90.00	89.67	89.37	90.52
θ_{T1}/deg	0.00	0.54	-0.68	0.05
θ_{T2}/deg	0.00	4.67	4.58	5.68
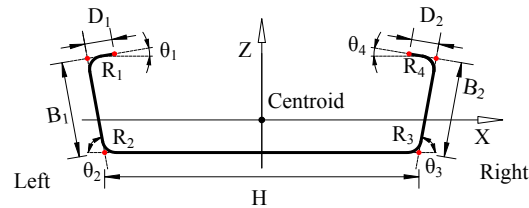
Figure 5-1: Symbol definitions of the cross section

The cross section model is first built in CUFSM and eigen buckling analysis is conducted to generate the expected imperfection modes. This is then converted to a shell element model in ABAQUS (via an input file). The pattern and magnitude of the geometric imperfections are discussed in the following section.

5.1.2 Shell element and mesh density

The ABAQUS shell element, S9R5, is used in the finite element model. S9R5 is a quadratic thin shell element using Kirchhoff's constraint. Each node of this element has five degree of freedoms (three displacement components and two in-surface rotation components) (Simulia 2007). It has been shown that this element can provide accurate predictions for thin-walled structures, and is more efficient than other alternatives: S4, S4R and S8R5 (Schafer et al. 2010). In the thickness direction, seven integration points are used when the cold roll-forming effect is ignored, and thirty-one integration points when through thickness residual stresses are modeled.

The effect of mesh density on the results is studied via a mesh sensitivity study. Five types of mesh density, termed Fine mesh, Medium mesh 1, Medium mesh 2, Medium mesh 3 and Coarse mesh (see Table 5-2, Table 5-3 and Table 5-4), are compared by using the short (L=12 inches), intermediate (L=24 inches) and long (L=48 inches) lipped channels (600S137-54) subjected to axial compression loading. These models use pin end boundary condition and 50% probability of exceedance imperfection magnitudes (Zeinoddini and Schafer 2012). The comparison focuses on the calculation time and the prediction accuracy for load capacity, as summarized in Table 5-2, Table 5-3 and Table 5-4.

155

Here we use the result from the Fine mesh as an accurate benchmark. All of the Medium meshes provide adequate prediction of the ultimate load. The Coarse mesh does not provide an accurate prediction although it saves a lot of time. In the Medium mesh, Medium 3 is the most efficient one. The final selected mesh of the short specimens, consistent with Medium 3, is shown in Figure 5-2.

Table 5-2: Mesh density studies on 12-inch long specimens subjected to axial compression

| Mesh | Number of elements | | | | | time (sec.) | $\dfrac{P_{FEM}}{P_y}$ |
	Web	Flange	Lip	Corner	Length		
Fine	30	8	5	16	120	851	0.47585
Medium 1	10	2	2	8	40	126	0.47552
Medium 2	10	2	2	4	40	72	0.47559
Medium 3	10	2	2	4	20	39	0.47593
Coarse	2	1	1	2	20	20	0.52076

Table 5-3 Mesh density studies on 24-inch long specimens subjected to axial compression

| Mesh | Number of elements | | | | | time (sec.) | $\dfrac{P_{FEM}}{P_y}$ |
	Web	Flange	Lip	Corner	Length		
Fine	30	8	5	16	240	1659	0.39608
Medium 1	10	2	2	8	80	235	0.39631
Medium 2	10	2	2	4	80	150	0.39628
Medium 3	10	2	2	4	40	71	0.39639
Coarse	2	1	1	2	40	33	0.43150

Table 5-4 Mesh density studies on 48-inch specimens subjected to axial compression

| Mesh | Number of elements | | | | | time (sec.) | $\dfrac{P_{FEM}}{P_y}$ |
	Web	Flange	Lip	Corner	Length		
Fine	30	8	5	16	480	4818	0.22487
Medium 1	10	2	2	8	160	518	0.22494
Medium 2	10	2	2	4	160	375	0.22493
Medium 3	10	2	2	4	80	179	0.22496
Coarse	2	1	1	2	80	84	0.23002
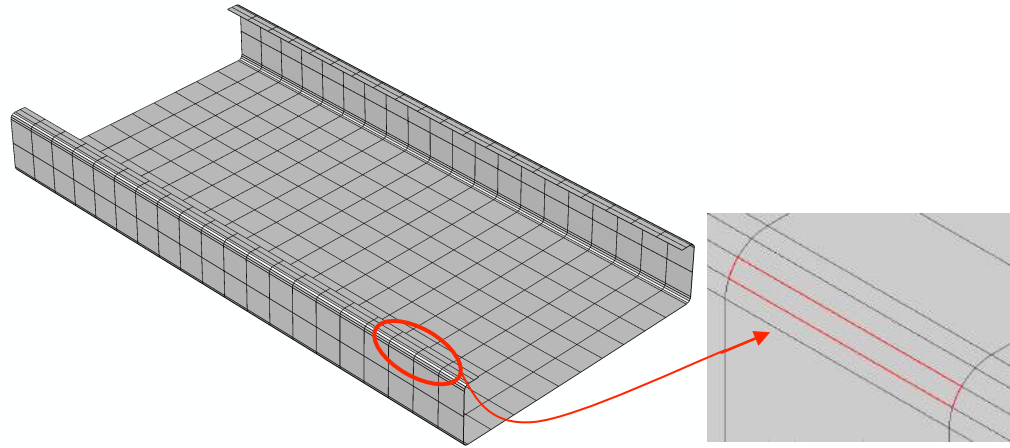
Figure 5-2: Mesh of the short specimens in finite element model

5.1.3 Boundary conditions

Figure 5-3 shows the comparison between the test setup (Chapter 3) and the finite element model. A reference node is built at the center of the clevis at each end. The coordinate of the reference point varies as different eccentricities applied to the specimens. The nodal degrees of freedoms at the end of the specimen are coupled to the reference point using a rigid body coupling. The length of the rigid link between the reference point and the end of the specimen is 6 in. in the longitudinal direction.

At the supporting end (i.e. top ref. point), all the translational degrees of freedom and the torsional degree of freedom of the reference point were constrained. At the loading end (i.e. bottom ref. point), the reference point was constrained in a similar way, except that the translational and rotational degree of freedom in the longitudinal direction were released. Concentrated force/displacement was applied at the reference point in the longitudinal direction.

157
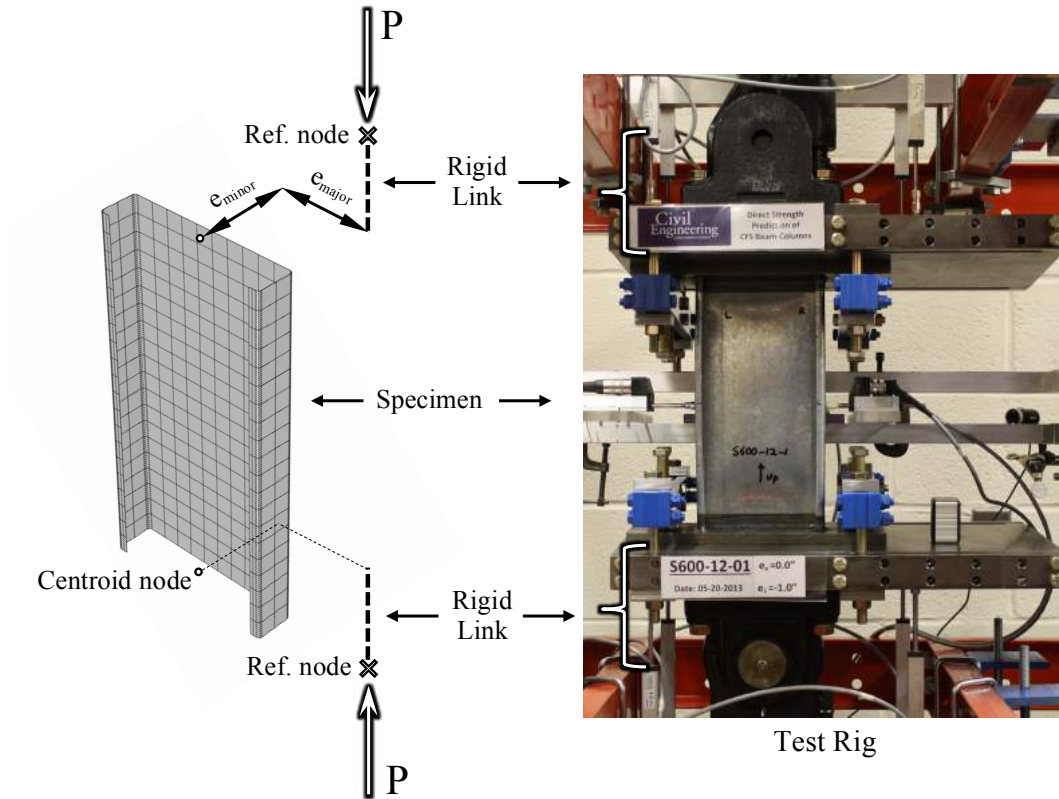
Figure 5-3: Comparison of finite element mode in ABAQUS and test setup

5.1.4 Geometric imperfection

The load capacity of thin-walled structures is sensitive to the geometric imperfection. There are two important parts in introducing the geometric imperfection: the distribution of imperfection and its corresponding magnitude.

Traditionally, buckling modes of the specimen are used as the imperfection distribution. For thin-walled members, three types of buckling modes are considered: local, distortional and global. Typical buckling modes of a lipped channel section in pure compression are shown in Figure 5-4. For short specimens, which typically do not fail in global buckling, a local buckling mode and/or distortional buckling mode imperfection should be introduced into the perfect model. For long specimens, which fail in interactive buckling, a combination of local and/or distortional, and/or global buckling mode imperfections should all be introduced into the perfect

158

model. However, using a uniform protocol, a linear combination of local, distortional, and global buckling modes of imperfection are introduced into all finite element models.

The sign of the imperfection is also important. For the local buckling mode and distortional buckling mode, the sign of the imperfection may imply flange buckling inward or outward. For global buckling, the sign of the imperfection may imply lips in tension or lips in compression buckling.

Figure 5-5 shows the signature curve of the nominal section subjected to axial compression provided by CUFSM. The local buckling half-wavelength of the 600S137-54 lipped channel is 4.33 in., and the distortional buckling half-wave length is 12.20 in. in compression. The global buckling length is equal to the length of specimen. In this report, to provide a uniform imperfection pattern, the buckling modes used for the imperfection distribution are all from axial compression eigen buckling mode shapes.
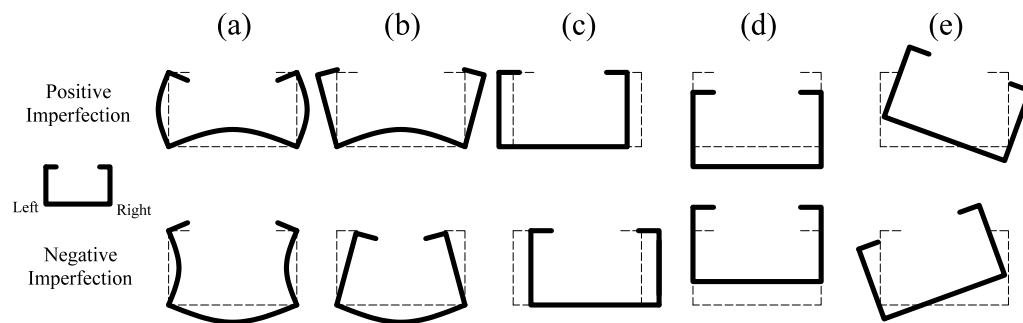
Figure 5-4: Typical buckling modes of Lipped Channel section
(a) Local, (b) Distortional, (c) Global-Camber, (d) Global-Bowl, (e) Global-Twist

The magnitude of the imperfection is studied in (Zeinoddini and Schafer 2012), where the imperfection magnitude is examined from a statistical viewpoint. The results, corresponding to 25%, 50% and 75% probability of exceedance (CDF), are shown in Table 5-5 for lipped channels. These magnitudes are used in validation of the finite element model. In this report, the

imperfection magnitudes in terms of "δ" or "Deg." corresponding to the 50% CDF (see Figure 5-5) are used as the default, where t and L depend on the specimens.

For global bow and camber, the maximum displacement is at the mid-height of the specimen, and the imperfection goes to zero at the end of the specimens by a sine function. For the global twist buckling mode, it is assumed the shape of the cross-section does not change, but rotates about the centroid. During the installation of the specimens in the test rig, the specimens were placed parallel to the loading machine with no rotation at the mid-height, but the ends were allowed to not be necessarily parallel to the machine due to the possible imperfections. Similarly, the cross-section in the simulations is not rotated at the mid-height, but the cross-section is rotated about the centroid to a specified degree ("Deg.") using a sine function. Fig. 9 shows the global twist buckling mode used in the simulations. The relative local rotation of the two ends are supposed to be in "Deg." as calculated per Table 5-5 (implemented as Deg./2 at each end, but in opposite directions with 0 Deg. at the mid-height.)

It should be noted that the distribution, magnitude, and sign of the imperfection are firmly related to the manufacturing of the specimens. So these parameters may vary along with different batches of specimens.

Table 5-5: Imperfection magnitudes δ or Deg. from (Zeinoddini and Schafer 2012)

CDF	Local (δ/t)	Distortional (δ/t)	Bowl (L/δ)	Camber (L/δ)	Twist (Deg/m)
25%	0.17	0.43	4755	6295	0.20
50%	0.31	0.75	2909	4010	0.30
75%	0.54	1.14	1659	2887	0.49
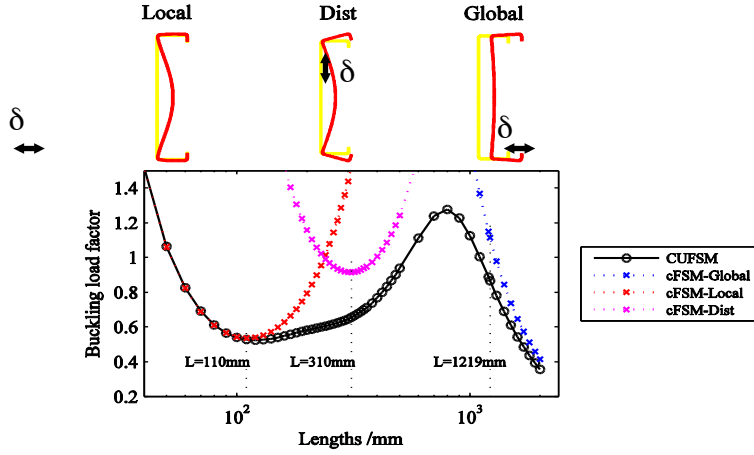
Figure 5-5: Signature curve of the nominal section: 600S137-54 lipped channel
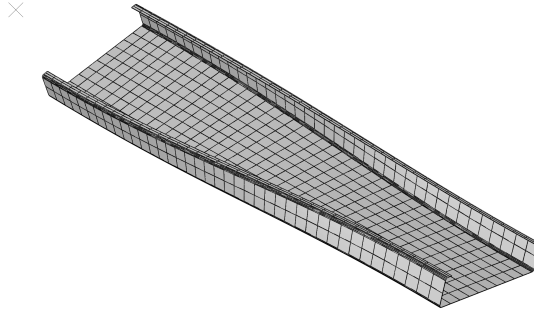
Figure 5-6: Global twist buckling mode (L=24 inches)

5.1.5 Material Model

In Chapter 3, the engineering stress-strain curve has already been obtained through tensile test. However, material properties inputted in ABAQUS use a plastic true stress-true strain curve. Equation 5.1 is used to transfer the engineering stress-strain into true stress-strain. Figure 5-7 shows the input stress-strain curve in ABAQUS. For the elastic part, the elastic Young's modulus is 29500 ksi, the yield stress is 53 ksi, and the Poisson ratio is 0.3. For the plastic part, von Mises yield rule, associated flow and isotropic hardening are employed.

$$\begin{cases} \varepsilon_{true} = \ln\left(1 + \varepsilon_e\right) \\ \sigma_{true} = \sigma_e\left(1 + \varepsilon_e\right) \end{cases} \tag{5.1}$$

161
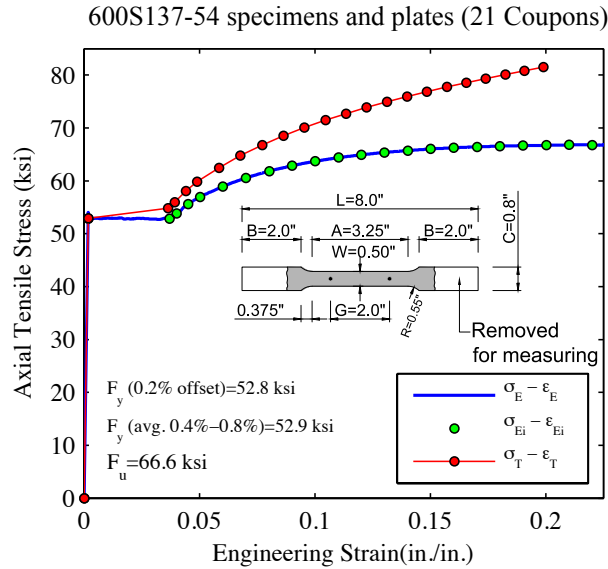
Figure 5-7: Material parameters used in finite element model

5.1.6 Cold rolling/forming effect

The cold rolling/forming effect is short for the effect of the roll-forming process on the material properties in the section, and on the member behavior. Usually, residual stresses and effective plastic strains are used to represent the effect of cold roll-forming. Residual stresses determine the current stress state when loading begins, while effective plastic strain records the forgoing loading history, and the size of the current yield surface.

In this report, the residual stress and effective plastic strain distribution model in (Moen et al. 2008) are used. Due to the high yield stress (53 ksi) and the small thickness of the specimens (0.056 in.), residual stresses and effective plastic strains in the flat region are ignored. Only the residual stresses and effective plastic strains in the corner regions are introduced into the finite element model. Figure 5-8 shows the residual stresses and effective plastic strains used in modeling. Thirty-one through thickness integration points are used when the roll-forming effect are considered.
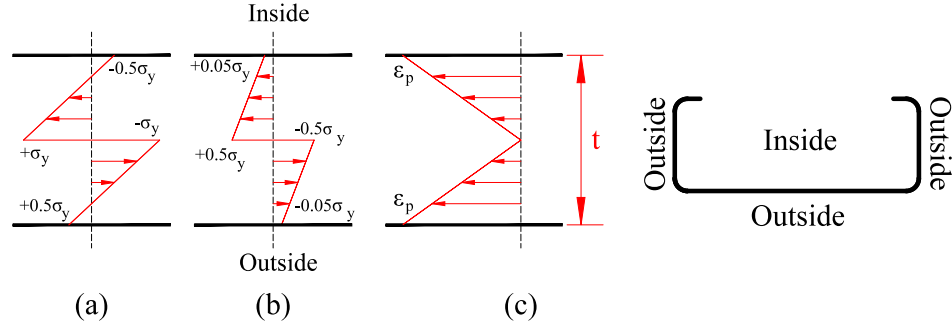
Figure 5-8: Residual stress and effective plastic strain in the corner regions
(a) residual stress in the transverse direction, (b) residual stress in the longitudinal direction,
(c) effective plastic strain, ε_p=0.26 (Moen et al. 2008)

5.1.7 Solution Method

For Eigen buckling analysis, ABAQUS offers the *Lanczos* and the *Subspace* iteration eigenvalue extraction methods. Here, we use *Lanczos* method and set the *minimum eigenvalue of interest* to zero to exclude negative eigenvalues.

For nonlinear collapse analysis, ABAQUS offers three methods to allow calculation in the post-buckling stage: displacement control, arc-length (Riks), and artificial damping. These approaches are studied in (Schafer et al. 2010), and the arc-length method (Riks) is recommended. In this report, we use arc-length method (Riks). As a rule of thumb to insure accuracy, before reaching peak load, about 20 steps are finished, by specifying the maximum arc length increment (typically ~0.05).

5.2 Eigen buckling analysis

Elastic buckling eigenvalues of the specimens are some of the most important parameters for the Direct Strength Method (DSM). One of the biggest advantages of DSM is to use software (e.g. CUFSM) to calculate elastic buckling loads of thin-walled members rather than simplified analytical equations; and use that prediction to determine strength. DSM predicts realistic strength based on the elastic buckling loads (global, distortional, and local) and empirical

formulas that link elastic buckling loads and strength. Since some assumptions have been made in CUFSM to simplify the eigen buckling calculation, the buckling loads of beam-columns calculated by CUFSM can be verified by using more general shell finite elements as available in ABAQUS. In addition, from the test setup presented in Chapter 3, we can observe there is a distance between the rotation center and the end of the specimen. The stiffness of this region is far more than the specimens. So this region works as a rigid link between the rotation center and the end of specimen. The rigid length effect on the elastic buckling critical loads are discussed in the second part of this section.

5.2.1 Elastic buckling of beam-columns in CUFSM vs. ABAQUS

As validation, eigen buckling analysis of the simple-simple (S-S) supported beam-columns are conducted by using CUFSM and ABAQUS. Three types of buckling modes: local, distortional, and global buckling are selected from the first 50 shell finite element eigen buckling modes by using the modal identification methodology (Li 2011). Comparisons are provided on buckling load and buckling mode.

5.2.1.1 Model simplification

In order to achieve the S-S boundary condition in ABAQUS some clarifications need to be made with respect to the shell finite element model presented in Section 5.1. First, the reference point and rigid body coupling are removed and a node at the mid height is constrained in the longitudinal translational degree of freedom. Second, the round corners of the specimen are ignored, because the modal identification methodology can only fully work on sections with clear fold lines. Figure 5-9 shows the simplified finite element model used in ABAQUS. Only the specimens with eccentricity in the minor axis are discussed here.

164
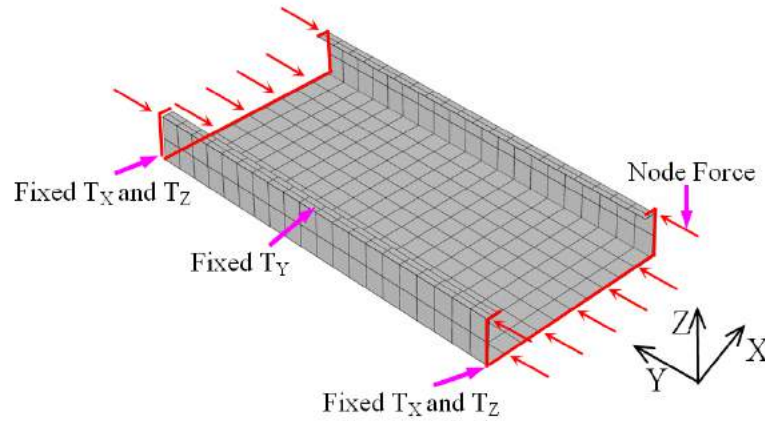
Figure 5-9: Finite element model for Eigen buckling analysis

5.2.1.2 Modal identification

Modal identification is a methodology to process the displacement result (buckling mode) to determine the participation factor of predefined pure buckling modes (local, distortional, and global). These predefined pure buckling modes are based on series of distinct mechanical assumptions. These assumptions are converted to restraint matrices and then used to form base vectors for identifying displacement. More details on modal identification are available in (Li 2011).

In this report, we use the criterion that the first buckling mode with a local buckling participation factor greater than 75% is the local buckling mode. If there is no buckling mode satisfying the upper condition, then we search for the first buckling mode with local buckling participation factor great than 50%. If there is also no buckling mode satisfying the upper condition, then the buckling mode with the maximum local buckling participation factor out of the first 50 is chosen. A similar searching method is used for finding the distortional and the global buckling modes.

5.2.1.3 Comparison to CUFSM results

Figure 5-10 and Figure 5-11 show the results for short beam-columns in the local and distortional buckling loads, respectively. The main buckling modes are shown on the right hand side of these figures.
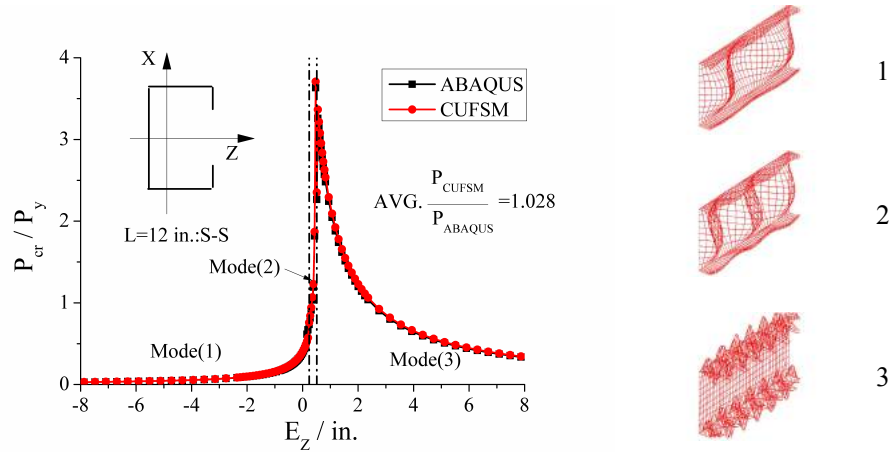
Figure 5-10: Local buckling load of 12 in. beam-columns
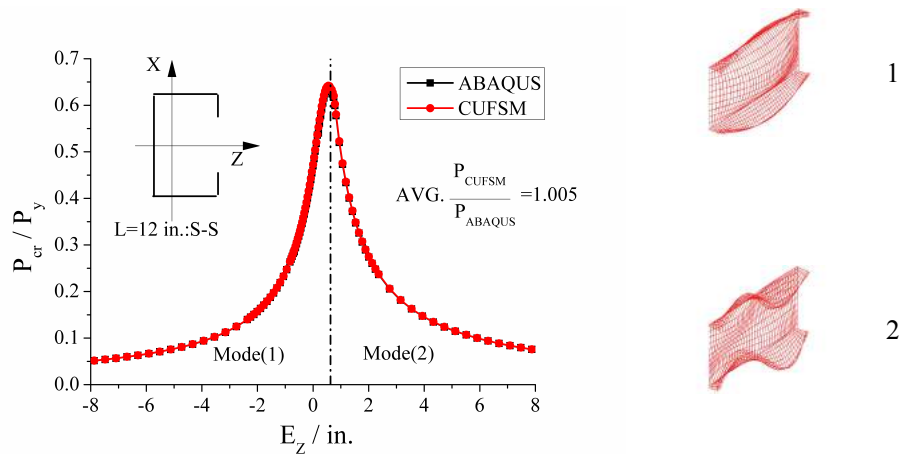
Figure 5-11: Distortional buckling load of 12 in. beam-columns

From Figure 5-10 and Figure 5-11, we conclude the SAFSM implemented in CUFSM can provide precise predictions on the local buckling and distortional buckling loads. Compared

166

to shell finite element models in ABAQUS, the predictions of CUFSM are modestly higher (less than 3%) presumably due to the idealized assumption made in the SAFSM shape functions.

As the eccentricity increases from the negative side (lips in tension) to positive side (lips in compression), the buckling load first increases and then decreases. The maximum buckling load is reached at a specimen with small positive eccentricity (lips in compression).

For local buckling, in Figure 5-10, all the specimens with negative eccentricity have two buckling waves in the web (mode 1). In the following narrow region around zero eccentricity, the number of buckling wave changes to three or more (mode 2). This is because the compression stress on the web has decreased. After this narrow region, the buckling mode changes to the flange buckling mode (mode 3). This is because the web is in tension and the flange is in compression in this case. The maximum buckling load is right at the point where the buckling mode shifts from the web to the flange.

For distortional buckling, in Figure 5-11, the specimens with negative (lips in tension) and small positive eccentricity (lips in compression) buckle mainly due to the web instabilities (mode 1). The specimens with large positive eccentricity buckle mainly due to the flange (mode 2). The maximum buckling load is at the point where the buckling mode shifts from the web to the flange.

Figure 5-12 and Figure 5-13 shows a similar comparison for 24 in. long beam-columns in local buckling and distortional buckling, respectively. The dominant buckling modes are shown on the right hand side of these figures. Behavior of the 24 in. long specimens is similar to that of the 12 in. long specimens.
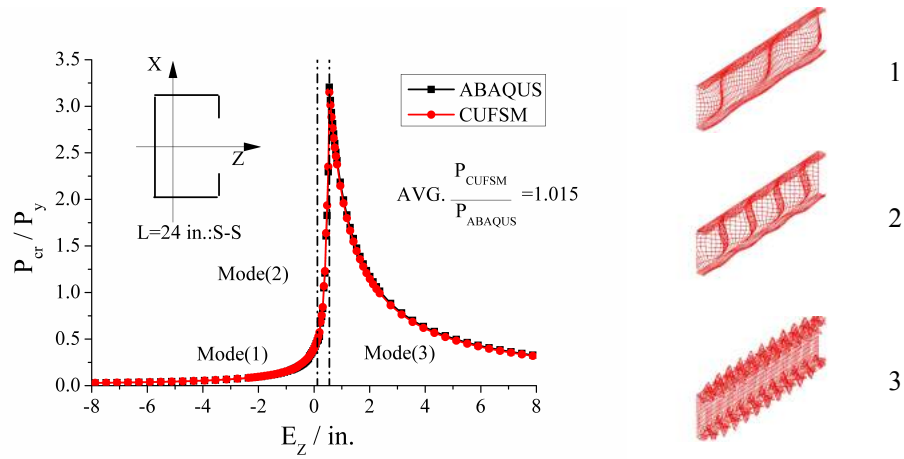
Figure 5-12: Comparison of local buckling load of 24 in. beam-columns
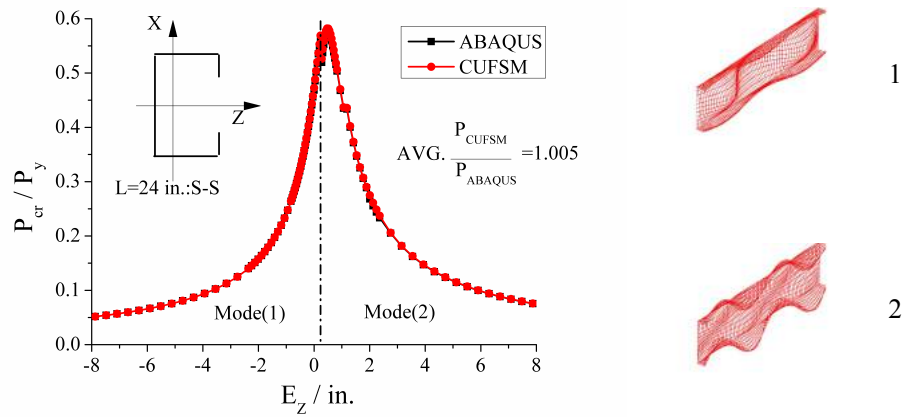
Figure 5-13: Comparison of distortional buckling load of 24 in. beam-columns

Figure 5-14 shows the comparison of 48 in. long beam-columns in global buckling. The dominant buckling modes are shown on the right hand side of this figure. Again, the SAFSM in CUFSM offers excellent predictions. For the specimens with negative eccentricity (lips in tension), the global buckling mode is flexural buckling in the minor axis (mode 1). For most of the specimens with positive eccentricity, the global buckling mode is lateral-torsional bucking (mode 2.1 and 2.2).

168
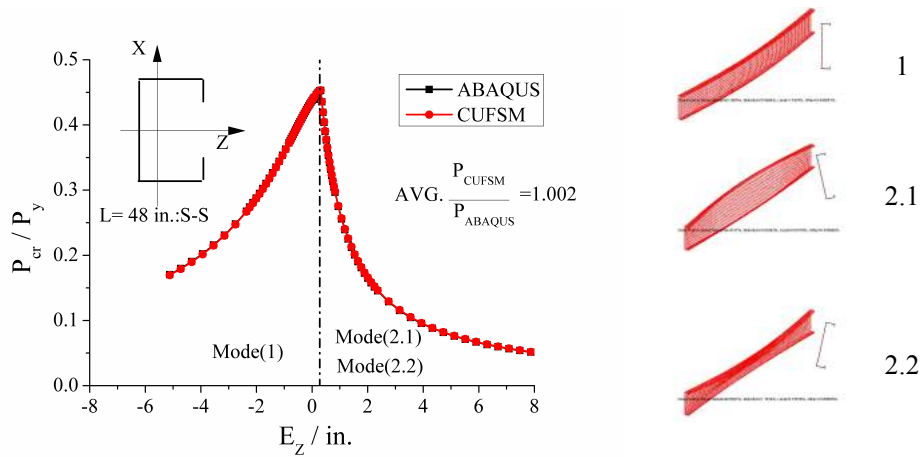
Figure 5-14: Global buckling load of 48 inches beam-columns

5.2.1 Effect of rigid ends on global bucking

Since the tested beam-column specimens (Chapter 3) used welded end plates, the specimens were fixed in warping, but they could still globally buckle between two swivel joints at the ends of specimens. The stiffness of the end regions is far more than the specimens, and therefore these regions work as a rigid link between the rotation center and the end of specimen. The rigid length can affect the global buckling critical loads. Notably, it is not possible to have different stiffness along the length in finite strip programs (i.e. modeling rigid lengths in CUFSM) and the global buckling prediction compared with the tests needs to be handled using other methods.

Table 5-6: Elastic global buckling analysis including the effect of rigid end links

Specimen	Length of the specimen	Total length (pined-pined)	CUTWP [15]		MASTAN 2			Equivalent effective length factor
			min buckling load	Mode	w/o rigid links	w/ rigid links	Rigid link effect	
	(in.)	(in.)	(kips)		(kips)	(kips)	(%)	
Short	12	24	53.1	Minor axis buckling	53.1	63.6	19.8%	0.91
Interm.	24	36	23.6	Minor axis buckling	23.6	24.9	5.7%	0.97
Long	48	60	8.5	Minor axis buckling	8.5	8.6	1.2%	0.99

169

Accordingly, single columns of 600S137-54 lipped channels have been modeled in MASTAN 2 (McGuire, William et al. 2000) to the length of the specimens (12, 24, and 48 in.), and rigid parts (using 10 times higher section properties in the end links) are added to the end of the columns before performing elastic eigen-buckling analyses. The total length of the columns including the rigid ends is always 12 in. longer than the specimens and are therefore 24, 36, and 60 in. for the short, intermediate, and long columns, respectively. Table 5-6 summarizes the elastic global buckling critical loads including the effect of rigid end links. The results show that the rigid links can affect the buckling critical loads up to 20% for the short members, but just 1.2% for the longest ones.

To simplify the global buckling load calculations, the minimum buckling load of the columns can also to be calculated by CUTWP [15]. CUTWP provides an analytical solution for global buckling of the columns, but is still not able to model variable stiffness along the length. The results in Table 5-6 show that the CUTWP results match the MASTAN results without the rigid links. While the global buckling mode of all columns is "minor axis flexural buckling," an effective equivalent effective length factor is calculated in Table 5-6 to account for the rigid links. Using the provided effective length factors in CUTWP or any other analytical calculation will result in the elastic buckling loads including effect of the rigid links.

5.3 Nonlinear collapse analysis

In this section, the shell finite element model presented in Section 5.1 is employed to perform geometric and material nonlinear collapse analyses. Considering the options for modeling imperfections, several options for the finite element models are prepared and a "best"

model is selected primarily through comparing against the test data of Chapter 3. This "best" model is then used to generate the P-M-M interaction strength surface and compare with the predictions of the AISI-S100-12 specifications.

Table 5-7: Options of finite element model

Options	Label	Section		Imperfection				Cold roll-forming	
		Nominal	Realistic	Positive	Negative	Local	Distortion	With	Without
1	PL-N-C	√		√		√		√	
2	PL-N-NC	√		√		√			√
3	NL-N-C	√			√	√		√	
4	NL-N-NC	√			√	√			√
5	PD-N-C	√		√			√	√	
6	PD-N-NC	√		√			√		√
7	ND-N-C	√			√		√	√	
8	ND-N-NC	√			√		√		√
9	PL-R-C		√	√		√		√	
10	PL-R-NC		√	√		√			√
11	NL-R-C		√		√	√		√	
12	NL-R-NC		√		√	√			√
13	PD-R-C		√	√			√	√	
14	PD-R-NC		√	√			√		√
15	ND-R-C		√		√		√	√	
16	ND-R-NC		√		√		√		√

PL: Positive local; ND: Negative local; PD: Positive distortional; ND: Negative distortional;
N: Nominal; R: Realistic; NC: Without cold-forming effect; C: With cold-forming effect.

5.3.1 Determination of the validation parameters

Several modeling parameters can be included in finding the "best" or validated model appropriate for parametric studies including, section geometries (dimensions), imperfection patterns, imperfection magnitude, roll-forming effects, combination of the imperfections, and more. To determine the most important parameters and to decrease the number of required iterations to find the proper modeling parameters, a sensitivity analysis on nominal versus measured cross-sectional dimensions has been made first on the short lipped channel members to decide whether it is necessary to use measured cross-sectional dimensions or not? Moreover, the effect of imperfection magnitude is studied separately to see which magnitude, 25% CDF, 50% CDF, or 75% CDF is most suitable for modeling the imperfections. Using proper cross-sectional dimensions and imperfection magnitude, several combinations of imperfections have been

examined to find the "best" imperfection combination for modeling, which in this case provides the best agreement with test results in terms of absolute strength and minimizing deviation in the predictions.

5.3.1.1 Studying the effect of cross-sectional dimensions

From Section 5.1, three parameters have been selected: the section geometry, the imperfection, and the cold roll-forming effect. For the section geometry, there are two options: nominal and measured. For the imperfection, as the specimens first selected are the short length ones (12 in.), there are four options: positive and negative 50% CDF local buckling mode imperfection; and 50% CDF distortional mode imperfection. For roll-forming/cold work effect, there are two options: with and without the roll-forming effect. In total, 16 combinations are studied, as shown in.

5.3.1.2 Validation with test specimens

For short (12 in. length) specimens, all of the 16 options when implemented in the shell element collapse model provide good predictions. The average ratio of prediction over the test results are all more than 90% with scatter less than 0.1. In Table 5-8, the top three options are: Option 3-nominal geometry, with negative 50% CDF local buckling mode imperfection, considering roll-forming/cold-work effect; Option 5-nominal geometry, with 50% CDF positive distortional buckling mode imperfection, considering roll-forming/cold-work effect; Option 7-nominal geometry, with positive 50% CDF distortional buckling mode imperfection, considering cold forming effect in Table 5-9, the parameters of the top three options are similar to those in Table 5-8, expect the geometry used is the actual section geometry.

172

In Table 5-8, the average ratio of the test results to the prediction of Option 1 is 1.056, which is 3.6% lower than the average ratio of Option 2 (1.092). The only difference of these two model types is whether the roll-forming/cold-work effect is considered. So, this means roll-forming/cold-work effect may increase the ultimate load by ~3.6%. The same conclusion can be drawn when comparing Option 3 and Option 4.

Table 5-8: Comparisons of finite element results and test results (Part 1-Nominal dimensions)

No.		Specimen	P_{Test}/P_{FEM}							
			1	2	3	4	5	6	7	8
1		S600-12-1	1.057	1.102	1.026	1.068	1.050	1.103	1.017	1.053
2		S600-12-19	1.192	1.225	1.151	1.179	1.118	1.154	1.138	1.166
3	Minor axis bending	S600-12-4	1.157	1.189	1.109	1.136	1.065	1.088	1.088	1.112
4		S600-12-5	1.023	1.056	1.050	1.070	1.049	1.092	1.196	1.237
5		S600-12-6	1.083	1.130	1.080	1.130	1.098	1.144	1.100	1.147
6		S600-12-8	1.094	1.150	1.100	1.158	1.118	1.174	1.033	1.091
7		S600-12-9	1.110	1.146	1.036	1.065	1.011	1.040	0.897	0.915
8	Major axis bending	S600-12-10	1.055	1.081	1.025	1.055	1.013	1.044	1.008	1.045
9		S600-12-11	1.019	1.046	1.022	1.059	0.992	1.022	1.016	1.055
10		S600-12-2	1.020	1.052	1.037	1.077	0.983	1.015	1.047	1.085
11		S600-12-13	0.906	0.938	0.943	0.981	0.890	0.921	0.942	0.980
12		S600-12-14	0.972	1.002	1.020	1.055	0.956	0.983	1.049	1.085
13	Bi-axial bending	S600-12-15	1.017	1.053	1.033	1.070	1.029	1.064	1.034	1.070
14		S600-12-16	1.060	1.093	1.000	1.027	0.965	0.988	0.982	1.005
15		S600-12-17	1.023	1.058	0.973	1.008	0.950	0.984	0.953	0.981
16		S600-12-3	1.134	1.172	1.055	1.086	1.032	1.063	0.970	0.966
17		S600-12-20	1.033	1.068	0.961	0.990	0.956	0.988	0.925	0.940
		Max.	1.192	1.225	1.151	1.179	1.118	1.174	1.196	1.237
		Min.	0.906	0.938	0.943	0.981	0.890	0.921	0.897	0.915
		Avg.	1.056	1.092	**1.037**	1.071	**1.016**	1.051	**1.023**	1.055
		Stdev.	0.069	0.071	**0.053**	0.055	**0.063**	0.069	**0.078**	0.085

The prediction of the failure mode is also used to rank Option 3, Option 5, and Option 7. Failure modes of the test specimens and the finite element models with different modes of imperfection are shown in Appendix G. The finite element failure modes employ the nominal geometry with cold roll-forming effect. It is clear that Option 3 and Option 7, i.e., models with

negative local/distortional buckling mode imperfections, can predict the failure mode better than Option 5, i.e., a model with positive distortional buckling mode imperfection.

Table 5-9: Comparisons of finite element results and test results (Part 2-Measured dimensions)

No.	Specimen	P_{Test}/P_{FEM}							
		9	10	11	12	13	14	15	16
1	S600-12-1	1.068	1.115	1.038	1.081	1.062	1.116	1.029	1.067
2	S600-12-19	1.204	1.240	1.164	1.193	1.129	1.165	1.152	1.181
3	S600-12-4	1.169	1.202	1.119	1.148	1.076	1.100	1.102	1.126
4	S600-12-5	1.031	1.064	1.058	1.077	1.054	1.098	1.210	1.250
5	S600-12-6	1.094	1.142	1.092	1.142	1.108	1.155	1.113	1.160
6	S600-12-8	1.106	1.165	1.112	1.279	1.132	1.188	1.044	1.102
7	S600-12-9	1.117	1.154	1.037	1.067	1.023	1.054	0.908	0.928
8	S600-12-10	1.074	1.101	1.051	1.086	1.032	1.065	1.031	1.071
9	S600-12-11	1.046	1.077	1.055	1.095	1.016	1.048	1.044	1.087
10	S600-12-2	1.039	1.073	1.057	1.098	0.999	1.032	1.061	1.100
11	S600-12-13	0.920	0.954	0.961	1.001	0.903	0.937	0.958	0.998
12	S600-12-14	0.981	1.014	1.032	1.068	0.961	0.991	1.058	1.096
13	S600-12-15	1.021	1.062	1.042	1.083	1.033	1.033	1.042	1.082
14	S600-12-16	1.064	1.098	1.000	1.027	0.970	0.993	0.983	1.007
15	S600-12-17	1.019	1.053	0.966	1.001	0.945	0.983	0.947	0.976
16	S600-12-3	1.140	1.177	1.055	1.087	1.041	1.074	0.951	0.954
17	S600-12-20	1.035	1.070	0.958	0.986	0.965	0.997	0.923	0.939
	Max.	1.204	1.240	1.164	1.279	1.132	1.188	1.210	1.250
	Min.	0.920	0.954	0.958	0.986	0.903	0.937	0.908	0.928
	Avg.	1.066	1.104	**1.047**	1.089	**1.026**	1.060	**1.033**	1.066
	Stdev.	0.069	0.071	**0.056**	0.073	**0.065**	0.070	**0.082**	0.089

Note: "Minor axis bending" spans No. 1–6; "Major axis bending" spans No. 7–9; "Bi-axial bending" spans No. 10–17.

Comparing Option 3 to Option 11, the only difference is the choice of the geometry parameter. The average ratio of the test to the prediction of Option 3 is 1.037 with a standard deviation of 0.053, while for Option 11 the same two respective statistics are 1.047 and 0.056. The prediction of Option 3 is modestly better than that of the Option 11. Similarly, we can conclude Option 5 is better than Option 13, and Option 7 is better than Option 15. Thus, for convenience, we can directly use the nominal geometry if desired.

Both Option 3 and Option 7 offer good predictions. Option 3 has a higher average ratio than Option 7, but also a lower scatter. So, to select the best simulation option for the short

specimens, finite element models with 25% CDF and 75% CDF imperfection magnitudes are used. Table 5-10 provides the results, while Figure 5-16 and Figure 5-15 provides the distribution of the results.

Table 5-10: Comparisons of the magnitude of imperfection on simulation results

Specimen	P_{Test}/P_{FEM}					
	Dist 25%	Dist 50%	Dist 75%	Local 25%	Local 50%	Local 75%
S600-12-1	1.016	1.017	1.015	1.023	1.026	1.034
S600-12-19	1.141	1.138	1.141	1.179	1.151	1.162
S600-12-4	1.093	1.088	0.962	1.103	1.109	1.120
S600-12-5	1.181	1.196	1.213	1.055	1.050	1.045
S600-12-6	1.093	1.100	1.110	1.080	1.080	1.083
S600-12-8	1.041	1.033	1.027	1.099	1.100	1.057
S600-12-9	1.013	0.897	0.911	1.029	1.036	1.049
S600-12-10	0.992	1.008	1.027	1.010	1.025	1.046
S600-12-11	1.000	1.016	1.033	1.006	1.022	1.044
S600-12-2	1.033	1.047	1.063	1.030	1.037	1.048
S600-12-13	0.933	0.942	0.952	0.934	0.943	0.955
S600-12-14	1.038	1.049	1.063	1.023	1.020	1.018
S600-12-15	1.029	1.034	1.040	1.029	1.033	1.039
S600-12-16	0.987	0.982	0.846	0.995	1.000	1.010
S600-12-17	0.957	0.953	0.930	0.968	0.973	0.984
S600-12-3	1.034	0.970	0.903	1.048	1.055	1.067
S600-12-20	0.934	0.925	0.850	0.953	0.961	0.976
Max.	1.181	1.196	1.213	1.179	1.151	1.162
Min.	0.933	0.897	0.846	0.934	0.943	0.955
Avg.	1.030	1.023	1.005	1.033	1.037	1.043
Stdev.	0.067	0.078	0.100	0.060	0.053	0.050
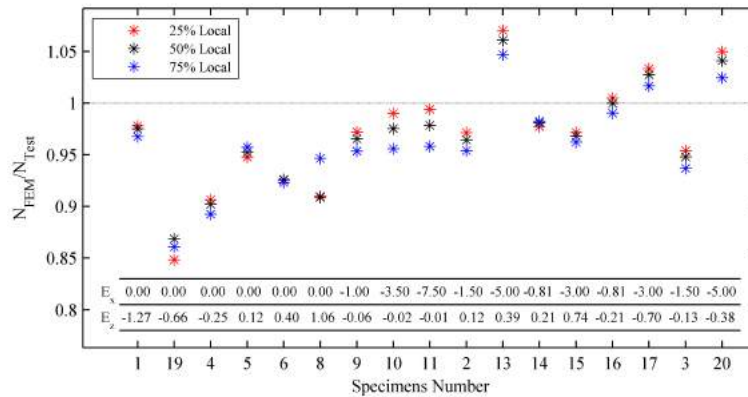
Figure 5-15: Effect of the magnitude of local imperfection on the simulation result Note: eccentricities are in inches.
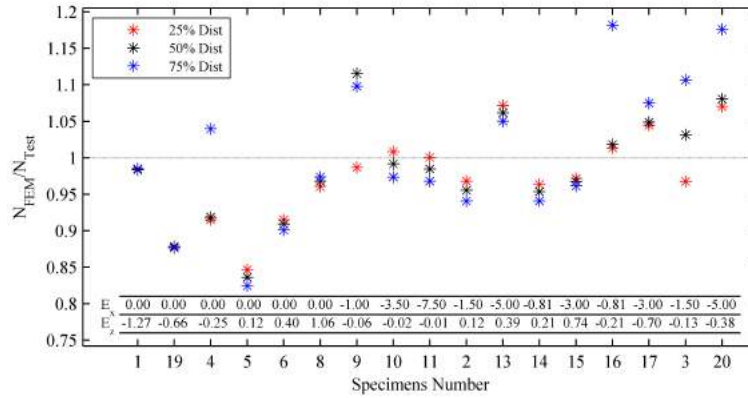
Figure 5-16: Effect of the magnitude of distortional imperfection on the simulation result. Note: eccentricities are in inches.

Compared to the finite element model with distortional buckling mode imperfections, the model with local buckling mode imperfections is more stable (i.e., less scatter in the predictions). (Most of the short length specimens failed in local buckling, so this is not surprising.) The scatter of the predictions of the finite element model with distortional buckling mode imperfection over the test results are 0.067, 0.078 and 0.100 for 25% CDF, 50% CDF and 75% CDF imperfection magnitude, respectively. For the model with local buckling mode imperfections, these values are 0.060, 0.053 and 0.050. So the "best" finite element model for the short specimens is Option 3, i.e. the finite element model with nominal cross section, with negative local buckling mode imperfection, and with roll-forming/cold-work included effect.
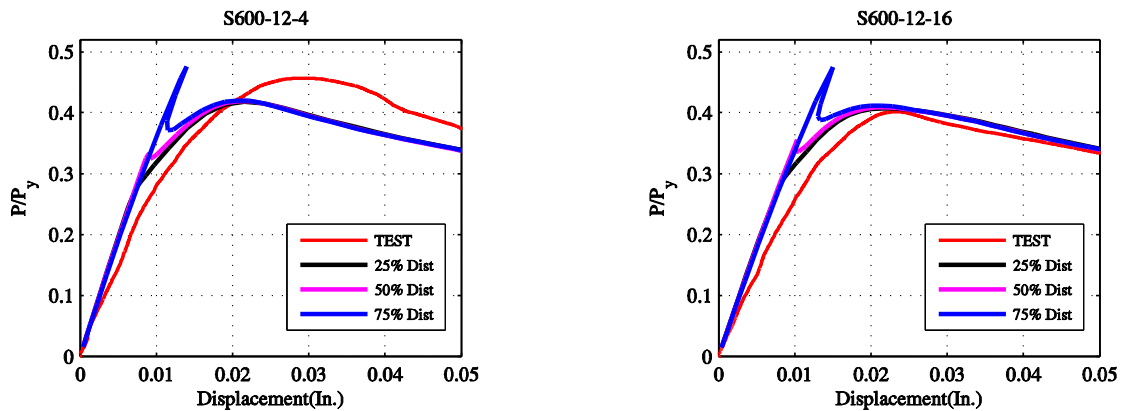
Figure 5-17: Load-displacement curves from finite element model with different magnitude of distortional buckling mode imperfection: Specimens 4 and 16

176
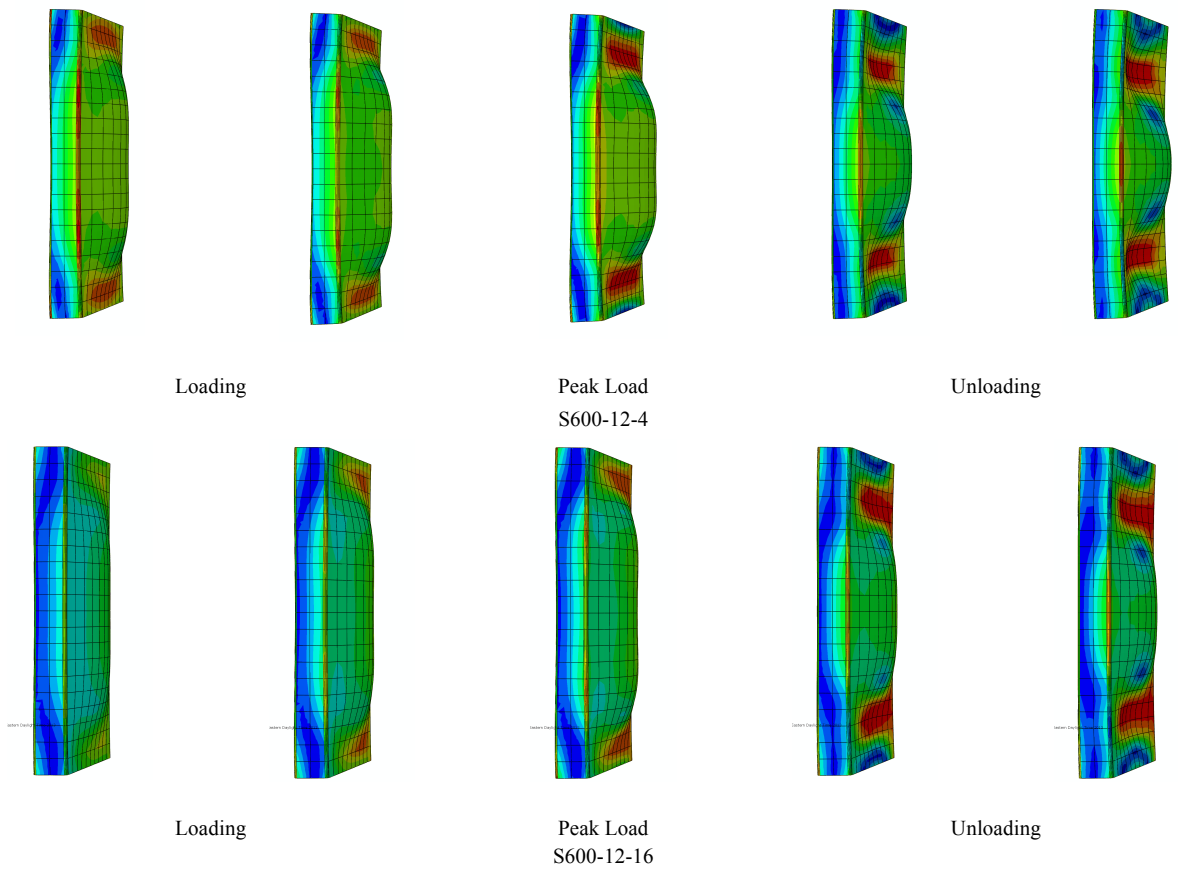
Figure 5-18: Changes of buckling mode from distortional buckling mode to local buckling mode: Specimens 4 and 16 with 75% CDF imperfection

The accuracy of the predictions of the finite element model with distortional buckling mode imperfections decreases as the magnitude of the imperfection increases. Typical load-displacement curves are shown in Figure 5-17. For the finite element model with 75% CDF imperfection, there is a sharp decrease just after the peak point, and after this drop, the curves with different levels of imperfection almost coincide. This is caused by the change of buckling mode, from distortional buckling mode (imperfection) to local buckling mode (actual response) (Figure 5-18). This phenomena is unstable and hard to reach in a real test.

5.3.2 Validating the FEM models including imperfection combinations

These preliminary models indicate that nominal geometric dimensions and 50% CDF imperfection magnitude, as in Table 5-5, is adequate. However, several combinations of the imperfections and also roll-forming/cold-work effects are included in finding the "best" model protocol (across all lengths), as summarized in Table 5-11. For the imperfection, there are eight options consisting of variations in the imperfection direction as positive (P) or negative (N) and using three different mode shapes including global (G) distortional (D) and local (L) modes, i.e. PGPDPL, PGNDNL, etc. For the roll-forming/cold-work effect, there are two options: with and without this forming effect. A total of 16 combinations are studied as shown in Table 5-11 and Figure 5-19.

Table 5-11: Options of finite element model

Option	Label	Global Positive	Global Negative	Distortional Positive	Distortional Negative	Local Positive	Local Negative	Cold roll-forming With	Cold roll-forming Without
1	PGNDNL-NC	√			√		√		√
2	PGNDPL-NC	√			√	√			√
3	PGPDNL-NC	√		√			√		√
4	PGPDPL-NC	√		√		√			√
5	NGNDNL-NC		√		√		√		√
6	NGNDPL-NC		√		√	√			√
7	NGPDNL-NC		√	√			√		√
8	NGPDPL-NC		√	√		√			√
9	PGNDNL-C	√			√		√	√	
10	PGNDPL-C	√			√	√		√	
11	PGPDNL-C	√		√			√	√	
12	PGPDPL-C	√		√		√		√	
13	NGNDNL-C		√		√		√	√	
14	NGNDPL-C		√		√	√		√	
15	NGPDNL-C		√	√			√	√	
16	NGPDPL-C		√	√		√		√	

PL: Positive local; ND: Negative local; PD: Positive distortional; ND: Negative distortional.
PG: Positive global; NG: Negative global; NC: Without cold-forming effect; C: With cold-forming effect.

PGPDPL(12 inch)   NGNDNL(12 inch)

PGPDPL(24 inch)

NGNDNL(24 inch)

PGPDPL(48 inch)   NGNDNL
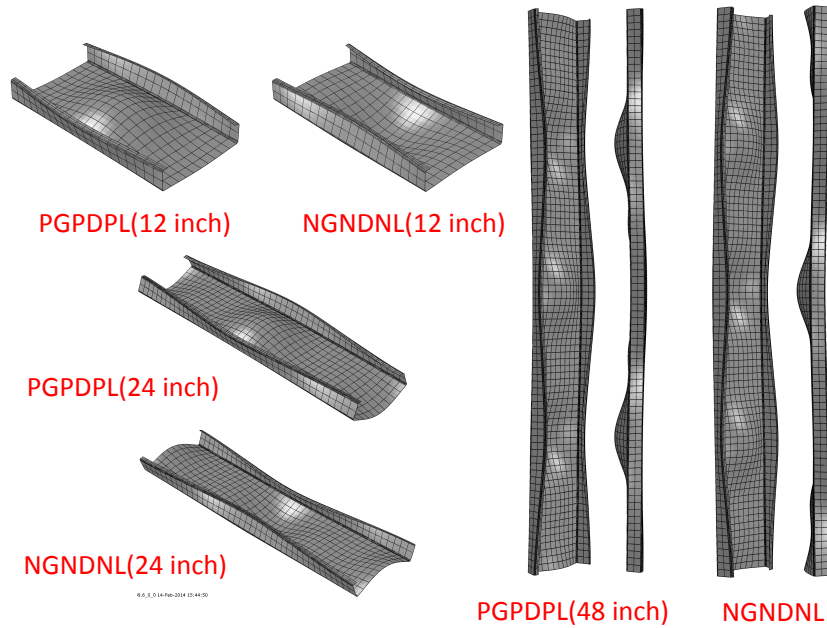
Figure 5-19: Typical imperfection patterns

5.3.2.1 Validation against the test results: Strength comparison

Shell finite element-based nonlinear material and geometric collapse analyses are conducted in ABAQUS. Comparisons of the finite element predictions and the test results are shown in Table 5-12 for the short length lipped channel specimens of Chapter 3.

For short specimens, the finite element models including the roll-forming/cold-work effect showed good results. The average P_{Test}/P_{FEM} ratios lie in the range of 1.03 to 1.07 with a standard deviation less than 0.07. Comparatively, the best models are Option 11 (NGPDNL-C) and Option 15 (PGPDNL-C). However, other options such as Option 13 (NGNDNL-C) can also be selected, as the results are very close to Options 11 and 15 in terms of failure statistics and observed collapse mechanisms. The average capacity predicted by the finite element models is lower than the test results. Introducing the global buckling imperfection did not meaningfully change the results for these short length specimens.

179

Table 5-12: Comparisons of finite element results and test results for 12 in. long specimens

No.	Specimen in the test	P_{Test}/P_{FEM} (Without cold roll-forming effect)								P_{Test}/P_{FEM} (With cold roll-forming effect)							
		1	2	3	4	5	6	7	8	9	10	11	12	13	14	15	16
1		S600-12-1	1.06	1.10	1.08	1.12	1.06	1.09	1.08	1.11	1.02	1.06	1.04	1.07	1.02	1.05	1.03	1.06
2		S600-12-19	1.18	1.24	1.20	1.23	1.17	1.22	1.19	1.22	1.15	1.20	1.17	1.20	1.14	1.19	1.16	1.19
3	Minor axis bending	S600-12-4	1.13	1.19	1.16	1.20	1.12	1.18	1.15	1.19	1.10	1.16	1.13	1.17	1.09	1.15	1.12	1.16
4		S600-12-5	1.21	1.05	1.00	1.07	1.23	1.06	1.02	1.07	1.18	1.02	0.98	1.04	1.19	1.03	1.00	1.03
5		S600-12-6	1.14	1.14	1.10	1.14	1.15	1.15	1.11	1.15	1.10	1.10	1.07	1.09	1.10	1.11	1.06	1.10
6		S600-12-8	1.09	1.09	1.17	1.17	1.10	1.09	1.18	1.18	1.04	1.03	1.12	1.11	1.04	1.03	1.13	1.12
7	Major axis bending	S600-12-9	1.05	1.14	1.08	1.16	1.04	1.13	1.07	1.14	1.03	1.11	1.05	1.12	1.02	1.09	1.04	1.11
8		S600-12-10	1.08	1.05	1.04	1.11	1.08	1.04	1.04	1.10	1.04	1.03	1.01	1.08	1.04	1.03	1.01	1.07
9		S600-12-11	1.08	1.00	1.02	1.07	1.09	1.02	1.03	1.07	1.04	0.98	0.99	1.04	1.04	0.99	1.00	1.04
10		S600-12-2	1.10	1.04	1.04	1.07	1.10	1.07	1.05	1.07	1.06	1.01	1.01	1.04	1.06	1.04	1.02	1.03
11		S600-12-13	0.99	0.96	0.96	0.95	1.00	0.97	0.96	0.95	0.95	0.92	0.92	0.91	0.96	0.93	0.93	0.92
12		S600-12-14	1.08	1.07	1.02	1.00	1.09	1.08	1.03	1.01	1.05	1.04	0.98	0.97	1.06	1.05	0.99	0.98
13	Bi-Axial bending	S600-12-15	1.08	1.06	1.06	1.07	1.08	1.07	1.06	1.07	1.04	1.02	1.02	1.03	1.05	1.03	1.03	1.04
14		S600-12-16	1.02	1.10	1.04	1.10	1.01	1.09	1.03	1.09	1.00	1.07	1.02	1.06	0.99	1.05	1.01	1.05
15		S600-12-17	1.00	1.06	1.02	1.05	0.99	1.06	1.02	1.05	0.97	1.03	0.99	1.02	0.96	1.02	0.98	1.01
16		S600-12-3	1.08	1.17	1.10	1.18	1.07	1.15	1.10	1.17	1.05	1.13	1.07	1.14	1.04	1.12	1.06	1.13
17		S600-12-20	0.98	1.06	1.01	1.07	0.97	1.05	1.00	1.07	0.95	1.03	0.97	1.04	0.94	1.02	0.97	1.03
	AVG.		1.08	1.09	1.07	1.10	1.08	1.09	1.07	1.10	1.04	1.05	1.03	1.07	1.04	1.05	1.03	1.06
	STDEV.		0.06	0.07	0.07	0.07	0.07	0.06	0.06	0.07	0.06	0.07	0.06	0.07	0.06	0.06	0.06	0.07
	MAX.		1.21	1.24	1.20	1.23	1.23	1.22	1.19	1.22	1.18	1.20	1.17	1.20	1.19	1.19	1.16	1.19
	MIN.		0.98	0.96	0.96	0.95	0.97	0.97	0.96	0.95	0.95	0.92	0.92	0.91	0.94	0.93	0.93	0.92

For Option 1 (PGNDNL-NC), the average P_{Test}/P_{FEM} ratio is 1.08, while for Option 9 (PGNDNL_C), the average P_{Test}/P_{FEM} ratio is 1.04. The only difference of these two options is the cold-work/roll-forming effect assumption. So, the effect of cold-work is again shown to increase the load carrying capacity by ~3%. Similar conclusions are drawn when Option 2 and Option 10 are compared. On average, the effect of cold-work increases the load carrying capacity by about 3% for these 12 in. specimens. (In general the effect of cold-work is a function of yield stress, thickness, corner radius, and the percentage of the total cross-section that is attributed to the corners – the important observation here is that inclusion of roll-forming residual stresses and strains is a small net benefit, as opposed to a detriment.)

By comparing Option 1 through Option 8, the difference of the average P_{Test}/P_{FEM} ratio is less than 0.03, which means the sign of the imperfection buckling mode is not critical in these short length specimens. Compared to the P_{Test}/P_{FEM} ratio of the specimens with positive eccentricities in minor axis, the P_{Test}/P_{FEM} ratio of the specimens with negative eccentricities in minor axis is higher. For the short members, the FEM predictions are systematically lower than the test results in minor axis bending.

In all the finite element options, Option 4 (PGPDPL-NC) shows the highest P_{Test}/P_{FEM} ratio. In this option, the imperfection creates outward flanges movement at the mid-height and the web moves towards the lips. Similar conclusion was drawn when the elastic post-buckling behavior of lipped channel member was studied (Dinis et al. 2007; Silvestre et al. 2006). Accordingly, outward flange buckling results in lower distortional post-buckling strength. For intermediate length specimens (24 in. long), the average P_{Test}/P_{FEM} ratios lie in the range of 1.05 to 1.10 with scatter (standard deviation of the test-to-predicted ratio) less than 0.09. Comparatively, the best model is Option 13 (NGNDNL-C). The capacity predicted by the finite element models is lower than the test results of most of the specimens.

None of the finite element modeling options provide fully satisfactory predictions for specimens: S600-24-7, S600-24-16, S600-24-17, S600-24-18, and S600-24-20. These five specimens have small eccentricity in the minor axis. In Figure 5-20, NON denotes a model without imperfection; PGPDPL denotes a model with positive global, distortional, and local buckling mode imperfection; 25, 50, and 75 correspond to 25% CDF, 50% CDF, and 75% CDF imperfection magnitudes from Table 5-5. For the member with +0.07 in. (+1.8 mm) eccentricity in the minor axis, the capacity of the model without imperfection is 22% higher than the capacity

of model with PGPDPL-75 imperfection. So, when the eccentricity in minor axis is very small, the load capacity of test specimen is quite sensitive to the imperfection.

Table 5-13: Comparisons of finite element results and test results for 24-inch specimens

No.	Specimen in the test	P_{Test}/P_{FEM} (Without cold roll-forming effect)								P_{Test}/P_{FEM} (With cold roll-forming effect)							
		1	2	3	4	5	6	7	8	9	10	11	12	13	14	15	16
1		S600-24-1	1.06	1.06	1.08	1.09	1.05	1.05	1.07	1.08	1.02	1.02	1.04	1.04	1.01	1.01	1.03	1.03
2		S600-24-2	1.06	1.06	1.07	1.08	1.04	1.05	1.06	1.06	1.03	1.04	1.05	1.05	1.02	1.02	1.03	1.04
3	Minor axis bending	S600-24-3	1.08	1.08	1.10	1.10	1.06	1.06	1.08	1.08	1.06	1.06	1.08	1.08	1.04	1.04	1.06	1.07
4		S600-24-6	0.96	0.99	0.91	0.96	0.98	1.01	0.95	1.00	0.95	0.97	0.90	0.95	0.97	0.99	0.94	0.99
5		S600-24-5	0.99	0.99	1.01	1.01	1.00	1.00	1.03	1.03	0.96	0.95	0.99	0.99	0.97	0.97	1.00	1.00
6		S600-24-4	1.03	1.03	1.05	1.05	1.04	1.04	1.07	1.06	0.99	0.99	1.02	1.01	1.00	1.00	1.03	1.02
7	Major axis bending	S600-24-7	1.23	1.23	1.26	1.27	1.20	1.20	1.23	1.24	1.20	1.21	1.23	1.24	1.17	1.17	1.20	1.21
8		S600-24-8	1.01	1.00	1.03	1.06	1.02	1.01	1.01	1.04	0.99	0.98	1.00	1.03	1.00	0.99	0.99	1.01
9		S600-24-9	1.03	1.01	1.00	1.02	1.04	1.02	1.00	1.02	1.01	0.99	0.97	1.00	1.02	1.00	0.96	1.00
10		S600-24-10	1.12	1.13	1.03	1.06	1.15	1.15	1.06	1.10	1.09	1.10	0.99	1.03	1.12	1.12	1.03	1.07
11		S600-24-11	1.06	1.02	0.98	1.05	1.08	1.04	1.00	1.07	1.02	0.99	0.96	1.02	1.04	1.00	0.97	1.03
12		S600-24-12	1.05	1.04	1.01	1.04	1.07	1.06	1.01	1.07	1.02	1.01	0.99	1.01	1.04	1.03	0.99	1.04
13	Bi-Axial bending	S600-24-13	1.02	0.97	1.04	1.05	1.04	0.99	1.06	1.07	0.99	0.95	1.01	1.01	1.00	0.96	1.02	1.03
14		S600-24-14	1.10	1.11	1.11	1.12	1.08	1.09	1.09	1.10	1.07	1.08	1.09	1.10	1.05	1.06	1.07	1.08
15		S600-24-15	1.05	1.07	1.06	1.07	1.04	1.05	1.05	1.06	1.03	1.04	1.04	1.04	1.01	1.03	1.03	1.03
16		S600-24-16	1.11	1.12	1.13	1.14	1.09	1.10	1.11	1.12	1.08	1.09	1.11	1.11	1.06	1.07	1.08	1.09
17		S600-24-17	1.11	1.13	1.12	1.15	1.10	1.11	1.11	1.14	1.08	1.10	1.09	1.12	1.07	1.08	1.08	1.10
18	Axial	S600-24-18	1.22	1.21	1.25	1.26	1.19	1.18	1.22	1.22	1.20	1.19	1.23	1.24	1.17	1.16	1.20	1.21
19	Major	S600-24-19	1.04	1.01	1.00	1.02	1.04	1.02	1.00	1.02	1.01	0.99	0.97	0.99	1.02	1.00	0.96	1.00
20	Axial	S600-24-20	1.28	1.28	1.32	1.33	1.25	1.25	1.28	1.29	1.27	1.26	1.30	1.31	1.23	1.23	1.27	1.27
	AVG.		1.08	1.08	1.08	1.10	1.08	1.07	1.07	1.09	1.05	1.05	1.05	1.07	1.05	1.05	1.05	1.07
	STDEV.		0.08	0.09	0.10	0.09	0.07	0.07	0.08	0.08	0.08	0.09	0.10	0.09	0.07	0.07	0.09	0.08
	MAX.		1.28	1.28	1.32	1.33	1.25	1.25	1.28	1.29	1.27	1.26	1.30	1.31	1.23	1.23	1.27	1.27
	MIN.		0.96	0.97	0.91	0.96	0.98	0.99	0.95	1.00	0.95	0.95	0.90	0.95	0.97	0.96	0.94	0.99
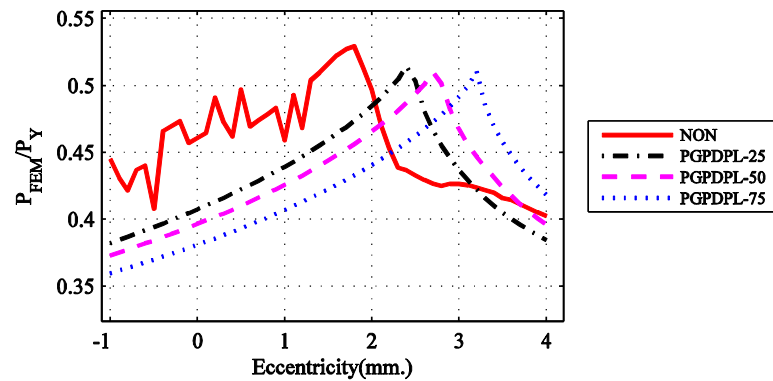
Figure 5-20: Finite element result for 24 inches long specimens with small eccentricities in minor axis. 25.4 mm=1 inch. (Note convergence in the model with no imperfections: NON, is unstable)

182

For Option 1 (PGNDNL-NC), the average P_{Test}/P_{FEM} ratio is 1.08, while for Option 9 (PGNDNL_C), the average P_{Test}/P_{FEM} ratio is 1.05. The only difference of these two options is whether the cold-work/roll-forming effect is considered or not. So, again, the effect of cold-work is to increase the load capacity by ~3%. A similar conclusion can be drawn when Option 2 and Option 10 are compared. On average, the effect of cold-work increases the load capacity by about ~3% for the 24 in. long specimens.

Just like the short specimens, the sign of the imperfection shape is not so critical in the 24 in. long specimens. However, outward flange buckling could result in slightly lower distortional buckling post-buckling strength and is considered to be more conservative.

According to Table 5-14 for long specimens, the average P_{Test}/P_{FEM} ratio of all modeling options is around 1.12 with a large scatter of 0.26. The large scatter is mainly caused by the results of the following four specimens: S600-48-7, S600-48-8, S600-48-16, and S600-48-18. If these four specimens are ignored, the average P_{Test}/P_{FEM} ratio is 1.01 with a scatter (standard deviation) of 0.06! Comparatively, the last four models: Option 13 (NGNDNL-C), 14 (NGNDPL-C), 15 (NGPDNL-C), and Option 16 (NGPDPL-C) are better than others. And, Option 13 (NGNDNL-C) is considered to be the "best" model in the comparisons.

The specimens in poor agreement (overly conservative) include the S600-48-18 which is the specimen under axial compression and the S600-48-7, S600-48-8 and S600-48-16 which are the specimens with small eccentricity in the minor axis. In these tests, similar phenomenon was observed: the load dropped sharply right after the peak load and the displacement in minor axis at the mid-height increased sharply. The experimental load equilibrium path was unstable for a while after the peak load for these four specimens, presumably friction in the rig joints provided

some artificial (unintentional) bracing support. Figure 5-21 shows the load-displacement curves of these test specimens. In these figures, the load-displacement curve from the test and the finite element modeling nearly coincide in the elastic range and also again deep in the post-buckling stage. This indicates that the finite element models follow a stable load path and achieve failure modes similar to the test results. In tests with larger eccentricities, or about axes where the specimen itself has greater rigidity (major axis or biaxial bending) this phenomena between the test and FE model was not observed.

Table 5-14: Comparisons of finite element results and test results for 48-inch specimens

No.	Specimen In the test	P_{Test}/P_{FEM} (Without cold roll-forming effect)								P_{Test}/P_{FEM} (With cold roll-forming effect)							
		1	2	3	4	5	6	7	8	9	10	11	12	13	14	15	16
1	S600-48-1	1.04	1.05	1.05	1.05	1.03	1.04	1.04	1.04	1.01	1.02	1.02	1.02	1.00	1.00	1.01	1.01
2	S600-48-2	1.05	1.05	1.05	1.05	1.03	1.03	1.03	1.03	1.03	1.03	1.04	1.04	1.02	1.02	1.02	1.02
3	S600-48-3	1.11	1.11	1.12	1.12	1.09	1.09	1.09	1.09	1.12	1.11	1.12	1.12	1.09	1.09	1.09	1.09
4	Minor axis bending S600-48-4	0.94	0.95	0.96	0.97	0.98	0.98	1.00	1.00	0.94	0.95	0.96	0.96	0.98	0.98	0.99	0.99
5	S600-48-5	0.95	0.95	0.96	0.96	0.97	0.97	0.99	0.98	0.94	0.94	0.94	0.94	0.96	0.95	0.97	0.96
6	S600-48-6	1.01	1.00	1.02	1.01	1.02	1.02	1.03	1.03	0.98	0.98	0.99	0.99	0.99	0.99	1.00	1.00
7	S600-48-7	1.75	1.76	1.75	1.75	1.69	1.69	1.68	1.68	1.75	1.75	1.75	1.75	1.69	1.69	1.68	1.68
8	Major axis bending S600-48-8	1.34	1.34	1.31	1.33	1.27	1.28	1.31	1.35	1.34	1.34	1.31	1.33	1.27	1.28	1.31	1.34
9	S600-48-9	1.09	1.09	1.09	1.11	1.03	1.01	1.01	1.04	1.08	1.08	1.08	1.10	1.02	1.00	1.00	1.03
10	S600-48-10	0.95	0.97	0.98	1.00	0.99	1.01	1.03	1.04	0.93	0.96	0.96	0.99	0.97	0.99	1.01	1.03
11	S600-48-11	0.94	0.95	0.96	0.98	1.00	1.01	1.03	1.04	0.95	0.95	0.96	0.98	1.00	1.01	1.02	1.04
12	S600-48-12	0.92	0.92	0.94	0.94	0.95	0.96	0.98	0.99	0.91	0.92	0.93	0.94	0.95	0.96	0.97	0.98
13	Bi-Axial bending S600-48-13	0.91	0.92	0.94	0.94	0.93	0.94	0.97	0.97	0.89	0.90	0.92	0.93	0.91	0.92	0.95	0.95
14	S600-48-14	1.14	1.14	1.14	1.14	1.11	1.11	1.11	1.11	1.14	1.14	1.14	1.14	1.11	1.11	1.11	1.11
15	S600-48-15	1.00	1.01	1.01	1.01	0.99	0.99	0.99	0.99	1.00	1.00	1.00	1.00	0.98	0.98	0.98	0.98
16	S600-48-16	1.36	1.36	1.36	1.36	1.32	1.32	1.32	1.32	1.36	1.36	1.36	1.36	1.32	1.32	1.32	1.32
17	S600-48-17	1.04	1.04	1.05	1.05	1.02	1.02	1.02	1.03	1.03	1.03	1.04	1.04	1.01	1.01	1.01	1.01
	Axial S600-48-18	1.77	1.77	1.76	1.76	1.71	1.71	1.70	1.70	1.77	1.77	1.76	1.76	1.71	1.71	1.70	1.70
	AVG.	1.13	1.13	1.14	1.14	1.12	1.12	1.13	1.14	1.12	1.12	1.13	1.13	1.11	1.11	1.12	1.13
	STDEV.	0.26	0.26	0.25	0.25	0.23	0.23	0.23	0.23	0.27	0.27	0.26	0.26	0.24	0.24	0.23	0.23
	MAX.	1.77	1.77	1.76	1.76	1.71	1.71	1.70	1.70	1.77	1.77	1.76	1.76	1.71	1.71	1.70	1.70
	MIN.	0.91	0.92	0.94	0.94	0.93	0.94	0.97	0.97	0.89	0.90	0.92	0.93	0.91	0.92	0.95	0.95
	Ignore S600-48-7, S600-48-8, S600-48-16, and S600-48-18																
	AVG.	1.01	1.01	1.02	1.02	1.01	1.01	1.02	1.03	1.00	1.00	1.01	1.01	1.00	1.00	1.01	1.01
	STDEV.	0.07	0.07	0.07	0.07	0.05	0.05	0.04	0.04	0.08	0.07	0.07	0.07	0.05	0.05	0.04	0.04
	MAX.	1.14	1.14	1.14	1.14	1.11	1.11	1.11	1.11	1.14	1.14	1.14	1.14	1.11	1.11	1.11	1.11
	MIN.	0.91	0.92	0.94	0.94	0.93	0.94	0.97	0.97	0.89	0.90	0.92	0.93	0.91	0.92	0.95	0.95

184
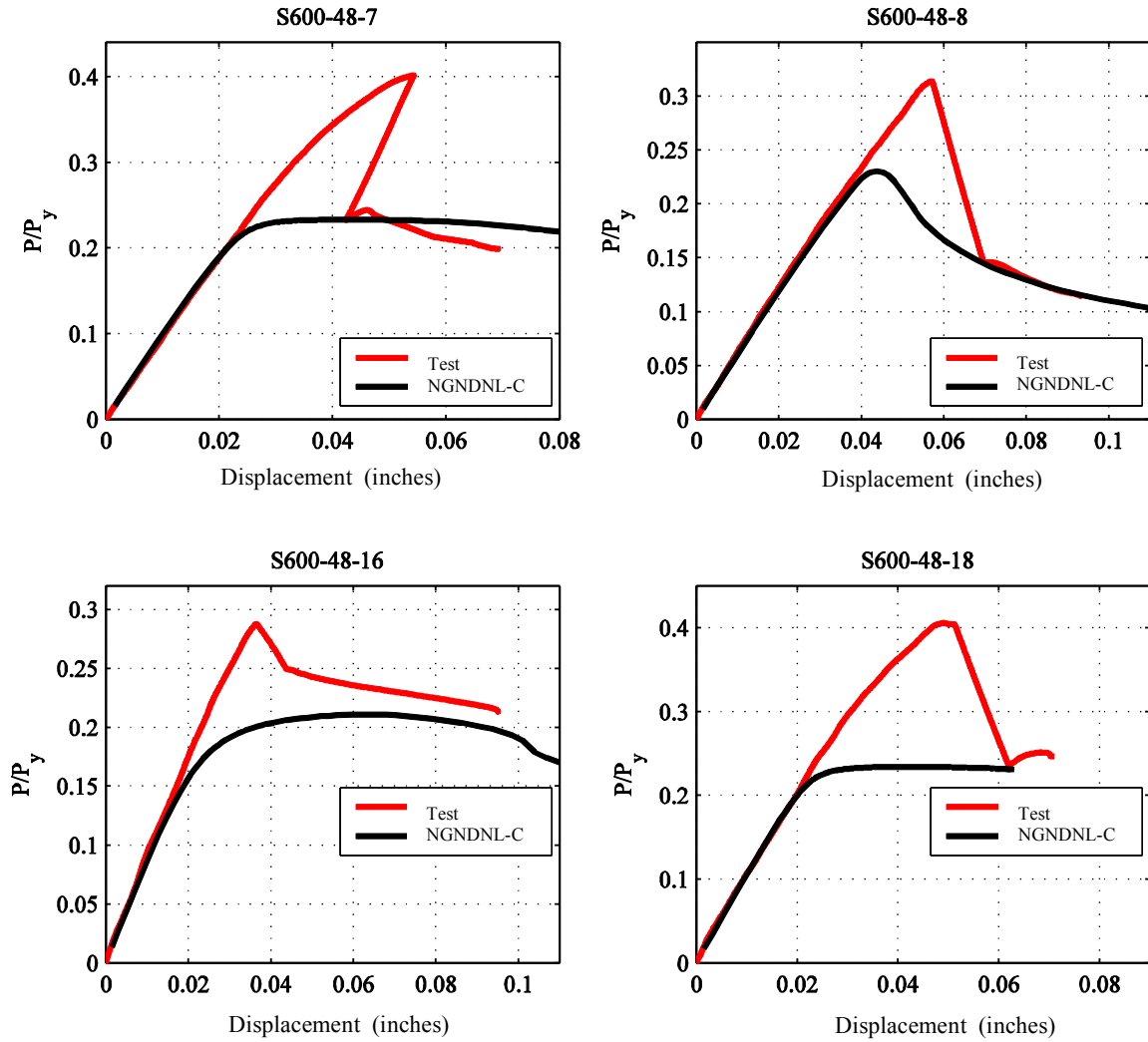
Figure 5-21: Load-displacement curve of S600-48-7, S600-48-7, S600-48-16, and S600-48-18

Figure 5-22 shows more precise results of the models with small eccentricities in the minor axis. In this figure, NON means the result from a finite element model without any imperfection; PGPDPL means the result from the finite element model with positive global, distortional, and local buckling mode imperfection; 25, 50, and 75 correspond to 25% CDF, 50% CDF, and 75% CDF in Figure 5-22. For members with +0.025 in (+0.1mm) eccentricity in minor axis, the capacity of the model without an imperfection is 42% higher than the capacity of model

with PGPDPL-75 imperfection. So, the load capacity of the specimen is highly sensitive to the imperfection in this region as illustrated in Figure 5-22.
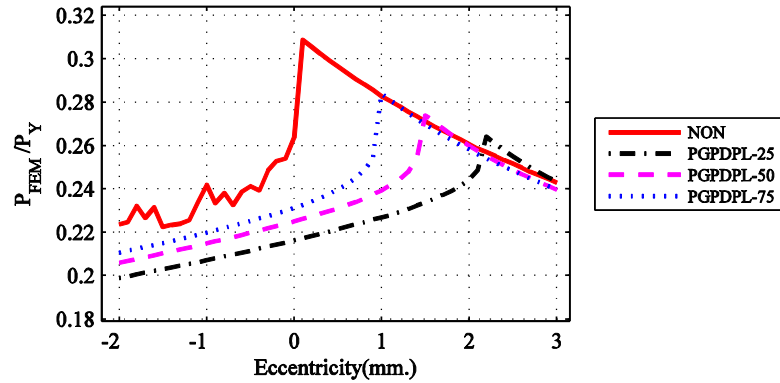
Figure 5-22: Finite element result for 48 inches long specimens with small eccentricities in minor axis. 25.4 mm=1 inch.

Note, the effect of cold-work in the long length specimens increased the load capacity of the specimens by about 1% on average. As the response becomes more elastic (i.e. for the longer columns) the cold-work, which influences the yielding response, becomes less important.

By comparing Option 1 through Option 8, the difference of the average P_{Test}/P_{FEM} ratio is less than 0.02, which means that the results are not highly sensitive to the sign of imperfection. However, outward flange deformation at the mid-height can result in slightly lower distortional buckling post-buckling strength.

5.3.2.2 Validation against the test results: Stiffness comparison

Table 5-17 to Table 5-17 show the stiffness calculation results for short, intermediate and long length lipped channel specimens, respectively. The initial stiffness of both the test specimens and the numerical model were calculated as secant stiffness at 40% of the specimen strength. Secant stiffness of the test data is subject to some initial accommodation.

Comparing the initial stiffness of the tested specimens to the FEM models provides a check on the models and the testing as it can be an indicator of how precise the specimens were set in the test rig at the desired eccentricities as well as estimate the existence of slack in the clamping of the end plates and swivel joints. Change in the provided eccentricities can meaningfully change the initial stiffness of the specimens. Minor detachment of the end plate and the loading plates or small movement in the swivel joints can also reduce the initial stiffness of the specimen. In general, the FEM models are expected to be stiffer than the physical models.

The stiffness from the finite element models matches the stiffness of the tested specimens, which means the specimens were almost at the targeted eccentricities. The average of the test to FEM stiffness for all short specimens is 0.83 and the standard deviation is around 0.12. The decrease in the test initial stiffness can also be justified by the high stiffness demand of the short specimens on the end plates and the clamps. As the failure of the specimen is a function of the force equilibrium and stress distribution on the cross section, any decrease in the initial stiffness may not affect the strength magnitude, although the failure may happen at a larger displacement.

For 24 in. specimens, the average axial K_{Test}/K_{FEM} ratio is 0.92 and the scatter is around 0.07. The results showed that the average of the test to FEM stiffness for 48-inch specimens is 0.99 and the scatter is around 0.10. Accordingly, the stiffness prediction of the longer (less flexural stiffness) is generally better than the shorter specimens. While the total stiffness comes from both the test setup (end plates and clamps) stiffness and the stiffness of the specimen, for longer specimens with lower flexural stiffness the deformation demand on the end plates and clamps is lower and the specimen stiffness is more contributing in the total stiffness.

Table 5-15 Comparison the initial stiffness of the finite element model and test result for the 12-inch long specimen

No.		Specimen	K(kip/inch)	K_{Test}/K_{FEM} (Without cold roll-forming effect)								K_{Test}/K_{FEM} (With cold roll-forming effect)							
			test	1	2	3	4	5	6	7	8	9	10	11	12	13	14	15	16
1	Minor axis bending	S600-12-1	138.08	0.85	0.88	0.95	0.96	0.84	0.86	0.94	0.94	0.86	0.90	0.96	0.97	0.85	0.88	0.96	0.95
2		S600-12-19	414.23	0.97	1.00	1.09	1.12	0.96	0.98	1.07	1.09	0.98	1.03	1.10	1.13	0.97	1.00	1.09	1.10
3		S600-12-4	877.55	0.96	0.97	1.04	1.08	0.96	0.95	1.04	1.05	0.97	0.99	1.05	1.09	0.96	0.96	1.05	1.06
4		S600-12-5	986.51	0.91	0.91	0.90	0.93	0.92	0.91	0.91	0.92	0.91	0.91	0.91	0.94	0.92	0.92	0.92	0.93
5		S600-12-6	730.03	0.92	0.91	0.88	0.89	0.93	0.93	0.89	0.90	0.92	0.91	0.88	0.89	0.93	0.93	0.89	0.90
6		S600-12-8	225.51	1.03	1.03	1.03	1.03	1.04	1.04	1.04	1.04	1.04	1.04	1.03	1.03	1.05	1.04	1.04	1.05
7	Major axis bending	S600-12-9	806.06	0.86	0.85	0.87	0.91	0.86	0.84	0.87	0.89	0.86	0.85	0.88	0.92	0.87	0.84	0.88	0.90
8		S600-12-10	287.53	0.83	0.82	0.82	0.84	0.83	0.82	0.82	0.83	0.83	0.82	0.82	0.84	0.83	0.82	0.82	0.83
9		S600-12-11	52.23	0.53	0.52	0.52	0.52	0.53	0.52	0.52	0.52	0.53	0.52	0.52	0.52	0.53	0.52	0.52	0.52
10	Bi-Axial bending	S600-12-2	605.09	0.78	0.76	0.75	0.78	0.78	0.77	0.75	0.77	0.78	0.77	0.75	0.78	0.78	0.77	0.75	0.77
11		S600-12-13	152.36	0.82	0.82	0.80	0.81	0.83	0.82	0.81	0.81	0.82	0.82	0.81	0.81	0.83	0.82	0.81	0.81
12		S600-12-14	735.52	0.80	0.79	0.76	0.79	0.81	0.79	0.77	0.79	0.80	0.79	0.77	0.79	0.81	0.80	0.77	0.79
13		S600-12-15	237.23	0.94	0.94	0.92	0.93	0.95	0.94	0.93	0.93	0.94	0.94	0.92	0.93	0.95	0.95	0.93	0.93
14		S600-12-16	787.40	0.91	0.90	0.96	1.00	0.90	0.88	0.96	0.97	0.91	0.91	0.97	1.01	0.91	0.89	0.97	0.98
15		S600-12-17	188.85	0.77	0.77	0.83	0.85	0.77	0.75	0.82	0.83	0.78	0.77	0.83	0.85	0.77	0.76	0.83	0.84
16		S600-12-3	581.02	0.76	0.75	0.78	0.81	0.77	0.74	0.78	0.80	0.77	0.75	0.79	0.82	0.77	0.74	0.79	0.80
17		S600-12-20	151.52	0.83	0.82	0.84	0.86	0.83	0.82	0.84	0.85	0.84	0.82	0.85	0.86	0.83	0.82	0.84	0.85
	Ave.			0.85	0.85	0.87	0.89	0.85	0.85	0.87	0.88	0.86	0.86	0.87	0.89	0.86	0.85	0.87	0.88
	Stdev.			0.11	0.12	0.13	0.14	0.11	0.12	0.13	0.13	0.12	0.12	0.14	0.14	0.12	0.12	0.14	0.13
	Max.			1.03	1.03	1.09	1.12	1.04	1.04	1.07	1.09	1.04	1.04	1.10	1.13	1.05	1.04	1.09	1.10
	Min.			0.53	0.52	0.52	0.52	0.53	0.52	0.52	0.52	0.53	0.52	0.52	0.52	0.53	0.52	0.52	0.52

Table 5-16 Comparison the initial stiffness of the finite element model and test result for the 24-inch long specimens

No.		Specimen	K(kip/inch)	K_{Test}/K_{FEM} (Without cold roll-forming effect)								K_{Test}/K_{FEM} (With cold roll-forming effect)							
			test	1	2	3	4	5	6	7	8	9	10	11	12	13	14	15	16
1	Minor axis bending	S600-24-1	48.99	0.96	0.99	0.98	0.97	0.94	0.97	0.96	0.95	0.98	1.01	0.99	0.98	0.96	0.99	0.97	0.97
2		S600-24-2	160.52	1.07	1.10	1.10	1.08	1.04	1.07	1.07	1.06	1.09	1.11	1.11	1.10	1.05	1.08	1.08	1.07
3		S600-24-3	408.98	0.93	0.96	0.98	0.95	0.91	0.94	0.95	0.93	0.94	0.97	0.99	0.96	0.91	0.94	0.96	0.94
4		S600-24-6	468.89	0.91	0.93	0.93	0.91	0.93	0.95	0.94	0.92	0.91	0.94	0.93	0.91	0.93	0.96	0.94	0.92
5		S600-24-5	183.94	0.97	0.97	0.96	0.96	0.99	0.99	0.98	0.98	0.97	0.97	0.96	0.96	0.99	1.00	0.98	0.98
6		S600-24-4	57.57	0.88	0.88	0.88	0.88	0.89	0.89	0.89	0.89	0.88	0.88	0.88	0.88	0.90	0.90	0.90	0.90
7	Major axis bending	S600-24-7	434.66	0.89	0.92	0.93	0.90	0.89	0.92	0.92	0.90	0.90	0.92	0.93	0.91	0.89	0.92	0.92	0.90
8		S600-24-8	181.60	0.86	0.88	0.87	0.86	0.85	0.87	0.87	0.86	0.86	0.88	0.88	0.86	0.86	0.87	0.87	0.86
9		S600-24-9	50.90	0.79	0.80	0.80	0.79	0.79	0.80	0.80	0.79	0.79	0.80	0.80	0.79	0.79	0.80	0.80	0.79
10	Bi-Axial bending	S600-24-10	383.43	0.89	0.91	0.91	0.89	0.89	0.92	0.91	0.89	0.89	0.92	0.92	0.90	0.89	0.92	0.91	0.89
11		S600-24-11	91.03	0.86	0.86	0.85	0.85	0.86	0.86	0.86	0.85	0.86	0.86	0.85	0.85	0.86	0.87	0.86	0.85
12		S600-24-12	496.93	1.08	1.10	1.09	1.07	1.10	1.13	1.11	1.08	1.08	1.10	1.09	1.07	1.10	1.13	1.11	1.09
13		S600-24-13	124.03	0.91	0.91	0.90	0.90	0.92	0.92	0.91	0.91	0.91	0.92	0.90	0.90	0.92	0.93	0.91	0.91
14		S600-24-14	398.44	0.96	0.98	1.01	0.98	0.93	0.96	0.98	0.96	0.97	0.99	1.02	0.99	0.93	0.96	0.98	0.97
15		S600-24-15	112.87	0.89	0.91	0.93	0.91	0.88	0.89	0.91	0.89	0.90	0.92	0.94	0.92	0.89	0.90	0.91	0.90
16		S600-24-16	357.56	0.89	0.91	0.93	0.90	0.87	0.90	0.91	0.89	0.89	0.92	0.94	0.91	0.88	0.91	0.92	0.89
17		S600-24-17	94.52	0.91	0.92	0.93	0.91	0.89	0.91	0.92	0.90	0.91	0.92	0.93	0.92	0.90	0.91	0.92	0.91
18	Axial	S600-24-18	489.79	0.91	0.93	0.94	0.92	0.89	0.93	0.93	0.91	0.91	0.93	0.95	0.92	0.90	0.93	0.94	0.91
19	Major	S600-24-19	50.42	0.78	0.79	0.79	0.78	0.78	0.79	0.79	0.78	0.79	0.79	0.79	0.79	0.78	0.79	0.79	0.78
20	Axial	S600-24-20	494.73	0.91	0.93	0.95	0.92	0.89	0.93	0.94	0.91	0.92	0.94	0.95	0.92	0.90	0.94	0.94	0.92
	Ave.			0.91	0.93	0.93	0.92	0.91	0.93	0.93	0.91	0.92	0.93	0.94	0.92	0.91	0.93	0.93	0.92
	Stdev.			0.07	0.08	0.08	0.07	0.07	0.08	0.08	0.07	0.08	0.08	0.08	0.08	0.08	0.08	0.08	0.08
	Max.			1.08	1.10	1.10	1.08	1.10	1.13	1.11	1.08	1.09	1.11	1.11	1.10	1.10	1.13	1.11	1.09
	Min.			0.78	0.79	0.79	0.78	0.78	0.79	0.79	0.78	0.79	0.79	0.79	0.79	0.78	0.79	0.79	0.78

Table 5-17 Comparison the initial stiffness of the finite element model and test result for the 48-inch long specimens

		Specimen	K(kip/inch)	K_{Test}/K_{FEM} (Without cold roll-forming effect)								K_{Test}/K_{FEM} (With cold roll-forming effect)							
			test	1	2	3	4	5	6	7	8	9	10	11	12	13	14	15	16
1		S600-48-1	16.90	1.07	1.07	1.06	1.05	1.03	1.03	1.03	1.02	1.08	1.09	1.07	1.07	1.05	1.06	1.05	1.04
2		S600-48-2	73.58	1.26	1.27	1.25	1.24	1.20	1.22	1.19	1.18	1.27	1.28	1.26	1.25	1.21	1.23	1.20	1.19
3	Minor axis bending	S600-48-3	248.70	1.34	1.37	1.34	1.32	1.25	1.28	1.25	1.24	1.33	1.37	1.33	1.32	1.24	1.28	1.24	1.24
4		S600-48-4	192.85	0.88	0.88	0.89	0.88	0.94	0.94	0.94	0.93	0.88	0.88	0.89	0.88	0.93	0.94	0.94	0.94
5		S600-48-5	68.94	0.98	0.98	0.97	0.97	1.02	1.02	1.01	1.02	0.99	0.99	0.98	0.98	1.03	1.03	1.02	1.03
6		S600-48-6	18.44	0.94	0.95	0.94	0.94	0.97	0.97	0.96	0.96	0.96	0.95	0.96	0.95	0.98	0.98	0.98	0.98
7		S600-48-7	249.69	0.95	0.97	0.96	0.94	0.93	0.95	0.95	0.93	0.95	0.96	0.96	0.94	0.93	0.95	0.95	0.93
8	Major axis bending	S600-48-8	157.73	0.98	0.99	1.00	0.98	0.99	0.99	1.00	0.98	0.98	0.99	0.99	0.98	0.98	0.99	0.99	0.98
9		S600-48-9	39.17	0.94	0.94	0.94	0.93	0.93	0.94	0.94	0.93	0.93	0.94	0.94	0.93	0.93	0.93	0.93	0.93
10		S600-48-11	251.10	1.07	1.09	1.09	1.07	1.09	1.10	1.11	1.09	1.07	1.08	1.08	1.07	1.08	1.10	1.10	1.08
11		S600-48-10	64.21	1.01	1.01	1.01	1.01	1.02	1.02	1.03	1.02	1.01	1.01	1.01	1.01	1.03	1.02	1.03	1.02
12		S600-48-12	200.77	0.87	0.87	0.87	0.86	0.90	0.91	0.91	0.90	0.86	0.87	0.87	0.86	0.91	0.91	0.91	0.90
13	Bi-Axial bending	S600-48-13	79.28	1.09	1.09	1.09	1.09	1.13	1.13	1.12	1.12	1.10	1.10	1.09	1.09	1.14	1.14	1.13	1.13
14		S600-48-14	247.30	1.23	1.25	1.23	1.21	1.15	1.18	1.16	1.13	1.23	1.25	1.23	1.21	1.15	1.17	1.15	1.13
15		S600-48-15	64.61	1.08	1.09	1.07	1.06	1.03	1.04	1.02	1.01	1.08	1.09	1.07	1.06	1.03	1.04	1.02	1.01
16		S600-48-16	214.02	0.99	1.01	1.00	0.98	0.95	0.97	0.96	0.94	0.98	1.00	0.99	0.97	0.94	0.96	0.95	0.93
17		S600-48-17	59.25	1.01	1.02	1.01	1.00	0.99	0.99	0.98	0.97	1.01	1.02	1.01	1.01	0.98	0.99	0.98	0.97
18	Axial	S600-48-18	264.68	0.94	0.96	0.96	0.94	0.93	0.95	0.94	0.92	0.94	0.96	0.95	0.93	0.93	0.94	0.94	0.92
	Ave.			1.04	1.05	1.04	1.03	1.02	1.03	1.03	1.02	1.04	1.05	1.04	1.03	1.03	1.04	1.03	1.02
	Stdev.			0.13	0.13	0.13	0.12	0.10	0.11	0.10	0.10	0.13	0.14	0.13	0.12	0.10	0.11	0.10	0.10
	Max.			1.34	1.37	1.34	1.32	1.25	1.28	1.25	1.24	1.33	1.37	1.33	1.32	1.24	1.28	1.24	1.24
	Min.			0.87	0.87	0.87	0.86	0.90	0.91	0.91	0.90	0.86	0.87	0.87	0.86	0.91	0.91	0.91	0.90

5.3.2.3 Load-displacement results

The load-displacement curves of the test specimens and the finite element models are compared in Appendix F for the "best" model determined in the previous sections (Option 13 (NGNDNL-C): negative global, distortional, and local imperfection and including cold-rolling effects). The results show how the predicted load-displacement curves match the test results.

5.3.2.4 Moment-rotation results

The moment-rotation curves of the test specimens and the finite element models are shown in Appendix I for the "best" model determined in the previous sections. The results show how the predicted moment-rotation results match the test results. It should be noted that

generally the moment rotation results of the longer specimens are in better agreement with the test results.

5.3.3 Interaction curves and comparison against DSM (AISI-S100-12) and test results

As shown in Figure 5-23 to Figure 5-25 the experimental results are compared to the predictions of the AISI-S100-12 specifications by utilizing the DSM method for nominal axial (P_n) and flexural (M_{nx}, M_{ny}) strengths in Appendix 1; and the interaction equations in AISI-S100 section C5.2: Combined Compressive Axial Load and bending. Accordingly, the following interaction equation,

$$\frac{\overline{P}}{\phi_c P_n} + \frac{C_{mx}\overline{M_x}}{\phi_b M_{nx}\alpha_x} + \frac{C_{mz}\overline{M_z}}{\phi_b M_{nz}\alpha_z} \leq 1.0 \tag{5.2}$$

where, $\overline{P}$, $\overline{M}_{x,y}$ are the required strengths, P_n, $M_{nx,nz}$ are the nominal strengths, $C_{mx,mz}$ are moment gradient coefficients, $\alpha_{x,y} = 1 - \overline{P}/P_{Ex,y}$ is the P-δ moment amplification factors, $P_{Ex,z} = \pi^2 EI/(K_{x,z}L_{x,z})$ are the Euler buckling loads, and $\phi_{c,b}$ are compressive and bending resistance factors.

Nominal strengths, were determined in accordance with the AISI-S100-12 Appendix 1 DSM method including inelastic reserve. Critical elastic local and distortional buckling axial load and moments were determined by CUFSM 4.06 finite strip program (Schafer and Adany 2006). To automatically identify local and distortional buckling the "FSM@cFSM-L_{cr}" was used (Li and Schafer 2010). "FSM@cFSM-L_{cr}" utilizes a straight-line cross-section definition to perform a constrained finite strip method (cFSM) analysis to determine local and distortional buckling loads and the corresponding half-wave lengths (L_{cr}). Knowing L_{cr} for both local and

distortional buckling, FSM can be utilized to determine the signature curve of the rounded-corner model. Local and distortional buckling loads at the associated L_{cr} are determined from the signature curve. Critical elastic column buckling and lateral-torsional beam buckling loads were determined from CUTWP (Sarawit 2006) with the effective lengths determined in Table 5-6. Where the ends moments on the specimens were almost equal and the member was bent in single curvature, $C_{mx,mz}$=1.0; and to compare with the test results resistance factors were assumed to be unity ($\phi_{c,b}$=1.0). Moreover, moment amplification factors ($\alpha_{x,z}$) were assumed to be 1.0, where the end-moment experimental results were compared to the specification predictions in Figure 5-23 to Figure 5-31.
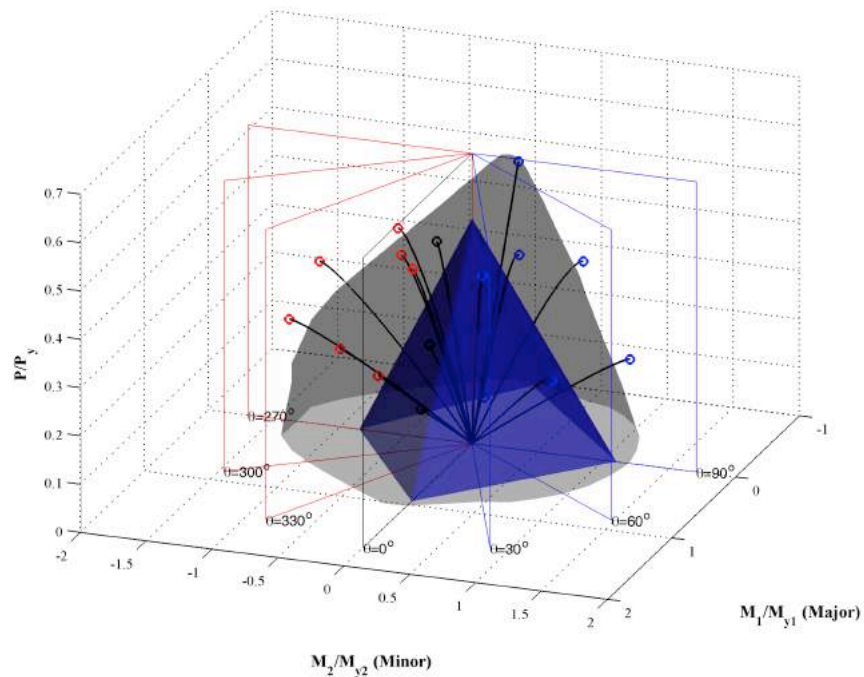
Figure 5-23: Test results (black lines and circles at the peak load; Short specimens: 12 inches) vs. AISI-S100-12 prediction (blue surface) and FEM results (gray surface)
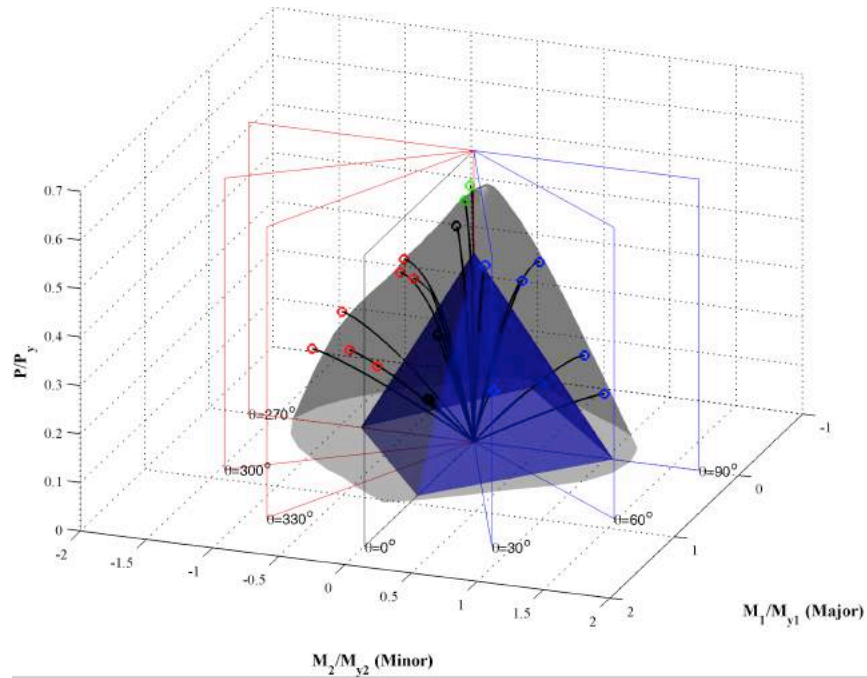
Figure 5-24: Test results (Intermediate specimens: 24 inches) vs. AISI-S100-12 prediction and FEM results
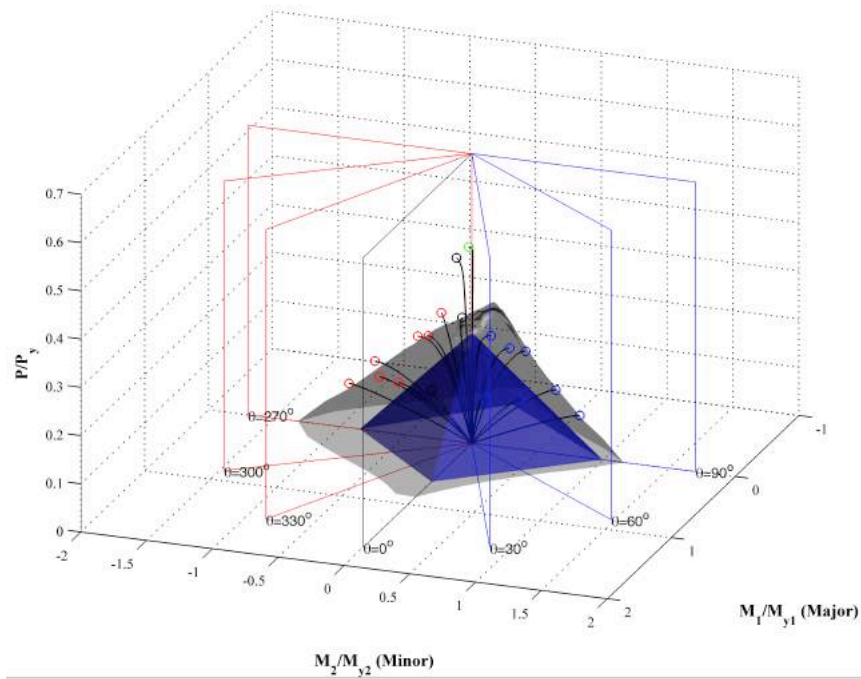
Figure 5-25: Test results (Long specimens: 48 inches) vs. AISI-S100-12 prediction and FEM results

For the DSM (AISI-S100-12) predictions, a correction was made to the distortional elastic buckling loads to address the actual clamped boundary conditions in the test rig. Clamped boundary conditions increase both the local and distortional elastic buckling loads; however, the

192

increase in local buckling critical load is negligible. For distortional buckling in short members this increase may be large, particularly when the distortional buckling half-wave length (L_{crd}) is comparable to the length of the element. To account for this phenomenon, an empirical increase had been developed for boosting up the distortional buckling critical load (Eq. 2.1).

It would be also possible to directly model the warping fixed end conditions in CUFSM 4.06; however, the signature curve does not exist in this case, and the results are slightly more complex – for simple design situations D_{boost} provides greater convenience. In the calculations L was assumed to be 12 in. for boosting up the distortional buckling; and 24 in. for global buckling calculations, where the length of the top and bottom rigid links must be included in the global length of the specimen between top and bottom pin joints.

The interaction curves at particular planes in the P-M_1-M_2 space that include available experimental results are illustrated in Figure 5-26 to Figure 5-31. In each figure, all available numerical (FEM), analytical (AISI-S100-12), and experimental results are compared together. To show the contribution of each of the limits states, the linear interaction equation (Eq. 4.2) was implemented to provide a distinct interaction curve for the several limit states: plastic limit, yield limit, global limit, distortional limit, and local limit.
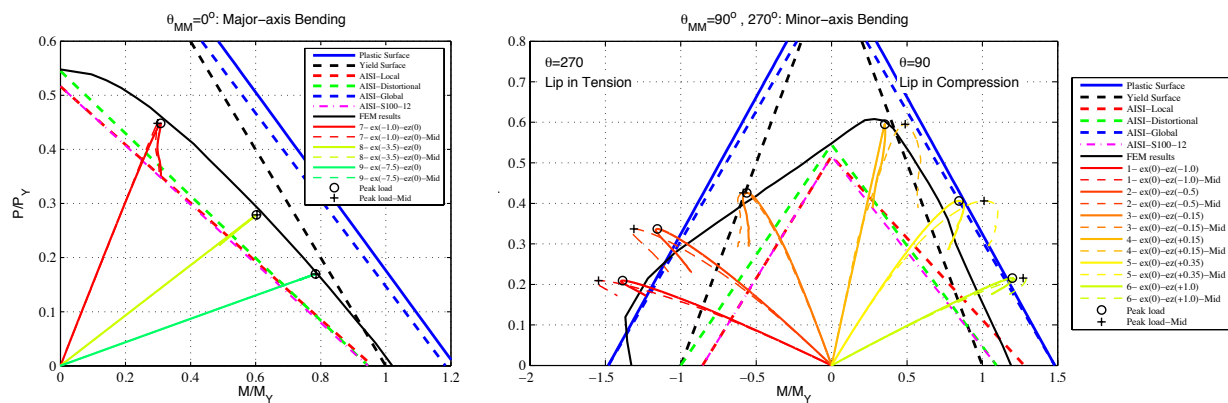
Figure 5-26: Test results (Short specimens: 12 inches) vs. AISI-S100-12 prediction and FEM results in principal axes (Slice of 3D)
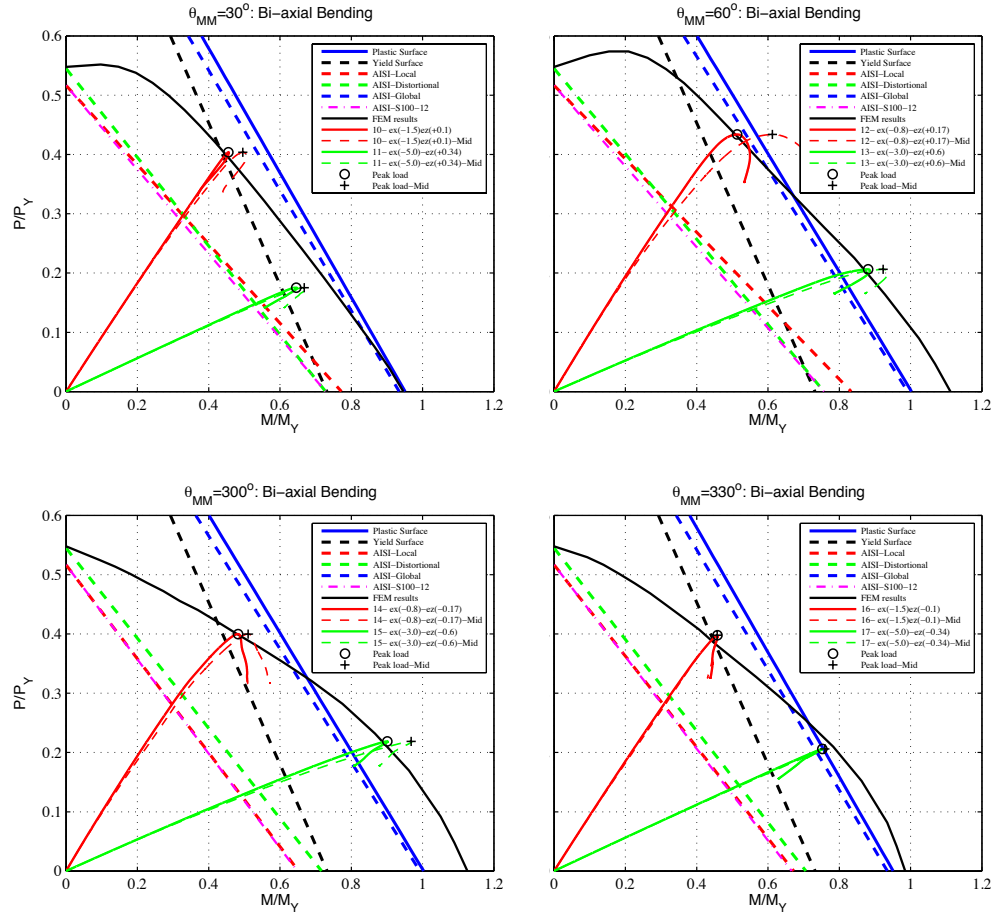
Figure 5-27: Test results (Short specimens: 12 inches) vs. AISI-S100-12 prediction and FEM results in non-principal axes
(Slice of 3D)
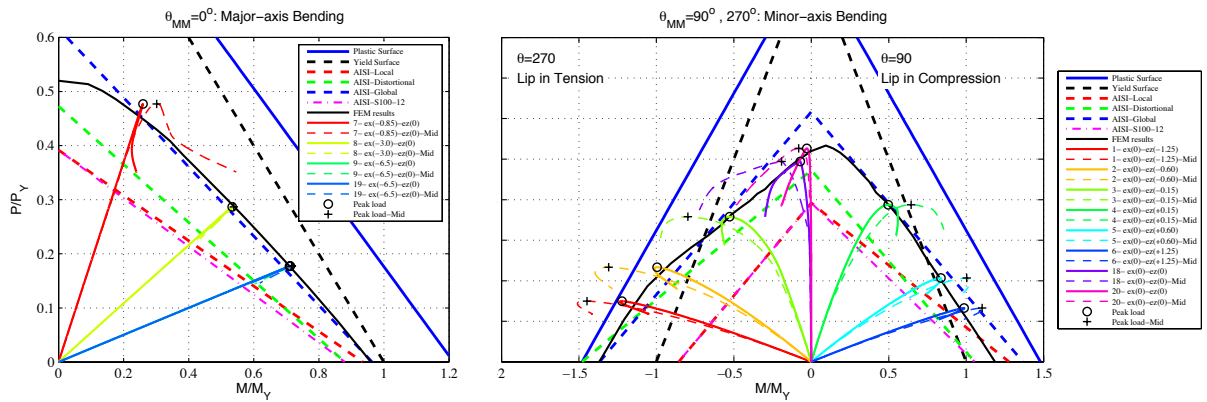
Figure 5-28: Test results (Intermediate specimens: 24 inches) vs. AISI-S100-12 prediction and FEM results in principal axes. (Slice of 3D)
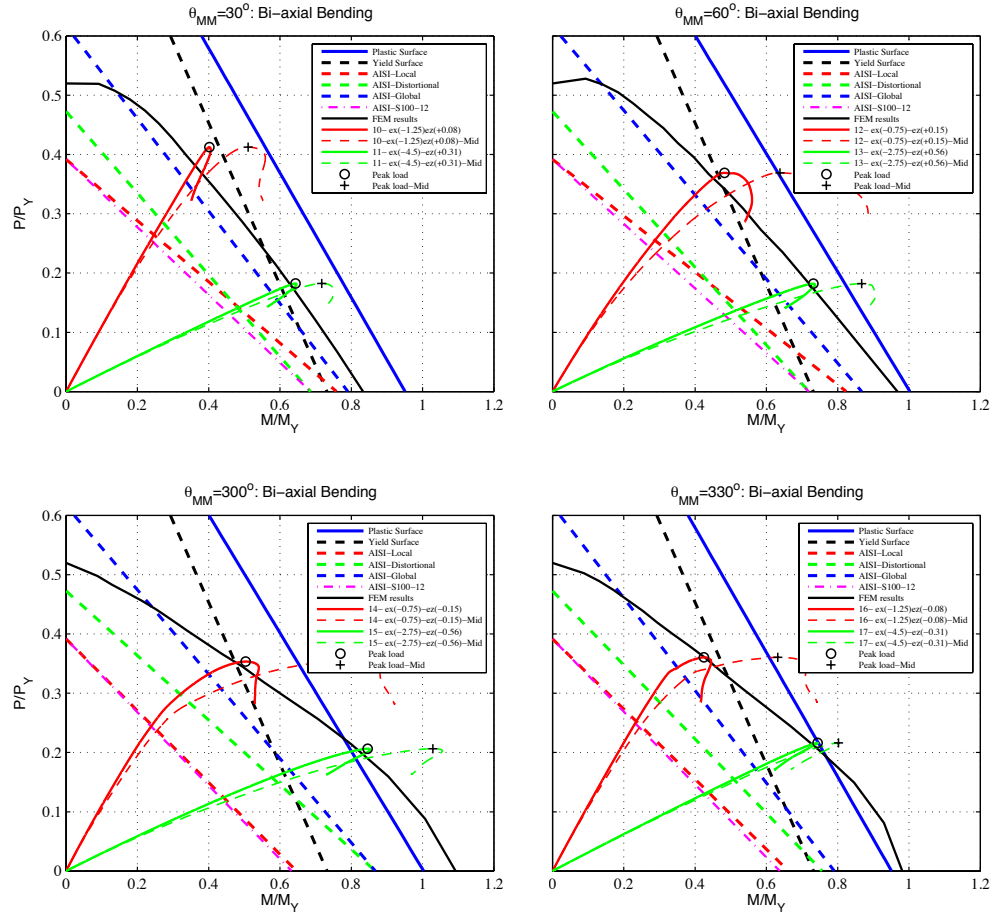
Figure 5-29: Test results (Intermediate specimens: 24 inches) vs. AISI-S100-12 prediction and FEM results in non-principal axes. (Slice of 3D)
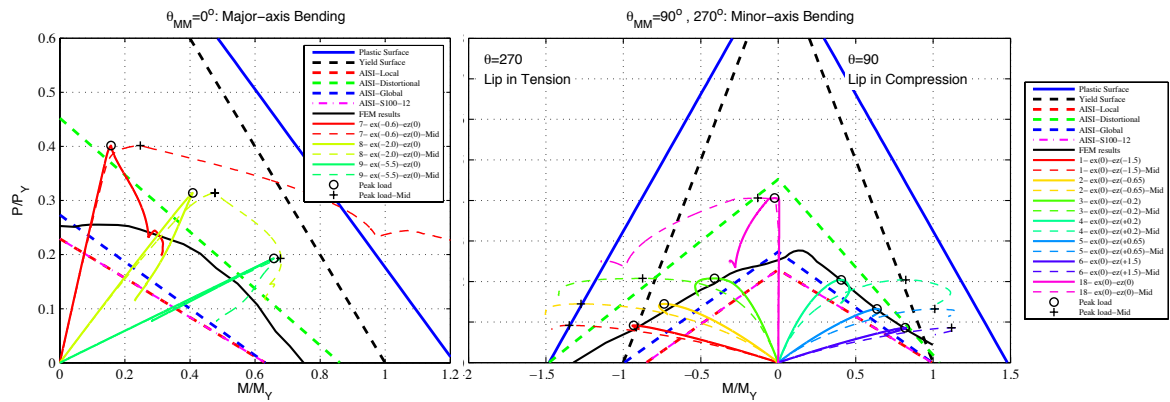
Figure 5-30: Test results (Long specimens: 48 inches) vs. AISI-S100-12 prediction and FEM results in principal axes.
(Slice of 3D)
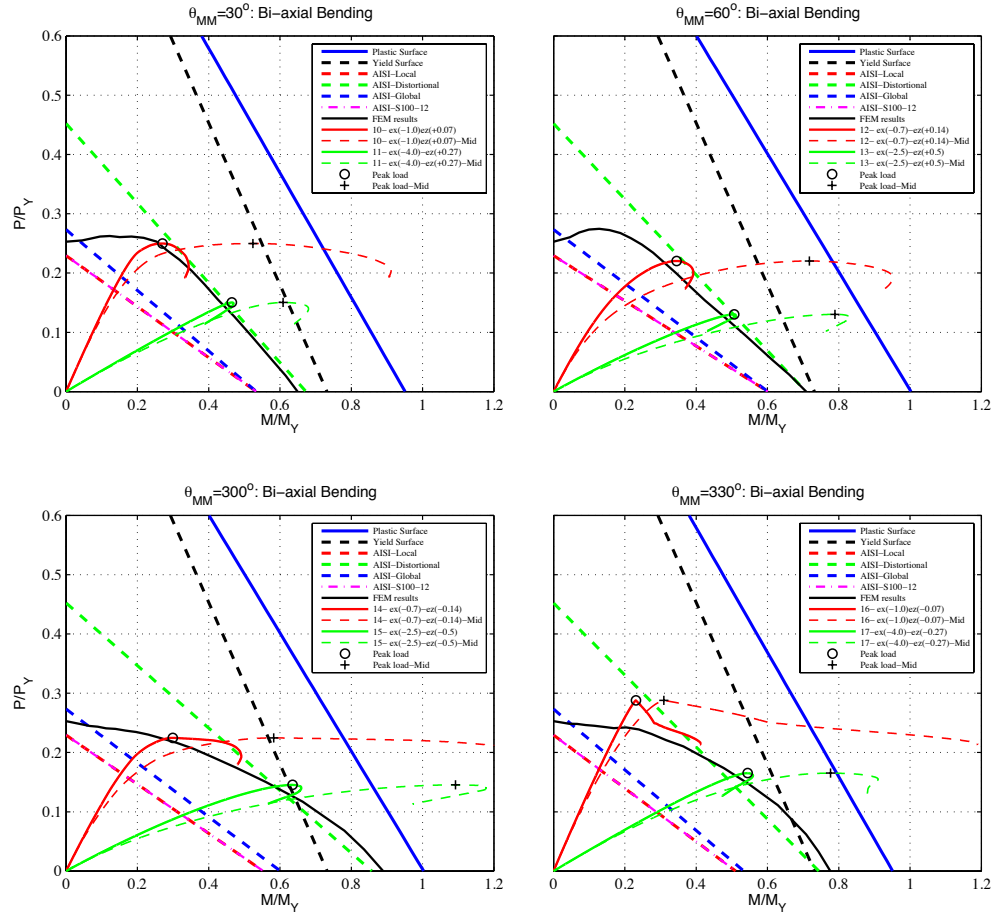
Figure 5-31: Test results (long specimens: 48 inches) vs. AISI-S100-12 prediction and FEM results in non-principal axes. (Slice of 3D)

Generally speaking, the AISI-S100-12 design method follows the experimental results, although it is quite conservative for short and intermediate specimens. The AISI-S100-12 specifications successfully predicted the failure mode of the specimens, although the results were quite conservative in terms of strength. For short and intermediate length specimens, all the specimens with negative minor axis bending (causing tension in the lips) failed in local buckling and all others with positive minor axis bending failed in the distortional mode. In short specimens, most of the failures occurred beyond the yield surface and for some beyond the plastic surface, indicating significant inelastic reserve (and even strain hardening). In short specimens, for almost all specimens, the global plastic surface was close to the plastic surface

indicating a high global buckling load (as desired) and minimal local-global interaction. In long specimens, the global buckling effect governed the behavior and therefore, due to local-global interaction, local buckling always happed prior to the distortional buckling. However, distortional buckling modes were also observed in the tests.

For each test the moments were calculated including the "e_x" and "e_z" eccentricities at the rigid end distances as well as with the additional P-δ moment due to mid-height displacements denoted with a "Mid" in the plots. The FE model (as discussed in Section 5.3.2) is in excellent agreement with the test except for axial and minor-axis bending where both AISI-S100-12 interaction curves and FE predictions remain consistently conservative.

Table 5-18 to Table 5-20 show the results using the P-M-M spaced as defined in Chapter 4. The results show that all FEM models for short, intermediate and long specimens provide reasonable prediction, however the coefficient of variation for β_{Test}/β_{FEM} for long specimens, which global buckling was more significant in the failure modes, are larger than the shorter specimens.

Table 5-18: Results summary for short specimens (12 in.): test results, FEM "best" model predictions

No.	Bending Axis	Specimen in the test	Measured Angles		Test result		FEM result		Comparison	
			θ_{MM}	ϕ_{PM}	K_{Test}	β_{Test}	K_{FEM}	β_{FEM}	K_{Test}/K_{FEM}	β_{Test}/β_{FEM}
			(deg.)	(deg.)	(kips/in.)	-	(kips/in.)	-	-	-
1	Minor	S600-12-1	270.0	79.8	138.1	1.40	152.8	1.30	0.90	1.08
2		S600-12-19	270.0	70.4	414.2	1.20	416.7	1.09	0.99	1.10
3		S600-12-4	270.0	43.8	877.5	0.71	942.1	0.69	0.93	1.02
4		S600-12-5	90.0	29.4	986.5	0.69	1137.9	0.72	0.87	0.96
5		S600-12-6	90.0	58.0	730.0	0.94	822.2	0.87	0.89	1.08
6		S600-12-8	90.0	78.5	225.5	1.22	217.4	1.00	1.04	1.22
7	Major	S600-12-9	340.1	33.0	806.1	0.54	992.9	0.55	0.81	0.99
8		S600-12-10	358.2	65.0	287.5	0.66	358.8	0.68	0.80	0.98
9		S600-12-11	360.0	77.7	52.2	0.80	101.4	0.81	0.51	0.99
10	Bi-Axial	S600-12-2	31.1	47.0	605.1	0.61	825.1	0.62	0.73	0.98
11		S600-12-13	29.8	74.2	152.4	0.67	189.2	0.76	0.81	0.87
12		S600-12-14	60.1	44.9	735.5	0.67	976.4	0.72	0.75	0.93
13		S600-12-15	60.7	75.1	237.2	0.90	255.1	0.92	0.93	0.98
14		S600-12-16	300.8	44.2	787.4	0.63	905.8	0.65	0.87	0.96
15		S600-12-17	299.9	74.8	188.9	0.93	244.8	0.97	0.77	0.95
16		S600-12-3	330.5	46.5	581.0	0.61	797.8	0.59	0.73	1.02
17		S600-12-20	330.2	74.2	151.5	0.78	185.3	0.81	0.82	0.96
								Average	0.83	1.01
								Standard deviation	0.12	0.08
								C.O.V	14.5%	7.8%

Table 5-19: Results summary for intermediate specimens (24"): test results, FEM "best" model predictions

No.	Bending Axis	Specimen in the test	Measured Angles		Test result		FEM result		Comparison	
			θ_{MM}	ϕ_{PM}	K_{Test}	β_{Test}	K_{FEM}	β_{FEM}	K_{Test}/K_{FEM}	β_{Test}/β_{FEM}
			(deg.)	(deg.)	(kips/in.)	-	(kips/in.)	-	-	-
1	Minor	S600-24-1	270.0	81.5	49.0	1.23	51.0	1.19	0.96	1.04
2		S600-24-2	270.0	72.3	160.5	1.02	152.4	1.07	1.05	0.96
3		S600-24-3	270.0	37.9	409.0	0.64	448.5	0.75	0.91	0.85
4		S600-24-6	90.0	38.1	468.9	0.63	503.4	0.68	0.93	0.93
5		S600-24-5	90.0	72.4	183.9	0.86	185.0	0.90	0.99	0.96
6		S600-24-4	90.0	81.1	57.6	0.99	64.3	0.99	0.90	1.00
7	Major	S600-24-7	6.5	28.2	434.7	0.54	489.1	0.51	0.89	1.07
8		S600-24-8	0.6	61.4	181.6	0.61	212.4	0.62	0.86	0.98
9		S600-24-9	359.7	75.9	50.9	0.73	64.3	0.73	0.79	1.01
10	Bi-Axial	S600-24-10	31.8	42.0	383.4	0.58	428.5	0.56	0.89	1.03
11		S600-24-11	33.3	73.1	91.0	0.67	105.8	0.69	0.86	0.97
12		S600-24-12	62.4	44.7	496.9	0.61	450.1	0.66	1.10	0.92
13		S600-24-13	60.9	73.9	124.0	0.75	134.4	0.83	0.92	0.91
14		S600-24-14	302.3	40.7	398.4	0.62	427.1	0.73	0.93	0.85
15		S600-24-15	300.8	73.1	112.9	0.87	127.5	0.94	0.89	0.93
16		S600-24-16	329.7	41.5	357.6	0.56	407.9	0.65	0.88	0.86
17		S600-24-17	330.0	72.5	94.5	0.77	105.4	0.79	0.90	0.98
18	Axial	S600-24-18	-	1.1	489.8	0.50	546.1	0.50	0.90	1.00
19	Major	S600-24-19	359.7	75.9	-	0.73	-	0.72	-	1.02
20	Axial	S600-24-20	-	1.1	-	0.53	-	0.51	-	1.04
								Average	0.92	0.97
								Standard deviation	0.07	0.07
								C.O.V	8.1%	6.8%

Table 5-20: Results summary for long specimens (48"): test results, FEM "best" model predictions

No.	Bending Axis	Specimen in the test	Measured Angles		Test result		FEM result		Comparison	
			θ_{MM}	ϕ_{PM}	K_{Test}	β_{Test}	K_{FEM}	β_{FEM}	K_{Test}/K_{FEM}	β_{Test}/β_{FEM}
			(deg.)	(deg.)	(kips/in.)	-	(kips/in.)	-	-	-
1		S600-48-1	270.0	83.0	16.8	0.94	16.5	1.02	1.02	0.92
2		S600-48-2	270.0	73.6	72.1	0.75	62.3	0.88	1.16	0.86
3	Minor	S600-48-3	270.0	45.3	252.5	0.46	201.3	0.65	1.25	0.70
4		S600-48-4	90.0	46.8	194.2	0.45	206.7	0.61	0.94	0.75
5		S600-48-5	90.0	73.7	68.4	0.65	67.9	0.77	1.01	0.84
6		S600-48-6	90.0	82.7	18.6	0.82	19.2	0.89	0.97	0.93
7		S600-48-7	2.4	20.2	249.0	0.43	269.1	0.28	0.93	1.53
8	Major	S600-48-8	11.1	51.3	158.8	0.52	160.7	0.39	0.99	1.31
9		S600-48-9	0.1	73.4	38.9	0.69	42.2	0.59	0.92	1.17
10		S600-48-11	33.4	36.2	252.0	0.37	230.7	0.44	1.09	0.84
11		S600-48-10	29.5	70.4	64.7	0.49	62.9	0.49	1.03	0.99
12		S600-48-12	60.5	41.0	202.7	0.41	222.4	0.54	0.91	0.76
13	Bi-Axial	S600-48-13	59.9	71.8	76.3	0.52	70.7	0.63	1.08	0.83
14		S600-48-14	301.0	39.7	192.8	0.37	218.3	0.51	0.88	0.74
15		S600-48-15	299.9	71.9	62.9	0.65	63.9	0.81	0.98	0.81
16		S600-48-16	329.6	35.3	211.8	0.37	227.6	0.34	0.93	1.10
17		S600-48-17	330.5	70.4	59.4	0.57	60.8	0.63	0.98	0.90
18	Axial	S600-48-18	-	0.9	217.4	0.41	287.9	0.26	0.76	1.59
								Average	0.99	0.98
								Standard deviation	0.10	0.22
								C.O.V	9.7%	22.7%

5.4 Finite element modeling protocols for cold-formed steel zee-section beam-column (Torabian et al. 2016b)

A series of material and geometric nonlinear collapse finite element analyses has been performed on a short Zee-section beam column (700Z225-60, L=305mm [12 in.]) using different imperfection patterns, imperfection magnitudes, residual stresses and strains, and geometric dimensions. The results are compared against the results of existing experiments on 21 short beam-columns to find an appropriate modeling protocol for numerical modeling of Zee-section beam-column. The complete details are provided in the following paper:

Torabian S., Amouzegar H., Tootkaboni M. and Schafer B.W. (2016). "Finite element modeling protocols and parametric analyses for short cold-formed steel zee-section beam-columns". *Structural Stability Research Council Annual Stability Conference 2015, SSRC 2015*, Orlando, Florida, April 12-15, 2016.

The selected modeling protocol consists of the following primary assumptions,

S9R5 shell elements are used, with transverse discretization of: 10 elements in the web, 2 elements in the flange and the lip, and 4 elements in the corner. The element aspect ratio is kept close to one throughout the mesh. The von Mises yield criteria, associated flow, and isotropic hardening with a s-e curve based on direct experimental measurement were assumed for modeling plasticity in the numerical models. Roll-forming effects (residual stresses and strains) are considered for the corners of the cross-section based on the method set forth by Moen et al. (2008), but are not shown to have a significant effect on the results. Measured (as opposed to nominal) geometric dimensions are implemented in the modeling. An imperfection pattern consisting of sympathetic local and distortional modes along with global modes (which were small in this study) was selected. The selected pattern causes inward distortional buckling for the flange under compression, which is consistent with the test results. The imperfection magnitude was determined based on Zhao et al. (2015) measurements (50%ile), which were determined based on direct measurements of the Zee-sections. This imperfection magnitude is consistent with the large 95%ile imperfections on lipped channels from Zeinoddini and Schafer (2012).

After using the modeling protocol to construct the strength surface of the tested specimen, it was found that the current AISI-S100-12 predictions for the beam-column strength of this section (using DSM method for anchor points and interaction equations) are quite conservative. The most conservative results were found to be under axial load and minor axis bending. The reserved capacity between the strength surfaces constructed by the AISI specification and the

numerical interaction surface show the potential for improving the current specification methods

for beam-column design.

Chapter 6 - Parametric study by nonlinear finite element modeling

6.1 Introduction

Chapter 5 has shown that the finite element models can accurately provide capacity predictions for the test specimens. Therefore, nonlinear FE models can be utilized to extend the results to other beam-columns with different cross-section properties, different material properties, and different member lengths. A comprehensive database for the strength surface of cold-formed steel beam-columns is provided in this chapter. The database can be utilized to evaluate the current beam-column design methods and also to develop the new beam-column DSM.

This chapter first introduces a modeling protocol for the finite element models for performing parametric studied. Consequently, several cross-sections selected out of a lipped channel product catalog (SFIA 2012), including the popular cross-sections in the previous experimental studies and actual constructions, are selected according to dimensionless parameters. Nonlinear collapse finite element analyses using the modeling protocol are performed, and the results are implemented to evaluate the prediction methods.

6.2 Modeling protocol

The general-purpose finite element program "ABAQUS" is employed to perform nonlinear collapse analyses on shell finite element models of cold-formed steel members. The geometric coordinates of the cross-section and the buckling shapes used to apply imperfections are generated from CUFSM. CUFSM 2D results, including cross-section data and buckling

shapes, are used to reproduce 3D models in ABAQUS using a custom MATLAB code. The parameters used in the finite element model are described in the following section.

6.2.1 Element and mesh properties

A 9-node quadratic shell element, S9R5, is used as the computational element in the models. Similar to the mesh described in Chapter 5: the maximum size of the element is assumed to be 15mm×15mm; the corners of the cross-section are meshed with 4 elements transversally; the minimum number of transverse elements in the web, flange, and lip is considered to be 4, 2 and 2, respectively. A schematic diagram of the cross-section mesh is shown in Figure 6-1. Typical mesh topology for the specimens in the parametric study is shown in Figure 6-2.
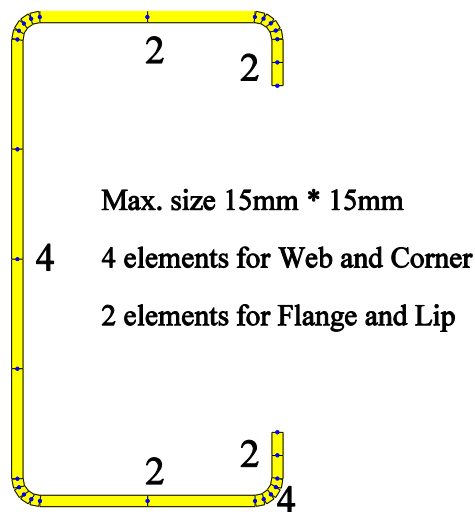
Figure 6-1: mesh rule in finite element model
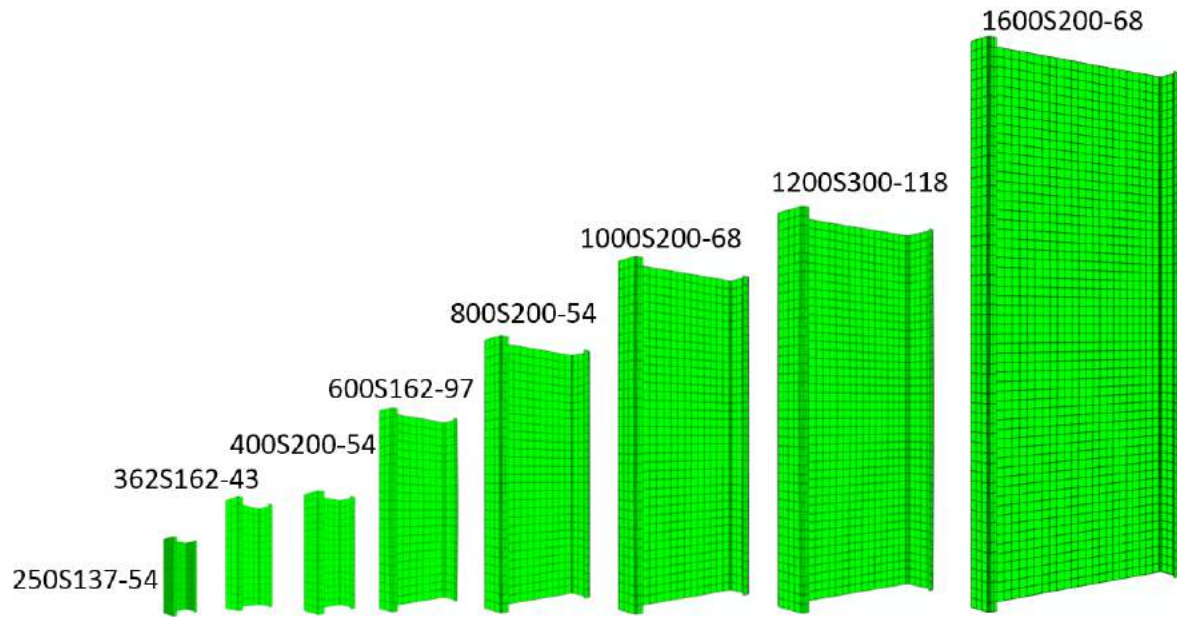
Figure 6-2: Typical mesh topology in the finite element model
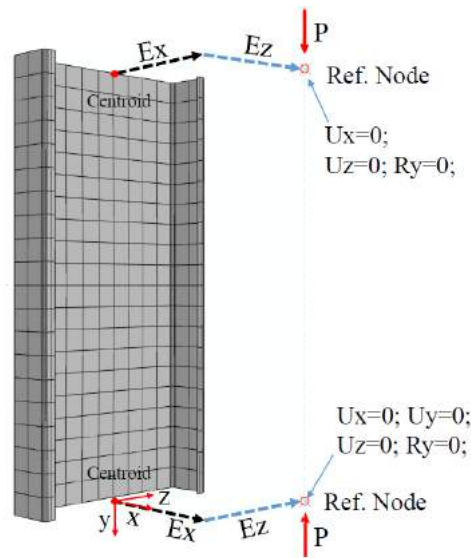
Figure 6-3: Boundary conditions of the finite element model in the parametric study

6.2.1 Boundary conditions

The boundary conditions are assumed to be identical to those considered in Chapter 5, except for the rigid link at the end of the specimens. In the physical tests, at the ends of the test

specimens (600S137-54 lipped channel), there were end plates, loading plates, and swivel joints between the loading plate and the MTS loading machine. These parts (all parts other than the lipped channel specimen) were simulated as rigid links in the finite element model. However, in the parametric study, there is no need to consider rigid links at the ends of the specimens. The finite element model including the boundary conditions is shown Figure 6-3.

6.2.2 Material model

The stress-strain curve of steel includes a pronounced yielding plateau after the yield point and then material enters the strain-hardening region for larger deformations. Typical stress-strain curves resulting from coupon testing are shown in Figure 6-4 (labeled as TEST). In Chapter 5, the stress remained in the yield plateau or in elastic region for almost all models. Accordingly, and conservatively, an elastic-perfectly-plastic engineering stress-strain material model is assumed to be adequate for the analysis of thin-walled members. (See (Shifferaw and Schafer 2012) for the impact of the strain hardening regime on inelastic reserve in CFS beams). For the elastic regime, a Young's modulus of 29500 ksi (2.03×10^5 MPa) is assumed, the yield stress is set at 33 ksi (228 MPa) or 50 ksi (345 MPa) consistent with assigned materials in available product catalogs, and the Poisson's ratio is 0.3. For the plastic part, von Mises yield criterion and associated flow rule are employed. Notably, ABAQUS uses true-stress strain as an input.
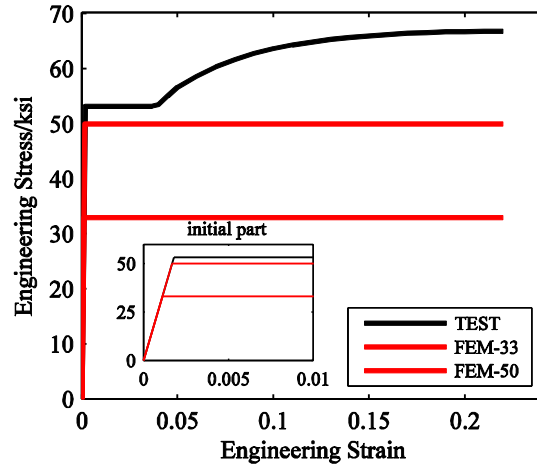
Figure 6-4: Engineering strain-stress curves

6.2.3 Cold-work/roll-forming effects

According to Chapter 5, the cold-work/roll-forming effect can increase the capacity of the 24 in.and 48 in. long specimens by 3% and 1%, respectively. However, to accurately include the cold-work/roll-forming effect thirty-one, through thickness integration points must be used. To save calculation time the cold-work/roll-forming effect in the parametric study is ignored and no residual stress is introduced into the finite element models.

6.2.4 Geometrical imperfections

In order to employ a generalized imperfection pattern for all of the specimens, three types of buckling modes: global, distortional, and local, obtained from the axial compression case, are introduced into all the beam-column finite element models. In Chapter 5, the same type of imperfections has been used, and it was concluded that the finite element models with PGPDPL (positive global, positive distortional, and positive local buckling imperfection patterns) provides the lower-bound prediction of the capacity. The most important reason is that the PDPL type of imperfection makes the flanges of the lipped channel cross-section move outward at the mid-

206

height. This type of imperfection provides lower post-buckling strength. In the parametric study, PDPL imperfection is considered in the finite element models to create the cross-sectional imperfection. For the global imperfection (bow and camber), the sign of the global imperfection is assigned to make the eccentricities at the mid-height of the specimens bigger. The selected shapes of the imperfections are schematically shown in Figure 6-5. The 50% CDF values in Table 5-5 are used for the imperfection magnitude.
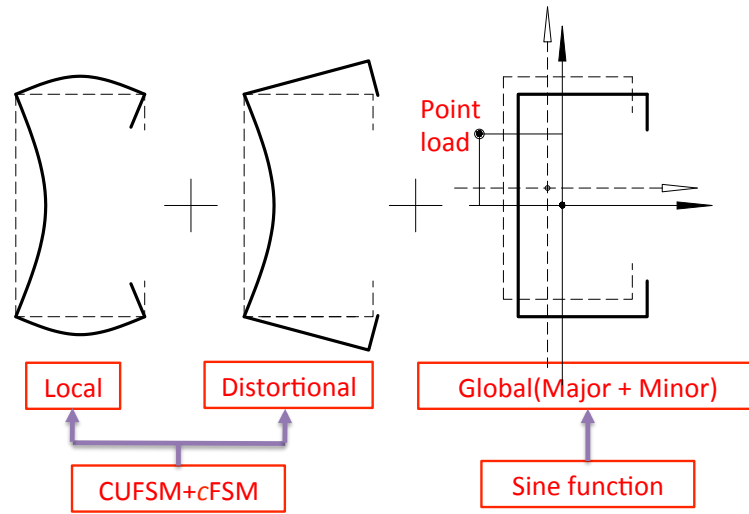
Figure 6-5: Imperfections used in the parametric study

6.2.5 Solution method

In the parametric study, the Riks arc-length method is implemented to solve the nonlinear collapse problem. Displacement is applied at the reference node for the majority of the specimens. Specimens with the greatest eccentricity (essentially a beam) have a force and moment applied at the reference node.

6.2.6 Length of the specimens

Two lengths, $3L_{crL}$ and $3L_{crD}$, are selected for each of section. L_{crL} and L_{crD}, are the local and the distortional buckling half-wave length of the cross-section, respectively. These two

length are automatically identified from the FSM result by using the "FSM@cFSM-L_{cr}" method (see Section 2.2.1).

The length of "$3L_{crL}$" is short and allows local buckling and the potential for local/distortional interaction. At this short length the distortional mode is significantly elevated due to the end boundary conditions and the global mode is essentially removed.

The length of "$3L_{crD}$" is intermediate and allows local buckling or distortional buckling and provides the potential for local/distortional, local/global, or distortional/global modes of failure. Using three times the distortional buckling half-wave length minimizes the boosting effect of the warping fixed end boundary conditions on distortional buckling and allows one distortional buckling half-wave to form at the middle of the specimen at a load near the ideal simply-supported minimum.

6.2.7 Number of loading points for each cross-section

The spherical coordinate system detailed in Chapter 1 is utilized to define the number of different loading/calculation points (model runs) for each section. In the M-M plane, twelve P-M curves, evenly distributed on the M-M plane (step of 30°), are considered. Due to the symmetric shape of the lipped channel section about the major axis, seven P-M curves are adequate to compose the P-M-M strength surface (the solid lines in the left part of the figure). For each of the P-M curves, eighteen points (step of 5°), evenly distributed in the P-M plane, are considered. Including one specimen for pure axial loading, a total of 127 loading/calculation points are considered for each P-M-M surface per selected cross-section, per selected length.
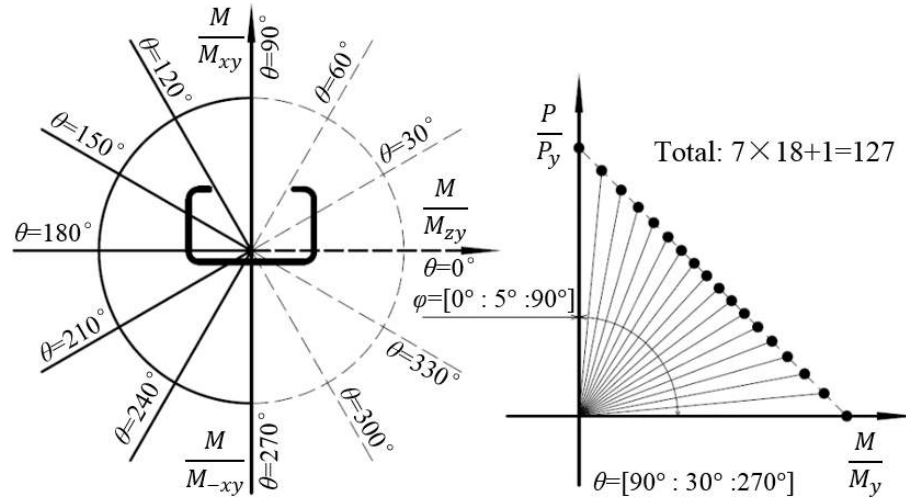
Figure 6-6: number of the calculation points

6.3 Cross-section selection

In the SFIA product catalog (SFIA 2012), there are 364 structural stud sections. The section depths range from 2.5 to 16 in.. It would take a prohibitively long time to get P-M-M strength surfaces for all cross-sections. Moreover, some of the cross-sections may never be used as beam-columns in real construction. So, first it is required to select sections for the parametric study.

6.3.1 Selection criteria

To select cross-sections from the product list, several parameters are considered. These parameters are listed below:

(1) Local and distortional slenderness.

Critical local, P_{crl}, and distortional, P_{crd}, axial buckling loads are calculated using CUFSM. To overcome having a non-unique minima in conventional finite strip models the "FSM@cFSM-L_{cr}" method is used to automatically identify the local and distortional buckling loads. Assuming the yield load for column global buckling,

209

$P_{ne=}P_y$, the local and distortional slenderness are determined for all cross sections as follows,

$$P_{nG} > P_y \rightarrow \lambda_L = \sqrt{\frac{P_y}{P_{crl}}}$$

$$P_{nG} \leq P_y \rightarrow \lambda_L = \sqrt{\frac{P_{nG}}{P_{crl}}}$$

(5.1)

(2) Depth-to-width ratio.

The depth-to-width ratio is calculated for all lipped channel sections in the product list.

(3) Local and distortional nominal capacity.

Using the calculated local and distortional slenderness, the axial nominal capacity of the cross section is also determined to identify the governing mode of failure of the specimens. To determine the axial nominal capacity, a modification on the elastic critical load is made regarding the clamped warping boundary condition assumed for the specimens. As discussed in the experimental studies, applying end moment via eccentric loading implies a warping fix end condition for the specimens. Warping fix end conditions result in a clamped end condition in distortional buckling and may result in a clamp end condition in local buckling as well. To account for the clamped distortional buckling end condition, an empirical relationship (Eq. 2.1) developed for boosting up the distortional buckling critical load is implemented to determine the elastic distortional buckling load and the associated distortional slenderness (Moen 2008). The shorter the physical length for the specimens, the higher the boosting effect on distortional buckling that is achieved. Accordingly, two sets of lengths are

considered for each cross-section. A length of $3L_{crl}$ is assumed for short specimens with high boosting in distortional buckling and $3L_{crd}$ is assumed for longer specimens with minimal boosting for elastic distortional buckling load. The boosting factor for short specimens is a function of $L_{crd}/(L=3L_{crl})$ ratio, but it is a constant number equal to 1.06 for longer specimens, where $L_{crd}/(L=3L_{crd})$ is always 0.33. The axial capacity of the specimens having either length is calculated for all cross-sections. The P_{crl}/P_{crd} ratio is used to help identify whether the specimen strength is governed by local or the distortional buckling.

(4) Popularity of the cross-section in the constructions and use in previous experiments.

6.3.2 Results

In total, 75 sections out of 364 sections in the product list have been selected for conducting a comprehensive parametric study on cold-formed steel lipped channel sections.

The names and the parameters used in the selection of the section are shown in Table 6-1. Comparison of the depth-to-width ratio of the selected sections with that of all the sections in the product list are shown in Figure 6-7 and Figure 6-8.

Comparison of the local and the distortional buckling slenderness of the selected sections with that of all the sections in the product list are shown in Figure 6-9 and Figure 6-10 respectively.

Comparison of the P_{crl}/P_{crd} ratio of the selected sections with that of all the sections in the SFIA product list are shown in Figure 6-11 and Figure 6-12.

211

Table 6-1: Properties of the selected sections

Num	Sections	Dimensions/mm *					F_y	Parameters					$3L_{Loc}$	$3L_{Dist}$
		Web	Flange	Lip	r	t	MPa	Web/Flange	λ_{Loc}	λ_{Dist}	L_{Loc}	L_{Dist}	P_{Loc}/P_{Dist}	
4	250S137-54	56.31	27.61	5.93	2.88	1.44	344.74	2.04	0.80	0.80	50	250	0.98	1.10
6	250S137-68	54.44	25.74	5.00	3.62	1.81	344.74	2.12	0.63	0.69	50	220	1.00	1.04
12	250S162-68	54.44	32.09	8.17	3.62	1.81	344.74	1.70	0.64	0.70	50	300	1.00	1.04
17	350S162-68	79.84	32.09	8.17	3.62	1.81	227.53	2.49	0.72	0.66	70	320	1.00	1.02
21	350S200-43	82.99	44.89	12.92	2.38	1.15	227.53	1.85	1.16	0.87	70	560	0.77	0.91
25	350S200-68	79.84	41.74	11.35	3.62	1.81	344.74	1.91	0.89	0.83	70	440	0.91	1.04
26	350S200-97	75.98	37.88	9.42	5.17	2.58	227.53	2.01	0.50	0.54	70	360	1.00	1.00
33	362S137-68	82.89	25.74	5.00	3.62	1.81	344.74	3.22	0.91	0.85	70	240	0.94	1.06
34	362S162-33	86.30	35.50	9.88	2.38	0.88	227.53	2.43	1.54	1.02	70	490	0.63	0.83
35	362S162-43	86.04	35.24	9.75	2.38	1.15	227.53	2.44	1.18	0.88	70	420	0.76	0.90
37	362S162-54	84.76	33.96	9.11	2.88	1.44	344.74	2.50	1.15	0.94	70	370	0.78	0.97
38	362S162-68	82.89	32.09	8.17	3.62	1.81	227.53	2.58	0.74	0.67	70	330	1.00	1.03
39	362S162-68	82.89	32.09	8.17	3.62	1.81	344.74	2.58	0.91	0.82	70	330	0.90	1.03
41	362S162-97	79.03	28.23	6.24	5.17	2.58	344.74	2.80	0.63	0.66	70	260	1.00	1.02
45	362S200-54	84.76	43.61	12.28	2.88	1.44	344.74	1.94	1.17	0.96	70	500	0.77	0.97
46	362S200-68	82.89	41.74	11.35	3.62	1.81	227.53	1.99	0.75	0.68	70	440	1.00	1.03
63	362S300-68	82.89	67.14	11.35	3.62	1.81	344.74	1.23	0.98	1.07	80	570	0.86	1.19
70	400S137-68	92.54	25.74	5.00	3.62	1.81	227.53	3.60	0.81	0.76	80	240	0.98	1.05
76	400S162-68	92.54	32.09	8.17	3.62	1.81	227.53	2.88	0.82	0.71	80	330	0.97	1.02
83	400S200-54	94.41	43.61	12.28	2.88	1.44	344.74	2.16	1.29	1.00	80	510	0.72	0.94
101	400S300-68	92.54	67.14	11.35	3.62	1.81	344.74	1.38	1.06	1.10	90	580	0.83	1.15
105	550S162-43	133.79	35.24	9.75	2.38	1.15	227.53	3.80	1.77	1.25	100	460	0.68	0.90
108	550S162-68	130.64	32.09	8.17	3.62	1.81	227.53	4.07	1.11	0.95	100	360	0.85	0.99
114	550S200-54	132.51	43.61	12.28	2.88	1.44	227.53	3.04	1.42	1.00	110	540	0.69	0.88
117	550S200-68	130.64	41.74	11.35	3.62	1.81	344.74	3.13	1.38	1.08	110	480	0.75	0.95
123	600S137-54	145.21	27.61	5.93	2.88	1.44	344.74	5.26	1.89	1.70	110	310	0.99	1.16
127	600S137-97	139.48	21.88	3.07	5.17	2.58	344.74	6.37	1.08	1.11	110	220	1.08	1.15
131	600S162-54	145.21	33.96	9.11	2.88	1.44	344.74	4.28	1.89	1.48	110	410	0.80	1.01
133	600S162-68	143.34	32.09	8.17	3.62	1.81	344.74	4.47	1.50	1.29	110	360	0.87	1.05
135	600S162-97	139.48	28.23	6.24	5.17	2.58	344.74	4.94	1.05	1.02	110	300	0.97	1.09
141	600S200-54	145.21	43.61	12.28	2.88	1.44	344.74	3.33	1.90	1.34	110	550	0.65	0.91
158	600S300-54	145.21	69.01	12.28	2.88	1.44	344.74	2.10	1.95	1.45	120	710	0.63	0.97
172	600S350-118	136.63	73.13	17.51	6.31	3.15	344.74	1.87	0.88	0.84	120	710	0.92	1.07
185	800S162-68	194.14	32.09	8.17	3.62	1.81	227.53	6.05	1.63	1.49	150	390	1.00	1.13
187	800S162-97	190.28	28.23	6.24	5.17	2.58	227.53	6.74	1.16	1.15	150	330	1.05	1.13
188	800S162-97	190.28	28.23	6.24	5.17	2.58	344.74	6.74	1.42	1.42	150	330	1.09	1.18
191	800S200-33	197.56	45.16	13.05	2.38	0.88	227.53	4.37	3.35	1.97	150	770	0.58	0.89
192	800S200-43	197.29	44.89	12.92	2.38	1.15	227.53	4.39	2.57	1.70	150	670	0.67	0.93
193	800S200-54	196.01	43.61	12.28	2.88	1.44	227.53	4.49	2.04	1.49	150	590	0.74	0.96
194	800S200-54	196.01	43.61	12.28	2.88	1.44	344.74	4.49	2.52	1.83	150	590	0.77	1.02

Num	Sections	Dimensions/mm *					F_y	Parameters						
								Web	λ_{Loc}	λ_{Dist}	L_{Loc}	L_{Dist}	$3L_{Loc}$	$3L_{Dist}$
		Web	Flange	Lip	r	t	MPa	Flange					P_{Loc}/P_{Dist}	
196	800S200-68	194.14	41.74	11.35	3.62	1.81	344.74	4.65	2.00	1.60	150	510	0.85	1.05
198	800S200-97	190.28	37.88	9.42	5.17	2.58	344.74	5.02	1.40	1.27	150	430	0.94	1.08
200	800S200-118	187.43	35.03	7.99	6.31	3.15	344.74	5.35	1.15	1.11	150	390	0.99	1.10
204	800S250-68	194.14	54.44	11.35	3.62	1.81	227.53	3.57	1.64	1.25	150	590	0.76	0.96
205	800S250-68	194.14	54.44	11.35	3.62	1.81	344.74	3.57	2.01	1.54	150	590	0.77	1.00
220	800S350-68	194.14	79.84	20.87	3.62	1.81	227.53	2.43	1.66	1.09	150	1030	0.60	0.84
227	1000S162-54	246.81	33.96	9.11	2.88	1.44	227.53	7.27	2.55	2.33	190	470	1.14	1.29
235	1000S200-43	248.09	44.89	12.92	2.38	1.15	227.53	5.53	3.19	2.28	190	710	0.82	1.07
237	1000S200-54	246.81	43.61	12.28	2.88	1.44	344.74	5.66	3.13	2.45	190	630	0.94	1.17
239	1000S200-68	244.94	41.74	11.35	3.62	1.81	344.74	5.87	2.49	2.12	190	550	1.01	1.19
241	1000S200-97	241.08	37.88	9.42	5.17	2.58	344.74	6.36	1.76	1.68	190	450	1.08	1.20
250	1000S250-97	241.08	50.58	9.42	5.17	2.58	344.74	4.77	1.76	1.59	190	510	0.99	1.14
253	1000S300-54	246.81	69.01	12.28	2.88	1.44	227.53	3.58	2.58	1.80	190	790	0.72	0.98
263	1000S350-68	244.94	79.84	20.87	3.62	1.81	227.53	3.07	2.06	1.29	190	1070	0.57	0.83
269	1200S162-54	297.61	33.96	9.11	2.88	1.44	227.53	8.76	3.08	2.98	220	490	1.33	1.47
274	1200S162-97	291.88	28.23	6.24	5.17	2.58	344.74	10.34	2.20	2.31	220	370	1.36	1.43
280	1200S200-68	295.74	41.74	11.35	3.62	1.81	344.74	7.08	2.99	2.71	220	580	1.17	1.35
287	1200S250-68	295.74	54.44	11.35	3.62	1.81	227.53	5.43	2.43	2.04	220	670	0.96	1.16
290	1200S250-97	291.88	50.58	9.42	5.17	2.58	344.74	5.77	2.11	1.98	220	550	1.10	1.25
300	1200S300-118	289.03	60.43	7.99	6.31	3.15	344.74	4.78	1.74	1.65	220	550	1.06	1.19
304	1200S350-68	295.74	79.84	20.87	3.62	1.81	344.74	3.70	3.02	1.91	220	1120	0.62	0.93
305	1200S350-97	291.88	75.98	18.94	5.17	2.58	227.53	3.84	1.71	1.27	220	910	0.73	0.94
308	1200S350-118	289.03	73.13	17.51	6.31	3.15	344.74	3.95	1.72	1.38	220	820	0.79	1.00
309	1400S200-54	348.41	43.61	12.28	2.88	1.44	227.53	7.99	3.55	3.18	250	670	1.22	1.43
324	1400S250-118	339.83	47.73	7.99	6.31	3.15	344.74	7.12	2.04	2.07	250	520	1.23	1.34
327	1400S300-68	346.54	67.14	11.35	3.62	1.81	227.53	5.16	2.84	2.38	250	760	1.01	1.23
336	1400S350-68	346.54	79.84	20.87	3.62	1.81	344.74	4.34	3.50	2.31	250	1030	0.74	1.03
337	1400S350-97	342.68	75.98	18.94	5.17	2.58	227.53	4.51	1.99	1.51	250	970	0.78	1.00
340	1400S350-118	339.83	73.13	17.51	6.31	3.15	344.74	4.65	2.00	1.66	250	850	0.87	1.08
341	1600S200-68	397.34	41.74	11.35	3.62	1.81	227.53	9.52	3.26	3.24	290	610	1.41	1.55
346	1600S200-118	390.63	35.03	7.99	6.31	3.15	344.74	11.15	2.40	2.53	290	490	1.41	1.48
347	1600S250-68	397.34	54.44	11.35	3.62	1.81	227.53	7.30	3.25	3.04	290	690	1.28	1.45
355	1600S300-97	393.48	63.28	9.42	5.17	2.58	227.53	6.22	2.30	2.22	290	650	1.20	1.33
361	1600S350-97	393.48	75.98	18.94	5.17	2.58	227.53	5.18	2.27	1.81	290	970	0.87	1.09
363	1600S350-118	390.63	73.13	17.51	6.31	3.15	227.53	5.34	1.86	1.59	290	890	0.92	1.08

Note: * All dimensions are measured at mid thickness, and the web, the flange, and the lip width means the straight part of the cross-section.
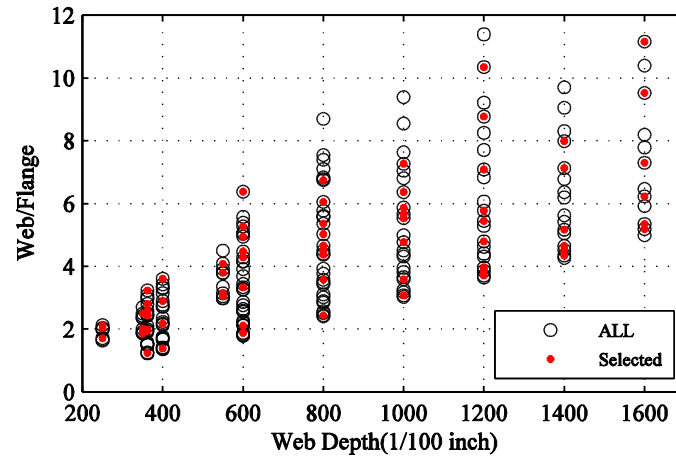
Figure 6-7: Depth-to-flange width distribution of the selected section
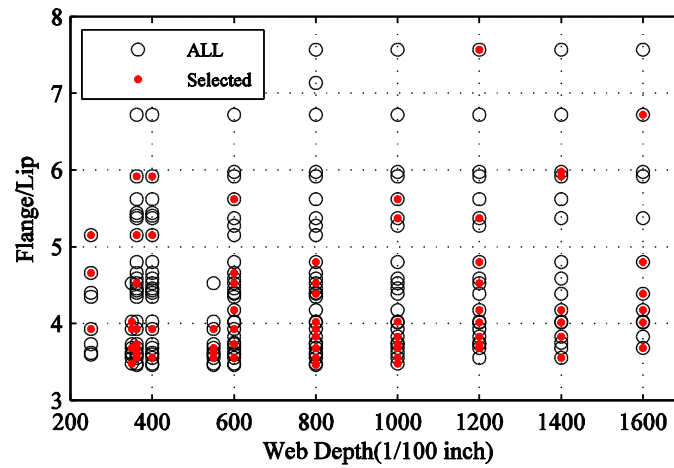
Figure 6-8: Flange width-to-lip width distribution of the selected section
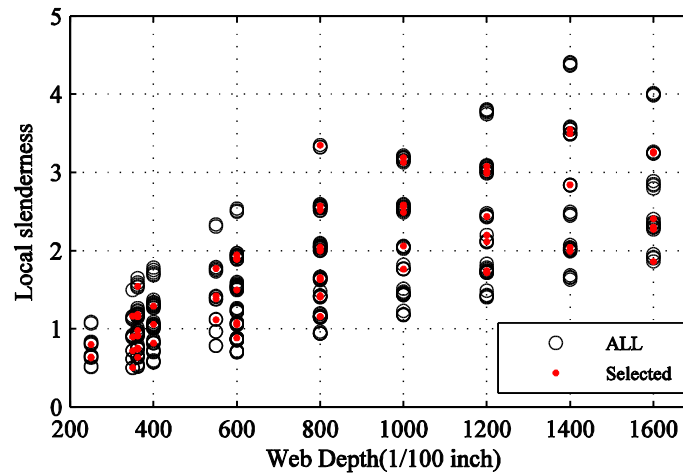
Figure 6-9: Local buckling slenderness distribution of the selected section

214
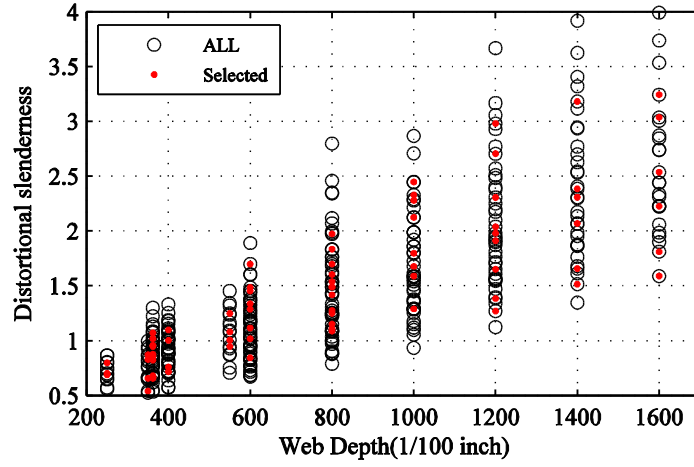
Figure 6-10: Distortional buckling slenderness distribution of the selected section
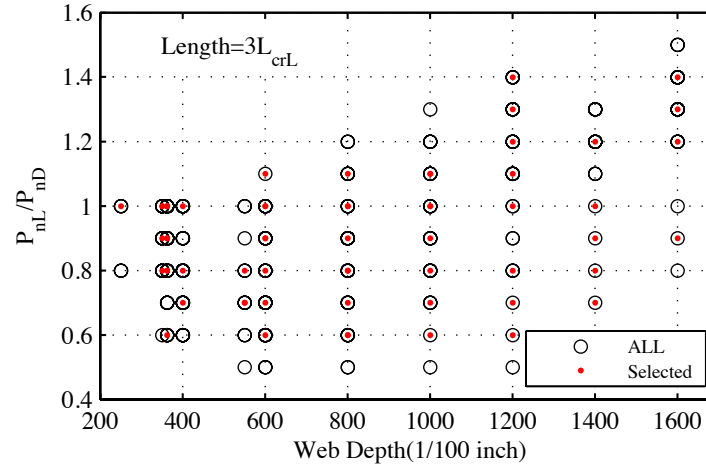
Figure 6-11: P_{nL}/P_{nD} Distribution of the selected section: $L=3L_{crL}$
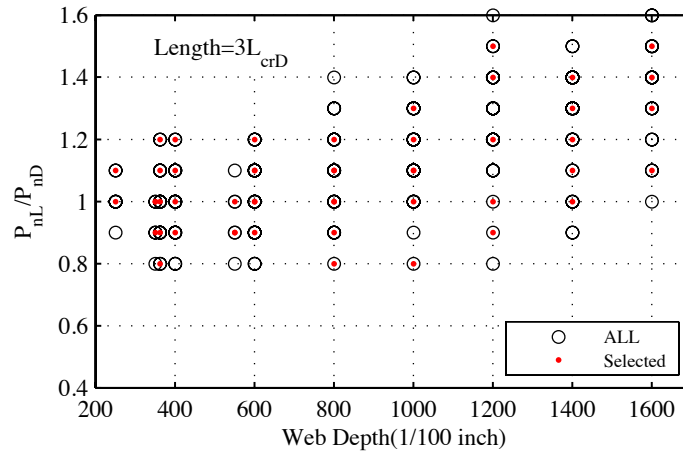
Figure 6-12: P_{nL}/P_{nD} Distribution of the selected section: $L=3L_{crD}$

In Figure 6-7 to Figure 6-12 we can see that the parameters of the selected sections cover well the range of the parameters of the sections in the full product list. Therefore, the selected section can be used to reasonably represent all sections in the product list.

6.4 Typical calculation results

According to the modeling protocol prescribed in the above sections the finite element analyses were carried out by using a computational Cluster in the Department of Civil Engineering at Johns Hopkins University. There are 75 types of cross-section, and for each of the sections, two lengths are considered, and for each length, there are 127 specimens with different eccentricities (127 load combinations). This is a total of 75×2×127=19050 models run to achieve 150 predicted strength surfaces.

Typical calculation results are shown in Figure 6-13.

250S137-54(50) L=150mm   250S137-54(50) L=750mm

216
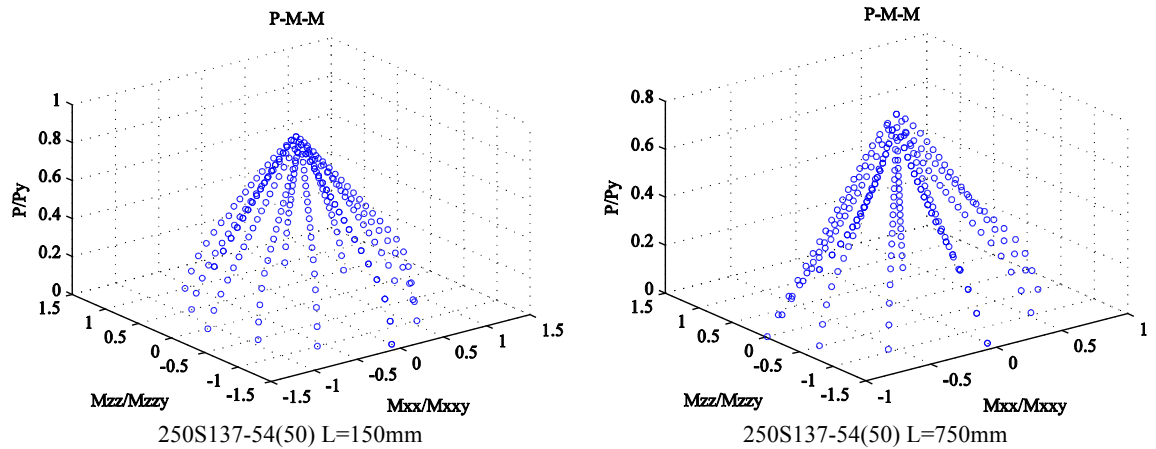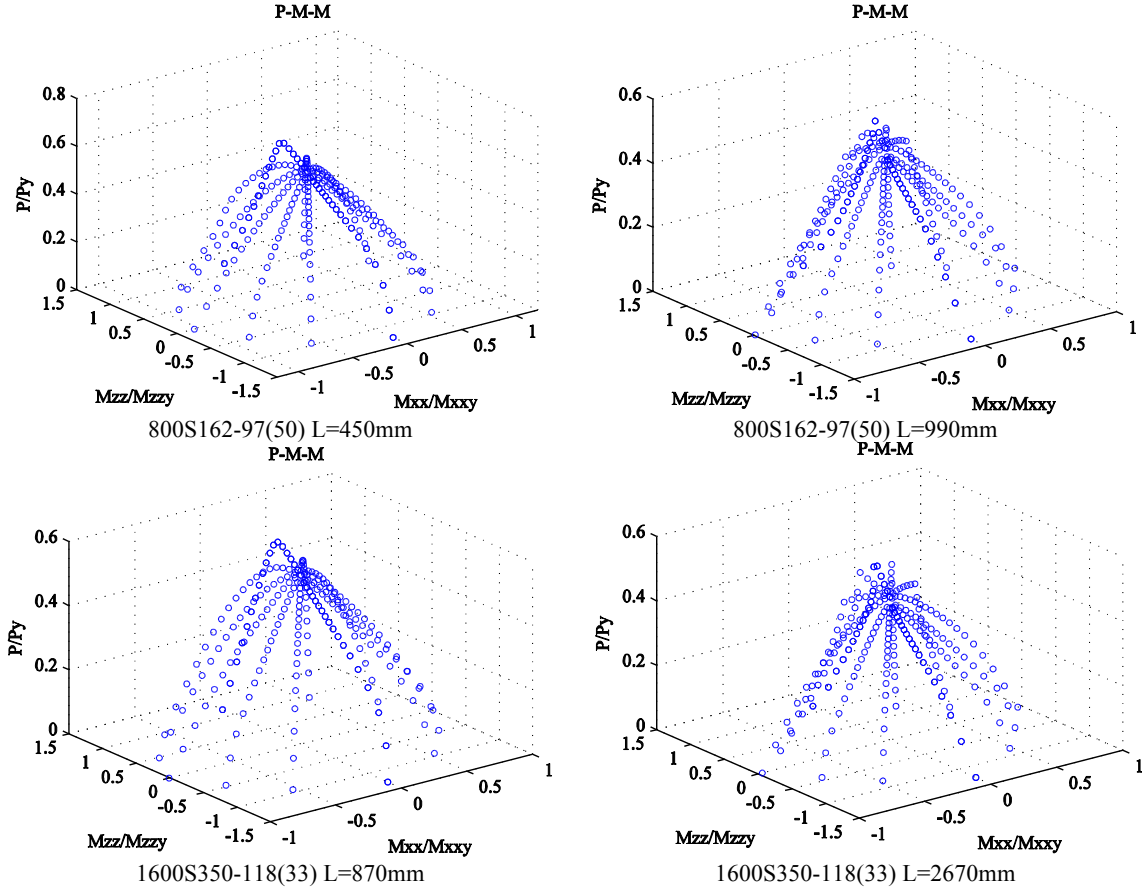
Figure 6-13: Typical strength surfaces in the parametric study (25.4 mm=1 in.)

6.5 Shape analysis on the beam-column interaction equation via parametric analyses

The results of collapse analyses on the 75 different lipped channels are summarized in Figure 6-14 to Figure 6-16 at the principal axes, including axial load-major axis bending, axial load-minor axis bending when the lips are in compression, and axial load-minor axis bending when lips are in tension. The results are normalized to the capacity of the member at the anchor points, known as P_n, M_{1n}, and M_{2n}.

The results clearly show the potential to depart from a linear interaction equation and improving the strength predictions. Additionally, more strength reserve in the case of axial load and minor axis bending is seen, as also found in the experimental results.

Average P-M interaction equations are provided for the strength surfaces (at principal surfaces) of the lipped channels studies in the parametric analyses. The results show a potential to provide a simplified method to incorporate nonlinear P-M interactions for any class of the cold-formed cross-sections such as lipped channels.
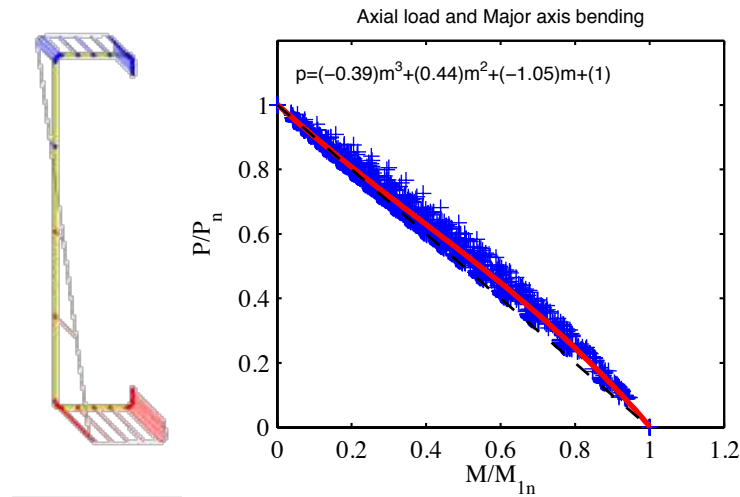
Figure 6-14: An average beam-column interaction equation for Major axis bending of lipped channels
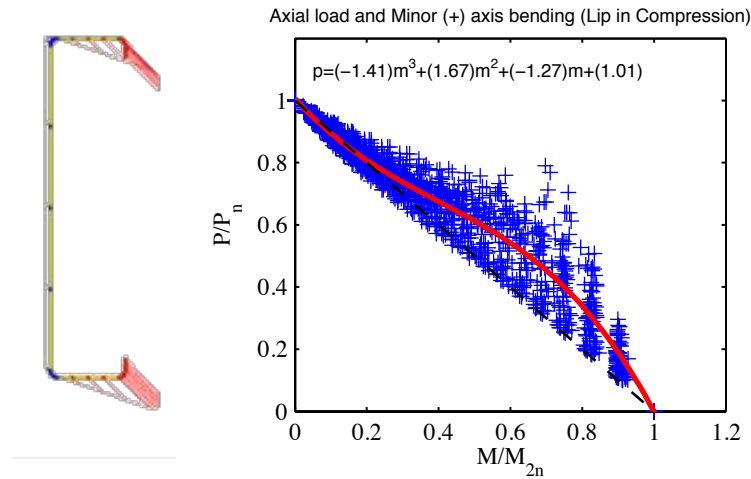
Figure 6-15: An average beam-column interaction equation for minor axis bending of lipped channels (lips in compression)
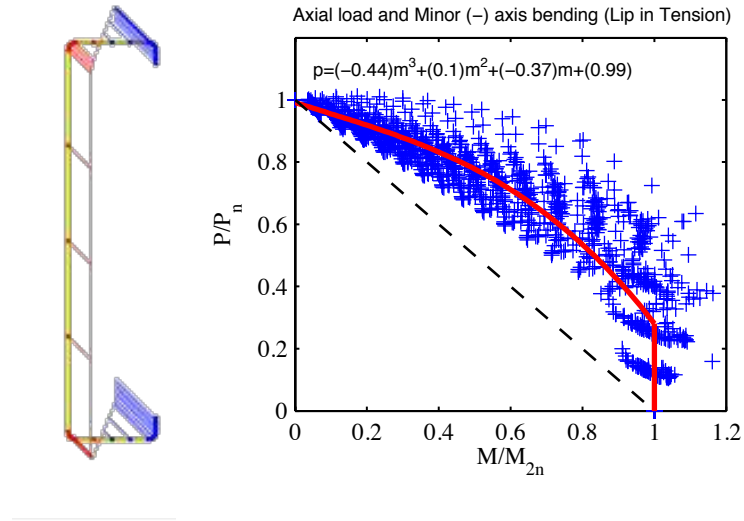
Figure 6-16: An average beam-column interaction equation for minor axis bending of lipped channels (lips in tension)

6.6 Comparison with the current the design method

To evaluate the results, the reliability index β_0 is determined based on the available test results and the parametric study results. Prediction methods include current AISI-S100-12 (DSM method) and the proposed beam-column DSM, as discussed in Chapter 4.

In the reliability analysis, C_ϕ, the calibration factor is set to 1.52 for LRFD method; M_m is mean value of material factor ($M_m = 1.05$ for combined axial load and bending); F_m is mean value of fabrication factor ($F_m = 1.00$ for combined axial load and bending); P_m is mean value of professional factor (P_m is assumed to be mean of the test-to-prediction ratio); β_0 is the target reliability index which is assumed to be 2.5 for structural members (LRFD). V_m is the coefficient of variation of the material factor ($V_m = 0.10$ for combined axial load and bending); V_F is the coefficient of variation of fabrication factor ($V_F = 0.05$ for combined axial load and bending); $C_P = (1+1/n)/m/(m-2)$ is the correction factor, where n in the number of the tests and m is

the degrees of freedom (n-1); as a huge number of simulations have been done, C_P is assumed to be 1.0; V_P is the coefficient of variation of the professional factor (V_P is assumed to be the coefficient of variation of the test-to-prediction ratio); and V_Q is coefficient of variation of load effect (V_Q =0.21 for LRFD method).

Mean test-to-prediction ratios and the associated standard deviations for both current AISI-S100-12 (DSM method) and the proposed beam-column DSM are summarized in Table 6-2 and Table 6-3 for all specimens. As shown in the the table, the reliability index is back-calculated from Eq. 5.2 for two different resistance factors; and the resistance factor is also calculated based on the target reliability of 2.5. Two resistance factors of 0.85 (typically for columns) and 0.9 (typically for beams) have be chosen due to having a beam-column member, which is not completly a beam nor a column.

Table 6-2: Reliability analysis of current AISI-S100-12 beam-column design method (linear interaction)

| Data Set | No. of models | AISI-S100-12 Linear Interaction | | | | |
		P_m	V_p	$\beta_0(\phi=0.85)$	$\beta_0(\phi=0.9)$	$\phi(\beta_0=2.5)$
All	19050	1.237	0.168	2.89	2.70	0.95
$15^\circ<\phi_{PM}<85^\circ$	13650	1.274	0.138	3.17	2.96	1.02

Table 6-3: Reliability analysis of the new proposed beam-column DSM

| Data Set | No. of models | New Beam-Column DSM | | | | |
		P_m	V_p	$\beta_0(\phi=0.85)$	$\beta_0(\phi=0.9)$	$\phi(\beta_0=2.5)$
All	19050	1.08	0.175	2.39	2.20	0.82
$15^\circ<\phi_{PM}<85^\circ$	13650	1.084	0.162	2.47	2.27	0.84

Notably, the new beam-column DSM is intended o provide the capacity under combined actions, but the capacity prediction at anchor points (pure compression and pure major and minor

bending moments) are assumed to be the same as the current AISI-S100-12 Specification. Accordingly, in Table 6-2 and Table 6-3 two data sets are considered. "All" includes all data points (anchor and non-anchor points) and "$15^{\circ} < \phi_{PM} < 85^{\circ}$" includes just loading conditions away from the anchor points. Although the difference is small, the results away from the anchor points provide a more independent assessment of the beam-column provisions and are more reasonable for reliability analyses.

The reliability analysis in Table 6-2 shows that the current beam-column design method in AISI-S100-12 is conservative. The calculated reliability index including all test specimens is 3.17 (ϕ=0.85) and 2.96 (ϕ=0.90), which is larger than the target reliability index of 2.5. Table 6-3 provides the reliability analysis for the new beam-column DSM. The calculated reliability index is 2.47 (ϕ=0.85) and 2.27 (ϕ=0.90), i.e. close to the target reliability index, but not conservative. It should be noted that the modeling methods used for simulation is a lower bound assumption (large compatible modal imperfections, no cold-work, no strain hardening, F_y = nominal values, etc.) and achieving a relatively low reliability index is expected.

Chapter 7 - Summary and Conclusions

This report summarizes developing of an advanced direct strength design method for thin-walled cold-formed steel (CFS) beam-columns via experimental and numerical approaches. A complete summary of a testing rig developed to study CFS beam-columns via eccentric loading is provided. The rig is fully developed and shown to reliably and efficiently produce beam-column capacities for axial load (P) and major (M_1) and minor (M_2) axis bending.

A lipped channel, 600S137-54 (53 ksi), and a Zee-section, 700Z225-60 (80 ksi), are specially selected and tested under P-M_1-M_2 loading. Totally 98 specimens have been tested including short (12 inches), intermediate (24 inches) and long (48 inches) specimens. Short specimens are supposed to show more local/distortional buckling; Intermediate specimens designed for distortional/local buckling and long specimens supposed to include global buckling along with local/distortional buckling. The test results are implemented to validate the newly proposed DSM for beam-columns.

A new design formulation in that directly incorporates stability under the actual applied P-M_1-M_2 action and inelastic reserve in bending is completed. This new Direct Strength Method (DSM) for beam-columns provides capacity predictions an average 20% higher than current design formulations, but remains conservative, where the method still reflects the current "beam" and "column" strengths of the current design specifications. The design relationships are provided in a specification-ready format for North American Specification for the design of cold-formed steel structural members. The new method will be proposed as an alternative design method to the current linear interaction method for designing members under combined actions.

A shell finite element (FE) model is validated against the testing and provides a reliable means to expand the predicted performance of the CFS beam-columns. A comprehensive parametric analysis on lipped channels using the verified modeling protocol has been performed to evaluate the current beam-column design method and the proposed beam-column DSM.

Reliability analyses of the current beam-column design method in the AISI specification and the new beam-column DSM using both test results and parametric analyses results showed that the current method is a conservative design method and the new proposed method could provide a more reasonable strength prediction.

As a technology transfer outcome, a beam-column stability and yield/plastic analysis tool is added to CUFSM that enables a universal and stand-alone tool to perform required stability and plastic analyses required for beam-columns in accordance to the proposed DSM method to ease the use of the developed method.

References

AISI. (2016). North American Specification for the design of cold-formed steel structural members. American Iron and Steel Institute, Washington, D.C.

Albermani, F., and Kitipornchai, S. (1990). "Elasto-plastic large deformation analysis of thin-walled structures." Engineering Structures, 12(1), 28–36.

Baptista, a. M. (2012a). "Resistance of steel I-sections under axial force and biaxial bending." Journal of Constructional Steel Research, Elsevier, 72, 1–11.

Baptista, a. M. (2012b). "Analytical evaluation of the elastic and plastic resistances of double symmetric rectangular hollow sections under axial force and biaxial bending." International Journal of Non-Linear Mechanics, Elsevier, 47(9), 1033–1044.

Baptista, A. M., and Muzeau, J.-P. (2006). "Analytical formulation of the elastic–plastic behaviour of bi-symmetrical steel shapes." Journal of Constructional Steel Research, 62(9), 872–884.

Baptista, A. M., and Muzeau, J.-P. (2008). "Analytical formulation for the deformations of I-shapes and RHS at the plastic strain ultimate limit state." Journal of Constructional Steel Research, 64(10), 1165–1177.

Chan, S. L., and Kitipornchait, S. (1987). "Geometric nonlinear analysis of asymmetric thin-walled beam-columns." 9, 243–254.

Charalampakis, a. E., and Koumousis, V. K. (2008). "Ultimate strength analysis of composite sections under biaxial bending and axial load." Advances in Engineering Software, 39(11), 923–936.

Dinis, P. B., Camotim, D., and Silvestre, N. (2007). "FEM-based analysis of the local-plate/distortional mode interaction in cold-formed steel lipped channel columns." Computers & Structures, 85(19-20), 1461–1474.

Hancock, G. . (2003). "Cold-formed steel structures." Journal of Constructional Steel Research, 59(4), 473–487.

Kalyanaraman, V., and Jayabalan, P. (1994). "Local buckling of stiffened and unstiffened elements under nonuniform compression." International Specialty Conference on Cold-Formed Steel Structures: Recent Research and Developments in Cold-Formed Steel Design and Construction, 1–9.

Kitipornchai, S., Zhu, K., Xiang, Y., and Al-Bermani, F. G. a. (1991). "Single-equation yield surfaces for monosymmetric and asymmetric sections." Engineering Structures, 13(4), 366–370.

Li, Z. (2011). "Finite strip modeling of thin-walled members." Ph.D. Thesis, Johns Hopkins University, Baltimore, Maryland.

Li, Z., Hanna, M. T., Ádány, S., and Schafer, B. W. (2011). "Impact of basis, orthogonalization, and normalization on the constrained Finite Strip Method for stability solutions of open thin-walled members." Thin-Walled Structures, 49(9), 1108–1122.

Li, Z., and Schafer, B. W. (2010). "Application of the finite strip method in cold-formed steel member design." Journal of Constructional Steel Research, Elsevier Ltd, 66(8-9), 971–980.

Loh, T. S. (1982a). Project AISI 1201-439: Combined axial load and bending in cold-formed steel memebrs, Progress report. Ithaca, New York.

Loh, T. S. (1982b). "Combined axial load and bending in cold-formed steel members." M.S. Thesis, Cornell University, Ithaca, New York.

Loh, T. S. (1985). "Combined axial load and bending in cold-formed steel members." Ph.D. Thesis, Cornell University, Ithaca, New York.

Loughlan, L. (1979). "Mode interaction in lipped channel column under concentric or eccentric loading." Ph.D. Thesis, Department of Mechanics of Materials, University of Strathclyde, Glasgow.

Macdonald, M., Heiyantuduwa, M. a., and Rhodes, J. (2008). "Recent developments in the design of cold-formed steel members and structures." Thin-Walled Structures, 46(7-9), 1047–1053.

McGuire, William, Gallagher, R. H., and Ziemian, R. D. (2000). Matrix structural analysis.

Miller, T. H., and Pekoz, T. (1994). "Load-Eccentricity effects on cold-formed steel lipped-channel columns." Journal of structural engineering, 120(3), 805–823.

Moen, C. D. (2008). "Direct strength design for cold-formed steel members with perforations." Ph.D. Thesis, Johns Hopkins University, Baltimore, Maryland.

Moen, C. D., Igusa, T., and Schafer, B. W. (2008). "Prediction of residual stresses and strains in cold-formed steel members." Thin-Walled Structures, 46(11), 1274–1289.

Mulligan, G. P. (n.d.). The influence of local buckling on the structural behavior of singly-symmetric cold-formed steel columns, Report No. 83-1.

NAS. (2012). North American Specification for the design of cold-formed steel structural members. Washington (DC, USA).

Padilla-Llano, D., Eatherton, M. R., and Moen, C. D. (2012). "Cyclic energy dissipation of cold-formed steel structural studs." 15th World Conference on Earthquake Engineering, Lisbon, Portugal.

Padilla, D., Eatherton, E., Moen, C. D., Bruce, T., and McAnallen, L. (2012a). "Cyclic energy dissipation of cold--formed steel studs experiencing Euler buckling." ASCE Structures Congress, Chicago, IL.

Padilla, D., Moen, C. D., Eatherton, M. R., McAnallen, L., and Bruce, T. (2012b). "Compression-tension hysteretic response of cold-formed steel C-section framing members." 21st International Specialty Conference on Cold-Formed Steel Structures, St. Louis, MO.

Papanikolaou, V. K. (2012). "Analysis of arbitrary composite sections in biaxial bending and axial load." Computers & Structures, Elsevier Ltd, 98-99, 33–54.

Pekoz, T. (1967). "Torsional-flexural buckling of thin-walled open sections under eccentric axial loading." Ph.D. Thesis, Cornell University, Ithaca, New York.

Pekoz, T. (1986). "Developement of a unified approach to the design of cold-formed steel members." Eighth International Specialty Conference on Cold-Formed Steel Structures, St. Louis, MO, 77–84.

Peterman, K. (2012). "Experiments on the stability of sheathed cold-formed steel studs under axial load and bending." (March), 119.

Rondal, J. (2000). "Cold formed steel members and structures: General Report." Journal of constructional steel research, 55, 155–158.

Sarawit, A. (2006). CUTWP thin-walled section properties.

Schafer, B. W. (2002). "Local, distortional, and euler buckling of thin-walled columns." Journal of Structural Engineering, 128(3), 289–299.

Schafer, B. W. (2008). "Review: The Direct Strength Method of cold-formed steel member design." Journal of Constructional Steel Research, 64(7-8), 766–778.

Schafer, B. W., and Adany, S. (2006). "Buckling analysis of cold-formed steel members using CUFSM: Conventional and Constrained Finite Strip Methods." Eighteenth international specialty conference on cold-formed steel structure: University of Missouri-Rolla, Rolla, MO, United States, Orlando, FL, United States.

Schafer, B. W., Li, Z., and Moen, C. D. (2010). "Computational modeling of cold-formed steel." Thin-Walled Structures, 48(10-11), 752–762.

Sfakianakis, M. G. (2002). "Biaxial bending with axial force of reinforced, composite and repaired concrete sections of arbitrary shape by fiber model and computer graphics." Advances in Engineering Software, 33(4), 227–242.

SFIA. (2012). Technical guide for cold-formed steel framing products. Steel Framing Industry Association, Falls Church, VA, US.

Shifferaw, Y. (2010). "Section capacity of cold-formed steel members by the Direct Strength Method." Ph.D. Thesis, Johns Hopkins University, Baltimore, Maryland.

Shifferaw, Y., and Schafer, B. W. (2010). "Towards a direct strength method for cold- formed steel beam-columns." Annual Stability Conference Structural Stability Research Council, 2010, SSRC 2010, Orlando, Florida, 613–630.

Shifferaw, Y., and Schafer, B. W. (2011). "Towards a cold-formed steel beam-column design by the Direct Strength Method." Proceedings of Eurosteel 2011: 6th European Conference on Steel and Composite Structures, Budapest, Hungary., 1785–1790.

Shifferaw, Y., and Schafer, B. W. (2012). "Inelastic bending capacity of cold-formed steel members." Journal of Structural Engineering, 138(4), 468–480.

Silvestre, N., Camotim, D., and Asce, M. (2006). "Local-plate and distortional postbuckling behavior of cold-formed steel lipped channel columns with intermediate stiffeners." Journal of Structural Engineering, 132(4), 529–540.

Simulia. (2007). ABAQUS/Standard User's Manual, Version 6.7. Pawtucket, RI.

Standards Australia. (2005). Cold-formed Steel Structures: NZS 4600. Standards Australia, Sydney, Australia.
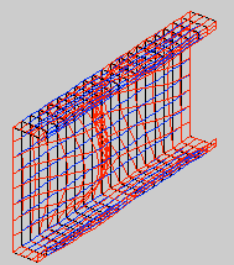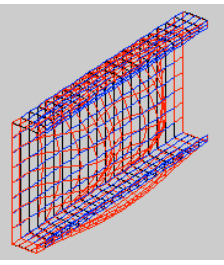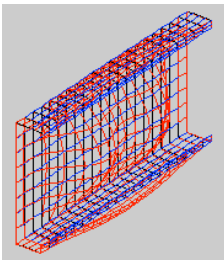
Torabian, S., Amouzegar, H., Tootkaboni, M., and Schafer, B. W. (2016a). "Finite element modeling protocols and parametric analyses for short cold-formed steel zee-section beam-columns." Annual Stability Conference Structural Stability Research Council, 2016, SSRC 2016, Orlando, Florida.

Torabian, S., Fratamico, D. C., and Schafer, B. W. (2015a). "Experiments on cold-formed steel Zee-shaped stub beam-columns." Structural Stability Research Council Annual Stability Conference 2015, SSRC 2015, Nashville, Tennessee.

Torabian, S., Fratamico, D. C., and Schafer, B. W. (2016b). "Experimental response of cold-formed steel Zee-section beam-columns." Thin-Walled Structures, 98, 496–517.

Torabian, S., Zheng, B., and Schafer, B. W. (2014a). "Reliability of the new DSM beam-column design method for cold-formed steel lipped channel." 22nd International Specialty Conference on Cold-Formed Steel Structures, November 2014, St. Louis, Missouri, USA.

Torabian, S., Zheng, B., and Schafer, B. W. (2014b). "Experimental study and modeling of cold-formed steel lipped channel stub beam-columns." Proceedings of the Annual Stability Conference Structural Stability Research Council, 2014, SSRC 2014, SSRC, Toronto, Canada.

Torabian, S., Zheng, B., and Schafer, B. W. (2014c). Direct strength prediction of cold-formed steel beam-columns. Baltimore. www.ce.jhu.edu/bschafer/dsmbeamcol.

Torabian, S., Zheng, B., and Schafer, B. W. (2015b). "Experimental response of cold-formed steel lipped channel beam-columns." Thin-Walled Structures, Elsevier, 89, 152–168.

Young, B. (2008). "Research on cold-formed steel columns." Thin-Walled Structures, 46(7-9), 731–740.

Yu, C., and Schafer, B. (2006). "Distortional buckling tests on cold-formed steel beams." Journal of structural engineering, 132, 515–528.

Yu, C., and Schafer, B. W. (2003). "Local buckling tests on cold-formed steel beams." Journal of Structural Engineering, 129, 1596-1606.

Zeinoddini, V. M., and Schafer, B. W. (2012). "Simulation of geometric imperfections in cold-formed steel members using spectral representation approach." Thin-Walled Structures, Elsevier, 60, 105–117.

228
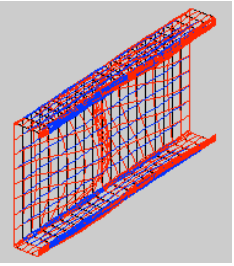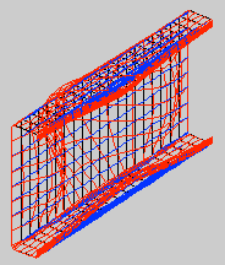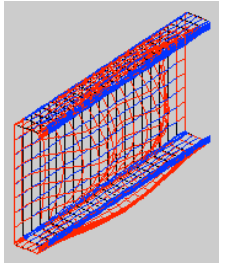
Zhao, X., Tootkaboni M., Schafer, B.W. (2015). "Laser-based Cross-Section Measurement of Cold-Formed Steel Members: Model Reconstruction and Application". Submitted to Thin-Walled Structures.
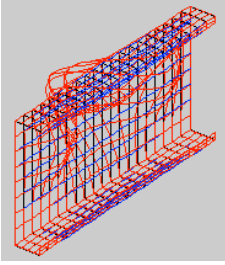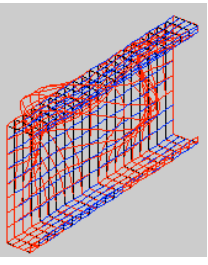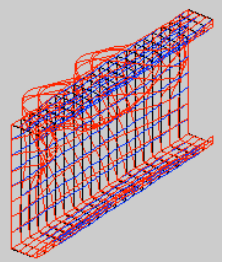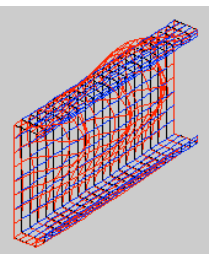
Appendix A - Elastic buckling analyses by CUFSM and CUTWP for identifying CFS beam-columns for testing program
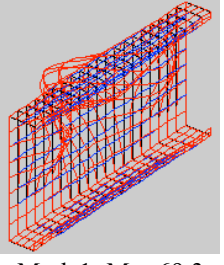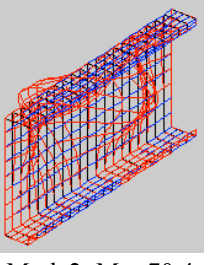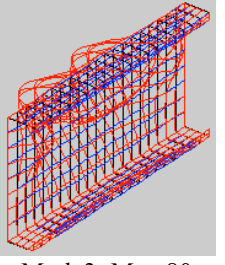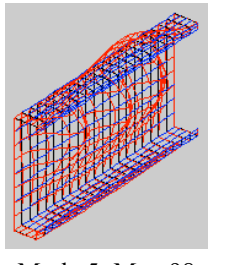
Table: Summary of the critical loads for 600S137-54 and 600S137-68

Section	B.C.	Length	Compression (kips)				Bending (kips-in)									
							Major				Minor					
													Lips in tension		Lips in compression	
			P_y	P_{crl}	P_{crd}	P_{cre}	M_y	M_{crl}	M_{crd}	M_{cre}	M_y	M_{crl}	M_{cre}	M_{crl}	M_{crd}	M_{cre}
600S137-54	C-C	12"	25.7	8.2	12.3	212.2	42.0	69.3	80.0	1111.1	4.9	6.2	36458.0	52.9	21.8	811.4
600S137-54	C-C	48"	25.7	7.2	10.6	13.3	42.0	65.0	60.0	70.0	4.9	5.4	2279.0	48.9	14.3	51.5
600S137-54	S.S/FSM@cFSM	-	25.7	7.3	9.1	-	42.0	65.3	57.5	-	4.9	5.4	-	49.1	13.7	-
600S137-54	S.S/boosted	12"	25.7	7.3	14.2	212.2	42.0	65.3	75.6	1111.1	4.9	5.4	36458.0	49.1	18.0	811.4
600S137-54	S.S/boosted	48"	25.7	7.3	9.4	13.3	42.0	65.3	58.6	70.0	4.9	5.4	2279.0	49.1	13.9	51.5
600S137-68	C-C	12"	32.0	16.0	22.3	263.1	51.5	128.7	123.7	1320.0	5.9	11.9	45097.0	105.7	32.5	953.0
600S137-68	C-C	48"	32.0	13.8	18.9	15.8	51.5	121.3	99.4	83.6	5.9	10.9	2820.0	97.1	23.0	61.2
600S137-68	S.S/FSM@cFSM	-	32.0	14.3	15.4	-	51.5	127.0	98.4	-	5.9	10.4	-	97.5	22.4	-
600S137-68	S.S/boosted	12"	32.0	14.3	21.9	263.1	51.5	127.0	129.2	1320.0	5.9	10.4	45097.0	97.5	28.0	953.0
600S137-68	S.S/boosted	48"	32.0	14.3	15.8	15.8	51.5	127.0	100.3	83.6	5.9	10.4	2820.0	97.5	22.8	61.2

Section	Local Buckling	Local Buckling	Distortional Buckling
600S137-54 12"-C-C Straight-line **Compression** FSM@cFSM	Mode1: D=9%, L=90%, P_{cl}=8.3 P_{cl}=7.3, L_{cr}=4.1"	Mode2: D=13%, L=86%, P_{cl}=8.4 P_{cl}=7.3, L_{cr}=4.1"	Mode 4:D=24%, L=74%, P_{cd}=12.3 P_{cd}=9.1, L_{cr}=12.6"
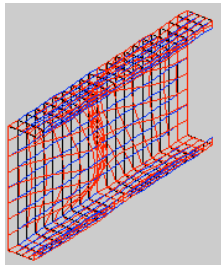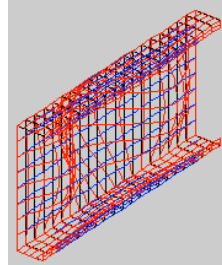
Section	Local Buckling	Local Buckling	Distortional Buckling
600S137-54 12"-C-C Round-corner **Compression** FSM@cFSM	Mode1: P_{cl}=8.2 P_{cl}=7.3, L_{cr}=4.1"	Mode2: P_{cl}=8.3 P_{cl}=7.3, L_{cr}=4.1"	Mode 4: P_{cd}=12.3 P_{cd}=9.1, L_{cr}=12.6"
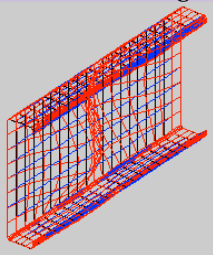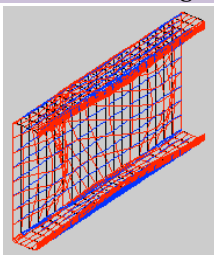
Section	Local Buckling	Local Buckling	Distortional Buckling	Distortional Buckling
600S137-54 12"-C-C Straight-line **Major Bending** FSM@cFSM	Mode1: D=18%, L=80%, M_{cl}=69.3 M_{cl}=65.3, L_{cr}=3.6"	Mode2: D=12%, L=87%, M_{cl}=70.4 M_{cl}=65.3, L_{cr}=3.6"	Mode3: D=25%, L=74%, M_{cd}=80 M_{cd}=57.5, L_{cr}=9.5"	Mode 4:D=32%, L=67%, M_{cd}=98 M_{cd}=57.5, L_{cr}=9.5"
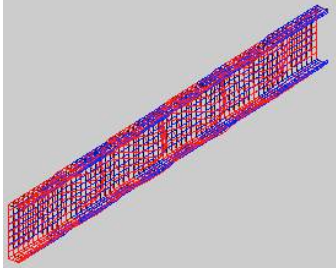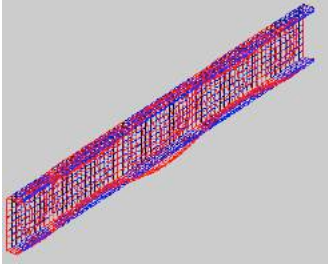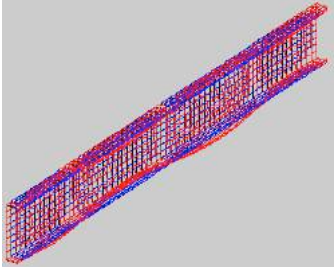
Section	Local Buckling	Local Buckling	Distortional Buckling	Distortional Buckling
600S137-54 12"-C-C Round-corner **Major Bending** FSM@cFSM	Mode1: M_{cl}=69.3 M_{cl}=65.3, L_{cr}=3.6"	Mode2: M_{cl}=70.4 M_{cl}=65.3, L_{cr}=3.6"	Mode3: M_{cd}=80 M_{cd}=57.5, L_{cr}=9.5"	Mode 5: M_{cd}=98 M_{cd}=57.5, L_{cr}=9.5"
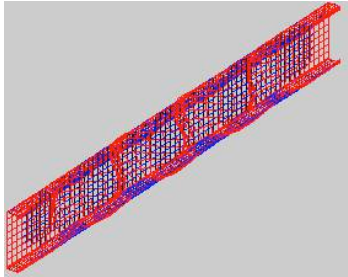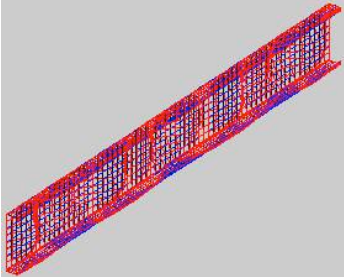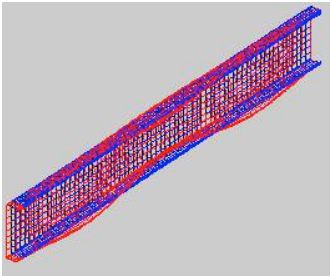
231

Section	Local Buckling	Local Buckling	Distortional Buckling	Distortional Buckling
600S137-54 12"-C-C Straight-line **Minor Bending Flange lip in compression** **FSM@cFSM**	 Mode7: D=19%, L=76%, M_{cl}=53.7 M_{cl}=49.1, L_{cr}=1.2"	 Mode8: D=27%, L=68%, M_{cl}=53.7 M_{cl}=49.1, L_{cr}=1.2"	 Mode1: D=61%, L=37.7%, M_{cd}=22.2 M_{cd}=13.7, L_{cr}=9.5"	 Mode 2:D=84%, L=13%, M_{cd}=22.5 M_{cd}=13.7, L_{cr}=9.5"
Section	Local Buckling	Local Buckling	Distortional Buckling	Distortional Buckling
600S137-54 12"-C-C Round-corner **Minor Bending Flange lip in compression** **FSM@cFSM**	 Mode7: M_{cl}=52.9 M_{cl}=49.1, L_{cr}=1.2"	 Mode8: M_{cl}=52.9 M_{cl}=49.1, L_{cr}=1.2"	 Mode1: M_{cd}=21.8 M_{cd}=13.7, L_{cr}=9.5"	 Mode 2: M_{cd}=22.1 M_{cd}=13.7, L_{cr}=9.5"
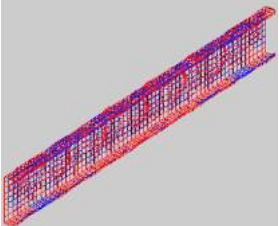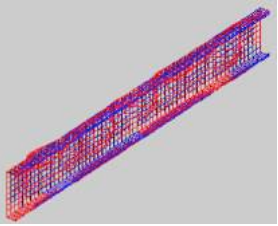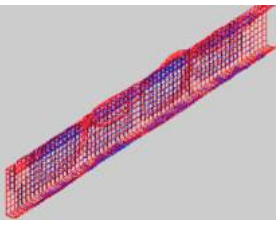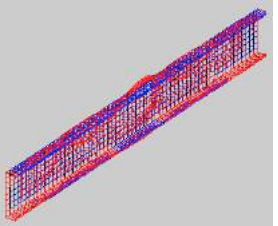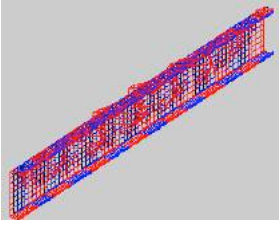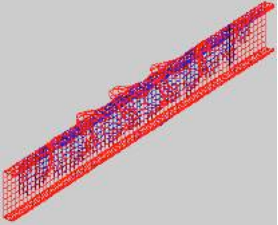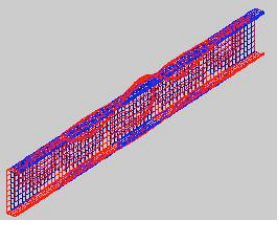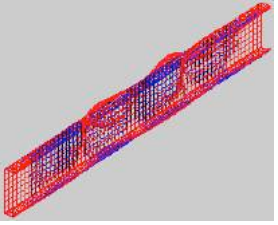
Section	Local Buckling	Local Buckling
600S137-54 12"-C-C Straight-line **Minor Bending Flange lip in tension** **FSM@cFSM**	 Mode1: D=7%, L=92%, M_{cl}=6.3 M_{cl}=5.4, L_{cr}=4.7"	 Mode2: D=8%, L=91%, M_{cl}=6.4 M_{cl}=65.3, L_{cr}=3.6"
Section	Local Buckling	Local Buckling
600S137-54 12"-C-C Round-corner **Minor Bending Flange lip in tension** **FSM@cFSM**	 Mode1: M_{cl}=6.2 M_{cl}=5.4, L_{cr}=4.7"	 Mode2: M_{cl}=6.2 M_{cl}=5.4, L_{cr}=4.7"
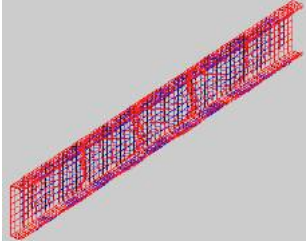
Section	Local Buckling	Distortional Buckling	Distortional Buckling
600S137-54 48"-C-C Straight-line **Compression** **FSM@cFSM**	Mode1: D=11%, L=88%, P_cl=7.3 P_cl=7.3, L_cr=4.1"	Mode9: D=46%, L=51%, P_cd=9.1 P_cd=9.1, L_cr=12.6"	Mode 10:D=50%, L=46%, P_cd=10.2 P_cd=9.1, L_cr=12.6"
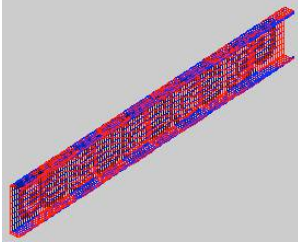
Section	Local Buckling	Distortional Buckling	Distortional Buckling
600S137-54 48"-C-C Round-corner **Compression** **FSM@cFSM**	Mode1: P_cl=7.2 P_cl=7.3, L_cr=4.1"	Mode9: P_cd=10.6 P_cd=9.1, L_cr=12.6"	Mode10: P_cd=10.6 P_cd=9.1, L_cr=12.6"
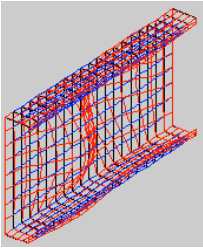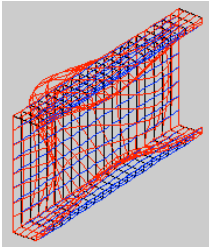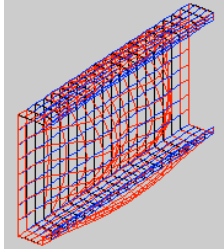
Section	Local Buckling	Local Buckling	Distortional Buckling	Distortional Buckling
600S137-54 48"-C-C Straight-line **Major Bending** **FSM@cFSM**	Mode3: D=12%, L=87%, M_cl=66.6 M_cl=65.3, L_cr=3.6"	Mode4: D=30%, L=69%, M_cl=67.0 M_cl=65.3, L_cr=3.6"	Mode1: D=79%, L=19%, M_cd=61.9 M_cd=57.5, L_cr=9.5"	Mode 2:D=76%, L=22%, M_cd=62.0 M_cd=57.5, L_cr=9.5"
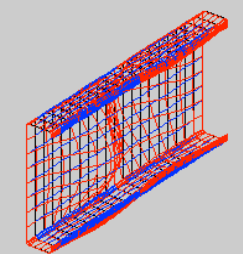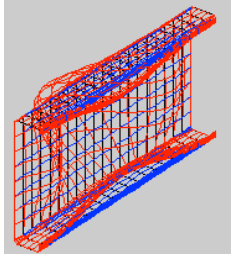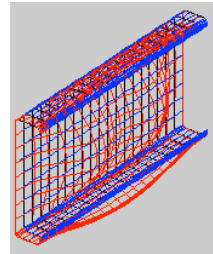
Section	Local Buckling	Local Buckling	Distortional Buckling	Distortional Buckling
600S137-54 48"-C-C Round-corner **Major Bending** **FSM@cFSM**	Mode3: M_cl=65.0 M_cl=65.3, L_cr=3.6"	Mode4: M_cl=65.0 M_cl=65.3, L_cr=3.6"	Mode1: M_cd=60 M_cd=57.5, L_cr=9.5"	Mode 2: M_cd=60.2 M_cd=57.5, L_cr=9.5"
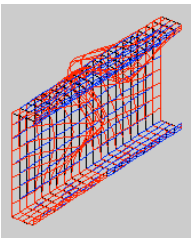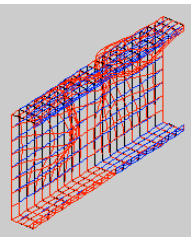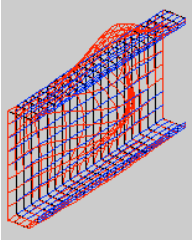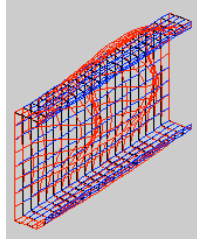
233

Section	Local Buckling	Distortional Buckling	Distortional Buckling
600S137-54 48"-C-C Straight-line **Minor Bending Flange lip in compression** **FSM@cFSM**	 Mode13: D=5%, L=93%, M_{cl}=50.5 M_{cl}=49.1, L_{cr}=1.2"	 Mode1: D=64%, L=35%, M_{cd}=14.3 M_{cd}=13.7, L_{cr}=9.5"	 Mode 3:D=87%, L=9%, M_{cd}=14.7 M_{cd}=13.7, L_{cr}=9.5"

Section	Local Buckling	Distortional Buckling	Distortional Buckling
600S137-54 48"-C-C Round-corner **Minor Bending Flange lip in compression** **FSM@cFSM**	 Mode13: M_{cl}=48.9 M_{cl}=49.1, L_{cr}=1.2"	 Mode1: M_{cd}=14.3 M_{cd}=13.7, L_{cr}=9.5"	 Mode 3:D=87%, L=9%, M_{cd}=14.6 M_{cd}=13.7, L_{cr}=9.5"
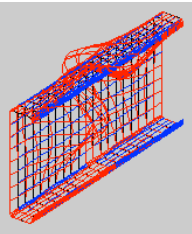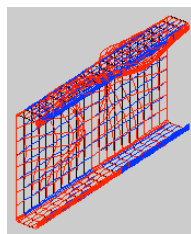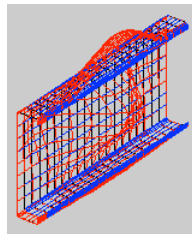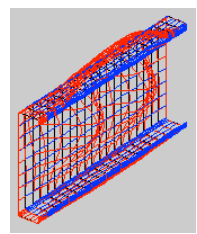
Section	Local Buckling
600S137-54 48"-C-C Straight-line **Minor Bending Flange lip in tension** **FSM@cFSM**	 Mode1: D=7%, L=92%, M_{cl}=5.5 M_{cl}=5.4, L_{cr}=4.7"
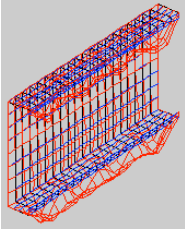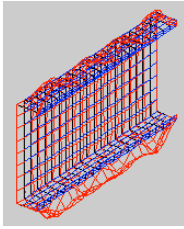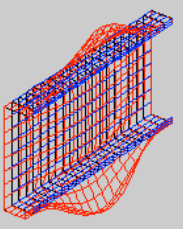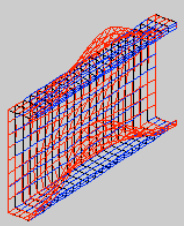
Section	Local Buckling
600S137-54 48"-C-C Round-corner **Minor Bending Flange lip in tension** **FSM@cFSM**	 Mode1: M_{cl}=5.4 M_{cl}=5.4, L_{cr}=4.7"
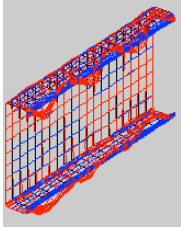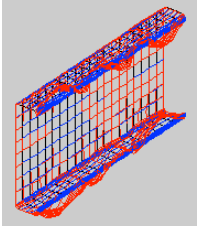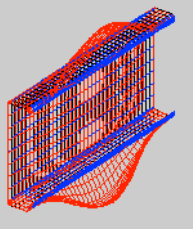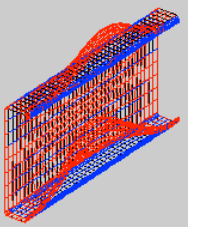
Section	Local Buckling	Local Buckling	Distortional Buckling
600S137-68 12"-C-C Straight-line **Compression** **FSM@cFSM**	Mode1: D=18%, L=81%, P_{cl}=15.6 P_{cl}=13.4, L_{cr}=4.1"	Mode2: D=24%, L=74%, P_{cl}=16.0 P_{cl}=13.4, L_{cr}=4.1"	Mode 3:D=35%, L=63%, P_{cd}=22.3 P_{cd}=15.4, L_{cr}=11"
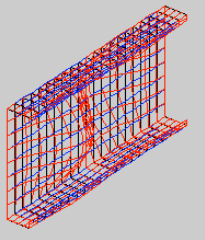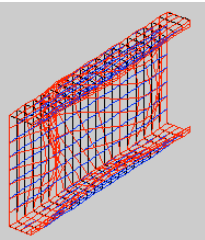
Section	Local Buckling	Local Buckling	Distortional Buckling
600S137-68 12"-C-C Round-corner **Compression** **FSM@cFSM**	Mode1: P_{cl}=16.0 P_{cl}=13.4, L_{cr}=4.1"	Mode2: P_{cl}=16.1 P_{cl}=13.4, L_{cr}=4.1"	Mode 3: P_{cd}=22.5 P_{cd}=15.4, L_{cr}=11"
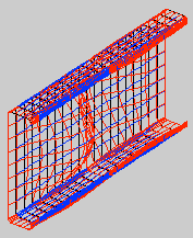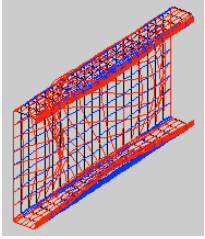
Section	Local Buckling	Local Buckling	Distortional Buckling	Distortional Buckling
600S137-68 12"-C-C Straight-line **Major Bending** **FSM@cFSM**	Mode2: D=36%, L=63%, M_{cl}=127.7 M_{cl}=127, L_{cr}=3.1"	Mode4: D=27%, L=72%, M_{cl}=153.1 M_{cl}=127, L_{cr}=3.1"	Mode1: D=49, L=49%, M_{cd}=122 M_{cd}=98.4, L_{cr}=9.5"	Mode 3:D=32%, L=67%, M_{cd}=145.3 M_{cd}=98.4, L_{cr}=9.5"
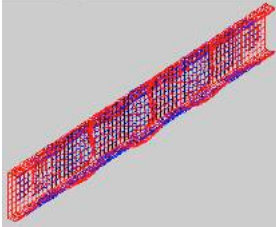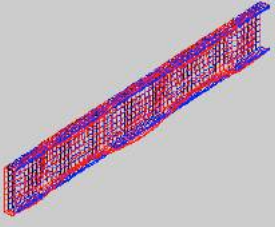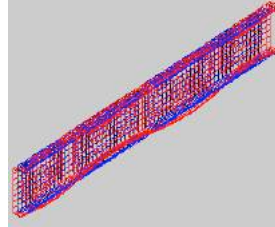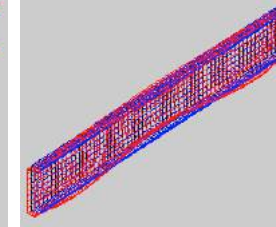
Section	Local Buckling	Local Buckling	Distortional Buckling	Distortional Buckling
600S137-68 12"-C-C Round-corner **Major Bending** **FSM@cFSM**	Mode2: M_{cl}=128.7 M_{cl}=127, L_{cr}=3.1"	Mode4: M_{cl}=152.7 M_{cl}=127, L_{cr}=3.1"	Mode1: M_{cd}=123.7 M_{cd}=98.4, L_{cr}=9.5"	Mode 3: M_{cd}=144.9 M_{cd}=98.4, L_{cr}=9.5"
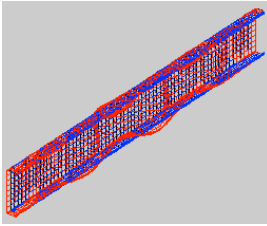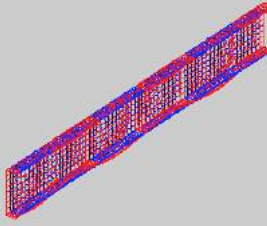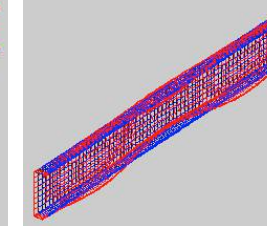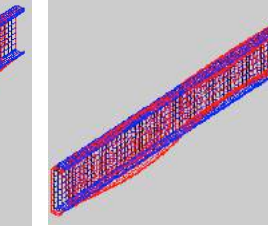
235

Section	Local Buckling	Local Buckling	Distortional Buckling	Distortional Buckling
600S137-68 12"-C-C Straight-line **Minor Bending Flange lip in compression** **FSM@cFSM**	Mode13: D=43%, L=50%, M_{cl}=99.7 M_{cl}=97.5, L_{cr}=1.2"	Mode 14: D=48%, L=48%, M_{cl}=99.8 M_{cl}=97.5, L_{cr}=1.2"	Mode1: D=62%, L=37%, M_{cd}=29.0 M_{cd}=22.4, L_{cr}=8.3"	Mode 2:D=82%, L=14%, M_{cd}=30.0 M_{cd}=22.4, L_{cr}=8.3"
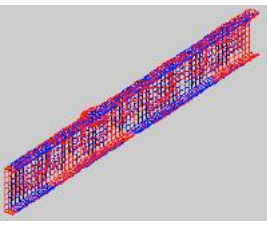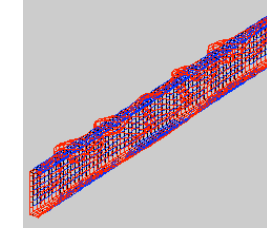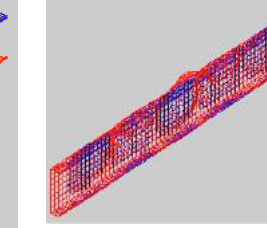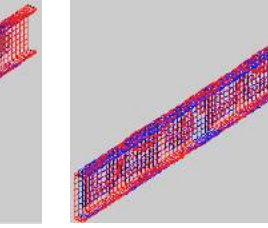
Section	Local Buckling	Local Buckling	Distortional Buckling	Distortional Buckling
600S137-68 12"-C-C Round-corner **Minor Bending Flange lip in compression** **FSM@cFSM**	Mode11: M_{cl}=105.7 M_{cl}=97.5, L_{cr}=1.2"	Mode12: M_{cl}=105.8 M_{cl}=97.5, L_{cr}=1.2"	Mode1: M_{cd}=32.5 M_{cd}=22.4, L_{cr}=8.3"	Mode 2: M_{cd}=33.5 M_{cd}=22.4, L_{cr}=8.3"
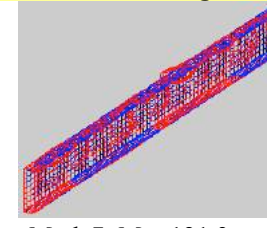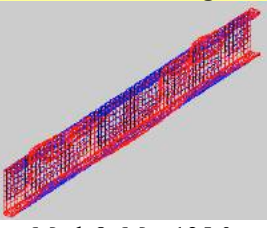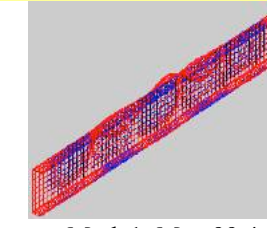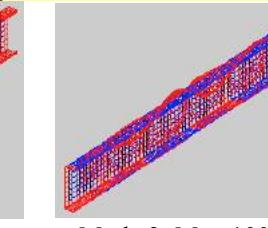
Section	Local Buckling	Local Buckling
600S137-68 12"-C-C Straight-line **Minor Bending Flange lip in tension** **FSM@cFSM**	Mode1: D=11%, L=88%, M_{cl}=12.0 M_{cl}=10.4, L_{cr}=4.7"	Mode2: D=11%, L=88%, M_{cl}=12.36 M_{cl}=10.4, L_{cr}=4.7"
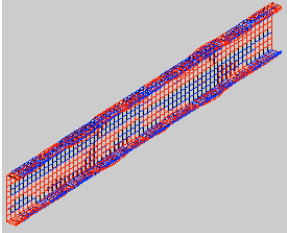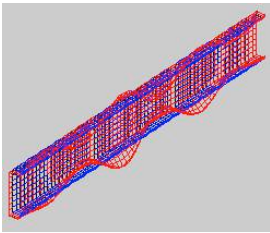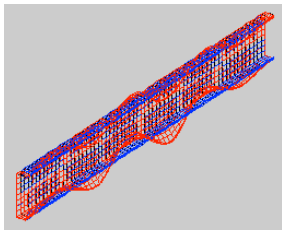
Section	Local Buckling	Local Buckling
600S137-68 12"-C-C Round-corner **Minor Bending Flange lip in tension** **FSM@cFSM**	Mode1: M_{cl}=11.9 M_{cl}=10.4, L_{cr}=4.7"	Mode2: M_{cl}=12.2 M_{cl}=10.4, L_{cr}=4.7"
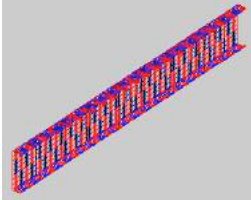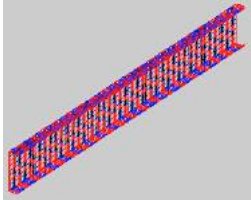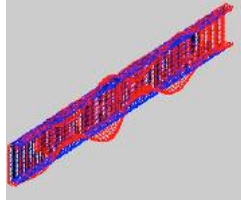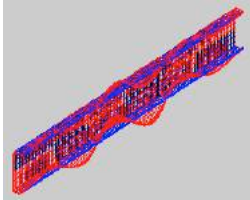
236

Section	Local Buckling	Distortional Buckling	Distortional Buckling	Distortional Buckling
600S137-68 48"-C-C Straight-line **Compression** **FSM@cFSM**	Mode1: D=28%, L=70%, P_{cl}=13.7 P_{cl}=13.4, L_{cr}=4.1"	Mode8: D=47%, L=50%, P_{cd}=15.0 P_{cd}=15.4, L_{cr}=11"	Mode 9:D=51%, L=44%, P_{cd}=18.0 P_{cd}=15.4, L_{cr}=11"	Mode 10:D=57%, L=30%, P_{cd}=21.2 P_{cd}=15.4, L_{cr}=11"
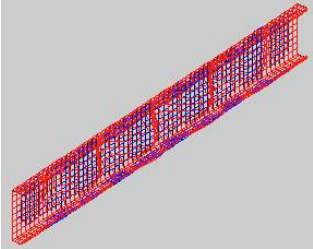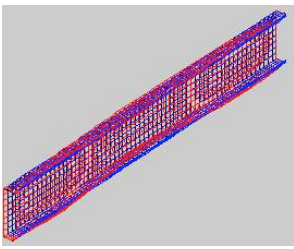
Section	Local Buckling	Distortional Buckling	Distortional Buckling	
600S137-68 48"-C-C Round-corner **Compression** **FSM@cFSM**	Mode1: P_{cl}=13.8 P_{cl}=13.4, L_{cr}=4.1"	Mode8: P_{cd}=16. P_{cd}=15.4, L_{cr}=11"	Mode 9: P_{cd}=18.9 P_{cd}=15.4, L_{cr}=11"	Mode 10: P_{cd}=27.7 P_{cd}=15.4, L_{cr}=11"
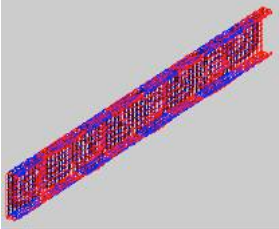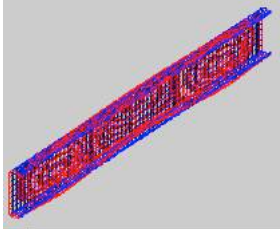
Section	Local Buckling	Local Buckling	Distortional Buckling	Distortional Buckling
600S137-68 48"-C-C Straight-line **Major Bending** **FSM@cFSM**	Mode7: D=37%, L=60%, M_{cl}=120.4 M_{cl}=127, L_{cr}=3.1"	Mode8: D=34%, L=64%, M_{cl}=121.6 M_{cl}=127, L_{cr}=3.1"	Mode1: D=83.0, L=14%, M_{cd}=96.7 M_{cd}=98.4, L_{cr}=9.5"	Mode 3:D=73%, L=24%, M_{cd}=104 M_{cd}=98.4, L_{cr}=9.5"

Section	Local Buckling	Local Buckling	Distortional Buckling	Distortional Buckling
600S137-68 48"-C-C Round-corner **Major Bending** **FSM@cFSM**	Mode7: M_{cl}=121.3 M_{cl}=127, L_{cr}=3.1"	Mode8: M_{cl}=125.0 M_{cl}=127, L_{cr}=3.1"	Mode1: M_{cd}=99.4 M_{cd}=98.4, L_{cr}=9.5"	Mode 3: M_{cd}=100.3 M_{cd}=98.4, L_{cr}=9.5"

237

Section	Local Buckling	Distortional Buckling	Distortional Buckling
600S137-68 48"-C-C Straight-line **Minor Bending Flange lip in compression** **FSM@cFSM**	Mode27: D=20%, L=50%, M_{cl}=388.1 M_{cl}=97.5, L_{cr}=1.2"	Mode1: D=63%, L=36%, M_{cd}=20.7 M_{cd}=22.4, L_{cr}=8.3"	Mode 3:D=86%, L=10%, M_{cd}=21.1 M_{cd}=22.4, L_{cr}=8.3"

Section	Local Buckling	Local Buckling	Distortional Buckling	Distortional Buckling
600S137-68 48"-C-C Round-corner **Minor Bending Flange lip in compression** **FSM@cFSM**	Mode16: M_{cl}=97.1 M_{cl}=97.5, L_{cr}=1.2"	Mode31: M_{cl}=165.3 M_{cl}=97.5, L_{cr}=1.2"	Mode1: M_{cd}=23.0 M_{cd}=22.4, L_{cr}=8.3"	Mode 3: M_{cd}=23.4 M_{cd}=22.4, L_{cr}=8.3"

Section	Local Buckling	Distortional Buckling
600S137-68 48"-C-C Straight-line **Minor Bending Flange lip in tension** **FSM@cFSM**	Mode1: D=11%, L=88%, M_{cl}=10.6 M_{cl}=10.4, L_{cr}=4.7"	Mode12: D=38%, L=45%, M_{cl}=26.9

Section	Local Buckling	Local Buckling
600S137-68 48"-C-C Round-corner **Minor Bending Flange lip in tension** **FSM@cFSM**	Mode1: M_{cl}=10.9 M_{cl}=10.4, L_{cr}=4.7"	Mode6: M_{cl}=25.2 M_{cl}=10.4, L_{cr}=4.7"

Appendix B - Loading plate details

Key Plan
SC. NTS

239

Part-1
SC. NTS

Plate Size: 12 x 20 x 1½

n= 2 pieces

VIEW A
SC. NTS

VIEW B
SC. NTS

20.0

12.0

3.0

0.500   1.500   2.00   2.00   2.00   2.00   2.00   2.00   2.00   2.00   1.500   0.500

3.125   5.750   3.125

3.625   5.750   10.625

$\frac{3}{8}$ 16 (Threading length=1 inch)

$\frac{5}{8}$ 11 (Threading length=1 inch)

(Thickness= 1½)

Ø0.25

Ø0.25

Thread (Only Top Plate)

1½

$\frac{3}{8}$

240
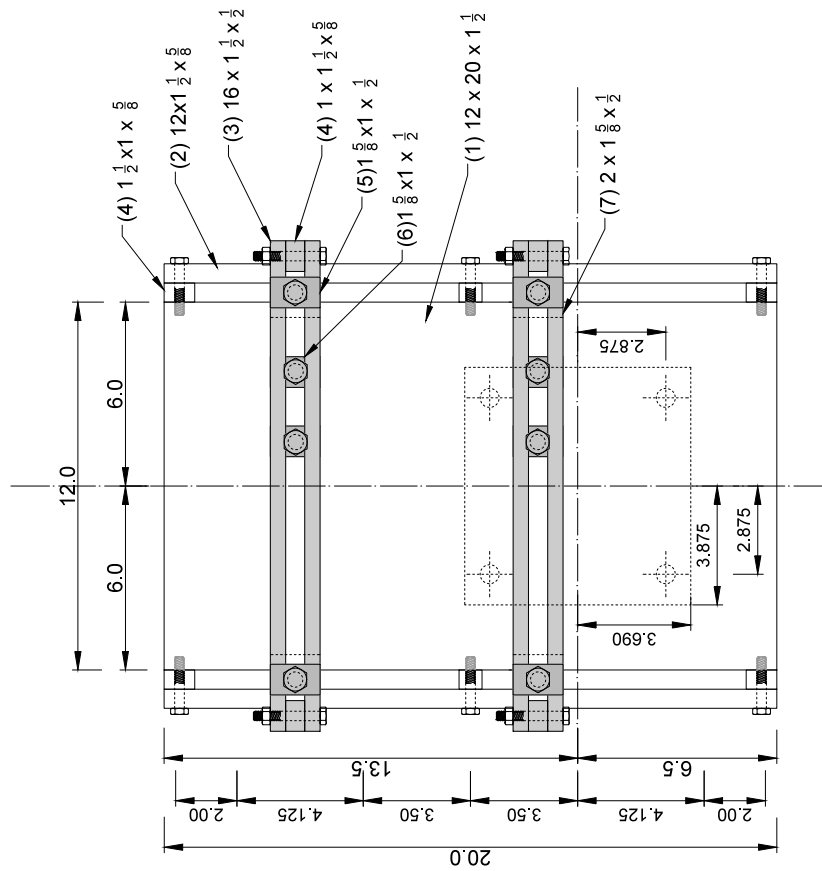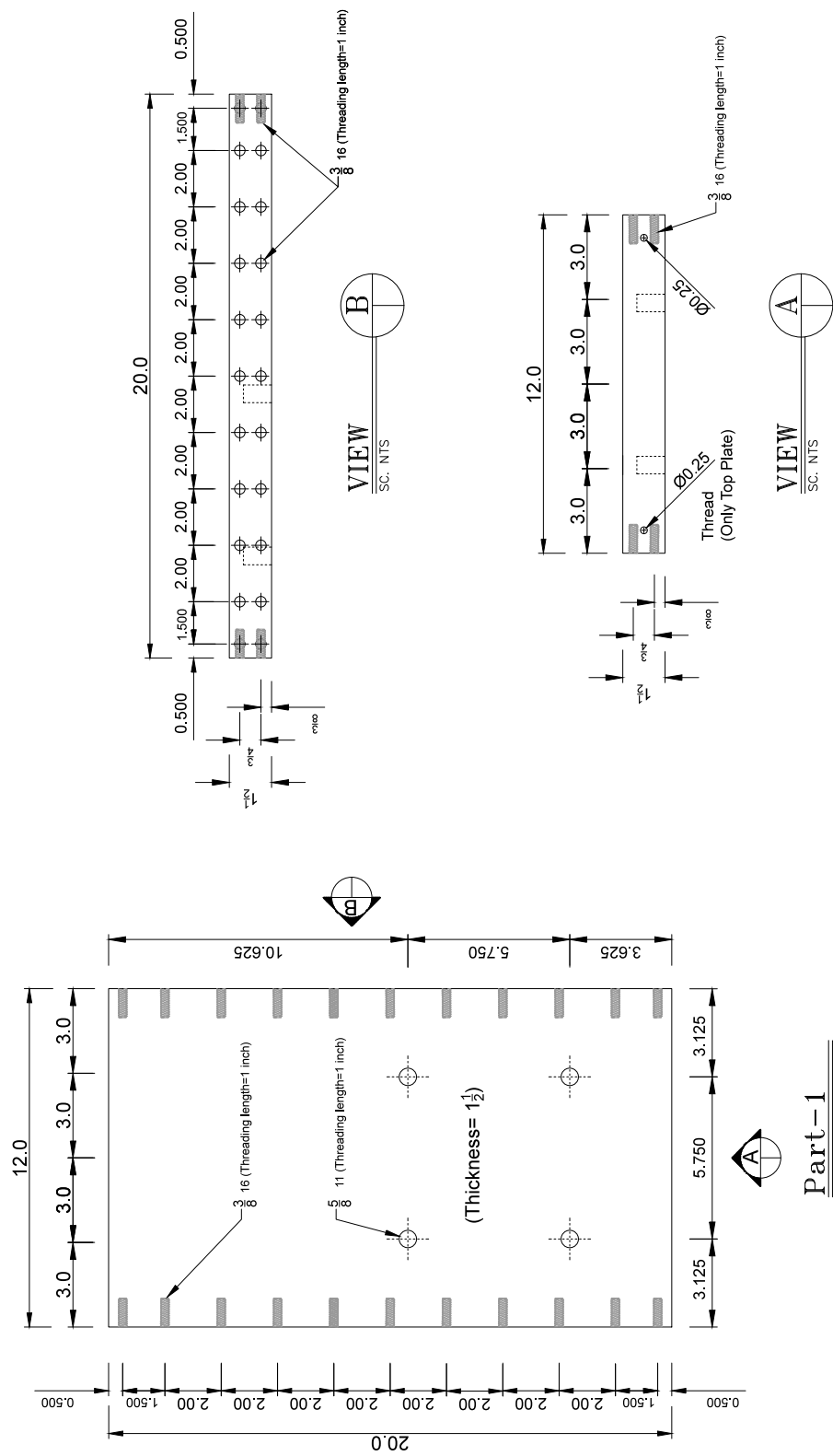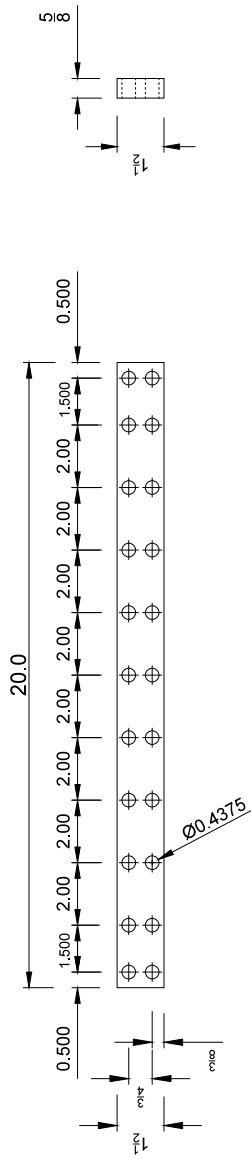
Part-2
SC. NTS
Bar Size: 12 x 1 $\frac{1}{2}$ x $\frac{5}{8}$

n= 4 pieces

Part-3
SC. NTS
Bar Size: 16 x 1 $\frac{1}{2}$ x $\frac{1}{2}$

n= 8 pieces

241

Part-5

SC. NTS

Plate: $1\frac{5}{8}$ x 1 x $\frac{1}{2}$

n= 8 pieces

$\frac{1}{2}$

1.0

Ø0.6250

$1\frac{9}{10}$

Part-7

SC. NTS

Plate: 2 x $1\frac{5}{8}$ x $\frac{1}{2}$

n= 8 pieces

$\frac{1}{2}$

2.0

Ø0.6250

$1\frac{9}{10}$
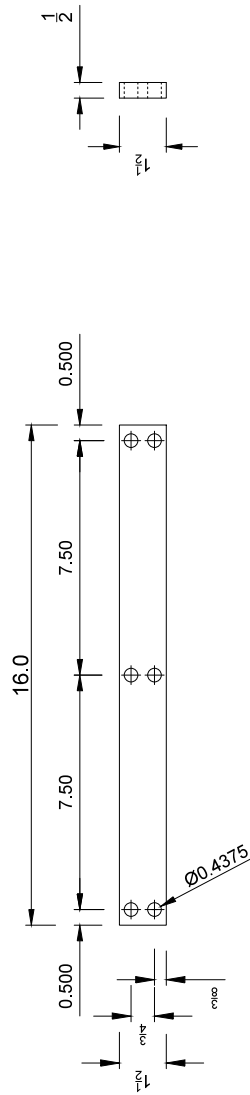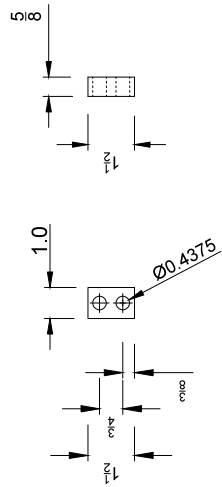
Part-4

SC. NTS

Plate: $1\frac{1}{2}$ x1 x $\frac{5}{8}$

n= 20 pieces

$\frac{5}{8}$

1.0

Ø0.4375

$1\frac{1}{2}$
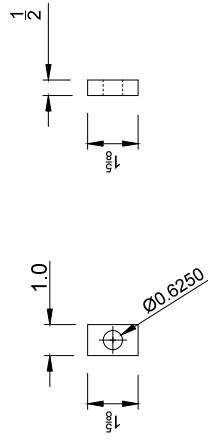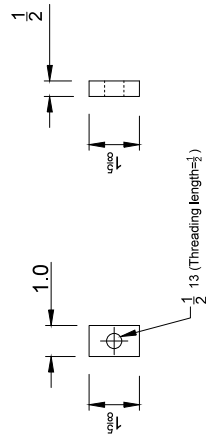
Part-6

SC. NTS

Plate: $1\frac{5}{8}$ x 1 x $\frac{1}{2}$

n= 8 pieces

$\frac{1}{2}$

1.0

$\frac{1}{2}$ 13 (Threading length=$\frac{1}{2}$)

$1\frac{9}{10}$
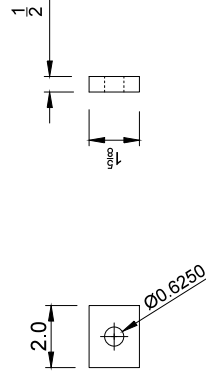
Appendix C - Material testing

ASTM E8/E8M – 11
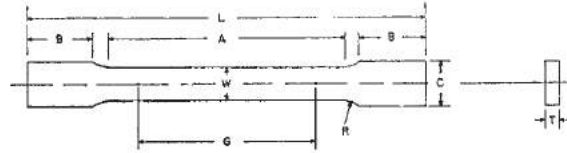
Dimensions

	Standard Specimens		Subsize Specimen
	Plate-Type, 40 mm [1.500 in.] Wide	Sheet-Type, 12.5 mm [0.500 in.] Wide	6 mm [0.250 in.] Wide
	mm [in.]	mm [in.]	mm [in.]
G—Gage length (Note 1 and Note 2)	200.0 ± 0.2 [8.00 ± 0.01]	50.0 ± 0.1 [2.000 ± 0.005]	25.0 ± 0.1 [1.000 ± 0.003]
W—Width (Note 3 and Note 4)	40.0 ± 2.0 [1.500 ± 0.125, -0.250]	12.5 ± 0.2 [0.500 ± 0.010]	6.0 ± 0.1 [0.250 ± 0.005]
T—Thickness (Note 5)		thickness of material	
R—Radius of fillet, min (Note 6)	25 [1]	12.5 [0.500]	6 [0.250]
L—Overall length, min (Note 2, Note 7, and Note 8)	450 [18]	200 [8]	100 [4]
A—Length of reduced section, min	225 [9]	57 [2.25]	32 [1.25]
B—Length of grip section, min (Note 9)	75 [3]	50 [2]	30 [1.25]
C—Width of grip section, approximate (Note 4 and Note 9)	50 [2]	20 [0.750]	10 [0.375]

Note 1—For the 40 mm [1.500 in.] wide specimen, punch marks for measuring elongation after fracture shall be made on the flat or on the edge of the specimen and within the reduced section. Either a set of nine or more punch marks 25 mm [1 in.] apart, or one or more pairs of punch marks 200 mm [8 in.] apart may be used.

Note 2—When elongation measurements of 40 mm [1.500 in.] wide specimens are not required, a minimum length of reduced section (A) of 75 mm [2.25 in.] may be used with all other dimensions similar to those of the plate-type specimen.

Note 3—For the three sizes of specimens, the ends of the reduced section shall not differ in width by more than 0.10, 0.05 or 0.02 mm [0.004, 0.002 or 0.001 in.], respectively. Also, there may be a gradual decrease in width from the ends to the center, but the width at each end shall not be more than 1 % larger than the width at the center.

Note 4—For each of the three sizes of specimens, narrower widths (W and C) may be used when necessary. In such cases the width of the reduced section should be as large as the width of the material being tested permits; however, unless stated specifically, the requirements for elongation in a product specification shall not apply when these narrower specimens are used.

Note 5—The dimension T is the thickness of the test specimen as provided for in the applicable material specifications. Minimum thickness of 40 mm [1.500 in.] wide specimens shall be 5 mm [0.188 in.]. Maximum thickness of 12.5 and 6 mm [0.500 and 0.250 in.] wide specimens shall be 19 and 6 mm [0.750 and 0.250 in.], respectively.

Note 6—For the 40 mm [1.500 in.] wide specimen, a 13 mm [0.500 in.] minimum radius at the ends of the reduced section is permitted for steel specimens under 690 MPa [100 000 psi] in tensile strength when a profile cutter is used to machine the reduced section.

Note 7—The dimension shown is suggested as a minimum. In determining the minimum length, the grips must not extend in to the transition section between Dimensions A and B, see Note 9.

Note 8—To aid in obtaining axial force application during testing of 6-mm [0.250-in.] wide specimens, the overall length should be as large as the material will permit, up to 200 mm [8.00 in.].

Note 9—It is desirable, if possible, to make the length of the grip section large enough to allow the specimen to extend into the grips a distance equal to two thirds or more of the length of the grips. If the thickness of 12.5 mm [0.500-in.] wide specimens is over 10 mm [0.375 in.], longer grips and correspondingly longer grip sections of the specimen may be necessary to prevent failure in the grip section.

Note 10—For the three sizes of specimens, the ends of the specimen shall be symmetrical in width with the center line of the reduced section within 2.5, 1.25 and 0.13 mm [0.10, 0.05 and 0.005 in.], respectively. However, for referee testing and when required by product specifications, the ends of the 12.5 mm [0.500 in.] wide specimen shall be symmetrical within 0.2 mm [0.01 in.].

Note 11—For each specimen type, the radii of all fillets shall be equal to each other within a tolerance of 1.25 mm [0.05 in.], and the centers of curvature of the two fillets at a particular end shall be located across from each other (on a line perpendicular to the centerline) within a tolerance of 2.5 mm [0.10 in.].

Note 12—Specimens with sides parallel throughout their length are permitted, except for referee testing, provided: (a) the above tolerances are used; (b) an adequate number of marks are provided for determination of elongation; and (c) when yield strength is determined, a suitable extensometer is used. If the fracture occurs at a distance of less than 2 W from the edge of the gripping device, the tensile properties determined may not be representative of the material. In acceptance testing, if the properties meet the minimum requirements specified, no further testing is required, but if they are less than the minimum requirements, discard the test and retest.

FIG. 1 Rectangular Tension Test Specimens

Figure C-1: ASTM E8/E8M-11 for Tension test specimens (coupons)

Table C-1: Measured thickness of the zinc-coated tensile coupons

No.	Specimen	Thickness of coated plate (in. $\times 10^{-3}$)														
		Start						End				Within the gauge length				
		t_{c1-1}	t_{c1-2}	t_{c1-3}	t_{c1-4}	t_{c1-5}	t_{c2-1}	t_{c2-2}	t_{c2-3}	t_{c2-4}	t_{c2-5}	t_{c1}	t_{c2}	t_{c3}	t_{c4}	t_{c5}
1	PL1-1	56.1	56	56.1	56.1	56	55.7	55.8	55.8	55.9	55.8	56.0	55.8	55.9	56	55.9
2	PL1-2	56.2	56.1	56.1	56.2	56.2	56.2	56.2	56.1	56.3	56.2	56.2	56	56.1	56.3	56.2
3	PL1-3	56.4	56.3	56.4	56.2	56.3	56.2	56.3	56.4	56.3	56.3	56.3	56.2	56.3	56.2	56.3
4	PL1-4	56	56.1	55.7	56.2	56	56.3	56.3	56.2	56.2	56	55.8	55.9	56	55.9	55.9
5	PL1-5	56	56.1	56.2	56.2	56.2	56.2	56.1	56.2	56.1	56.2	56.3	56	56.2	56.2	56.2
6	PL1-6	56.3	56.4	56.2	56.4	56.3	56.3	56.4	56.4	56.4	56.5	56.2	56.3	56.3	56.3	56.2
7	PL2-1	56.2	56.3	56.2	56.5	56.1	55.9	56	56.2	56	56.2	56.2	56.3	56.1	56.3	56.3
8	PL2-2	56.1	55.9	56	55.9	56	56	56.1	56.2	55.9	56.1	56.1	56.2	56.1	56.1	56.1
9	PL2-3	55.9	56	56.1	56.2	56.2	56.2	55.9	56	55.9	56	56.1	56.1	56	56.2	56.2
10	600-12-1-F (L)	56.4	56.3	56.4	56.4	56.6	56.5	56.5	56.4	56.5	56.5	56.4	56.5	56.5	56.4	56.4
11	600-12-1-W	55.8	55.6	56	55.9	55.7	55.8	55.8	55.7	55.9	55.9	55.8	55.7	55.9	55.9	55.8
12	600-12-2-F (R)	55.9	56	56.1	56.1	56	55.9	55.9	55.8	55.9	56.1	55.9	56.2	55.8	56	56.1
13	600-12-2-W	56.3	56.4	56.2	56.3	56.3	56.5	56.4	56.4	56.3	56.3	56.1	56.3	56.3	56.3	56.1
14	600-24-1-F (R)	55.8	56.1	55.9	55.7	55.8	55.6	55.7	56.1	55.9	56.1	56.1	56.1	56	56.1	56
15	600-24-1-W	56.2	56.4	56.5	56.4	56.4	56.6	56.1	56.3	56	56	56.1	56.2	56.3	56.2	56.4
16	600-24-2-F (L)	56.5	56.4	56.4	56.3	56.5	56.5	56.8	56.7	56.8	57	56.6	56.4	56.5	56.4	56.6
17	600-24-2-W	55.9	56	55.9	56.2	56.1	55.9	56	55.8	56.1	55.9	56	55.9	55.8	55.7	56
18	600-48-1-F (R)	55.7	55.8	55.8	55.8	55.5	55.1	55.5	55.3	55.6	55.5	55.4	55.3	55.6	55.5	55.3
19	600-48-1-W	55.8	55.7	55.9	55.9	55.8	55.9	55.6	55.9	55.6	55.8	55.5	55.7	56	55.7	55.9
20	600-48-2-F (L)	56.6	56.6	56.8	56.5	56.6	56.3	56.3	56.6	56.3	56.6	56.5	56.6	56.7	56.9	56.4
21	600-48-2-W	55.9	55.8	56	55.7	56.1	56.2	56	56.3	56.2	56.2	56.2	55.5	55.9	55.9	56.1

Table C-2: Measured thickness of the uncoated tensile coupons

No.	Specimen	Thickness of uncoated plate (in. $\times 10^{-3}$)														
		Start						End				Within the gauge length				
		t_{c1-1}	t_{c1-2}	t_{c1-3}	t_{c1-4}	t_{c1-5}	t_{c2-1}	t_{c2-2}	t_{c2-3}	t_{c2-4}	t_{c2-5}	t_{c1}	t_{c2}	t_{c3}	t_{c4}	t_{c5}
1	PL1-1	55.5	55.6	55.7	55.5	55.7	55.5	55.6	55.6	55.6	55.4					
2	PL1-2	55.8	55.5	55.7	55.8	55.7	55.9	55.8	55.6	55.8	55.7					
3	PL1-3	55.8	55.8	55.7	55.9	55.8	55.6	55.7	55.6	55.5	55.8					
4	PL1-4	55.5	55.4	55.4	55.3	55.4	55.5	55.6	55.5	55.5	55.4	55.3	55.5	55.4	55.5	55.4
5	PL1-5	55.3	55.5	55.5	55.3	55.5	55.5	55.4	55.6	55.6	55.5	55.3	55.5	55.3	55.5	55.4
6	PL1-6	55.5	55.6	55.7	55.6	55.5	55.7	55.8	55.8	55.7	55.8	55.7	55.6	55.6	55.6	55.7
7	PL2-1	55.5	55.4	55.6	55.4	55.5	55.5	55.7	55.6	55.6	55.7					
8	PL2-2	55.4	55.5	55.5	55.4	55.5	55.5	55.4	55.6	55.5	55.6					
9	PL2-3	55.5	55.3	55.4	55.4	55.4	55.3	55.4	55.6	55.5	55.6					
10	600-12-1-F (L)	55.5	55.6	55.7	55.6	55.7	55.4	55.7	55.6	55.6	55.6					
11	600-12-1-W	55.2	55.4	55.1	55.2	55.2	55.2	55	55.2	55.3	55.1					
12	600-12-2-F (R)	54.8	55	55	54.9	55	54.9	55	55.1	55	54.8					
13	600-12-2-W	55.8	55.8	55.8	55.8	55.6	55.8	55.7	55.7	55.7	55.6					
14	600-24-1-F (R)	54.9	55.1	54.8	55.1	55.2	55	55	55.1	55.1	55					
15	600-24-1-W	55.6	55.5	55.8	55.7	55.8	55.7	55.6	55.6	55.8	55.6					
16	600-24-2-F (L)	55.7	55.8	55.9	55.8	55.8	56	56.1	55.8	56.1	56.1					
17	600-24-2-W	55.3	55.5	55.3	55.2	55.5	55.3	55.5	55.5	55.3	55.5					
18	600-48-1-F (R)	54.8	54.5	54.9	54.5	54.7	54.6	54.6	54.8	54.7	54.7					
19	600-48-1-W	55.5	55.3	55.3	55.4	55.4	55.4	55.3	55.4	55.3	55.3					
20	600-48-2-F (L)	55.8	55.9	55.8	55.7	55.8	56	55.8	55.7	55.9	56					
21	600-48-2-W	55.1	55.5	55.5	55.4	55.5	55.5	55.5	55.5	55.4	55.3					

Table C-3: Measured width of the tensile coupons within the gauge length

No.	Specimen	W_1	W_2	W_3	W_4	W_5	$W_{ave.}$	C.O.V.	W_{min}	$W_{min}/W_{ave.}$
1	PL1-1	0.4995	0.4995	0.5000	0.4990	0.4990	0.4994	0.08%	0.4990	0.999
2	PL1-2	0.4995	0.4995	0.5000	0.4995	0.4995	0.4996	0.04%	0.4995	1.000
3	PL1-3	0.5000	0.5000	0.5000	0.5000	0.4995	0.4999	0.04%	0.4995	0.999
4	PL1-4	0.5000	0.5000	0.5000	0.4995	0.5000	0.4999	0.04%	0.4995	0.999
5	PL1-5	0.5000	0.4995	0.5000	0.4990	0.5000	0.4997	0.09%	0.4990	0.999
6	PL1-6	0.5000	0.5000	0.5000	0.4995	0.4995	0.4998	0.05%	0.4995	0.999
7	PL2-1	0.5000	0.5000	0.5015	0.5000	0.4990	0.5001	0.18%	0.4990	0.998
8	PL2-2	0.4995	0.4990	0.4995	0.4990	0.4990	0.4992	0.05%	0.4990	1.000
9	PL2-3	0.4995	0.4990	0.5000	0.4995	0.4995	0.4995	0.07%	0.4990	0.999
10	600-12-1-F (L)	0.4990	0.4990	0.4990	0.4990	0.4990	0.4990	0.00%	0.4990	1.000
11	600-12-1-W	0.4990	0.4990	0.4990	0.4985	0.4985	0.4988	0.05%	0.4985	0.999
12	600-12-2-F (R)	0.5000	0.5000	0.5005	0.4995	0.4990	0.4998	0.11%	0.4990	0.998
13	600-12-2-W	0.5000	0.4990	0.4990	0.5000	0.5000	0.4996	0.11%	0.4990	0.999
14	600-24-1-F (R)	0.4990	0.4995	0.4995	0.4990	0.4990	0.4992	0.05%	0.4990	1.000
15	600-24-1-W	0.4990	0.4990	0.4990	0.4980	0.4990	0.4988	0.09%	0.4980	0.998
16	600-24-2-F (L)	0.4990	0.4985	0.4990	0.4990	0.4990	0.4989	0.04%	0.4985	0.999
17	600-24-2-W	0.4990	0.4990	0.4995	0.5000	0.5005	0.4996	0.13%	0.4990	0.999
18	600-48-1-F (R)	0.5000	0.4995	0.4995	0.4990	0.4985	0.4993	0.11%	0.4985	0.998
19	600-48-1-W	0.5000	0.4990	0.5000	0.5005	0.4990	0.4997	0.13%	0.4990	0.999
20	600-48-2-F (L)	0.4990	0.4990	0.4995	0.4990	0.4990	0.4991	0.04%	0.4990	1.000
21	600-48-2-W	0.4990	0.4985	0.4985	0.4990	0.4980	0.4986	0.08%	0.4980	0.999

Table C-4: Average thickness of coated plate, uncoated plate and zinc-coating

No.	Specimen	Average coated thickness (in. $\times 10^{-3}$)					Average uncoated thickness (in. $\times 10^{-3}$)					Average thickness of zinc coating (in. $\times 10^{-3}$)				
		Start	End	Middle	All		Start	End	Middle	All		Start	End	Middle	All	
		t_{c1}	t_{c2}	t_c	t	C.O.V	t_{uc1}	t_{uc2}	t_{uc}	$t_{uc\text{-}ave.}$	C.O.V	t_{z1}	t_{z2}	t_z	$t_{z\text{-}ave}$	C.O.V
1	PL1-1	56.06	55.80	55.92	55.93	0.23%	55.60	55.54		55.57	0.17%	0.46	0.26		0.37	38%
2	PL1-2	56.16	56.20	56.16	56.17	0.14%	55.70	55.76		55.73	0.21%	0.46	0.44		0.45	19%
3	PL1-3	56.32	56.30	56.26	56.29	0.13%	55.80	55.64		55.72	0.22%	0.52	0.66		0.59	26%
4	PL1-4	56.00	56.20	55.90	56.03	0.32%	55.40	55.50	55.42	55.44	0.15%	0.60	0.70	0.48	0.62	27%
5	PL1-5	56.14	56.16	56.18	56.16	0.15%	55.42	55.52	55.40	55.45	0.19%	0.72	0.64	0.78	0.71	15%
6	PL1-6	56.32	56.40	56.26	56.33	0.16%	55.58	55.76	55.64	55.66	0.18%	0.74	0.64	0.62	0.68	16%
7	PL2-1	56.26	56.06	56.24	56.19	0.27%	55.48	55.62		55.55	0.19%	0.78	0.44		0.62	37%
8	PL2-2	55.98	56.06	56.12	56.05	0.18%	55.46	55.52		55.49	0.13%	0.52	0.54		0.53	20%
9	PL2-3	56.08	56.00	56.12	56.07	0.21%	55.40	55.48		55.44	0.19%	0.68	0.52		0.60	33%
10	600-12-1-F (L)	56.42	56.48	56.44	56.45	0.13%	55.62	55.58		55.60	0.17%	0.80	0.90		0.85	14%
11	600-12-1-W	55.80	55.82	55.82	55.81	0.19%	55.22	55.16		55.19	0.20%	0.58	0.66		0.62	32%
12	600-12-2-F (R)	56.02	55.92	56.00	55.98	0.22%	54.94	54.96		54.95	0.18%	1.08	0.96		1.02	17%
13	600-12-2-W	56.30	56.38	56.22	56.30	0.19%	55.76	55.70		55.73	0.15%	0.54	0.68		0.61	18%
14	600-24-1-F (R)	55.86	55.88	56.06	55.93	0.31%	55.02	55.04		55.03	0.21%	0.84	0.84		0.84	25%
15	600-24-1-W	56.38	56.20	56.24	56.27	0.32%	55.68	55.66		55.67	0.19%	0.70	0.54		0.62	35%
16	600-24-2-F (L)	56.42	56.76	56.50	56.56	0.34%	55.80	56.02		55.91	0.27%	0.62	0.74		0.68	23%
17	600-24-2-W	56.02	55.94	55.88	55.95	0.23%	55.36	55.42		55.39	0.22%	0.66	0.52		0.59	33%
18	600-48-1-F (R)	55.72	55.40	55.42	55.51	0.38%	54.68	54.68		54.68	0.24%	1.04	0.72		0.88	31%
19	600-48-1-W	55.82	55.76	55.76	55.78	0.26%	55.38	55.34		55.36	0.13%	0.44	0.42		0.43	25%
20	600-48-2-F (L)	56.62	56.42	56.62	56.55	0.31%	55.80	55.88		55.84	0.19%	0.82	0.54		0.68	33%
21	600-48-2-W	55.90	56.18	55.92	56.00	0.39%	55.40	55.44		55.42	0.24%	0.50	0.74		0.62	35%

Table C-5: Average uncoated thickness (t_{uc}) and coupon width (W)

No.	Specimen	Uncoated thickness (in. X10-3) t_{uc}	Width (in.) W
1	PL1-1	55.57	0.4994
2	PL1-2	55.73	0.4996
3	PL1-3	55.72	0.4999
4	PL1-4	55.42	0.4999
5	PL1-5	55.40	0.4997
6	PL1-6	55.64	0.4998
7	PL2-1	55.55	0.5001
8	PL2-2	55.49	0.4992
9	PL2-3	55.44	0.4995
10	600-12-1-F (L)	55.60	0.4990
11	600-12-1-W	55.19	0.4988
12	600-12-2-F (R)	54.95	0.4998
13	600-12-2-W	55.73	0.4996
14	600-24-1-F (R)	55.03	0.4992
15	600-24-1-W	55.67	0.4988
16	600-24-2-F (L)	55.91	0.4989
17	600-24-2-W	55.39	0.4996
18	600-48-1-F (R)	54.68	0.4993
19	600-48-1-W	55.36	0.4997
20	600-48-2-F (L)	55.84	0.4991
21	600-48-2-W	55.42	0.4986
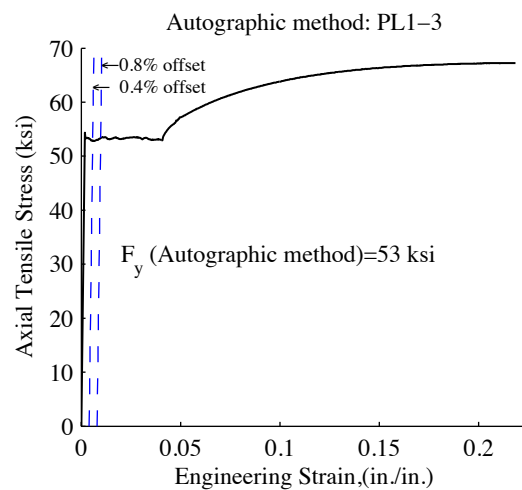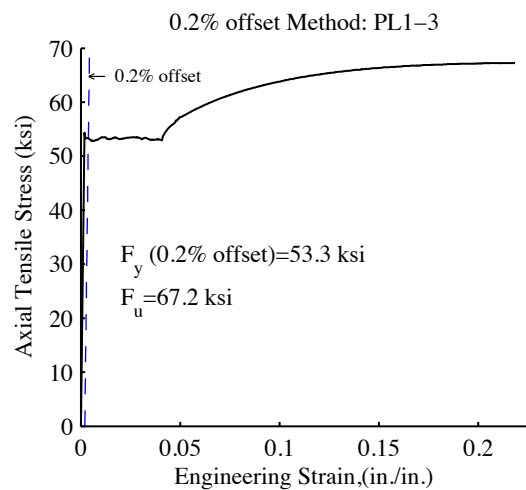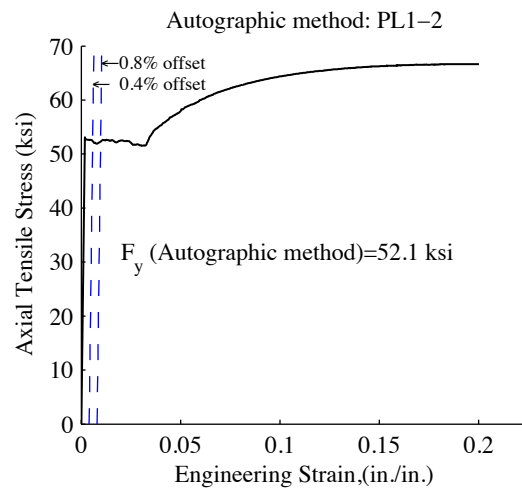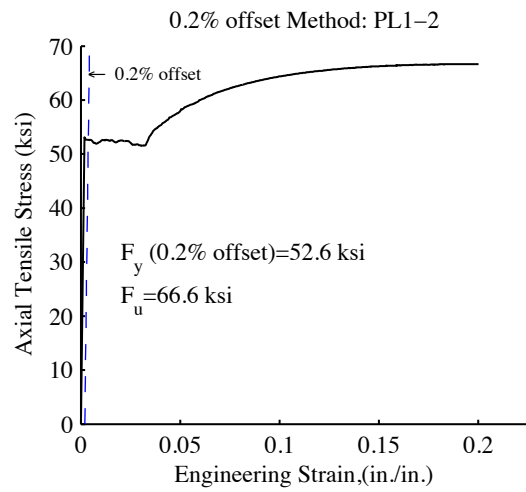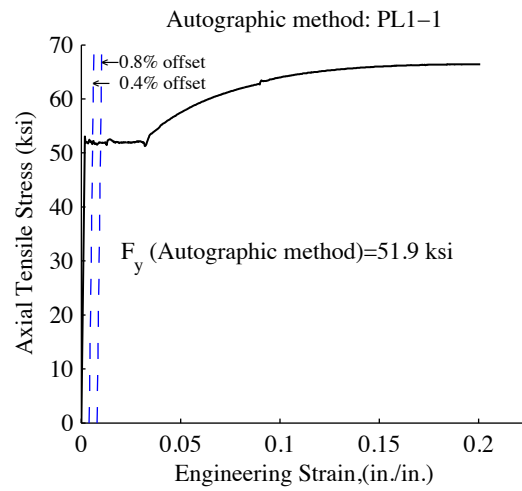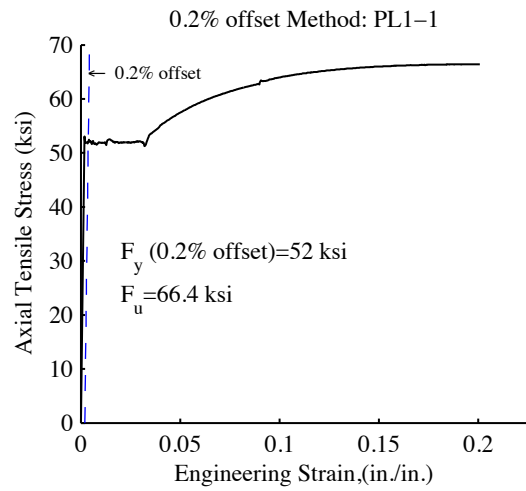
Figure C-2: Test results (PL1-1 to PL1-3)
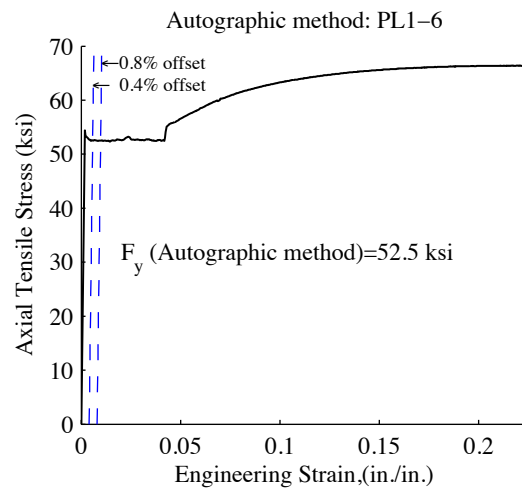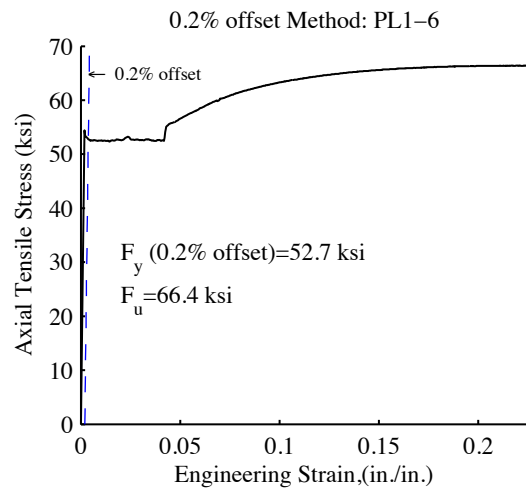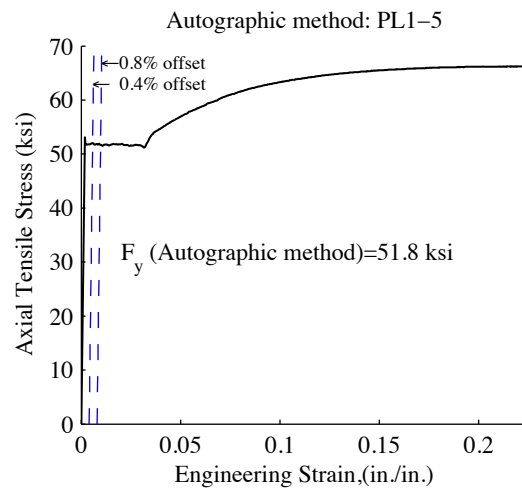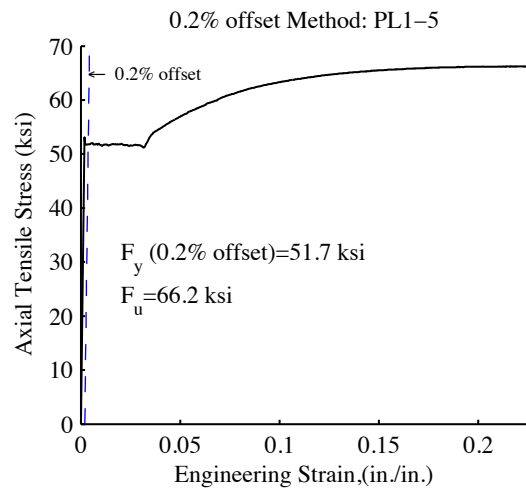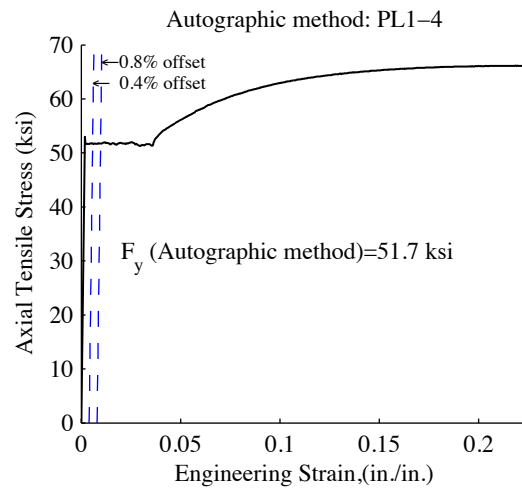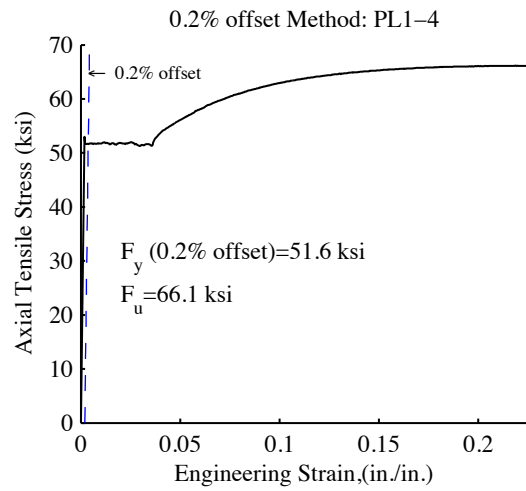
Figure C-3: Test results (PL1-4 to PL1-6)
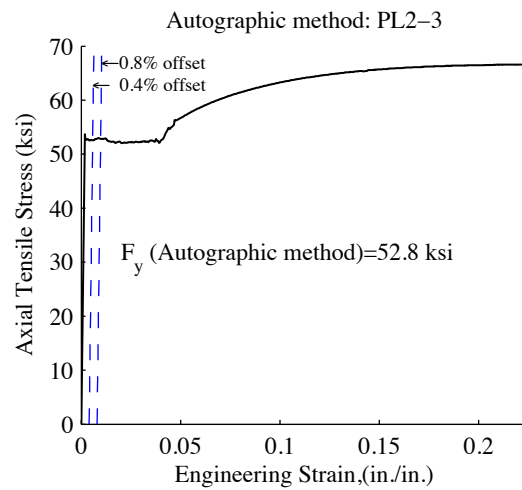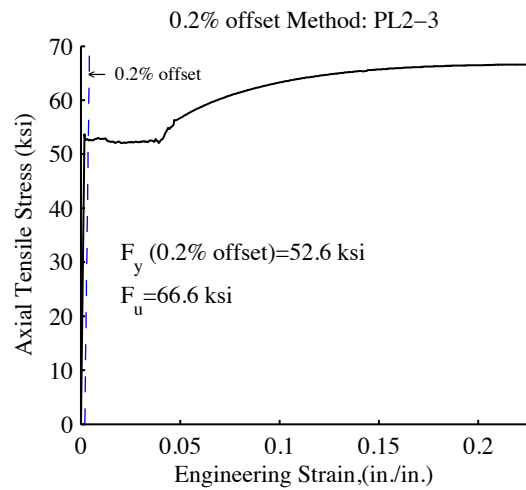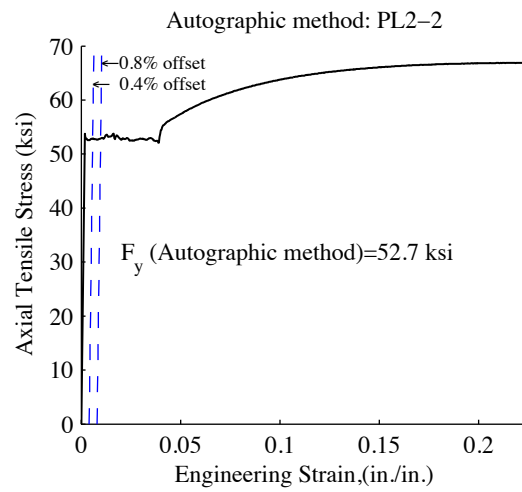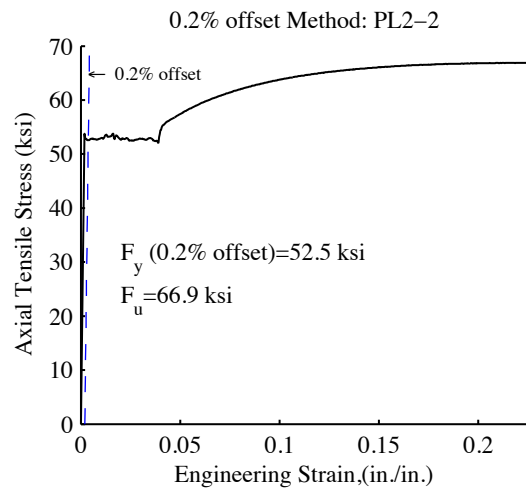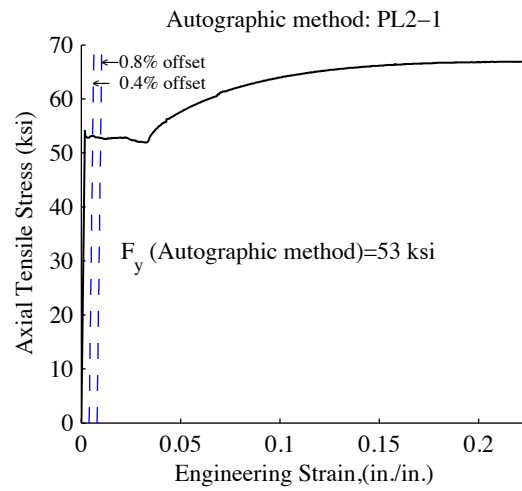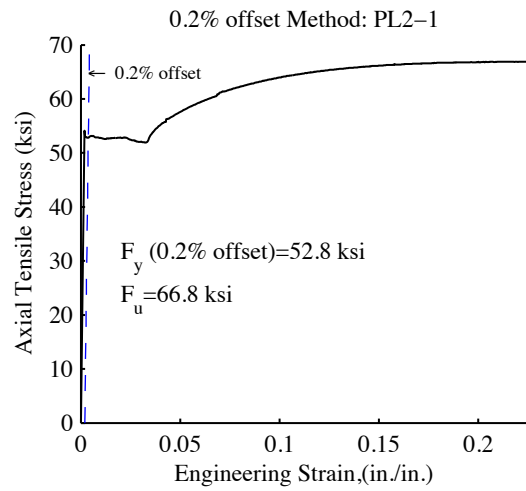
Figure C-4: Test results (PL2-1 to PL2-3)
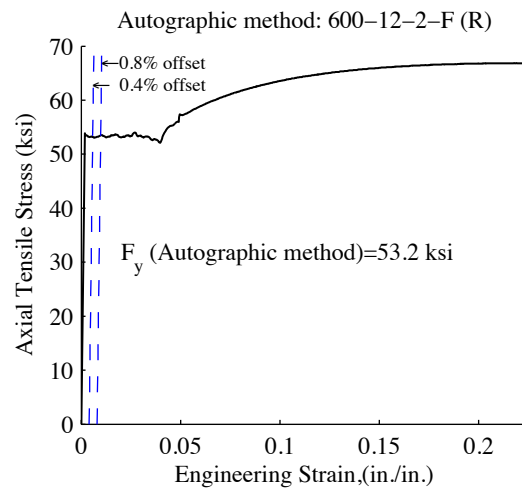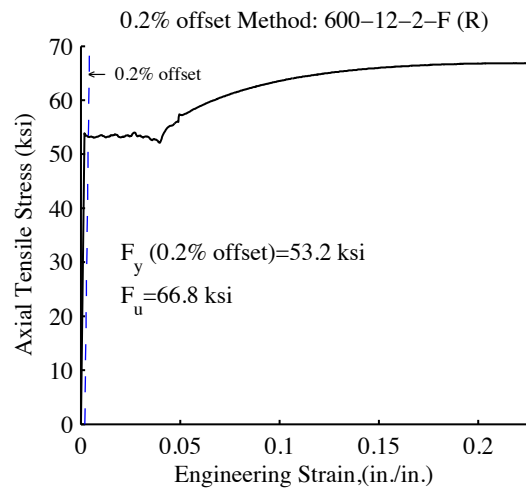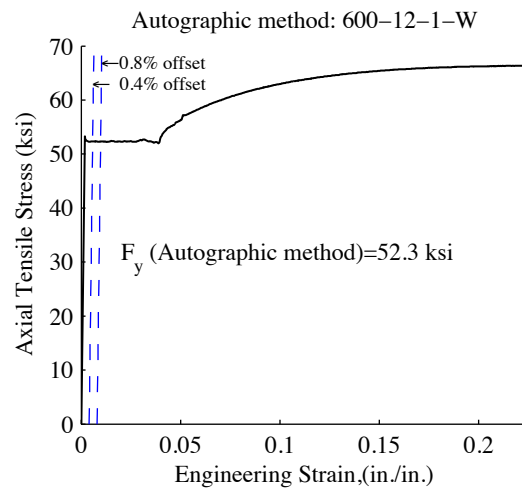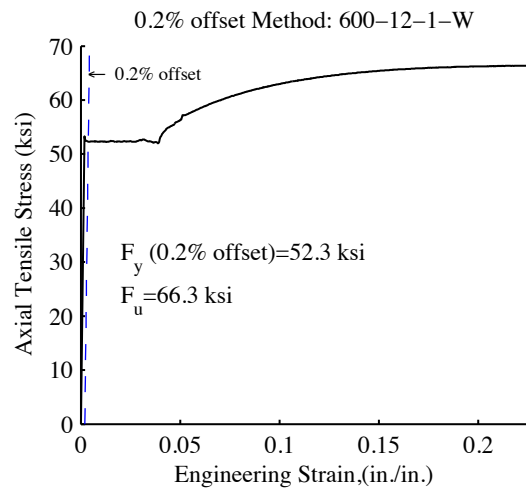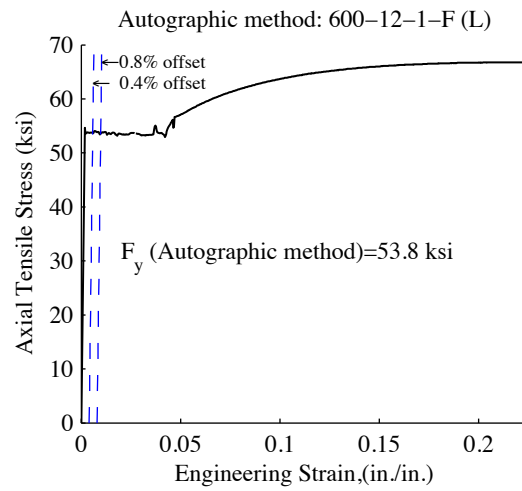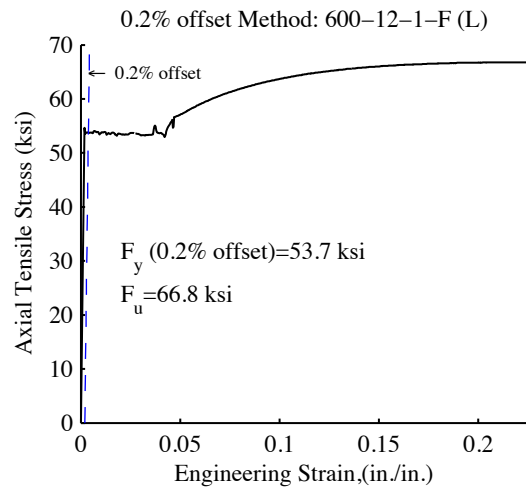
Figure C-5: Tension Test results (600-12 specimens)
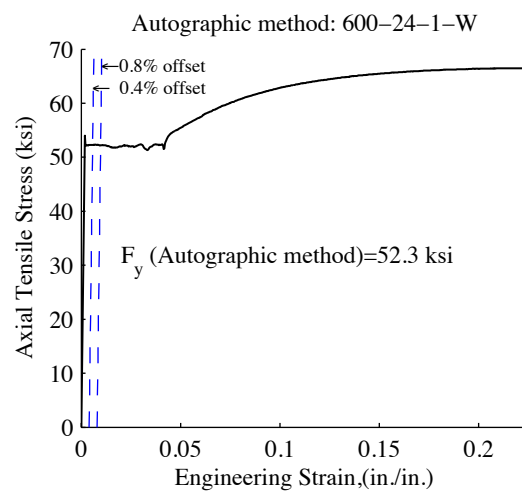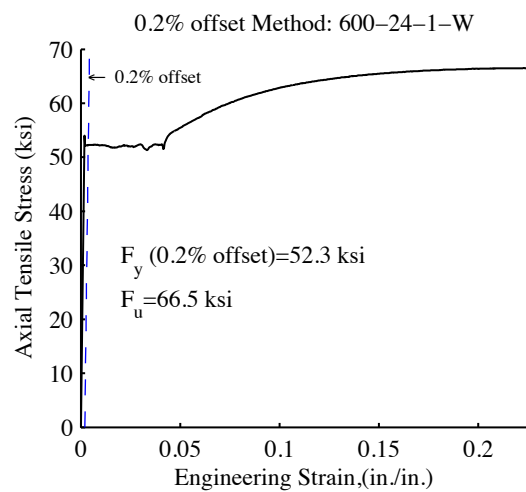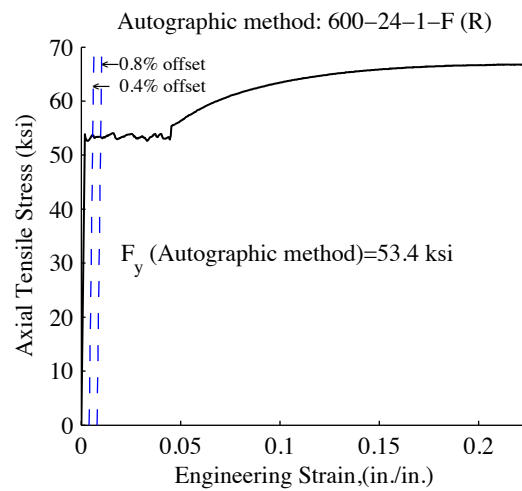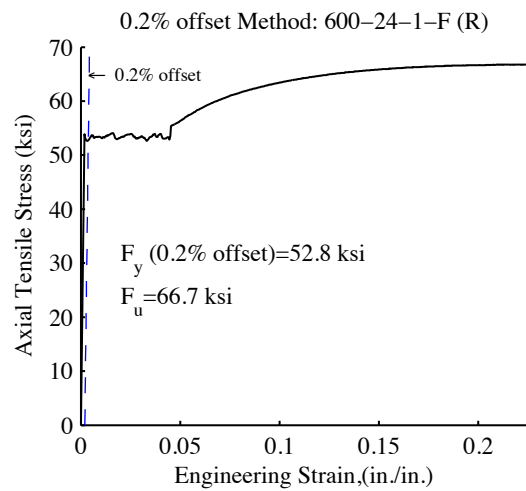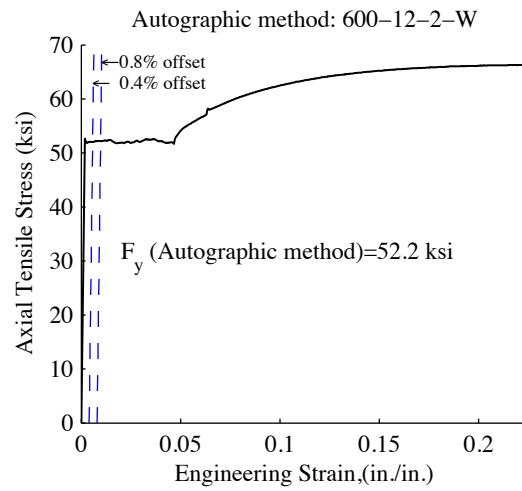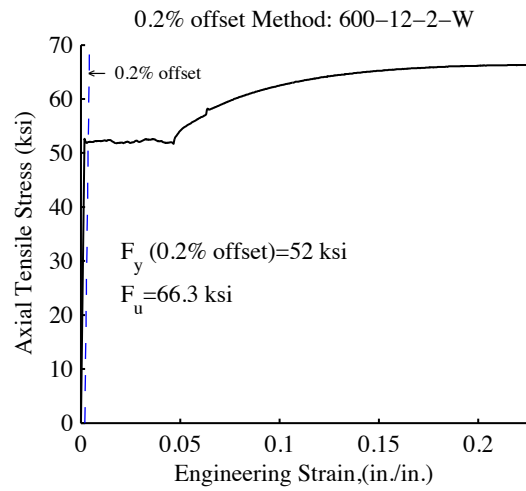
Figure C-6: Tension Test results (600-12 & 24 specimens)
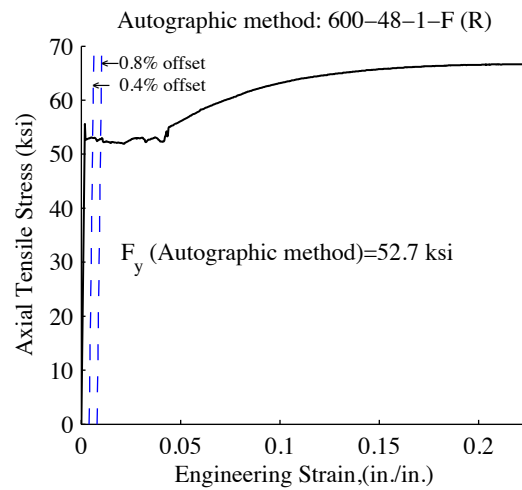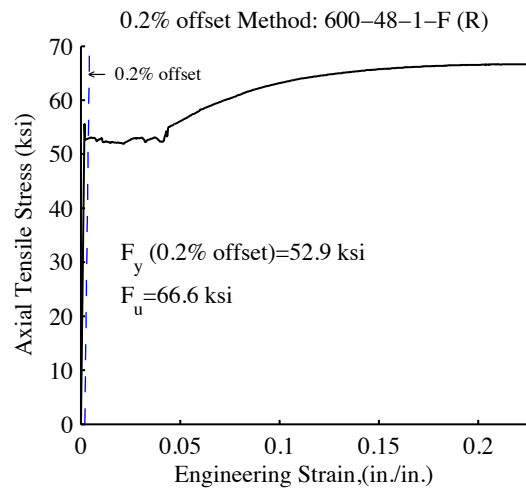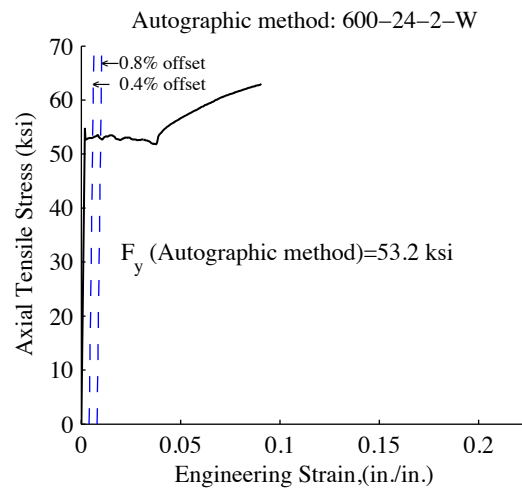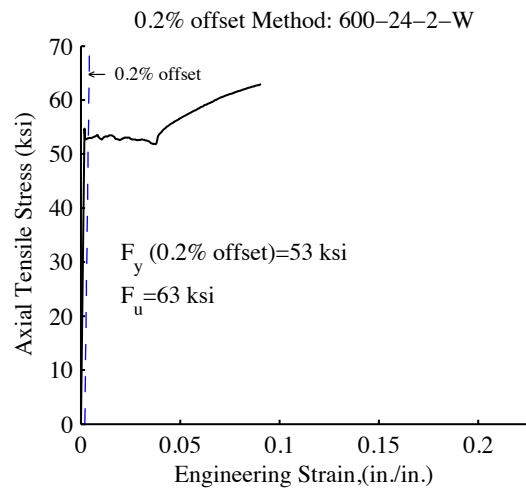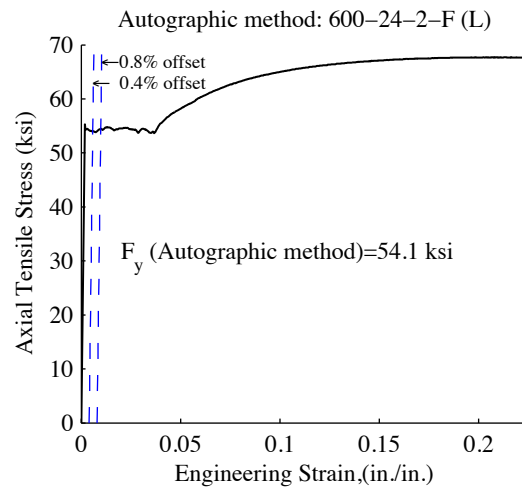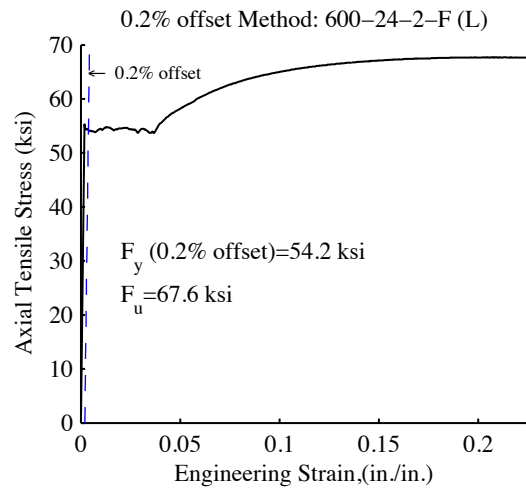
Figure C-7: Tension Test results (600-24 & 48 specimens)
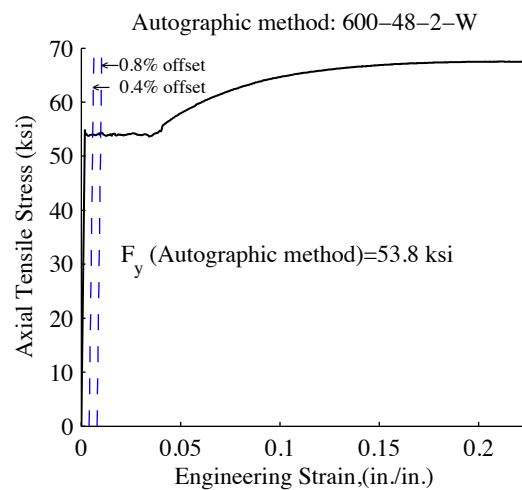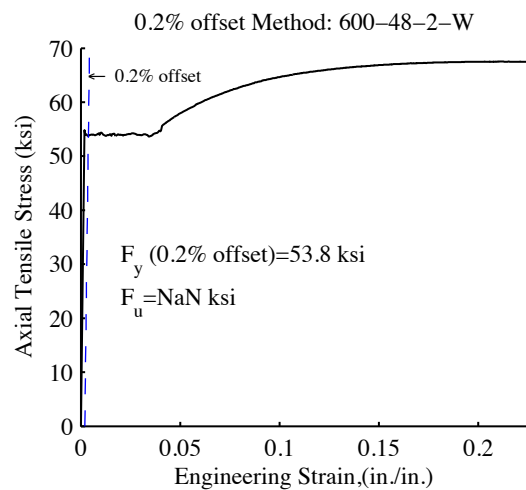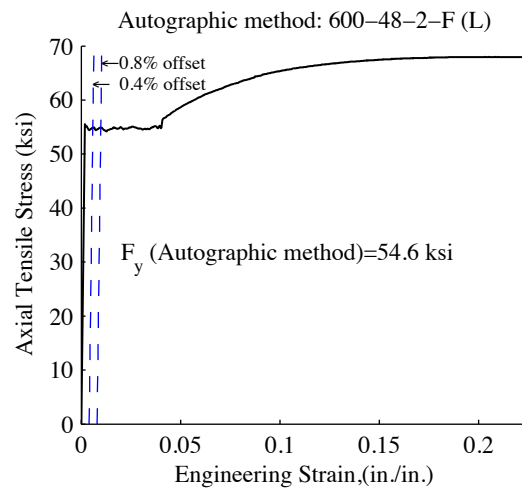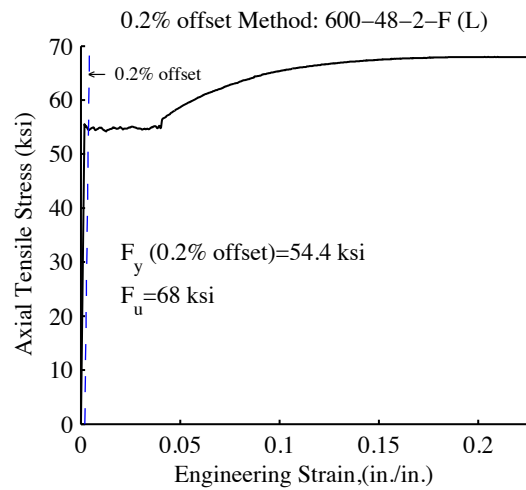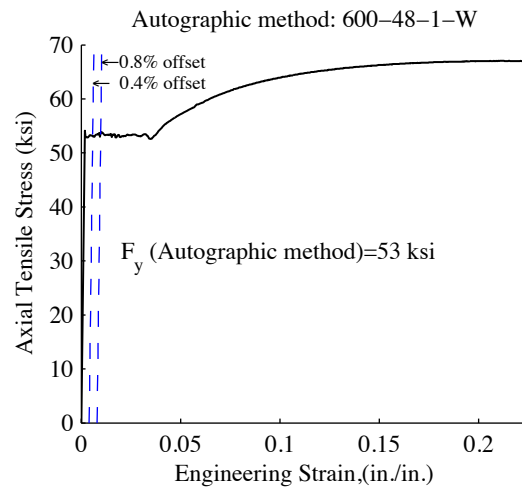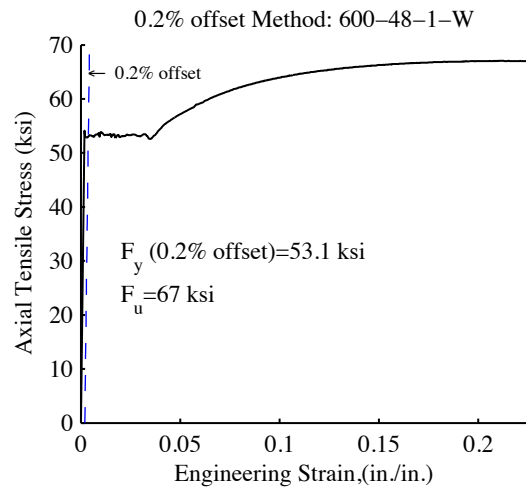
Figure C-8: Tension Test results (600-48 specimens)

Appendix D - Dimension measurement results
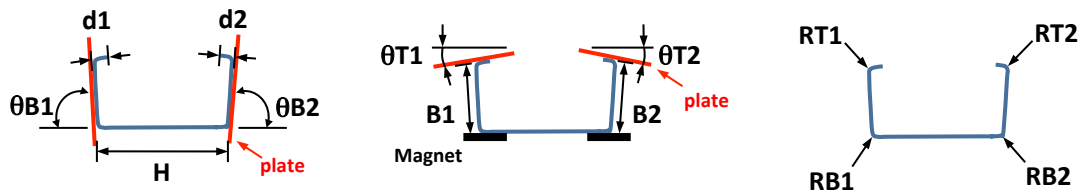
Figure D-1: Dimension Measurement parameters (Positive)
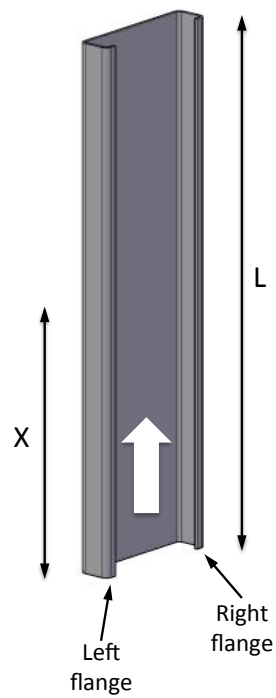
Figure D-2: Direction and length definitions

Positive (+)   Negative(-)

Figure D-3: Sign Convention

Table D-1: Dimension Measurements: 600S137-54 (L=12 inches)- Raw data

Specimen	X	H	B1	B2	D1	D2	RT1	RT2	RB1	RB2	θT1	θT2	θB1	θB2
	in	in.	in.	in.	in.	in.	in.	in.	in.	in.	deg.	deg.	deg.	deg.
	3	6.013	1.396	1.355	0.370	0.417	0.156	0.203	0.141	0.141	1.14	3.55	89.40	86.10
S600-12-1	6	6.015	1.395	1.362	0.368	0.409	0.156	0.203	0.141	0.141	1.62	3.03	89.40	85.70
	9	6.003	1.381	1.361	0.428	0.380	0.156	0.203	0.141	0.141	0.95	0.54	87.90	86.40
	3	6.002	1.441	1.316	0.386	0.396	0.156	0.203	0.141	0.125	-4.46	3.91	88.10	89.80
S600-12-2	6	6.002	1.414	1.316	0.390	0.390	0.156	0.203	0.141	0.125	2.57	5.44	-88.60	-89.90
	9	5.989	1.437	1.353	0.396	0.395	0.156	0.203	0.141	0.125	-1.07	8.40	88.30	89.00
	3	6.012	1.421	1.330	0.366	0.405	0.156	0.203	0.156	0.141	0.22	6.48	89.40	87.20
S600-12-3	6	5.994	1.403	1.340	0.387	0.409	0.156	0.203	0.156	0.141	1.82	2.12	-89.90	86.60
	9	5.991	1.382	1.371	0.379	0.418	0.156	0.203	0.156	0.141	1.90	3.15	88.00	86.40
	3	6.007	1.410	1.307	0.361	0.406	0.156	0.203	0.141	0.141	1.13	10.20	89.80	89.70
S600-12-4	6	5.996	1.420	1.310	0.364	0.408	0.156	0.203	0.141	0.141	-0.79	9.01	89.30	89.00
	9	5.996	1.407	1.326	0.360	0.408	0.156	0.203	0.141	0.141	2.13	8.86	88.80	88.30
	3	6.007	1.430	1.302	0.365	0.402	0.156	0.188	0.141	0.141	-0.03	8.61	89.30	89.50
S600-12-5	6	6.009	1.425	1.306	0.364	0.402	0.156	0.188	0.141	0.141	3.38	7.67	89.30	89.60
	9	6.023	1.425	1.319	0.361	0.401	0.156	0.188	0.141	0.141	1.93	7.73	89.20	88.50
	3	5.991	1.320	1.320	0.372	0.363	0.156	0.203	0.141	0.141	-0.48	8.64	88.60	87.50
S600-12-6	6	6.017	1.391	1.354	0.372	0.400	0.156	0.203	0.141	0.141	-0.97	7.80	88.90	87.00
	9	6.024	1.412	1.346	0.371	0.414	0.156	0.203	0.141	0.141	-3.36	6.66	89.80	86.70
	3	5.985	1.440	1.301	0.379	0.396	0.156	0.188	0.141	0.125	-2.39	5.04	89.10	89.80
S600-12-7	6	5.981	1.421	1.310	0.378	0.396	0.156	0.188	0.141	0.125	-1.05	6.49	-89.40	-89.90
	9	5.994	1.449	1.324	0.378	0.398	0.156	0.188	0.141	0.125	-2.43	7.87	89.50	89.20
	3	5.998	1.401	1.358	0.371	0.401	0.141	0.203	0.125	0.141	0.73	1.56	89.60	-87.40
S600-12-8	6	5.990	1.417	1.360	0.382	0.402	0.141	0.203	0.125	0.141	2.56	1.20	-89.30	-86.80
	9	5.987	1.399	1.364	0.389	0.414	0.141	0.203	0.125	0.141	-0.09	-0.45	87.30	-86.90
	3	5.995	1.416	1.325	0.375	0.401	0.156	0.219	0.141	0.141	0.95	5.70	89.60	-87.10
S600-12-9	6	5.989	1.398	1.344	0.377	0.407	0.156	0.219	0.141	0.141	-0.37	4.01	-88.90	-86.60
	9	5.986	1.386	1.344	0.385	0.418	0.156	0.219	0.141	0.141	1.08	3.14	87.10	-87.00
	3	6.009	1.407	1.343	0.366	0.412	0.156	0.188	0.125	0.141	0.96	2.38	-89.10	-87.20
S600-12-10	6	6.021	1.401	1.345	0.356	0.399	0.156	0.188	0.125	0.141	-0.13	1.55	-89.10	-86.70
	9	6.005	1.404	1.340	0.375	0.413	0.156	0.188	0.125	0.141	0.59	4.27	88.40	-86.90
	3	6.002	1.424	1.318	0.381	0.399	0.156	0.172	0.156	0.125	0.50	4.70	-88.00	89.80
S600-12-11	6	6.001	1.430	1.331	0.381	0.380	0.156	0.172	0.156	0.125	1.27	4.96	-88.50	89.60
	9	5.994	1.429	1.325	0.383	0.396	0.156	0.172	0.156	0.125	1.17	7.04	90.00	88.80
	3	5.992	1.406	1.351	0.366	0.399	0.156	0.188	0.156	0.156	1.34	3.10	-89.60	-86.40
S600-12-12	6	6.004	1.393	1.363	0.373	0.401	0.156	0.188	0.156	0.156	-1.80	0.42	-90.00	-86.30
	9	5.992	1.394	1.364	0.392	0.409	0.156	0.188	0.156	0.156	0.87	1.20	88.40	-86.30
	3	5.998	1.440	1.303	0.380	0.405	0.156	0.172	0.141	0.125	-1.74	1.32	-88.40	90.00
S600-12-13	6	6.001	1.452	1.305	0.380	0.396	0.156	0.172	0.141	0.125	-1.03	6.45	-88.70	-89.50
	9	6.002	1.432	1.327	0.383	0.398	0.156	0.172	0.141	0.125	1.03	3.74	90.00	89.10
	3	5.993	1.447	1.297	0.392	0.399	0.156	0.188	0.156	0.141	-1.41	6.10	-88.30	-89.30
S600-12-14	6	5.999	1.440	1.308	0.384	0.388	0.156	0.188	0.156	0.141	-0.13	6.69	-88.40	-89.90
	9	5.993	1.437	1.317	0.390	0.399	0.156	0.188	0.156	0.141	0.71	6.87	-89.50	89.50
	3	6.003	1.411	1.322	0.364	0.404	0.156	0.203	0.156	0.141	2.31	4.19	-89.30	89.20
S600-12-15	6	6.006	1.417	1.314	0.355	0.406	0.156	0.203	0.156	0.141	2.26	1.00	89.70	88.80
	9	6.002	1.423	1.337	0.351	0.410	0.156	0.203	0.156	0.141	1.94	3.79	89.00	87.70
	3	5.993	1.437	1.311	0.390	0.401	0.156	0.188	0.141	0.125	-2.90	6.64	-88.90	-89.50
S600-12-16	6	5.995	1.443	1.303	0.386	0.393	0.156	0.188	0.141	0.125	-1.27	7.00	-89.40	-89.80
	9	5.993	1.436	1.333	0.379	0.395	0.156	0.188	0.141	0.125	0.16	8.64	90.00	89.40
	3	6.010	1.428	1.307	0.372	0.399	0.156	0.188	0.156	0.141	-1.49	6.51	-89.80	90.00
S600-12-17	6	6.014	1.408	1.312	0.365	0.394	0.156	0.188	0.156	0.141	1.39	6.83	89.20	89.30
	9	6.016	1.422	1.319	0.374	0.402	0.156	0.188	0.156	0.141	1.39	6.19	88.50	88.00
	3	5.993	1.409	1.358	0.363	0.400	0.156	0.203	0.141	0.156	-0.23	4.89	-89.60	-173.00
S600-12-18	6	5.989	1.386	1.380	0.359	0.405	0.156	0.203	0.141	0.156	1.37	0.29	89.80	-86.60
	9	5.984	1.386	1.402	0.368	0.418	0.156	0.203	0.141	0.156	1.38	-3.45	88.00	-86.20
	3	6.018	0.424	1.349	0.362	0.400	0.156	0.203	0.156	0.141	-0.98	4.06	-89.20	-86.20
S600-12-19	6	6.006	1.413	1.392	0.370	0.404	0.156	0.203	0.156	0.141	-0.36	2.82	89.50	-86.20
	9	5.997	1.412	1.339	0.381	0.416	0.156	0.203	0.156	0.141	0.03	2.04	88.00	-86.30
	3	6.025	1.425	1.306	0.378	0.395	0.156	0.188	0.156	0.141	-0.04	9.51	-89.80	-89.70
S600-12-20	6	6.019	1.427	1.304	0.363	0.393	0.156	0.188	0.156	0.141	0.45	8.54	-89.30	89.20
	9	6.008	1.426	1.303	0.377	0.398	0.156	0.188	0.156	0.141	2.34	9.23	87.90	88.40

255

Table D-2: Dimension Measurements: 600S137-54 (L=24 inches)- Raw data

Specimen	X	H	B1	B2	D1	D2	RT1	RT2	RB1	RB2	θT1	θT2	θB1	θB2
	in	in.	in.	in.	in.	in.	in.	in.	in.	in.	deg.	deg.	deg.	deg.
S600-24-1	6	5.998	1.429	1.309	0.351	0.407	0.156	0.203	0.125	0.141	-0.34	2.88	89.90	90.00
	12	6.005	1.425	1.327	0.358	0.404	0.156	0.203	0.125	0.141	-0.86	2.64	89.50	-88.70
	18	5.999	1.417	1.355	0.362	0.401	0.156	0.203	0.125	0.141	-2.73	4.98	89.60	-87.20
S600-24-2	6	6.005	1.426	1.335	0.363	0.403	0.156	0.203	0.141	0.141	-1.26	5.11	90.00	-89.80
	12	6.007	1.423	1.315	0.357	0.399	0.156	0.203	0.141	0.141	-1.03	6.49	89.80	-88.80
	18	6.005	1.420	1.368	0.376	0.406	0.156	0.203	0.141	0.141	-1.69	3.09	88.90	-86.80
S600-24-3	6	6.025	1.428	1.317	0.371	0.388	0.156	0.203	0.141	0.156	-0.03	4.20	89.90	-89.30
	12	6.013	1.420	1.340	0.362	0.391	0.156	0.203	0.141	0.156	-1.26	4.25	89.80	-88.70
	18	6.003	1.411	1.366	0.365	0.396	0.156	0.203	0.141	0.156	-1.17	3.45	89.30	-86.70
S600-24-4	6	5.990	1.446	1.314	0.380	0.389	0.156	0.203	0.141	0.125	-2.31	5.07	-88.60	-89.50
	12	5.985	1.434	1.318	0.374	0.396	0.156	0.203	0.141	0.125	-0.79	3.92	90.00	89.80
	18	6.004	1.425	1.318	0.361	0.404	0.156	0.203	0.141	0.125	0.18	7.39	88.40	88.60
S600-24-5	6	5.984	1.441	1.319	0.377	0.392	0.156	0.203	0.125	0.125	-0.50	0.02	-88.90	-89.80
	12	5.996	1.425	1.329	0.365	0.391	0.156	0.203	0.125	0.125	-0.04	1.18	-89.40	90.00
	18	6.007	1.410	1.359	0.359	0.401	0.156	0.203	0.125	0.125	2.19	1.78	88.40	-88.50
S600-24-6	6	5.999	1.441	1.305	0.381	0.385	0.156	0.203	0.141	0.141	0.02	3.99	-88.70	-89.30
	12	5.993	1.428	1.323	0.373	0.388	0.156	0.203	0.141	0.141	-0.56	4.91	-89.10	89.90
	18	6.012	1.423	1.352	0.361	0.393	0.156	0.203	0.141	0.141	1.46	4.79	89.80	88.90
S600-24-7	6	5.999	1.436	1.325	0.367	0.397	0.156	0.203	0.125	0.125	-2.92	3.00	-88.00	-89.80
	12	5.992	1.416	1.330	0.364	0.398	0.156	0.203	0.125	0.125	-0.48	3.61	-89.30	90.00
	18	6.004	1.419	1.348	0.358	0.401	0.156	0.203	0.125	0.125	2.49	4.15	89.10	89.20
S600-24-8	6	5.994	1.430	1.323	0.382	0.384	0.156	0.203	0.125	0.141	0.28	3.19	-89.00	-89.40
	12	5.997	1.422	1.332	0.369	0.390	0.156	0.203	0.125	0.141	0.57	2.51	-89.50	-89.40
	18	6.009	1.420	1.336	0.358	0.394	0.156	0.203	0.125	0.141	2.40	4.18	88.50	89.10
S600-24-9	6	6.010	1.429	1.342	0.358	0.396	0.156	0.203	0.141	0.141	-0.84	5.90	-89.80	-89.30
	12	6.009	1.436	1.321	0.360	0.398	0.156	0.203	0.141	0.141	-0.90	4.97	89.50	-88.50
	18	6.002	1.424	1.372	0.361	0.405	0.156	0.203	0.141	0.141	-1.25	2.96	89.40	-87.10
S600-24-10	6	6.009	1.434	1.317	0.357	0.405	0.156	0.203	0.141	0.141	0.72	4.70	-89.90	90.00
	12	6.005	1.418	1.335	0.358	0.401	0.156	0.203	0.141	0.141	0.42	2.81	89.70	-89.00
	18	5.990	1.430	1.363	0.362	0.407	0.156	0.203	0.141	0.141	1.41	2.93	88.90	-87.00
S600-24-11	6	5.990	1.438	1.356	0.373	0.396	0.156	0.203	0.141	0.141	-2.24	5.97	-88.80	-89.80
	12	5.996	1.433	1.328	0.369	0.417	0.156	0.203	0.141	0.141	-1.86	5.81	89.90	-90.00
	18	6.013	1.420	1.327	0.363	0.397	0.156	0.203	0.141	0.141	0.12	5.48	88.50	89.00
S600-24-12	6	6.011	1.414	1.311	0.362	0.404	0.156	0.203	0.141	0.141	0.24	6.50	89.70	-89.80
	12	6.016	1.443	1.327	0.354	0.400	0.156	0.203	0.141	0.141	-0.97	5.43	89.80	-88.70
	18	6.010	1.411	1.356	0.362	0.407	0.156	0.203	0.141	0.141	-1.58	4.93	89.30	-87.30
S600-24-13	6	6.014	1.406	1.318	0.351	0.408	0.156	0.203	0.125	0.141	2.30	4.82	89.60	89.90
	12	6.018	1.430	1.322	0.354	0.402	0.156	0.203	0.125	0.141	0.59	6.02	89.90	-89.10
	18	6.001	1.389	1.359	0.357	0.408	0.156	0.203	0.125	0.141	2.68	1.65	89.20	-87.40
S600-24-14	6	6.011	1.400	1.367	0.357	0.415	0.156	0.203	0.125	0.141	0.20	5.18	89.60	-87.20
	12	6.003	1.419	1.342	0.350	0.410	0.156	0.203	0.125	0.141	-1.84	5.02	-89.50	-89.90
	18	5.995	1.411	1.304	0.355	0.408	0.156	0.203	0.125	0.141	-0.99	1.79	90.00	90.00
S600-24-15	6	5.987	1.452	1.303	0.381	0.386	0.156	0.203	0.125	0.125	-1.74	4.93	-89.30	-89.60
	12	5.986	1.430	1.302	0.372	0.388	0.156	0.203	0.125	0.125	-1.03	5.31	89.90	89.90
	18	6.007	1.424	1.325	0.367	0.391	0.156	0.203	0.125	0.125	0.36	6.36	88.30	89.00
S600-24-16	6	6.005	1.439	1.304	0.352	0.409	0.156	0.203	0.125	0.141	-0.82	7.75	89.60	89.60
	12	6.006	1.433	1.326	0.356	0.403	0.156	0.203	0.125	0.141	-0.56	5.81	89.50	-88.80
	18	5.995	1.423	1.319	0.371	0.404	0.156	0.203	0.125	0.141	-1.34	3.37	88.80	-87.10
S600-24-17	6	6.001	1.431	1.315	0.349	0.409	0.156	0.203	0.125	0.141	-1.43	6.15	89.90	89.90
	12	6.002	1.422	1.321	0.349	0.400	0.156	0.203	0.125	0.141	-1.02	6.71	89.90	-88.90
	18	6.003	1.419	1.355	0.365	0.400	0.156	0.203	0.125	0.141	-2.12	3.99	89.40	-87.10
S600-24-18	6	6.001	1.447	1.306	0.368	0.401	0.156	0.203	0.141	0.141	-1.93	3.88	-89.40	-89.80
	12	5.992	1.452	1.315	0.364	0.394	0.156	0.203	0.141	0.141	-1.66	3.94	-89.20	-89.70
	18	6.008	1.433	1.319	0.366	0.388	0.156	0.203	0.141	0.141	0.07	6.07	88.80	88.80
S600-24-19	6	5.992	1.446	1.311	0.371	0.392	0.156	0.203	0.141	0.125	-1.24	3.40	-88.70	-89.80
	12	5.991	1.433	1.316	0.368	0.393	0.156	0.203	0.141	0.125	0.03	5.19	90.00	89.70
	18	6.011	1.417	1.324	0.359	0.394	0.156	0.203	0.141	0.125	1.10	6.08	88.80	88.70
S600-24-20	6	6.005	1.430	1.323	0.361	0.398	0.156	0.203	0.125	0.141	-0.77	7.15	89.20	89.90
	12	6.004	1.430	1.340	0.362	0.392	0.156	0.203	0.125	0.141	-0.40	5.13	89.70	-88.40
	18	5.998	1.431	1.358	0.369	0.405	0.156	0.203	0.125	0.141	-0.86	2.09	88.70	-86.50

Specimen	X	H	B1	B2	D1	D2	RT1	RT2	RB1	RB2	θT1	θT2	θB1	θB2
	in	in.	in.	in.	in.	in.	in.	in.	in.	in.	deg.	deg.	deg.	deg.
	6	6.006	1.450	1.339	0.375	0.393	0.156	0.188	0.141	0.156	-1.34	3.04	-88.80	89.90
	15	6.005	1.446	1.339	0.362	0.374	0.156	0.188	0.141	0.156	1.00	6.96	89.30	89.30
S600-48-1	24	6.011	1.407	1.370	0.363	0.407	0.156	0.188	0.141	0.156	-0.21	5.99	89.10	88.80
	33	6.012	1.417	1.309	0.356	0.411	0.156	0.188	0.141	0.156	-0.20	5.54	89.40	89.20
	42	6.003	1.429	1.349	0.368	0.411	0.156	0.188	0.141	0.156	1.20	0.73	86.40	-87.90
	6	6.007	1.444	1.344	0.372	0.395	0.156	0.203	0.141	0.156	-1.25	4.46	-88.50	-89.50
	15	6.018	1.424	1.338	0.369	0.403	0.156	0.203	0.141	0.156	-1.82	4.69	89.30	90.00
S600-48-2	24	6.008	1.415	1.335	0.358	0.402	0.156	0.203	0.141	0.156	1.68	7.36	89.40	89.10
	33	6.006	1.441	1.320	0.355	0.407	0.156	0.203	0.141	0.156	1.43	6.97	89.70	89.40
	42	6.004	1.421	1.345	0.373	0.405	0.156	0.203	0.141	0.156	0.86	5.97	89.20	-87.40
	6	5.989	1.426	1.345	0.377	0.392	0.156	0.203	0.156	0.156	0.22	3.18	-89.10	90.00
	15	6.004	1.420	1.346	0.375	0.394	0.156	0.203	0.156	0.156	1.15	5.59	89.10	90.00
S600-48-3	24	6.008	1.432	1.321	0.367	0.397	0.156	0.203	0.156	0.156	0.28	3.50	88.80	89.40
	33	6.014	1.431	1.320	0.358	0.399	0.156	0.203	0.156	0.156	0.61	6.58	89.50	89.60
	42	5.999	1.403	1.364	0.365	0.402	0.156	0.203	0.156	0.156	-2.67	4.50	89.20	-87.40
	6	5.996	1.425	1.318	0.379	0.394	0.156	0.203	0.141	0.156	-1.96	4.98	-89.20	-89.60
	15	6.013	1.421	1.315	0.368	0.404	0.156	0.203	0.141	0.156	-1.63	8.17	89.60	89.50
S600-48-4	24	6.004	1.415	1.331	0.360	0.402	0.156	0.203	0.141	0.156	-1.58	10.00	89.40	89.10
	33	6.010	1.406	1.338	0.352	0.407	0.156	0.203	0.141	0.156	-3.18	7.60	89.40	89.60
	42	5.999	1.431	1.393	0.363	0.404	0.156	0.203	0.141	0.156	-2.50	2.23	89.70	-87.60
	6	5.999	1.446	1.315	0.368	0.400	0.156	0.203	0.141	0.156	-4.35	7.41	-89.10	-89.60
	15	6.003	1.429	1.332	0.366	0.397	0.156	0.203	0.141	0.156	0.42	5.94	89.80	89.60
S600-48-5	24	6.007	1.429	1.321	0.360	0.398	0.156	0.203	0.141	0.156	-0.74	5.11	89.10	89.30
	33	6.015	1.431	1.324	0.348	0.408	0.156	0.203	0.141	0.156	-1.26	0.65	89.60	89.50
	42	5.999	1.420	1.403	0.368	0.402	0.156	0.203	0.141	0.156	-2.85	2.81	89.10	-87.20
	6	5.990	1.441	1.335	0.364	0.403	0.156	0.188	0.156	0.141	-1.36	5.43	-88.90	90.00
	15	6.007	1.405	1.333	0.364	0.400	0.156	0.188	0.156	0.141	-1.05	6.71	89.40	89.40
S600-48-6	24	5.999	1.427	1.334	0.353	0.404	0.156	0.188	0.156	0.141	-2.32	4.13	89.00	89.00
	33	6.011	1.445	1.317	0.350	0.406	0.156	0.188	0.156	0.141	-1.46	4.94	90.00	89.30
	42	5.995	1.434	1.357	0.361	0.412	0.156	0.188	0.156	0.141	-3.02	5.44	89.30	-87.70
	6	6.003	1.438	1.311	0.383	0.393	0.156	0.203	0.141	0.172	-2.13	2.63	-88.90	90.00
	15	6.003	1.404	1.326	0.366	0.399	0.156	0.203	0.141	0.172	0.91	4.85	89.70	89.30
S600-48-7	24	6.010	1.426	1.311	0.356	0.408	0.156	0.203	0.141	0.172	0.99	6.56	89.10	89.30
	33	6.008	1.424	1.314	0.348	0.410	0.156	0.203	0.141	0.172	0.78	7.41	89.40	89.70
	42	6.014	1.399	1.359	0.364	0.407	0.156	0.203	0.141	0.172	0.10	5.75	89.10	-87.40
	6	5.999	1.432	1.313	0.371	0.397	0.156	0.203	0.141	0.156	-2.36	4.56	-88.90	-89.90
	15	6.030	1.409	1.312	0.365	0.399	0.156	0.203	0.141	0.156	0.58	4.49	90.00	89.50
S600-48-8	24	6.019	1.440	1.327	0.357	0.401	0.156	0.203	0.141	0.156	1.86	6.35	89.50	89.10
	33	6.006	1.404	1.325	0.349	0.404	0.156	0.203	0.141	0.156	-0.28	2.08	89.90	89.60
	42	5.993	1.398	1.368	0.351	0.414	0.156	0.203	0.141	0.156	-0.68	2.75	89.70	-87.70
	6	5.991	1.430	1.351	0.374	0.399	0.156	0.203	0.141	0.156	-1.52	5.16	-88.90	89.70
	15	6.006	1.403	1.318	0.377	0.395	0.156	0.203	0.141	0.156	1.25	7.75	89.40	89.60
S600-48-9	24	6.009	1.427	1.320	0.364	0.396	0.156	0.203	0.141	0.156	0.56	5.13	89.30	89.50
	33	6.016	1.412	1.330	0.359	0.402	0.156	0.203	0.141	0.156	1.94	3.48	90.00	89.80
	42	5.995	1.401	1.360	0.371	0.408	0.156	0.203	0.141	0.156	1.08	4.05	89.30	-87.60
	6	5.985	1.424	1.324	0.377	0.390	0.156	0.203	0.141	0.156	-1.97	3.89	-88.80	90.00
	15	6.002	1.412	1.314	0.365	0.399	0.156	0.203	0.141	0.156	0.53	1.53	89.40	89.70
S600-48-10	24	6.006	1.412	1.332	0.358	0.403	0.156	0.203	0.141	0.156	1.66	6.82	89.10	89.20
	33	6.015	1.414	1.323	0.351	0.403	0.156	0.203	0.141	0.156	0.42	6.93	89.80	89.80
	42	5.991	1.408	1.343	0.361	0.406	0.156	0.203	0.141	0.156	-0.64	5.92	89.20	-87.40
	6	5.996	1.427	1.323	0.377	0.392	0.156	0.203	0.141	0.141	-0.57	3.48	-88.90	-89.90
	15	5.998	1.419	1.332	0.370	0.398	0.156	0.203	0.141	0.141	-0.73	4.94	89.30	89.50
S600-48-11	24	6.010	1.407	1.313	0.359	0.403	0.156	0.203	0.141	0.141	-0.25	6.31	89.00	89.40
	33	5.999	1.426	1.321	0.351	0.409	0.156	0.203	0.141	0.141	0.23	5.89	89.50	89.50
	42	6.002	1.421	1.360	0.367	0.404	0.156	0.203	0.141	0.141	-2.82	1.37	89.40	-87.40
	6	5.996	1.447	1.307	0.376	0.393	0.141	0.203	0.141	0.141	-1.51	1.90	-88.70	-89.70
	15	6.010	1.417	1.336	0.367	0.397	0.141	0.203	0.141	0.141	-0.17	8.23	89.70	89.80
S600-48-12	24	6.008	1.406	1.323	0.356	0.400	0.141	0.203	0.141	0.141	0.34	2.07	89.00	89.30
	33	6.007	1.421	1.324	0.352	0.402	0.141	0.203	0.141	0.141	0.99	4.07	89.50	89.90
	42	6.000	1.406	1.359	0.363	0.406	0.141	0.203	0.141	0.141	-1.27	3.88	89.70	-87.40
	6	6.001	1.434	1.320	0.387	0.385	0.141	0.203	0.125	0.141	-2.14	3.98	-89.20	89.80
	15	6.000	1.429	1.308	0.374	0.397	0.141	0.203	0.125	0.141	0.36	7.20	89.50	89.30
S600-48-13	24	6.008	1.419	1.310	0.353	0.408	0.141	0.203	0.125	0.141	0.81	5.83	89.00	89.10
	33	6.008	1.432	1.325	0.356	0.411	0.141	0.203	0.125	0.141	1.77	4.76	89.30	89.30
	42	5.997	1.406	1.342	0.363	0.411	0.141	0.203	0.125	0.141	0.09	5.02	89.30	-87.70
	6	5.998	1.398	1.314	0.378	0.390	0.141	0.203	0.125	0.141	-2.19	5.31	-88.70	-89.50
	15	6.005	1.417	1.327	0.364	0.400	0.141	0.203	0.125	0.141	0.19	5.35	89.60	89.70
S600-48-14	24	6.012	1.406	1.339	0.351	0.408	0.141	0.203	0.125	0.141	1.12	5.48	89.20	89.10
	33	6.007	1.429	1.296	0.350	0.410	0.141	0.203	0.125	0.141	0.06	6.21	89.40	89.70
	42	5.993	1.443	1.320	0.364	0.407	0.141	0.203	0.125	0.141	-0.65	2.80	89.30	-87.40
	6	5.998	1.434	1.309	0.373	0.393	0.156	0.203	0.125	0.141	-2.76	6.31	-88.60	-89.80
	15	6.008	1.410	1.320	0.368	0.395	0.156	0.203	0.125	0.141	-1.00	6.28	89.50	89.30
S600-48-15	24	6.009	1.417	1.316	0.359	0.401	0.156	0.203	0.125	0.141	-0.64	6.66	89.10	89.10
	33	6.007	1.428	1.318	0.353	0.408	0.156	0.203	0.125	0.141	-1.46	5.97	89.50	89.50
	42	5.991	1.418	1.356	0.365	0.409	0.156	0.203	0.125	0.141	-1.91	2.06	89.10	-87.70
	6	6.002	1.442	1.306	0.379	0.392	0.156	0.203	0.125	0.141	-3.52	4.45	-88.90	90.00
	15	6.010	1.425	1.296	0.376	0.394	0.156	0.203	0.125	0.141	-1.49	7.26	89.70	89.80
S600-48-16	24	6.007	1.416	1.326	0.361	0.399	0.156	0.203	0.125	0.141	0.13	6.86	89.00	89.40
	33	6.007	1.429	1.325	0.354	0.407	0.156	0.203	0.125	0.141	0.68	6.51	89.30	89.40
	42	5.993	1.398	1.371	0.361	0.406	0.156	0.203	0.125	0.141	-1.34	2.98	89.40	-87.40
	6	5.997	1.425	1.318	0.382	0.391	0.156	0.203	0.125	0.141	-1.35	4.57	-89.20	89.50
	15	6.011	1.419	1.306	0.373	0.399	0.156	0.203	0.125	0.141	-0.29	4.13	89.20	89.80
S600-48-17	24	6.010	1.416	1.318	0.359	0.406	0.156	0.203	0.125	0.141	0.47	1.75	88.80	89.50
	33	6.002	1.447	1.409	0.355	0.407	0.156	0.203	0.125	0.141	-1.29	5.10	89.40	89.90
	42	5.994	1.418	1.355	0.363	0.409	0.156	0.203	0.125	0.141	-2.31	1.12	89.20	-87.20
	6	5.997	1.438	1.324	0.376	0.391	0.141	0.203	0.125	0.141	-3.24	5.55	-88.60	89.30
	15	6.010	1.420	1.317	0.366	0.398	0.141	0.203	0.125	0.141	-0.79	7.37	89.40	90.00
S600-48-18	24	6.003	1.420	1.342	0.354	0.405	0.141	0.203	0.125	0.141	0.26	6.15	89.10	89.60
	33	6.003	1.418	1.350	0.350	0.406	0.141	0.203	0.125	0.141	1.29	6.54	89.60	90.00
	42	5.988	1.400	1.383	0.354	0.408	0.141	0.203	0.125	0.141	-0.49	5.02	89.70	-87.10

Table D-4: Dimension Measurements: 600S137-54 (L=12 inches)- Centerline

Specimen	h	b1	b2	d1	d2	rT1	rT2	rB1	rB2	θT1	θT2	θB1	θB2	t (avg.)	L (avg.)
	in.	in.	in.	in.	in.	in.	in.	in.	in.	deg.	deg.	deg.	deg.	10⁻⁴ in.	in.
S600-12-1	5.733	1.098	1.019	0.211	0.206	0.128	0.175	0.113	0.113	1.62	3.03	89.4	85.7	559	11.75
S600-12-2	5.736	1.117	0.988	0.233	0.187	0.128	0.175	0.112	0.097	2.57	5.44	-88.6	-89.9	563	12.03
S600-12-3	5.697	1.090	0.997	0.230	0.206	0.128	0.175	0.128	0.112	1.82	2.12	-89.9	86.6	563	11.75
S600-12-4	5.714	1.123	0.967	0.207	0.205	0.128	0.175	0.113	0.113	-0.79	9.01	89.3	89.0	559	11.69
S600-12-5	5.727	1.128	0.978	0.207	0.215	0.128	0.159	0.113	0.113	3.38	7.67	89.3	89.6	561	11.70
S600-12-6	5.735	1.094	1.011	0.215	0.197	0.128	0.175	0.112	0.112	-0.97	7.80	88.9	87.0	563	11.75
S600-12-7	5.715	1.124	0.998	0.221	0.209	0.128	0.160	0.113	0.097	-1.05	6.49	-89.4	-89.9	560	12.04
S600-12-8	5.724	1.151	1.017	0.241	0.199	0.113	0.175	0.097	0.113	2.56	1.20	-89.3	-86.8	554	11.62
S600-12-9	5.707	1.101	0.985	0.220	0.189	0.129	0.191	0.113	0.113	-0.37	4.01	-88.9	-86.6	553	11.65
S600-12-10	5.755	1.119	1.017	0.199	0.212	0.129	0.160	0.097	0.113	-0.13	1.55	-89.1	-86.7	553	11.60
S600-12-11	5.719	1.117	1.035	0.224	0.209	0.128	0.144	0.128	0.097	1.27	4.96	-88.5	89.6	561	12.06
S600-12-12	5.691	1.080	1.020	0.216	0.214	0.128	0.159	0.128	0.128	-1.80	0.42	-90.0	-86.3	563	11.64
S600-12-13	5.735	1.155	1.009	0.223	0.225	0.128	0.144	0.113	0.097	-1.03	6.45	-88.7	-89.5	562	12.07
S600-12-14	5.702	1.127	0.980	0.227	0.201	0.128	0.159	0.128	0.113	-0.13	6.69	-88.4	-89.9	561	11.64
S600-12-15	5.709	1.104	0.971	0.198	0.203	0.128	0.175	0.128	0.112	2.26	1.00	89.7	88.8	563	11.75
S600-12-16	5.729	1.146	0.991	0.229	0.206	0.129	0.160	0.113	0.097	-1.27	7.00	-89.4	-89.8	553	11.68
S600-12-17	5.717	1.095	0.984	0.208	0.207	0.128	0.159	0.128	0.112	1.39	6.83	89.2	89.3	563	11.72
S600-12-18	5.692	1.089	1.021	0.202	0.202	0.128	0.175	0.113	0.128	1.37	0.29	89.8	-86.6	562	12.12
S600-12-19	5.709	1.100	1.049	0.213	0.201	0.128	0.175	0.128	0.112	-0.36	2.82	89.5	-86.2	564	12.06
S600-12-20	5.722	1.114	0.976	0.206	0.206	0.128	0.159	0.128	0.113	0.45	8.54	-89.3	89.2	561	11.60

Table D-5: Dimension Measurements: 600S137-54 (L=24 inches)- Centerline

Specimen	h	b1	b2	d1	d2	rT1	rT2	rB1	rB2	θT1	θT2	θB1	θB2	t (avg.)	L (avg.)
	in.	in.	in.	in.	in.	in.	in.	in.	in.	deg.	deg.	deg.	deg.	10⁻⁴ in.	in.
S600-24-1	5.739	1.143	0.984	0.201	0.201	0.128	0.175	0.097	0.113	-0.86	2.64	89.5	-88.7	561	24.16
S600-24-2	5.725	1.126	0.972	0.200	0.196	0.128	0.175	0.113	0.113	-1.03	6.49	89.8	-88.8	562	24.08
S600-24-3	5.716	1.123	0.981	0.205	0.188	0.128	0.175	0.113	0.128	-1.26	4.25	89.8	-88.7	562	23.72
S600-24-4	5.719	1.137	0.990	0.217	0.193	0.128	0.175	0.113	0.097	-0.79	3.92	90.0	89.8	562	23.65
S600-24-5	5.746	1.143	1.001	0.208	0.188	0.128	0.175	0.097	0.097	-0.04	1.18	-89.4	90.0	562	24.06
S600-24-6	5.711	1.131	0.980	0.216	0.185	0.114	0.161	0.099	0.099	-0.56	4.91	-89.1	89.9	839	24.16
S600-24-7	5.742	1.134	1.002	0.207	0.195	0.128	0.175	0.097	0.097	-0.48	3.61	-89.3	90.0	561	23.66
S600-24-8	5.731	1.140	0.989	0.212	0.187	0.128	0.175	0.097	0.113	0.57	2.51	-89.5	-89.4	561	24.09
S600-24-9	5.727	1.139	0.978	0.203	0.195	0.128	0.175	0.113	0.113	-0.90	4.97	89.5	-88.5	561	23.69
S600-24-10	5.723	1.121	0.992	0.201	0.198	0.128	0.175	0.113	0.113	0.42	2.81	89.7	-89.0	562	23.65
S600-24-11	5.714	1.136	0.985	0.212	0.214	0.128	0.175	0.112	0.112	-1.86	5.81	89.9	-90.0	564	24.21
S600-24-12	5.734	1.146	0.984	0.197	0.197	0.128	0.175	0.112	0.112	-0.97	5.43	89.8	-88.7	565	24.21
S600-24-13	5.752	1.148	0.979	0.197	0.199	0.128	0.175	0.097	0.113	0.59	6.02	89.9	-89.1	562	23.71
S600-24-14	5.737	1.137	0.999	0.193	0.207	0.128	0.175	0.097	0.113	-1.84	5.02	-89.5	-89.9	562	23.66
S600-24-15	5.736	1.148	0.974	0.215	0.185	0.128	0.175	0.097	0.097	-1.03	5.31	89.9	89.9	563	24.09
S600-24-16	5.740	1.151	0.983	0.199	0.200	0.128	0.175	0.097	0.113	-0.56	5.81	89.5	-88.8	563	23.71
S600-24-17	5.736	1.140	0.978	0.192	0.197	0.128	0.175	0.097	0.113	-1.02	6.71	89.9	-88.9	561	23.68
S600-24-18	5.710	1.155	0.972	0.207	0.191	0.128	0.175	0.112	0.112	-1.66	3.94	-89.2	-89.7	563	24.09
S600-24-19	5.725	1.136	0.988	0.211	0.190	0.128	0.175	0.113	0.097	0.03	5.19	90.0	89.7	561	24.14
S600-24-20	5.738	1.148	0.997	0.205	0.189	0.128	0.175	0.097	0.112	-0.40	5.13	89.7	-88.4	563	23.71

Table D-6: Dimension Measurements: 600S137-54 (L=48 inches)- Centerline

Specimen	h	b1	b2	d1	d2	rT1	rT2	rB1	rB2	θT1	θT2	θB1	θB2	t (avg.)	L (avg.)
	in.	in.	in.	in.	in.	in.	in.	in.	in.	deg.	deg.	deg.	deg.	10⁻⁴ in.	in.
S600-48-1	5.712	1.126	0.993	0.204	0.207	0.128	0.159	0.112	0.128	0.20	6.16	89.3	89.1	565	48.02
S600-48-2	5.713	1.129	0.969	0.204	0.198	0.128	0.175	0.113	0.128	0.43	6.34	89.5	89.5	563	48.05
S600-48-3	5.696	1.115	0.967	0.210	0.191	0.128	0.175	0.128	0.128	0.68	5.22	89.1	89.7	564	47.83
S600-48-4	5.712	1.117	0.966	0.203	0.199	0.128	0.175	0.112	0.128	-2.13	8.59	89.5	89.4	564	48.05
S600-48-5	5.711	1.132	0.964	0.201	0.195	0.128	0.175	0.112	0.128	-0.53	3.90	89.5	89.5	565	47.75
S600-48-6	5.708	1.113	0.997	0.199	0.213	0.128	0.159	0.128	0.113	-1.61	5.26	89.5	89.2	561	48.25
S600-48-7	5.694	1.121	0.939	0.200	0.200	0.128	0.175	0.113	0.144	0.89	6.27	89.4	89.4	561	47.78
S600-48-8	5.721	1.120	0.959	0.200	0.196	0.128	0.175	0.112	0.128	0.72	4.31	89.8	89.4	564	47.78
S600-48-9	5.713	1.117	0.961	0.210	0.192	0.128	0.175	0.113	0.128	1.25	5.45	89.6	89.6	563	48.05
S600-48-10	5.710	1.115	0.961	0.201	0.196	0.128	0.175	0.112	0.128	0.87	5.09	89.4	89.6	564	48.05
S600-48-11	5.721	1.120	0.976	0.203	0.198	0.128	0.175	0.113	0.113	-0.25	5.71	89.3	89.5	561	48.04
S600-48-12	5.727	1.133	0.981	0.217	0.194	0.113	0.175	0.113	0.113	0.39	4.79	89.4	89.7	561	47.78
S600-48-13	5.739	1.161	0.968	0.220	0.200	0.112	0.175	0.097	0.112	0.98	5.93	89.3	89.2	563	48.00
S600-48-14	5.742	1.151	0.974	0.214	0.200	0.112	0.175	0.097	0.112	0.46	5.68	89.4	89.5	564	47.74
S600-48-15	5.742	1.137	0.972	0.203	0.196	0.128	0.175	0.097	0.112	-1.03	6.30	89.4	89.3	563	48.05
S600-48-16	5.742	1.142	0.969	0.207	0.194	0.128	0.175	0.097	0.112	-0.23	6.88	89.3	89.5	564	47.78
S600-48-17	5.742	1.146	0.998	0.206	0.198	0.128	0.175	0.097	0.112	-0.37	3.66	89.1	89.7	563	48.05
S600-48-18	5.739	1.153	0.990	0.216	0.197	0.113	0.175	0.097	0.113	0.25	6.69	89.4	89.9	561	47.75

258

Appendix E - Procedure for Stripping zinc coating

(Consulted with Dr. Daniel R. Kuespert, Homewood Laboratory Safety Advocate)

E.1 Choosing acid

One of the most common chemicals suitable for stripping galvanized coating off the cold-formed steel products is Hydrochloride acid (HCl). Hydrochloric acid when combined with a base (neutralization reaction) will react violently and produce water, salt and heat (heat of neutralization). Hydrochloric acid in contact with common metals reacts to produce flammable and potentially explosive hydrogen gas. A third type of reaction involves the dilution of Hydrochloric acid with water. A large amount of heat is released when strong acids are mixed with water. By adding water to acid, extremely concentrated solution of acid initially formed. So much heat is released that the solution may boil very violently, splashing concentrated acid out of the container. However, by adding acid to the solution that forms is very dilute and the small amount of heat released is not enough to vaporize and spatter it. So Always Add Acid to water, and never the reverse.

More information:

http://www.northstarchemical.com

http://www.stickmanscience.com/chem/

E.1.1 Acid concentration

Working with highly concentrated or strong hydrochloric acid needs to have experience and preparing certain conditions. Typically, there is no need to use strong acid for removing the zinc coating. The minimum concentrate examined before was 36.5mg/1mL HCl which is also named "1N" or "1M" or 1Molar HCl.

It would be better to buy diluted 1N HCl rather than concentrated form. If diluted form is not available, the concentrated form should be diluted to get the reduced concentration. The common concentrated form of HCL is 36.5~37% HCL which is 12 Molar or 12N HCl.

The amount of concentered HCl should be minimized regarding using and handling problems—less material is less risk. If the quantities are larger than 125 mL (e.g. 250mL batches, etc.), and this is the first time of handling strong acids, It is suggested to do everything under the supervision from someone in a chemistry lab who is experienced with the materials.

There is an easy formulation for determining the required amount of 12N HCl which is needed to get certain amount of 1N acid through dilution:

Molarity Initial x Volume Initial = Molarity Final x Volume Final

For example:

12N HCl x 10 mL = 1N x 120 mL

So, 10 mL of concentrated 12N HCl could be added to 110 mL distilled water to make 120 mL 1N HCl. (Again remember, Always **Add Acid to water**, and never the reverse!).

Providing acid

In the Homewood campus of the Johns Hopkins University, acid could be provided through the Mudd Hall Supply Store located in the basement of Mudd. The budget number of the project is needed for purchasing. The catalog could be found in the following link:

http://rocfy.com/order/JHU%20Supply%20Store%20Catalog.htm

It should be noted that the diluted 1N HCl is often available and it would also be possible to place order for that.

E.1.2 Acid handling and storage

Generally acid container should be handled in safe container designed for handling hazardous materials. This kind of containers could be provided in Mudd Hall Supply Store or it could be found in the chemistry labs. Probably, some labs in Mechanical Engineering (ME) also have this kind of containers.

After purchasing the acid, the acid bottle should be kept in a safe place. The best place is a safe box designed for storing acid and other hazardous or high corrosive materials.

Required safety dressing and equipment

The required dressing while diluting acid or stripping the zinc

Work with corrosives like HCl **absolutely requires** an eyewash/safety shower unit within about 10 seconds travel. That's the amount of time you've typically got after a splash to prevent deep burns and permanent damage.

E.1.3 Required safety equipment

Minimum personal protective equipment would be a lab coat, clothing that fully covers the extremities, closed-toe shoes (preferably not canvas or woven), appropriate gloves, chemical splash goggles, and a face shield. An acid apron is recommended as well if 1 gal bottles are used (try to order 250mL-1L instead).

The gloves should be washed before removing and to check them over for pinholes before using each time.

E.2 Striping procedure

Given the previous sections, the striping procedure itself includes the following steps:

1. Cleaning the surface

2. Place the specimen in the acid bath very carefully to avoid splashes

3. Recording the time

4. Flipping the part to make sure about uniform acid contact

5. Looking at the hydrogen bubbles

6. Putting the specimens in the water tank

7. Taking out the specimens in the towel

8. Washing the specimens with a large plenty of water

9. Trying the specimens

10. Redo the process if necessary

11. Return the waste acid to the bottle

12. Washing all the containers and tools with water

E.3 Waste acid

The most important points about the waste acid are first storage of the waste acid and second the place to dump waste acid. Most probably, hydrogen is still produced even after removing the specimens. According, the bottle cap should not keep tight. As an alternative a specials cap including a small hole should be used to prevent accumulation of hydrogen in the bottle.

Once a week and at a certain time, all waste chemicals and hazardous materials (HAZMAT) are placed in one special place to be taken out to a safe place.

Appendix F - Beam-Column experiment results

All the test results including raw load-displacement from the MTS load cell and internal position transducer and other processed data provided by 15 other position transducers are presented herein for all tested specimens. Furthermore, dimension measurements made for placing the specimens inside the rig are reposted to show the testing procedure.

To document each test event, test results are presentment individually for each single test specimen. All data analyses and comparisons are made in the main report.

The results are presented in the same format for all tested specimens, but as some improvements were made to the test procedure throughout the experimental program, minor changes to the data presentation format are expected. However, all the test results provide the same data with the same precision.

F.1 Experiment results: Short Specimens (S600-12)

1- S600-12-e$_x$(0)-e$_z$(-1.0)

Tested Specimen:	S600-12-1
Cross-section:	600S137-54 (SSMA Designation)
Date:	May 20th 2013

Left (L)   z   Right (R)

x

(Bottom to Top View)

Measured cross-section:

(Centroid position for the middle of the tested specimen)

0.3031

2.9916   3.0218

Test Description:	- Lipped C-channel Beam-column Test (Loading rate: 0.0025 in./sec) - Minor axis (Lips in tension) bending moment and axial compression
Target eccentricity in x-dir (e$_{x0}$):	0.0 (in.)
Target eccentricity in z-dir (e$_{z0}$):	-1.0 (in.)
Provided ave. ecc. in x-dir (e$_x$):	~0.0 (in.)
Provided ave. ecc. in z-dir (e$_z$)-Top:	-1.077 (in.) Provided ave. ecc in z-dir (e$_z$)-Bot: -1.073 (in.)
Initial end plate angles:	θ_{xT}= -0.42^o , θ_{zT}= 0.21^o , θ_{xB}= 1.0^o , θ_{zB}= 0.13^o

Beam-Column Specimen: S600-12-1
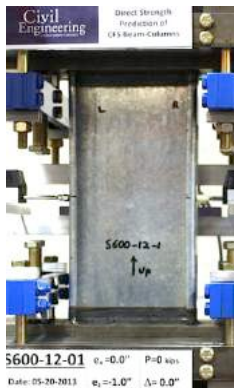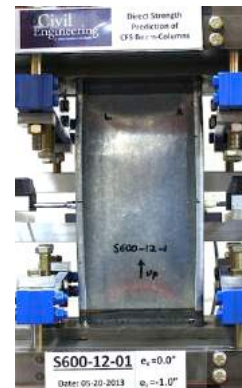
P=2.308 kips	P=3.239 kips	P=5.706 kips	P=4.729 kips
40% P$_m$	57% P$_m$	100% P$_m$	83% P$_m$

Note: Symmetric web local buckling (one big half wave) along with consistent flange deformations was observed.
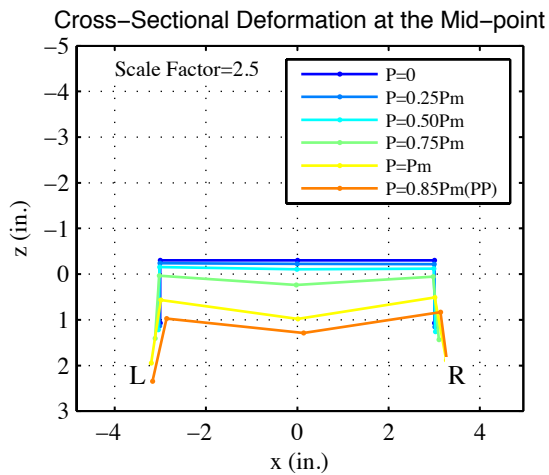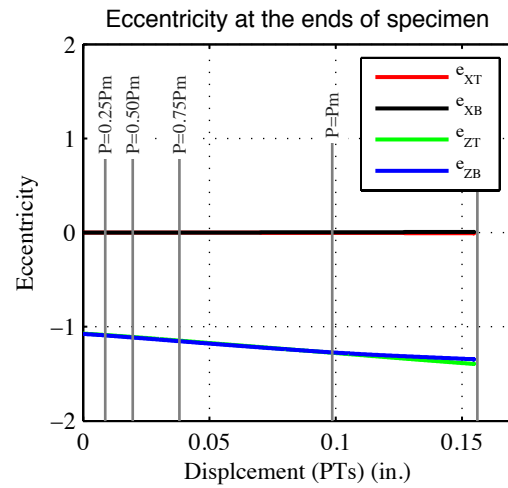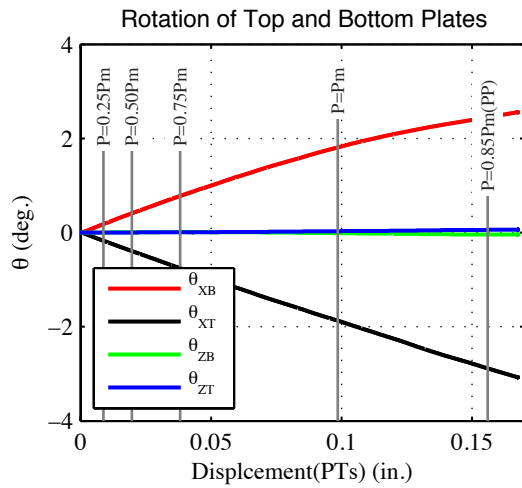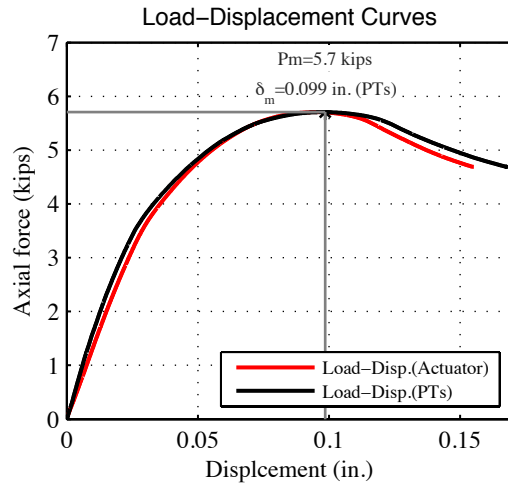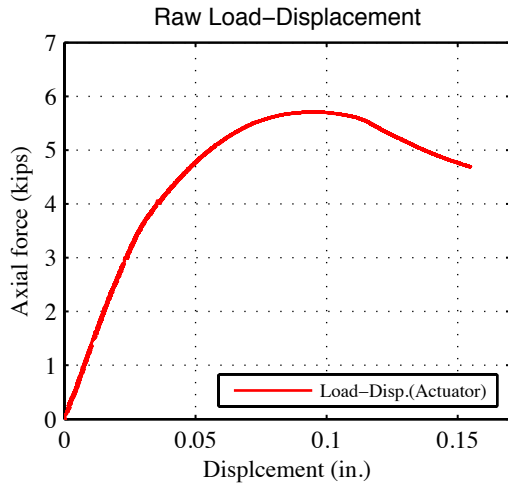
Specimen (S600-12-1) at post-peak stage (PP)

2- S600-12-e$_x$(0)-e$_z$(-0.50)

Tested Specimen:	S600-12-19
Cross-section:	600S137-54 (SSMA Designation)
Date:	May 13th 2013

Left (L) z Right (R)

x

(Bottom to Top View)

Measured cross-section:

(Centroid position for the middle of the tested specimen)

0.3005

2.9582 — 3.0437

Test Description:	- Lipped C-channel Beam-column Test (Loading rate: 0.0025 in./sec) - Minor axis (Lips in Tension) bending and axial compression
Target eccentricity in x-dir (e$_{x0}$):	0.0 (in.)
Target eccentricity in z-dir (e$_{z0}$):	-0.50 (in.)
Provided ave. ecc. in x-dir (e$_x$):	~0.0 (in.)
Provided ave. ecc. in z-dir (e$_z$)-Top:	-0.538 (in.) Provided ave. ecc in z-dir (e$_z$)-Bot: -0.543 (in.)
Initial end plate angles:	θ_{xT}= -0.56^o , θ_{zT}= 0.09^o , θ_{xB}=0.47^o , θ_{zB}= 0.20^o

Beam-Column Specimen: S600-12-19
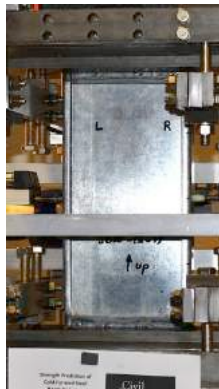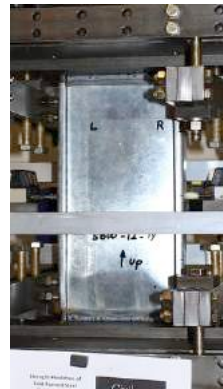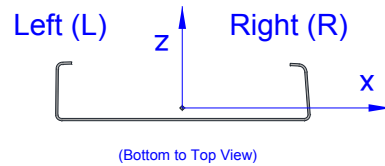
P=0.99 kips	P=8.3 kips	P=9.3 kips	P=6.0 kips
11% P$_m$	89% P$_m$	100% P$_m$	65% P$_m$

Note: Web local buckling was the prominent failure mode (1 big half wave). Flange deformations were very small. Specimen squashed at the bottom part.

MTS Raw Load−Displacement

Load−Displacement Curves

Pm=9.332 kips

δ_m =0.043 in. (PTs)

Load−Disp.(Actuator)
Load−Disp.(PTs)

Rotation of Top and Bottom Plates

P=0.25Pm
P=0.50Pm
P=0.75Pm
P=Pm
P=0.85Pm(PP)

θ_{XB}
θ_{XT}
θ_{ZB}
θ_{ZT}

Eccentricity at the ends of specimen

P=0.25Pm
P=0.50Pm
P=0.75Pm
P=Pm
P=0.85Pm(PP)

e_{XT}
e_{XB}
e_{ZT}
e_{ZB}

Cross−Sectional Deformation at the Mid−point

Scale Factor=2.5

P=0
P=0.25Pm
P=0.50Pm
P=0.75Pm
P=Pm
P=0.85Pm(PP)

L   R

Specimen (S600-12-19) at post-peak stage (PP)

3- S600-12-e$_x$(0)-e$_z$(-0.15)

Tested Specimen:	S600-12-4
Cross-section:	600S137-54 (SSMA Designation)
Date:	May 21th 2013

Left (L)   z   Right (R)

x

(Bottom to Top View)

Measured cross-section:

(Centroid position for the middle of the tested specimen)

0.2992

2.9598   3.0353

Test Description:	- Lipped C-channel Beam-column Test (Loading rate: 0.0025 in./sec) - Minor axis (Lips in tension) bending moment and axial compression	
Target eccentricity in x-dir (e$_{x0}$):	0.0 (in.)	
Target eccentricity in z-dir (e$_{z0}$):	-0.15 (in.)	
Provided ave. ecc. in x-dir (e$_x$):	~0.0 (in.)	
Provided ave. ecc. in z-dir (e$_z$)-Top:	-0.178 (in.)	Provided ave. ecc in z-dir (e$_z$)-Bot: -0.191 (in.)
Initial end plate angles:	θ_{xT}= -0.80^o , θ_{zT}= 0.10^o , θ_{xB}= -0.08^o , θ_{zB}= 0.13^o	

Beam-Column Specimen: S600-12-4
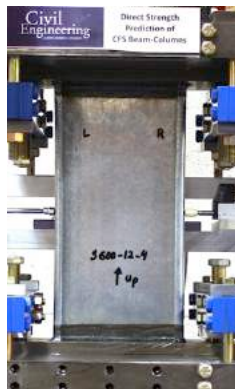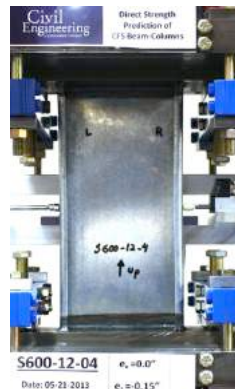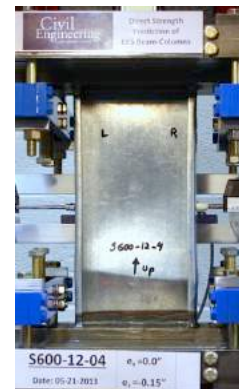
P=3.04 kips	P=8.27 kips	P=12.50 kips	P=8.036 kips
24% P$_m$	66% P$_m$	100% P$_m$	64% P$_m$
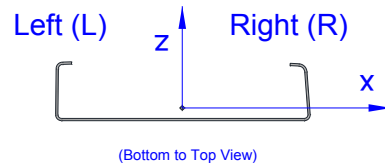
Note: Web local buckling was the prominent failure mode (3 half waves). Specimen squashed at the bottom part.

MTS Raw Load−Displacement

Axial force (kips)

Load−Disp.(Actuator)

Displcement (in.)

Load−Displacement Curves

Pm=12.54 kips

δ_m =0.029 in. (PTs)

Axial force (kips)

Load−Disp.(Actuator)
Load−Disp.(PTs)

Displcement (in.)

Rotation of Top and Bottom Plates

P=0.25Pm
P=0.50Pm
P=0.75Pm
P=Pm
P=0.85Pm(PP)

θ (deg.)

θ_{XB}
θ_{XT}
θ_{ZB}
θ_{ZT}

Displcement(PTs) (in.)

Eccentricity at the ends of specimen

P=0.25Pm
P=0.50Pm
P=0.75Pm
P=Pm
P=0.85Pm(PP)

Eccentricity

e_{XT}
e_{XB}
e_{ZT}
e_{ZB}

Displcement (PTs) (in.)

Cross−Sectional Deformation at the Mid−point

Scale Factor=3.5

P=0
P=0.25Pm
P=0.50Pm
P=0.75Pm
P=Pm
P=0.85Pm(PP)

z (in.)

L

R

x (in.)

Specimen (S600-12-4) at post-peak stage (PP)

269

4- S600-12-e$_x$(0)-e$_z$(+0.15)

Tested Specimen:	S600-12-5
Cross-section:	600S137-54 (SSMA Designation)
Date:	May 23th 2013

Left (L)   z   Right (R)

x

(Bottom to Top View)

Measured cross-section:

(Centroid position for the middle of the tested specimen)

0.2992

2.9689   3.0398

Test Description:	- Lipped C-channel Beam-column Test (Loading rate: 0.0025 in./sec) - Minor axis (Lips in compression) bending and axial compression	
Target eccentricity in x-dir (e$_{x0}$):	0.0 (in.)	
Target eccentricity in z-dir (e$_{z0}$):	+0.15 (in.)	
Provided ave. ecc. in x-dir (e$_x$):	~0.0 (in.)	
Provided ave. ecc. in z-dir (e$_z$)-Top:	+0.115 (in.)	Provided ave. ecc in z-dir (e$_z$)-Bot: +0.102 (in.)
Initial end plate angles:	θ_{xT}= -0.42^o , θ_{zT}= 0.04^o , θ_{xB}= 0.17^o , θ_{zB}= 0.31^o	

Beam-Column Specimen: S600-12-5
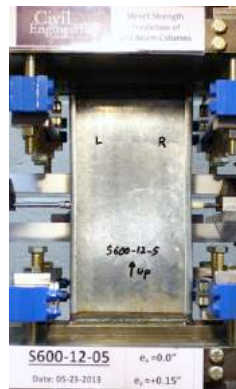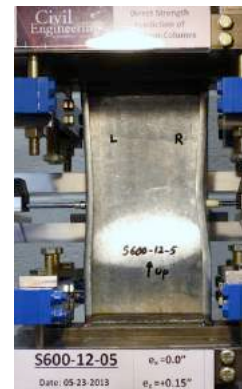
P=7.42 kips	P=10.42 kips	P=16.2 kips	P=12.3 kips
45% P$_m$	63% P$_m$	98% P$_m$	75% P$_m$
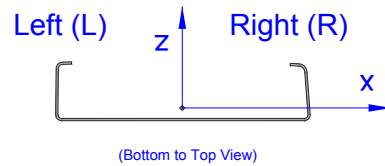
Note: Web local buckling (3 half waves) and consequent and consistent flange deformations were observed.

MTS Raw Load–Displacement

Load–Displacement Curves

Pm=16.54 kips
δ_m=0.027 in. (PTs)

Load–Disp.(Actuator)
Load–Disp.(PTs)

Rotation of Top and Bottom Plates

P=0.25Pm
P=0.50Pm
P=0.75Pm
P=Pm
P=0.85Pm(PP)

θ_{XB}
θ_{XT}
θ_{ZB}
θ_{ZT}

Eccentricity at the ends of specimen

P=0.25Pm
P=0.50Pm
P=0.75Pm
P=Pm
P=0.85Pm(PP)

e_{XT}
e_{XB}
e_{ZT}
e_{ZB}

Cross–Sectional Deformation at the Mid–point

Scale Factor=3.5

P=0
P=0.25Pm
P=0.50Pm
P=0.75Pm
P=Pm
P=0.85Pm(PP)

L

R

Specimen (S600-12-5) at post-peak stage (PP)

271

5- S600-12-e$_x$(0)-e$_z$(+0.35)

Tested Specimen:	S600-12-6
Cross-section:	600S137-54 (SSMA Designation)
Date:	May 28th 2013

Left (L)   z   Right (R)

x

(Bottom to Top View)

Measured cross-section:

(Centroid position for the middle of the tested specimen)

0.3006

2.9861   3.0303

Test Description:	- Lipped C-channel Beam-column Test (Loading rate: 0.0025 in./sec) - Minor axis (Lips in compression) bending and axial compression
Target eccentricity in x-dir (e$_{x0}$):	0.0 (in.)
Target eccentricity in z-dir (e$_{z0}$):	+0.35 (in.)
Provided ave. ecc. in x-dir (e$_x$):	~0.0 (in.)
Provided ave. ecc. in z-dir (e$_z$)-Top:	+0.311 (in.) Provided ave. ecc in z-dir (e$_z$)-Bot: +0.304 (in.)
Initial end plate angles:	θ_{xT}= -0.21^o , θ_{zT}= 0.50^o , θ_{xB}= 0.34^o , θ_{zB}= -0.43^o

Beam-Column Specimen: S600-12-6
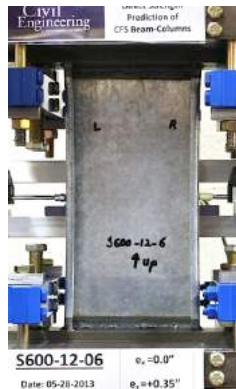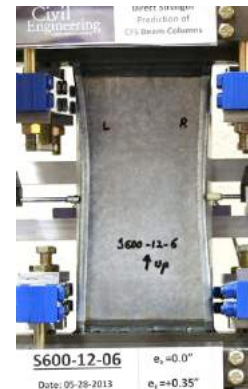
P=6.516 kips	P=9.547 kips	P=11.30 kips	P=8.882 kips
58% P$_m$	85% P$_m$	100% P$_m$	79% P$_m$

Note: Flange distortional buckling (inward deformation) of both flanges occurred. The web deformed consistent to the deformations of the flanges.

MTS Raw Load−Displacement

Load−Displacement Curves

Pm=11.3 kips

δ_m=0.027 in. (PTs)

Rotation of Top and Bottom Plates

P=0.25Pm
P=0.50Pm
P=0.75Pm
P=Pm
P=0.85Pm(PP)

θ_{XB}
θ_{XT}
θ_{ZB}
θ_{ZT}

Eccentricity at the ends of specimen

P=0.25Pm
P=0.50Pm
P=0.75Pm
P=Pm
P=0.85Pm(PP)

e_{XT}
e_{XB}
e_{ZT}
e_{ZB}

Cross−Sectional Deformation at the Mid−point

Scale Factor=2.5

P=0
P=0.25Pm
P=0.50Pm
P=0.75Pm
P=Pm
P=0.85Pm(PP)

L   R
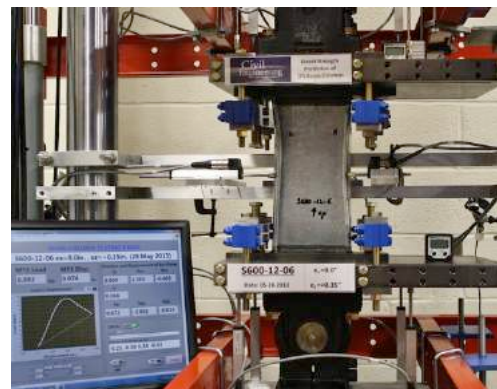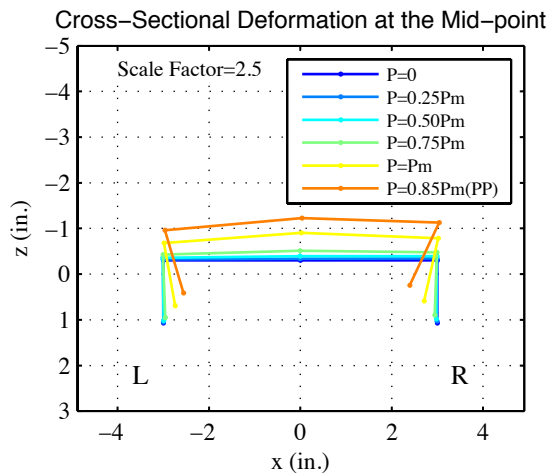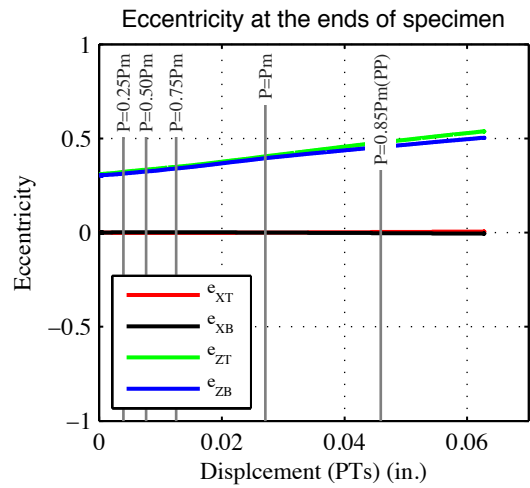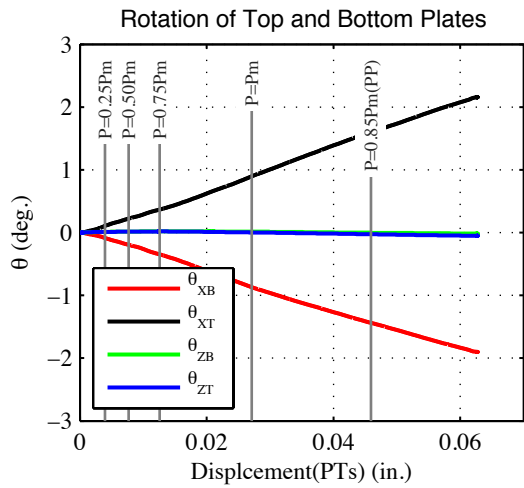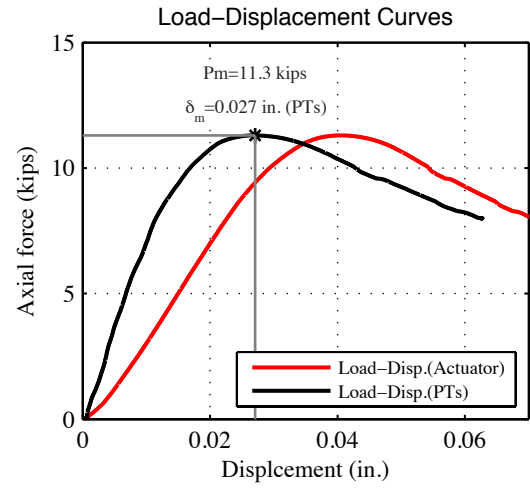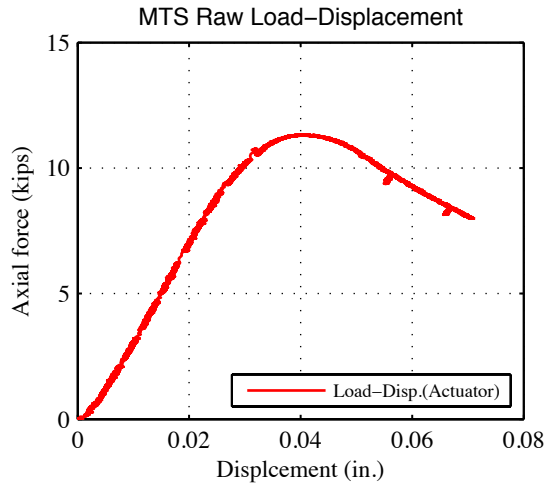
Specimen (S600-12-6) at post-peak stage (PP)

273

6- S600-12-e$_x$(0)-e$_z$(+1.0)

Tested Specimen:	S600-12-8
Cross-section:	600S137-54 (SSMA Designation)
Date:	July 3rd 2013

Left (L)   z   Right (R)

x

(Bottom to Top View)

Measured cross-section:

(Centroid position for the middle of the tested specimen)

0.3098

2.9628   3.0266

Test Description:	- Lipped C-channel Beam-column Test (Loading rate: 0.0025 in./sec) - Minor axis (Lips in compression) bending and axial compression
Target eccentricity in x-dir (e$_{x0}$):	0.0 (in.)
Target eccentricity in z-dir (e$_{z0}$):	+1.0 (in.)
Provided ave. ecc. in x-dir (e$_x$):	~0.0 (in.)
Provided ave. ecc. in z-dir (e$_z$)-Top:	+0.927 (in.) Provided ave. ecc in z-dir (e$_z$)-Bot: +0.973 (in.)
Initial end plate angles:	θ_{xT}= -0.84^o , θ_{zT}= +0.28^o , θ_{xB}= 0.62^o , θ_{zB}= +0.50^o

Beam-Column Specimen: S600-12-8
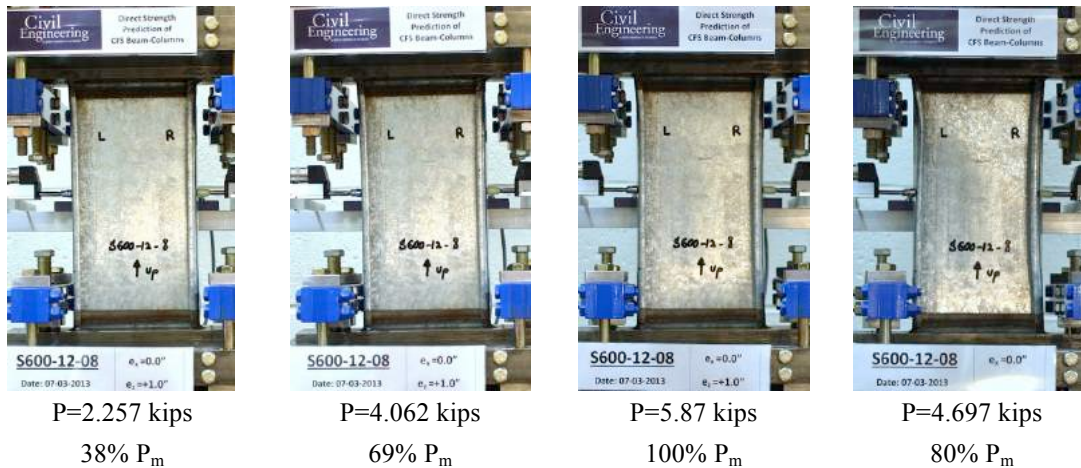
P=2.257 kips	P=4.062 kips	P=5.87 kips	P=4.697 kips
38% P$_m$	69% P$_m$	100% P$_m$	80% P$_m$

Note: Flange distortional buckling (inward deformation) in the right flange and a little smaller deformation in the left flange were observed. The web deformed consistent to the flange deformations.

MTS Raw Load–Displacement

Load–Displacement Curves

Pm=5.87 kips
δ_m =0.052 in. (PTs)

Rotation of Top and Bottom Plates

Eccentricity at the ends of specimen

Cross–Sectional Deformation at the Mid–point

Scale Factor=2.5
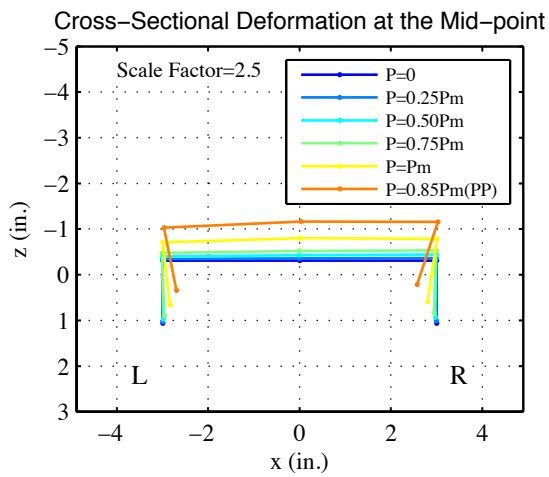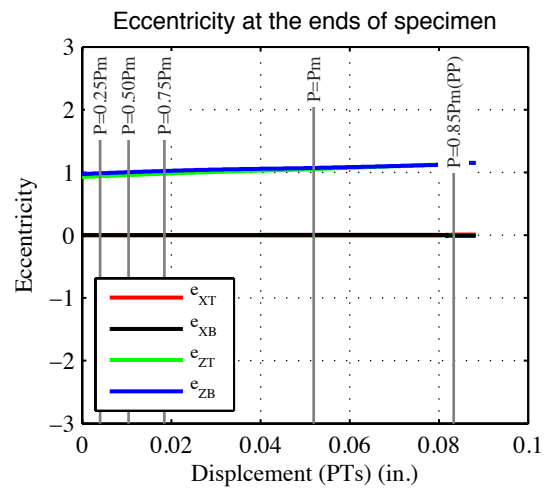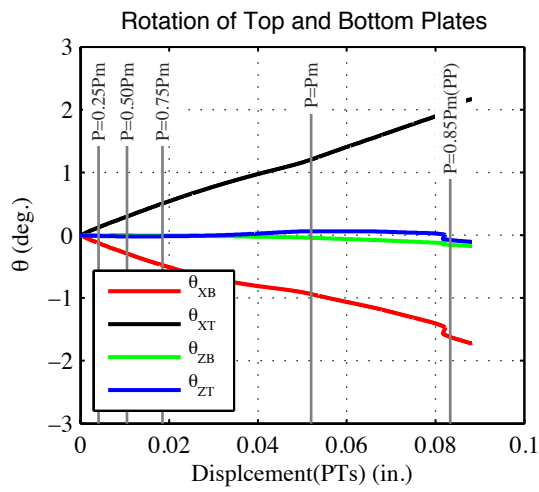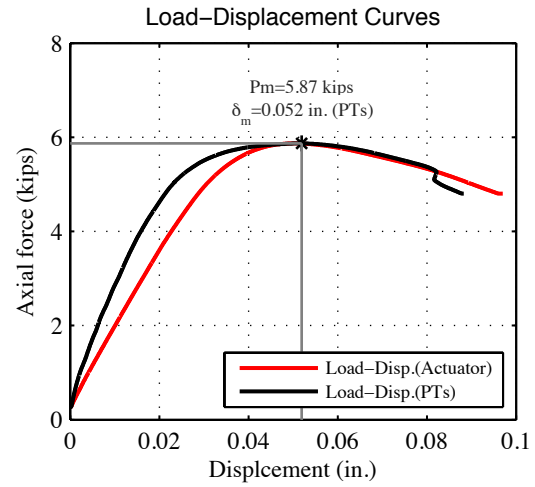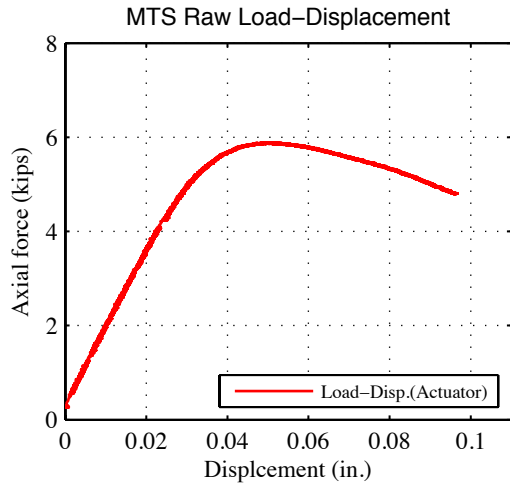
Specimen (S600-12-8) at post-peak stage (PP)

7- S600-12-e$_x$(-1.0)-e$_z$(0.0)

Tested Specimen:	S600-12-9	
Cross-section:	600S137-54 (SSMA Designation)	
Date:	July 4th 2013	

Left (L)   z   Right (R)

x

(Bottom to Top View)

Measured cross-section:

(Centroid position for the middle of the tested specimen)

0.3023

2.9675 ———— 3.0211

Test Description:	- Lipped C-channel Beam-column Test (Loading rate: 0.00125 in./sec) - Major axis bending and axial compression		
Target eccentricity in x-dir (e$_{x0}$):	-1.0 (in.)		
Target eccentricity in z-dir (e$_{z0}$):	0.0 (in.)		
Provided ave. ecc. in x-dir (e$_x$):	-1.0 (in.)		
Provided ave. ecc. in z-dir (e$_z$)-Top:	-0.068 (in.)	Provided ave. ecc in z-dir (e$_z$)-Bot:	-0.017 (in.)
Initial end plate angles:	θ_{xT}= -0.70^o , θ_{zT}= -0.31^o , θ_{xB}= 0.87^o , θ_{zB}= +0.63^o		

Beam-Column Specimen: S600-12-9
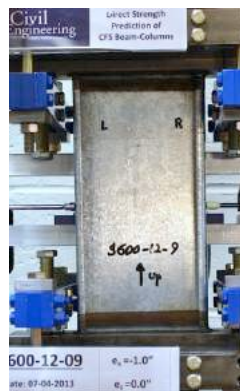
P=4.77 kips	P=9.37 kips	P=12.21 kips	P=9.72 kips
39% P$_m$	77% P$_m$	100% P$_m$	80% P$_m$
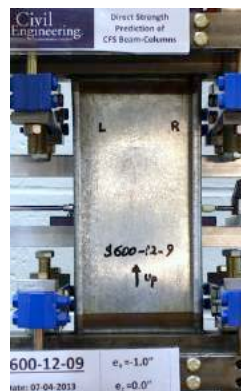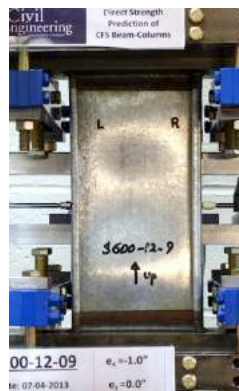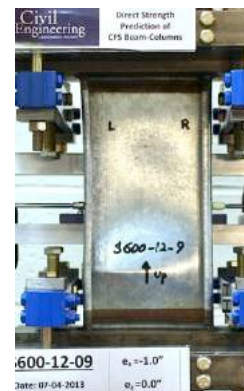
Note: Unsymmetrical (almost symmetric) web buckling (3 half waves visible at about P=8.0 kips) and a small left flange inward deformation (distortional buckling) occurred.

MTS Raw Load-Displacement

Load-Displacement Curves

Pm=12.216 kips
δ_m =0.021 in. (PTs)

Rotation of Top and Bottom Plates

P=0.25Pm
P=0.50Pm
P=0.75Pm
P=Pm
P=0.85Pm(PP)

θ_{XB}
θ_{XT}
θ_{ZB}
θ_{ZT}

Eccentricity at the ends of specimen

P=0.25Pm
P=0.50Pm
P=0.75Pm
P=Pm
P=0.85Pm(PP)

e_{XT}
e_{XB}
e_{ZT}
e_{ZB}

Cross-Sectional Deformation at the Mid-point

Scale Factor=3.5

P=0
P=0.25Pm
P=0.50Pm
P=0.75Pm
P=Pm
P=0.85Pm(PP)

L   R
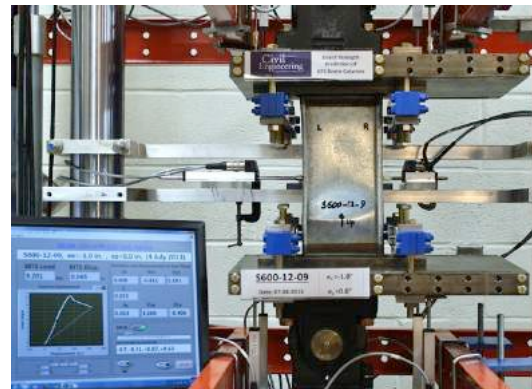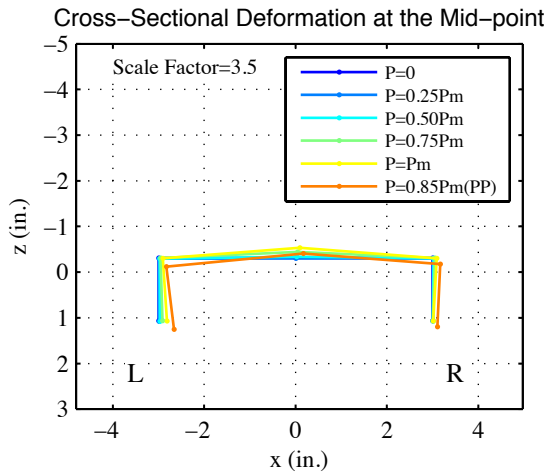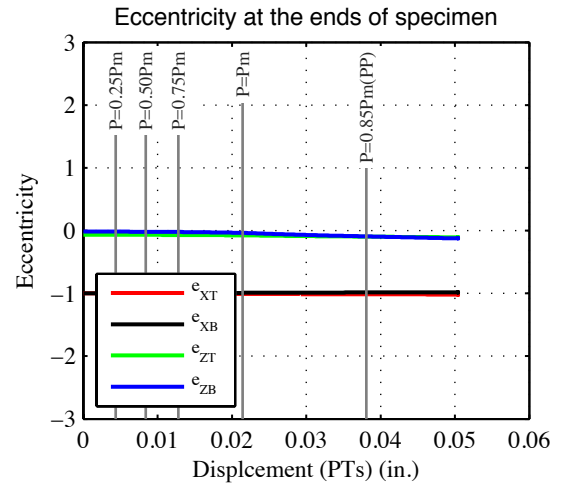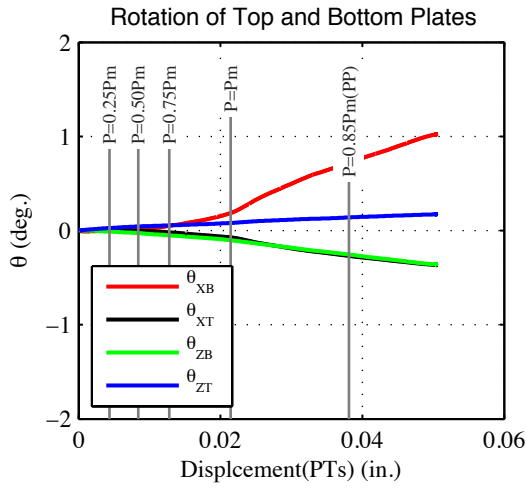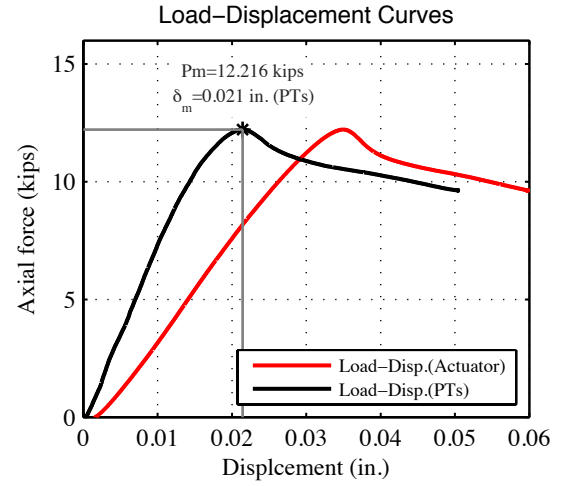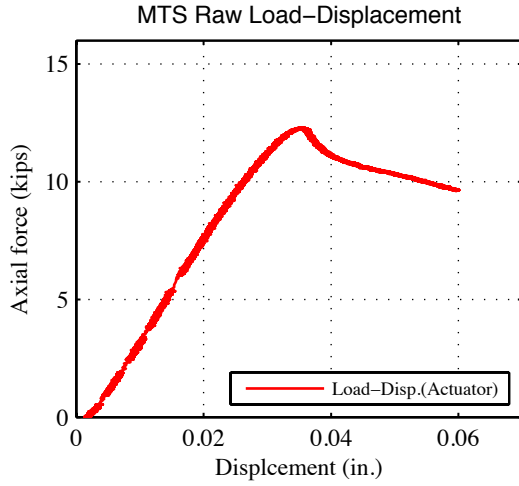
Specimen (S600-12-9) at post-peak stage (PP)

8- S600-12-e$_x$(-3.5)-e$_z$(0.0)

Tested Specimen:	S600-12-10
Cross-section:	600S137-54 (SSMA Designation)
Date:	July 5th 2013

Left (L)   z   Right (R)

x

(Bottom to Top View)

Measured cross-section:

(Centroid position for the middle of the tested specimen)

0.3011

2.9918   3.0287

Test Description:	- Lipped C-channel Beam-column Test (Loading rate: 0.00125 in./sec) - Major axis bending and axial compression	
Target eccentricity in x-dir (e$_{x0}$):	-3.50 (in.)	
Target eccentricity in z-dir (e$_{z0}$):	0.0 (in.)	
Provided ave. ecc. in x-dir (e$_x$):	-3.50 (in.)	
Provided ave. ecc. in z-dir (e$_z$)-Top:	-0.016 (in.)	Provided ave. ecc in z-dir (e$_z$)-Bot: -0.01 (in.)
Initial end plate angles:	θ_{xT}= -0.90^o , θ_{zT}= -0.05^o , θ_{xB}= +0.36^o , θ_{zB}= -0.01^o	

Beam-Column Specimen: S600-12-10
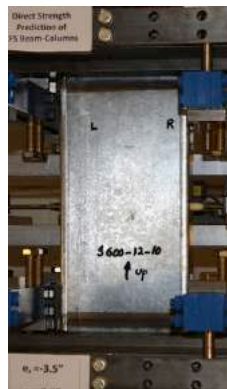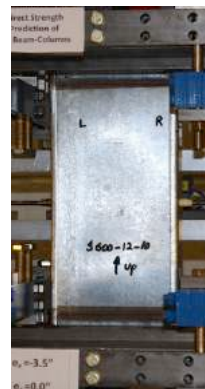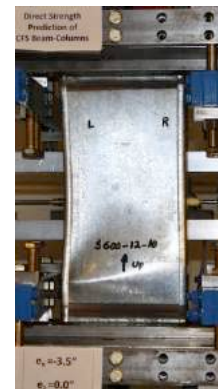
P=3.67 kips	P=6.01 kips	P=7.06 kips	P=6.01 kips
52% P$_m$	85% P$_m$	100% P$_m$	85% P$_m$

Note: Unsymmetrical web buckling (seemed like 3 half-waves) and left flange distortional buckling were observed.

MTS Raw Load−Displacement

Load−Displacement Curves

Pm=7.602 kips
δ$_m$ =0.035 in. (PTs)

Rotation of Top and Bottom Plates

Eccentricity at the ends of specimen

Cross−Sectional Deformation at the Mid−point

Scale Factor=3.5
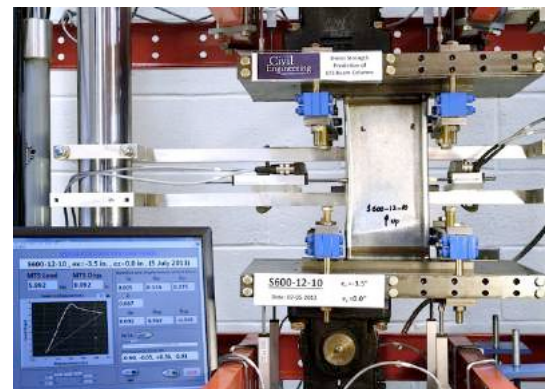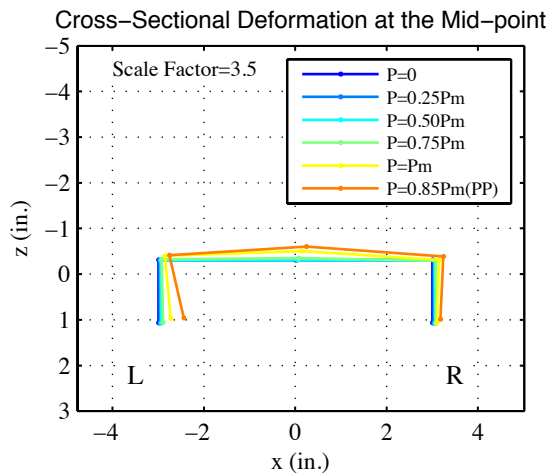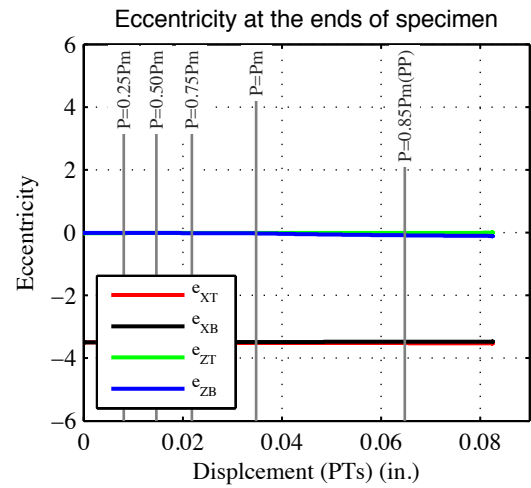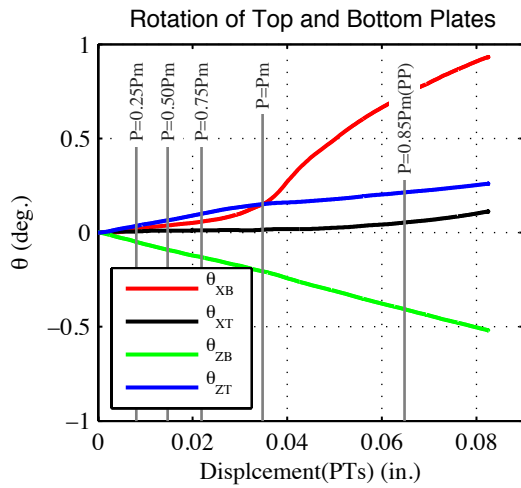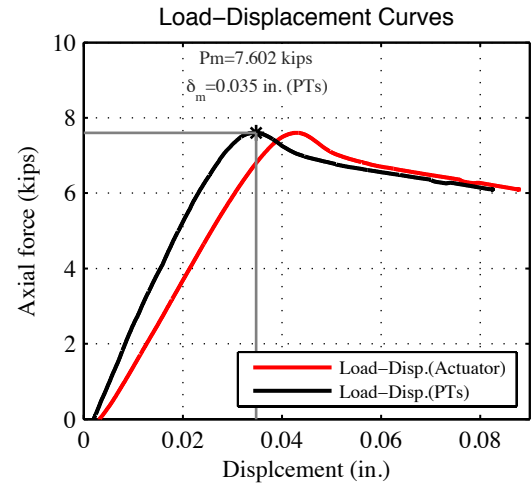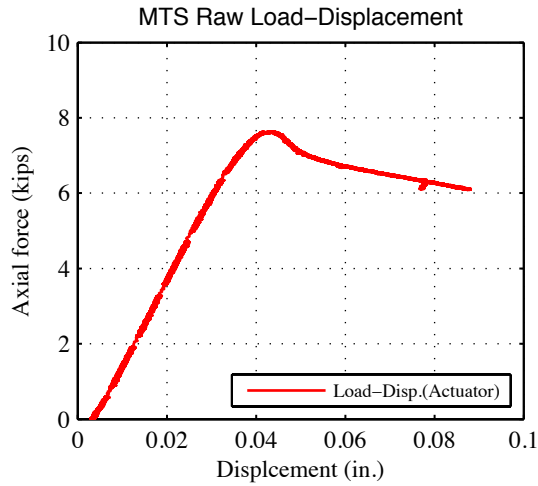
Specimen (S600-12-10) at post-peak stage (PP)

279

9- S600-12-e$_x$(-7.5)-e$_z$(0.0)

Tested Specimen:	S600-12-11
Cross-section:	600S137-54 (SSMA Designation)
Date:	July 8th 2013

Left (L)   z   Right (R)

x

(Bottom to Top View)

Measured cross-section:

(Centroid position for the middle of the tested specimen)

0.3056

2.9699   3.0309

Test Description:	- Lipped C-channel Beam-column Test (Loading rate: 0.00125 in./sec) - Major axis bending and axial compression
Target eccentricity in x-dir (e$_{x0}$):	-7.50 (in.)
Target eccentricity in z-dir (e$_{z0}$):	0.0 (in.)
Provided ave. ecc. in x-dir (e$_x$):	-7.50 (in.)
Provided ave. ecc. in z-dir (e$_z$)-Top:	0.0045 (in.) Provided ave. ecc in z-dir (e$_z$)-Bot: -0.003 (in.)
Initial end plate angles:	θ_{xT}= +0.58^o , θ_{zT}= -0.69^o , θ_{xB}= +0.81^o , θ_{zB}= -0.56^o

Beam-Column Specimen: S600-12-11
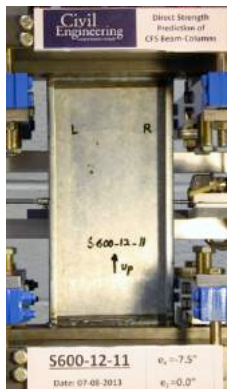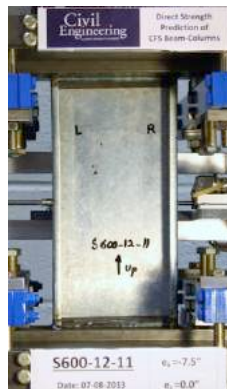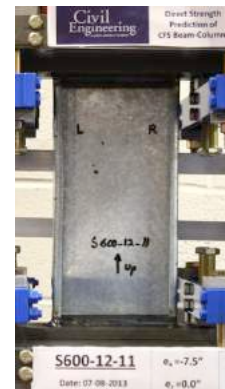
P=1.497 kips	P=3.04 kips	P=4.62 kips	P=-- kips
32% P$_m$	65% P$_m$	100% P$_m$	Unloaded

Note: Unsymmetrical web buckling (at about P=4.5 kips) and left flange distortional buckling (at about P=1.5 kips) were observed.

MTS Raw Load–Displacement

Load–Displacement Curves

Pm=4.622 kips
δ_m=0.099 in. (PTs)

Rotation of Top and Bottom Plates

Eccentricity at the ends of specimen

Cross–Sectional Deformation at the Mid–point

Scale Factor=3.5
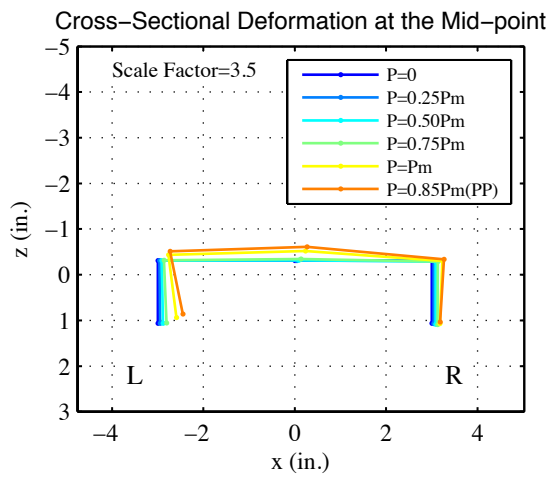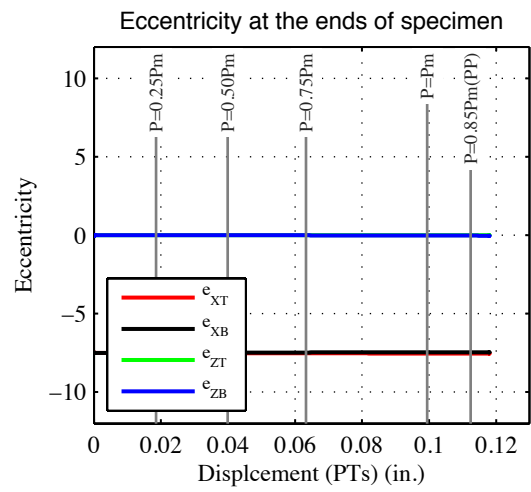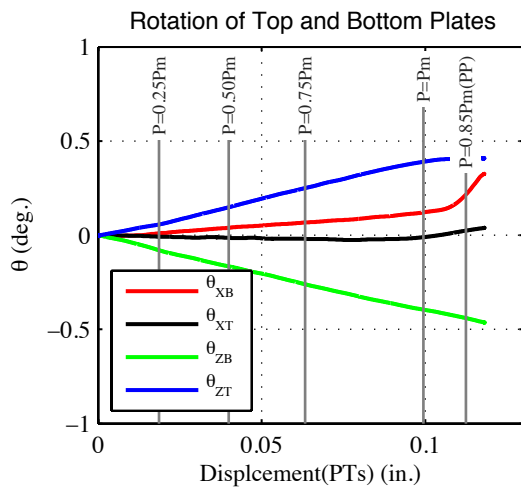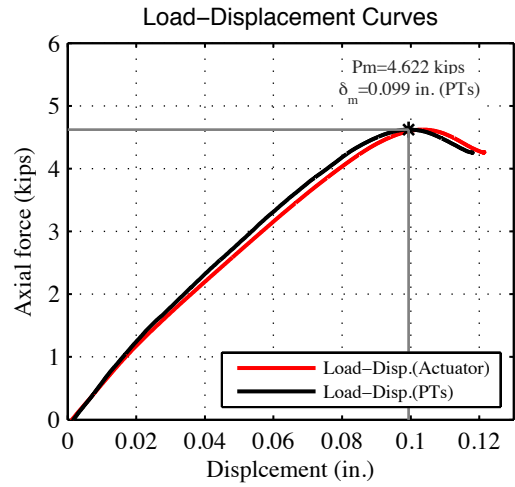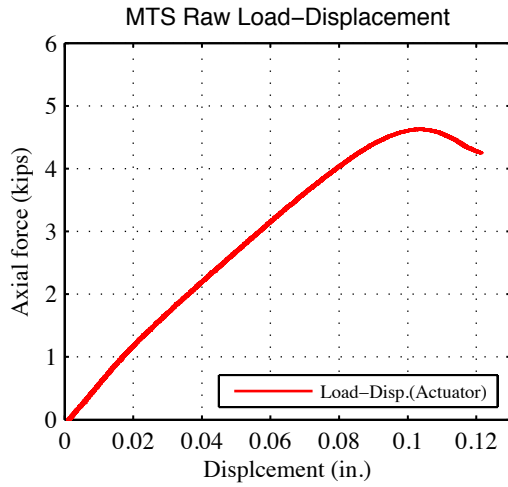
Specimen (S600-12-11) at post-peak stage (PP)

10- S600-12-e_x(-1.5)-e_z(0.10)

Tested Specimen:	S600-12-02
Cross-section:	600S137-54 (SSMA Designation)
Date:	July 11th 2013

Left (L) | Right (R)

z

x

(Bottom to Top View)

Measured cross-section:

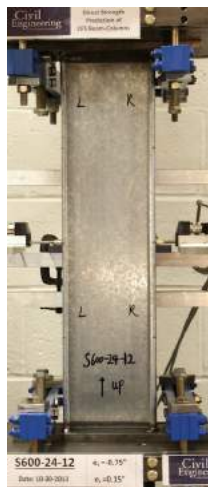(Centroid position for the middle of the tested specimen)

0.3005

2.9582   3.0437

Test Description:	- Lipped C-channel Beam-column Test (Loading rate: 0.0025 in./sec) - Bi-axial bending and axial compression	
Target eccentricity in x-dir (e_{x0}):	-1.5 (in.)	
Target eccentricity in z-dir (e_{z0}):	+0.1019 (in.)	
Provided ave. ecc. in x-dir (e_x):	-1.5 (in.)	
Provided ave. ecc. in z-dir (e_z)-Top:	+0.107 (in.)	Provided ave. ecc in z-dir (e_z)-Bot: +0.107 (in.)
Initial end plate angles:	θ_{xT}= -1.12^o , θ_{zT}= +0.13^o , θ_{xB}= +0.37^o , θ_{zB}= +0.52^o	

Beam-Column Specimen: S600-12-02
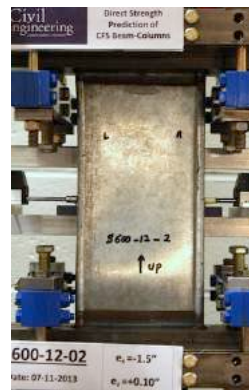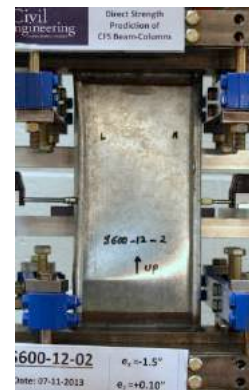
P=2.53 kips	P=8.05 kips	P=11 kips	P=9.22 kips
23% P_m	73% P_m	100% P_m	84% P_m

Note: Inward movement (distortional buckling) of the left flange and a very small right flange deformation (mostly in post-peak stage) were observed. The web buckling (3 half waves) consistent with flange deformations was seen.

MTS Raw Load–Displacement

Load–Displacement Curves

Pm=11 kips
δ_m =0.022 in. (PTs)

Rotation of Top and Bottom Plates

P=0.25Pm
P=0.50Pm
P=0.75Pm
P=Pm
P=0.85Pm(PP)

Eccentricity at the ends of specimen

P=0.25Pm
P=0.50Pm
P=0.75Pm
P=Pm
P=0.85Pm(PP)

Cross−Sectional Deformation at the Mid−point

Scale Factor=3.5

P=0
P=0.25Pm
P=0.50Pm
P=0.75Pm
P=Pm
P=0.85Pm(PP)

L   R
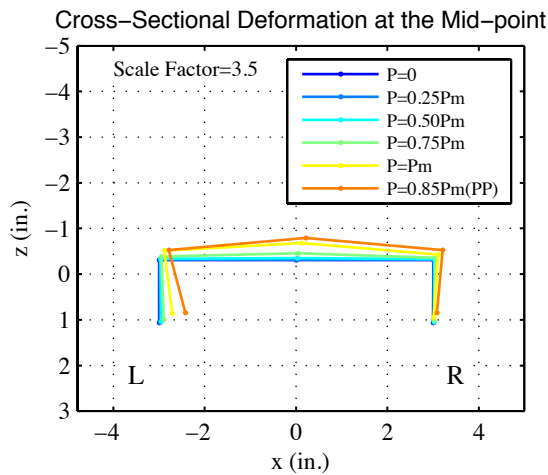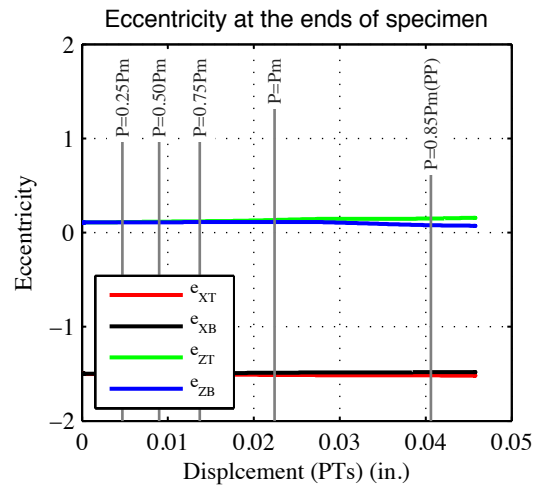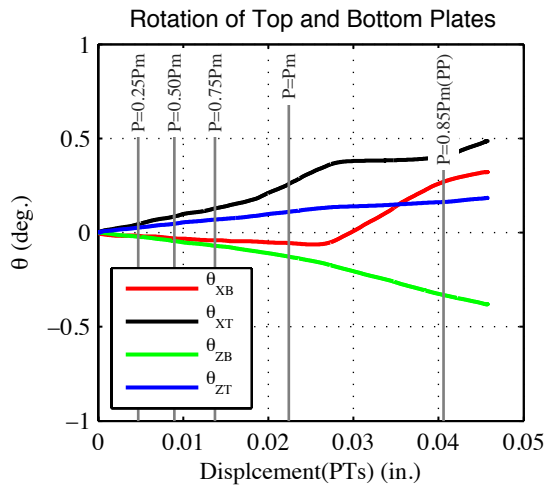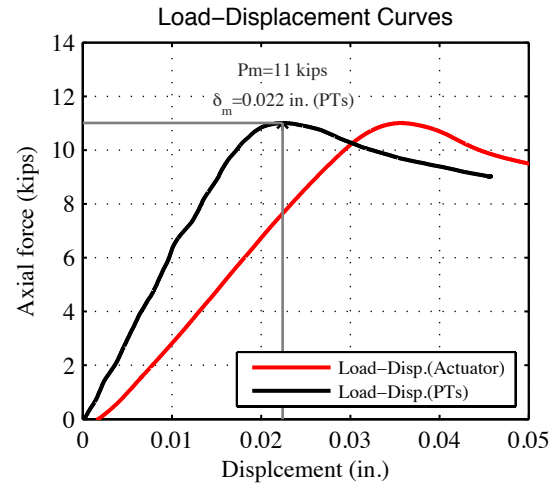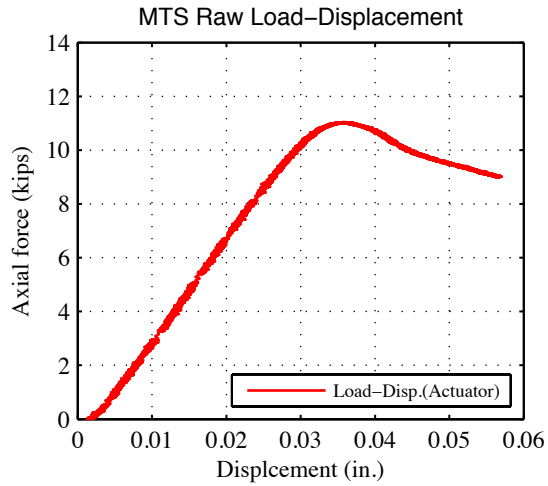
Specimen (S600-12-2) at post-peak stage (PP)

283

11- S600-12-e$_x$(-5.0)-e$_z$(0.34)

Tested Specimen:	S600-12-13
Cross-section:	600S137-54 (SSMA Designation)
Date:	July 9th 2013

Left (L)   z   Right (R)

x

(Bottom to Top View)

Measured cross-section:

(Centroid position for the middle of the tested specimen)

0.3069

2.9540 ——|—— 3.0467

Test Description:	- Lipped C-channel Beam-column Test (Loading rate: 0.0017 in./sec) - Bi-axial bending and axial compression	
Target eccentricity in x-dir (e$_{x0}$):	-5.0 (in.)	
Target eccentricity in z-dir (e$_{z0}$):	0.3397 (in.)	
Provided ave. ecc. in x-dir (e$_x$):	-5.0 (in.)	
Provided ave. ecc. in z-dir (e$_z$)-Top:	0.3425 (in.)	Provided ave. ecc in z-dir (e$_z$)-Bot: 0.332 (in.)
Initial end plate angles:	θ_{xT}= -1.04^o , θ_{zT}= +0.74^o , θ_{xB}= 0.0^o , θ_{zB}= +1.20^o	

Beam-Column Specimen: S600-12-13

P=1.53 kips	P=3.01 kips	P=4.78 kips	P=3.76 kips
32% P$_m$	63% P$_m$	100% P$_m$	79% P$_m$

Note: Inward movement (distortional buckling) of the left flange and a smaller right flange movement (mostly in post-peak stage) were observed. A web deformation consistent with the flange movements was occurred.

284

MTS Raw Load–Displacement

Load–Displacement Curves

Pm=4.78 kips

δ_m=0.052 in. (PTs)

Rotation of Top and Bottom Plates

P=0.25Pm
P=0.50Pm
P=0.75Pm
P=Pm
P=0.85Pm(PP)

θ_{XB}
θ_{XT}
θ_{ZB}
θ_{ZT}

Eccentricity at the ends of specimen

P=0.25Pm
P=0.50Pm
P=0.75Pm
P=Pm
P=0.85Pm(PP)

e_{XT}
e_{XB}
e_{ZT}
e_{ZB}

Cross–Sectional Deformation at the Mid–point

Scale Factor=3.5

P=0
P=0.25Pm
P=0.50Pm
P=0.75Pm
P=Pm
P=0.85Pm(PP)

L   R
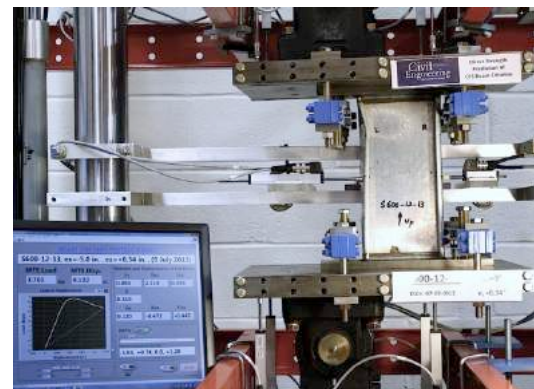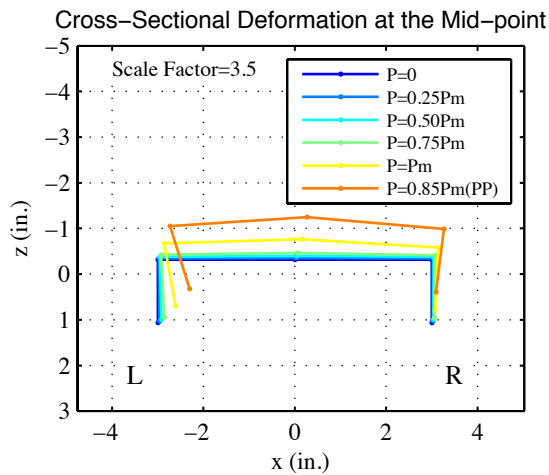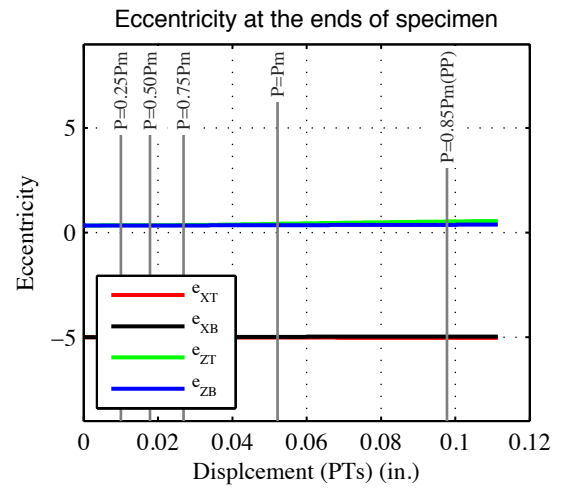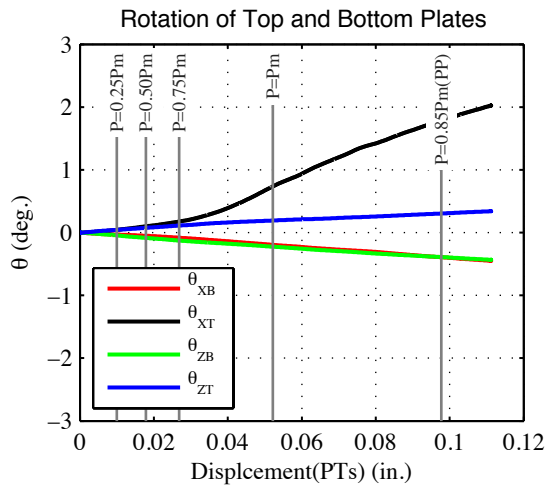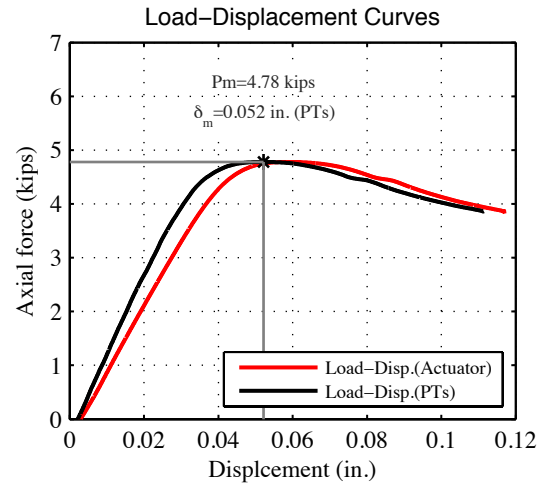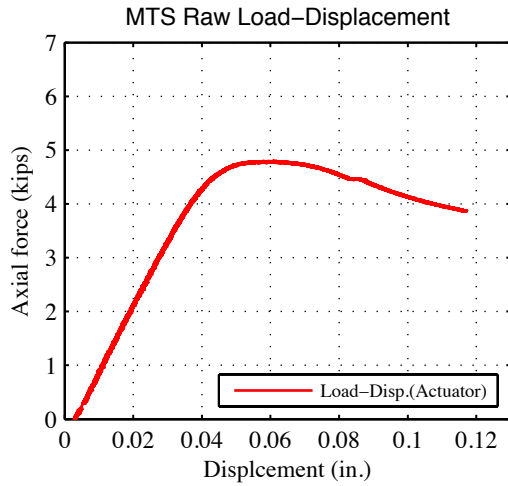
Specimen (S600-12-13) at post-peak stage (PP)

12- S600-12-e$_x$(-0.8)-e$_z$(0.17)

Tested Specimen:	S600-12-14		
Cross-section:	600S137-54 (SSMA Designation)		
Date:	July 10th 2013		

Left (L)   z   Right (R)

x

(Bottom to Top View)

Measured cross-section:

(Centroid position for the middle of the tested specimen)

0.3043

2.9511   3.0474

Test Description:	- Lipped C-channel Beam-column Test (Loading rate: 0.0017 in./sec) - Bi-axial bending and axial compression	
Target eccentricity in x-dir (e$_{x0}$):	-0.8125 (in.)	
Target eccentricity in z-dir (e$_{z0}$):	0.1656 (in.)	
Provided ave. ecc. in x-dir (e$_x$):	-0.80 (in.)	
Provided ave. ecc. in z-dir (e$_z$)-Top:	0.160 (in.) Provided ave. ecc in z-dir (e$_z$)-Bot:	0.172 (in.)
Initial end plate angles:	θ_{xT}= -0.85^o , θ_{zT}= -0.09^o , θ_{xB}= +0.21^o , θ_{zB}= +0.34^o	

Beam-Column Specimen: S600-12-14
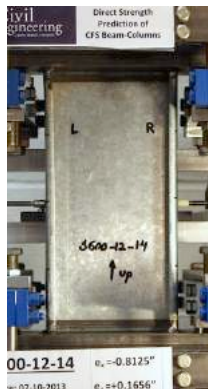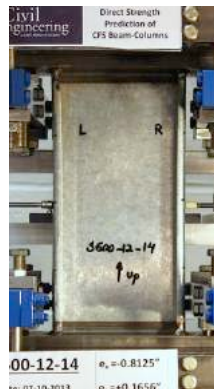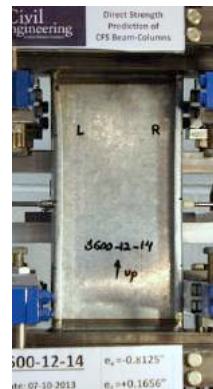
P=3.54 kips	P=8.83 kips	P=11.81 kips	P=9.44 kips
30% P$_m$	65% P$_m$	100% P$_m$	80% P$_m$

Note: Left flange inward movement (distortional buckling) was the main failure mode of the specimen and a smaller right flange movement occurred mostly in post-peak stage. A web deformation consistent with the flange movements was seen.

Cross−Sectional Deformation at the Mid−point
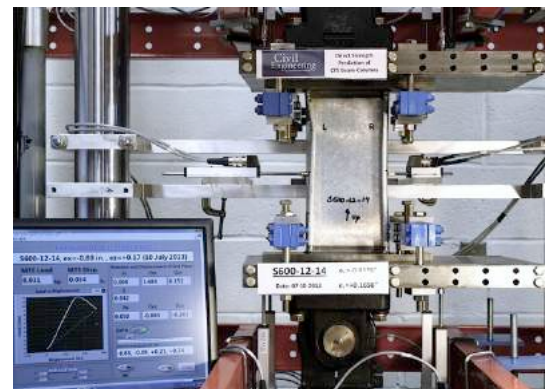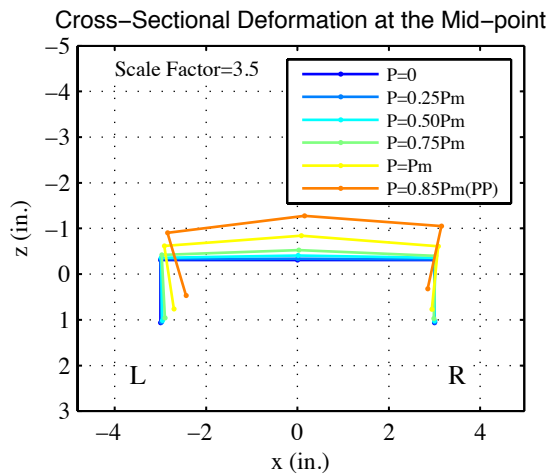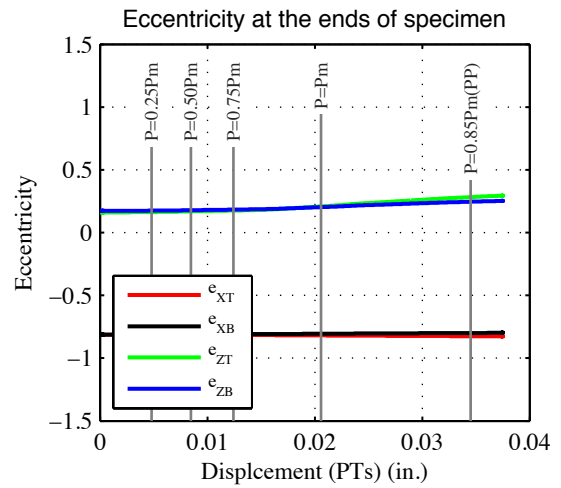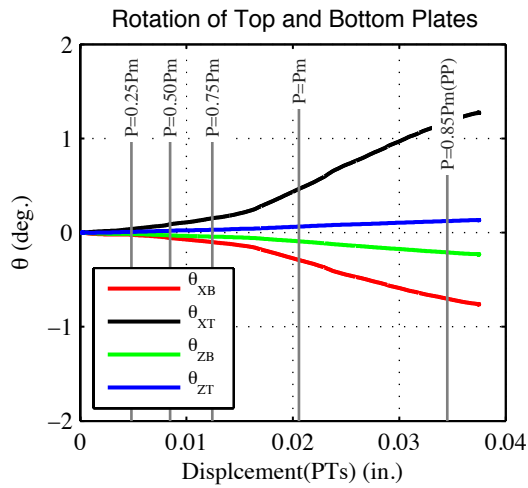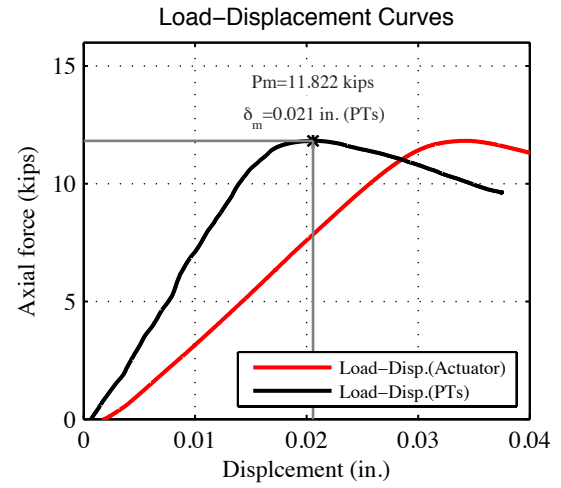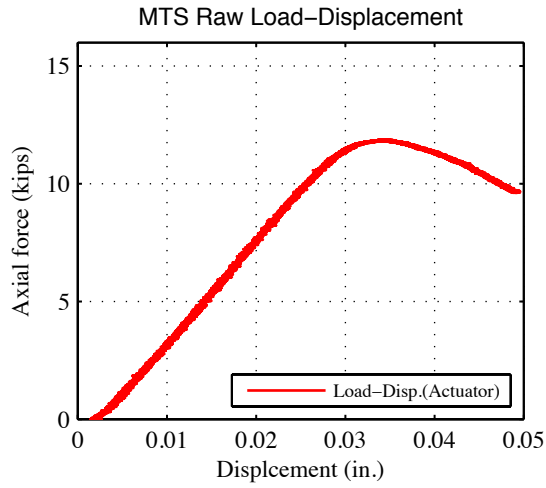
Specimen (S600-12-14) at post-peak stage (PP)

## 13- S600-12-e$_x$(-3.0)-e$_z$(0.6)

Tested Specimen:	S600-12-15
Cross-section:	600S137-54 (SSMA Designation)
Date:	July 11th 2013

Left (L)   z   Right (R)

x

(Bottom to Top View)

Measured cross-section:

(Centroid position for the middle of the tested specimen)

0.2993

2.9831   3.0485

Test Description:	- Lipped C-channel Beam-column Test (Loading rate: 0.0025 in./sec) - Bi-axial bending and axial compression	
Target eccentricity in x-dir (e$_{x0}$):	-3.0 (in.)	
Target eccentricity in z-dir (e$_{z0}$):	0.6115 (in.)	
Provided ave. ecc. in x-dir (e$_x$):	-3.0 (in.)	
Provided ave. ecc. in z-dir (e$_z$)-Top:	0.620 (in.) Provided ave. ecc in z-dir (e$_z$)-Bot: 0.637 (in.)	
Initial end plate angles:	θ_{xT}= -0.71^o , θ_{zT}= +0.3^o , θ_{xB}= +0.31^o , θ_{zB}= +0.86^o	
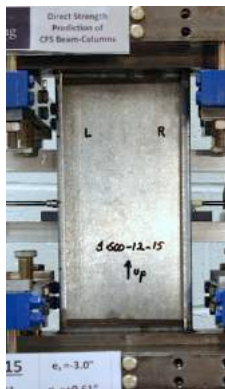
Beam-Column Specimen: S600-12-15

P=1.36 kips	P=4.24 kips	P=5.62 kips	P=4.55 kips
24% P$_m$	75% P$_m$	100% P$_m$	80% P$_m$

Note: Flange distortional buckling resulted in outward movement of both flanges. Web buckling was not observed until the post-peak stage. The web deformation was consistent to the flange outward movement.

MTS Raw Load–Displacement

Load–Displacement Curves

Pm=5.625 kips

δ_m=0.053 in. (PTs)

Rotation of Top and Bottom Plates

P=0.25Pm P=0.50Pm P=0.75Pm P=Pm P=0.85Pm(PP)

Eccentricity at the ends of specimen

P=0.25Pm P=0.50Pm P=0.75Pm P=Pm P=0.85Pm(PP)

Cross–Sectional Deformation at the Mid–point

Scale Factor=3.5

P=0
P=0.25Pm
P=0.50Pm
P=0.75Pm
P=Pm
P=0.85Pm(PP)

L   R
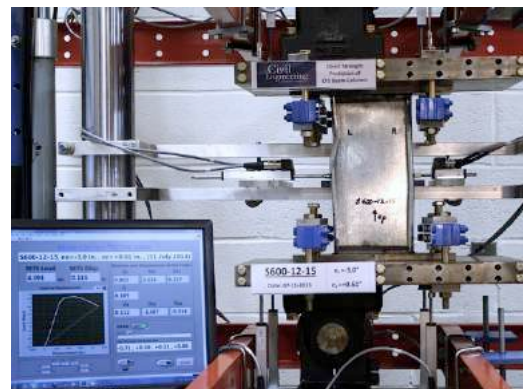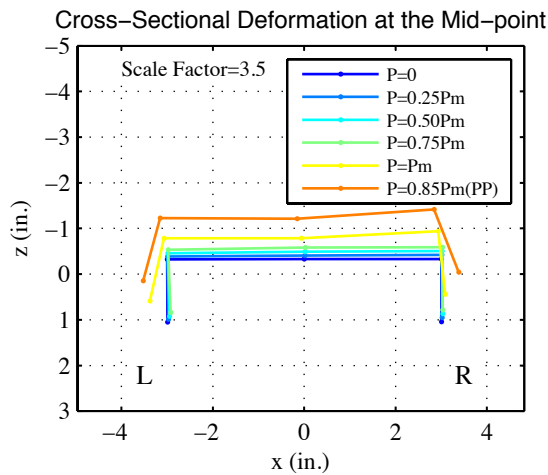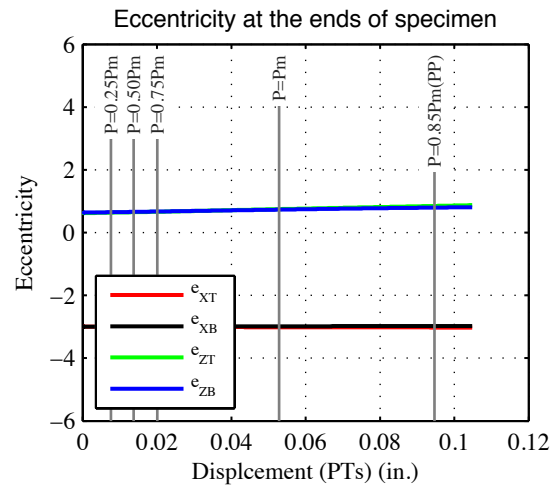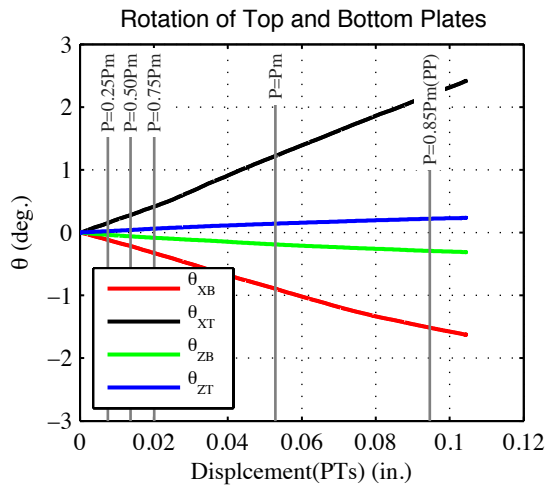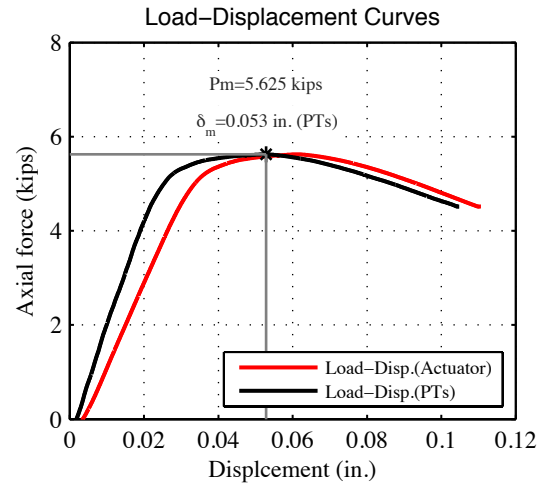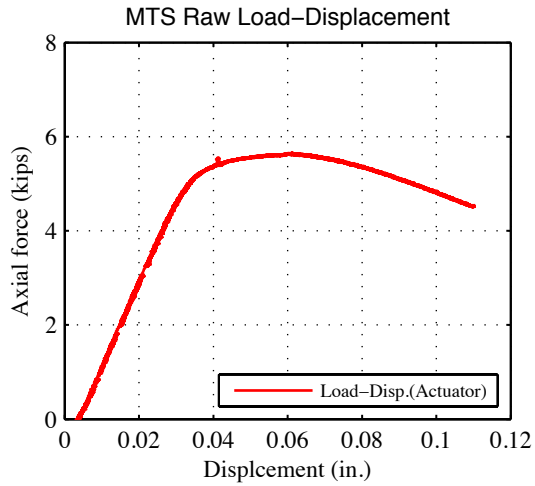
Specimen (S600-12-15) at post-peak stage (PP)

14- S600-12-e$_x$(-0.8)-e$_z$(-0.17)

Tested Specimen:	S600-12-16
Cross-section:	600S137-54 (SSMA Designation)
Date:	July 12th 2013

Left (L)   z   Right (R)

x

(Bottom to Top View)

Measured cross-section:

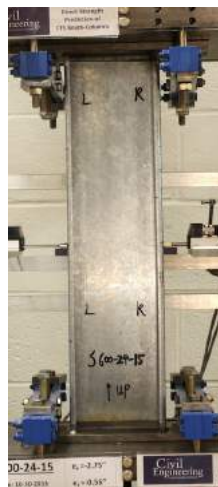(Centroid position for the middle of the tested specimen)

0.3047

2.9463   3.0485

Test Description:	- Lipped C-channel Beam-column Test (Loading rate: 0.0025 in./sec) - Bi-axial bending and axial compression	
Target eccentricity in x-dir (e$_{x0}$):	-0.8125 (in.)	
Target eccentricity in z-dir (e$_{z0}$):	-0.1656 (in.)	
Provided ave. ecc. in x-dir (e$_x$):	-0.8125 (in.)	
Provided ave. ecc. in z-dir (e$_z$)-Top:	-0.163 (in.)	Provided ave. ecc in z-dir (e$_z$)-Bot: -0.158 (in.)
Initial end plate angles:	θ_{xT}= -1.03^o , θ_{zT}= +0.04^o , θ_{xB}= +0.31^o , θ_{zB}= +0.19^o	

Beam-Column Specimen: S600-12-16

P=3.03 kips	P=8.0 kips	P=10.8 kips	P=9.5 kips
28% P$_m$	74% P$_m$	100% P$_m$	87% P$_m$

Note: Unsymmetrical web local buckling (3 half-waves visible at about P=6.5 kips). Flange local buckling of the left flange within the post-peak stage and consistent with the web buckling

MTS Raw Load–Displacement

Load–Displacement Curves

Pm=10.896 kips

δ_m=0.024 in. (PTs)

Rotation of Top and Bottom Plates

P=0.25Pm
P=0.50Pm
P=0.75Pm
P=Pm
P=0.85Pm(PP)

θ_{XB}
θ_{XT}
θ_{ZB}
θ_{ZT}

Eccentricity at the ends of specimen

P=0.25Pm
P=0.50Pm
P=0.75Pm
P=Pm
P=0.85Pm(PP)

e_{XT}
e_{XB}
e_{ZT}
e_{ZB}

Cross−Sectional Deformation at the Mid−point

Scale Factor=3.5

P=0
P=0.25Pm
P=0.50Pm
P=0.75Pm
P=Pm
P=0.85Pm(PP)

L   R
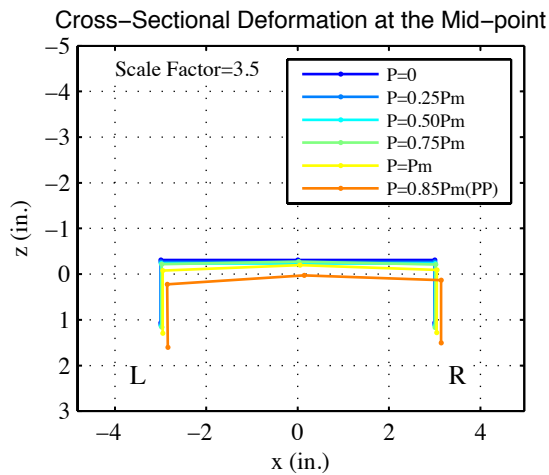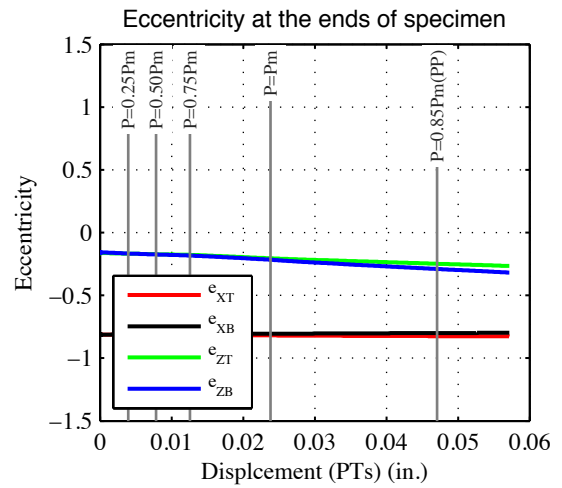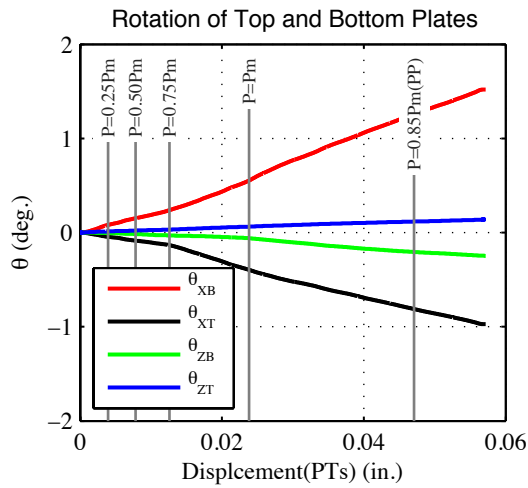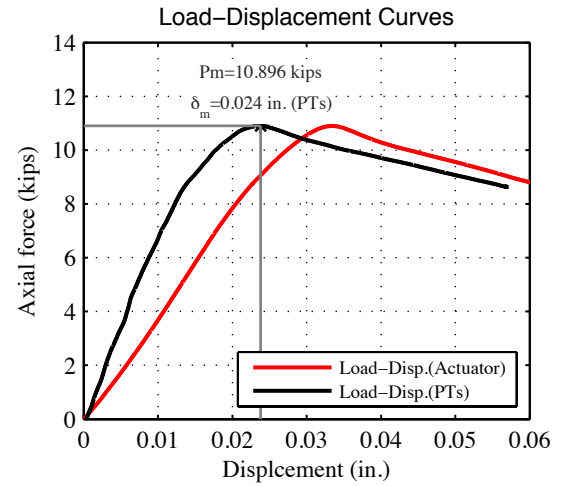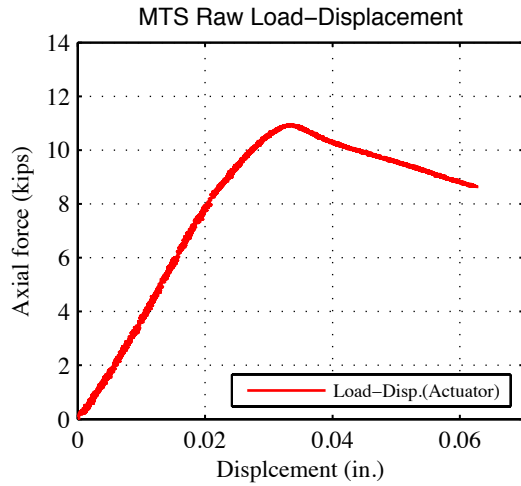
Specimen (S600-12-16) at post-peak stage (PP)

15- S600-12-e$_x$(-3.0)-e$_z$(-0.6)

Tested Specimen:	S600-12-17
Cross-section:	600S137-54 (SSMA Designation)
Date:	July 12th 2013

Left (L)   z   Right (R)

x

(Bottom to Top View)

Measured cross-section:

(Centroid position for the middle of the tested specimen)

0.2977

2.9923   3.0486

Test Description:	- Lipped C-channel Beam-column Test (Loading rate: 0.0025 in./sec) - Bi-axial bending and axial compression	
Target eccentricity in x-dir (e$_{x0}$):	-3.0 (in.)	
Target eccentricity in z-dir (e$_{z0}$):	-0.6115 (in.)	
Provided ave. ecc. in x-dir (e$_x$):	-3.0 (in.)	
Provided ave. ecc. in z-dir (e$_z$)-Top:	-0.612 (in.)	Provided ave. ecc in z-dir (e$_z$)-Bot: -0.615 (in.)
Initial end plate angles:	θ_{xT}= -1.93^o , θ_{zT}= -0.12^o , θ_{xB}= +0.16^o , θ_{zB}= +1.31^o	

Beam-Column Specimen: S600-12-17

P=1.65 kips	P=4.57 kips	P=5.96 kips	P=4.98 kips
27% P$_m$	77% P$_m$	100% P$_m$	83% P$_m$

Note: Almost symmetric web local buckling (one big half wave) and consequent flange outward movement. Flange local buckling of the left flange within the post-peak stage.

MTS Raw Load–Displacement

Load–Displacement Curves

Pm=5.963 kips

δ_m=0.049 in. (PTs)

Rotation of Top and Bottom Plates

Eccentricity at the ends of specimen

Cross–Sectional Deformation at the Mid–point
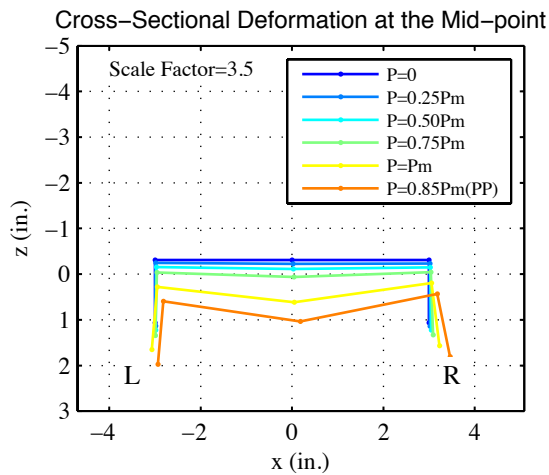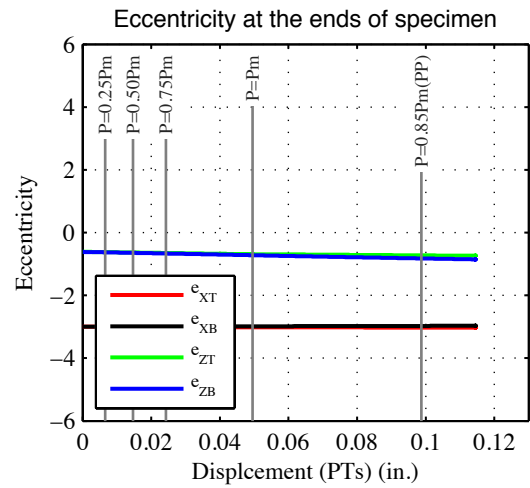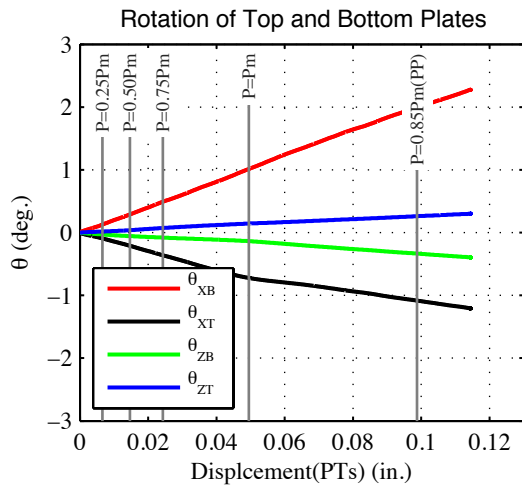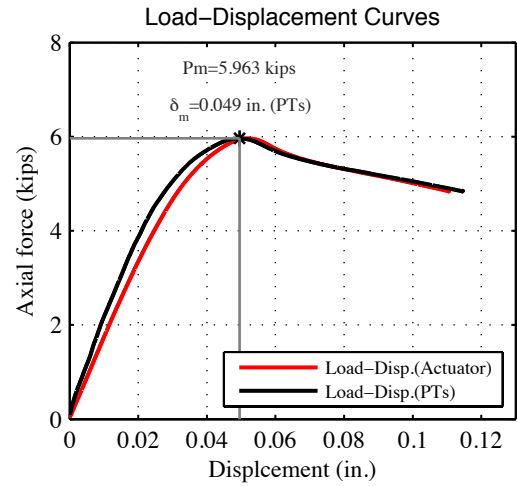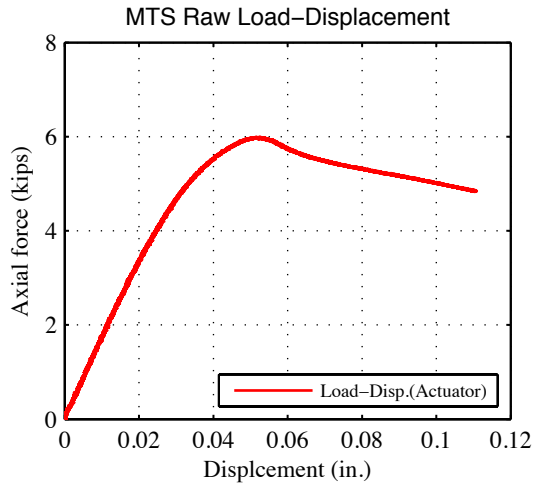
Specimen (S600-12-17) at post-peak stage (PP)

16- S600-12-e_x(-1.5)-e_z(-0.1)

Tested Specimen:	S600-12-3
Cross-section:	600S137-54 (SSMA Designation)
Date:	July 13th 2013

Left (L)   z   Right (R)

x

(Bottom to Top View)

Measured cross-section:

(Centroid position for the middle of the tested specimen)

0.3025

2.9647   3.0276

Test Description:	- Lipped C-channel Beam-column Test (Loading rate: 0.0025 in./sec) - Bi-axial bending and axial compression
Target eccentricity in x-dir (e_{x0}):	-1.5 (in.)
Target eccentricity in z-dir (e_{z0}):	-0.1019 (in.)
Provided ave. ecc. in x-dir (e_x):	-1.5 (in.)
Provided ave. ecc. in z-dir (e_z)-Top:	-0.105 (in.) Provided ave. ecc in z-dir (e_z)-Bot: -0.095 (in.)
Initial end plate angles:	θ_{xT}= -1.33^o , θ_{zT}= -0.23^o , θ_{xB}= +0.55^o , θ_{zB}= +0.03^o

Beam-Column Specimen: S600-12-3

P=3.37 kips	P=7.47 kips	P=10.85 kips	P=9.5 kips
31% P_m	69% P_m	100% P_m	87% P_m
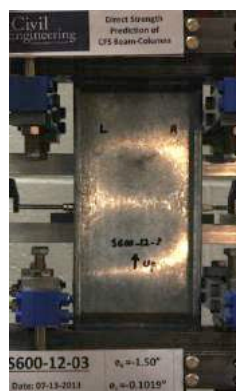
Note: Unsymmetrical (but almost symmetric) web local buckling (3 half-waves) and compression flange (left flange) local buckling. Web buckling was visible at about P=7.0 kips.

MTS Raw Load–Displacement

Load–Displacement Curves

Rotation of Top and Bottom Plates

Eccentricity at the ends of specimen

Cross−Sectional Deformation at the Mid−point
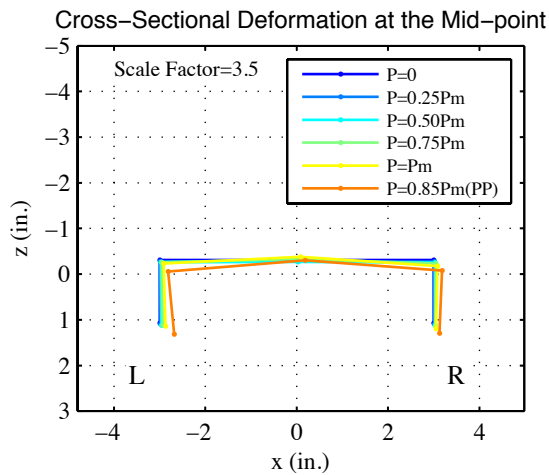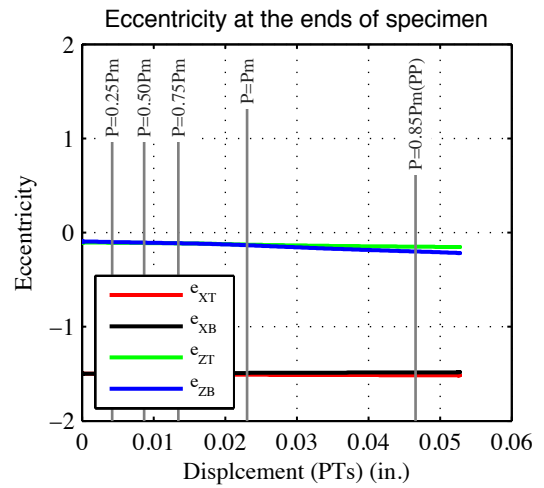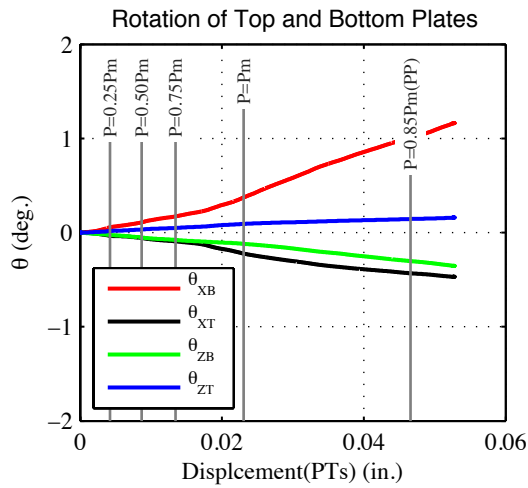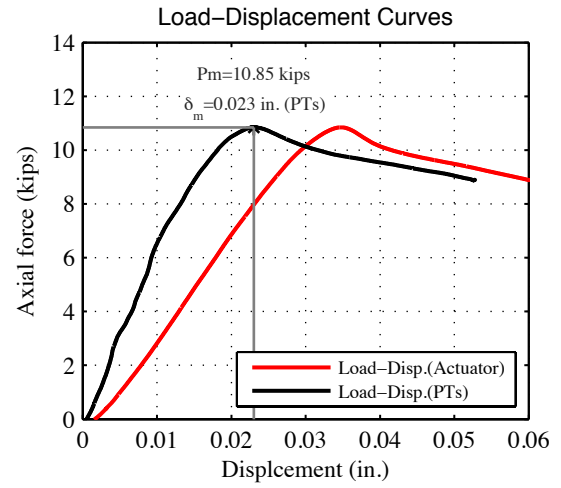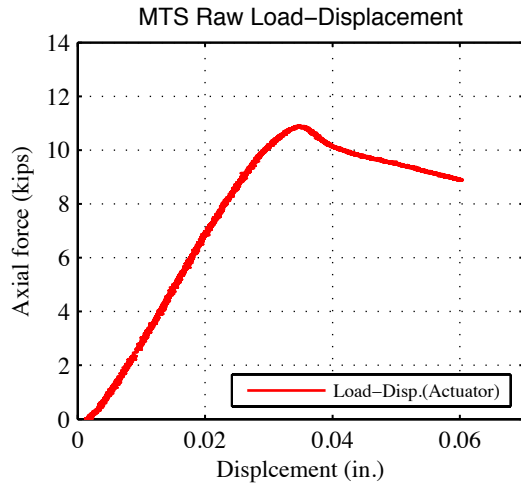
Specimen (S600-12-3) at post-peak stage (PP)

17- S600-12-e$_x$(-5.0)-e$_z$(-0.34)

Tested Specimen:	S600-12-20
Cross-section:	600S137-54 (SSMA Designation)
Date:	July 13th 2013

Left (L)   z   Right (R)

x

(Bottom to Top View)

Measured cross-section:

(Centroid position for the middle of the tested specimen)

0.2984

2.9718   3.0599

Test Description:	- Lipped C-channel Beam-column Test (Loading rate: 0.0025 in./sec) - Bi-axial bending and axial compression	
Target eccentricity in x-dir (e$_{x0}$):	-5.0 (in.)	
Target eccentricity in z-dir (e$_{z0}$):	-0.3397 (in.)	
Provided ave. ecc. in x-dir (e$_x$):	-5.0 (in.)	
Provided ave. ecc. in z-dir (e$_z$)-Top:	-0.335 (in.) Provided ave. ecc in z-dir (e$_z$)-Bot:	-0.338 (in.)
Initial end plate angles:	θ_{xT}= -1.30^o , θ_{zT}= -0.14^o , θ_{xB}= +0.60^o , θ_{zB}= +0.05^o	

Beam-Column Specimen: S600-12-20

P=1.7 kips	P=4.2 kips	P=5.61 kips	P=4.76 kips
30% P$_m$	75% P$_m$	100% P$_m$	84% P$_m$
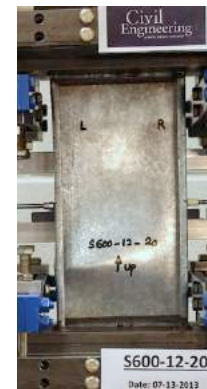
Note: Unsymmetrical web local buckling and left flange local buckling (3-half waves). Twisting was seen after the peak load. Web buckling was visible at about P=+5.0 kips.

MTS Raw Load–Displacement

Load–Displacement Curves

Pm=5.616 kips

δ_m=0.047 in. (PTs)

Rotation of Top and Bottom Plates

Eccentricity at the ends of specimen

Cross–Sectional Deformation at the Mid–point

Scale Factor=3.5
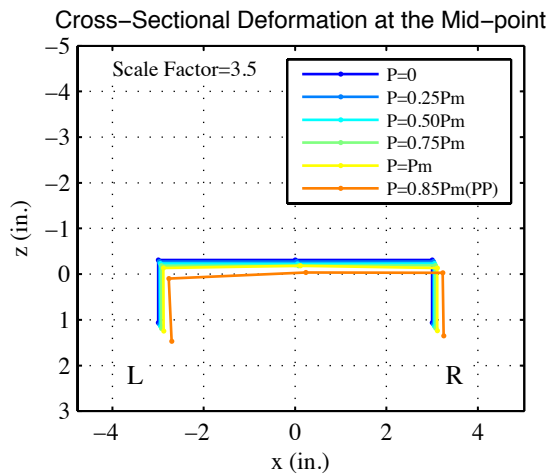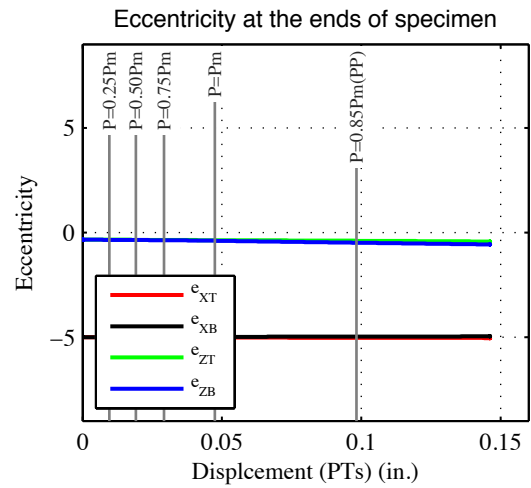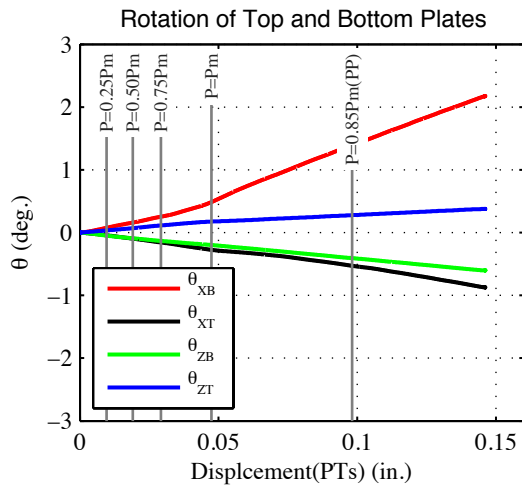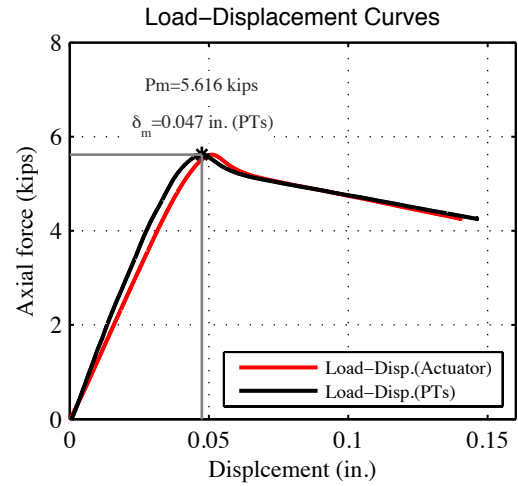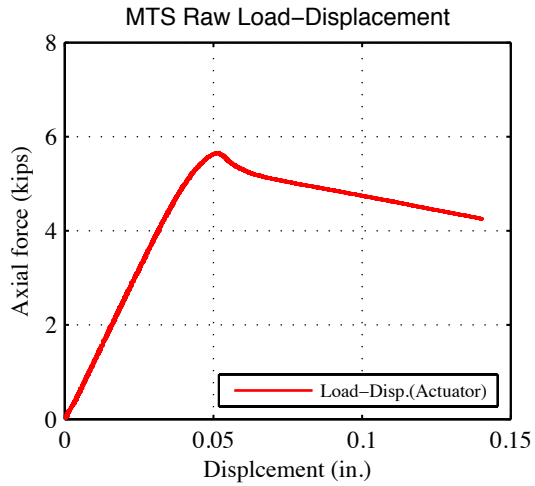
Specimen (S600-12-20) at post-peak stage (PP)

F.2 Experiment results: Intermediate Specimens (S600-24)

1- S600-24-e_x(0)-e_z(-1.25)

Tested Specimen:	S600-24-1 (L=24 inches)
Cross-section:	600S137-54 (AISI-S200-12 nomenclature)
Date:	October 22th 2013
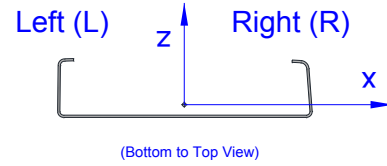
Left (L)   z   Right (R)

x

(Bottom to Top View)

Measured cross-section:

(Centroid position for the middle of the tested specimen)

0.3029

2.9788   3.0364
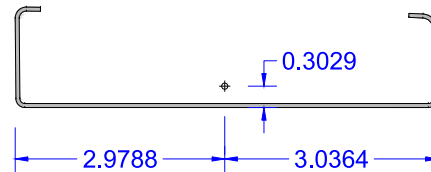
Test Description:	- Lipped C-channel Beam-column Test (Loading rate: 4.2×10^{-5} in./sec) - Minor axis (Lips in tension) bending moment and axial compression
Target eccentricity in x-dir (e_{x0}): 0.0 (in.)	Target eccentricity in z-dir (e_{z0}): -1.25 (in.)
Provided ave. ecc. in x-dir (e_x): ~0.0 (in.)	
Provided ave. ecc. in z-dir (e_z)-Top: -1.279 (in.)	Provided ave. ecc in z-dir (e_z)-Bot: -1.285 (in.)
Initial end plate angles:	θ_{xT}= -1.71^o , θ_{zT}= 0.84^o , θ_{xB}= 0.66^o , θ_{zB}= 0.59^o

Beam-Column Specimen: S600-24-1
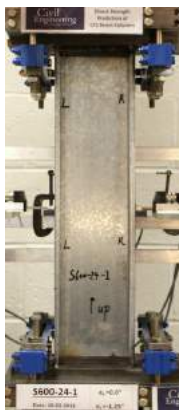
P=1.387 kips	P=3.076 kips	P=4.074 kips	P=3.387 kips
34% P_m	76% P_m	100% P_m	83% P_m (post-peak)

Note: Symmetric web local buckling along with consistent small flange deformations. Visible buckling waves at P=2.7 kips (3 half-waves).
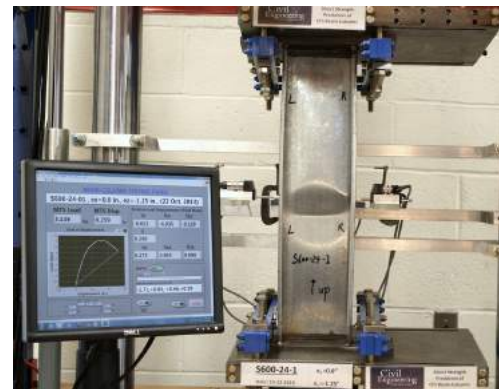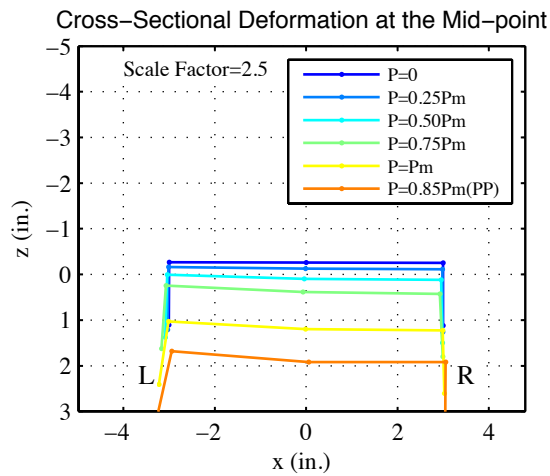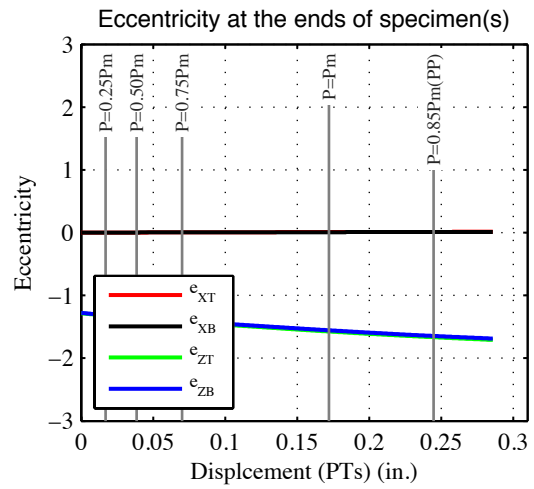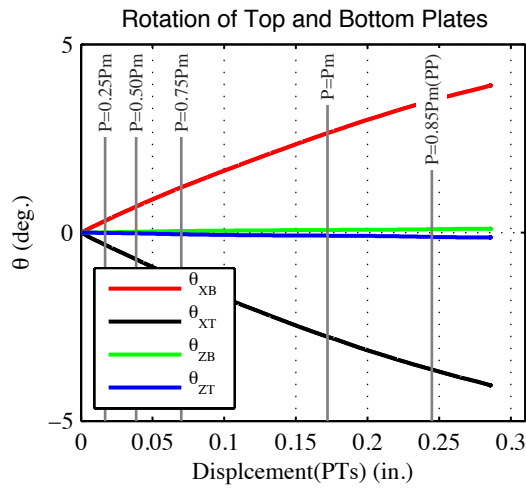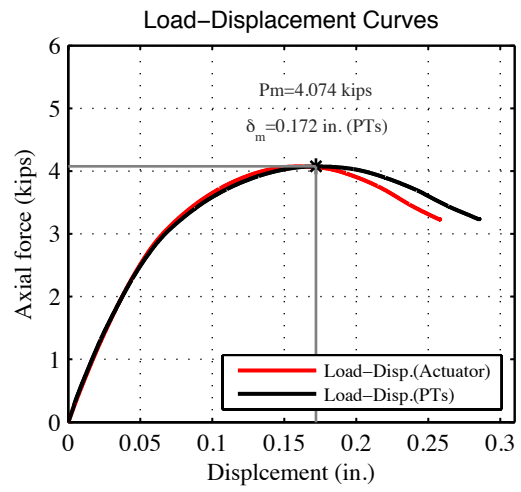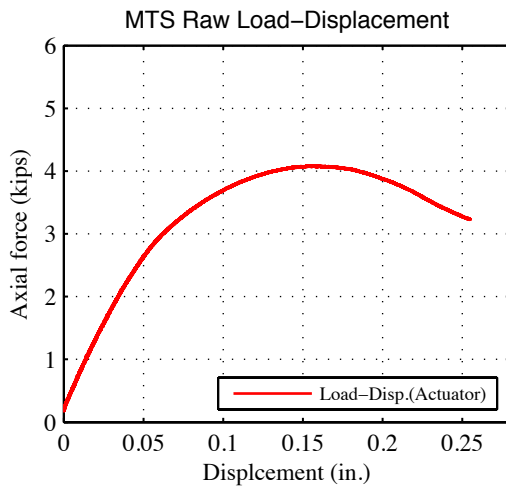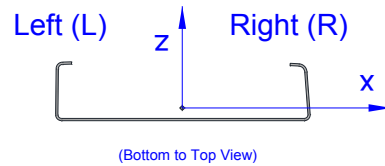
Specimen (S600-24-1) at post-peak stage (PP)

2- S600-24-e_x(0)-e_z(-0.6)

Tested Specimen:	S600-24-2 (L=24 inches)
Cross-section:	600S137-54 (AISI-S200-12 nomenclature)
Date:	October 23th 2013

Left (L) z Right (R)

x

(Bottom to Top View)

Measured cross-section:

(Centroid position for the middle of the tested specimen)

0.2995

2.9650   3.0424

Test Description:	- Lipped C-channel Beam-column Test (Loading rate: 6.6×10^{-5} in./sec) - Minor axis (Lips in tension) bending moment and axial compression
Target eccentricity in x-dir (e_{x0}): 0.0 (in.)	Target eccentricity in z-dir (e_{z0}): -0.6 (in.)
Provided ave. ecc. in x-dir (e_x): ~0.0 (in.)	
Provided ave. ecc. in z-dir (e_z)-Top: -0.609 (in.)	Provided ave. ecc in z-dir (e_z)-Bot: -0.595 (in.)
Initial end plate angles: θ_{xT}= -1.08^{o} , θ_{zT}= 0.74^{o} , θ_{xB}= 0.28^{o} , θ_{zB}= 1.18^{o}	

Beam-Column Specimen: S600-24-2

P=2.536 kips	P=5.318 kips	P=6.358 kips	P=5.280 kips
40% P_m	84% P_m	100% P_m	83% P_m (post-peak)

Note: Web local buckling (one big half wave at the mid-height) and consistent small flange deformations. Visible buckling waves at P=3.9 kips (5 half-waves).

MTS Raw Load–Displacement

Axial force (kips) vs. Displcement (in.)

Legend: Load−Disp.(Actuator)

Load–Displacement Curves

Axial force (kips) vs. Displcement (in.)

Pm=6.357 kips

δ_m =0.088 in. (PTs)

Legend: Load−Disp.(Actuator), Load−Disp.(PTs)

Rotation of Top and Bottom Plates

θ (deg.) vs. Displcement(PTs) (in.)

P=0.25Pm, P=0.50Pm, P=0.75Pm, P=Pm, P=0.85Pm(PP)

Legend: θ_{XB}, θ_{XT}, θ_{ZB}, θ_{ZT}

Eccentricity at the ends of specimen(s)

Eccentricity vs. Displcement (PTs) (in.)

P=0.25Pm, P=0.50Pm, P=0.75Pm, P=Pm, P=0.85Pm(PP)

Legend: e_{XT}, e_{XB}, e_{ZT}, e_{ZB}

Cross−Sectional Deformation at the Mid−point

z (in.) vs. x (in.)

Scale Factor=2.5

Legend: P=0, P=0.25Pm, P=0.50Pm, P=0.75Pm, P=Pm, P=0.85Pm(PP)

L   R

Specimen (S600-24-2) at post-peak stage (PP)

301

3- S600-24-e$_x$(0)-e$_z$(-0.15)

Tested Specimen:	S600-24-3 (L=24 inches)
Cross-section:	600S137-54 (AISI-S200-12 nomenclature)
Date:	October 24th 2013

Left (L)   z   Right (R)

x

(Bottom to Top View)

Measured cross-section:

(Centroid position for the middle of the tested specimen)

0.3028

2.9763   3.0407

Test Description:	- Lipped C-channel Beam-column Test (Loading rate: 6.6×10^{-5} in./sec)
	- Minor axis (Lips in tension) bending moment and axial compression

Target eccentricity in x-dir (e$_{x0}$):	0.0 (in.)	Target eccentricity in z-dir (e$_{z0}$): -0.15 (in.)
Provided ave. ecc. in x-dir (e$_x$):	~0.0 (in.)	
Provided ave. ecc. in z-dir (e$_z$)-Top:	-0.160 (in.)	Provided ave. ecc in z-dir (e$_z$)-Bot: -0.139 (in.)
Initial end plate angles:	θ_{xT}= -1.56^o , θ_{zT}= 0.71^o , θ_{xB}= 0.30^o , θ_{zB}= 0.38^o	

Beam-Column Specimen: S600-24-3

P=4.068 kips	P=7.156 kips	P=9.747 kips	P=7.661 kips
42% P$_m$	73% P$_m$	100% P$_m$	79% P$_m$ (post-peak)

Note: Web local buckling (3 half-waves) along with consistent small flange deformations. Small offset of the mid-wave from the mid-height.

MTS Raw Load−Displacement

Load−Displacement Curves

Pm=9.747 kips

δ_m=0.047 in. (PTs)

Eccentricity at the ends of specimen(s)

P=0.25Pm P=0.50Pm P=0.75Pm P=Pm P=0.85Pm(PP)

Eccentricity at the ends of specimen(s)

P=0.25Pm P=0.50Pm P=0.75Pm P=Pm P=0.85Pm(PP)

Cross−Sectional Deformation at the Mid−point

Scale Factor=2.5

P=0
P=0.25Pm
P=0.50Pm
P=0.75Pm
P=Pm
P=0.85Pm(PP)

L   R
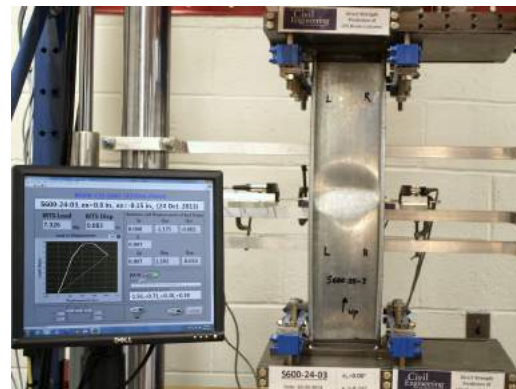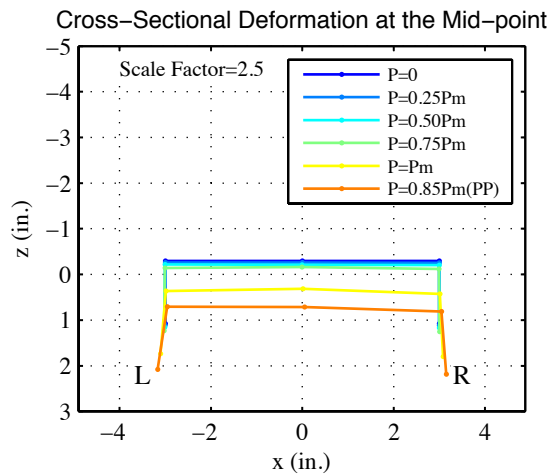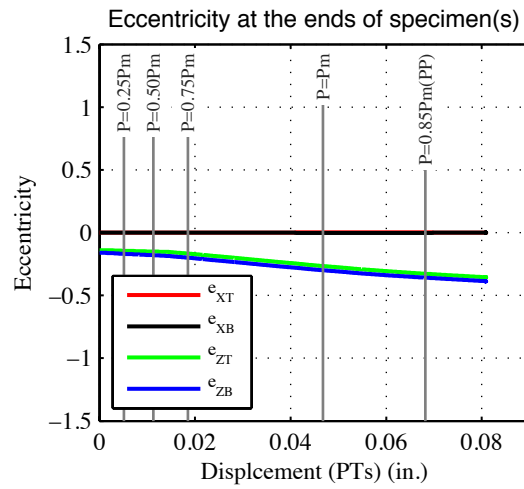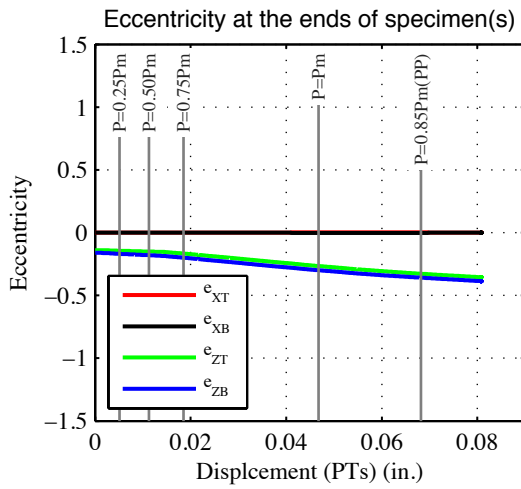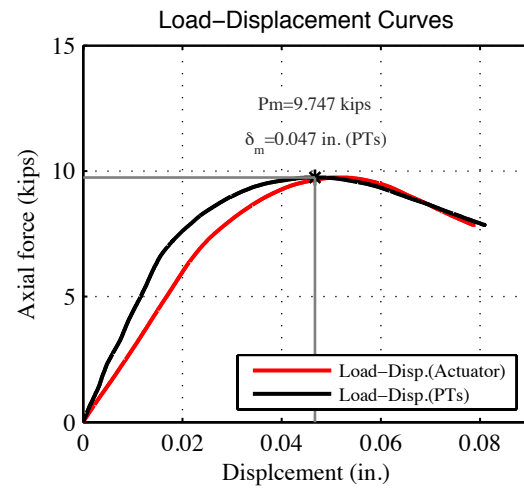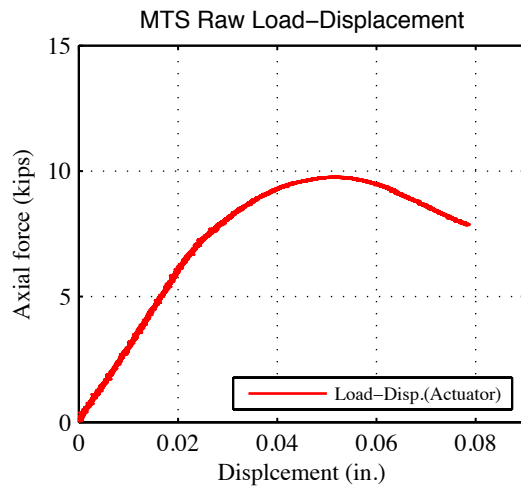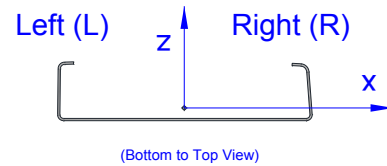
Specimen (S600-24-3) at post-peak stage (PP)

4- S600-24-e$_x$(0)-e$_z$(0.15)

Tested Specimen:	S600-24-6 (L=24 inches)
Cross-section:	600S137-54 (AISI-S200-12 nomenclature)
Date:	October 28th 2013

Left (L)   z   Right (R)   x

(Bottom to Top View)

Measured cross-section:

(Centroid position for the middle of the tested specimen)

0.2936

2.9439   3.0213

Test Description:	- Lipped C-channel Beam-column Test (Loading rate: 6.6×10^{-5} in./sec) - Minor axis (Lips in compression) bending moment and axial compression

Target eccentricity in x-dir (e$_{x0}$):	0.0 (in.)	Target eccentricity in z-dir (e$_{z0}$):	+0.15 (in.)
Provided ave. ecc. in x-dir (e$_x$):	~0.0 (in.)		
Provided ave. ecc. in z-dir (e$_z$)-Top:	+0.153 (in.)	Provided ave. ecc in z-dir (e$_z$)-Bot:	+0.149 (in.)
Initial end plate angles:	θ_{xT}= -1.6^o , θ_{zT}= 0.20^o , θ_{xB}= 1.12^o , θ_{zB}= 1.24^o		

Beam-Column Specimen: S600-24-6
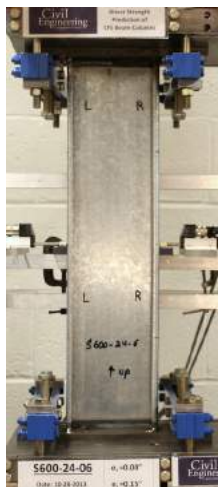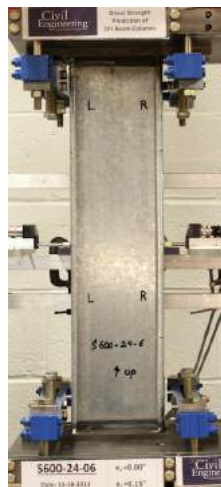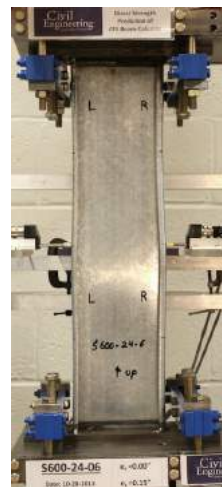
P=3.735 kips	P=8.136 kips	P=10.558 kips	P=8.722 kips
35% P$_m$	77% P$_m$	100% P$_m$	83% P$_m$ (post-peak)

Note: Distortional local buckling in both flanges along with consistent web deformations. Visible distortional buckling waves at P=8.0 kips.
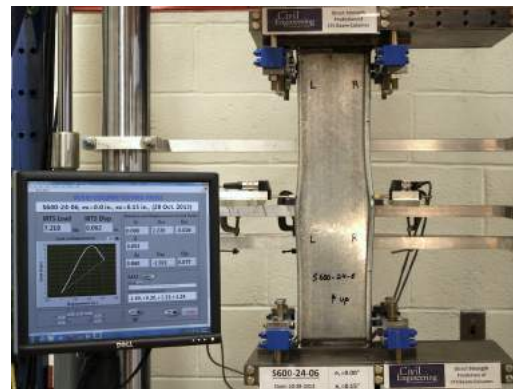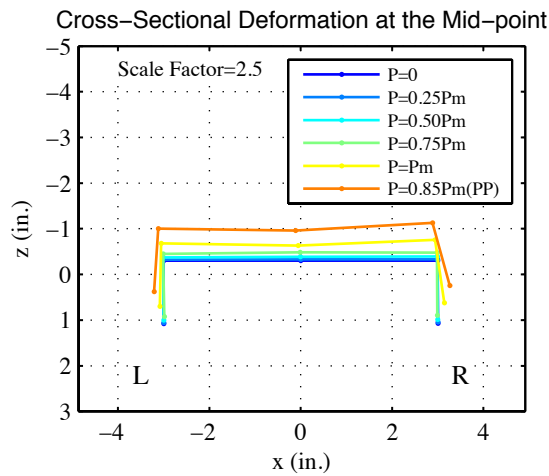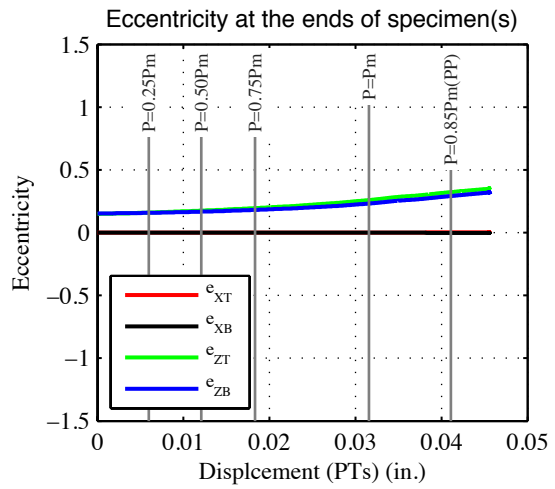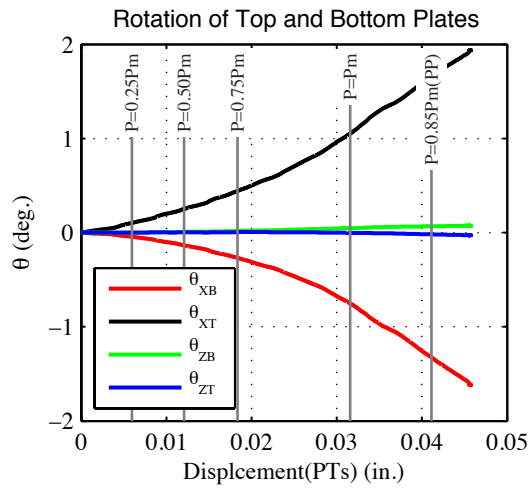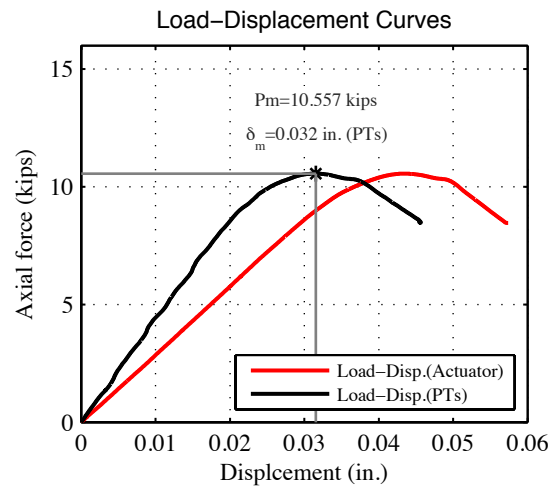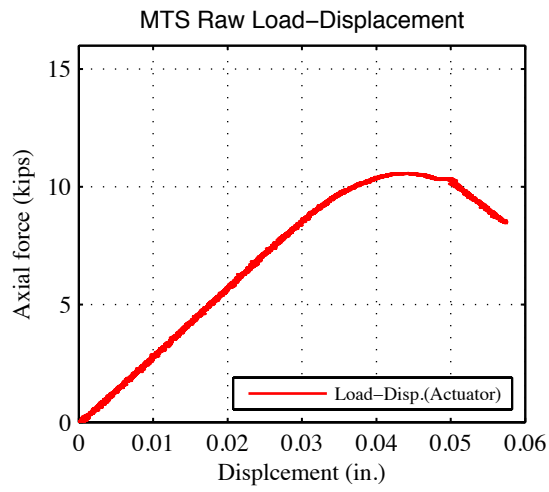
Specimen (S600-24-6) at post-peak stage (PP)

5- S600-24-e$_x$(0)-e$_z$(0.6)

Tested Specimen:	S600-24-5 (L=24 inches)
Cross-section:	600S137-54 (AISI-S200-12 nomenclature)
Date:	October 25th 2013

Left (L)   z   Right (R)

x

(Bottom to Top View)

Measured cross-section:

(Centroid position for the middle of the tested specimen)

0.3030

2.9793   3.0289

Test Description:	- Lipped C-channel Beam-column Test (Loading rate: 6.6×10^{-5} in./sec) - Minor axis (Lips in compression) bending moment and axial compression
Target eccentricity in x-dir (e$_{x0}$):	0.0 (in.) Target eccentricity in z-dir (e$_{z0}$): +0.6 (in.)
Provided ave. ecc. in x-dir (e$_x$):	~0.0 (in.)
Provided ave. ecc. in z-dir (e$_z$)-Top:	+0.614 (in.) Provided ave. ecc in z-dir (e$_z$)-Bot: +0.600 (in.)
Initial end plate angles:	θ_{xT}= -1.3^o , θ_{zT}= 0.67^o , θ_{xB}= 0.48^o , θ_{zB}= 0.06^o

Beam-Column Specimen: S600-24-5
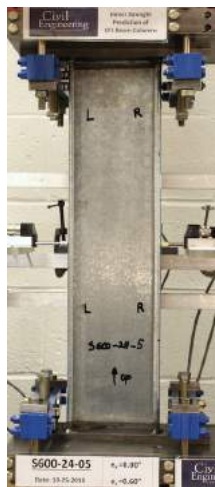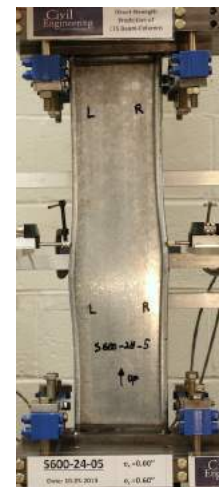
P=2.646 kips	P=4.03 kips	P=5.630 kips	P=4.787 kips
47% P$_m$	72% P$_m$	100% P$_m$	85% P$_m$ (post-peak)

Note: Flange distortional buckling along with very small consistent web deformations. Visible distortional buckling wave at P=4.0 first in the left flange.

MTS Raw Load–Displacement

Load–Displacement Curves

Pm=5.629 kips

δ_m =0.055 in. (PTs)

Rotation of Top and Bottom Plates

Eccentricity at the ends of specimen(s)

Cross–Sectional Deformation at the Mid–point
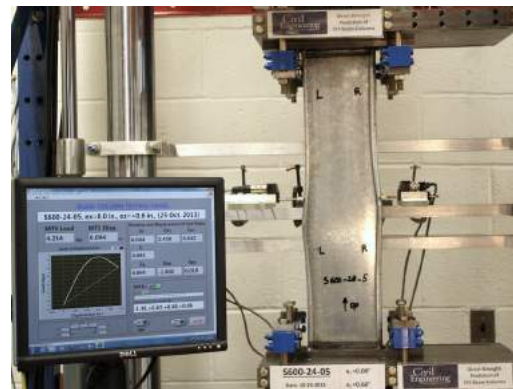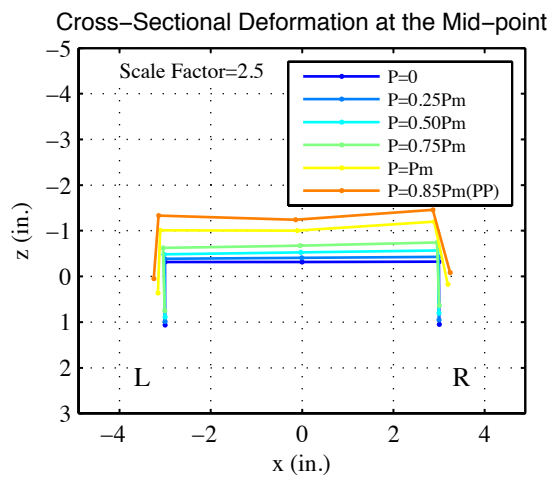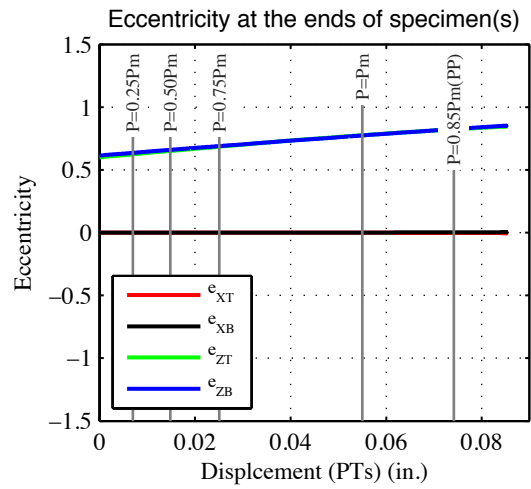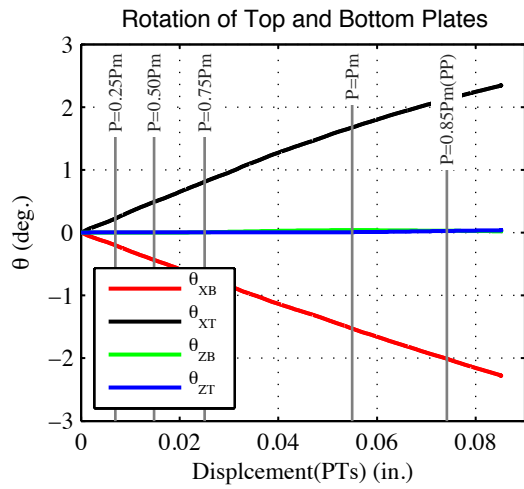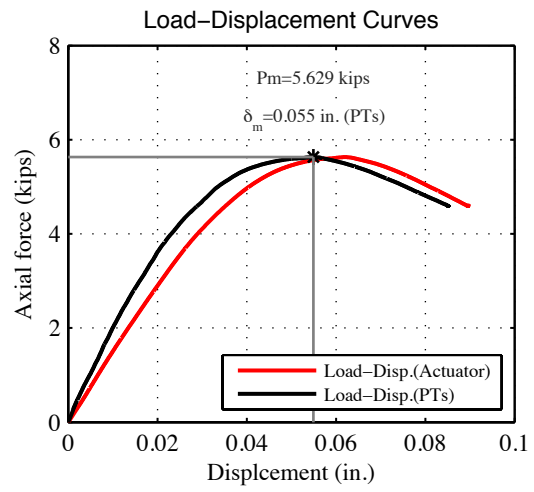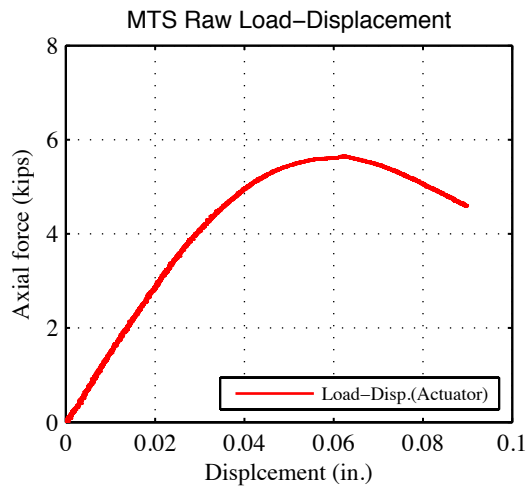
Specimen (S600-24-5) at post-peak stage (PP)

6- S600-24-e$_x$(0)-e$_z$(1.25)

Tested Specimen:	S600-24-4 (L=24 inches)
Cross-section:	600S137-54 (AISI-S200-12 nomenclature)
Date:	October 24th 2013

Left (L)   z   Right (R)

x

(Bottom to Top View)

Measured cross-section:

(Centroid position for the middle of the tested specimen)

0.3045

2.9533   3.0319

Test Description:	- Lipped C-channel Beam-column Test (Loading rate: 6.6×10^{-5} in./sec) - Minor axis (Lips in compression) bending moment and axial compression
Target eccentricity in x-dir (e$_{x0}$):	0.0 (in.) Target eccentricity in z-dir (e$_{z0}$): +1.25 (in.)
Provided ave. ecc. in x-dir (e$_x$):	~0.0 (in.)
Provided ave. ecc. in z-dir (e$_z$)-Top:	+1.2495 (in.) Provided ave. ecc in z-dir (e$_z$)-Bot: +1.212 (in.)
Initial end plate angles:	θ_{xT}= -1.36^o , θ_{zT}= 0.25^o , θ_{xB}= 0.23^o , θ_{zB}= 1.08^o

Beam-Column Specimen: S600-24-4
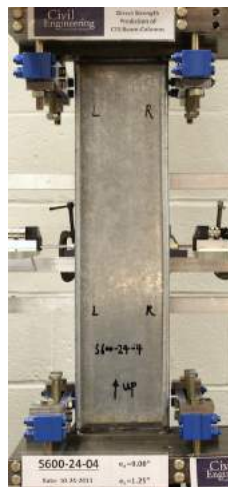
P=1.273 kips	P=2.829 kips	P=3.618 kips	P=2.924 kips
35% P$_m$	78% P$_m$	100% P$_m$	81% P$_m$ (post-peak)

Note: Distortional buckling in both flanges and consistent small web deformations. Larger initial imperfection in the right flange resulted in initiation of buckling.

MTS Raw Load–Displacement

Load–Displacement Curves

Pm=3.618 kips

δ_m =0.097 in. (PTs)

Load–Disp.(Actuator)
Load–Disp.(PTs)

Rotation of Top and Bottom Plates

P=0.25Pm
P=0.50Pm
P=0.75Pm
P=Pm
P=0.85Pm(PP)

θ_{XB}
θ_{XT}
θ_{ZB}
θ_{ZT}

Eccentricity at the ends of specimen(s)

P=0.25Pm
P=0.50Pm
P=0.75Pm
P=Pm
P=0.85Pm(PP)

e_{XT}
e_{XB}
e_{ZT}
e_{ZB}

Cross–Sectional Deformation at the Mid–point

Scale Factor=2.5

P=0
P=0.25Pm
P=0.50Pm
P=0.75Pm
P=Pm
P=0.85Pm(PP)

L

R

Specimen (S600-24-4) at post-peak stage (PP)

7- S600-24-e_x(-0.85)-e_z(0.0)

Tested Specimen:	S600-24-7 (L=24 inches)
Cross-section:	600S137-54 (AISI-S200-12 nomenclature)
Date:	October 23th 2013

Left (L)   z   Right (R)

x

(Bottom to Top View)

Measured cross-section:

(Centroid position for the middle of the tested specimen)

0.3019

2.9682   3.0234

Test Description:	- Lipped C-channel Beam-column Test (Loading rate: 6.6×10^{-5} in./sec) - Major axis bending and axial compression
Target eccentricity in x-dir (e_{x0}): -0.85 (in.)	Target eccentricity in z-dir (e_{z0}): 0.0 (in.)
Provided ave. ecc. in x-dir (e_x): -0.87 (in.)	
Provided ave. ecc. in z-dir (e_z)-Top: 0.004 (in.)	Provided ave. ecc in z-dir (e_z)-Bot: 0.020 (in.)
Initial end plate angles:	θ_{xT}= -1.20^o , θ_{zT}= -0.25^o , θ_{xB}= 0.25^o , θ_{zB}= 0.26^o

Beam-Column Specimen: S600-24-7
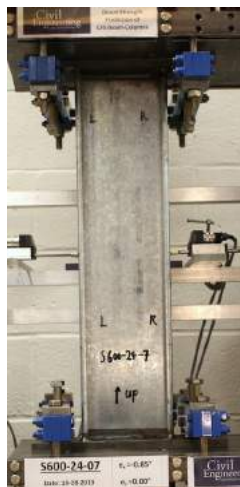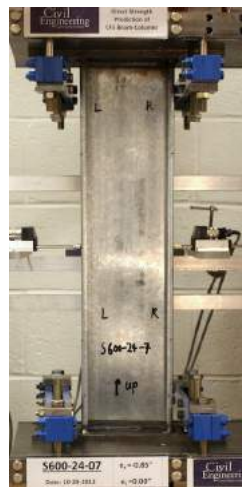
P=4.552 kips	P=9.467 kips	P=12.980 kips	P=9.955 kips
35% P_m	73% P_m	100% P_m	77% P_m (post-peak)

Note: Local buckling waves in the web at P=7kips followed by flange distortional buckling of the left flange at P=10 kips and the consistent web deformations.

MTS Raw Load−Displacement

Load−Displacement Curves

Pm=13.003 kips

δ_m =0.043 in. (PTs)

Rotation of Top and Bottom Plates

P=0.25Pm
P=0.50Pm
P=0.75Pm
P=Pm
P=0.85Pm(PP)

θ_{XB}
θ_{XT}
θ_{ZB}
θ_{ZT}

Eccentricity at the ends of specimen(s)

P=0.25Pm
P=0.50Pm
P=0.75Pm
P=Pm
P=0.85Pm(PP)

e_{XT}
e_{XB}
e_{ZT}
e_{ZB}

Cross−Sectional Deformation at the Mid−point

Scale Factor=2.5

P=0
P=0.25Pm
P=0.50Pm
P=0.75Pm
P=Pm
P=0.85Pm(PP)

L   R
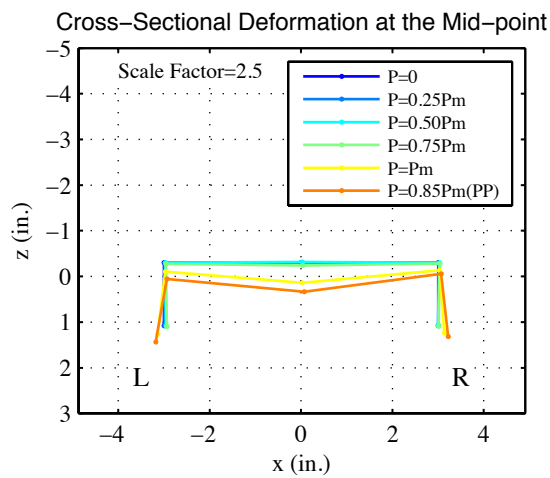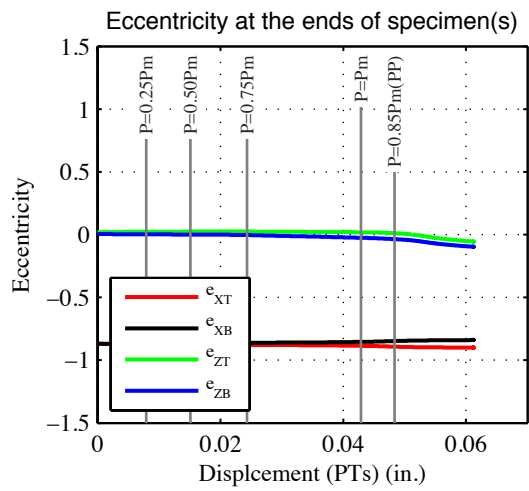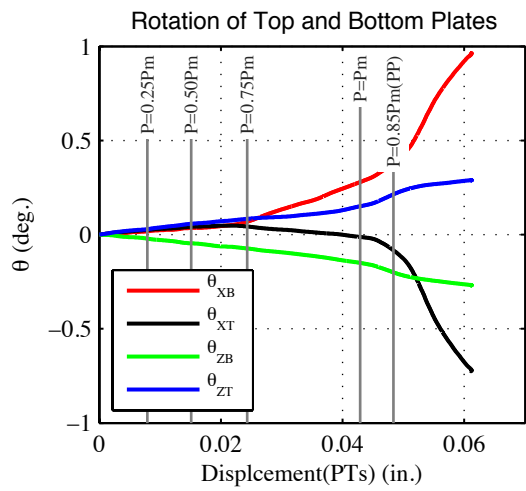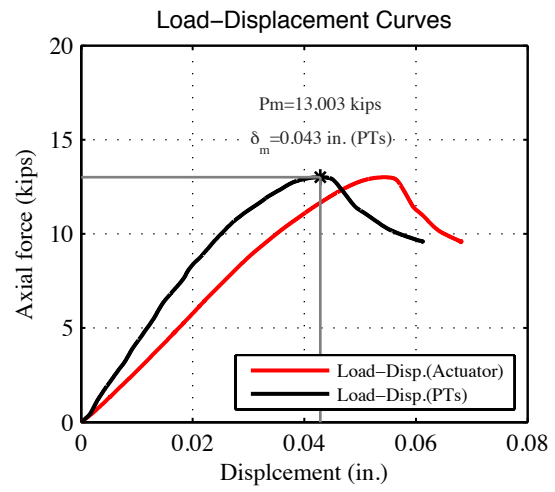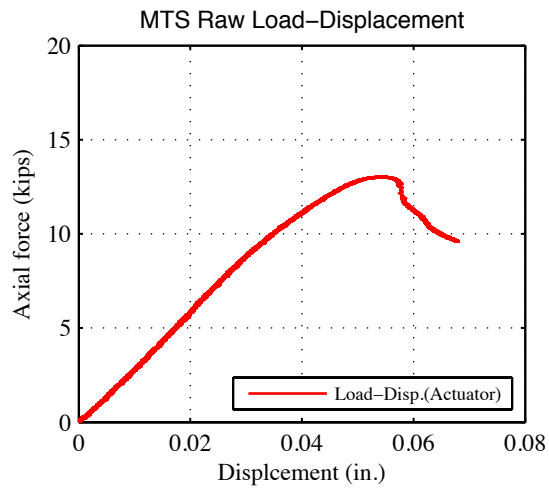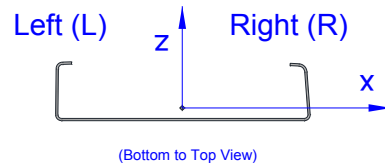
Specimen (S600-24-7) at post-peak stage (PP)

311

8- S600-24-e$_x$(-3.0)-e$_z$(0.0)

Tested Specimen:	S600-24-8 (L=24 inches)
Cross-section:	600S137-54 (AISI-S200-12 nomenclature)
Date:	October 28th 2013

Left (L) z Right (R)

x

(Bottom to Top View)

Measured cross-section:

(Centroid position for the middle of the tested specimen)

0.3028

2.9650   3.0320

Test Description:	- Lipped C-channel Beam-column Test (Loading rate: 6.6×10^{-5} in./sec) - Major axis bending and axial compression

Target eccentricity in x-dir (e$_{x0}$):	-3.0 (in.)	Target eccentricity in z-dir (e$_{z0}$):	0.0 (in.)

Provided ave. ecc. in x-dir (e$_x$): -3.0 (in.)

Provided ave. ecc. in z-dir (e$_z$)-Top: 0.003 (in.)   Provided ave. ecc in z-dir (e$_z$)-Bot: 0.003 (in.)

Initial end plate angles: θ_{xT}= -1.45 , θ_{zT}= 0.53^o , θ_{xB}= 0.45^o , θ_{zB}= -0.09^o

Beam-Column Specimen: S600-24-8

P=3.062 kips	P=7.220 kips	P=7.803 kips	P=6.572 kips
40% P$_m$	92% P$_m$	100% P$_m$	84% P$_m$ (post-peak)
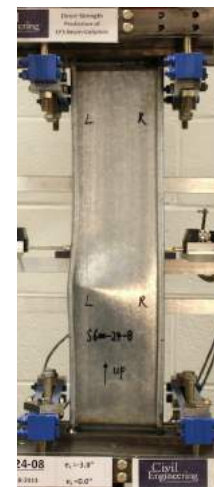
Note: Flange distortional buckling of the left flange first at P=6.8 kips followed by consistent web deformations. Maximum flange movement at one-third of the height.

MTS Raw Load–Displacement

Load–Displacement Curves

Pm=7.817 kips

δ_m=0.055 in. (PTs)

Rotation of Top and Bottom Plates

P=0.25Pm
P=0.50Pm
P=0.75Pm
P=Pm
P=0.85Pm(PP)

θ_{XB}
θ_{XT}
θ_{ZB}
θ_{ZT}

Eccentricity at the ends of specimen(s)

P=0.25Pm
P=0.50Pm
P=0.75Pm
P=Pm
P=0.85Pm(PP)

e_{XT}
e_{XB}
e_{ZT}
e_{ZB}

Cross−Sectional Deformation at the Mid−point

Scale Factor=2.5

P=0
P=0.25Pm
P=0.50Pm
P=0.75Pm
P=Pm
P=0.85Pm(PP)

L   R
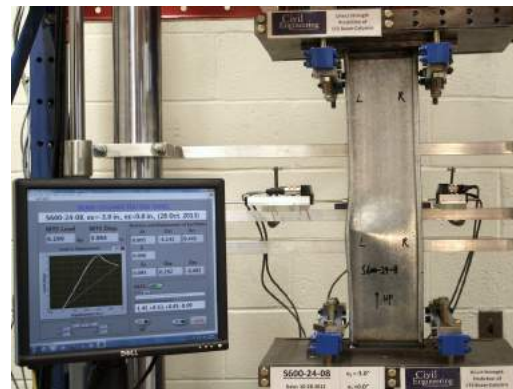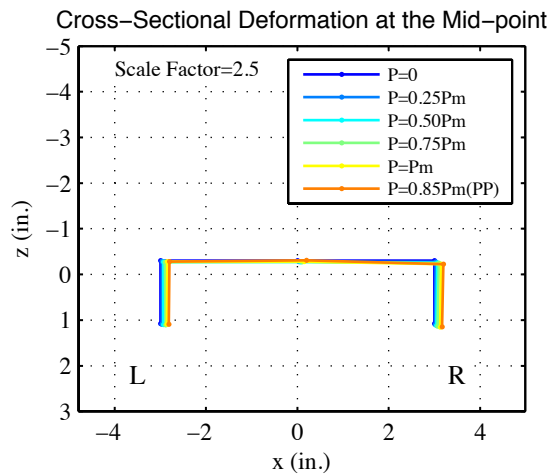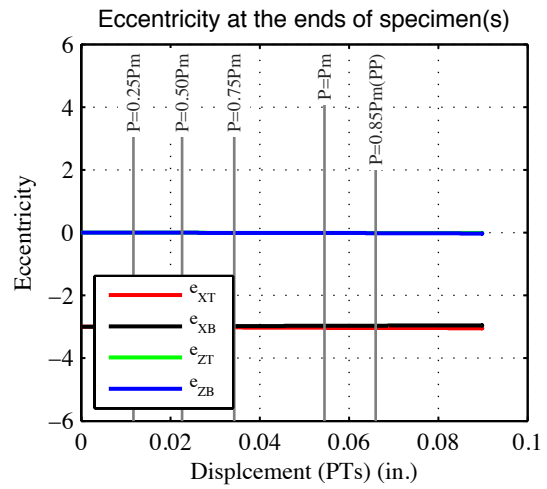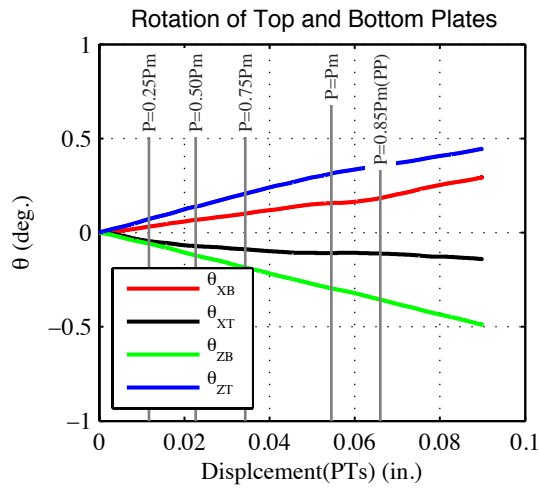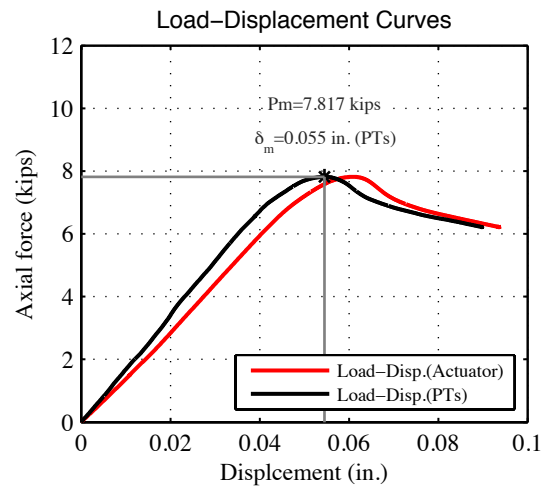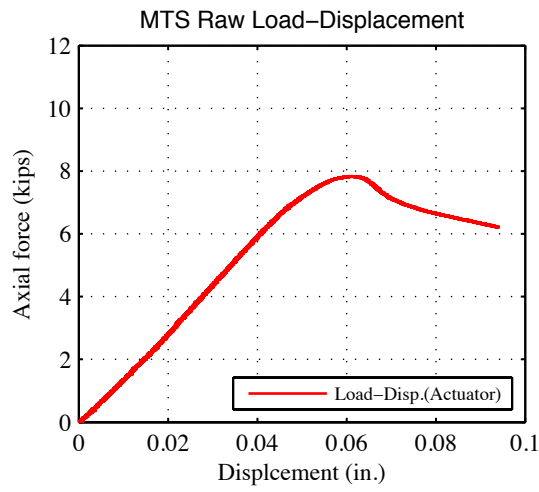
Specimen (S600-24-8) at post-peak stage (PP)

313

9- S600-24-e$_x$(-6.5)-e$_z$(0.0)

Tested Specimen:	S600-24-9 (L=24 inches)
Cross-section:	600S137-54 (AISI-S200-12 nomenclature)
Date:	October 28th 2013

Left (L)   z   Right (R)

x

(Bottom to Top View)

Measured cross-section:

(Centroid position for the middle of the tested specimen)

0.2995

2.9650   3.0424

Test Description:	- Lipped C-channel Beam-column Test (Loading rate: 6.6×10^{-5} in./sec) - Major axis bending and axial compression
Target eccentricity in x-dir (e$_{x0}$): -6.5 (in.)	Target eccentricity in z-dir (e$_{z0}$): 0.0 (in.)
Provided ave. ecc. in x-dir (e$_x$): -6.5 (in.)	
Provided ave. ecc. in z-dir (e$_z$)-Top: 0.006 (in.)	Provided ave. ecc in z-dir (e$_z$)-Bot: -0.012 (in.)
Initial end plate angles:	θ_{xT}= -1.71^o , θ_{zT}= 0.76^o , θ_{xB}= 0.17^o , θ_{zB}= 0.81^o

Beam-Column Specimen: S600-24-9

| P=2.013 kips | P=4.028 kips | P=4.831 kips | P=4.013 kips |
| 42% P$_m$ | 83% P$_m$ | 100% P$_m$ | 83% P$_m$ (post-peak) |

Note: Flange distortional buckling of the left flange first at P=4.0 kips followed by consistent web deformations. Large inward flange movement at the end of the test.

MTS Raw Load–Displacement

Load–Displacement Curves

Pm=4.837 kips

δ_m=0.113 in. (PTs)

Rotation of Top and Bottom Plates

Eccentricity at the ends of specimen(s)

Cross–Sectional Deformation at the Mid–point
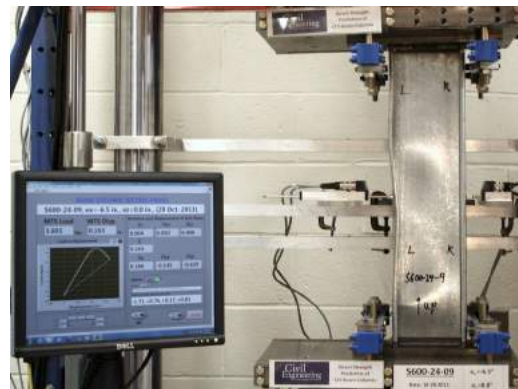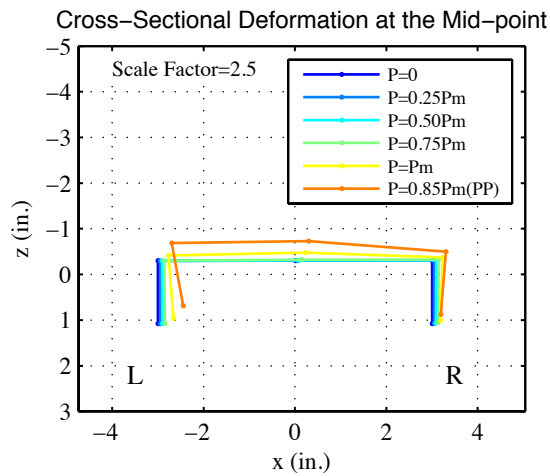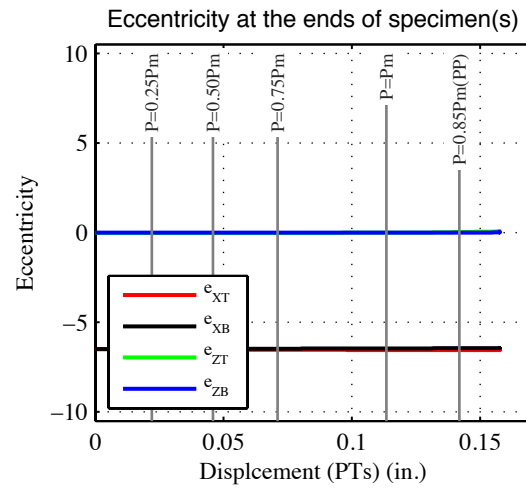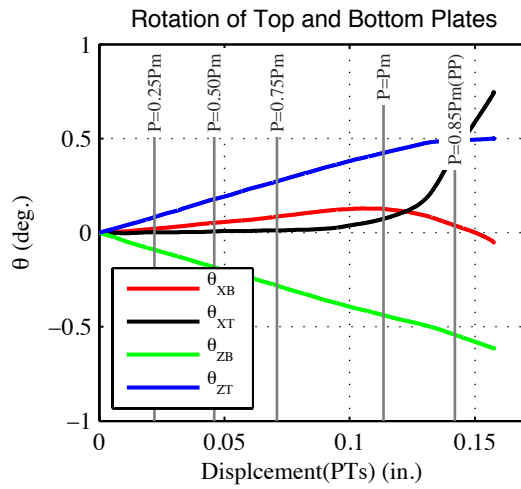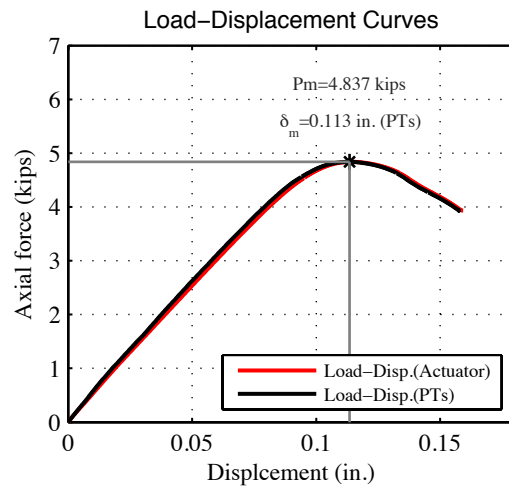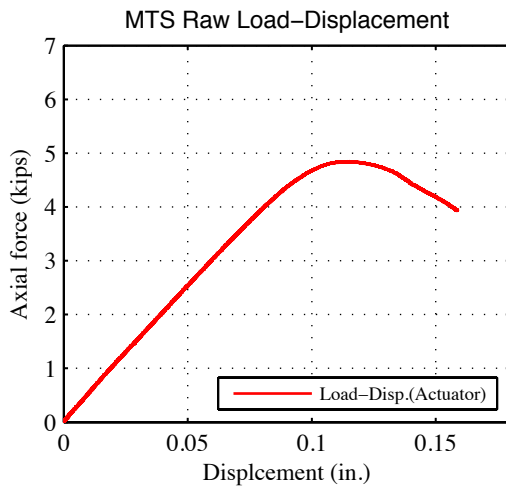
Specimen (S600-24-9) at post-peak stage (PP)

10- S600-24-e_x(-1.25)-e_z(0.09)

Tested Specimen:	S600-24-10 (L=24 inches)
Cross-section:	600S137-54 (AISI-S200-12 nomenclature)
Date:	October 29th 2013

Left (L)   z   Right (R)

x

(Bottom to Top View)

Measured cross-section:

(Centroid position for the middle of the tested specimen)

0.3028

2.9825   3.0285

Test Description:	- Lipped C-channel Beam-column Test (Loading rate: 6.6×10^{-5} in./sec) - Bi-axial bending and axial compression
Target eccentricity in x-dir (e_{x0}): -1.25 (in.)	Target eccentricity in z-dir (e_{z0}): +0.085 (in.)
Provided ave. ecc. in x-dir (e_x): -1.25 (in.)	
Provided ave. ecc. in z-dir (e_z)-Top: 0.088 (in.)	Provided ave. ecc in z-dir (e_z)-Bot: 0.094 (in.)
Initial end plate angles: θ_{xT}= -1.49^o , θ_{zT}= 1.12^o , θ_{xB}= 0.29^o , θ_{zB}= 0.51^o	

Beam-Column Specimen: S600-24-10

P=4.224 kips	P=8.844 kips	P=11.215 kips	P=9.45 kips
38% P_m	79% P_m	100% P_m	84% P_m (post-peak)

Note: Web local buckling and flange distortional buckling of the left flange first at P=7.0 kips. Large inward flange movement at the mid-height at the end of the test.

MTS Raw Load−Displacement

Load−Displacement Curves

Pm=11.242 kips

δ_m=0.038 in. (PTs)

Rotation of Top and Bottom Plates

Eccentricity at the ends of specimen(s)

Cross−Sectional Deformation at the Mid−point

Scale Factor=2.5
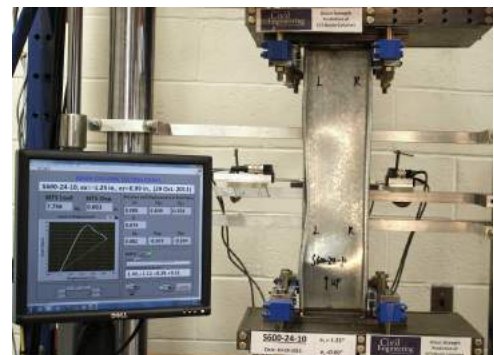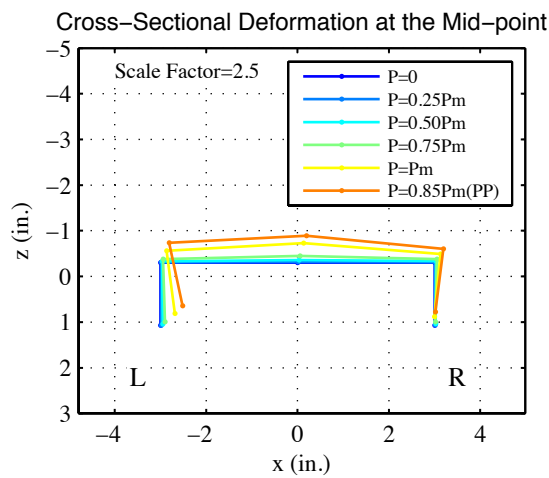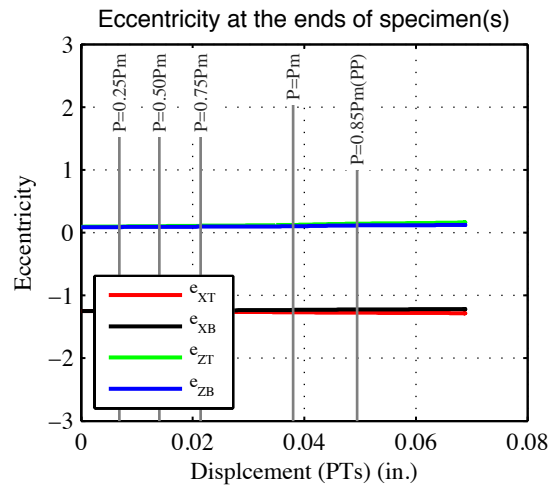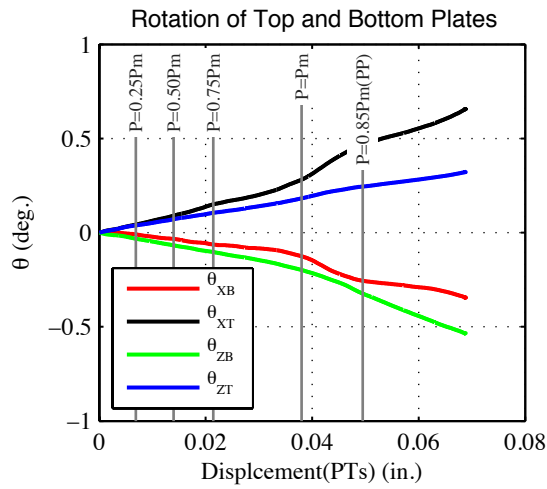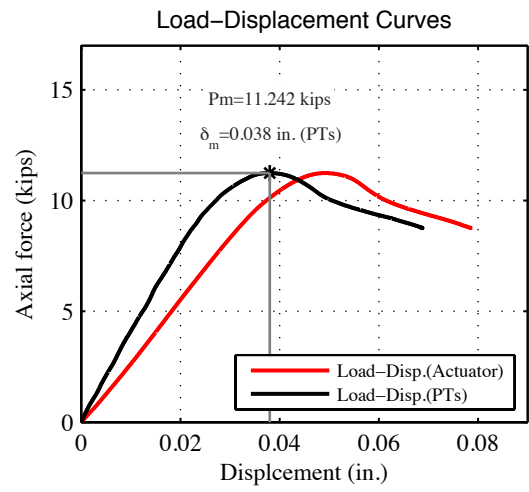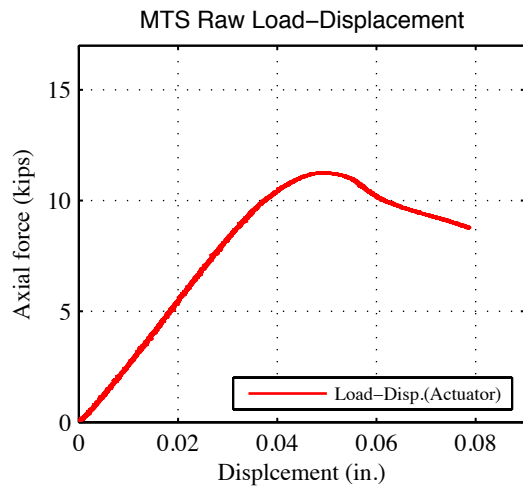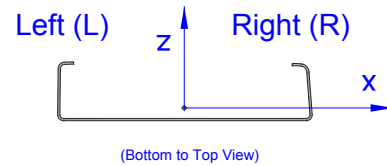
Specimen (S600-24-10) at post-peak stage (PP)

11- S600-24-e$_x$(-4.50)-e$_z$(0.31)

Tested Specimen:	S600-24-11 (L=24 inches)
Cross-section:	600S137-54 (AISI-S200-12 nomenclature)
Date:	October 29th 2013

Left (L) z Right (R)

x

(Bottom to Top View)

Measured cross-section:

(Centroid position for the middle of the tested specimen)

0.3070

2.9643   3.0301

Test Description:	- Lipped C-channel Beam-column Test (Loading rate: 7.5×10^{-5} in./sec) - Bi-axial bending and axial compression
Target eccentricity in x-dir (e$_{x0}$): -4.50 (in.)	Target eccentricity in z-dir (e$_{z0}$): +0.31 (in.)
Provided ave. ecc. in x-dir (e$_x$): -4.50 (in.)	
Provided ave. ecc. in z-dir (e$_z$)-Top: 0.331 (in.)	Provided ave. ecc in z-dir (e$_z$)-Bot: 0.365 (in.)
Initial end plate angles: θ_{xT}= -1.04^o , θ_{zT}= -0.17^o , θ_{xB}= 0.37^o , θ_{zB}= 0.70^o	

Beam-Column Specimen: S600-24-11

P=2.547 kips	P=3.993 kips	P=4.962 kips	P=4.015 kips
51% P$_m$	80% P$_m$	100% P$_m$	81% P$_m$ (post-peak)
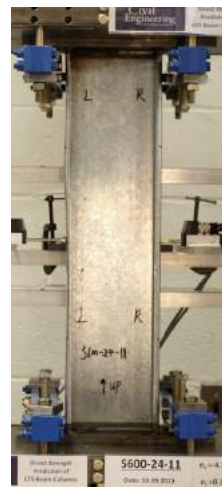
Note: Flange distortional buckling of the left flange first visible at P=4.0 kips. Outward flange buckling at two-third of the height at the end of the test.

MTS Raw Load−Displacement

Load−Displacement Curves

Pm=4.967 kips

δ_m =0.064 in. (PTs)

Rotation of Top and Bottom Plates

Eccentricity at the ends of specimen(s)

Cross−Sectional Deformation at the Mid−point

Scale Factor=2.5
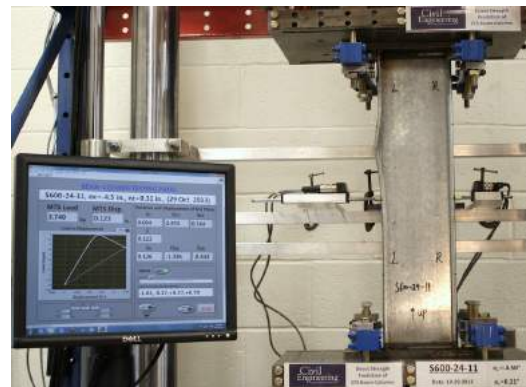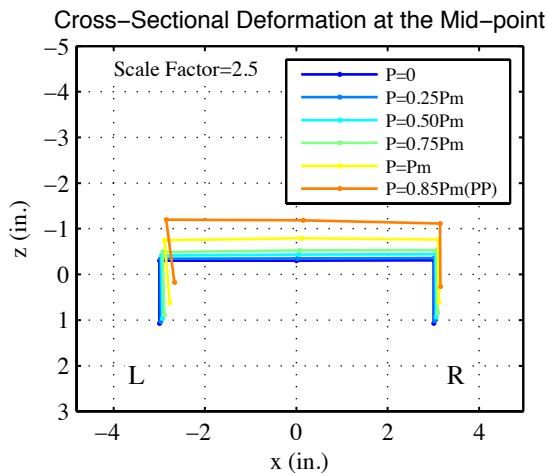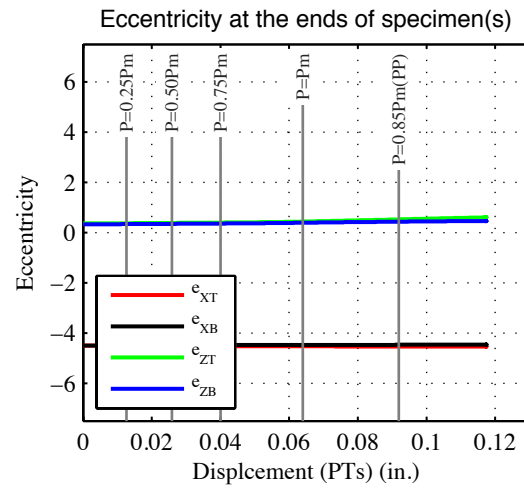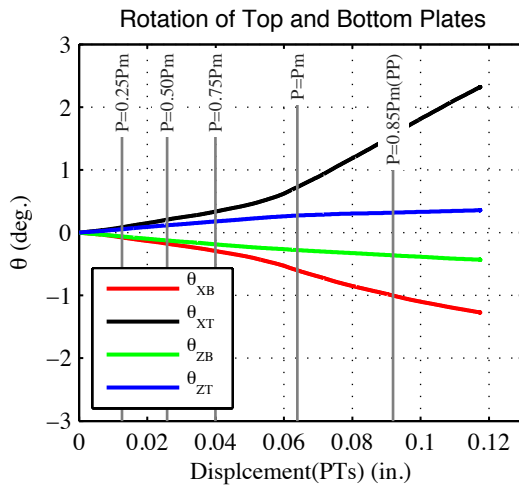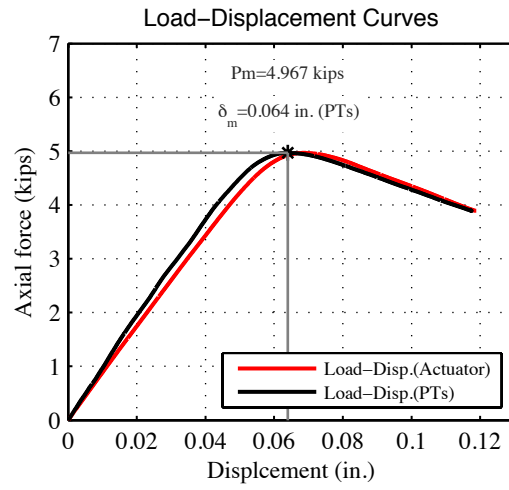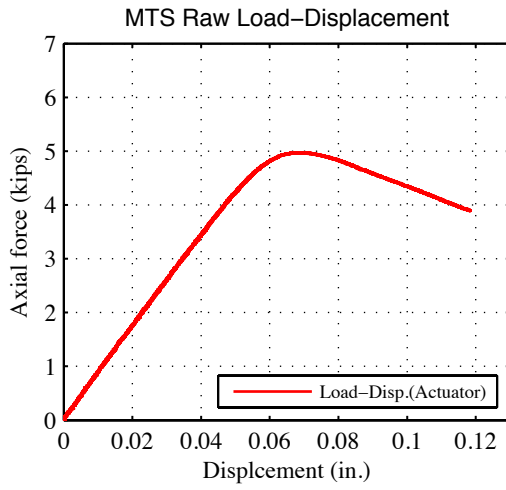
Specimen (S600-24-11) at post-peak stage (PP)

319

12- S600-24-e_x(-0.75)-e_z(0.15)

Tested Specimen:	S600-24-10 (L=24 inches)	
Cross-section:	600S137-54 (AISI-S200-12 nomenclature)	
Date:	October 30th 2013	

Left (L)   z   Right (R)

x

(Bottom to Top View)

Measured cross-section:

(Centroid position for the middle of the tested specimen)

0.3038

2.9717   3.0467

Test Description:	- Lipped C-channel Beam-column Test (Loading rate: 7.5×10^{-5} in./sec) - Bi-axial bending and axial compression
Target eccentricity in x-dir (e_{x0}): -0.75 (in.)	Target eccentricity in z-dir (e_{z0}): +0.15 (in.)
Provided ave. ecc. in x-dir (e_x): -0.75 (in.)	
Provided ave. ecc. in z-dir (e_z)-Top: 0.169 (in.)	Provided ave. ecc in z-dir (e_z)-Bot: 0.169 (in.)
Initial end plate angles:	θ_{xT}= -2.23^o , θ_{zT}= 0.51^o , θ_{xB}= 0.09^o , θ_{zB}= 0.52^o
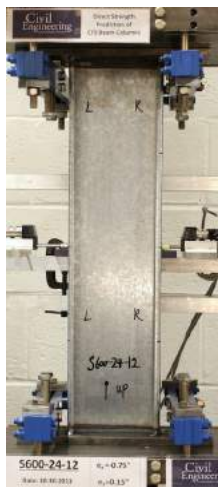
Beam-Column Specimen: S600-24-12

P=4.173 kips	P=8.14 kips	P=10.045 kips	P=7.932 kips
41% P_m	81% P_m	100% P_m	79% P_m (post-peak)
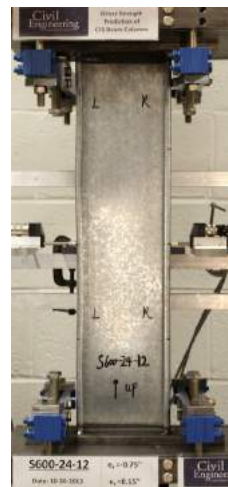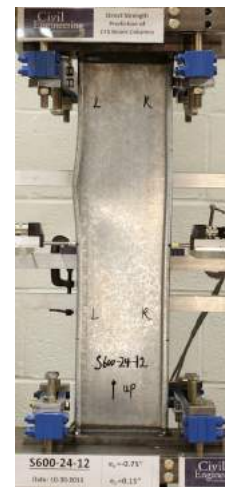
Note: Flange distortional buckling of the left flange. Outward flange buckling at two-third of the height at the end of the test.

MTS Raw Load−Displacement

Load−Displacement Curves

Pm=10.056 kips

δ_m =0.028 in. (PTs)

Rotation of Top and Bottom Plates

Eccentricity at the ends of specimen(s)

Cross−Sectional Deformation at the Mid−point

Scale Factor=2.5
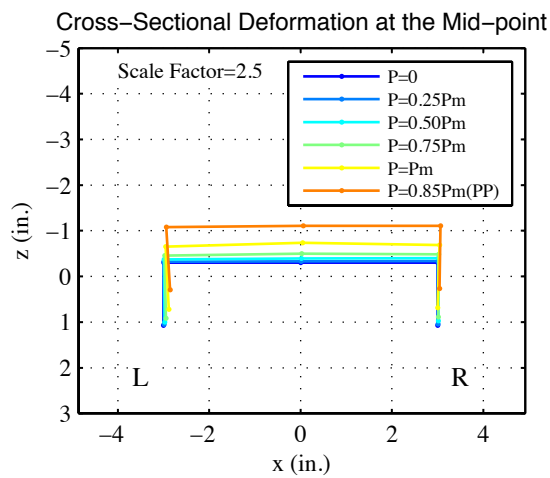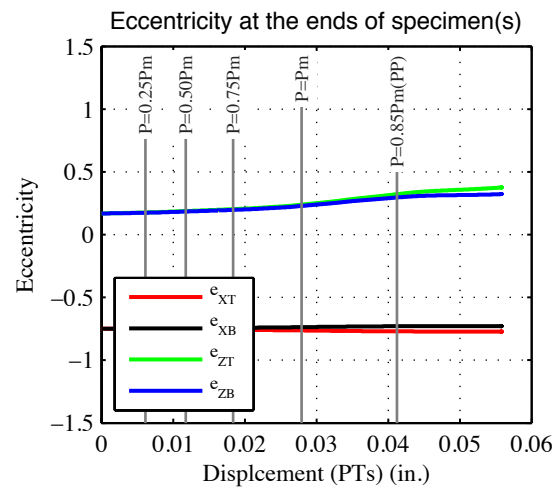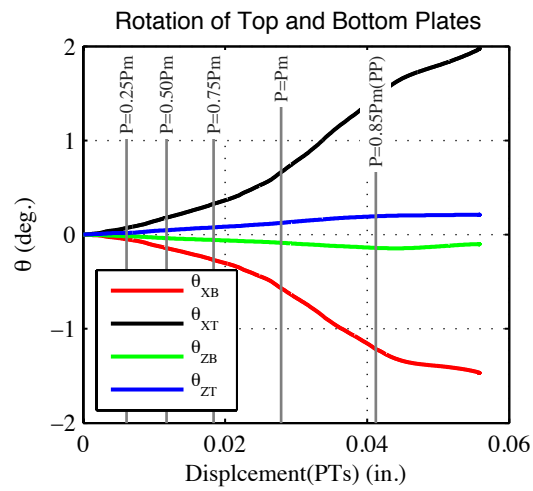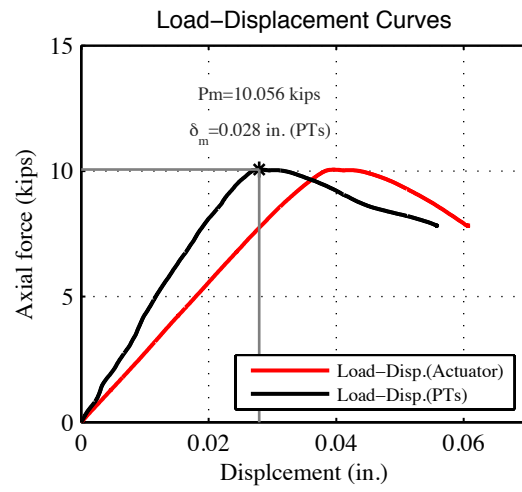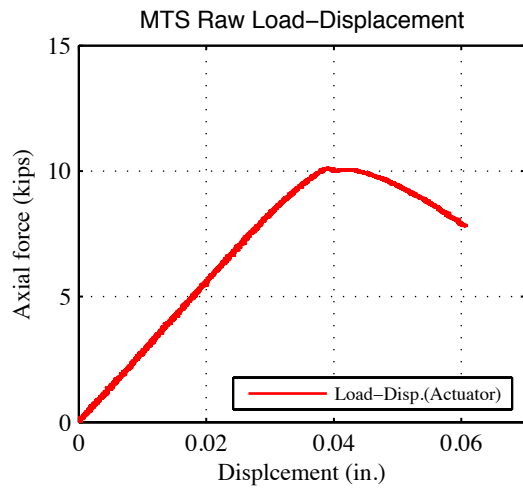
Specimen (S600-24-12) at post-peak stage (PP)

13- S600-24-e$_x$(-2.75)-e$_z$(0.56)

Tested Specimen:	S600-24-13 (L=24 inches)
Cross-section:	600S137-54 (AISI-S200-12 nomenclature)
Date:	October 30th 2013

Left (L)   z   Right (R)
x
(Bottom to Top View)

Measured cross-section:

(Centroid position for the middle of the tested specimen)

0.3006

2.9726   3.0456

Test Description:	- Lipped C-channel Beam-column Test (Loading rate: 6.6×10^{-5} in./sec) - Bi-axial bending and axial compression
Target eccentricity in x-dir (e$_{x0}$): -2.75 (in.)	Target eccentricity in z-dir (e$_{z0}$): +0.56 (in.)
Provided ave. ecc. in x-dir (e$_x$): -2.75 (in.)	
Provided ave. ecc. in z-dir (e$_z$)-Top: 0.592 (in.)	Provided ave. ecc in z-dir (e$_z$)-Bot: 0.572 (in.)
Initial end plate angles:	θ_{xT}= -1.1^o , θ_{zT}= 0.66^o , θ_{xB}= 0.30^o , θ_{zB}= 1.26^o

Beam-Column Specimen: S600-24-13

P=2.072 kips	P=3.832 kips	P=4.955 kips	P=3.931 kips
42% P$_m$	77% P$_m$	100% P$_m$	79% P$_m$ (post-peak)

Note: Flange distortional buckling of the left flange first visible at P=4.0 kips. Outward flange buckling at one-third of the height at the end of the test.

MTS Raw Load−Displacement

Load−Displacement Curves

Rotation of Top and Bottom Plates

Eccentricity at the ends of specimen(s)

Cross−Sectional Deformation at the Mid−point
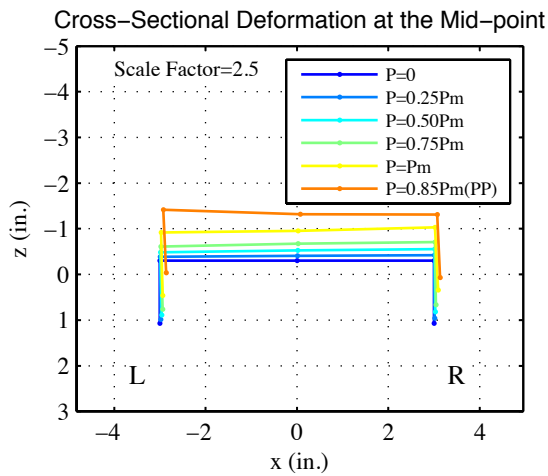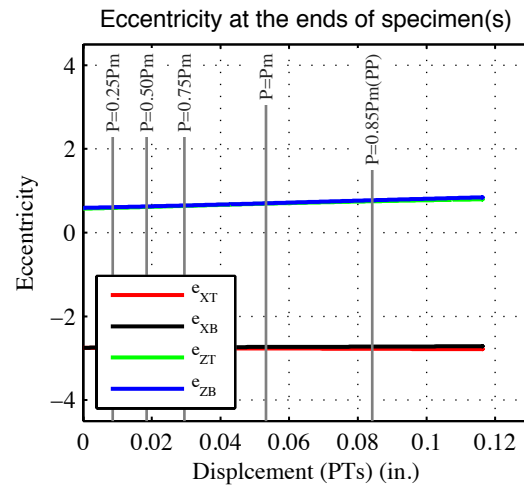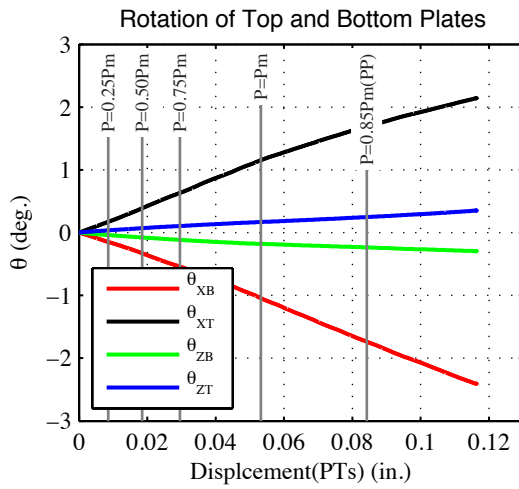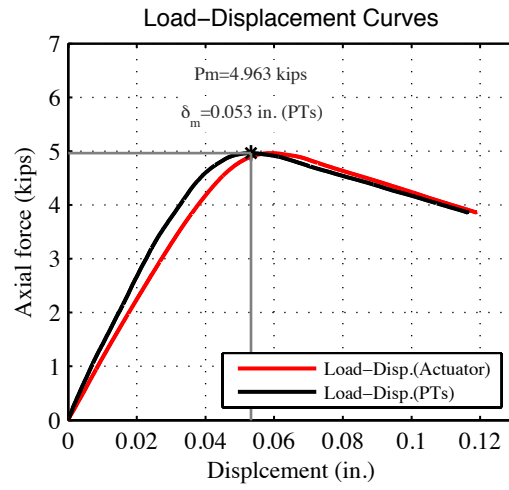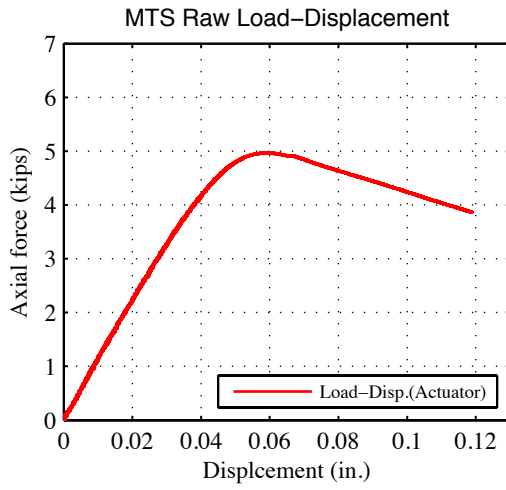
Specimen (S600-24-13) at post-peak stage (PP)

14- S600-24-e$_x$(-0.75)-e$_z$(-0.15)

Tested Specimen:	S600-24-14 (L=24 inches)
Cross-section:	600S137-54 (AISI-S200-12 nomenclature)
Date:	October 30th 2013

Left (L)   z   **Right (R)**   x

(Bottom to Top View)

Measured cross-section:

(Centroid position for the middle of the tested specimen)

0.3036

2.9812   3.0220

Test Description:	- Lipped C-channel Beam-column Test (Loading rate: 6.6×10^{-5} in./sec) - Bi-axial bending and axial compression
Target eccentricity in x-dir (e$_{x0}$): -0.75 (in.)	Target eccentricity in z-dir (e$_{z0}$): -0.15 (in.)

Provided ave. ecc. in x-dir (e$_x$):	-0.75 (in.)	
Provided ave. ecc. in z-dir (e$_z$)-Top:	-0.141 (in.)	Provided ave. ecc in z-dir (e$_z$)-Bot: -0.139 (in.)
Initial end plate angles:	θ_{xT}= -1.38^o , θ_{zT}= 0.05^o , θ_{xB}= 0.41^o , θ_{zB}= 0.91^o	

Beam-Column Specimen: S600-24-14
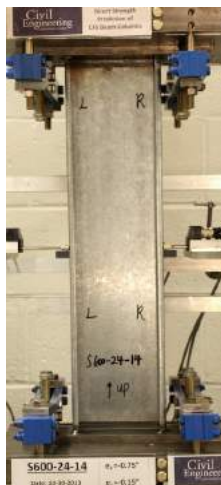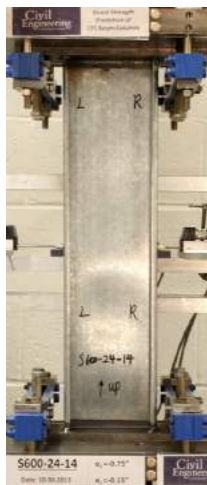
P=4.189 kips	P=7.903 kips	P=9.631 kips	P=7.763 kips
43% P$_m$	82% P$_m$	100% P$_m$	81% P$_m$ (post-peak)

Note: Web local buckling first visible at P=6.0 kips. Very small outward flange movement consistent with the web buckling.

324

MTS Raw Load−Displacement

Load−Displacement Curves

Pm=9.631 kips

δ_m =0.045 in. (PTs)

Load−Disp.(Actuator)

Load−Disp.(Actuator)
Load−Disp.(PTs)

Rotation of Top and Bottom Plates

P=0.25Pm
P=0.50Pm
P=0.75Pm
P=Pm
P=0.85Pm(PP)

θ_{XB}
θ_{XT}
θ_{ZB}
θ_{ZT}

Eccentricity at the ends of specimen(s)

P=0.25Pm
P=0.50Pm
P=0.75Pm
P=Pm
P=0.85Pm(PP)

e_{XT}
e_{XB}
e_{ZT}
e_{ZB}

Cross−Sectional Deformation at the Mid−point

Scale Factor=2.5

P=0
P=0.25Pm
P=0.50Pm
P=0.75Pm
P=Pm
P=0.85Pm(PP)

L   R
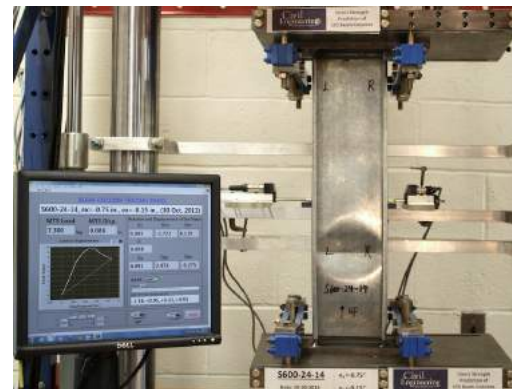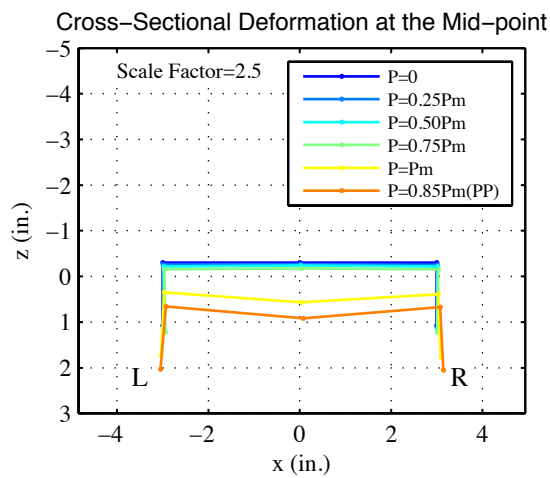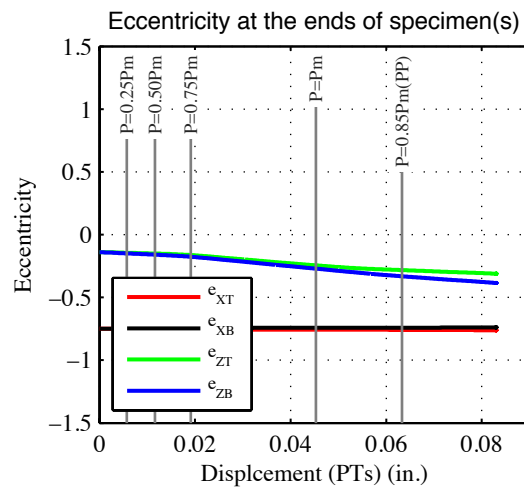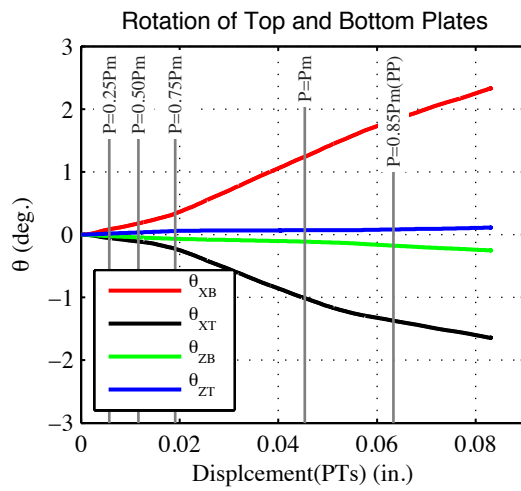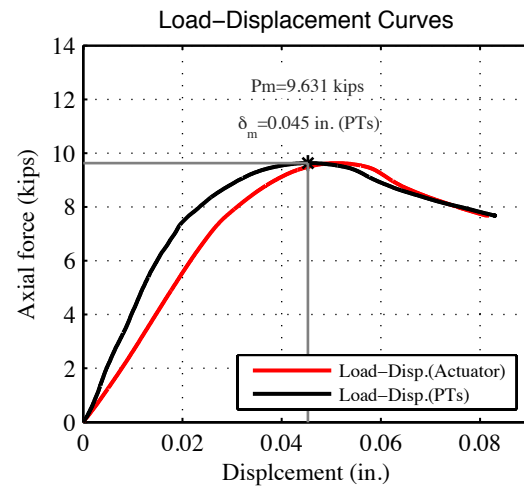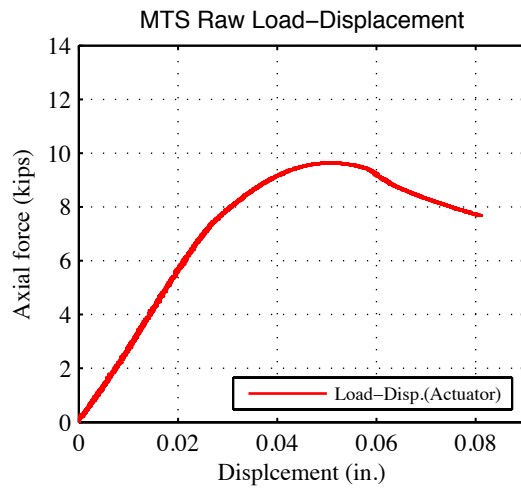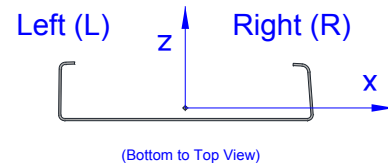
Specimen (S600-24-14) at post-peak stage (PP)

15- S600-24-e$_x$(-2.75)-e$_z$(-0.56)

Tested Specimen:	S600-24-15 (L=24 inches)
Cross-section:	600S137-54 (AISI-S200-12 nomenclature)
Date:	October 30th 2013

Left (L)   z   Right (R)

x

(Bottom to Top View)

Measured cross-section:

(Centroid position for the middle of the tested specimen)

0.2997

2.9442   3.0420

Test Description:	- Lipped C-channel Beam-column Test (Loading rate: 7.5×10^{-5} in./sec) - Bi-axial bending and axial compression
Target eccentricity in x-dir (e$_{x0}$): -2.75 (in.)	Target eccentricity in z-dir (e$_{z0}$): -0.56 (in.)
Provided ave. ecc. in x-dir (e$_x$): -2.75 (in.)	
Provided ave. ecc. in z-dir (e$_z$)-Top: -0.521 (in.)	Provided ave. ecc in z-dir (e$_z$)-Bot: -0.565 (in.)
Initial end plate angles: θ_{xT}= -1.66^o , θ_{zT}= 0.52^o , θ_{xB}= 0.06^o , θ_{zB}= 0.88^o	
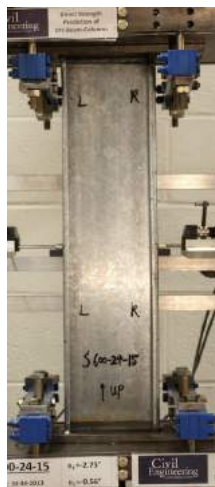
Beam-Column Specimen: S600-24-15

P=2.058 kips	P=4.202 kips	P=5.621 kips	P=4.477 kips
37% P$_m$	74% P$_m$	100% P$_m$	80% P$_m$ (post-peak)
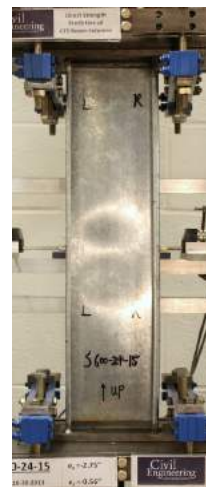
Note: Web local buckling first visible at P=4.3 kips (3 half-waves) and then turned into 5 half-waves. Very small outward flange movement.

MTS Raw Load–Displacement

Load–Displacement Curves

Pm=5.623 kips

δ_m=0.085 in. (PTs)

Rotation of Top and Bottom Plates

Eccentricity at the ends of specimen(s)

Cross–Sectional Deformation at the Mid–point

Scale Factor=2.5
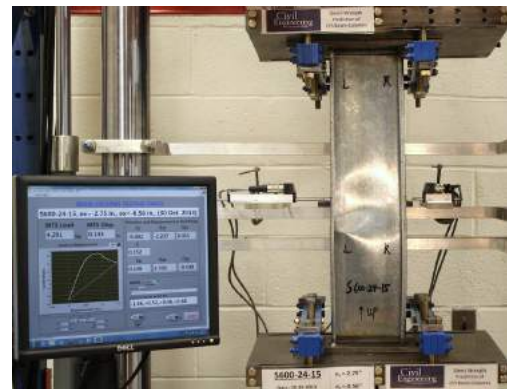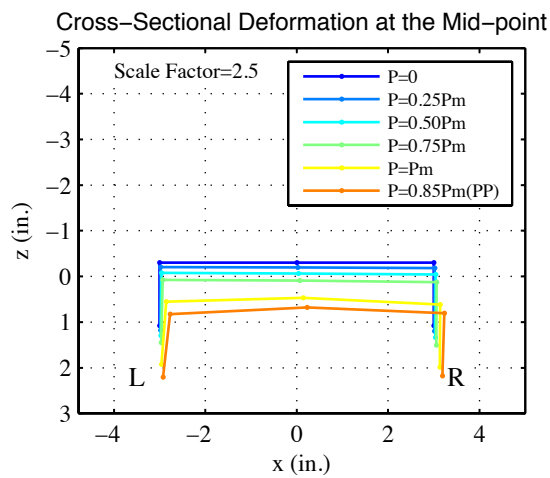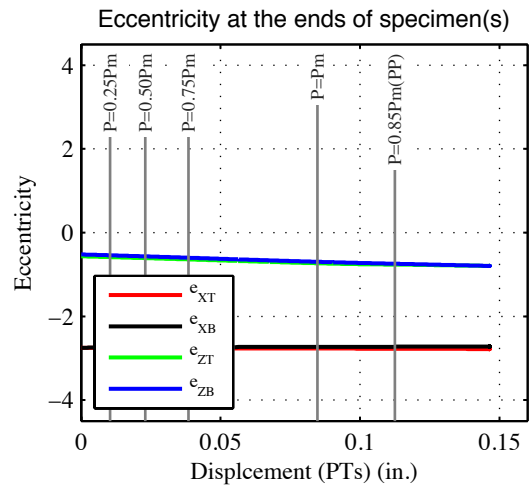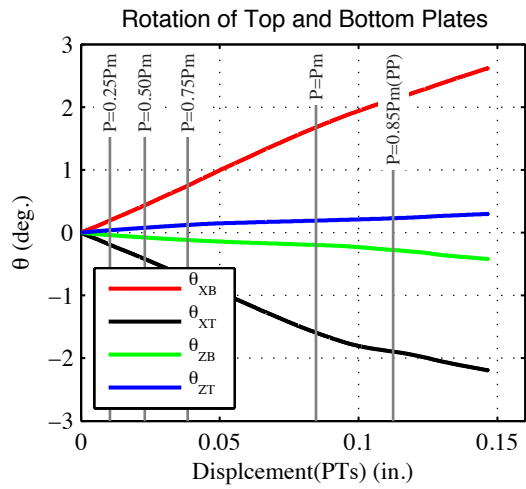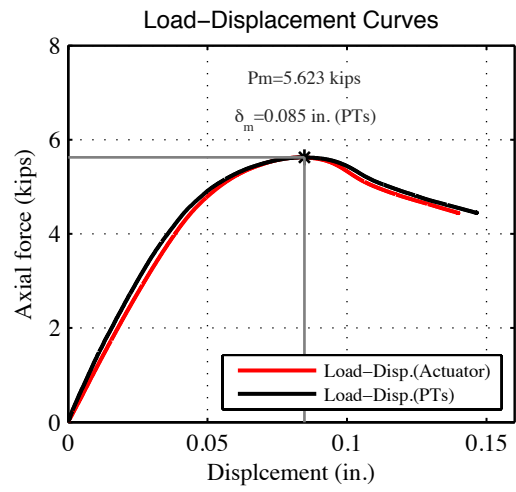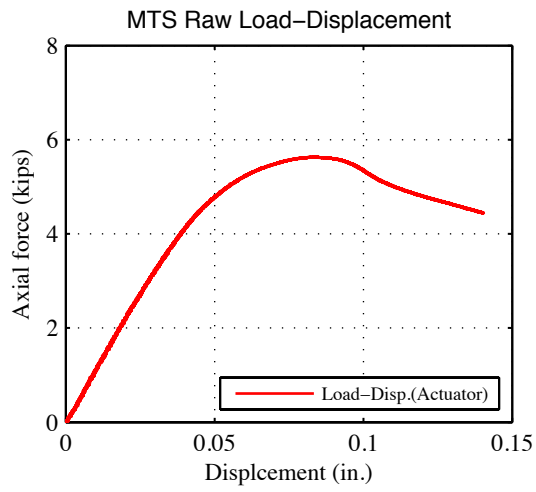
Specimen (S600-24-15) at post-peak stage (PP)

327

16- S600-24-e$_x$(-1.25)-e$_z$(0.09)

Tested Specimen:	S600-24-16 (L=24 inches)
Cross-section:	600S137-54 (AISI-S200-12 nomenclature)
Date:	October 31th 2013

Left (L)   z   Right (R)

x

(Bottom to Top View)

Measured cross-section:

(Centroid position for the middle of the tested specimen)

0.3026

2.9744   3.0419

Test Description:	- Lipped C-channel Beam-column Test (Loading rate: 6.6×10^{-5} in./sec) - Bi-axial bending and axial compression
Target eccentricity in x-dir (e$_{x0}$): -1.25 (in.)	Target eccentricity in z-dir (e$_{z0}$): -0.085 (in.)
Provided ave. ecc. in x-dir (e$_x$): -1.25 (in.)	
Provided ave. ecc. in z-dir (e$_z$)-Top: -0.078 (in.)	Provided ave. ecc in z-dir (e$_z$)-Bot: -0.094 (in.)
Initial end plate angles: $\theta_{xT} = -1.35^o$, $\theta_{zT} = 0.53^o$, $\theta_{xB} = 0.53^o$, $\theta_{zB} = 0.31^o$	

Beam-Column Specimen: S600-24-16

P=4.436 kips	P=9.024 kips	P=9.804 kips	P=7.726 kips
45% P$_m$	92% P$_m$	100% P$_m$	79% P$_m$ (post-peak)

Note: Unsymmetrical web local buckling first visible at P=7.0 kips. Very small outward flange movement consistent with the web buckling.

MTS Raw Load–Displacement

Load–Displacement Curves

Pm=9.826 kips

δ_m =0.042 in. (PTs)

Rotation of Top and Bottom Plates

Eccentricity at the ends of specimen(s)

Cross–Sectional Deformation at the Mid–point
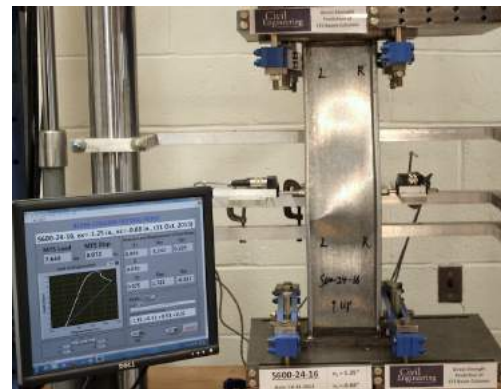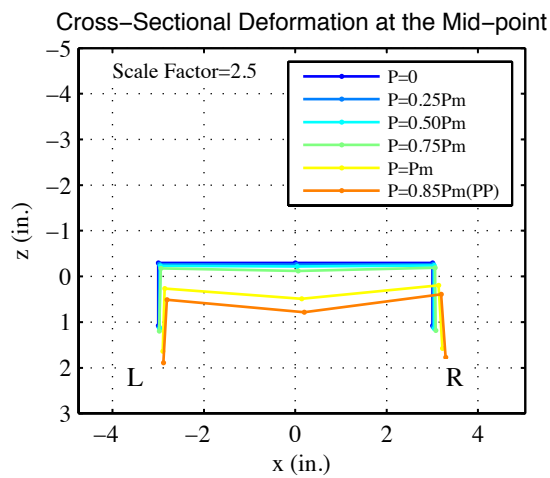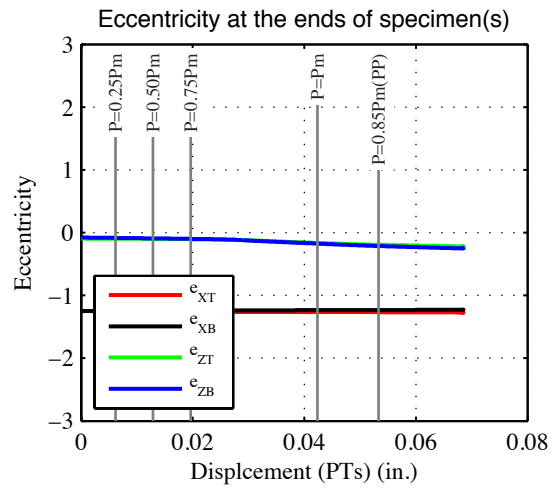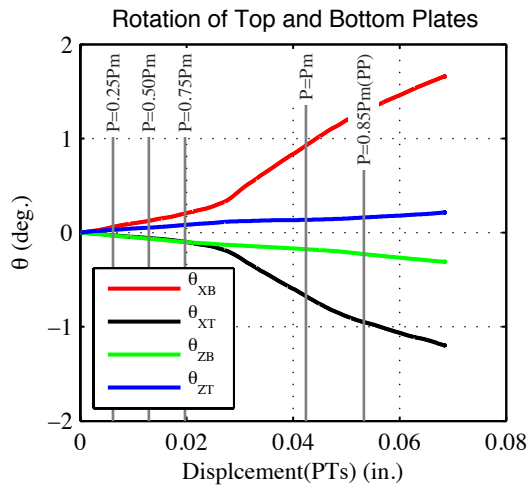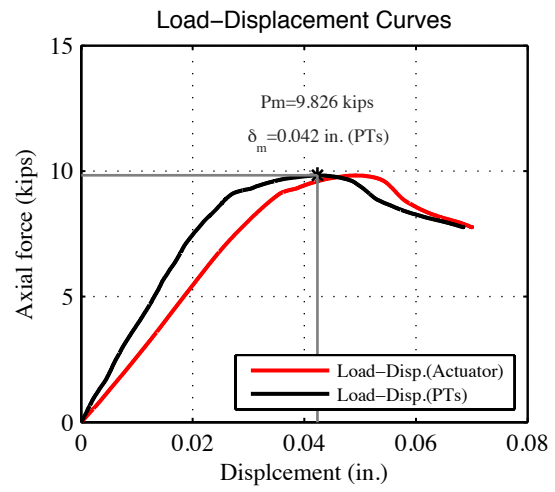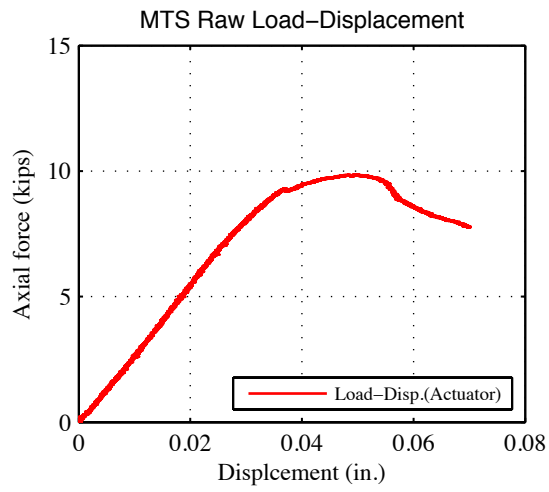
Specimen (S600-24-16) at post-peak stage (PP)

17- S600-24-e$_x$(-4.5)-e$_z$(-0.31)

Tested Specimen:	S600-24-17 (L=24 inches)
Cross-section:	600S137-54 (AISI-S200-12 nomenclature)
Date:	October 31th 2013

Left (L)   z   Right (R)   x

(Bottom to Top View)

Measured cross-section:

(Centroid position for the middle of the tested specimen)

0.2988

2.9655   3.0364

Test Description:	- Lipped C-channel Beam-column Test (Loading rate: 7.5×10^{-5} in./sec) - Bi-axial bending and axial compression
Target eccentricity in x-dir (e$_{x0}$): -4.50 (in.)	Target eccentricity in z-dir (e$_{z0}$): -0.31 (in.)
Provided ave. ecc. in x-dir (e$_x$): -4.50 (in.)	
Provided ave. ecc. in z-dir (e$_z$)-Top: -0.310 (in.)	Provided ave. ecc in z-dir (e$_z$)-Bot: -0.302 (in.)
Initial end plate angles:	θ_{xT}= -1.24^o , θ_{zT}= 0.71^o , θ_{xB}= 0.61^o , θ_{zB}= -0.06^o

Beam-Column Specimen: S600-24-17
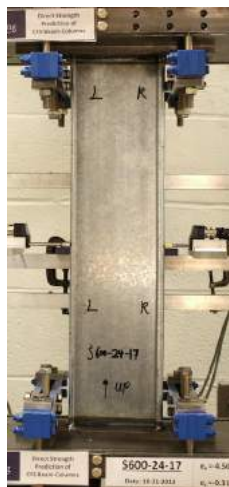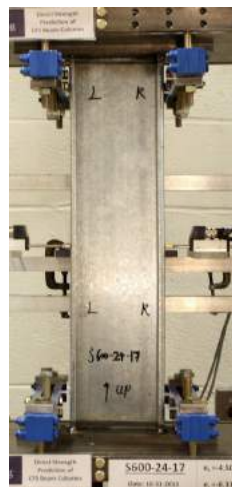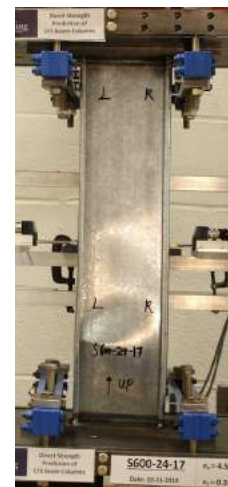
P=2.986 kips	P=4.028 kips	P=5.812 kips	P=4.637 kips
51% P$_m$	68% P$_m$	99% P$_m$	80% P$_m$ (post-peak)

Note: Unsymmetrical web local buckling first visible at P=4.5 kips. Very small flange movement. Fast strength drop at the maximum.

MTS Raw Load−Displacement

Load−Displacement Curves

Pm=5.892 kips

δ_m =0.081 in. (PTs)

Rotation of Top and Bottom Plates

Eccentricity at the ends of specimen(s)

Cross−Sectional Deformation at the Mid−point
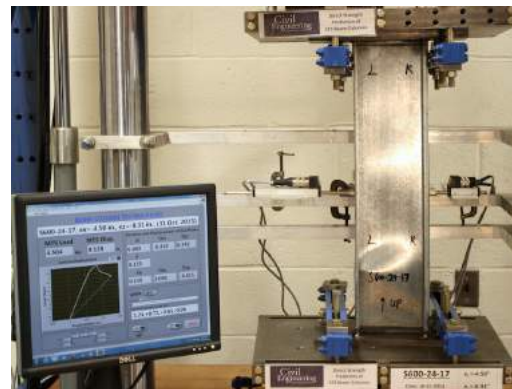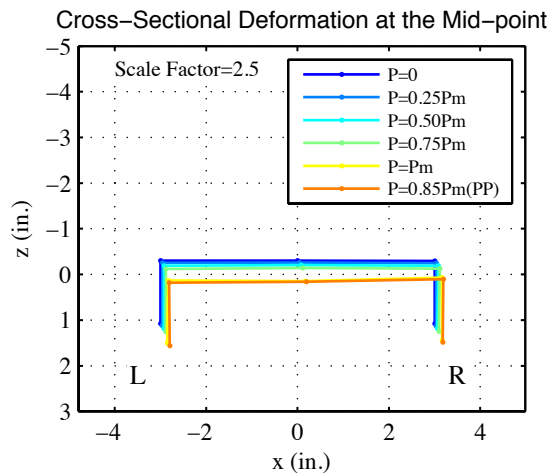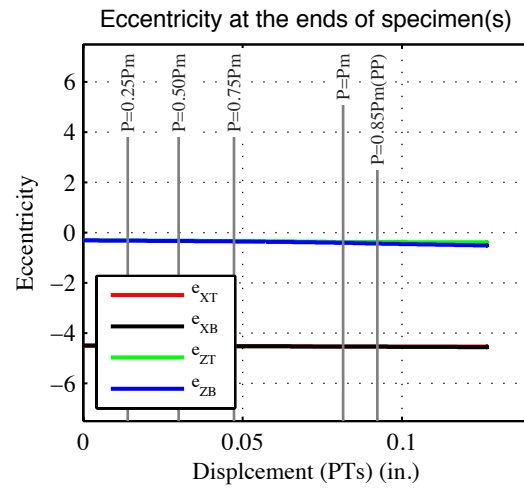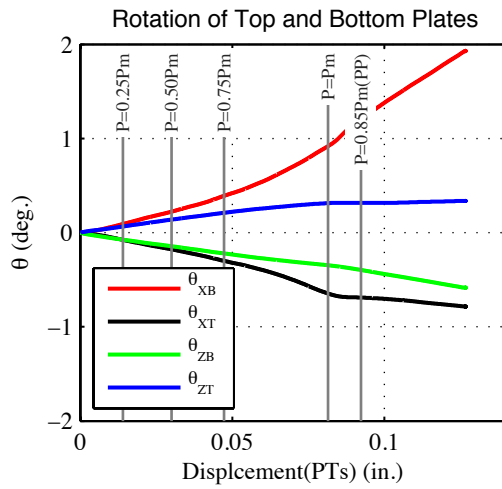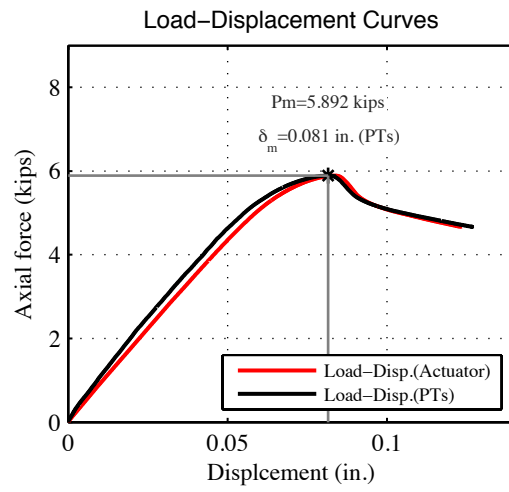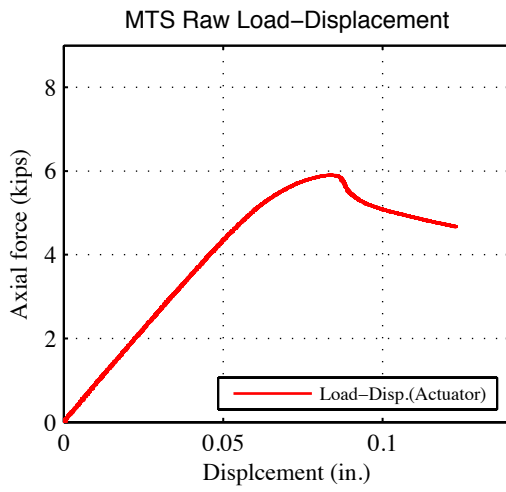
Specimen (S600-24-17) at post-peak stage (PP)

331

18- S600-24-e$_x$(0.0)-e$_z$(0.0)

Tested Specimen:	S600-24-18 (L=24 inches)
Cross-section:	600S137-54 (AISI-S200-12 nomenclature)
Date:	November 1st 2013

Left (L)   z   Right (R)

x

(Bottom to Top View)

Measured cross-section:

(Centroid position for the middle of
the tested specimen)

0.3053

2.9496   3.0406

Test Description:	- Lipped C-channel Beam-column Test (Loading rate: 6.0×10^{-5} in./sec) - Axial compression (Column test)	
Target eccentricity in x-dir (e$_{x0}$): 0.0 (in.)	Target eccentricity in z-dir (e$_{z0}$): 0.0 (in.)	
Provided ave. ecc. in x-dir (e$_x$): ~0.0 (in.)		
Provided ave. ecc. in z-dir (e$_z$)-Top: -0.020 (in.)	Provided ave. ecc in z-dir (e$_z$)-Bot: 0.013 (in.)	
Initial end plate angles:	θ_{xT}= -1.54^o , θ_{zT}= 0.76^o , θ_{xB}= 0.07^o , θ_{zB}= 0.21^o	

Beam-Column Specimen: S600-24-18

P=5.701 kips	P=8.975 kips	P=13.231 kips	P=10.408 kips
42% P$_m$	67% P$_m$	98% P$_m$	77% P$_m$ (post-peak)
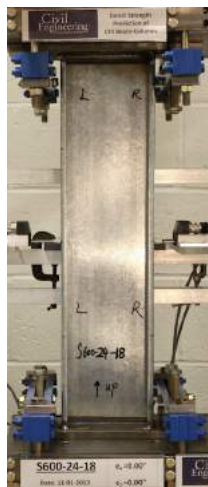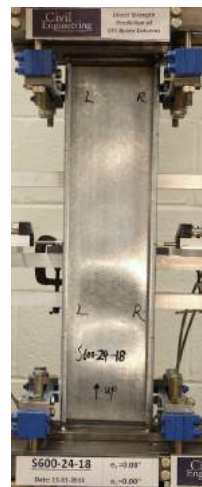
Note: Web local buckling first visible at P=7 kips (5 half-waves). Very small flange movement consistent with the web buckling. Fast strength drop at the maximum load.

MTS Raw Load–Displacement

Axial force (kips)

Displcement (in.)

Load–Disp.(Actuator)

Load–Displacement Curves

Pm=13.468 kips

δ_m=0.037 in. (PTs)

Axial force (kips)

Displcement (in.)

Load–Disp.(Actuator)
Load–Disp.(PTs)

Rotation of Top and Bottom Plates

P=0.25Pm
P=0.50Pm
P=0.75Pm
P=Pm
P=0.85Pm(PP)

θ (deg.)

Displcement(PTs) (in.)

θ_{XB}
θ_{XT}
θ_{ZB}
θ_{ZT}

Eccentricity at the ends of specimen(s)

P=0.25Pm
P=0.50Pm
P=0.75Pm
P=Pm
P=0.85Pm(PP)

Eccentricity

Displcement (PTs) (in.)

e_{XT}
e_{XB}
e_{ZT}
e_{ZB}

Cross−Sectional Deformation at the Mid−point

Scale Factor=2.5

P=0
P=0.25Pm
P=0.50Pm
P=0.75Pm
P=Pm
P=0.85Pm(PP)

z (in.)

L   R

x (in.)

Specimen (S600-24-18) at post-peak stage (PP)

19- S600-24-e$_x$(-6.50)-e$_z$(0.0)---Repeating Test #9

Tested Specimen:	S600-24-19 (L=24 inches)
Cross-section:	600S137-54 (AISI-S200-12 nomenclature)
Date:	December 11th 2013

Left (L)   z   Right (R)

x

(Bottom to Top View)

Measured cross-section:

(Centroid position for the middle of the tested specimen)

0.3021

2.9563   3.0399

Test Description:	- Lipped C-channel Beam-column Test (Loading rate: 6.6×10^{-5} in./sec) - Major-axis bending and axial compression
Target eccentricity in x-dir (e$_{x0}$): -6.50 (in.)	Target eccentricity in z-dir (e$_{z0}$): 0.0 (in.)
Provided ave. ecc. in x-dir (e$_x$): -6.50 (in.)	
Provided ave. ecc. in z-dir (e$_z$)-Top: -0.031 (in.)	Provided ave. ecc in z-dir (e$_z$)-Bot: 0.042 (in.)
Initial end plate angles:	θ_{xT}= - , θ_{zT}= - , θ_{xB}= - , θ_{zB}= -

Beam-Column Specimen: S600-24-19

P=1.747 kips	P=3.856 kips	P=4.802 kips	P=3.821 kips
36% P$_m$	80% P$_m$	100% P$_m$	79% P$_m$ (post-peak)

Note: Flange distortional buckling of the left flange followed by consistent web deformations. Large inward flange movement at the end of the test.

MTS Raw Load−Displacement

Load−Displacement Curves

Rotation of Top and Bottom Plates

Eccentricity at the ends of specimen(s)

Cross−Sectional Deformation at the Mid−point
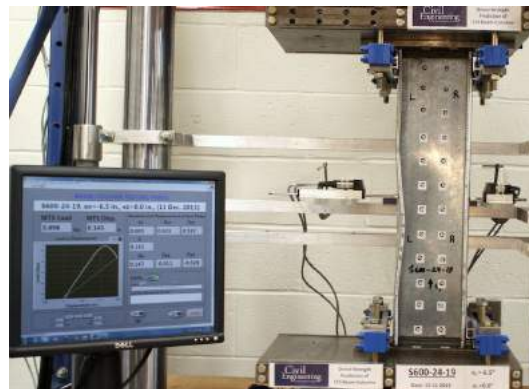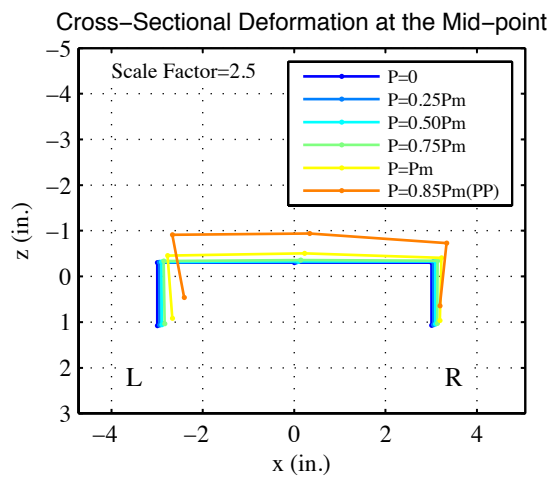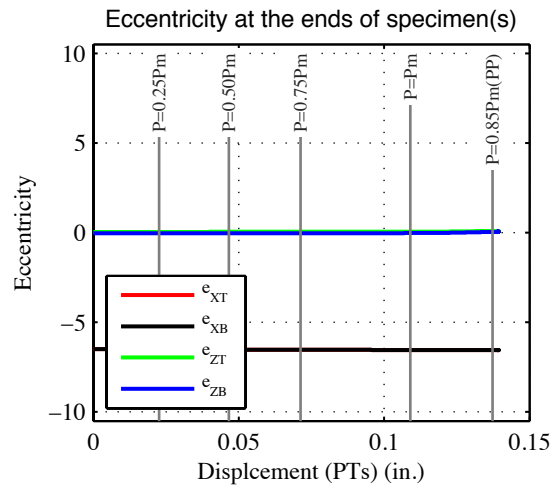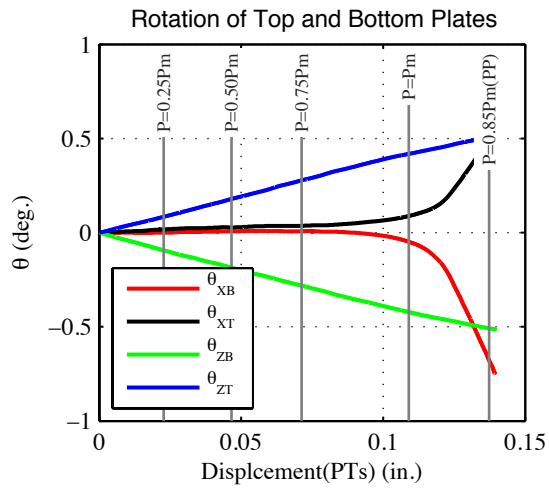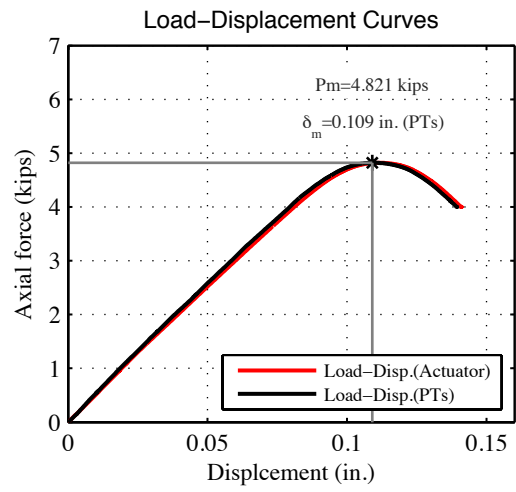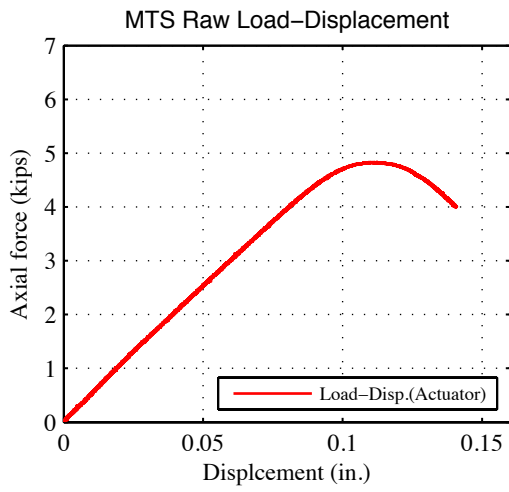
Specimen (S600-24-19) at post-peak stage (PP)

20- S600-24-e$_x$(0.0)-e$_z$(0.0)---Repeating Test #18

Tested Specimen:	S600-24-20 (L=24 inches)
Cross-section:	600S137-54 (AISI-S200-12 nomenclature)
Date:	December 12th 2013

Left (L)   z   Right (R)

x

(Bottom to Top View)

Measured cross-section:

(Centroid position for the middle of
the tested specimen)

0.3036

2.9696   3.0396

Test Description:	- Lipped C-channel Beam-column Test (Loading rate: 6.0×10^{-5} in./sec) - Axial compression (Column test)

Target eccentricity in x-dir (e$_{x0}$):	0.0 (in.)	Target eccentricity in z-dir (e$_{z0}$):	0.0 (in.)
Provided ave. ecc. in x-dir (e$_x$):	0.0 (in.)		
Provided ave. ecc. in z-dir (e$_z$)-Top:	-0.017 (in.)	Provided ave. ecc in z-dir (e$_z$)-Bot:	0.019 (in.)
Initial end plate angles:	θ_{xT}= - , θ_{zT}= - , θ_{xB}= - , θ_{zB}= -		
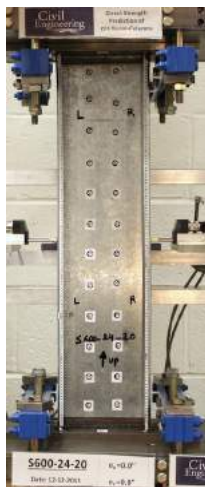
Beam-Column Specimen: S600-24-20

P=6.499 kips	P=11.142 kips	P=14.316 kips	P=10.649 kips
38% P$_m$	79% P$_m$	100% P$_m$	84% P$_m$ (post-peak)
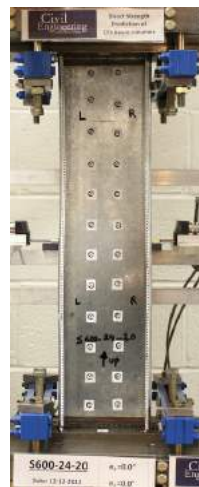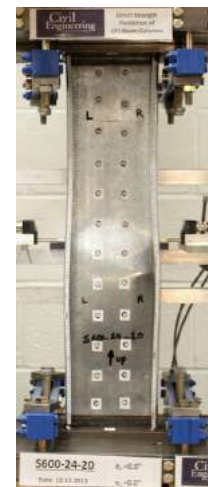
Note: Web local buckling (3 half-waves). Small flange movement consistent with the web buckling. Fast strength drop at the maximum load.

MTS Raw Load−Displacement

Load−Displacement Curves

Pm=14.339 kips

δ_m =0.046 in. (PTs)

Load−Disp.(Actuator)
Load−Disp.(PTs)

Rotation of Top and Bottom Plates

P=0.25Pm
P=0.50Pm
P=0.75Pm
P=Pm
P=0.85Pm(PP)

θ_{XB}
θ_{XT}
θ_{ZB}
θ_{ZT}

Eccentricity at the ends of specimen(s)

P=0.25Pm
P=0.50Pm
P=0.75Pm
P=Pm
P=0.85Pm(PP)

e_{XT}
e_{XB}
e_{ZT}
e_{ZB}

Cross−Sectional Deformation at the Mid−point

Scale Factor=2.5

P=0
P=0.25Pm
P=0.50Pm
P=0.75Pm
P=Pm
P=0.85Pm(PP)

L   R
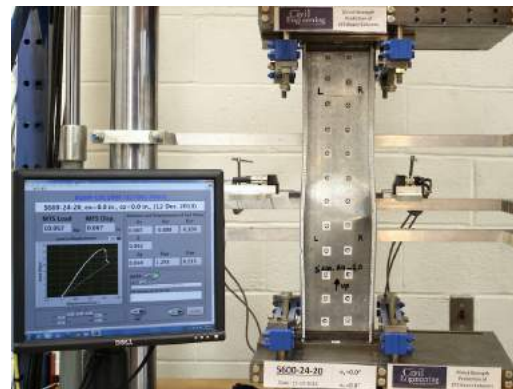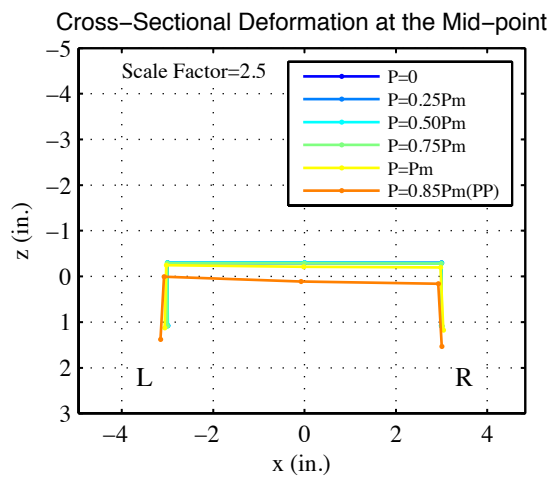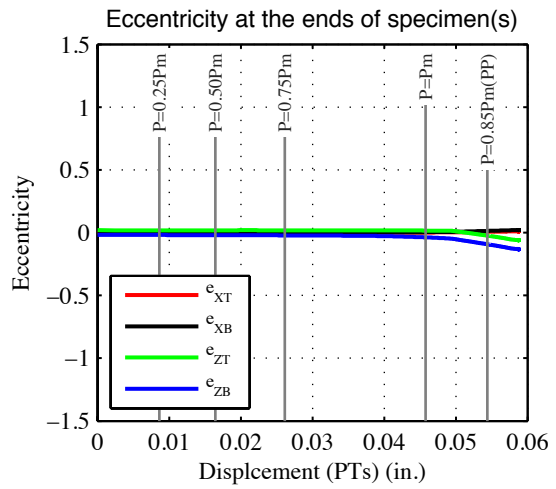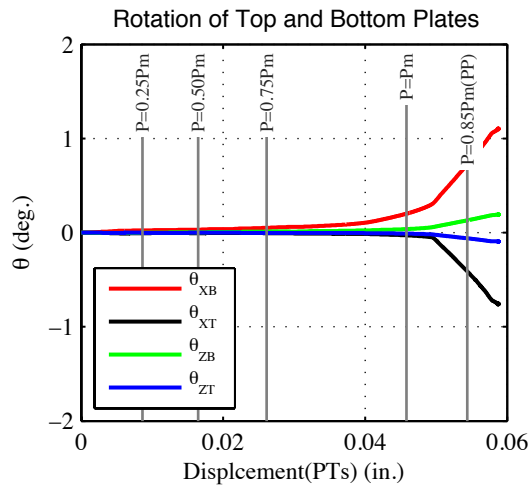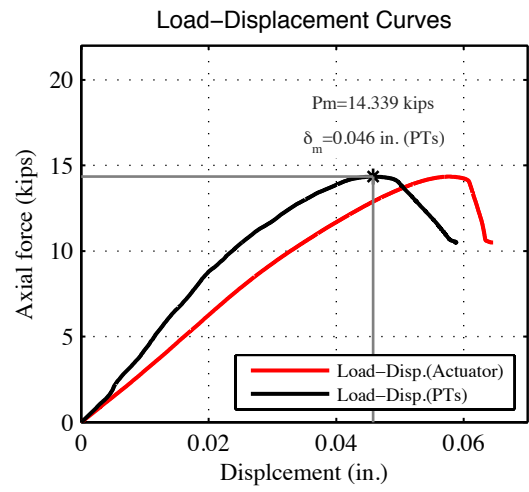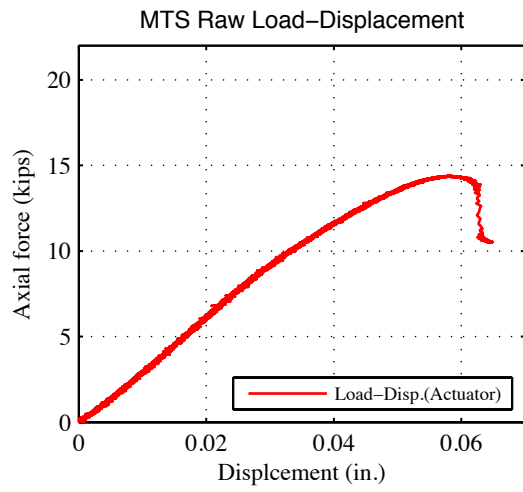
Specimen (S600-24-20) at post-peak stage (PP)

F.3 Experiment results: Long Specimens (S600-48)

1- S600-48-e_x(0)-e_z(-1.50)

Tested Specimen:	S600-48-1 (L=48 inches)
Cross-section:	600S137-54 (AISI-S200-12 nomenclature)
Date:	August 22th 2013

Left (L)   z   Right (R)   x

(Bottom to Top View)

Measured cross-section:
(Centroid position for the middle of
the tested specimen)

0.3034

2.9918   3.0499

Test Description:	- Lipped C-channel Beam-column Test (Loading rate: 4.2×10^{-5} in./sec)
	- Minor axis (Lips in tension) bending moment and axial compression

Target eccentricity in x-dir (e_{x0}): 0.0 (in.)   Target eccentricity in z-dir (e_{z0}): -1.50 (in.)

Provided ave. ecc. in x-dir (e_x): ~0.0 (in.)

Provided ave. ecc. in z-dir (e_z)-Top: -1.552 (in.)   Provided ave. ecc in z-dir (e_z)-Bot: -1.570 (in.)

Initial end plate angles: θ_{xT}= -1.18^o , θ_{zT}= 0.72^o , θ_{xB}= 0.31^o , θ_{zB}= 0.82^o

Beam-Column Specimen: S600-48-1

P=1.06 kips	P=2.007 kips	P=2.498 kips	P=2.231 kips
42% P_m	40% P_m	100% P_m	89% P_m (post-peak)

Note: Large local buckling half-wave at the middle at P=2.3 kips. 5 local buckling half-waves around the maximum and in the post-peak. Large global out of plane movement of the specimen in the Z-direction.

MTS Raw Load−Displacement

Load−Displacement Curves

Pm=2.499 kips
δ_m=0.299 in. (PTs)

Rotation of Top and Bottom Plates

Eccentricity at the ends of specimen(s)

Cross−Sectional Deformation at the Mid−point
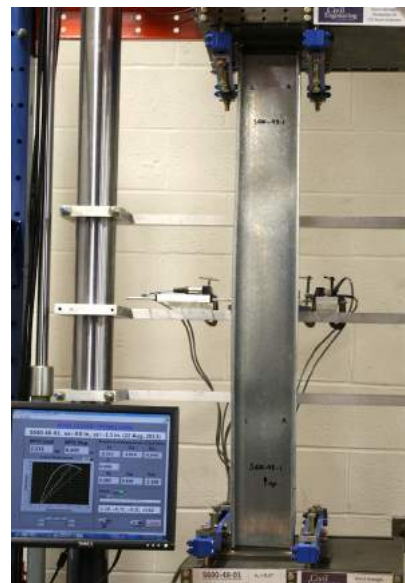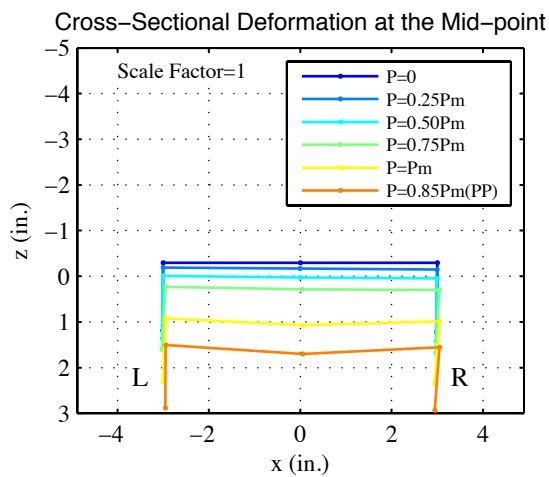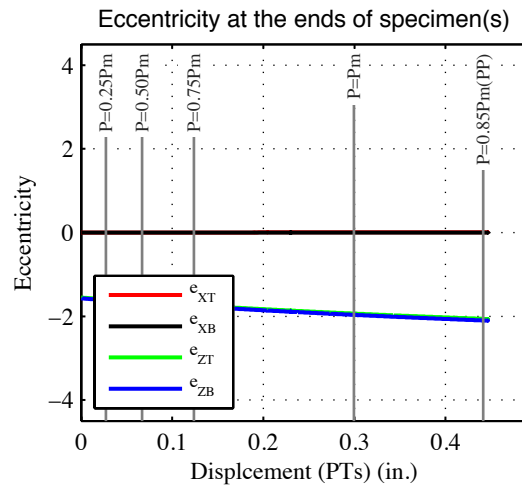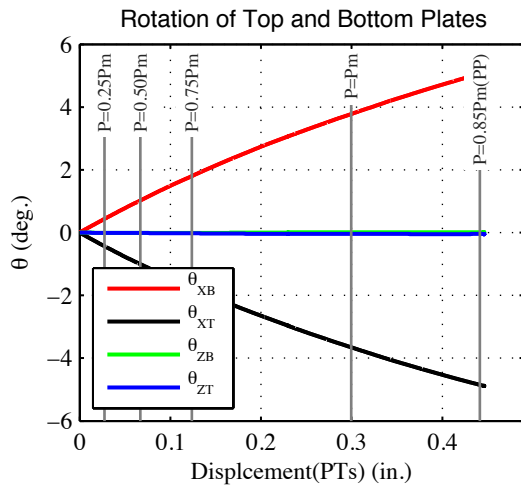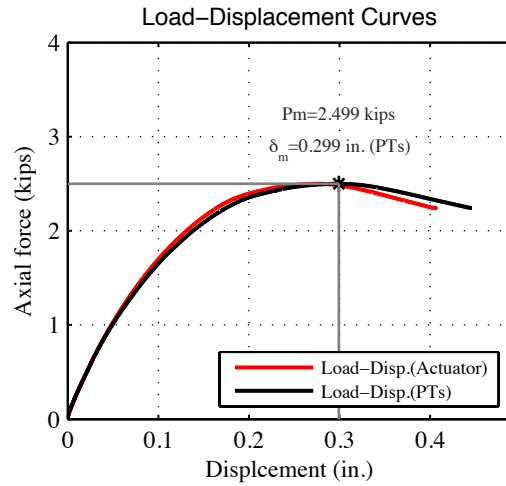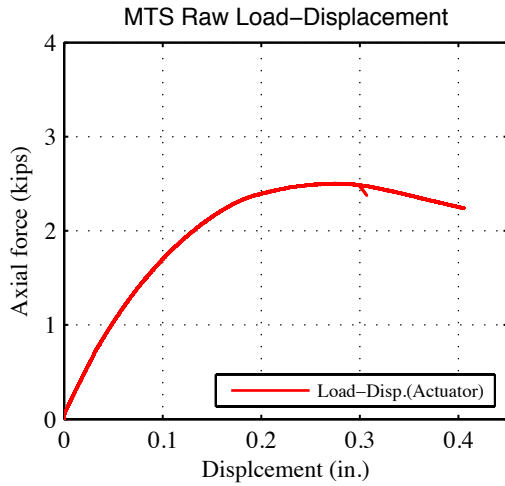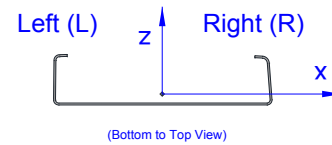
Specimen (S600-48-1) at post-peak stage (PP)

2- S600-48-e_x(0)-e_z(-0.65)

Tested Specimen:	S600-48-2 (L=48 inches)
Cross-section:	600S137-54 (AISI-S200-12 nomenclature)
Date:	August 30th 2013

Left (L) z Right (R)

x

(Bottom to Top View)

Measured cross-section:
(Centroid position for the middle of the tested specimen)

0.3034

2.9918   3.0499

Test Description:	- Lipped C-channel Beam-column Test (Loading rate: 9.0×10^{-5} in./sec) - Minor axis (Lips in tension) bending moment and axial compression

Target eccentricity in x-dir (e_{x0}): 0.0 (in.)   Target eccentricity in z-dir (e_{z0}): -0.60 (in.)

Provided ave. ecc. in x-dir (e_x):   ~0.0 (in.)

Provided ave. ecc. in z-dir (e_z)-Top: -0.696 (in.)   Provided ave. ecc in z-dir (e_z)-Bot: -0.610 (in.)

Initial end plate angles: θ_{xT}= -1.40^o , θ_{zT}= 0.39^o , θ_{xB}= 0.32^o , θ_{zB}= 0.36^o

Beam-Column Specimen: S600-48-2

P=1.962 kips	P=3.015 kips	P=3.949 kips	P=3.328 kips
50% P_m	76% P_m	100% P_m	84% P_m (post-peak)

Note: Several local buckling half-waves along the length around P=3.5 kips. Following the pick load, web plastic deformations at mid-height of the specimen. Large global out-of-plane movement of the specimen in the Z-direction.

MTS Raw Load–Displacement

Load–Displacement Curves

Pm=3.946 kips
δ_m=0.149 in. (PTs)

Rotation of Top and Bottom Plates

Eccentricity at the ends of specimen

Cross–Sectional Deformation at the Mid–point
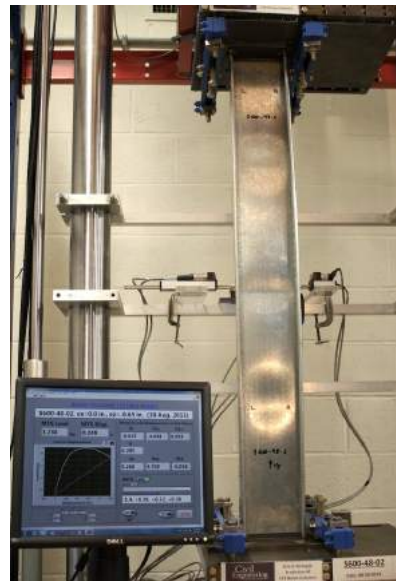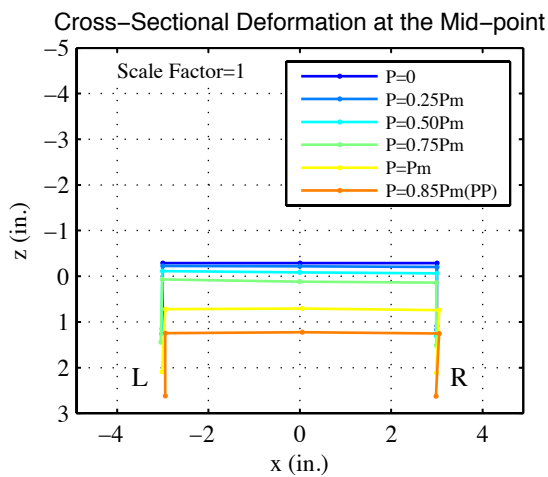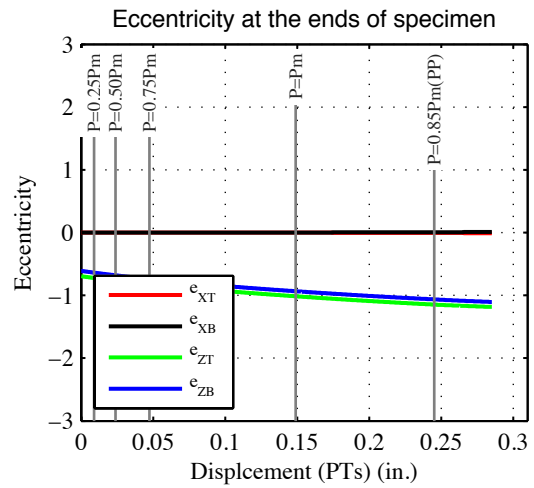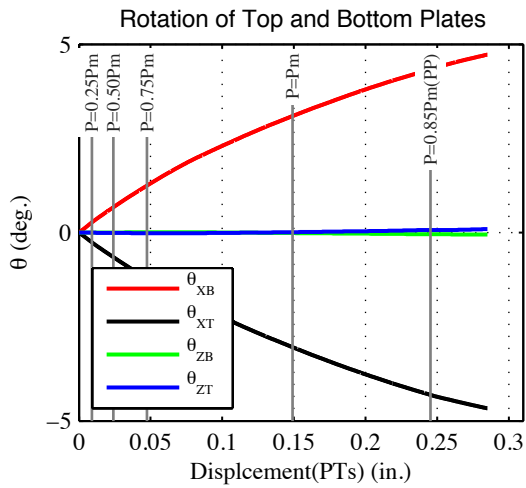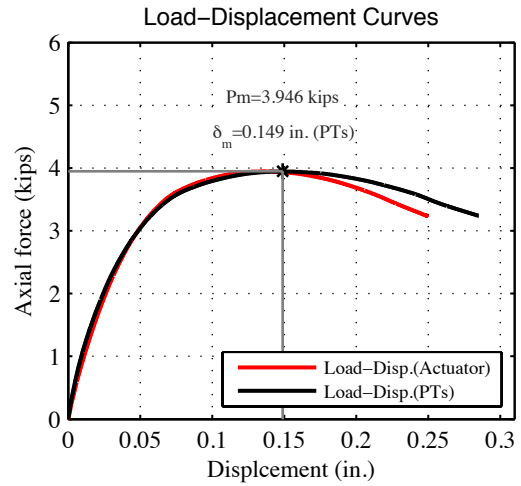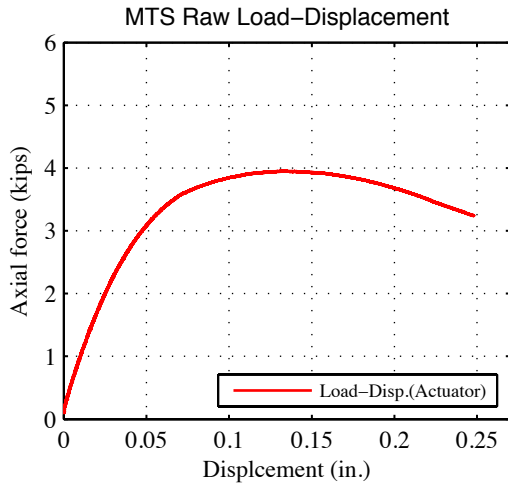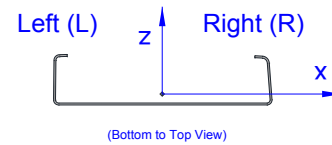
Specimen (S600-48-2) at post-peak stage (PP)

3- S600-48-e$_x$(0)-e$_z$(-0.20)

Tested Specimen:	S600-48-3 (L=48 inches)	
Cross-section:	600S137-54 (AISI-S200-12 nomenclature)	
Date:	September 3rd 2013	

Left (L)   z   Right (R)
x
(Bottom to Top View)

Measured cross-section:
(Centroid position for the middle of the tested specimen)

0.3028
2.9844   3.0465

Test Description:	- Lipped C-channel Beam-column Test (Loading rate: 9.0×10^{-5} in./sec) - Minor axis (Lips in tension) bending moment and axial compression

Target eccentricity in x-dir (e$_{x0}$):	0.0 (in.)	Target eccentricity in z-dir (e$_{z0}$):	-0.20 (in.)
Provided ave. ecc. in x-dir (e$_x$):	~0.0 (in.)		
Provided ave. ecc. in z-dir (e$_z$)-Top:	-0.196 (in.)	Provided ave. ecc in z-dir (e$_z$)-Bot:	-0.193 (in.)
Initial end plate angles:	θ_{xT}= -1.21^o , θ_{zT}= 0.42^o , θ_{xB}= 0.22^o , θ_{zB}= 0.35^o		

Beam-Column Specimen: S600-48-3

P=3.104 kips	P=3.911 kips	P=5.652 kips	P=4.527 kips
55% P$_m$	69% P$_m$	100% P$_m$	80% P$_m$ (post-peak)

Note: Several local buckling half-waves along the length around P=5.0 kips. Following the pick load, web plastic deformations at mid-height of the specimen. Large global out-of-plane movement of the specimen in the Z-direction.

MTS Raw Load–Displacement

Load–Displacement Curves

Pm=5.657 kips

δ_m=0.057 in. (PTs)

Eccentricity at the ends of specimen

Eccentricity at the ends of specimen

Cross−Sectional Deformation at the Mid−point

Scale Factor=1
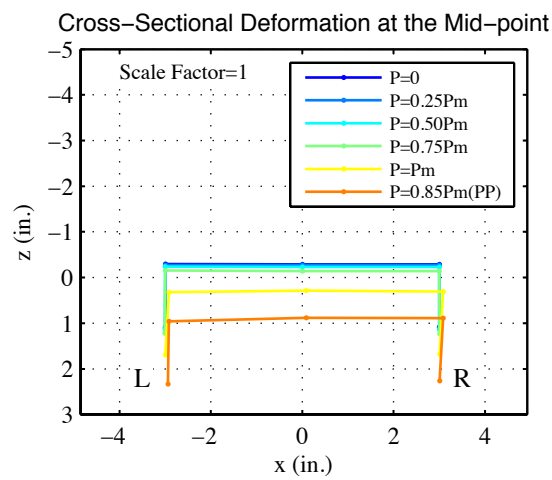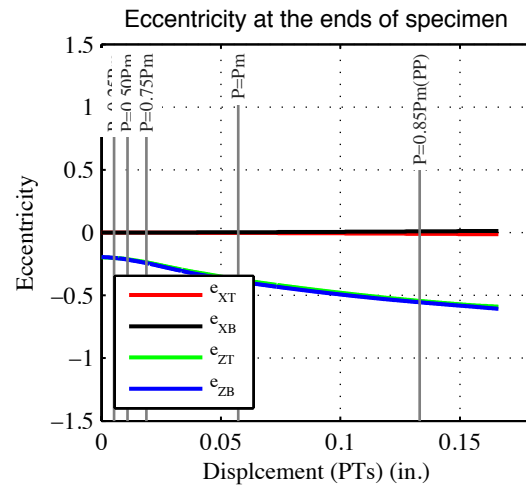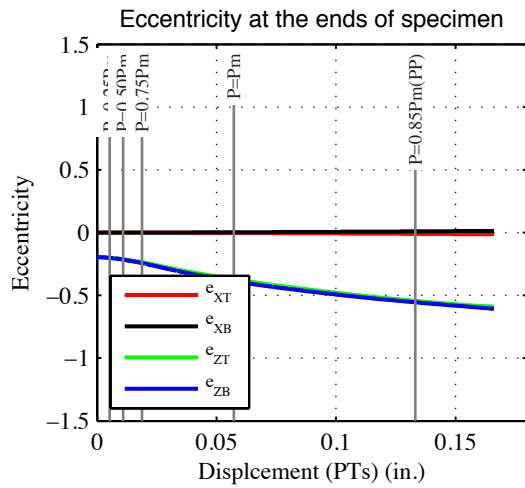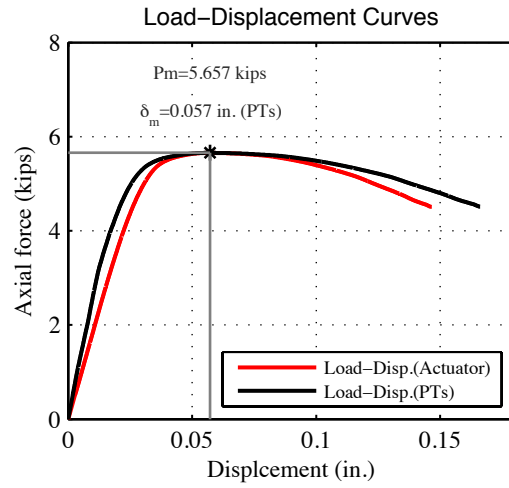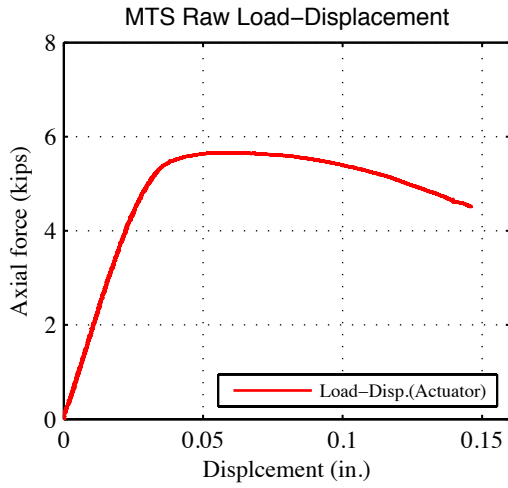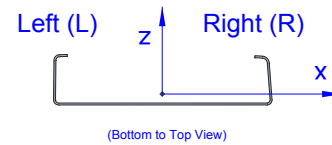
Specimen (S600-48-3) at post-peak stage (PP)

4- S600-48-e$_x$(0)-e$_z$(0.2)

Tested Specimen:	S600-48-4 (L=48 inches)
Cross-section:	600S137-54 (AISI-S200-12 nomenclature)
Date:	September 4th 2013

Left (L) z Right (R)

x

(Bottom to Top View)

Measured cross-section:
(Centroid position for the middle
of the tested specimen)

0.2991

2.9771   3.0512

Test Description:	- Lipped C-channel Beam-column Test (Loading rate: 9.0×10^{-5} in./sec) - Minor axis (Lips in compression) bending moment and axial compression

Target eccentricity in x-dir (e$_{x0}$):	0.0 (in.)	Target eccentricity in z-dir (e$_{z0}$):	+0.20 (in.)

Provided ave. ecc. in x-dir (e$_x$):   ~0.0 (in.)

Provided ave. ecc. in z-dir (e$_z$)-Top:	0.202 (in.)	Provided ave. ecc in z-dir (e$_z$)-Bot:	0.207 (in.)

Initial end plate angles: θ_{xT}= -1.07^o , θ_{zT}= 0.41^o , θ_{xB}= 0.09^o , θ_{zB}= 0.20^o

Beam-Column Specimen: S600-48-4

P=2.887 kips	P=5.125 kips	P=5.554 kips	P=4.553 kips
52% P$_m$	92% P$_m$	100% P$_m$	82% P$_m$ (post-peak)

Note: 5 distortional buckling half-waves in both flanges along with consistent web deformations. Global out-of-plane movement of the specimen in the negative Z-direction.

MTS Raw Load–Displacement

Load–Displacement Curves

Pm=5.561 kips

δ_m =0.048 in. (PTs)

Rotation of Top and Bottom Plates

Eccentricity at the ends of specimen

Cross-Sectional Deformation at the Mid-point
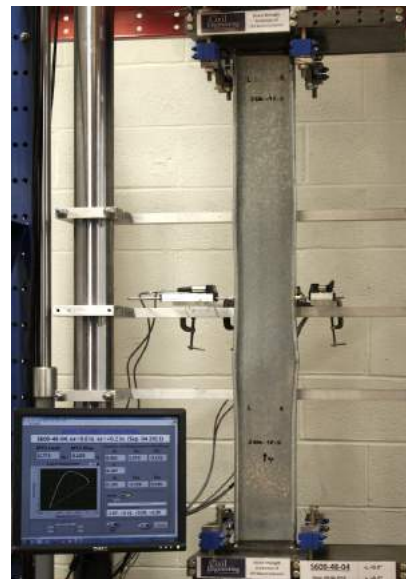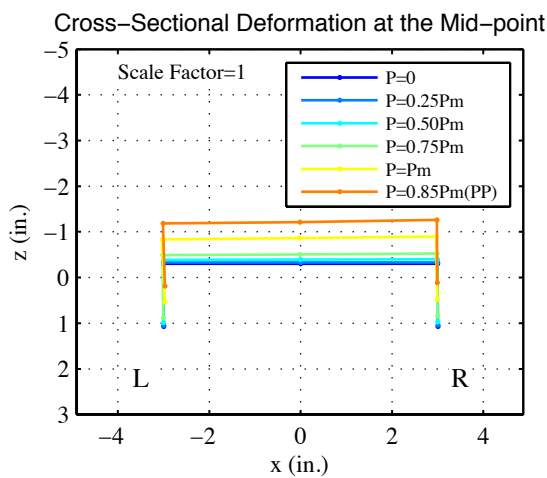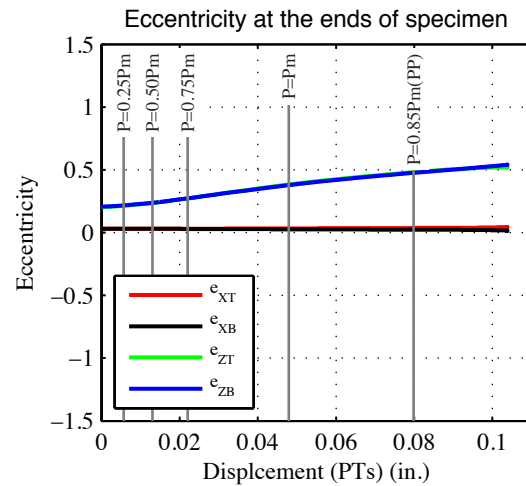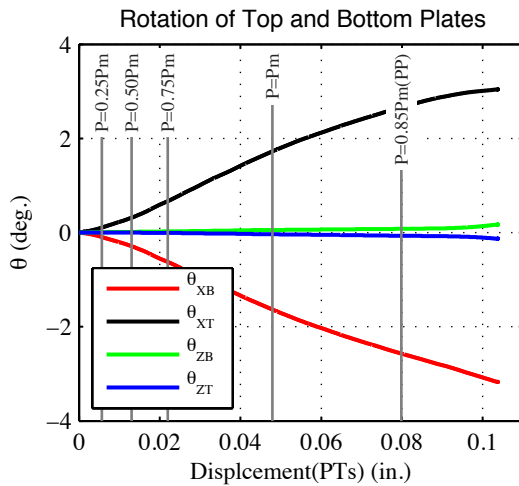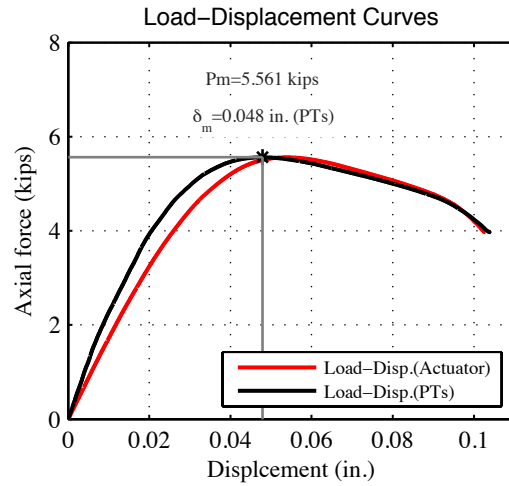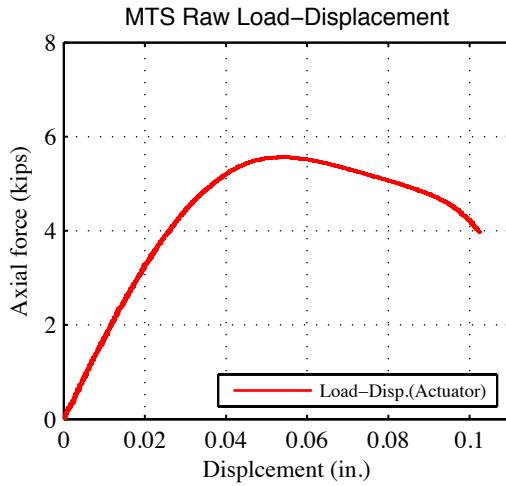
Specimen (S600-48-4) at post-peak stage (PP)

5- S600-48-e$_x$(0)-e$_z$(0.65)

Tested Specimen:	S600-48-5 (L=48 inches)
Cross-section:	600S137-54 (AISI-S200-12 nomenclature)
Date:	September 5th 2013

Left (L)   z   Right (R)

x

(Bottom to Top View)

Measured cross-section:
(Centroid position for the middle of the tested specimen)

0.2991

2.9771   3.0512

Test Description:	- Lipped C-channel Beam-column Test (Loading rate: 9.0×10^{-5} in./sec) - Minor axis (Lips in compression) bending moment and axial compression
Target eccentricity in x-dir (e$_{x0}$):	0.0 (in.) Target eccentricity in z-dir (e$_{z0}$): +0.65 (in.)
Provided ave. ecc. in x-dir (e$_x$):	~0.0 (in.)
Provided ave. ecc. in z-dir (e$_z$)-Top: 0.650 (in.)	Provided ave. ecc in z-dir (e$_z$)-Bot: 0.669 (in.)
Initial end plate angles:	θ_{xT}= -1.29^o , θ_{zT}= 0.16^o , θ_{xB}= 0.66^o , θ_{zB}= 0.32^o

Beam-Column Specimen: S600-48-5

P=2.167 kips	P=2.919 kips	P=3.60 kips	P=2.785 kips
60% P$_m$	81% P$_m$	100% P$_m$	77% P$_m$ (post-peak)

Note: 5 distortional buckling half-waves in both flanges along with consistent web deformations first at around P=2.6 kips. Global out-of-plane movement of the specimen in the negative Z-direction.

MTS Raw Load–Displacement

Load–Displacement Curves

Pm=3.602 kips

δ_m=0.101 in. (PTs)

Rotation of Top and Bottom Plates

Eccentricity at the ends of specimen

Cross–Sectional Deformation at the Mid–point
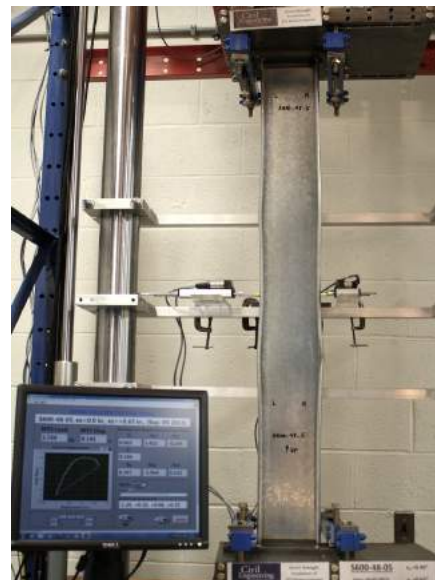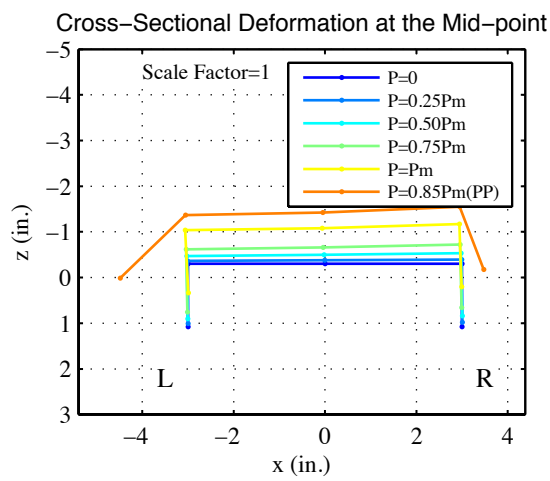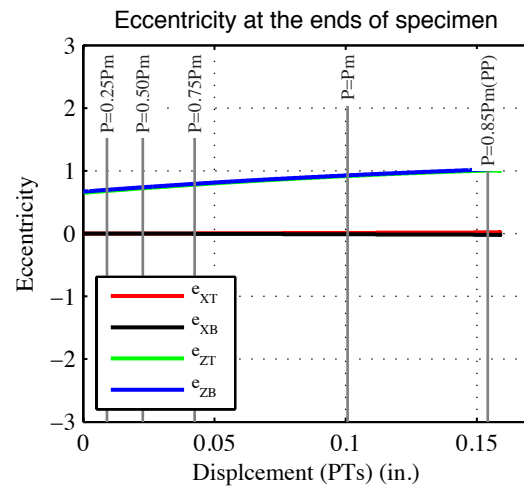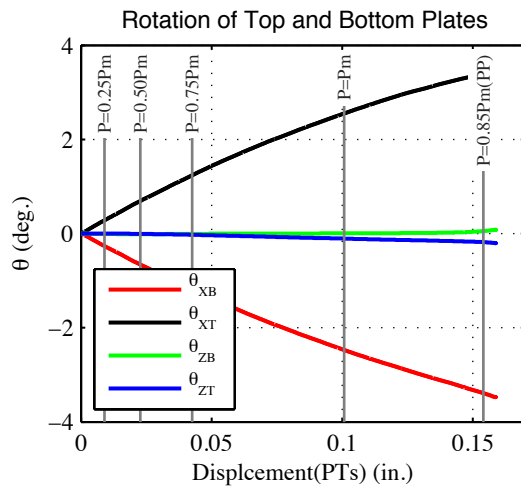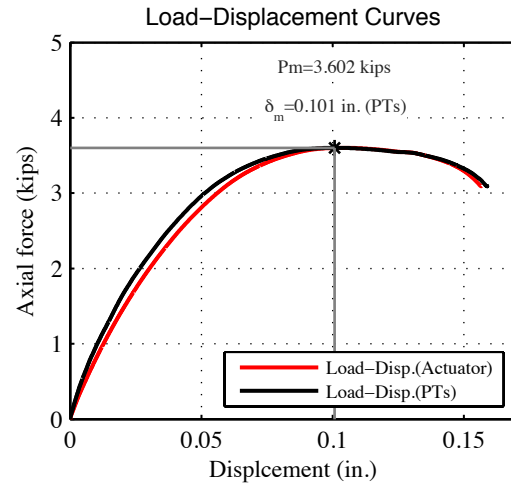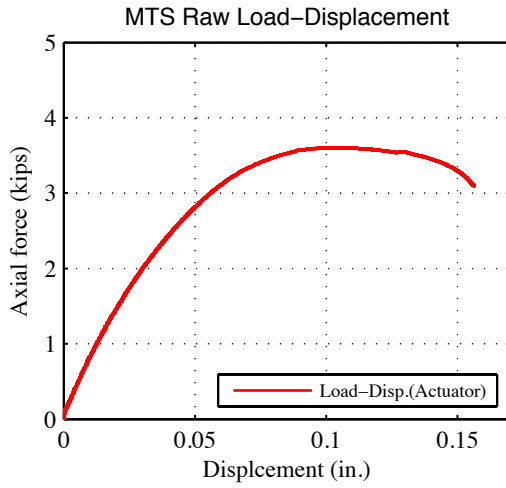
Specimen (S600-48-5) at post-peak stage (PP)

6- S600-48-e$_x$(0)-e$_z$(+1.5)

Tested Specimen:	S600-48-6 (L=48 inches)	
Cross-section:	600S137-54 (AISI-S200-12 nomenclature)	
Date:	September 2nd 2013	

Left (L)   z   Right (R)
x
(Bottom to Top View)

Measured cross-section:
(Centroid position for the middle of the tested specimen)

0.3029
2.9855   3.0432

Test Description:	- Lipped C-channel Beam-column Test (Loading rate: 9.0×10^{-5} in./sec) - Minor axis (Lips in compression) bending moment and axial compression

Target eccentricity in x-dir (e$_{x0}$):	0.0 (in.)	Target eccentricity in z-dir (e$_{z0}$): +1.50 (in.)	
Provided ave. ecc. in x-dir (e$_x$):	~0.0 (in.)		
Provided ave. ecc. in z-dir (e$_z$)-Top:	1.511 (in.)	Provided ave. ecc in z-dir (e$_z$)-Bot:	1.505 (in.)
Initial end plate angles:	θ_{xT}= -1.14^o , θ_{zT}= 0.64^o , θ_{xB}= 0.17^o , θ_{zB}= 0.54^o		

Beam-Column Specimen: S600-48-6

P=1.015 kips	P=1.892 kips	P=2.328 kips	P=1.866 kips
43% P$_m$	81% P$_m$	100% P$_m$	80% P$_m$ (post-peak)

Note: 5 distortional buckling half-waves in both flanges along with consistent web deformations visible around P=2.2 kips. Large global out-of-plane movement of the specimen in the negative Z-direction.

MTS Raw Load–Displacement

Load–Displacement Curves

Pm=2.338 kips
δ_m=0.216 in. (PTs)

Rotation of Top and Bottom Plates

Eccentricity at the ends of specimen

Cross−Sectional Deformation at the Mid−point
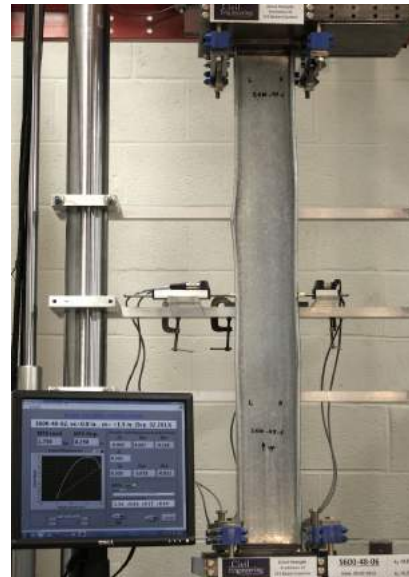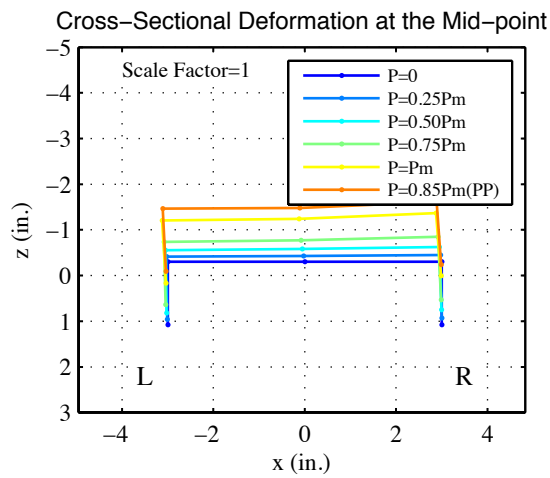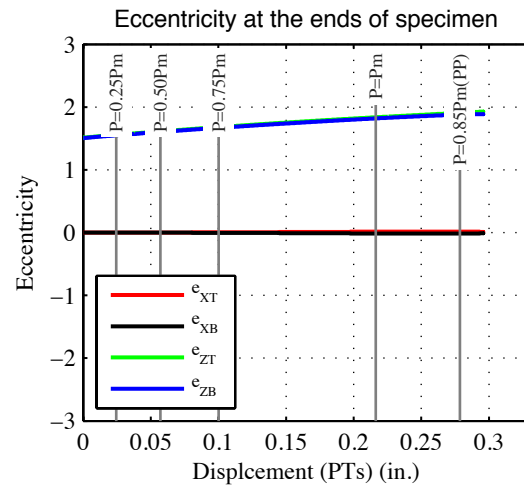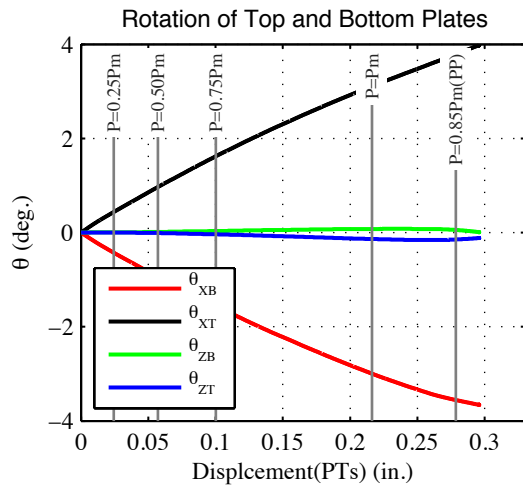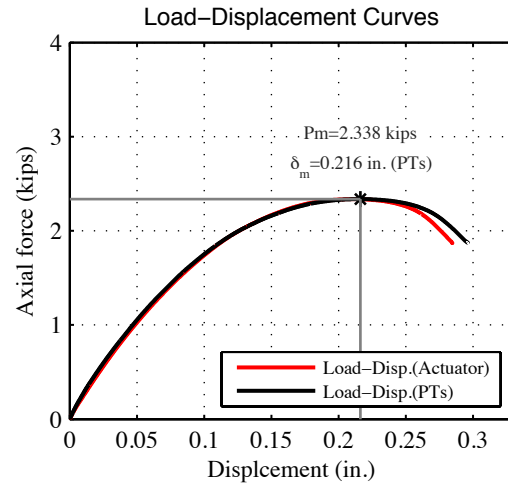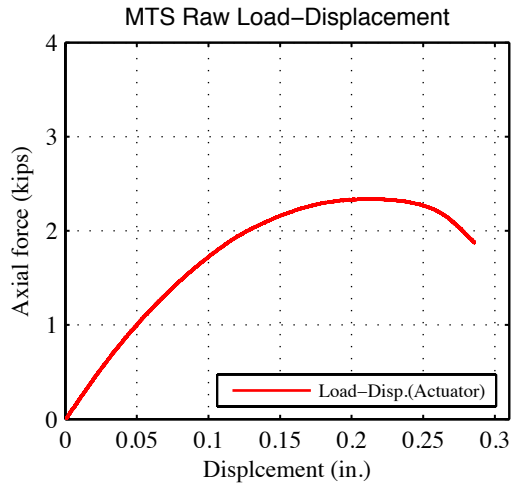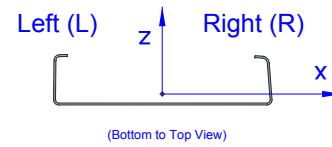
Specimen (S600-48-6) at post-peak stage (PP)

7- S600-48-e$_x$(-0.6)-e$_z$(0.0)

Tested Specimen:	S600-48-7 (L=48 inches)
Cross-section:	600S137-54 (AISI-S200-12 nomenclature)
Date:	September 30th 2013

Left (L)   z   Right (R)   x

(Bottom to Top View)

Measured cross-section:
(Centroid position for the middle of the tested specimen)

0.2993

2.9999   3.0290

Test Description:	- Lipped C-channel Beam-column Test (Loading rate: 7.5×10^{-5} in./sec) - Major axis bending moment and axial compression
Target eccentricity in x-dir (e$_{x0}$): -0.6 (in.)	Target eccentricity in z-dir (e$_{z0}$): 0.0 (in.)
Provided ave. ecc. in x-dir (e$_x$): -0.6 (in.)	
Provided ave. ecc. in z-dir (e$_z$)-Top: 0.005 (in.)	Provided ave. ecc in z-dir (e$_z$)-Bot: 0.001 (in.)
Initial end plate angles:	θ_{xT}= -2.26^o , θ_{zT}= -0.45^o , θ_{xB}= 0.16^o , θ_{zB}= 0.54^o

Beam-Column Specimen: S600-48-7

P=4.816 kips	P=8.269 kips	P=10.878 kips	P=6.233 kips
44% P$_m$	76% P$_m$	99% P$_m$	57% P$_m$ (post-peak)

Note: Several web buckling half-waves visible around P=7.5 kips. Flange deformations consistent with the web buckling. Sudden strength drop and global out-of-plane movement of the specimen in the Z-direction.

MTS Raw Load−Displacement

Load−Displacement Curves

Pm=10.942 kips

δ_m=0.054 in. (PTs)

Rotation of Top and Bottom Plates

P=0.25Pm
P=0.50Pm
P=0.75Pm
P=0.85Pm(PP)

θ_{XB}
θ_{XT}
θ_{ZB}
θ_{ZT}

Eccentricity at the ends of specimen

P=0.25Pm
P=0.50Pm
P=0.75Pm
P=0.85Pm(PP)

e_{XT}
e_{XB}
e_{ZT}
e_{ZB}

Cross−Sectional Deformation at the Mid−point

Scale Factor=1

P=0
P=0.25Pm
P=0.50Pm
P=0.75Pm
P=Pm
P=0.85Pm(PP)

L   R
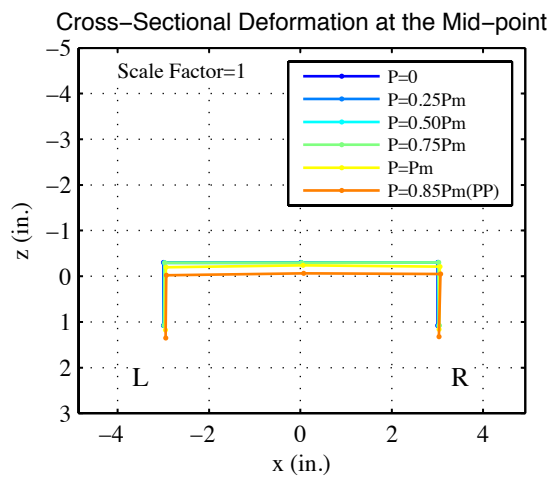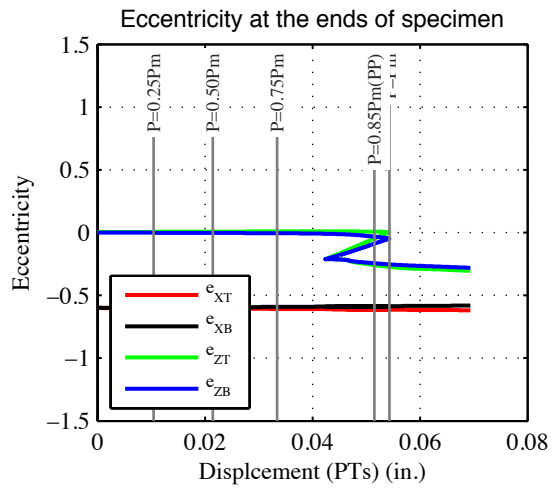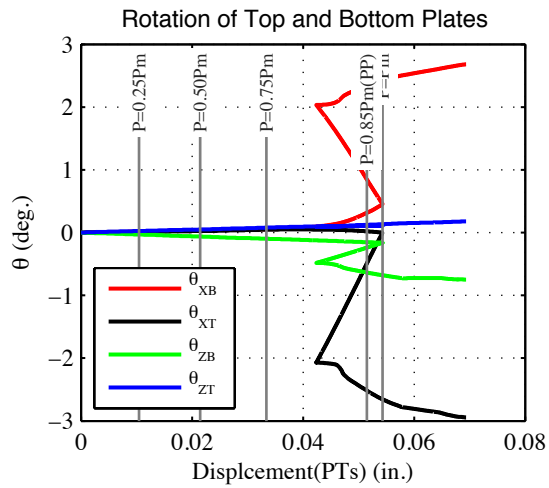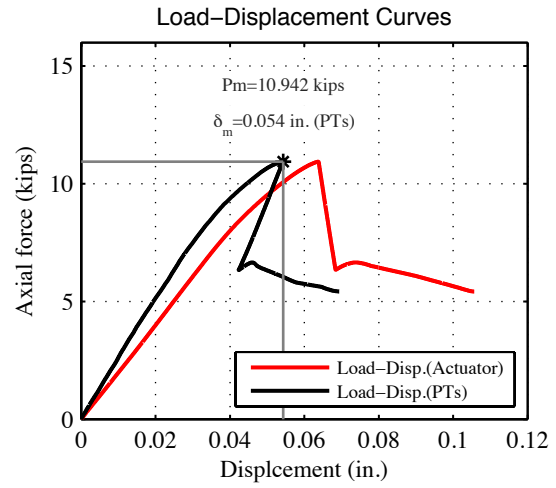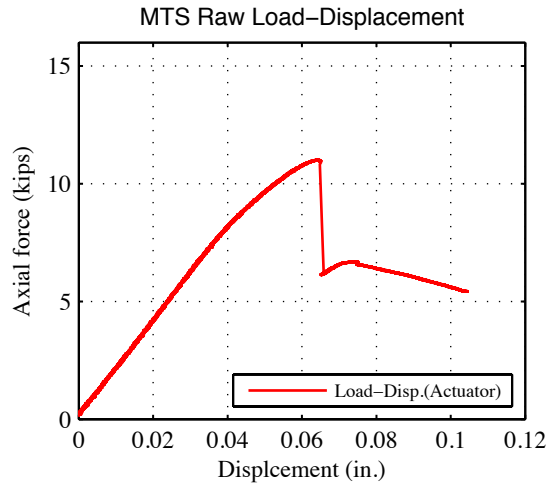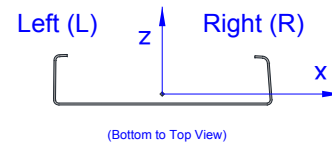
Specimen (S600-48-7) at post-peak stage (PP)

351

8- S600-48-e$_x$(-2.0)-e$_z$(0.0)

Tested Specimen:	S600-48-8 (L=48 inches)
Cross-section:	600S137-54 (AISI-S200-12 nomenclature)
Date:	September 30th 2013

Left (L) z Right (R)

x

(Bottom to Top View)

Measured cross-section:
(Centroid position for the middle of the tested specimen)

0.2992

3.0000 ——— 3.0314

Test Description:	- Lipped C-channel Beam-column Test (Loading rate: 7.5×10^{-5} in./sec) - Major axis bending moment and axial compression
Target eccentricity in x-dir (e$_{x0}$): -2.0 (in.)	Target eccentricity in z-dir (e$_{z0}$): 0.0 (in.)
Provided ave. ecc. in x-dir (e$_x$): -2.0 (in.)	
Provided ave. ecc. in z-dir (e$_z$)-Top: 0.015 (in.)	Provided ave. ecc in z-dir (e$_z$)-Bot: 0.078 (in.)
Initial end plate angles:	θ_{xT}= -1.49^o , θ_{zT}= 0.51^o , θ_{xB}= 0.38^o , θ_{zB}= 0.45^o

Beam-Column Specimen: S600-48-8

P=4.530 kips	P=6.104 kips	P=8.552 kips	P=3.918 kips
53% P$_m$	71% P$_m$	100% P$_m$	46% P$_m$ (post-peak)

Note: Flange distortional buckling half-waves in the left flange visible around P=7.0 kips. Web deformations consistent with the flange buckling. Sudden strength drop and global out-of-plane movement of the specimen in the Z-direction.
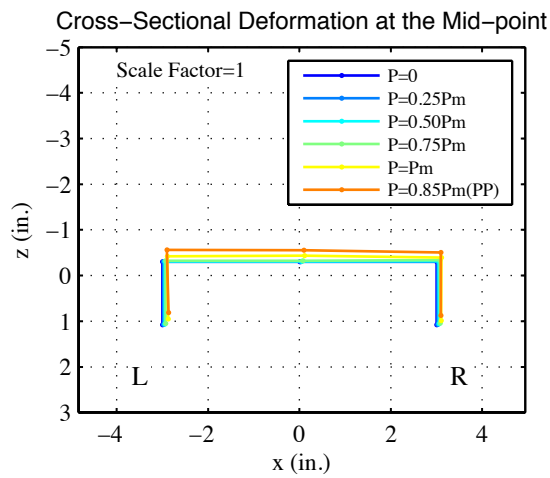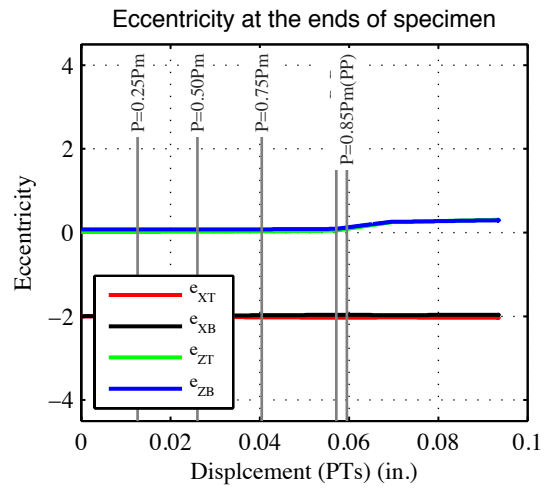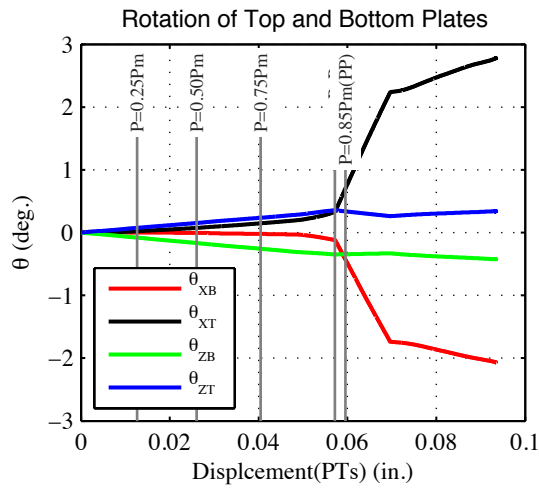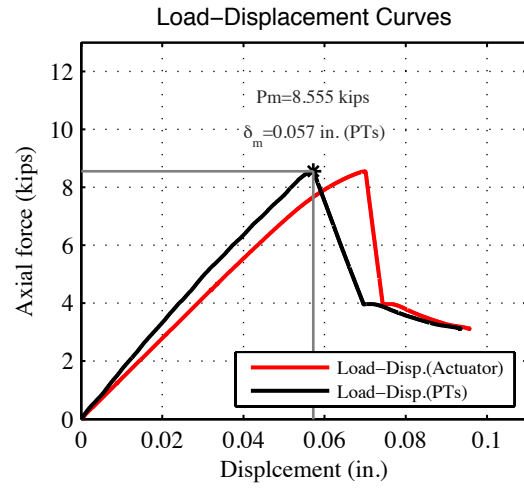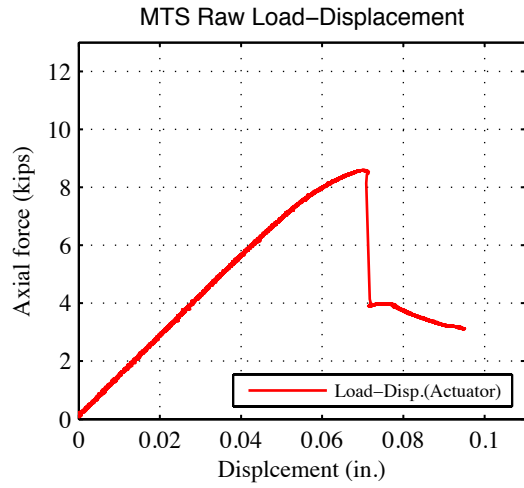
Specimen (S600-48-8) at post-peak stage (PP)

9- S600-48-e$_x$(-5.5)-e$_z$(0.0)

Tested Specimen:	S600-48-9 (L=48 inches)
Cross-section:	600S137-54 (AISI-S200-12 nomenclature)
Date:	October 1st 2013

Left (L) z Right (R)

x

(Bottom to Top View)

Measured cross-section:
(Centroid position for the middle of the tested specimen)

0.2974

2.9774 — 3.0474

Test Description:	- Lipped C-channel Beam-column Test (Loading rate: $7.5×10^{-5}$ in./sec) - Major axis bending moment and axial compression

Target eccentricity in x-dir (e$_{x0}$):	-5.5 (in.)	Target eccentricity in z-dir (e$_{z0}$):	0.0 (in.)
Provided ave. ecc. in x-dir (e$_x$):	-5.5 (in.)		
Provided ave. ecc. in z-dir (e$_z$)-Top:	-0.010 (in.)	Provided ave. ecc in z-dir (e$_z$)-Bot:	0.014 (in.)
Initial end plate angles:	θ_{xT}= -0.92^o , θ_{zT}= 0.39^o , θ_{xB}= 0.24^o , θ_{zB}= 0.13^o		

Beam-Column Specimen: S600-48-9

P=2.565 kips	P=4.019 kips	P=5.261 kips	P=2.296 kips
49% P$_m$	76% P$_m$	100% P$_m$	44% P$_m$ (post-peak)

Note: Flange distortional buckling half-waves in the left flange visible at around P=4.0 kips. Web deformations consistent with the flange buckling. Sudden strength drop and global out-of-plane movement of the specimen in the Z-direction.

MTS Raw Load–Displacement

Load–Displacement Curves

Pm=5.262 kips

δ_m=0.131 in. (PTs)

Rotation of Top and Bottom Plates

P=0.25Pm
P=0.50Pm
P=0.75Pm
P=Pm
P=0.85Pm(PP)

θ_{XB}
θ_{XT}
θ_{ZB}
θ_{ZT}

Eccentricity at the ends of specimen

P=0.25Pm
P=0.50Pm
P=0.75Pm
P=Pm
P=0.85Pm(PP)

e_{XT}
e_{XB}
e_{ZT}
e_{ZB}

Cross–Sectional Deformation at the Mid–point

Scale Factor=1

P=0
P=0.25Pm
P=0.50Pm
P=0.75Pm
P=Pm
P=0.85Pm(PP)

L   R
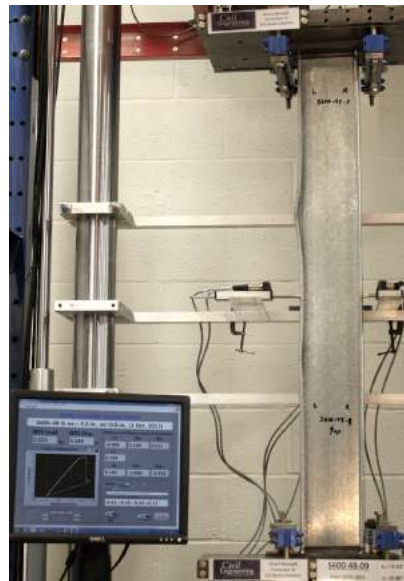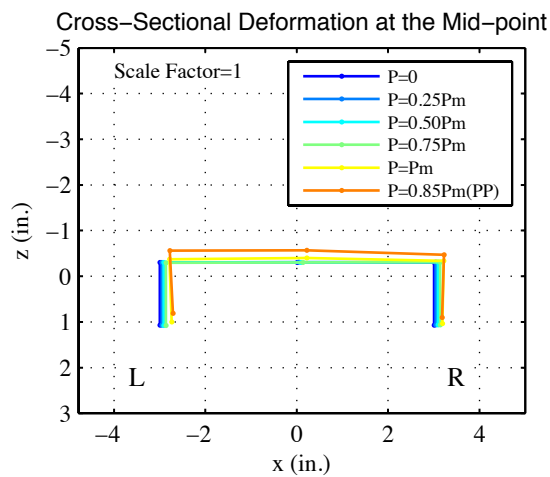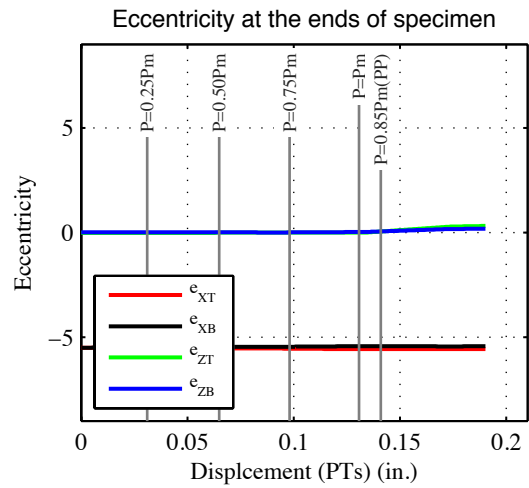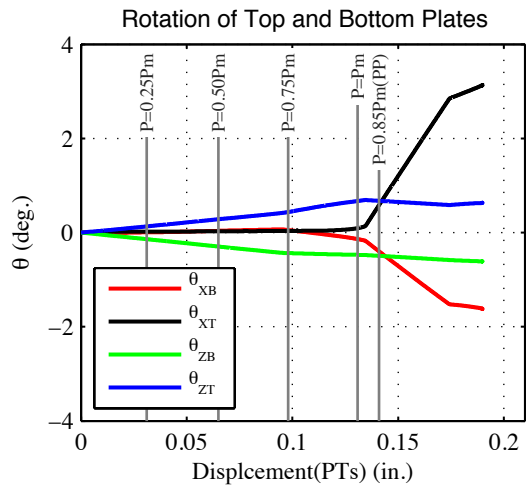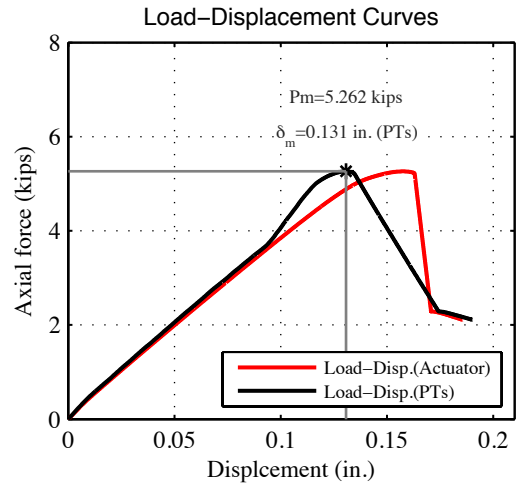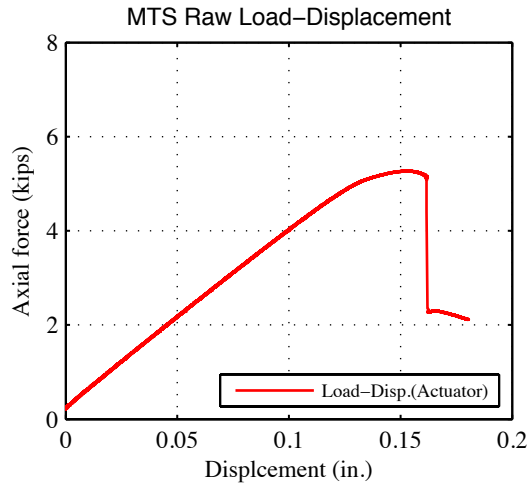
Specimen (S600-48-9) at post-peak stage (PP)

10- S600-48-e$_x$(-1.0)-e$_z$(0.07)

Tested Specimen:	S600-48-11 (L=48 inches)
Cross-section:	600S137-54 (AISI-S200-12 nomenclature)
Date:	October 1st 2013

Left (L)   z   Right (R)
x
(Bottom to Top View)

Measured cross-section:
(Centroid position for the middle of the tested specimen)

0.2987
2.9800   3.0406

| Test Description: | - Lipped C-channel Beam-column Test (Loading rate: 7.5×10^{-5} in./sec) |
| | - Biaxial bending moment and axial compression |

Target eccentricity in x-dir (e$_{x0}$):   -1.0 (in.)   Target eccentricity in z-dir (e$_{z0}$):   0.07 (in.)

Provided ave. ecc. in x-dir (e$_x$):   -1.0 (in.)

Provided ave. ecc. in z-dir (e$_z$)-Top: -0.079 (in.)   Provided ave. ecc in z-dir (e$_z$)-Bot: 0.076 (in.)

Initial end plate angles: θ_{xT}= -1.19^o , θ_{zT}= 0.40^o , θ_{xB}= 0.27^o , θ_{zB}= 0.33^o

Beam-Column Specimen: S600-48-11

P=3.072 kips	P=5.095 kips	P=6.805 kips	P=5.20 kips
45% P$_m$	75% P$_m$	100% P$_m$	76% P$_m$ (post-peak)

Note: Flange distortional buckling half-waves in the left flange visible at around P=4.0 kips. Small web deformations consistent with the flange buckling.

MTS Raw Load−Displacement

Load−Displacement Curves

Pm=6.806 kips

δ_m =0.035 in. (PTs)

Rotation of Top and Bottom Plates

P=0.25Pm

P=0.50Pm

P=0.75Pm

P=Pm

P=0.85Pm(PP)

Eccentricity at the ends of specimen

P=0.25Pm

P=0.50Pm

P=0.75Pm

P=Pm

P=0.85Pm(PP)

Cross−Sectional Deformation at the Mid−point

Scale Factor=1

P=0
P=0.25Pm
P=0.50Pm
P=0.75Pm
P=Pm
P=0.85Pm(PP)
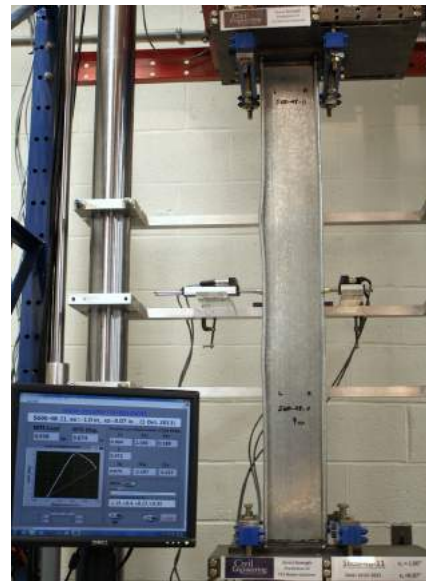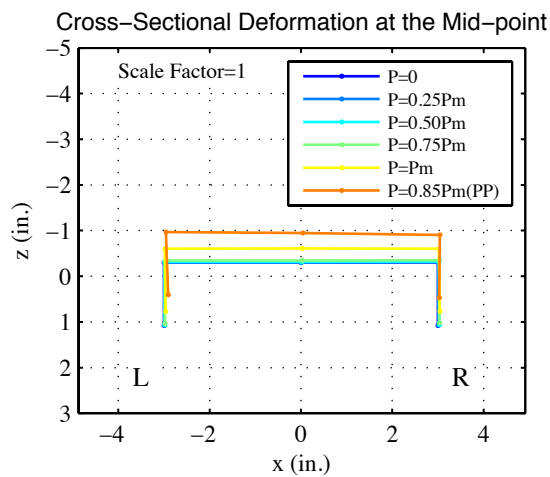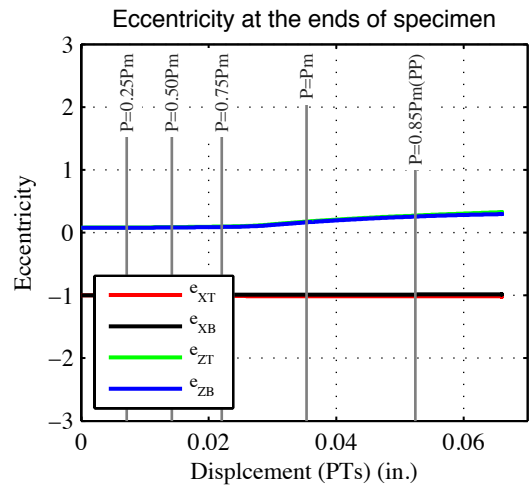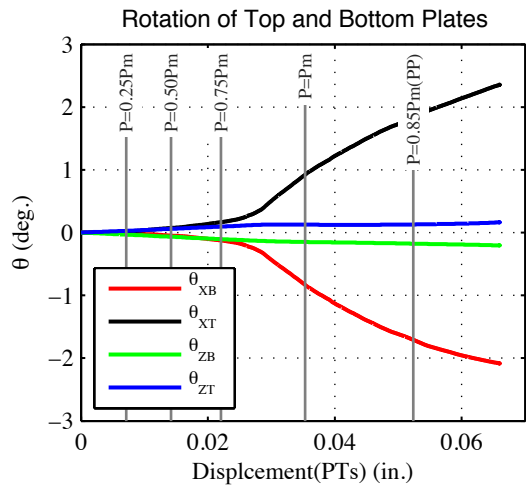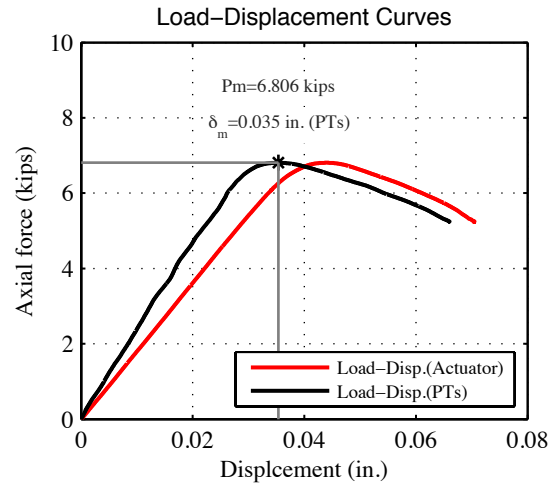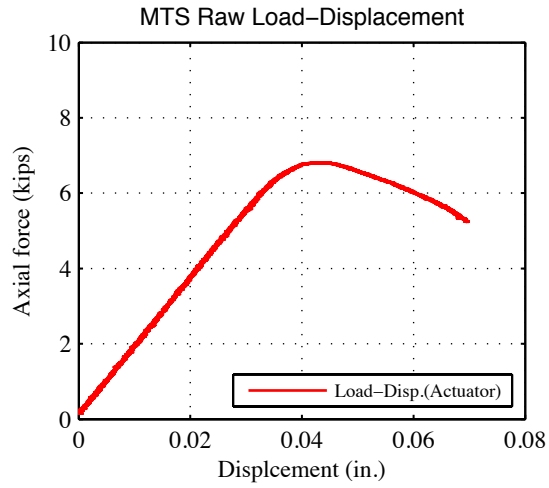
Specimen (S600-48-11) at post-peak stage (PP)

11- S600-48-e$_x$(-4.0)-e$_z$(0.27)

Tested Specimen:	S600-48-10 (L=48 inches)
Cross-section:	600S137-54 (AISI-S200-12 nomenclature)
Date:	November 1st 2013

Left (L) z Right (R) x
(Bottom to Top View)

Measured cross-section:
(Centroid position for the middle of the tested specimen)

0.2987
2.9800   3.0406

Test Description:	- Lipped C-channel Beam-column Test (Loading rate: 7.5×10^{-5} in./sec)
	- Biaxial bending moment and axial compression

Target eccentricity in x-dir (e$_{x0}$):	-4.0 (in.)	Target eccentricity in z-dir (e$_{z0}$):	0.0 (in.)

Provided ave. ecc. in x-dir (e$_x$):	-4.0 (in.)		
Provided ave. ecc. in z-dir (e$_z$)-Top:	0.238 (in.)	Provided ave. ecc in z-dir (e$_z$)-Bot:	0.295 (in.)
Initial end plate angles:	θ_{xT}= -0.92^o , θ_{zT}= 0.33^o , θ_{xB}= 0.12^o , θ_{zB}= 0.18^o		

Beam-Column Specimen: S600-48-10

P=2.023 kips	P=3.685 kips	P=4.095 kips	P=3.354 kips
49% P$_m$	90% P$_m$	100% P$_m$	82% P$_m$ (post-peak)

Note: Flange distortional buckling half-waves in the left flange visible at around P=3.0 kips. Small web deformations consistent with the flange buckling.

MTS Raw Load–Displacement

Load–Displacement Curves

Pm=4.096 kips

δ_m =0.075 in. (PTs)

Load–Disp.(Actuator)

Load–Disp.(Actuator)
Load–Disp.(PTs)

Rotation of Top and Bottom Plates

P=0.25Pm
P=0.50Pm
P=0.75Pm
P=Pm
P=0.85Pm(PP)

θ_{XB}
θ_{XT}
θ_{ZB}
θ_{ZT}

Eccentricity at the ends of specimen

P=0.25Pm
P=0.50Pm
P=0.75Pm
P=Pm
P=0.85Pm(PP)

e_{XT}
e_{XB}
e_{ZT}
e_{ZB}

Cross–Sectional Deformation at the Mid–point

Scale Factor=1

P=0
P=0.25Pm
P=0.50Pm
P=0.75Pm
P=Pm
P=0.85Pm(PP)

L   R
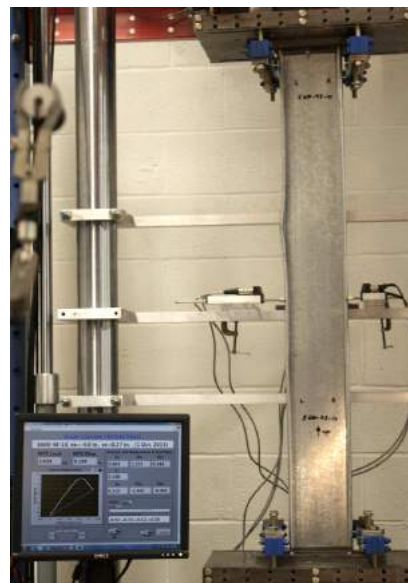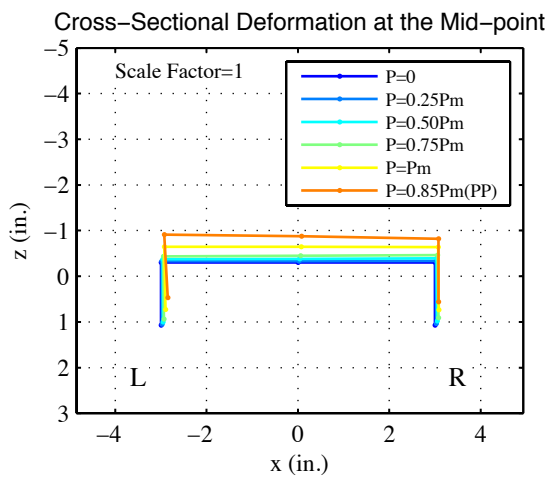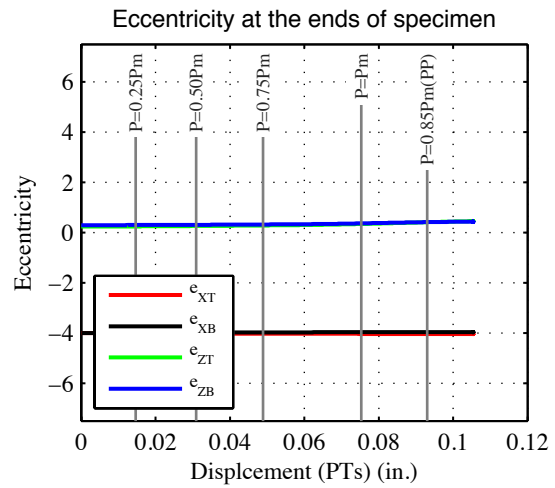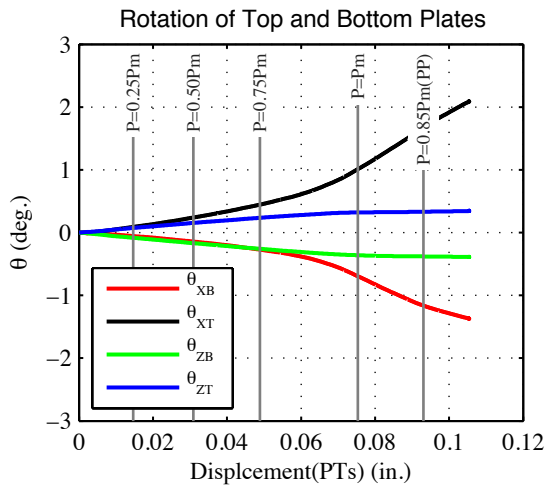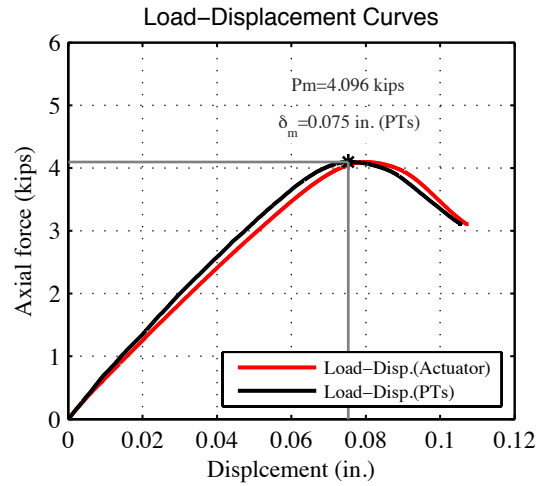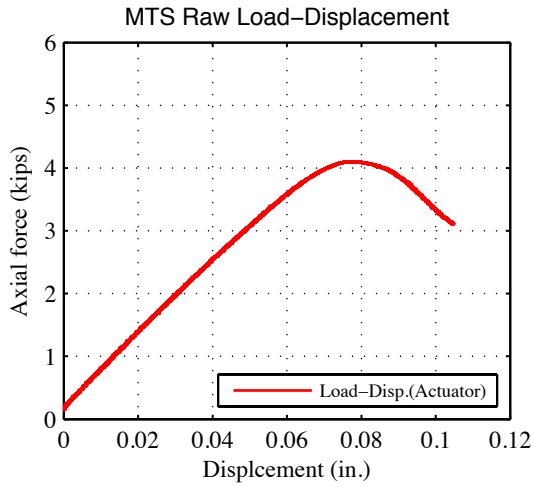
Specimen (S600-48-10) at post-peak stage (PP)

12- S600-48-e$_x$(-0.7)-e$_z$(0.14)

Tested Specimen:	S600-48-12 (L=48 inches)
Cross-section:	600S137-54 (AISI-S200-12 nomenclature)
Date:	October 2nd 2013

Left (L)   z   Right (R)

x

(Bottom to Top View)

Measured cross-section:
(Centroid position for the middle of the tested specimen)

0.3005

2.9857   3.0426

Test Description:	- Lipped C-channel Beam-column Test (Loading rate: $7.5×10^{-5}$ in./sec) - Biaxial bending moment and axial compression

Target eccentricity in x-dir (e$_{x0}$):	-0.7 (in.)	Target eccentricity in z-dir (e$_{z0}$):	0.14 (in.)
Provided ave. ecc. in x-dir (e$_x$):	-0.7 (in.)		
Provided ave. ecc. in z-dir (e$_z$)-Top:	0.143 (in.)	Provided ave. ecc in z-dir (e$_z$)-Bot:	0.149 (in.)
Initial end plate angles:	θ_{xT}= -1.36^o , θ_{zT}= 0.35^o , θ_{xB}= 0.10^o , θ_{zB}= 0.39^o		

Beam-Column Specimen: S600-48-12

P=3.059 kips	P=5.066 kips	P=5.998 kips	P=4.771 kips
51% P$_m$	84% P$_m$	100% P$_m$	80% P$_m$ (post-peak)

Note: Flange distortional buckling half-waves in the left flange visible at around P=5.0 kips. Small web deformations consistent with the flange buckling.
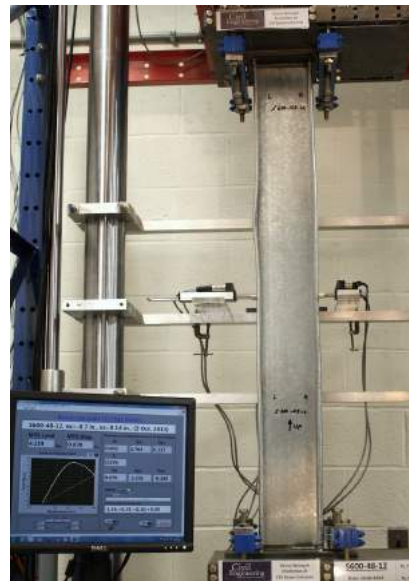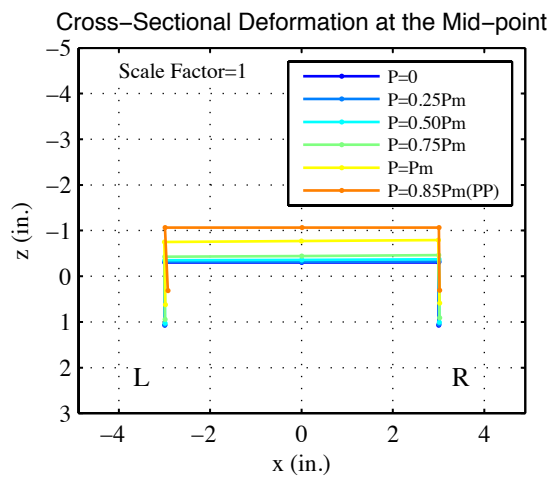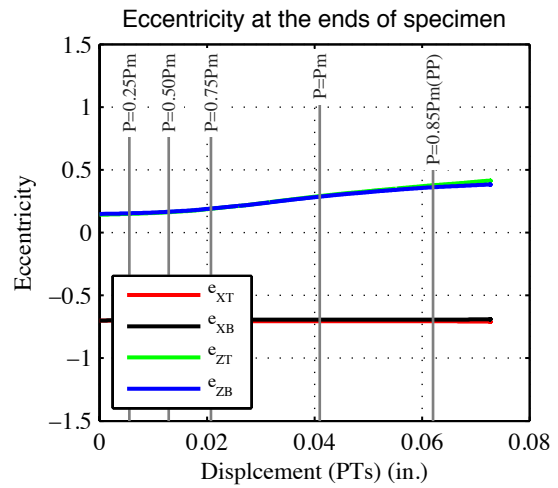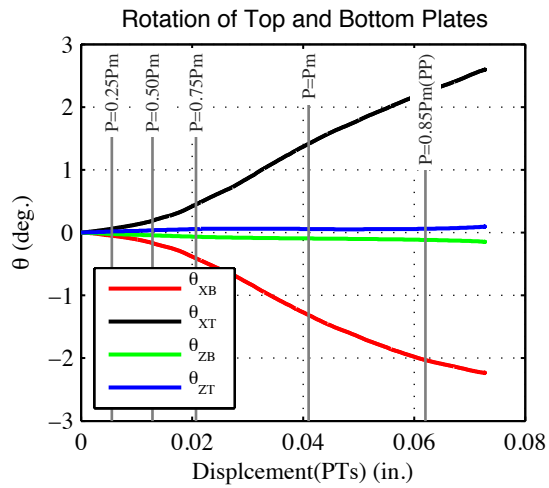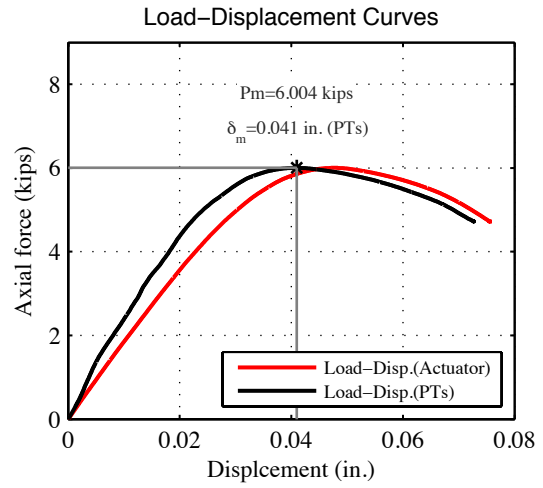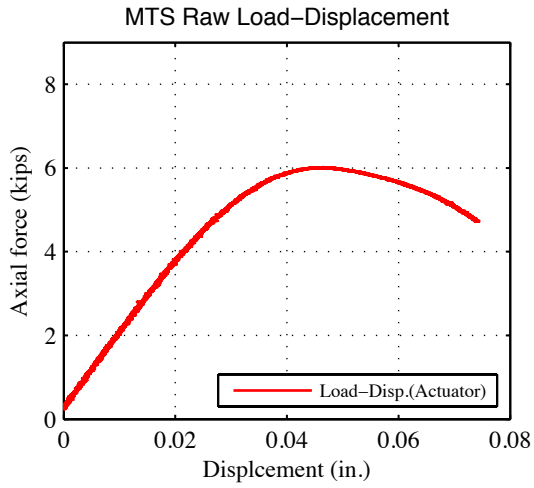
Specimen (S600-48-12) at post-peak stage (PP)

13- S600-48-e$_x$(-2.5)-e$_z$(0.51)

Tested Specimen:	S600-48-13 (L=48 inches)
Cross-section:	600S137-54 (AISI-S200-12 nomenclature)
Date:	October 3rd 2013

Left (L)   z   Right (R)

x

(Bottom to Top View)

Measured cross-section:
(Centroid position for the middle
of the tested specimen)

0.3009

2.9753   3.0567

Test Description:	- Lipped C-channel Beam-column Test (Loading rate: 7.5×10^{-5} in./sec) - Biaxial bending moment and axial compression

Target eccentricity in x-dir (e$_{x0}$): -2.5 (in.)   Target eccentricity in z-dir (e$_{z0}$): 0.51 (in.)

Provided ave. ecc. in x-dir (e$_x$): -2.5 (in.)

Provided ave. ecc. in z-dir (e$_z$)-Top: 0.492 (in.)   Provided ave. ecc in z-dir (e$_z$)-Bot: 0.523 (in.)

Initial end plate angles: θ_{xT}= -1.19^o , θ_{zT}= 0.41^o , θ_{xB}= 0.25^o , θ_{zB}= 0.26^o

Beam-Column Specimen: S600-48-13

P=2.167 kips	P=2.686 kips	P=3.551 kips	P=2.858 kips
61% P$_m$	76% P$_m$	100% P$_m$	80% P$_m$ (post-peak)

Note: Flange distortional buckling half-waves in the left flange visible at around P=3.0 kips. Small web deformations consistent with the flange buckling. Global movement in the Z-direction at the end of the test.

MTS Raw Load–Displacement

Load–Displacement Curves

Pm=3.552 kips

δ_m=0.075 in. (PTs)

Rotation of Top and Bottom Plates

P=0.25Pm
P=0.50Pm
P=0.75Pm
P=Pm
P=0.85Pm(PP)

θ_{XB}
θ_{XT}
θ_{ZB}
θ_{ZT}

Eccentricity at the ends of specimen

P=0.25Pm
P=0.50Pm
P=0.75Pm
P=Pm
P=0.85Pm(PP)

e_{XT}
e_{XB}
e_{ZT}
e_{ZB}

Cross–Sectional Deformation at the Mid–point

Scale Factor=1

P=0
P=0.25Pm
P=0.50Pm
P=0.75Pm
P=Pm
P=0.85Pm(PP)

L   R
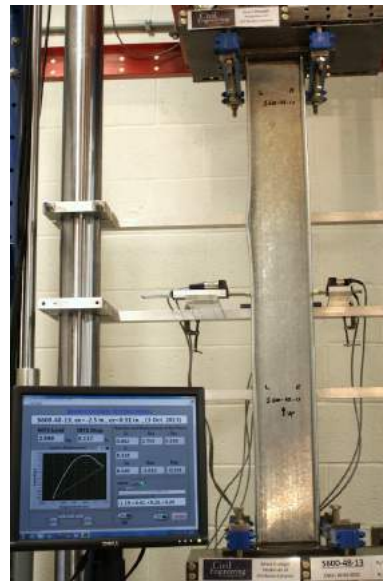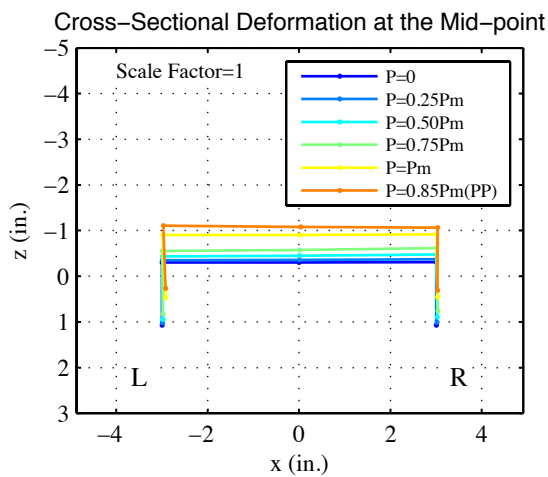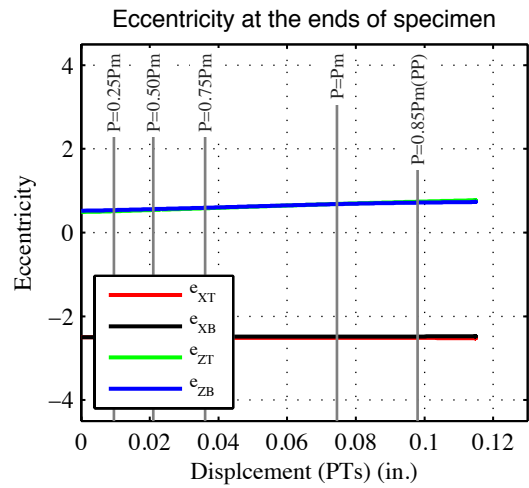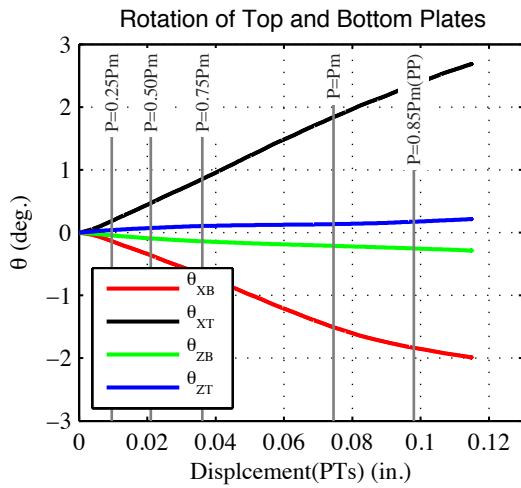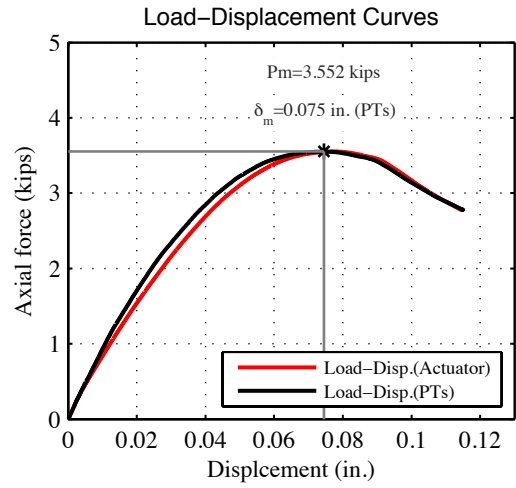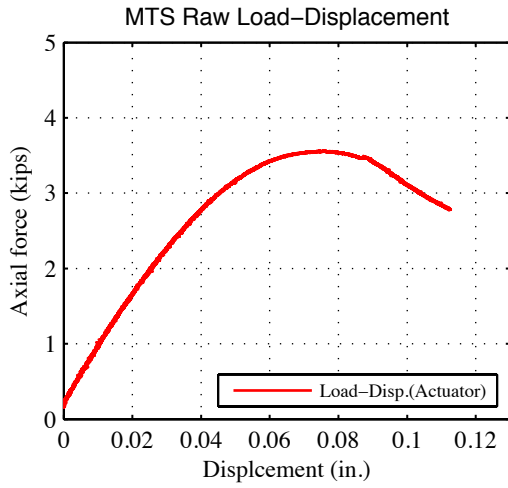
Specimen (S600-48-13) at post-peak stage (PP)

14- S600-48-e$_x$(-0.7)-e$_z$(-0.14)

Tested Specimen:	S600-48-14 (L=48 inches)
Cross-section:	600S137-54 (AISI-S200-12 nomenclature)
Date:	October 3rd 2013

Left (L) z Right (R)

x

(Bottom to Top View)

Measured cross-section:
(Centroid position for the middle of the tested specimen)

0.2996

2.9812   3.0467

Test Description:	- Lipped C-channel Beam-column Test (Loading rate: 7.5×10^{-5} in./sec) - Biaxial bending moment and axial compression

Target eccentricity in x-dir (e$_{x0}$):	-0.7 (in.)	Target eccentricity in z-dir (e$_{z0}$):	-0.14 (in.)

Provided ave. ecc. in x-dir (e$_x$):	-0.7 (in.)		
Provided ave. ecc. in z-dir (e$_z$)-Top:	-0.140 (in.)	Provided ave. ecc in z-dir (e$_z$)-Bot:	-0.134 (in.)
Initial end plate angles:	θ_{xT}= -1.08^o , θ_{zT}= 0.52^o , θ_{xB}= 0.43^o , θ_{zB}= 0.40^o		

Beam-Column Specimen: S600-48-14

P=2.223 kips	P=5.130 kips	P=6.094 kips	P=4.987 kips
36% P$_m$	84% P$_m$	100% P$_m$	81% P$_m$ (post-peak)

Note: Several local buckling half-waves along the length (symmetric about the mid-height) at around P=3.0 kips. Following the pick load, web plastic deformations at mid-height of the specimen.

MTS Raw Load–Displacement

Load–Displacement Curves

Pm=6.123 kips

δ_m=0.035 in. (PTs)

Rotation of Top and Bottom Plates

Eccentricity at the ends of specimen

Cross–Sectional Deformation at the Mid–point
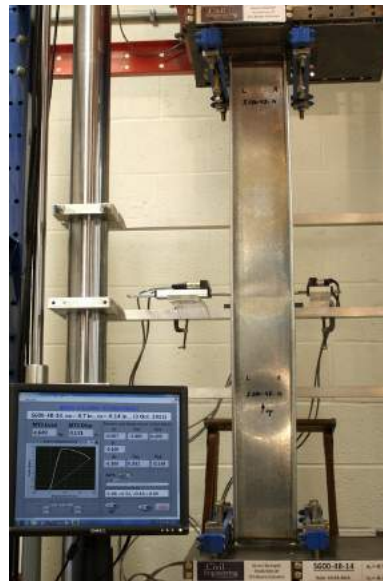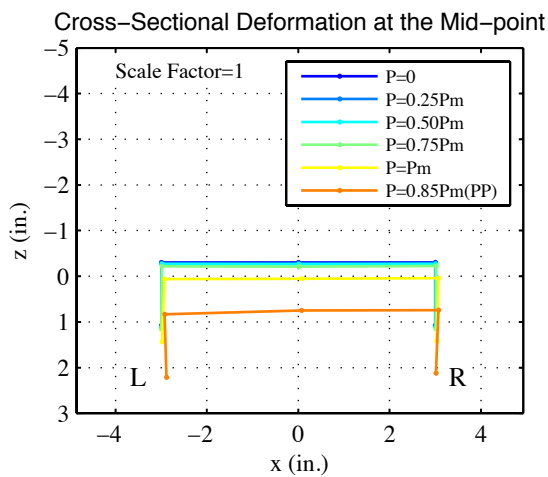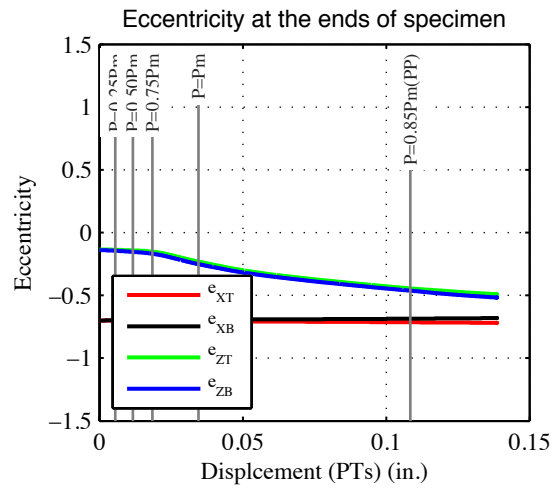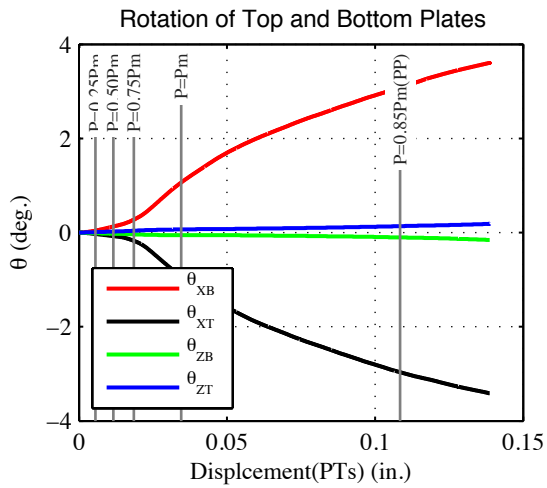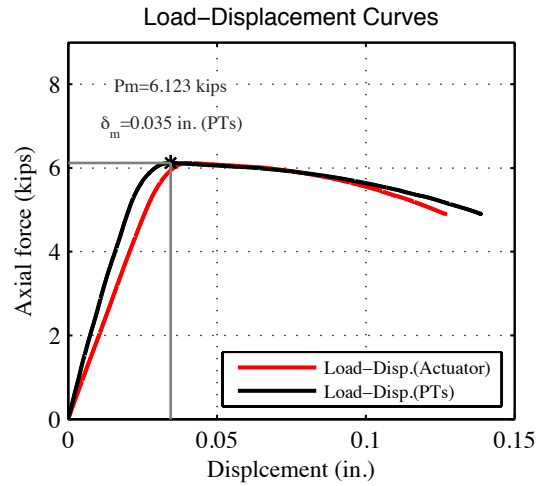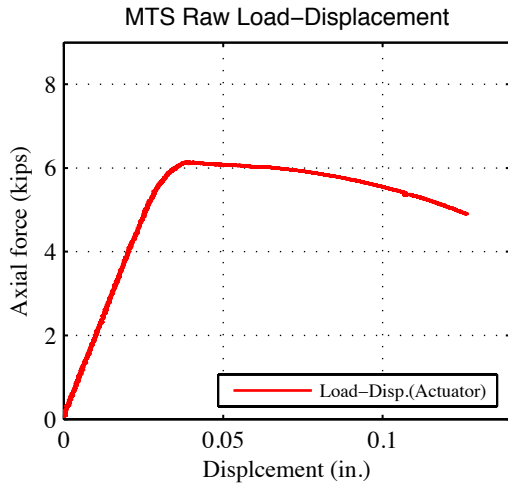
Specimen (S600-48-14) at post-peak stage (PP)

365

15- S600-48-e$_x$(-2.5)-e$_z$(-0.51)

Tested Specimen:	S600-48-15 (L=48 inches)
Cross-section:	600S137-54 (AISI-S200-12 nomenclature)
Date:	October 4nd 2013

Left (L) z Right (R) x

(Bottom to Top View)

Measured cross-section:
(Centroid position for the middle
of the tested specimen)

0.2990

2.9782 — 3.0528

Test Description:	- Lipped C-channel Beam-column Test (Loading rate: 7.5×10^{-5} in./sec) - Biaxial bending moment and axial compression

Target eccentricity in x-dir (e$_{x0}$):	-2.50 (in.)	Target eccentricity in z-dir (e$_{z0}$):	-0.51 (in.)
Provided ave. ecc. in x-dir (e$_x$):	-2.50 (in.)		
Provided ave. ecc. in z-dir (e$_z$)-Top:	-0.524 (in.)	Provided ave. ecc in z-dir (e$_z$)-Bot:	-0.499 (in.)
Initial end plate angles:	θ_{xT}= -1.27^o , θ_{zT}= 0.48^o , θ_{xB}= 0.27^o , θ_{zB}= 0.38^o		

Beam-Column Specimen: S600-48-15

P=2.128 kips	P=3.226 kips	P=3.954 kips	P=3.201 kips
54% P$_m$	81% P$_m$	100% P$_m$	81% P$_m$ (post-peak)

Note: Several local buckling half-waves along the length (One larger half-wave at the mid height) visible at around P=3.2 kips. Consistent flange outward movement at the end of the test.

MTS Raw Load−Displacement

Load−Displacement Curves

Pm=3.96 kips

δ_m=0.132 in. (PTs)

Rotation of Top and Bottom Plates

Eccentricity at the ends of specimen

Cross−Sectional Deformation at the Mid−point

Scale Factor=1
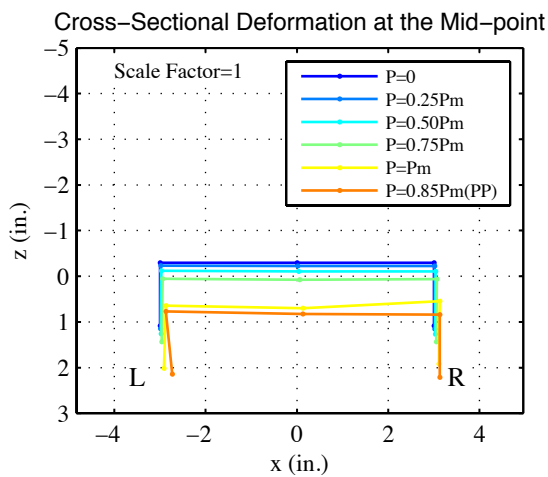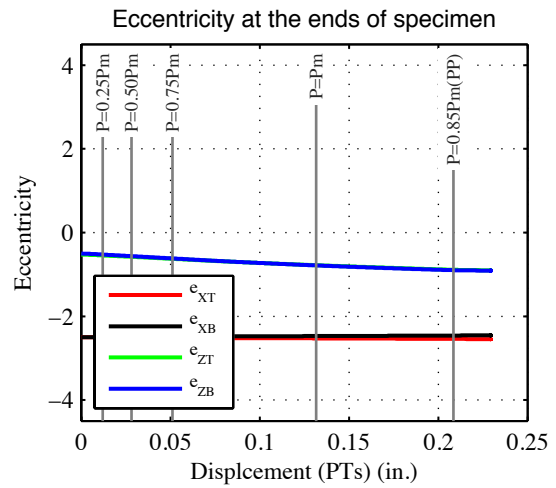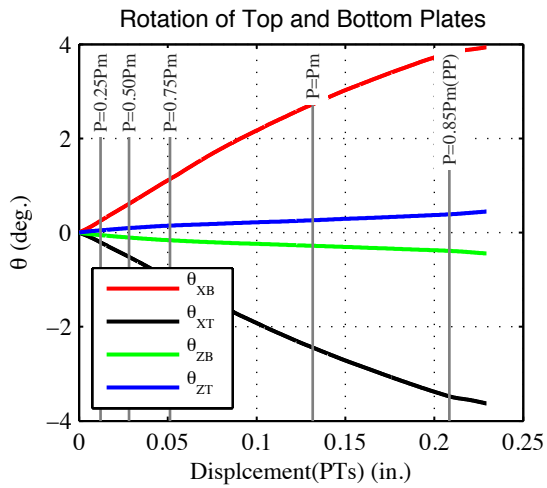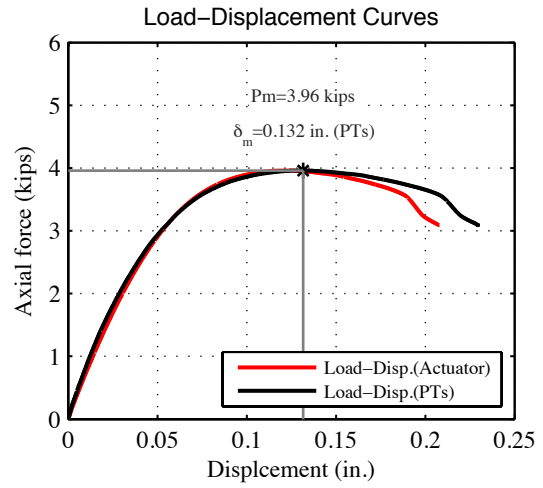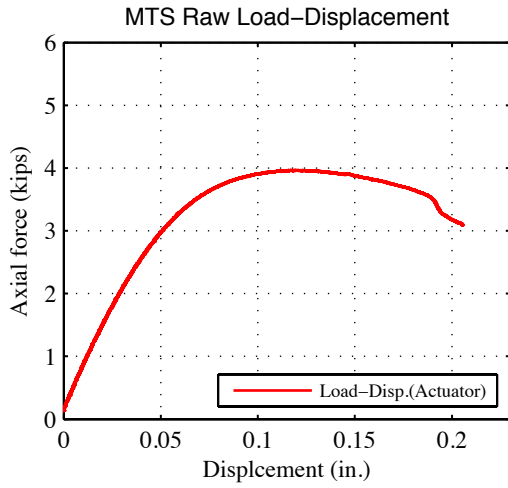
Specimen (S600-48-15) at post-peak stage (PP)

16- S600-48-e$_x$(-1.0)-e$_z$(-0.07)

Tested Specimen:	S600-48-16 (L=48 inches)
Cross-section:	600S137-54 (AISI-S200-12 nomenclature)
Date:	October 10nd 2013

Left (L)   z   Right (R)
x
(Bottom to Top View)

Measured cross-section:
(Centroid position for the middle of the tested specimen)

0.2994
2.9753   3.0545

Test Description:	- Lipped C-channel Beam-column Test (Loading rate: 7.5×10^{-5} in./sec) - Biaxial bending moment and axial compression
Target eccentricity in x-dir (e$_{x0}$): -1.0 (in.)	Target eccentricity in z-dir (e$_{z0}$): -0.07 (in.)

Provided ave. ecc. in x-dir (e$_x$):	-1.0 (in.)	
Provided ave. ecc. in z-dir (e$_z$)-Top: -0.077 (in.)		Provided ave. ecc in z-dir (e$_z$)-Bot: -0.061 (in.)
Initial end plate angles:	θ_{xT}= -1.01^o , θ_{zT}= 0.57^o , θ_{xB}= 0.34^o , θ_{zB}= 0.35^o	

Beam-Column Specimen: S600-48-16

P=3.623 kips	P=6.187 kips	P=7.84 kips	P=6.36 kips
46% P$_m$	79% P$_m$	100% P$_m$	81% P$_m$ (post-peak)

Note: Several local buckling half-waves along the length. Consistent flange movements. Sudden strength drop at the maximum load.

MTS Raw Load−Displacement

Load−Displacement Curves

Pm=7.846 kips

δ_m=0.037 in. (PTs)

Rotation of Top and Bottom Plates

Eccentricity at the ends of specimen

Cross−Sectional Deformation at the Mid−point
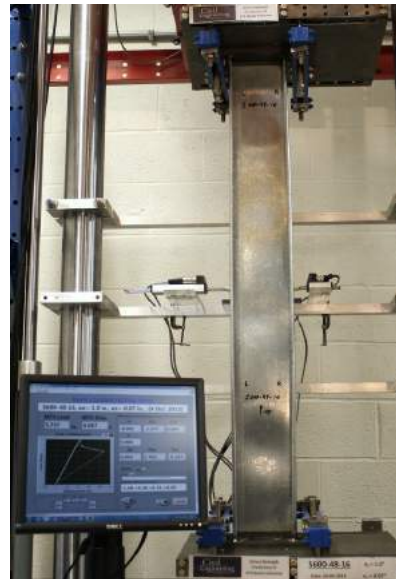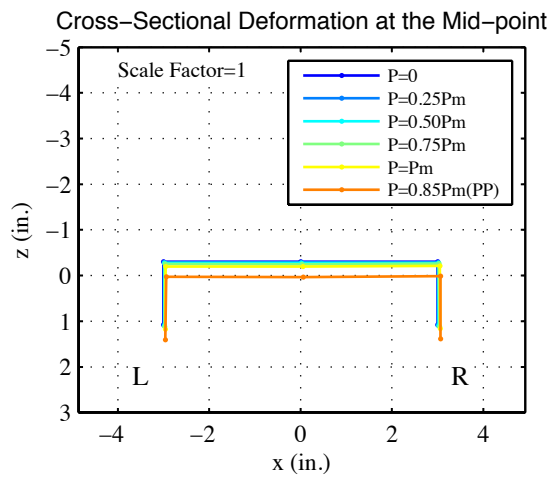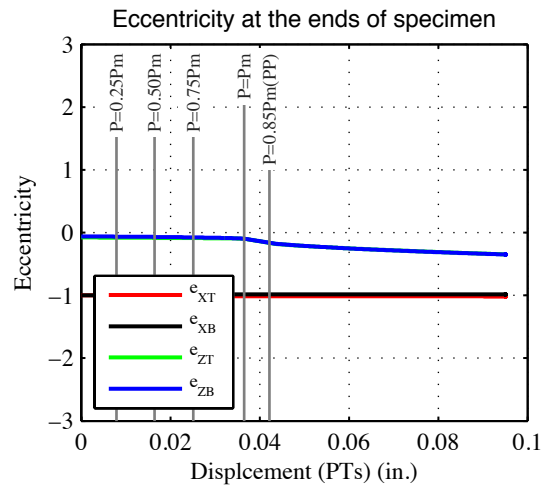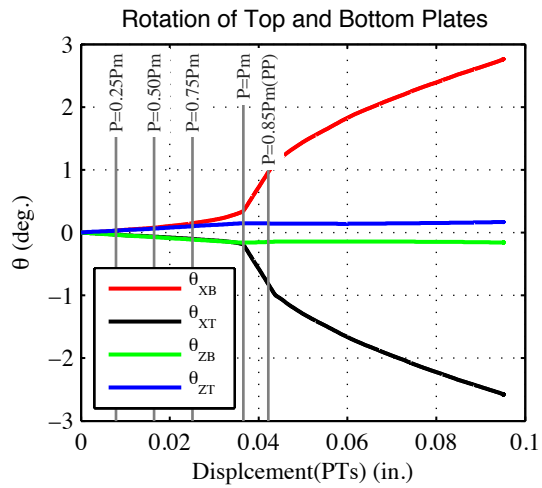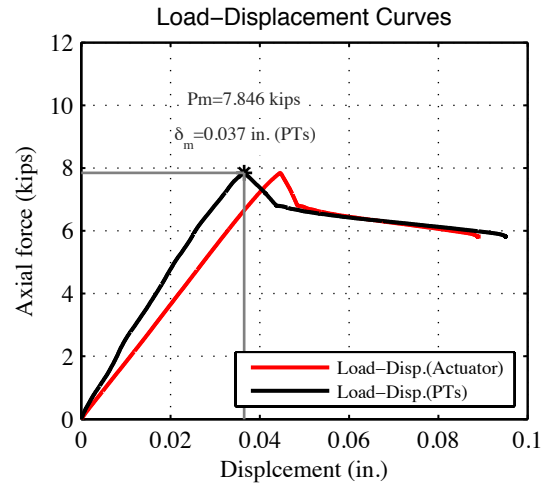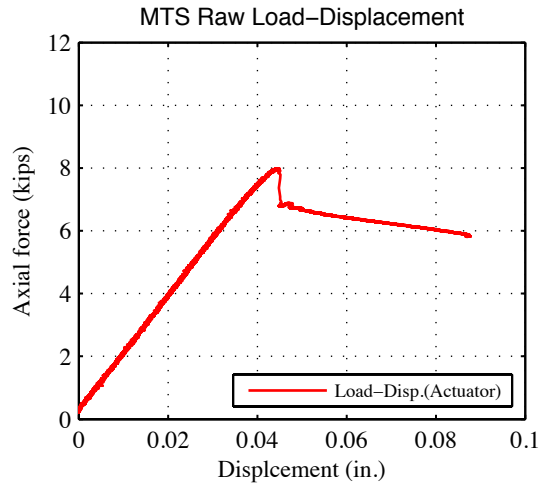
Specimen (S600-48-16) at post-peak stage (PP)

17- S600-48-e$_x$(-4.0)-e$_z$(-0.27)

Tested Specimen:	S600-48-17 (L=48 inches)
Cross-section:	600S137-54 (AISI-S200-12 nomenclature)
Date:	October 10nd 2013

Left (L) z Right (R) x
(Bottom to Top View)

Measured cross-section:
(Centroid position for the middle of the tested specimen)

0.3053
2.9909   3.0396

Test Description:	- Lipped C-channel Beam-column Test (Loading rate: 7.5×10^{-5} in./sec) - Biaxial bending moment and axial compression
Target eccentricity in x-dir (e$_{x0}$): -4.0 (in.)	Target eccentricity in z-dir (e$_{z0}$): -0.27 (in.)

Provided ave. ecc. in x-dir (e$_x$):	-2.50 (in.)
Provided ave. ecc. in z-dir (e$_z$)-Top: -0.290 (in.)	Provided ave. ecc in z-dir (e$_z$)-Bot: -0.242 (in.)
Initial end plate angles:	θ_{xT}= -1.01^o , θ_{zT}= 0.57^o , θ_{xB}= 0.34^o , θ_{zB}= 0.35^o
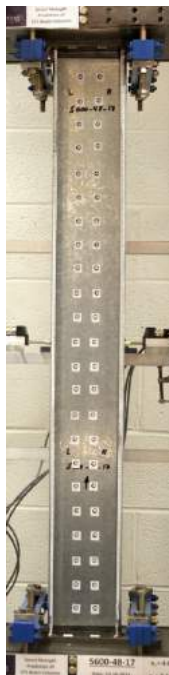
Beam-Column Specimen: S600-48-17

P=2.365 kips	P=3.714 kips	P=4.501 kips	P=3.349 kips
53% P$_m$	83% P$_m$	100% P$_m$	74% P$_m$ (post-peak)
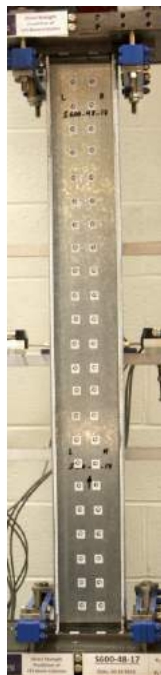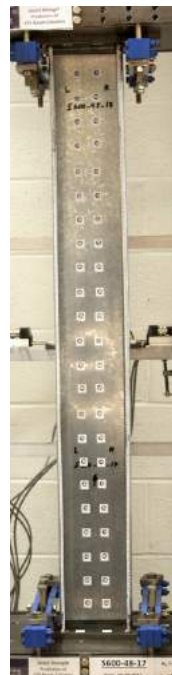
Note: Several local buckling half-waves along the length. One larger unsymmetrical half-wave at the mid height visible at around P=4 kips. Consistent small flange movement at the end of the test.

MTS Raw Load–Displacement

Load–Displacement Curves

Pm=4.501 kips

δ_m=0.103 in. (PTs)

Rotation of Top and Bottom Plates

Eccentricity at the ends of specimen

Cross−Sectional Deformation at the Mid−point
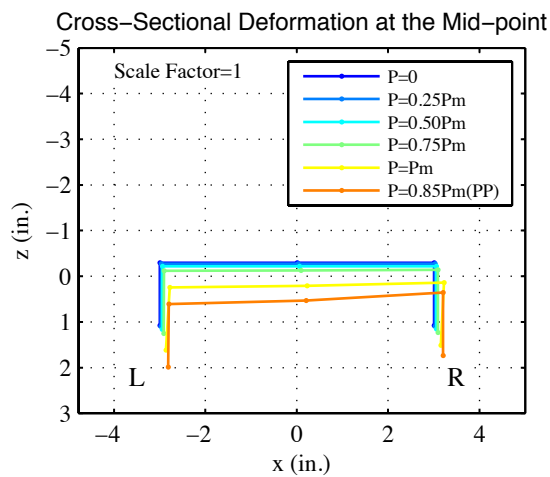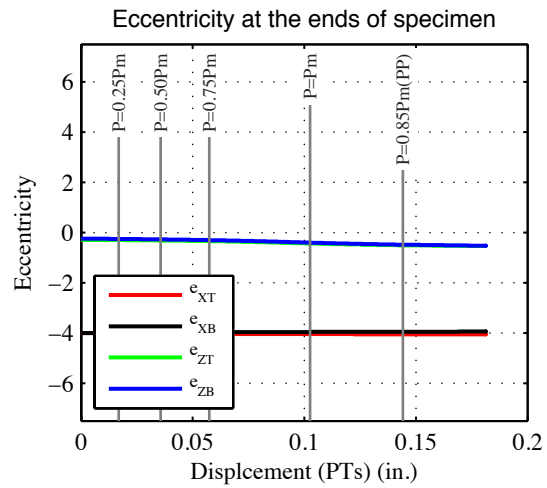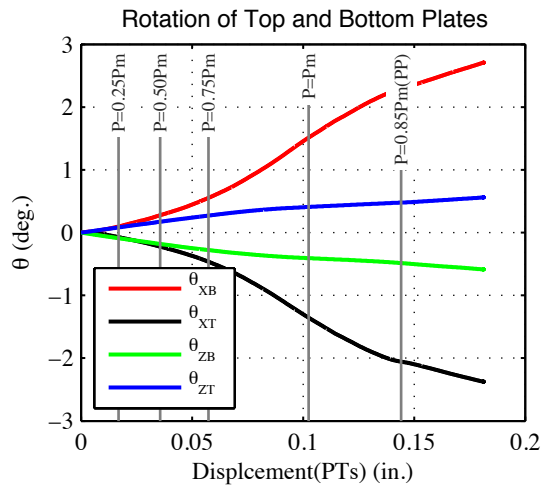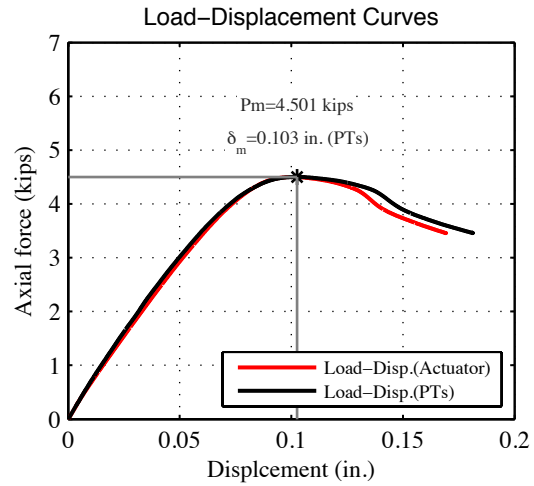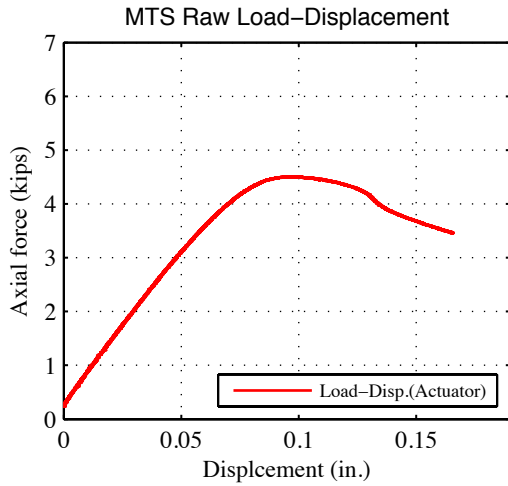
Specimen (S600-48-17) at post-peak stage (PP)

18- S600-48-e$_x$(0.0)-e$_z$(0.0)

Tested Specimen:	S600-48-18 (L=48 inches)
Cross-section:	600S137-54 (AISI-S200-12 nomenclature)
Date:	October 11nd 2013

Left (L)   z   Right (R)   x

(Bottom to Top View)

Measured cross-section:
(Centroid position for the middle
of the tested specimen)

0.3020

2.9811   3.0378
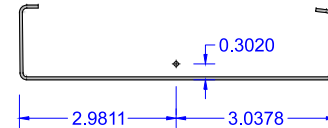
Test Description:	- Lipped C-channel Beam-column Test (Loading rate: 7.5×10^{-5} in./sec)
	- Axial compression (Column test)

Target eccentricity in x-dir (e$_{x0}$):	0.0 (in.)	Target eccentricity in z-dir (e$_{z0}$):	0.0 (in.)

Provided ave. ecc. in x-dir (e$_x$):	0.0 (in.)		
Provided ave. ecc. in z-dir (e$_z$)-Top:	0.006 (in.)	Provided ave. ecc in z-dir (e$_z$)-Bot:	0.000 (in.)
Initial end plate angles:	θ_{xT}= -1.18^o , θ_{zT}= 0.46^o , θ_{xB}= 0.15^o , θ_{zB}= 0.24^o		
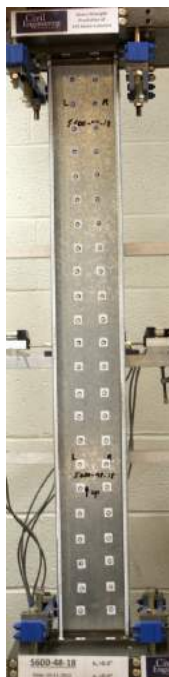
Beam-Column Specimen: S600-48-18

P=5.223 kips	P=8.231 kips	P=11.009 kips	P=6.410 kips
47% P$_m$	75% P$_m$	100% P$_m$	58% P$_m$ (post-peak)

Note: Several local buckling half-waves along the length visible at around P=5 kips. Consistent flange movements along the length. Sudden Strength drop at the maximum load.

MTS Raw Load–Displacement

Load–Displacement Curves

Pm=11.056 kips

δ_m=0.049 in. (PTs)

Rotation of Top and Bottom Plates

P=0.25Pm
P=0.50Pm
P=0.75Pm
P=Pm
P=0.85Pm(PP)

Eccentricity at the ends of specimen

P=0.25Pm
P=0.50Pm
P=0.75Pm
P=Pm
P=0.85Pm(PP)

Cross–Sectional Deformation at the Mid–point

Scale Factor=1

P=0
P=0.25Pm
P=0.50Pm
P=0.75Pm
P=Pm
P=0.85Pm(PP)

L   R
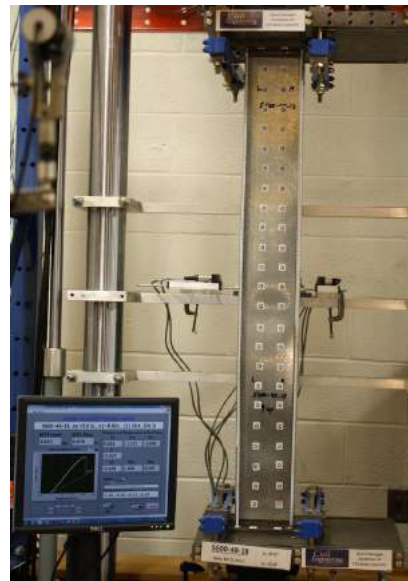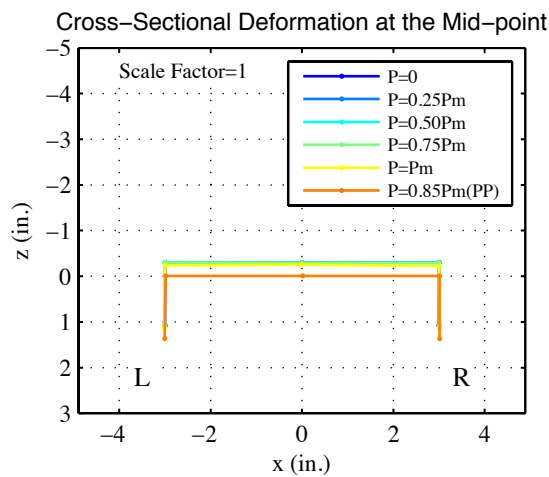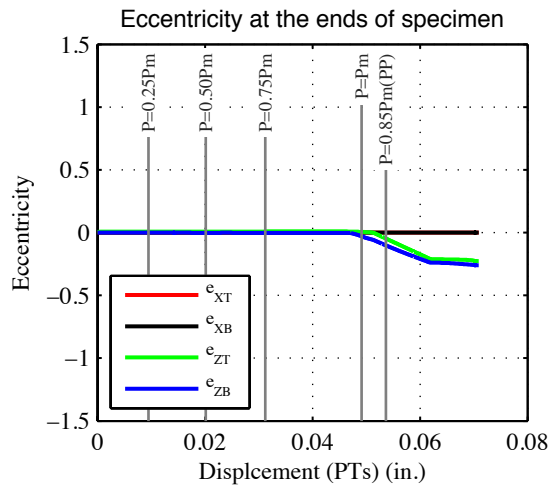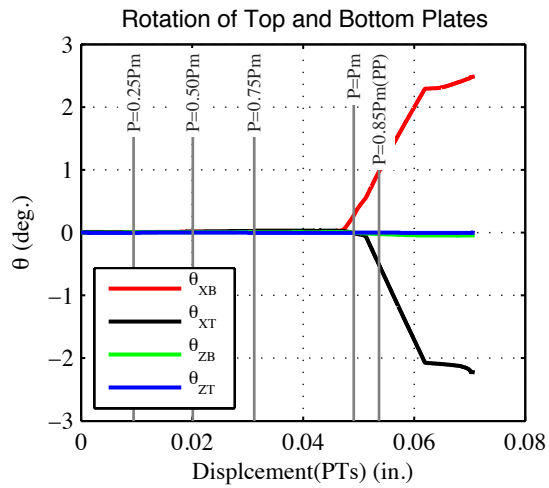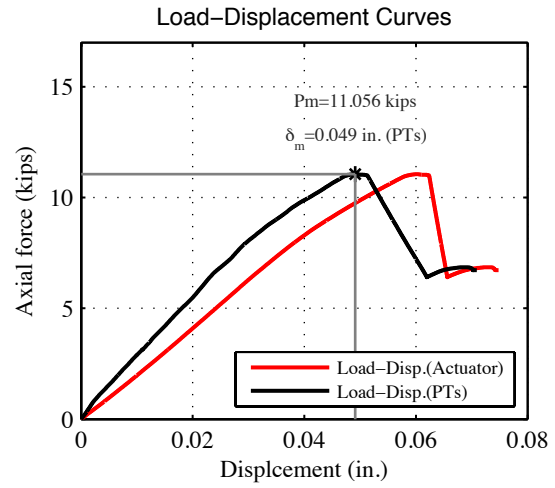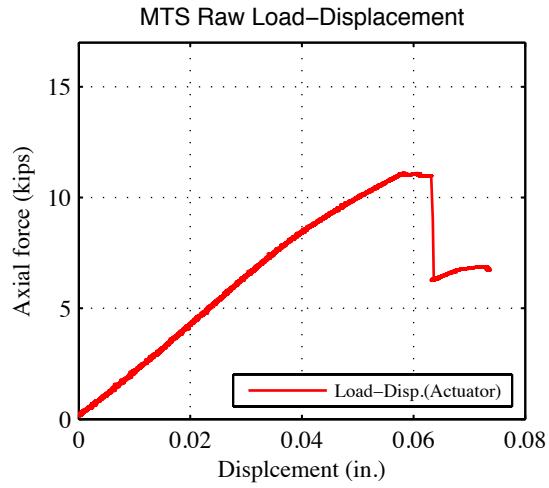
Specimen (S600-48-18) at post-peak stage (PP)

Appendix G - Comparison of failure modes: Test vs. FEM

G.1 Failure modes: Short Specimens (S600-12)

The failure modes are calculated by using finite element models for 4 options (PGNDPL-C, NGNDNL-C, PGPDPL-C, NGPDNL-C) in the report: the model with nominal cross section; with positive or negative global, local, and distortional buckling mode of imperfection; and with residual stress.
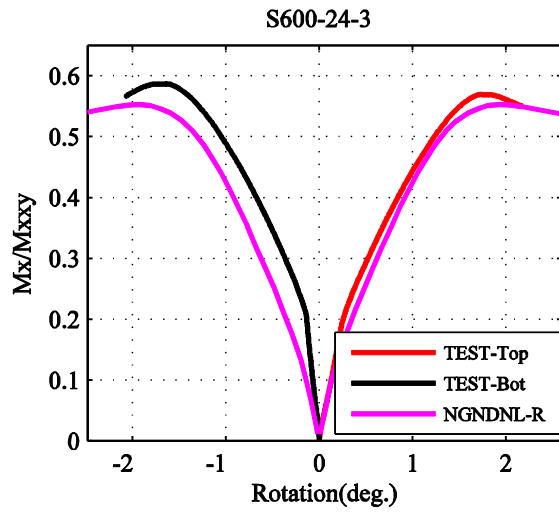
Comparisons showed a quite reasonable agreement. However, failure shapes are not completely same as the observed failure shapes, but the failure modes in the models and in the observations are qualitatively consisted in terms of identification of local web buckling (LWB) or flange distortional buckling (FDB).

(a) Positive Distortional and Positive Local   (b) Positive Distortional and Negative Local

(c) Negative Distortional and Positive Local   (d) Negative Distortional and Negative Local
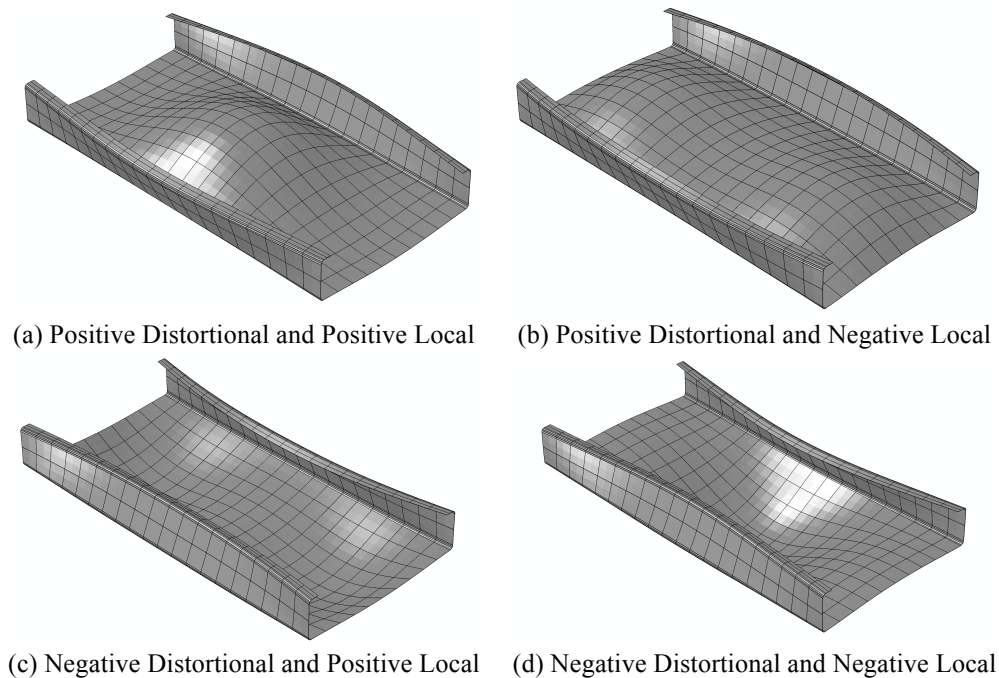
Figure G-1: Combined buckling shapes (Global buckling shape in not shown)

374

Test	PGNDPL	S600-12-1 NGNDNL	PGPDPL	NGPDNL

S600-12-2

S600-12-3

S600-12-4

Test	PGNDPL	S600-12-5 NGNDNL	PGPDPL	NGPDNL

S600-12-6

S600-12-8

S600-12-9

Test	PGNDPL	S600-12-10 NGNDNL	PGPDPL	NGPDNL

S600-12-11

S600-12-13

S600-12-14

Test	PGNDPL	S600-12-15 NGNDNL	PGPDPL	NGPDNL

S600-12-16

S600-12-17

S600-12-19

S600-12-20

| Test | PGNDPL | NGNDNL | PGPDPL | NGPDNL |
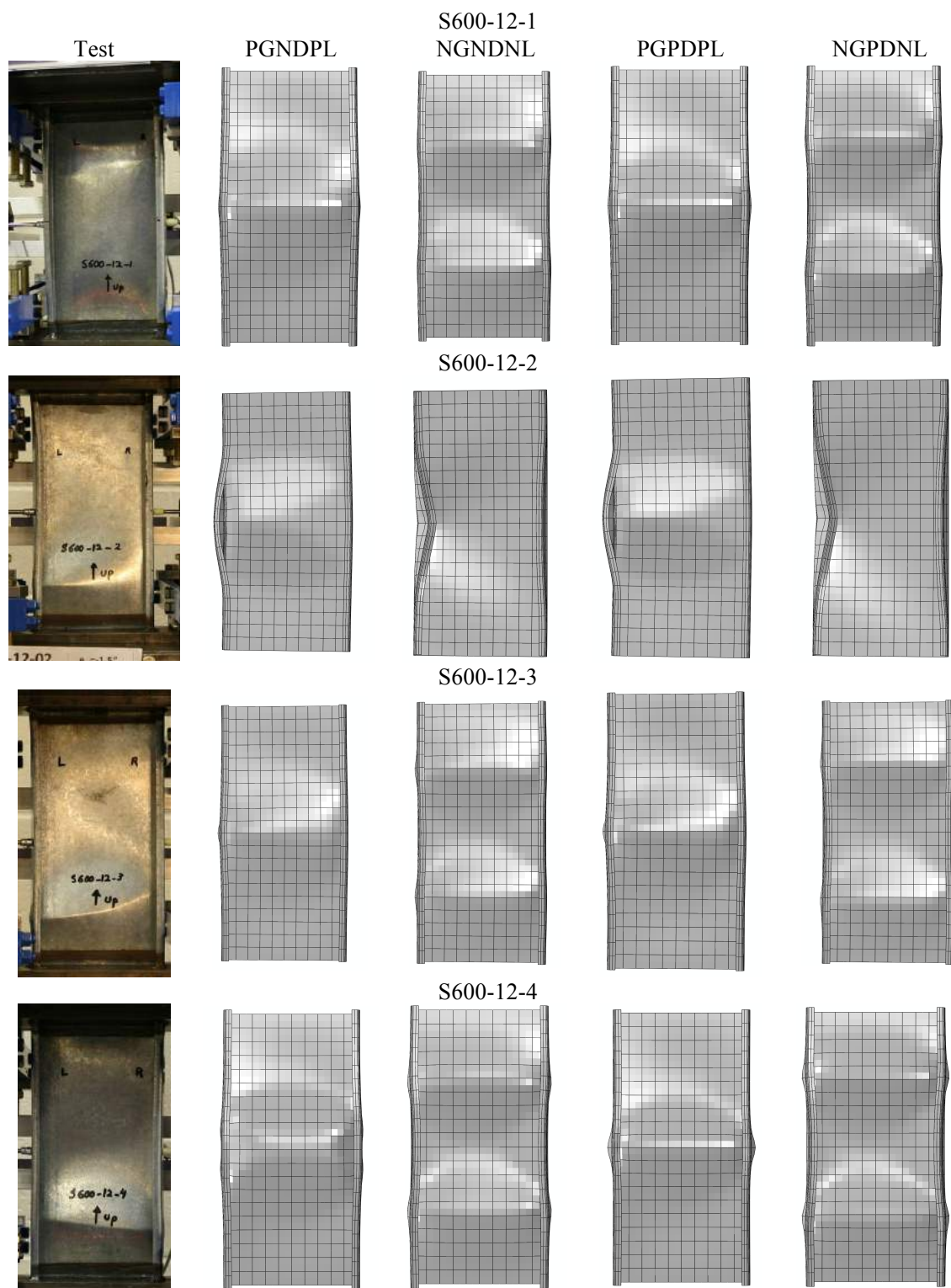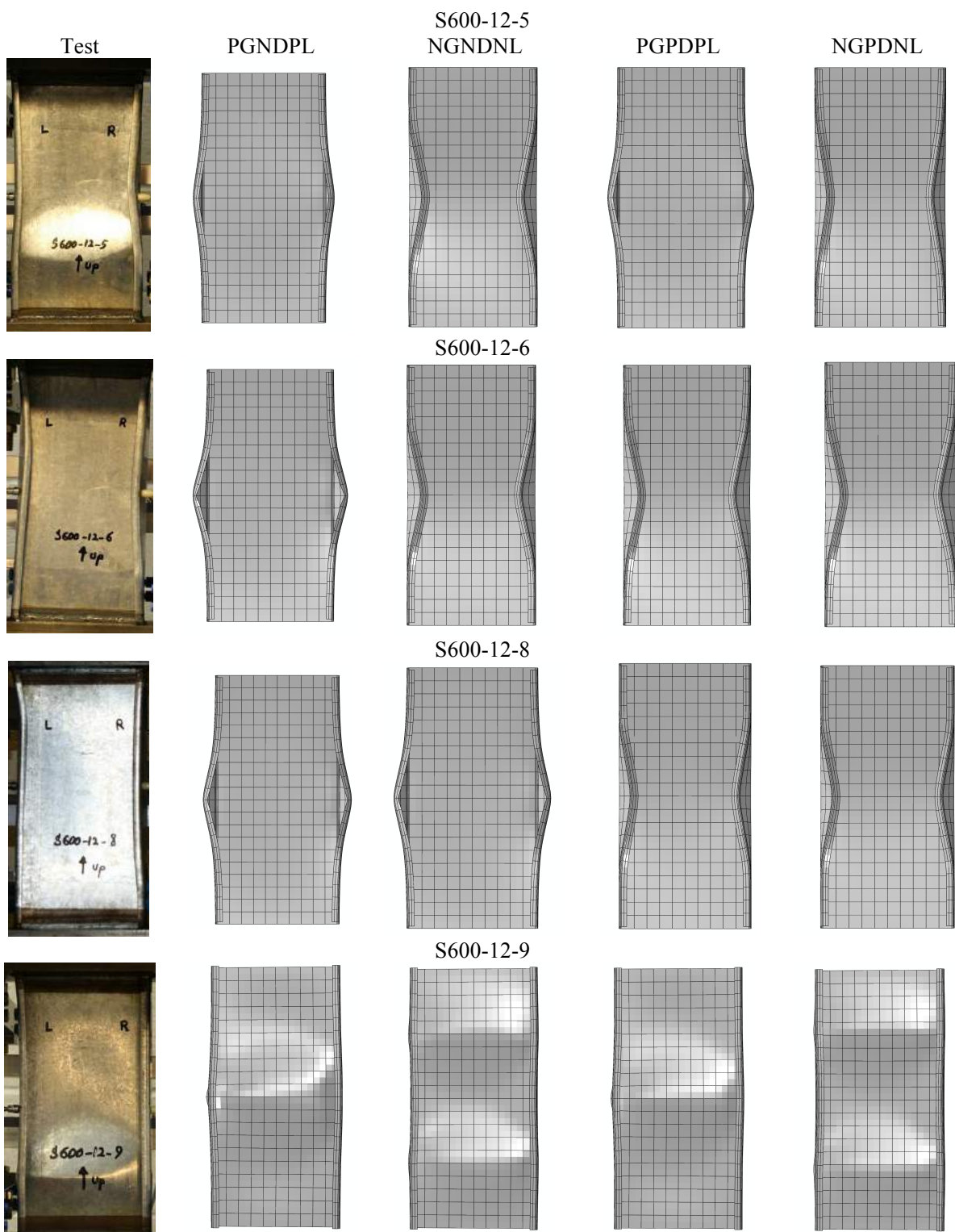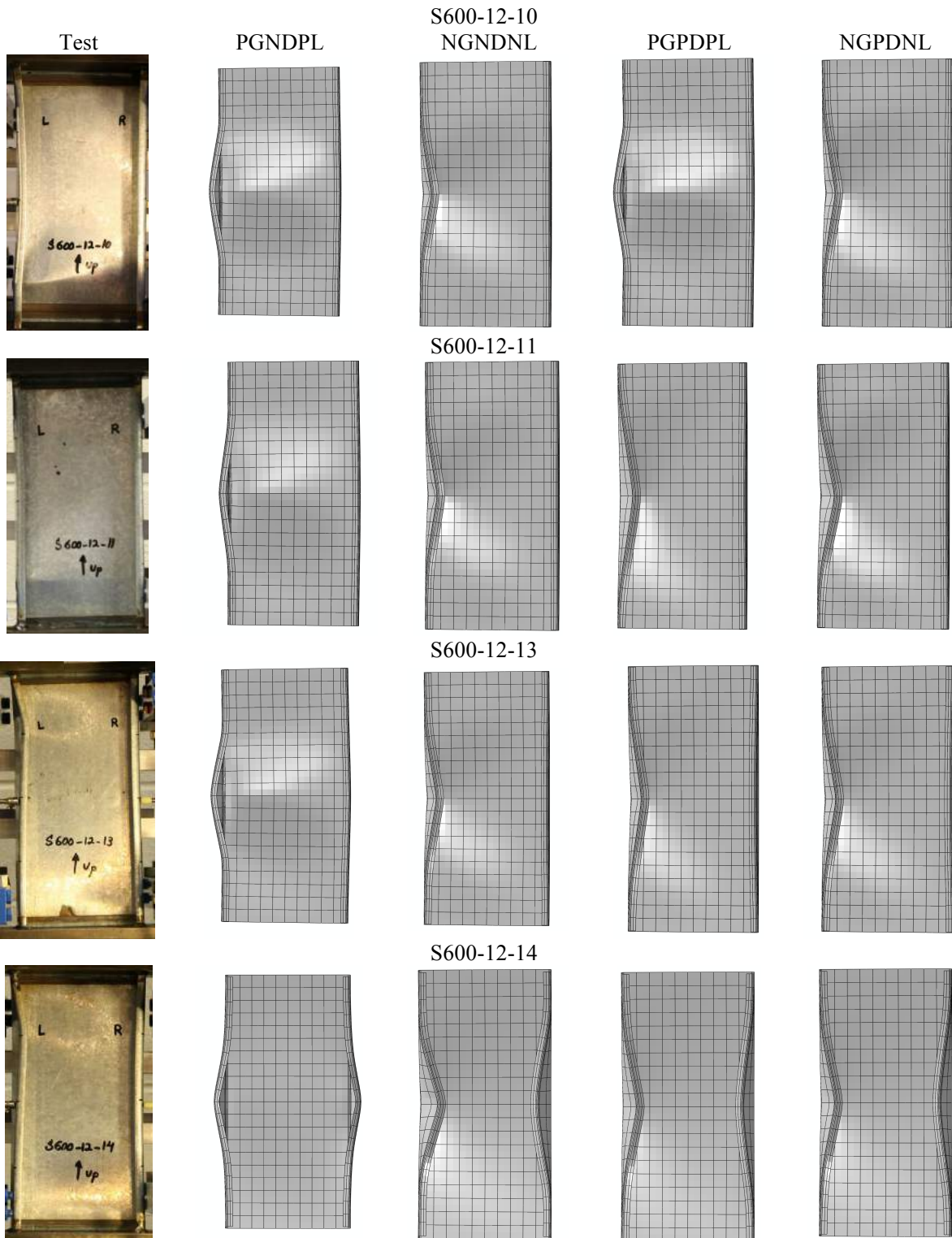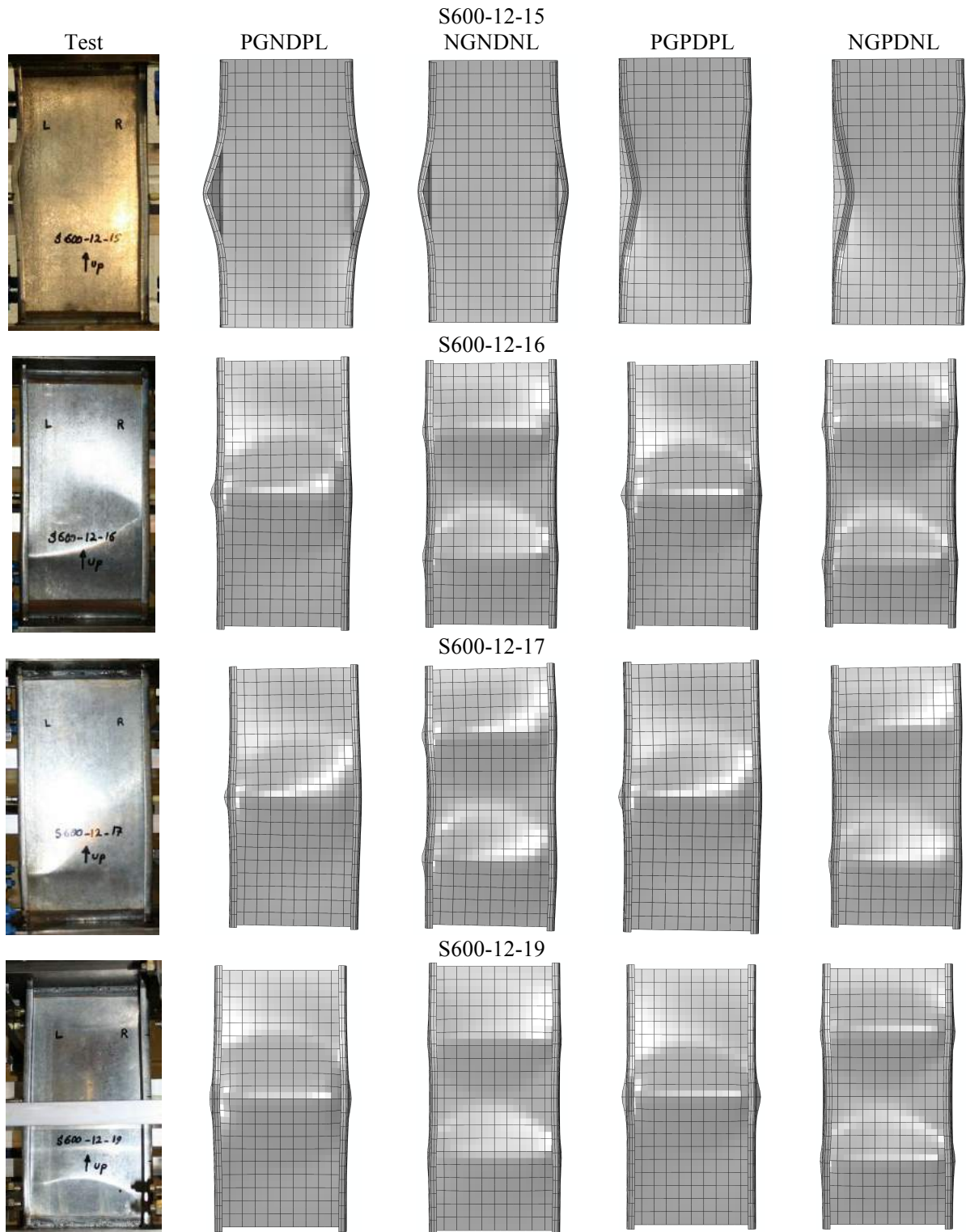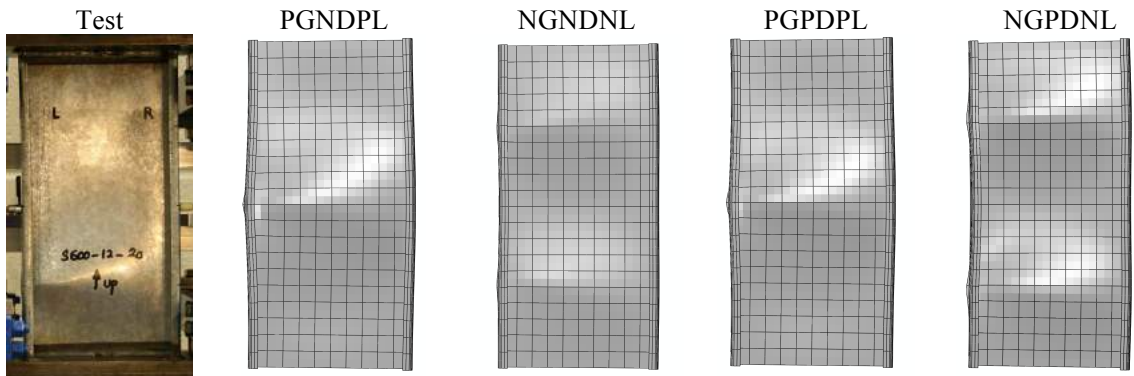
G.2 Failure modes: Intermediate Specimens (S600-24)

The failure modes are calculated by using finite element models for 2 options (NGNDNL-C/PGPDPL-C) in the report: the model with nominal cross section; with positive/negative global, local, and distortional buckling mode of imperfection; and with residual stress.

Comparisons showed a quite reasonable agreement. However, failure shapes are not completely same as the observed failure shapes, but the failure modes in the models and in the observations are qualitatively consisted in terms of identification of local web buckling (LWB) or flange distortional buckling (FDB)

(a) Negative Global buckling mode

(b) Positive Global buckling mode

(c) Negative Distortional buckling mode

(d) Positive Distortional buckling mode

(e) Negative Local buckling mode

(f) Positive Local buckling mode
Figure G-2: All buckling modes
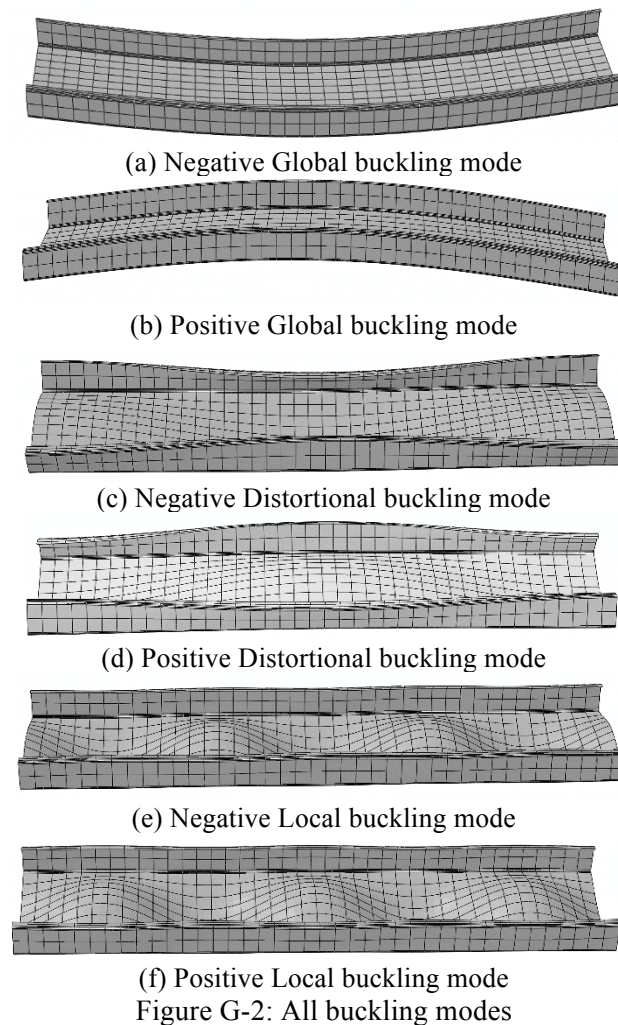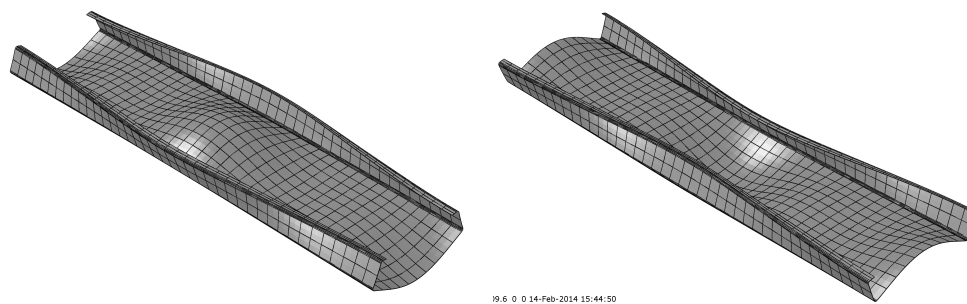
PGPDPL   NGNDNL

Figure G-3: Combined buckling modes

S600-24-1
Test   PGPDPL   NGNDNL

S600-24-4
Test   PGPDPL   NGNDNL

S600-48-2

S600-48-5

S600-48-3

S600-24-6

382

S600-24-7

S600-24-10

S600-24-8

S600-24-11

S600-24-9

S600-24-12

Test S600-24-13 PGPDPL NGNDNL

Test S600-24-16 PGPDPL NGNDNL

S600-24-14

S600-24-17

S600-24-15

S600-24-18
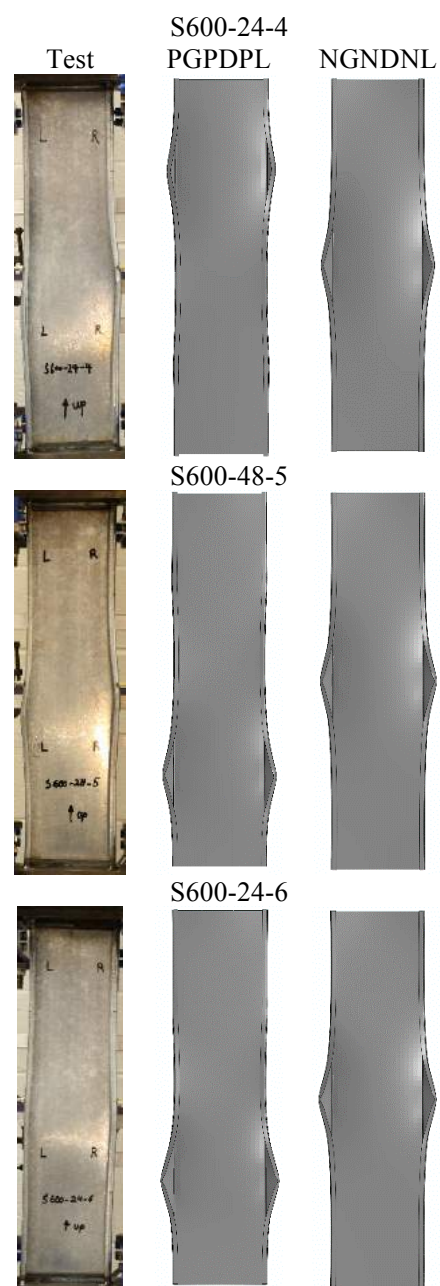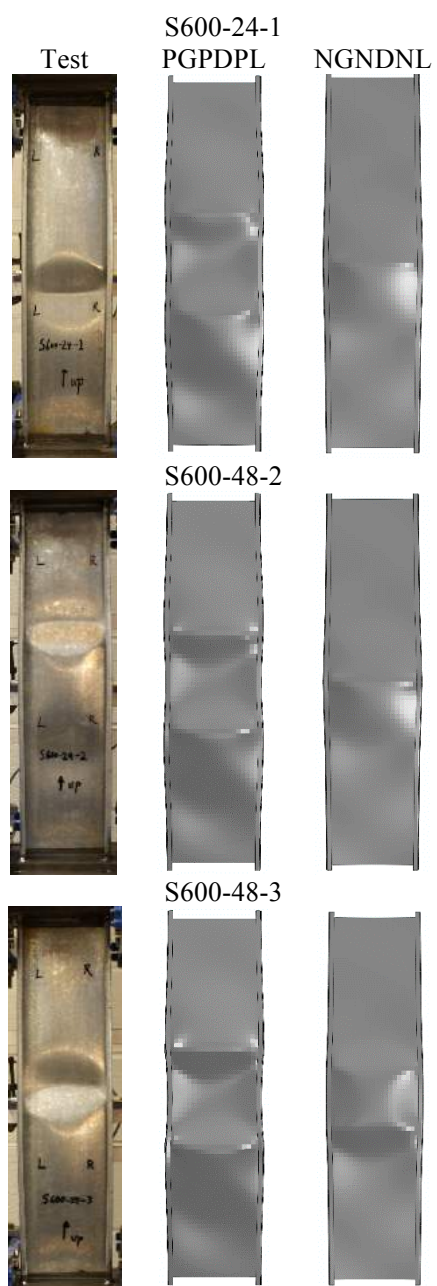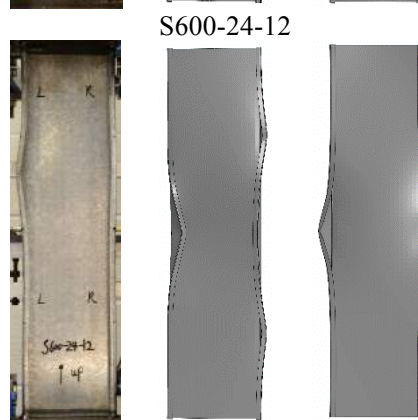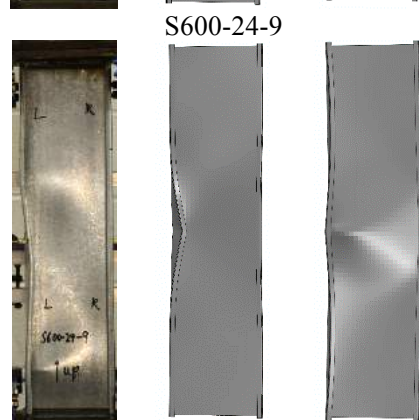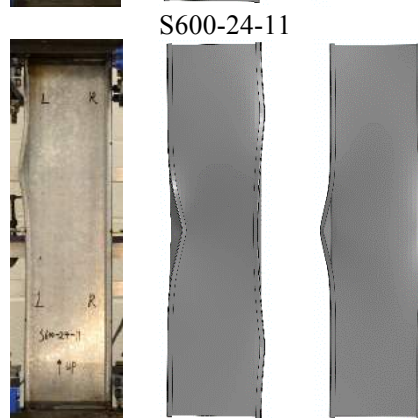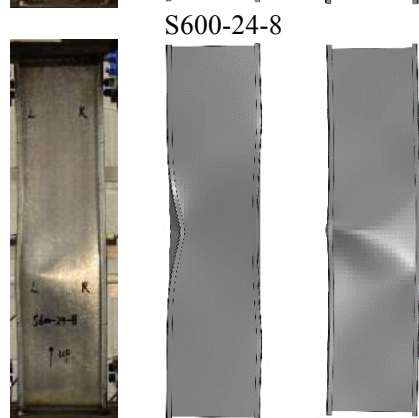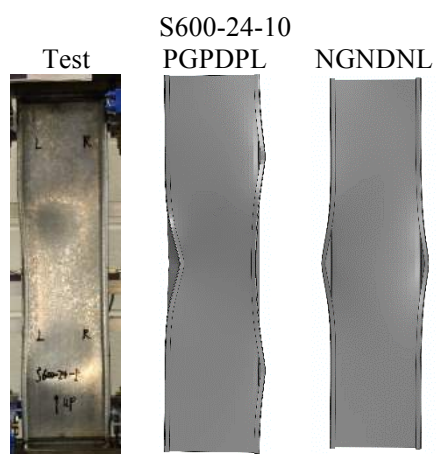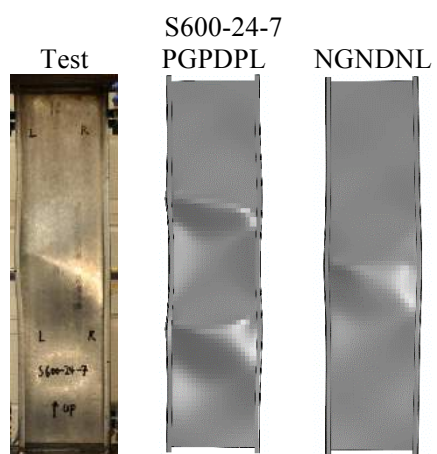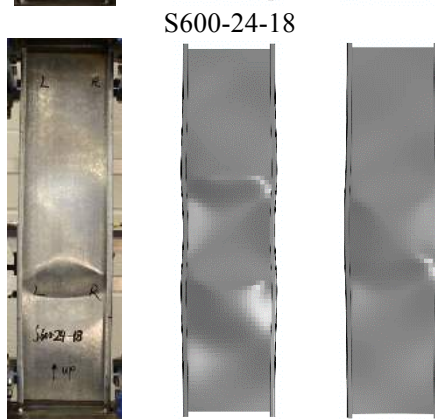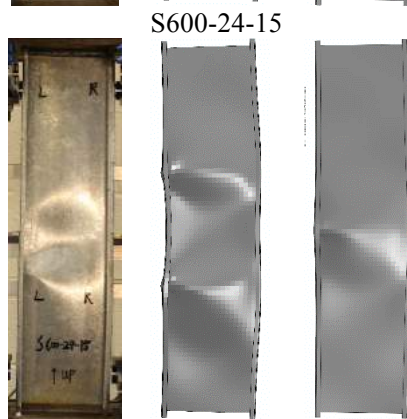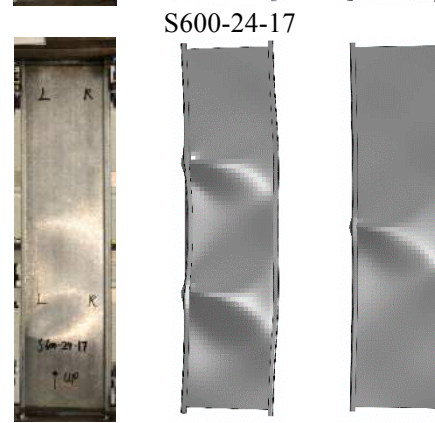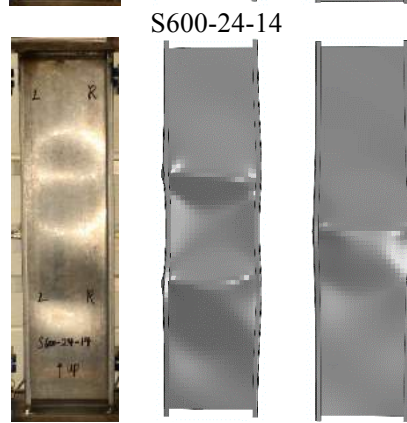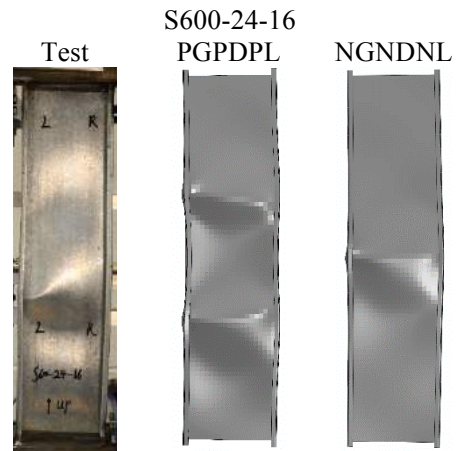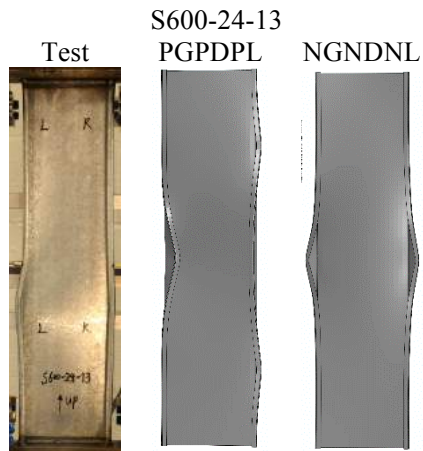
G.3 Failure modes: Long Specimens (S600-48)

The failure modes are calculated by using finite element models options NGNDNL-C/PFPDPL-C in the report: the model with nominal cross section; with positive/negative global, local, and distortional buckling mode of imperfection; and with residual stress.

Failure shapes are not completely same as the observed failure shapes, but the failure modes in the models and in the observations are qualitatively consisted in terms of identification of local web buckling (LWB) or flange distortional buckling (FDB).
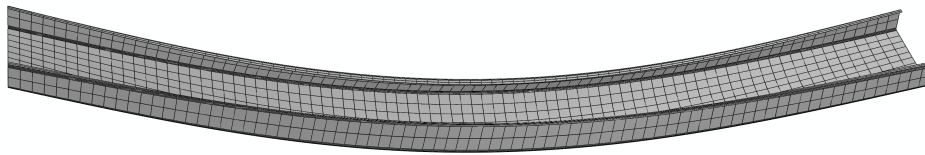
(a) Negative Global buckling mode
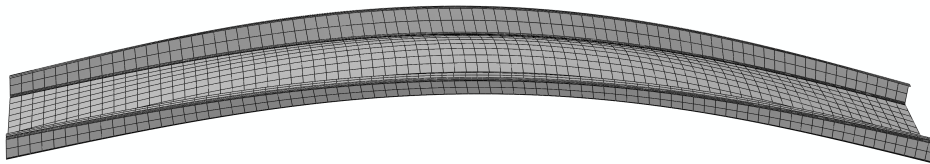
(b) Positive Global buckling mode

Figure G-4: Global buckling modes

(a) Negative Global buckling mode (NGNDNL)
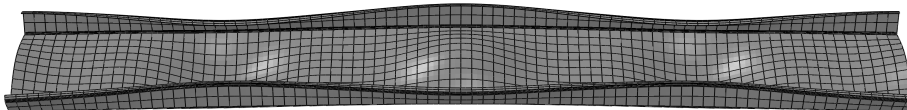
(b) Positive Global buckling mode (PGPDPL)

Figure G-5: Combined buckling modes

S600-48-1

Test PGPDPL NGNDNL

S600-48-4

Test PGPDPL NGNDNL

S600-48-2

S600-48-5

S600-48-3

S600-48-6

S600-48-7
Test   PGPDPL   NGNDNL

S600-48-10
Test   PGPDPL   NGNDNL

S600-48-8
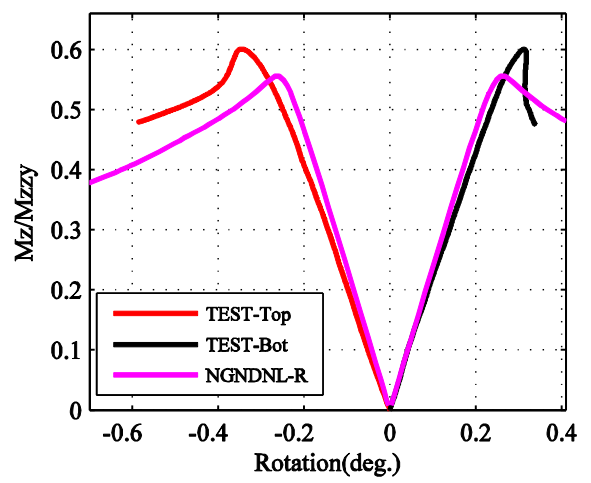
S600-48-11

S600-48-9

S600-48-12

S600-48-13
Test   PGPDPL   NGNDNL

S600-48-16
Test   PGPDPL   NGNDNL

S600-48-14

S600-48-17

S600-48-15

S600-48-18
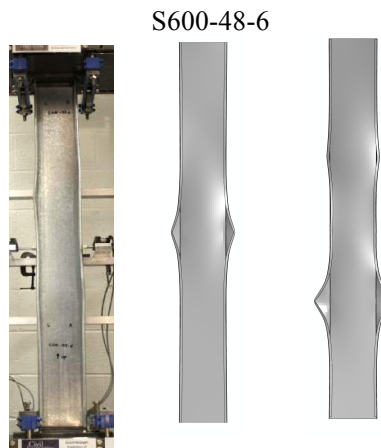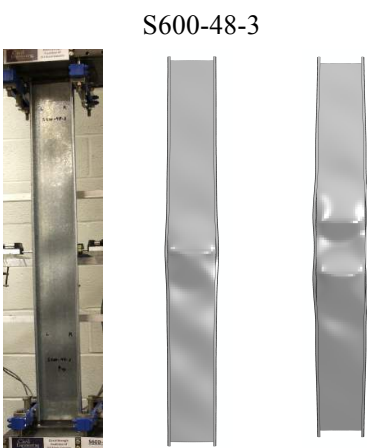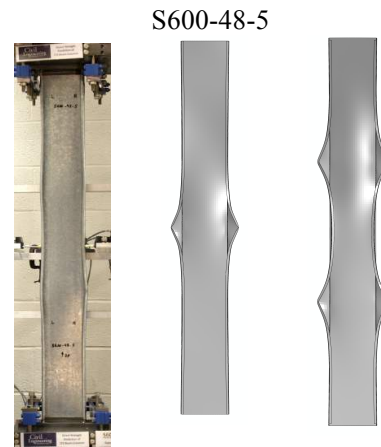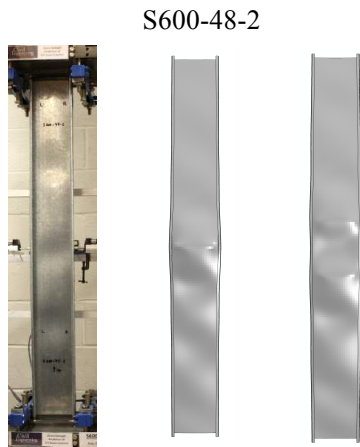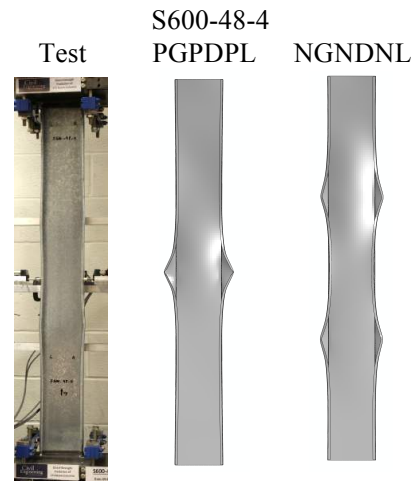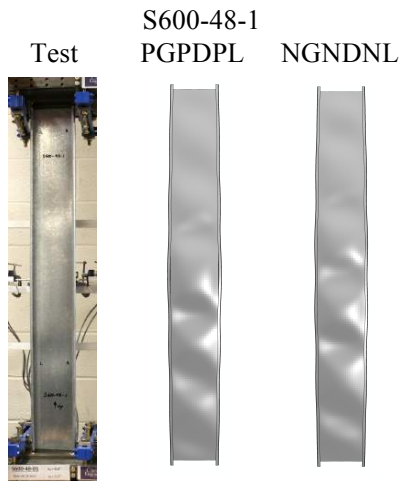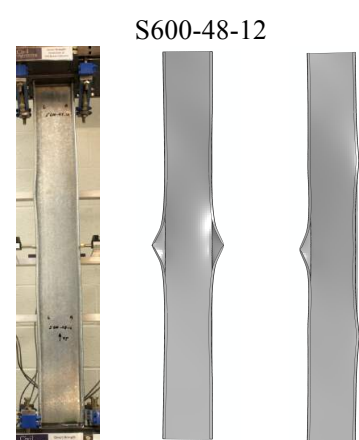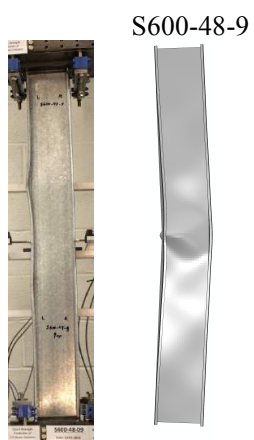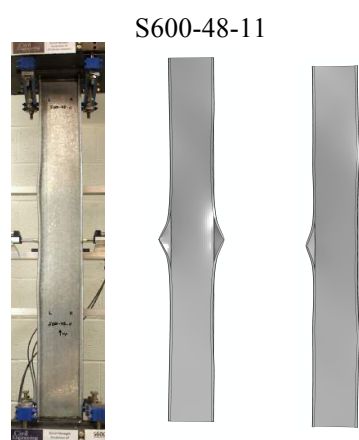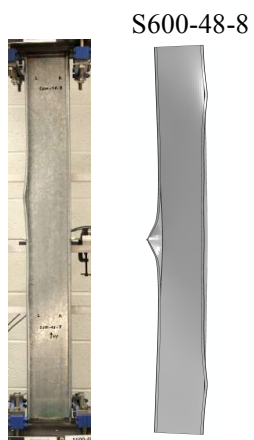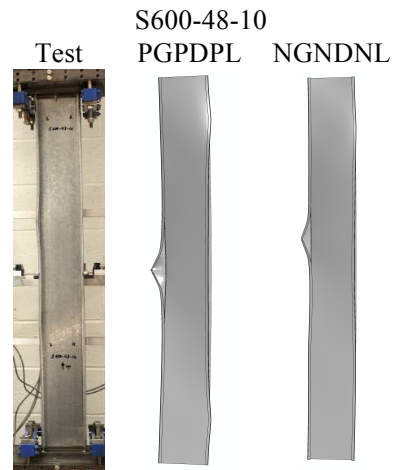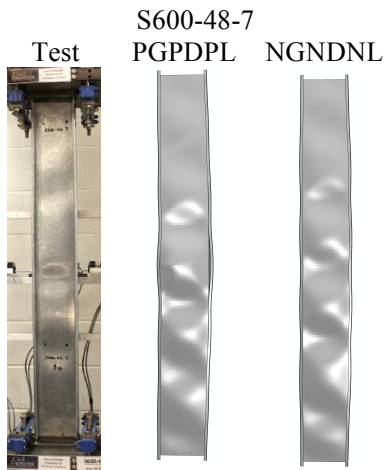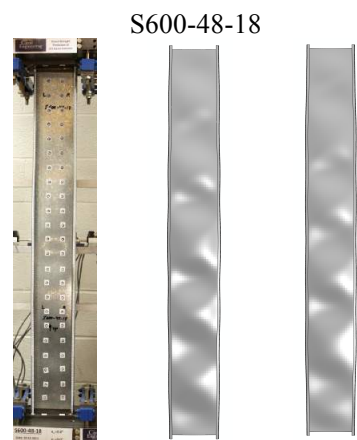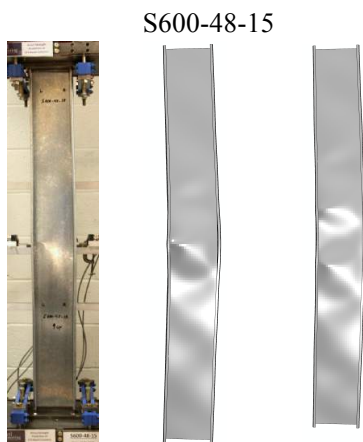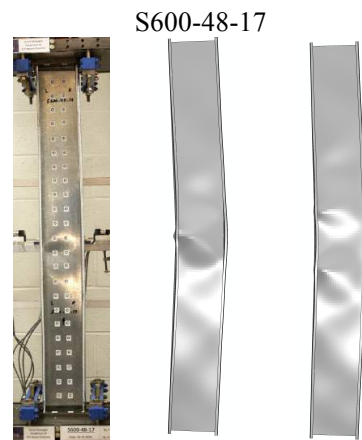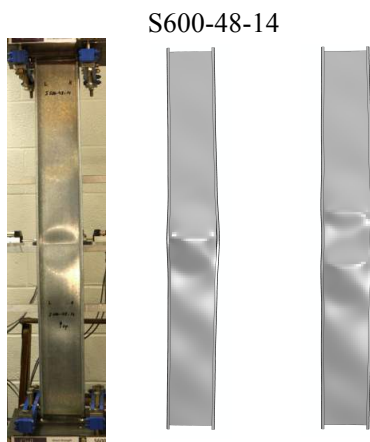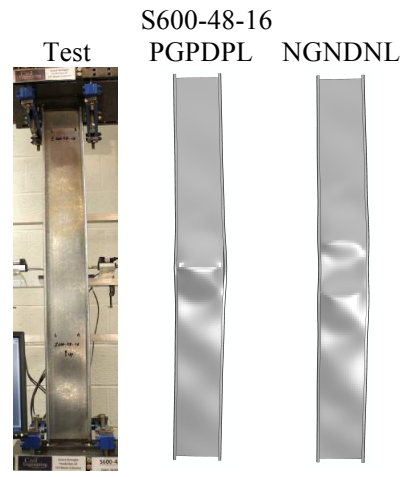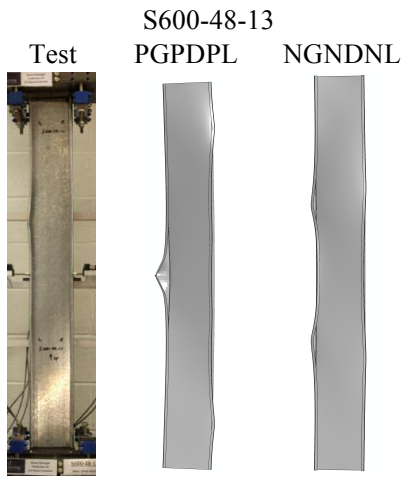
Appendix H - Load-displacement curves: Test vs. FEM

H.1 Load-displacement curves: Short Specimens (S600-12)

The load-diplacement curves are calculated by using finite element models Option NGPDNL-R (NGPDNL-R in the report): the model with nominal cross section; with negative global, negative local, and positive distortional buckling mode of imperfection; and with residual stress. The displacement is the axial shortening of the members.

390

S600-12-20
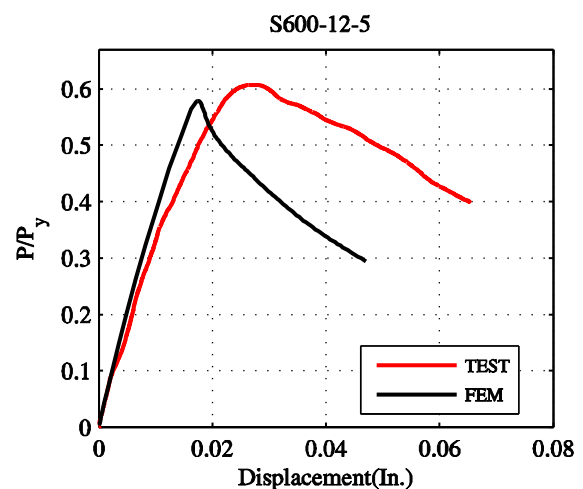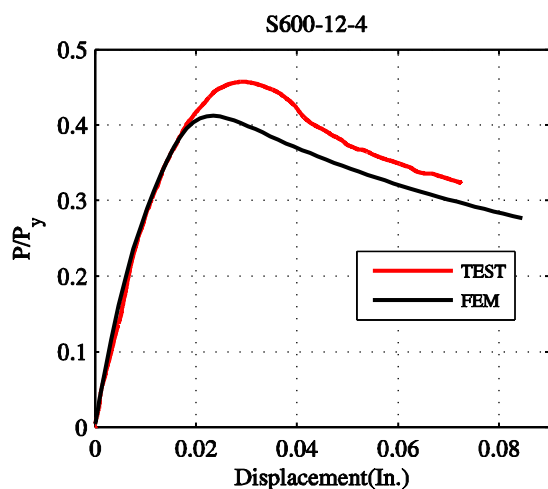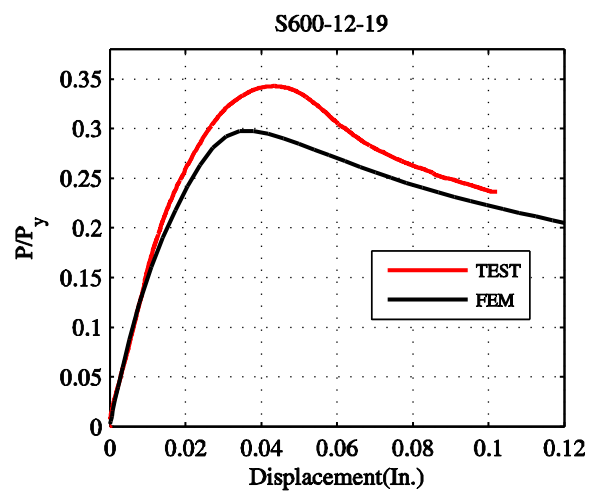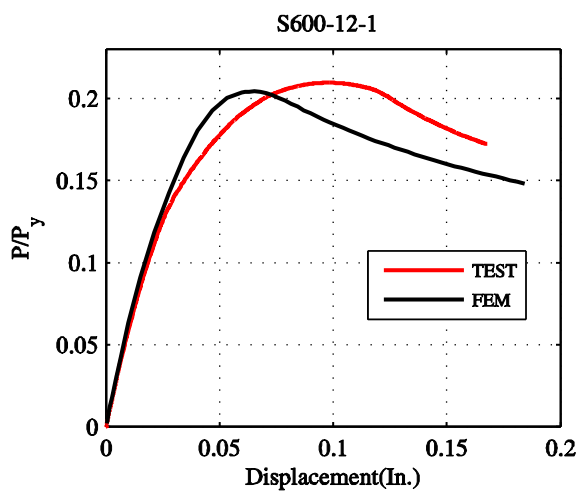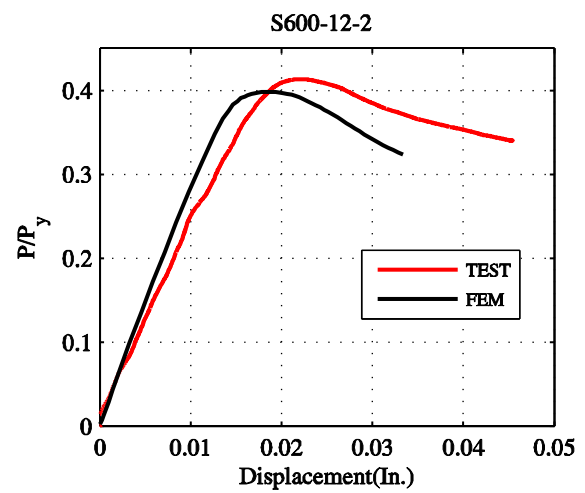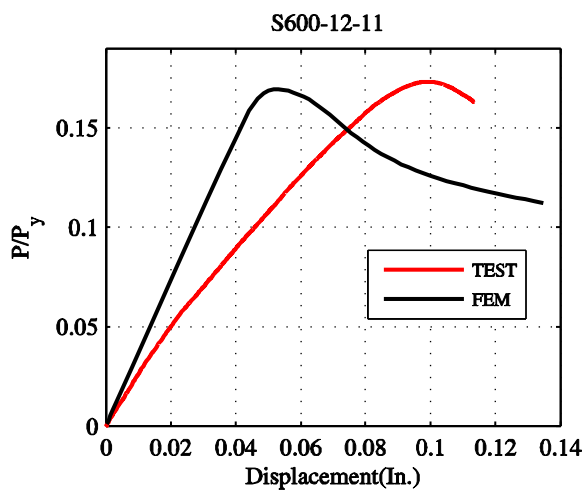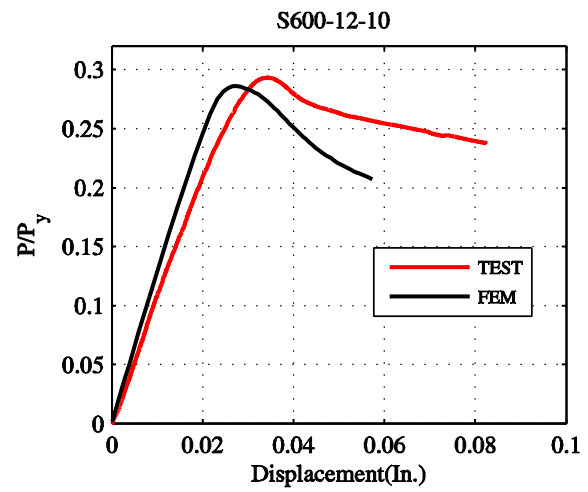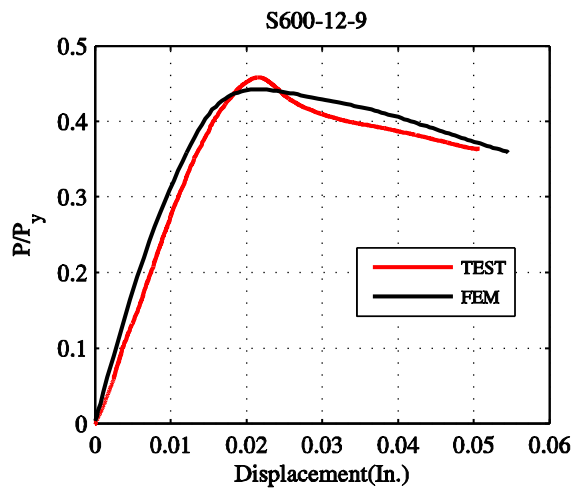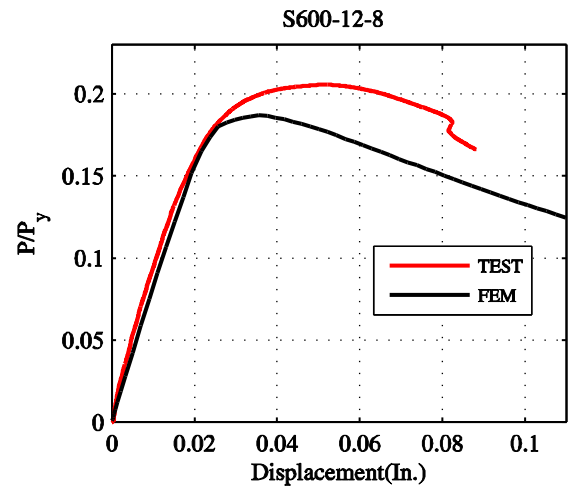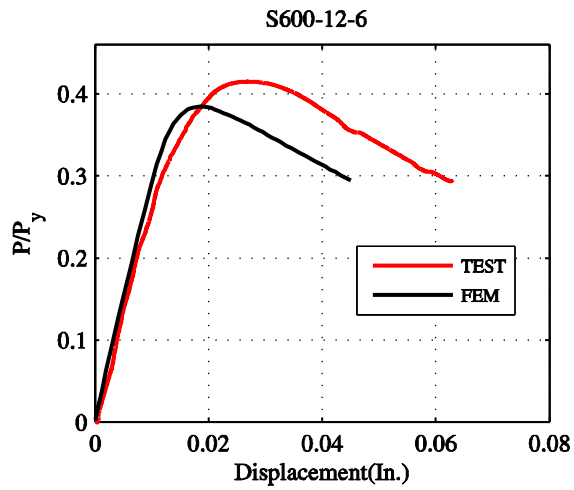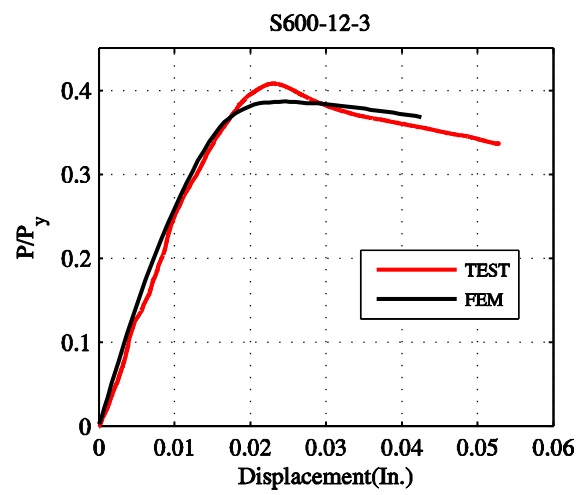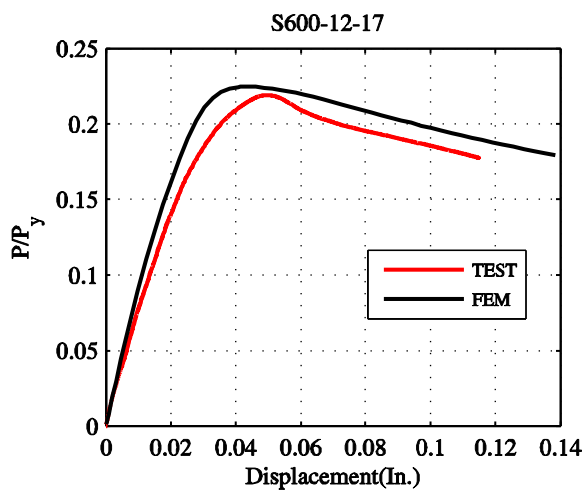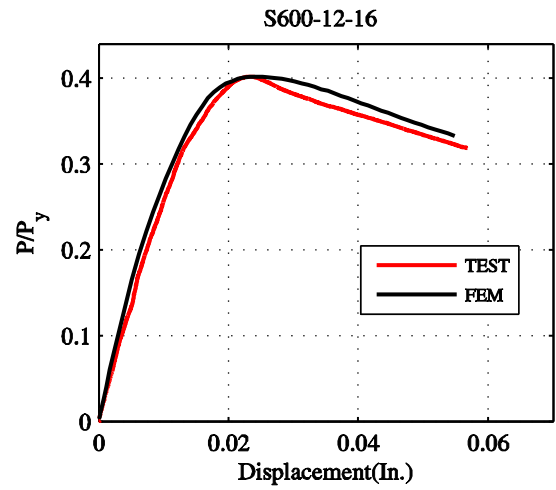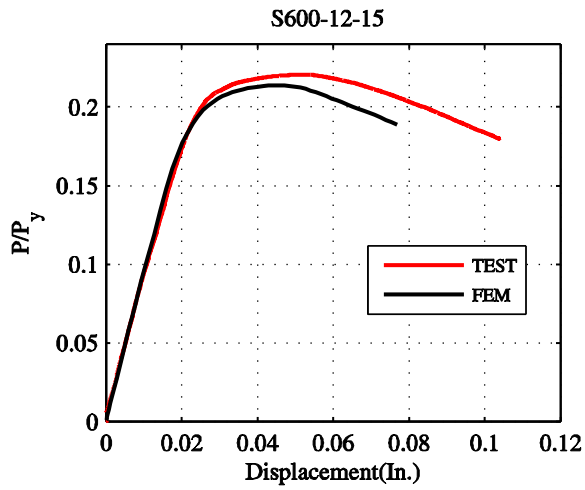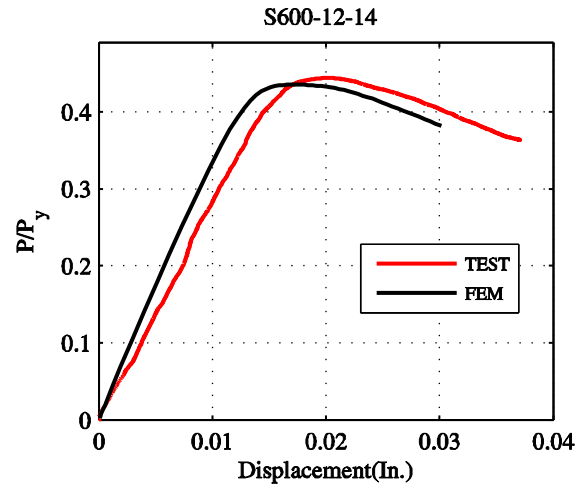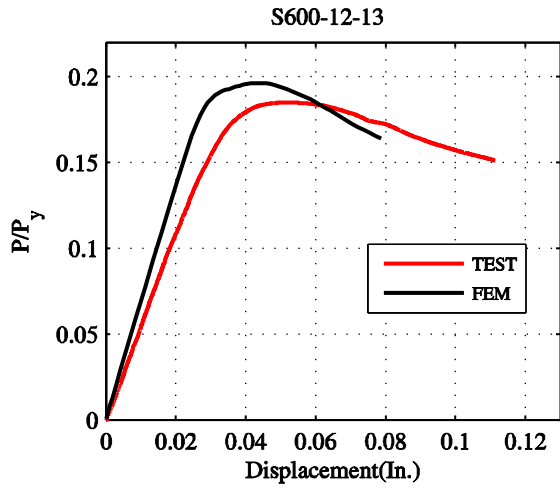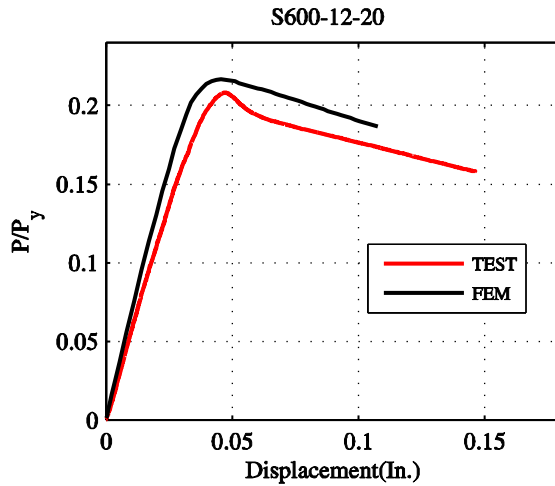
H.2 Load-displacement curves: Intermediate Specimens (S600-24)

The load-displacement curves are calculated by using finite element models Option NGNDNL-R (NGNDNL-C in the report): the model with nominal cross section; with negative global, local, and distortional buckling mode of imperfection; and with residual stress. The displacement is the axial shortening of the members.

S600-24-1

S600-24-2

S600-24-3

S600-24-4

S600-24-5

S600-24-6

S600-24-7

S600-24-8

S600-24-15

S600-24-16

S600-24-17

S600-24-18

S600-24-19

S600-24-20
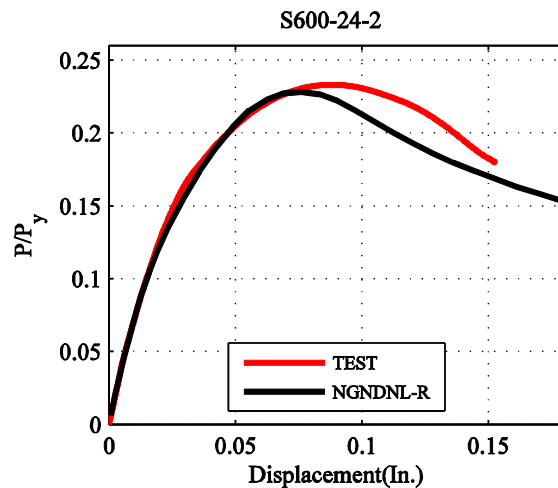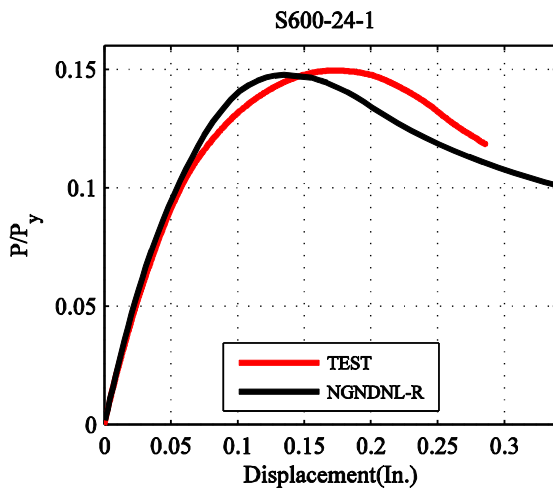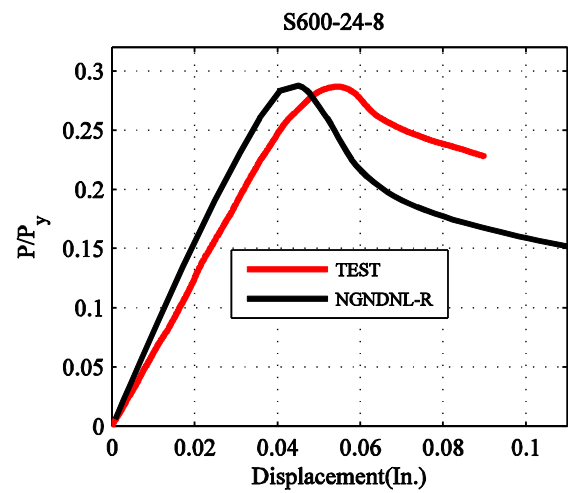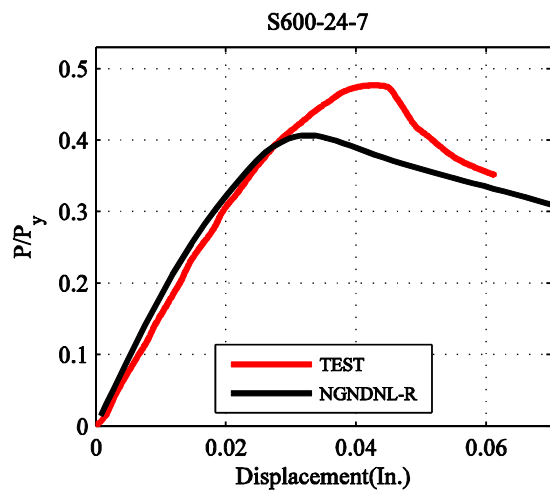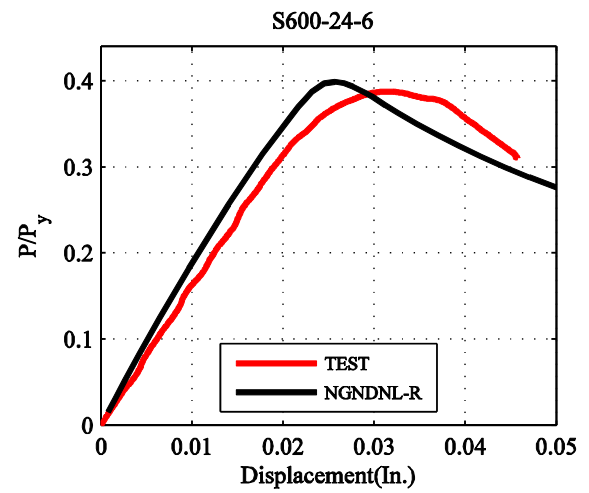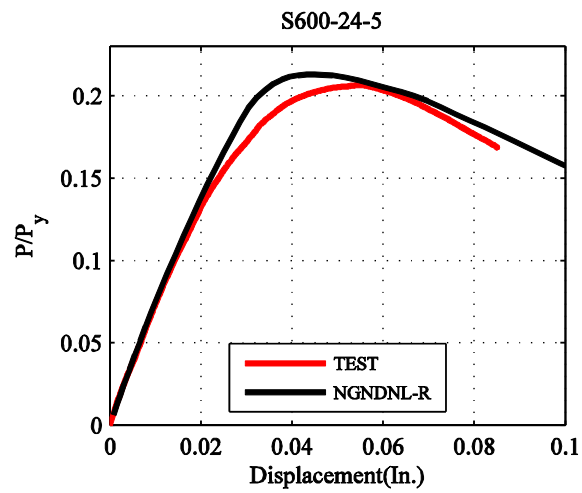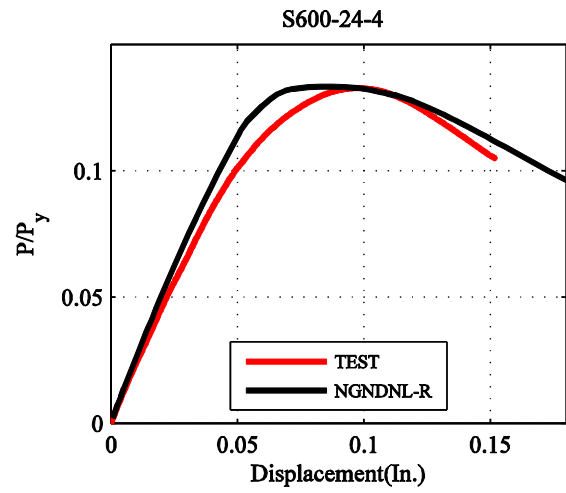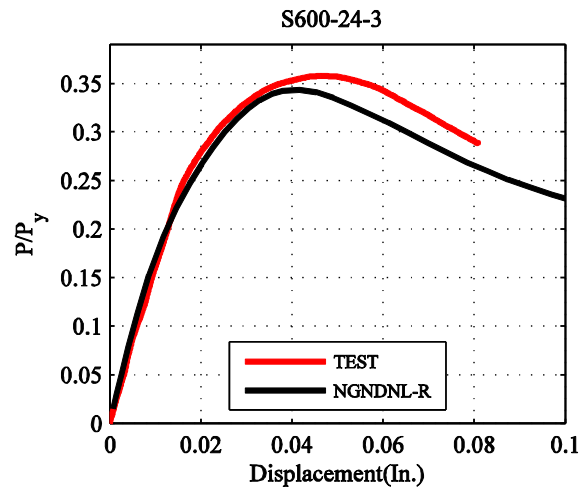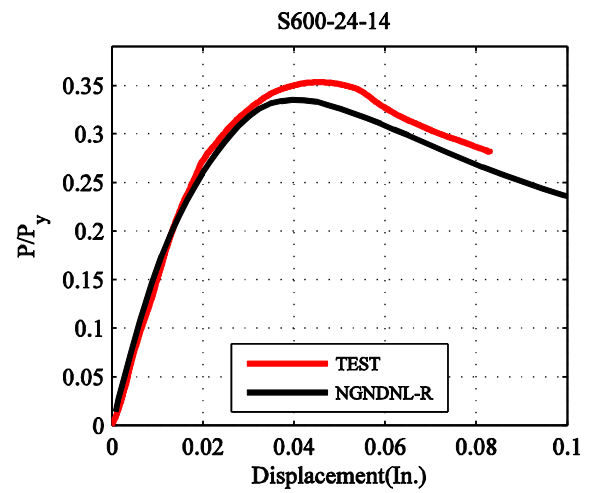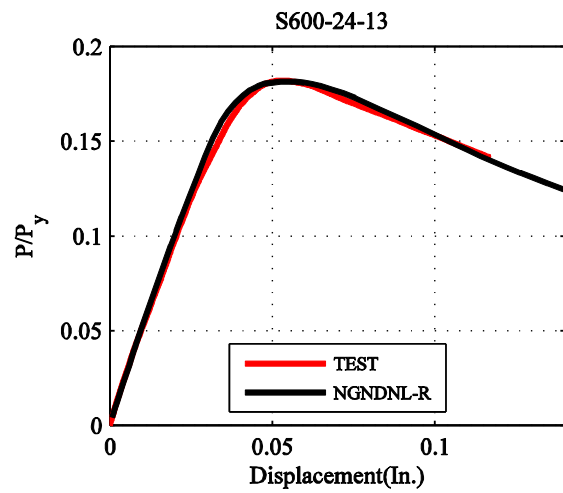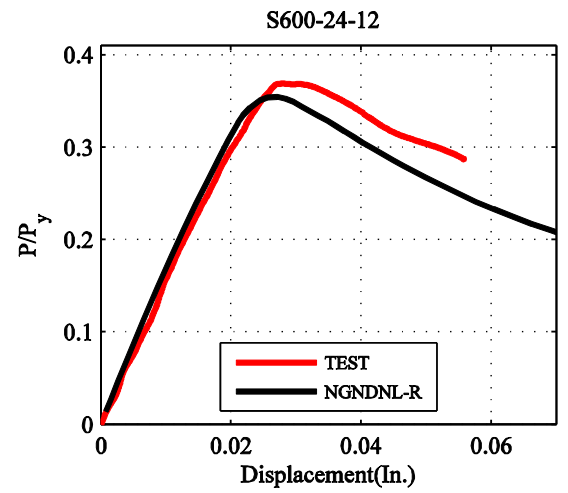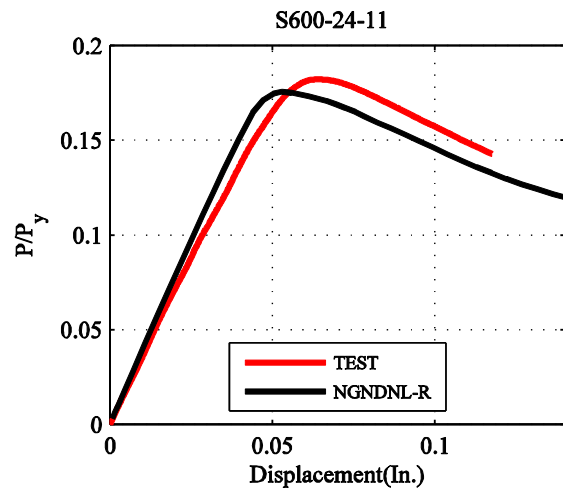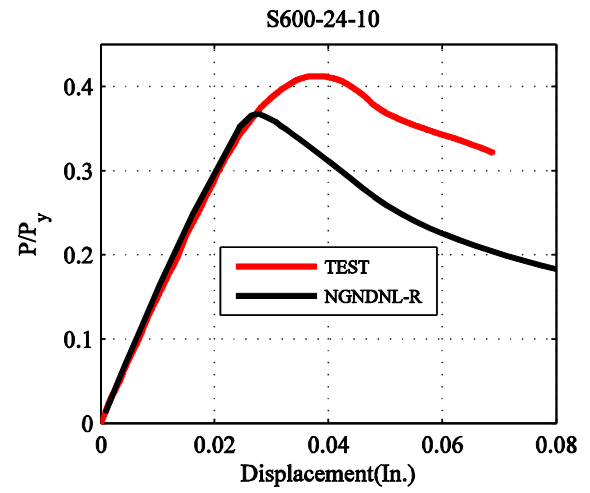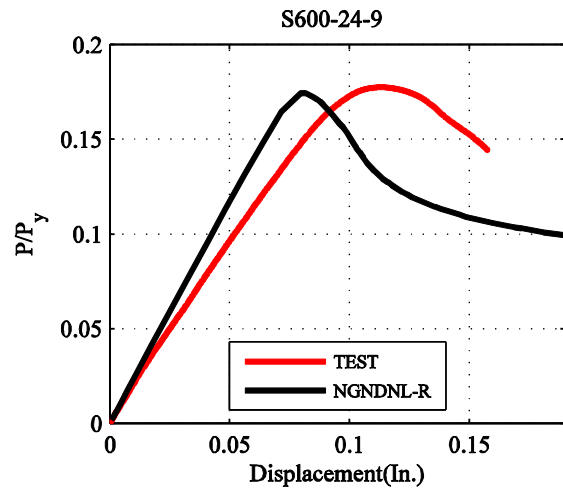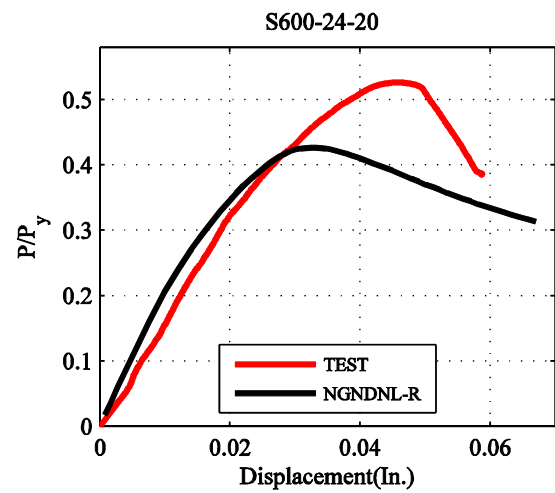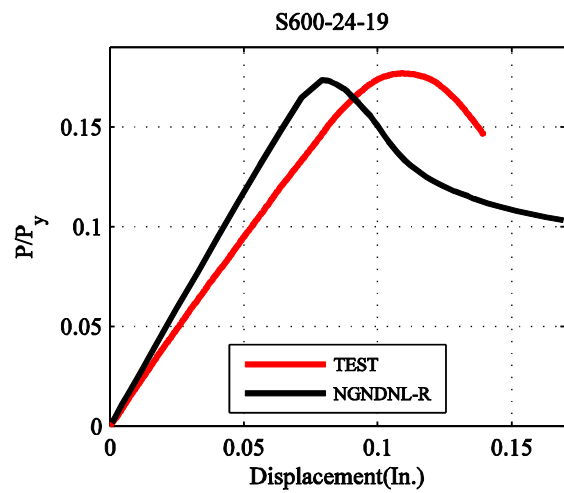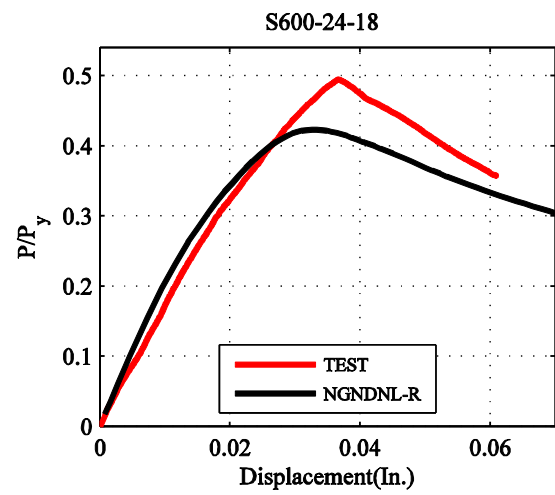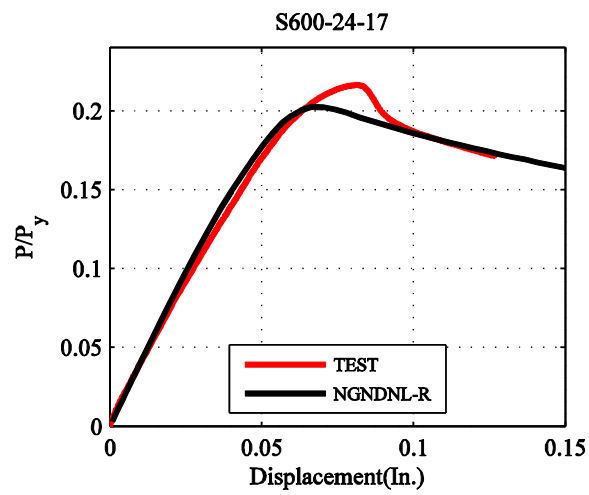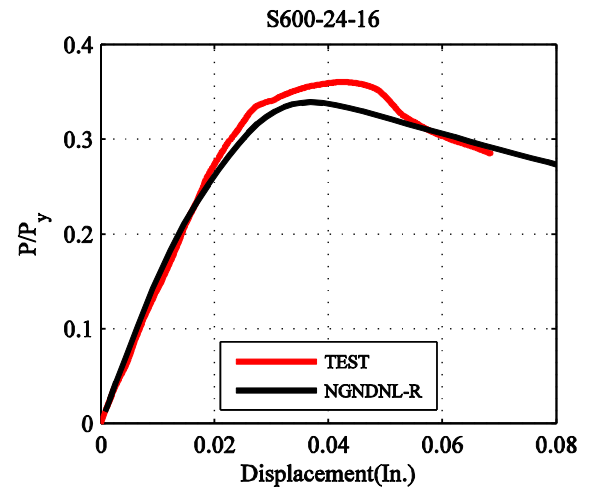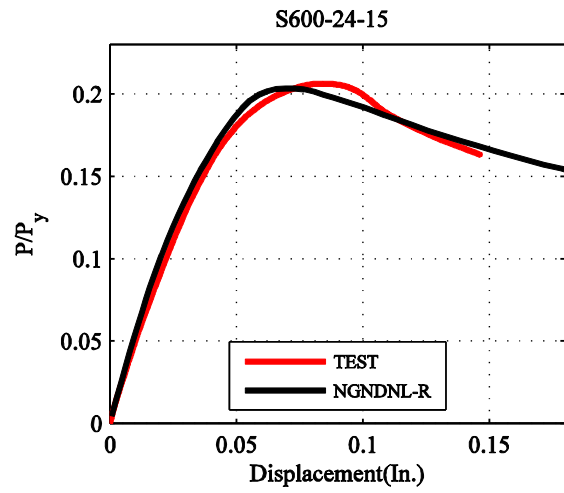
H.3 Load-displacement curves: Long Specimens (S600-48)

The Load-displacement curves are calculated by using finite element models Option NGNDNL-C in the report: the model with nominal cross section; with negative global, local, and distortional buckling mode of imperfection; and with residual stress. The displacement is the axial shortening of the members.
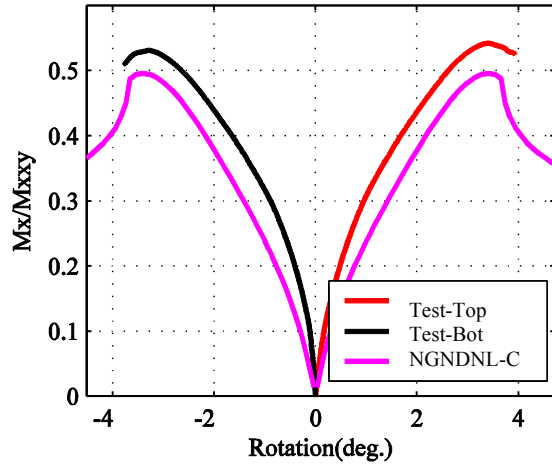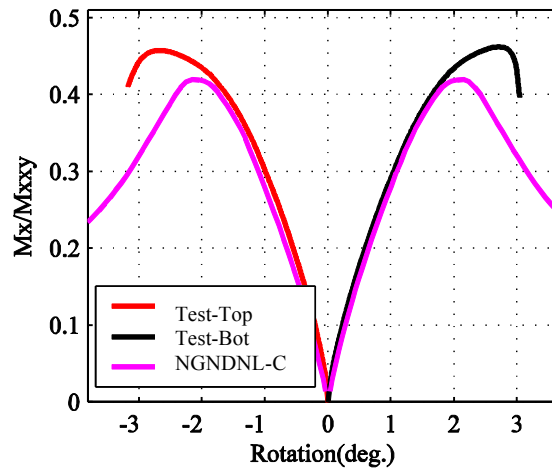
S600-48-5

S600-48-6

S600-48-7

S600-48-8

S600-48-9

S600-48-10

397

S600-48-11

S600-48-12

S600-48-13

S600-48-14

S600-48-15

S600-48-16

398

S600-48-17

S600-48-18
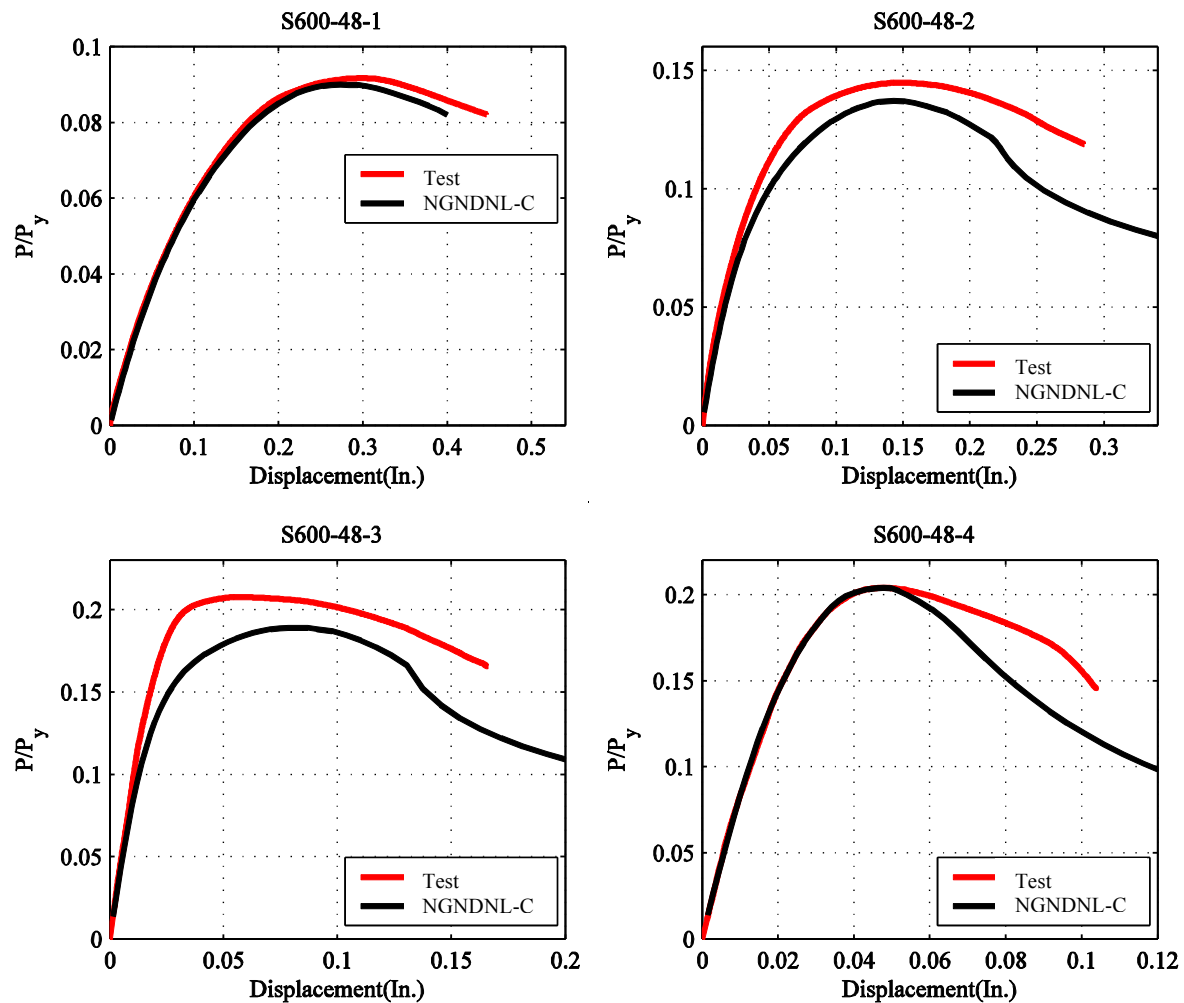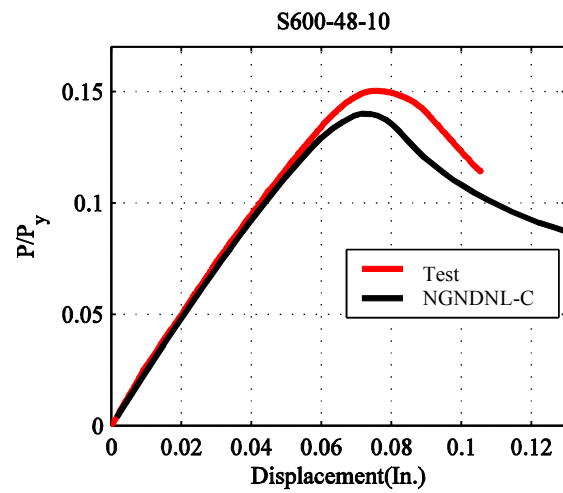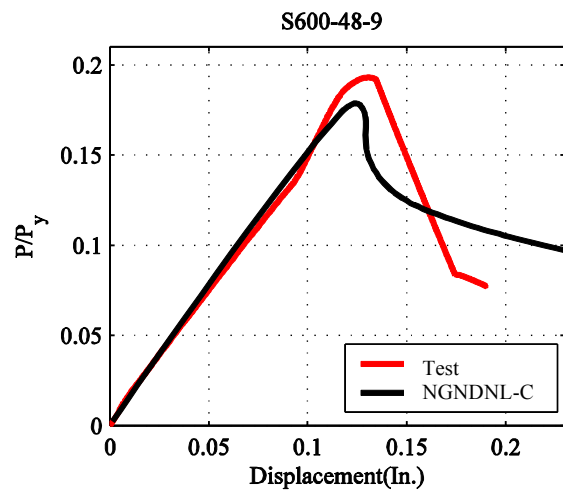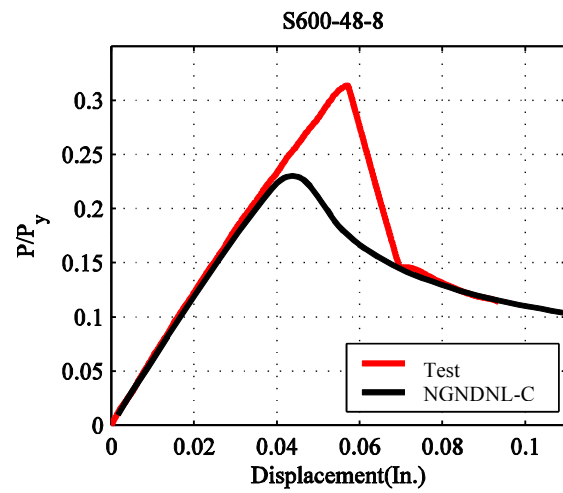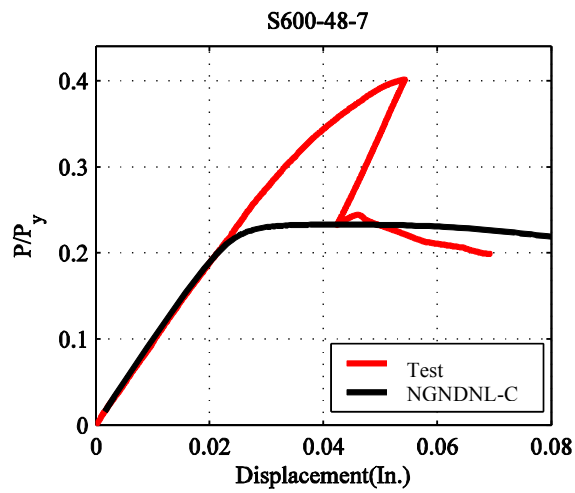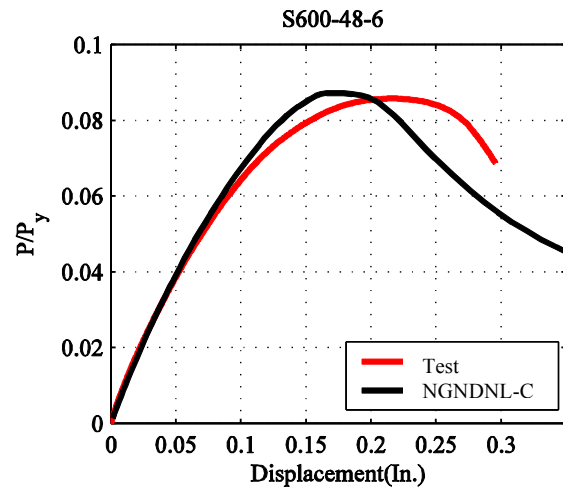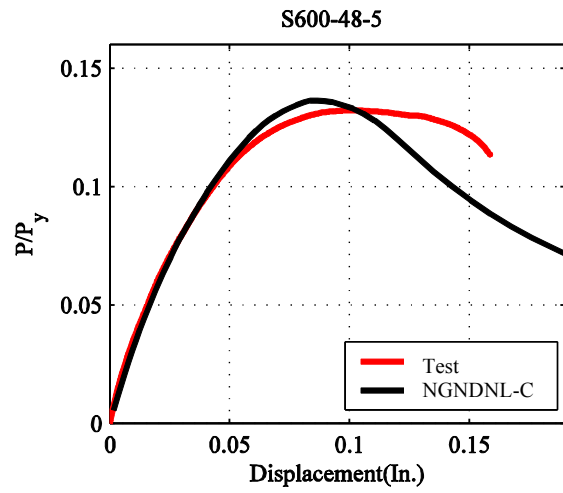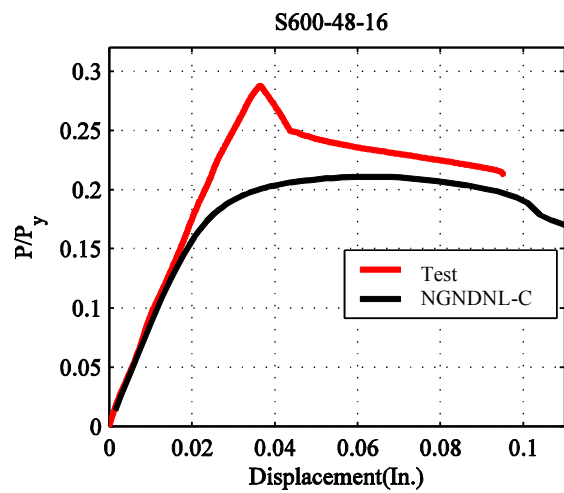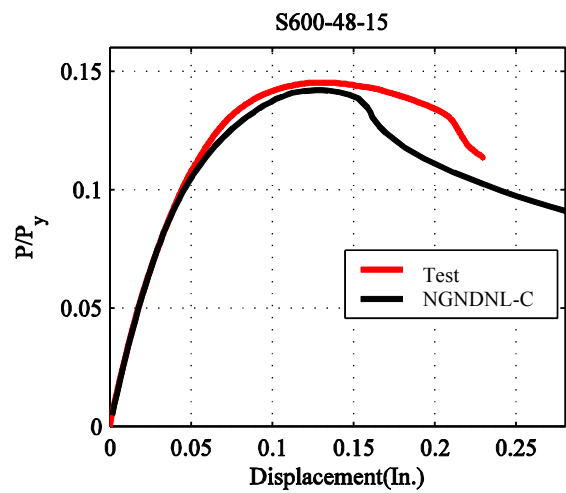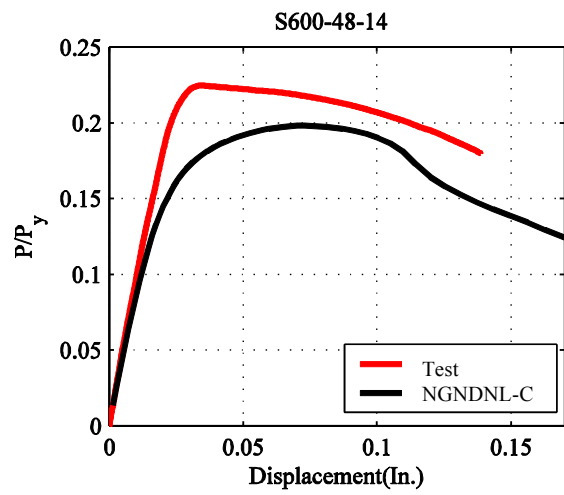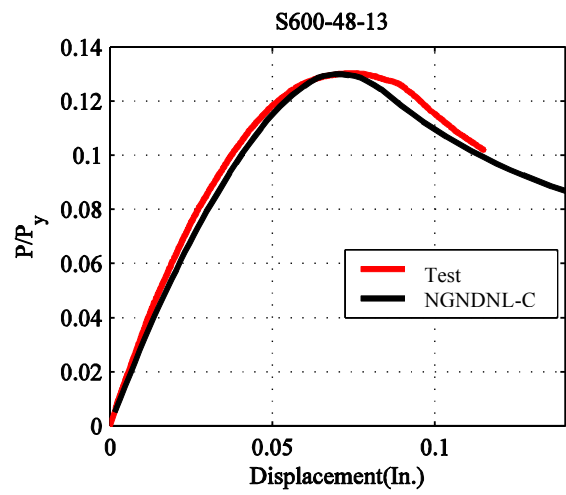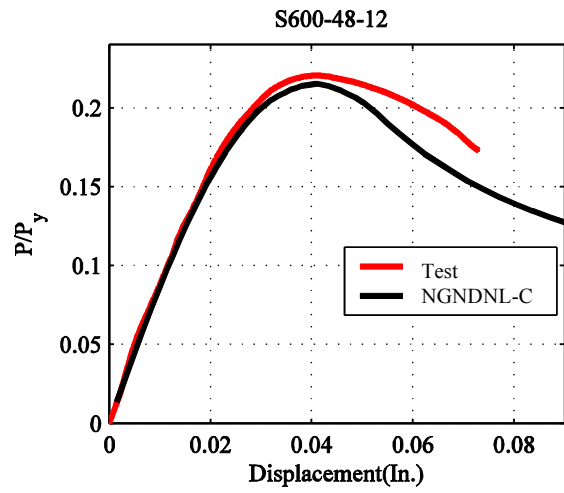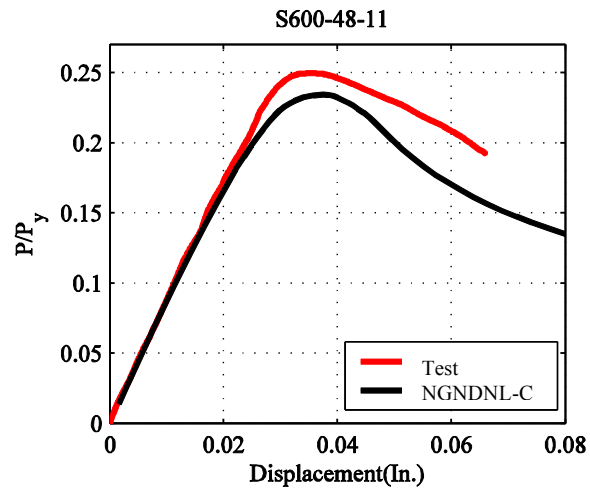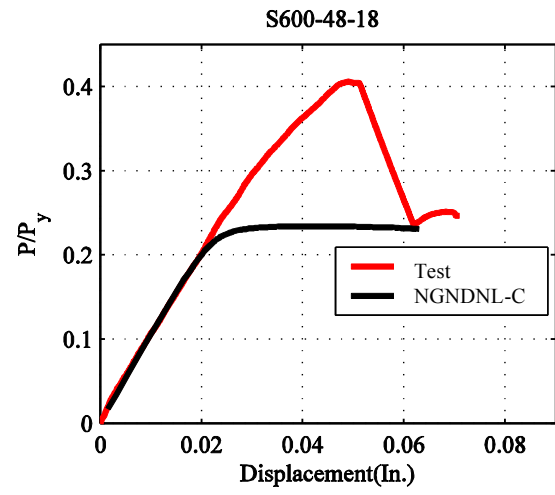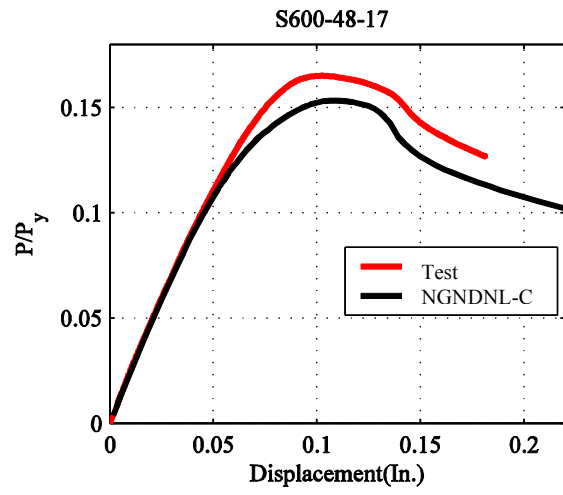
Appendix I - Moment-rotation curves: Test vs. FEM

I.1 Moment-rotation curves: Short Specimens (S600-12)

The moment-rotation curves are calculated by using finite element models Option NGPDNL-R (NGPDNL-C in the report): the model with nominal cross section; with negative global, negative local, and positive distortional buckling mode of imperfection; and with residual stress.

(a) Front view (b) Side-view
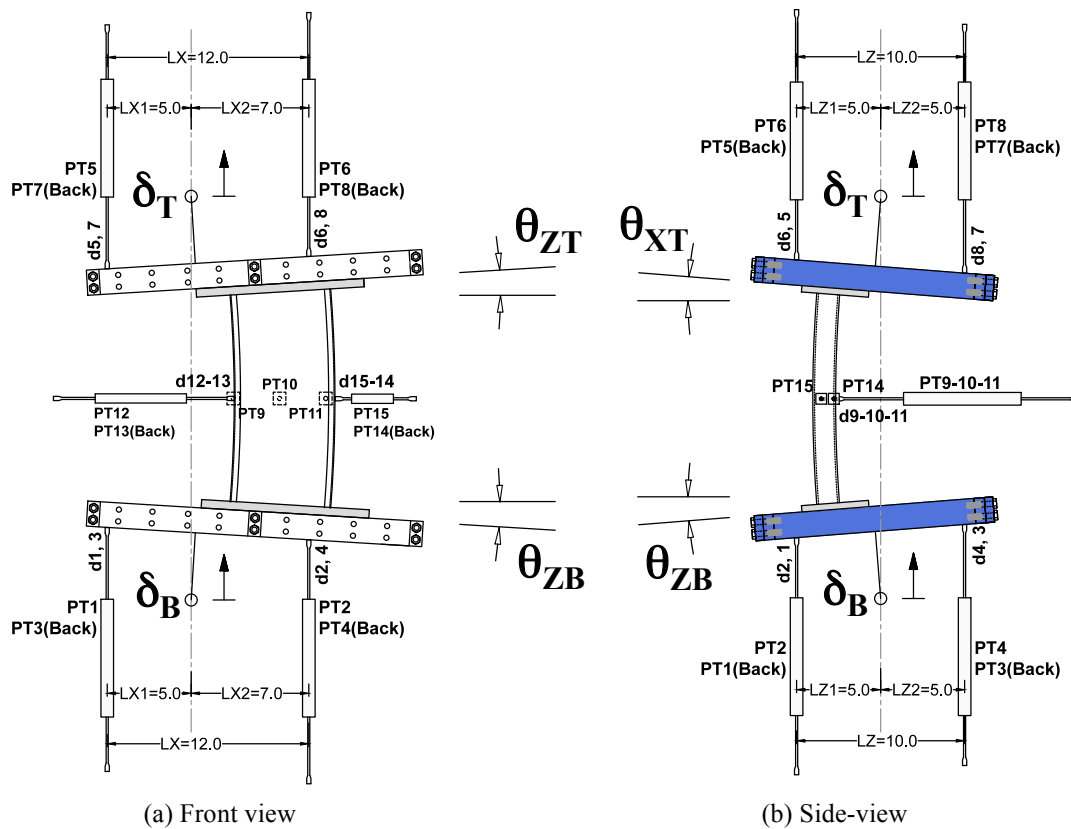
Figure I-1: Top and bottom plate movements and rotations

M$_x$-θ$_x$ (Minor axis)   **M$_z$-θ$_z$ (Major axis)**
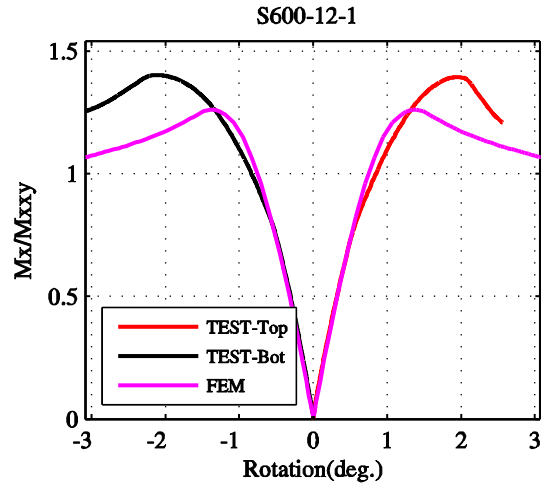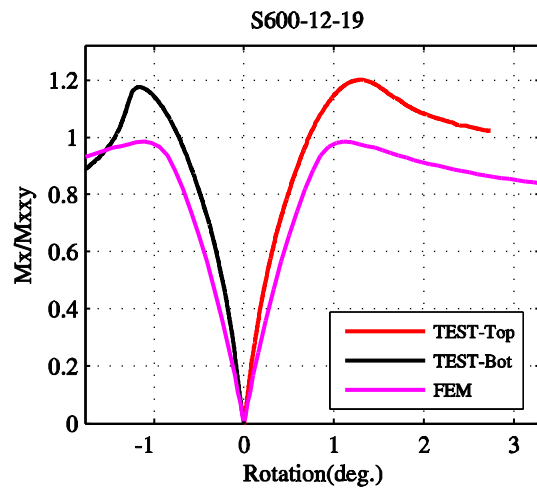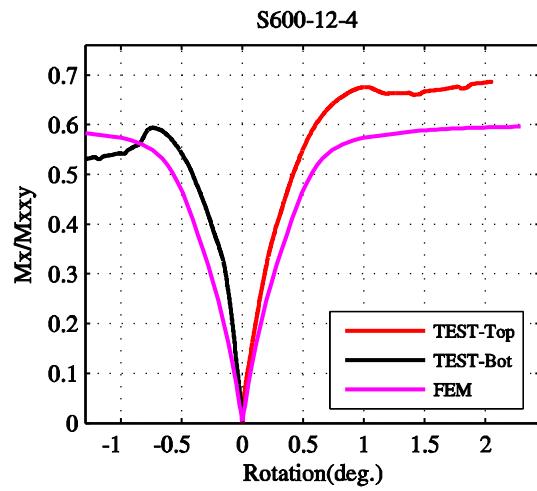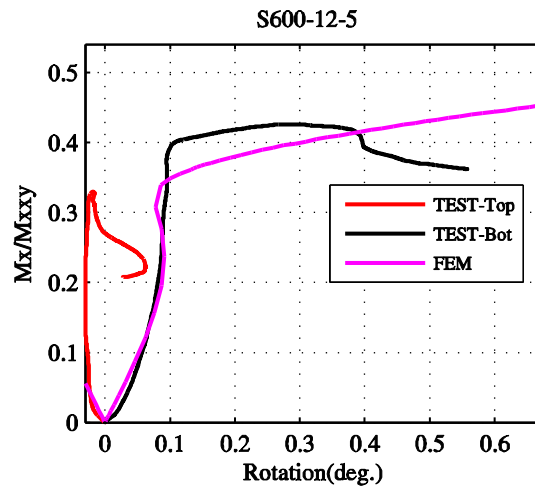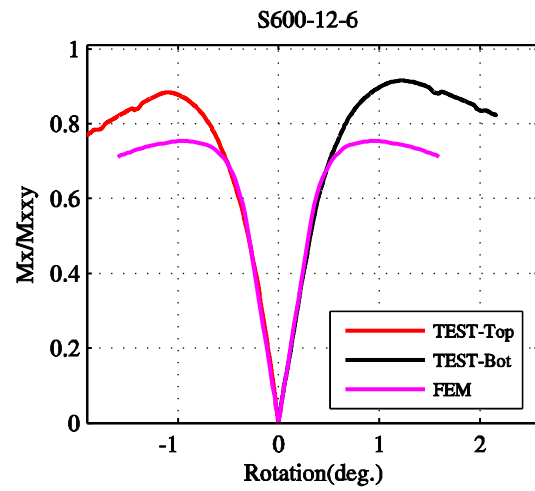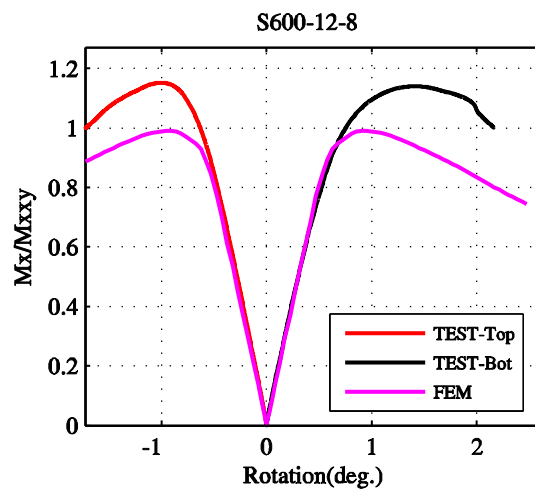
S600-12-1

N/A

S600-12-19

N/A

S600-12-4

N/A

M$_x$-θ$_x$ (Minor axis)   **M$_z$-θ$_z$ (Major axis)**

S600-12-5

N/A

S600-12-6

N/A

S600-12-8

N/A

402

M$_x$-θ$_x$ (Minor axis)   **M$_z$-θ$_z$ (Major axis)**

S600-12-9

S600-12-9

S600-12-10

S600-12-10

S600-12-11

S600-12-11

403

M_x-θ_x (Minor axis)

M_z-θ_z (Major axis)

S600-12-11

S600-12-11

S600-12-2

S600-12-2

S600-12-13

S600-12-13

M$_x$-θ_x (Minor axis)

M$_z$-θ_z (Major axis)

S600-12-14

S600-12-14

S600-12-15

S600-12-15

S600-12-16

S600-12-16

M_x-θ_x (Minor axis)

S600-12-17

S600-12-3

S600-12-20

M_z-θ_z (Major axis)

S600-12-17

S600-12-3

S600-12-20

406
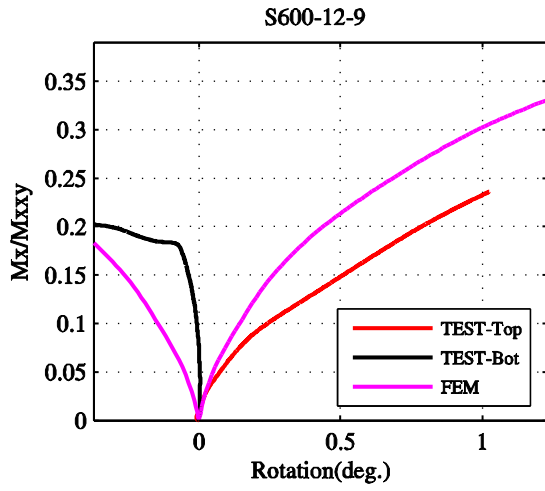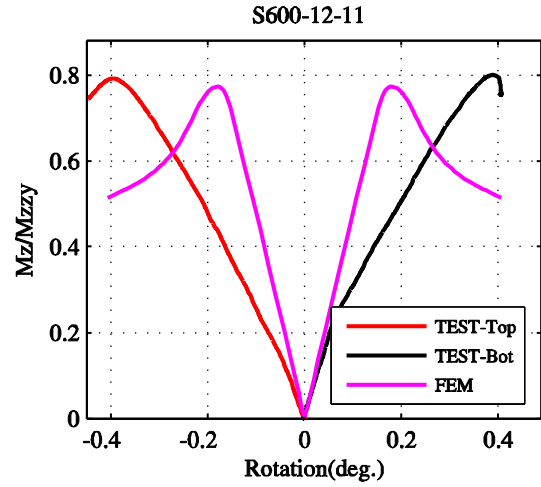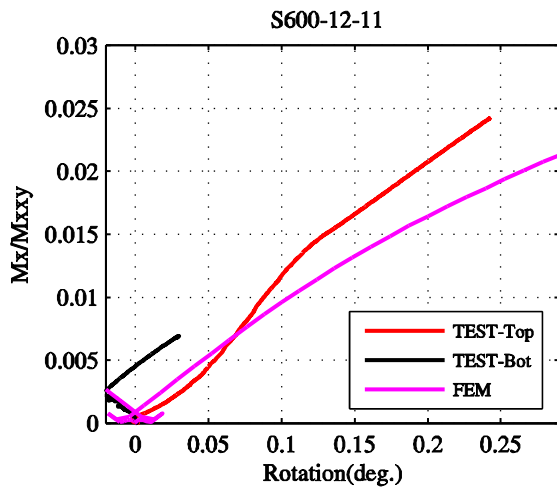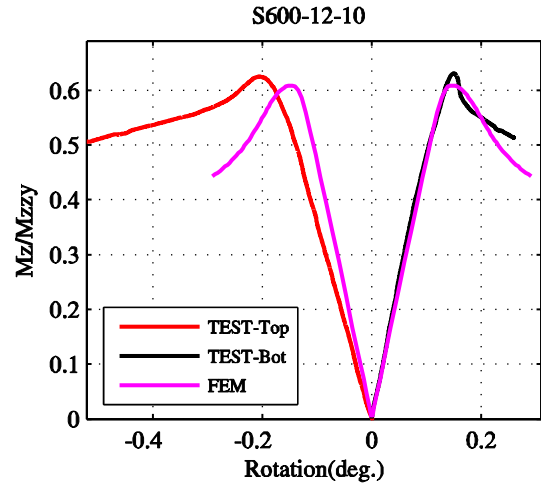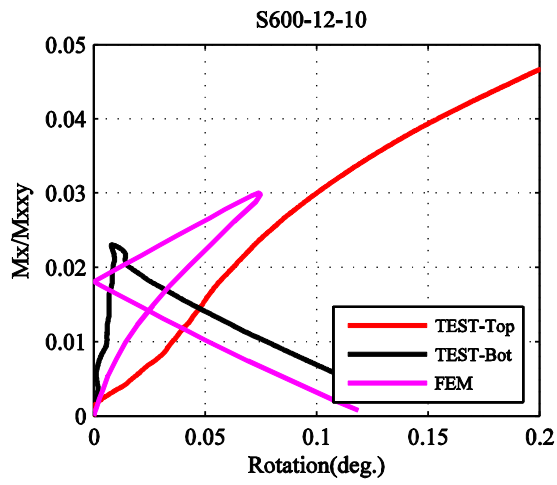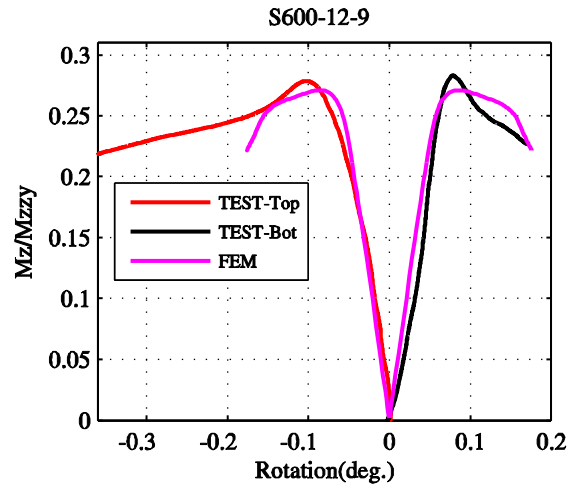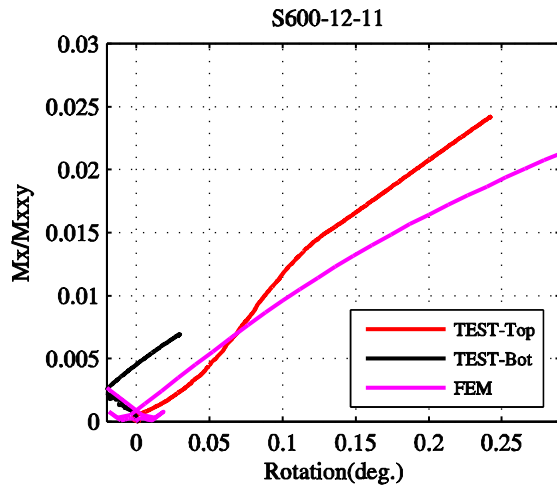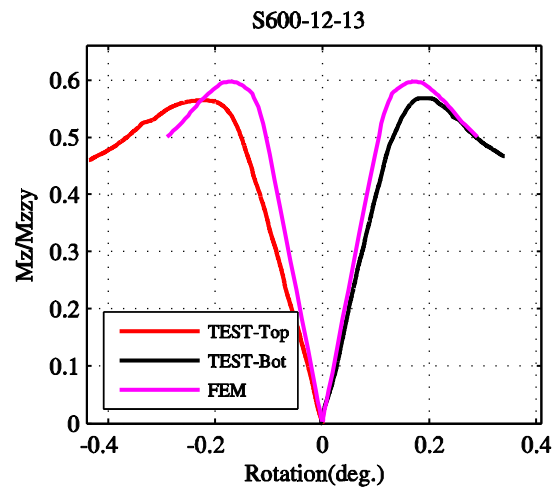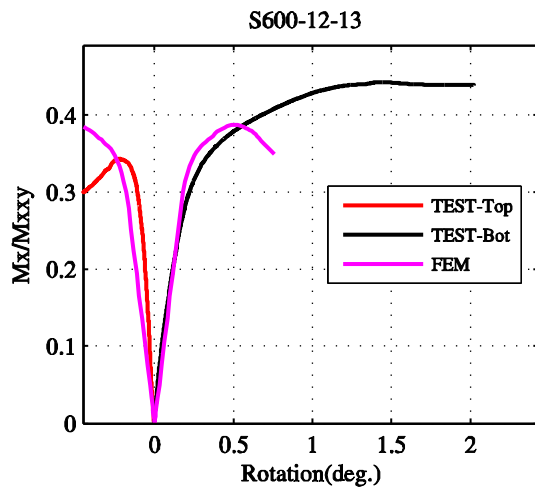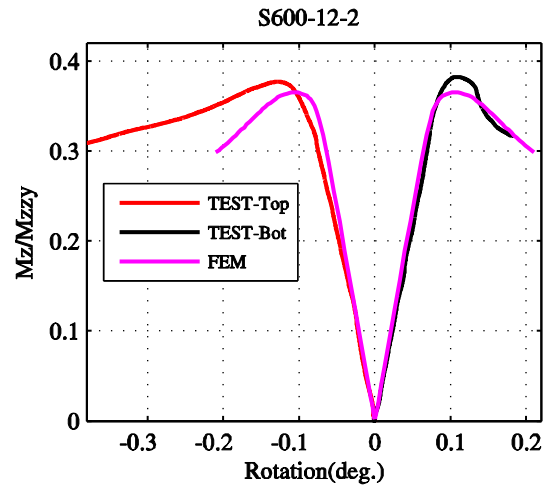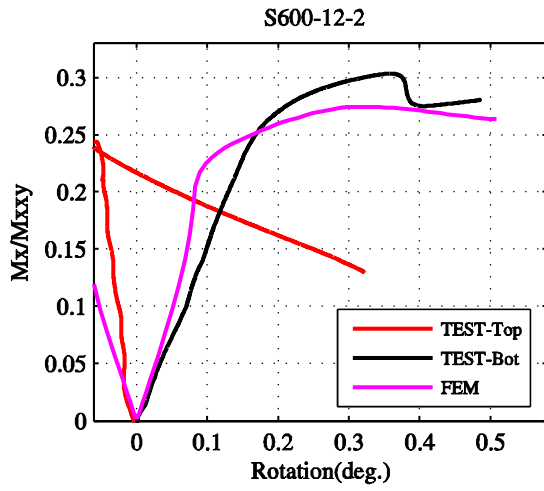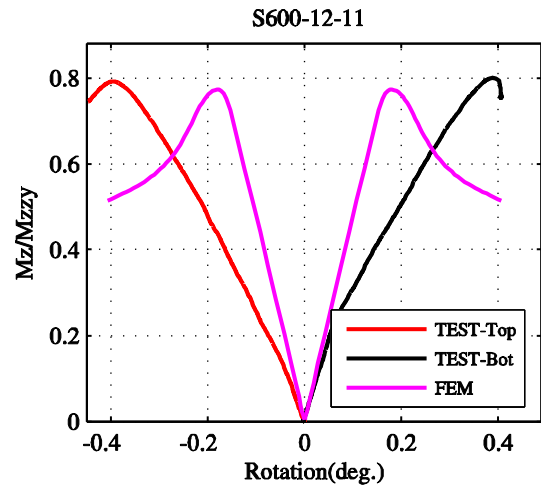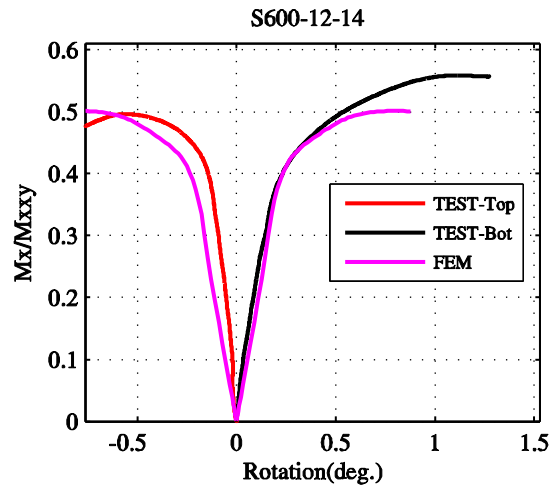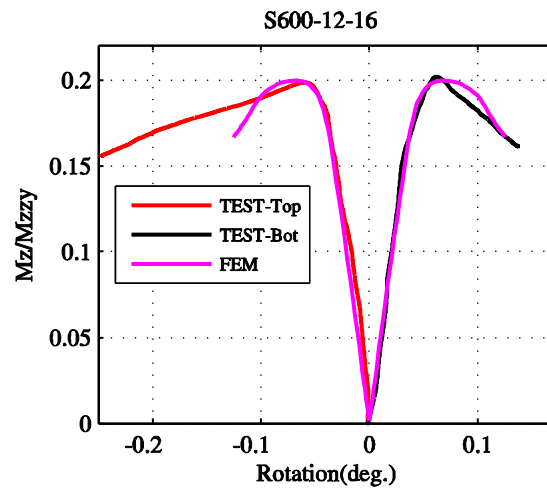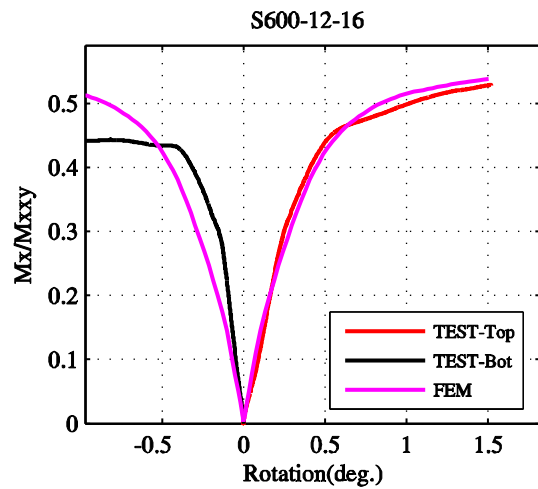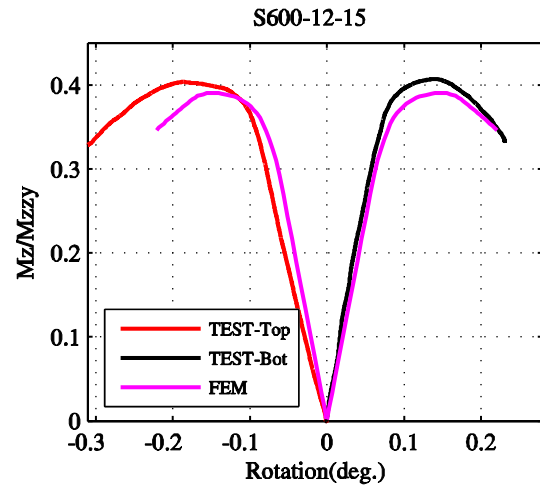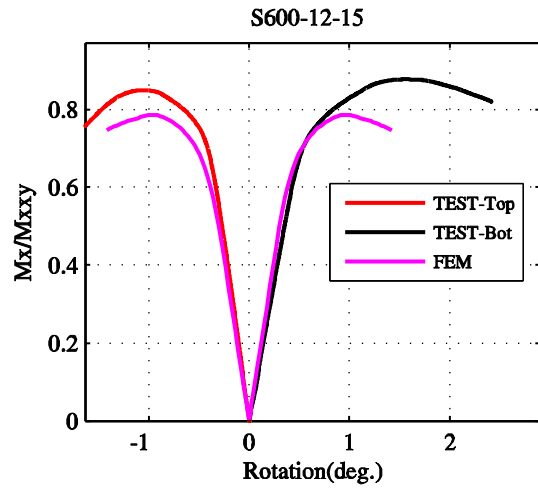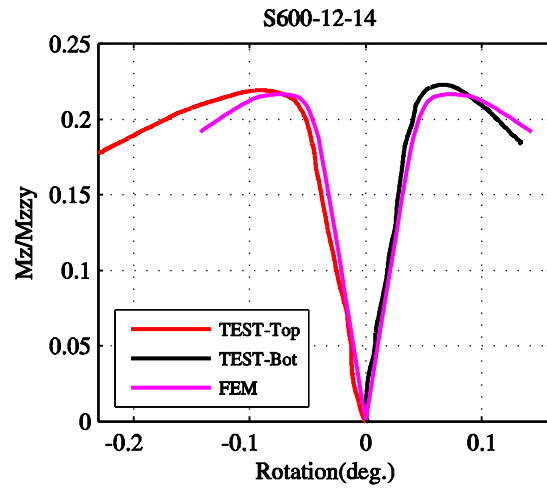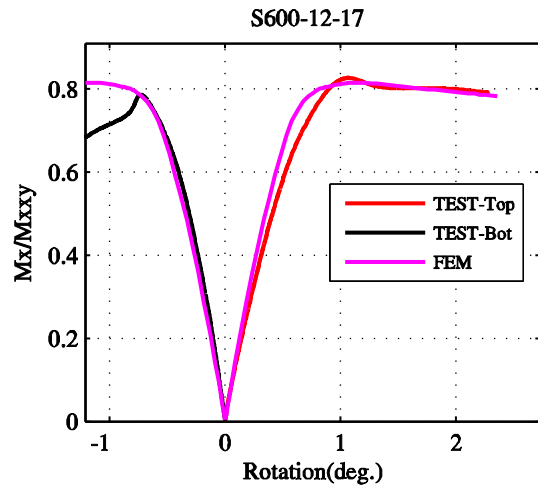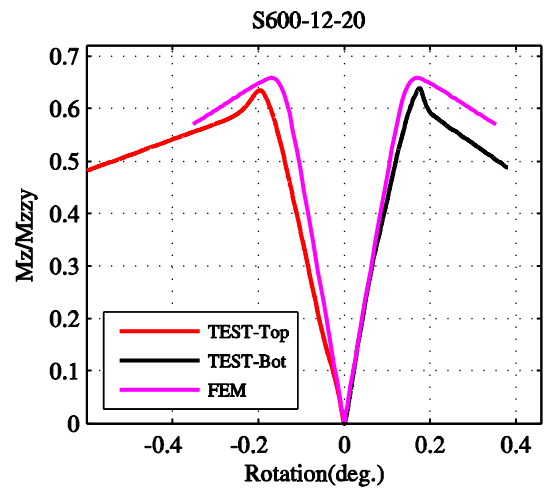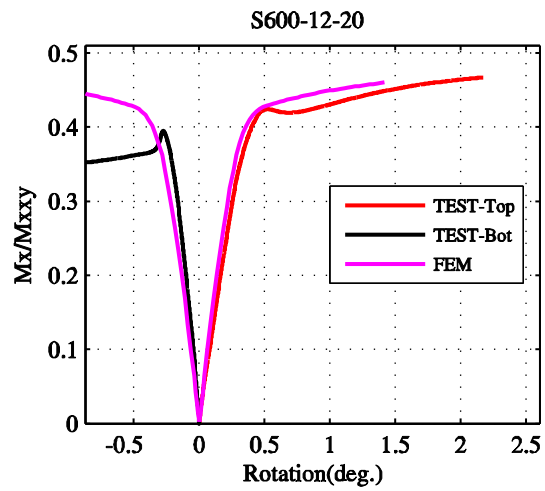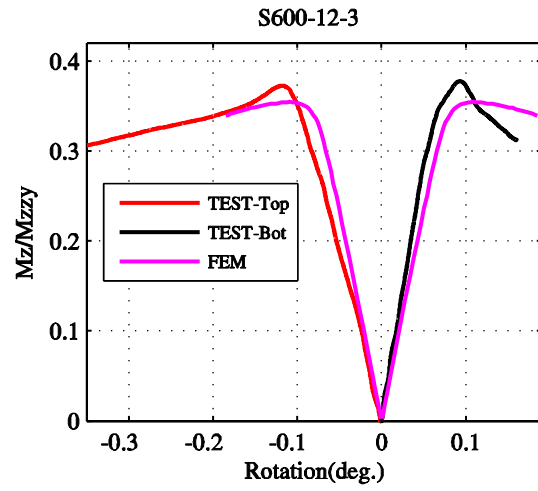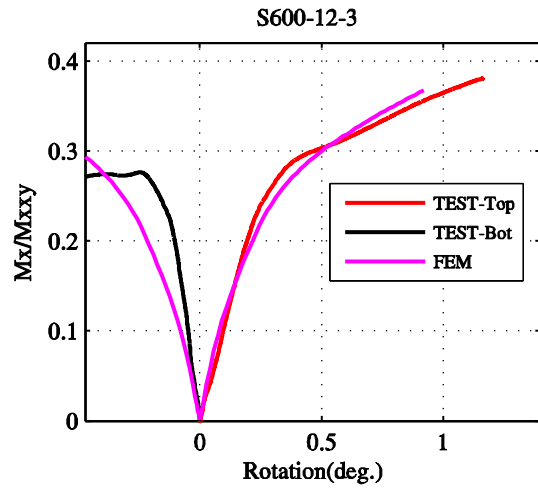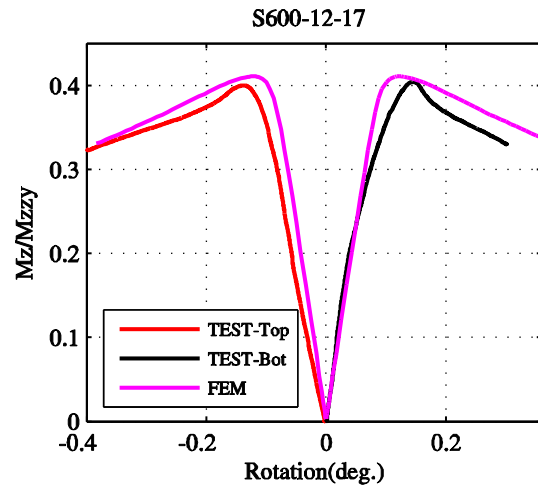
I.2 Moment-rotation curves: Intermediate Specimens (S600-24)

The moment-rotation curves are calculated by using finite element models Option NGNDNL-R (NGNDNL-C in the report): the model with nominal cross section; with negative global, local, and distortional buckling mode of imperfection; and with residual stress.

M_x-θ_x (Minor axis)   **M_z-θ_z (Major axis)**

S600-24-1

N/A

S600-24-2

N/A

M_x-θ_x (Minor axis)   **M_z-θ_z (Major axis)**

S600-24-3

N/A

S600-24-4

N/A

S600-24-5

N/A

M$_x$-θ$_x$ (Minor axis)   **M$_z$-θ$_z$ (Major axis)**

S600-24-6

N/A

S600-24-7

S600-24-7

S600-24-8

S600-24-8

M$_x$-θ$_x$ (Minor axis)   **M$_z$-θ$_z$ (Major axis)**

410

M_x-θ_x (Minor axis)

S600-24-12

S600-24-13

S600-24-14

M_z-θ_z (Major axis)

S600-24-12

S600-24-13

S600-24-14

411
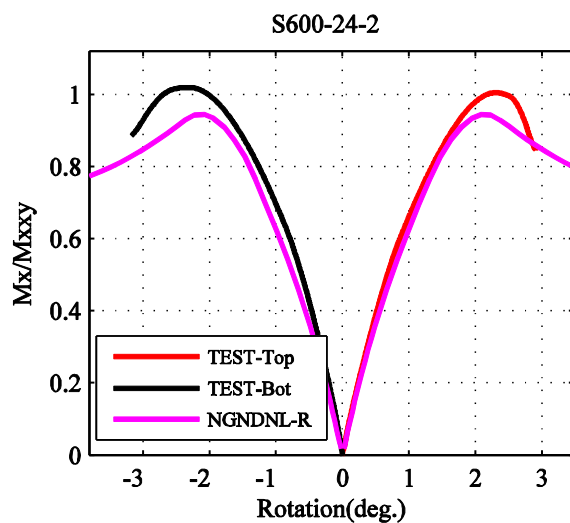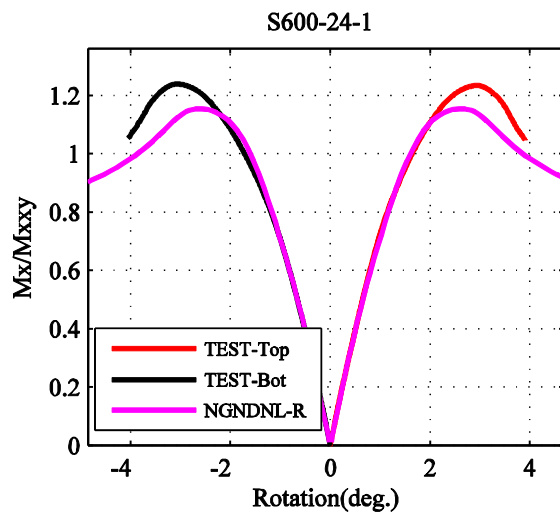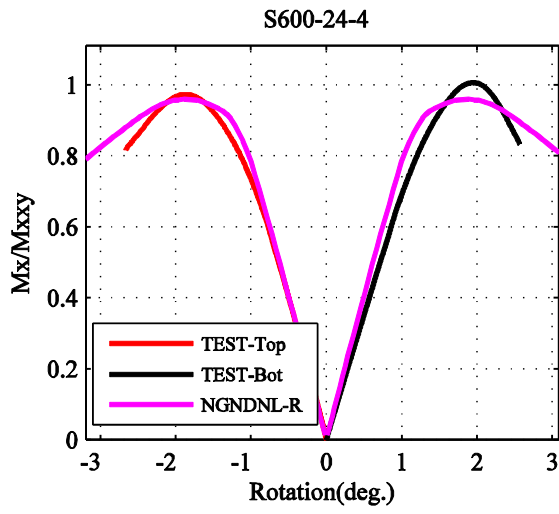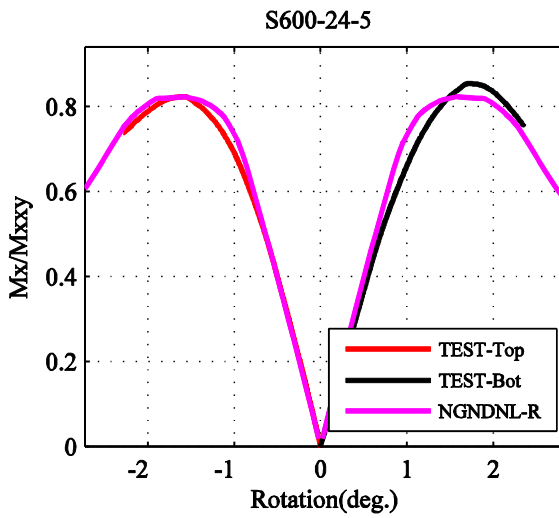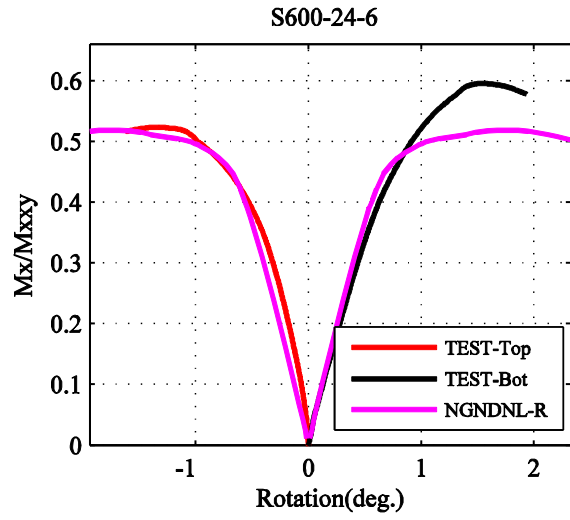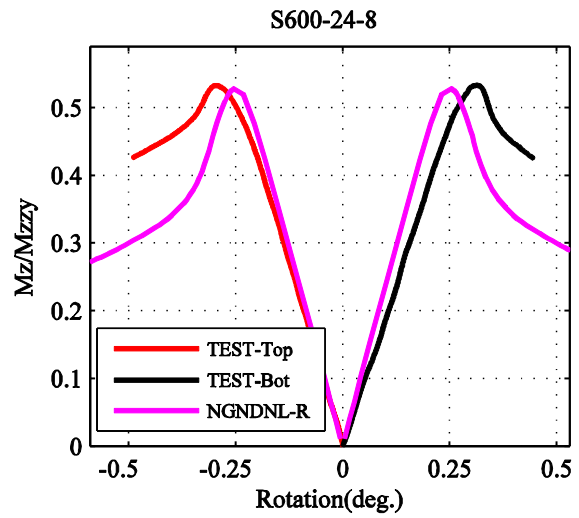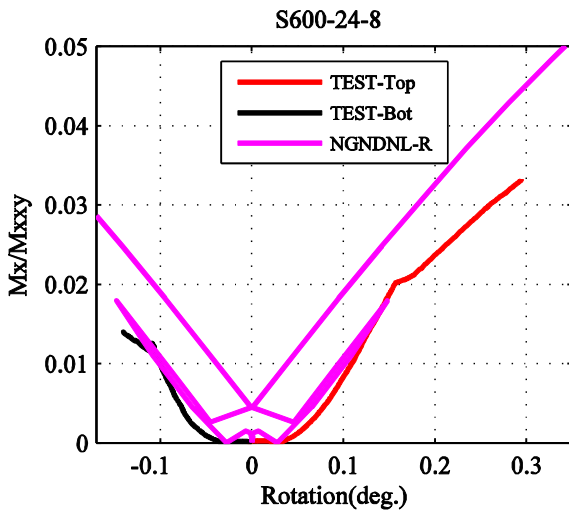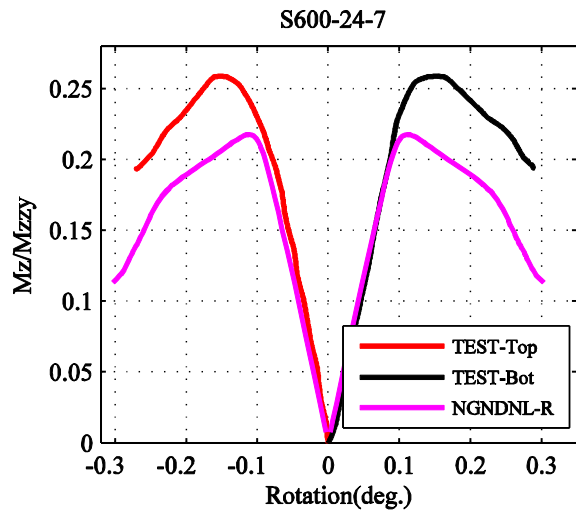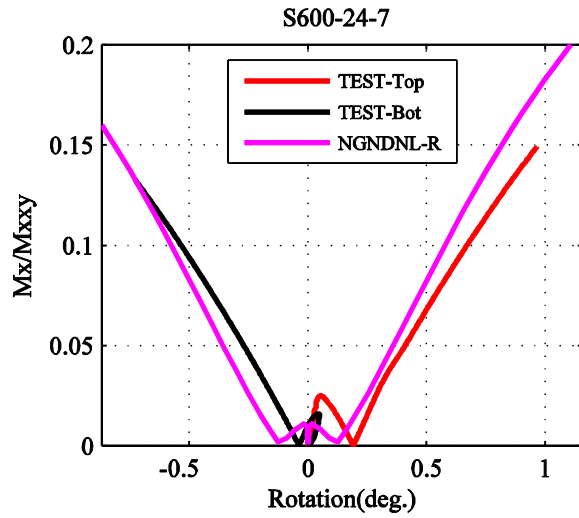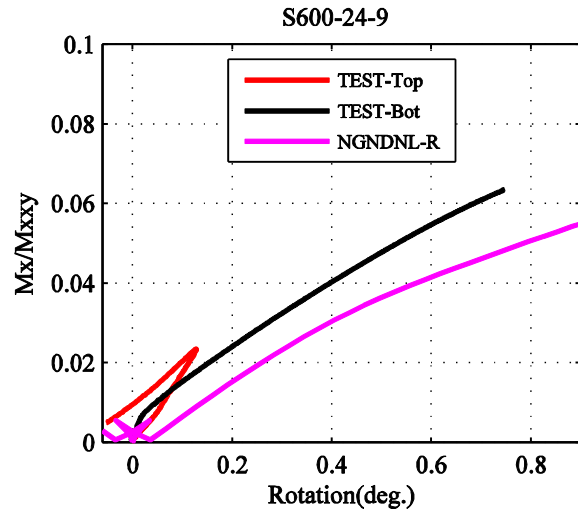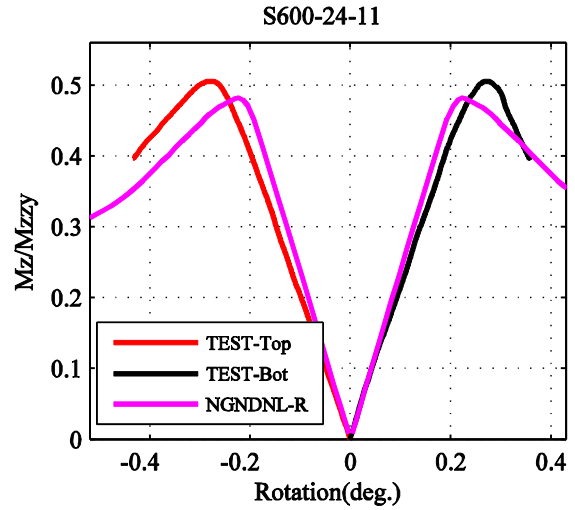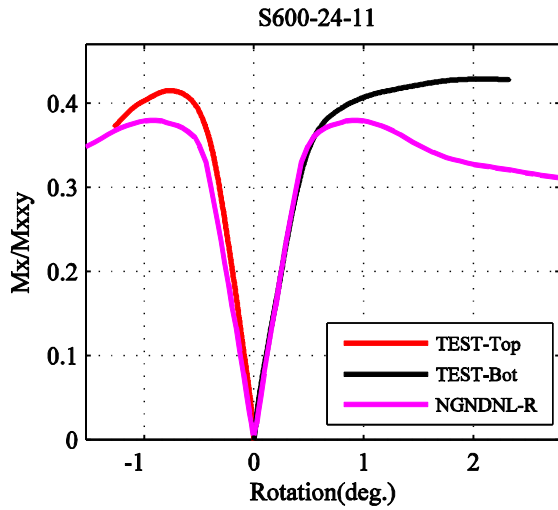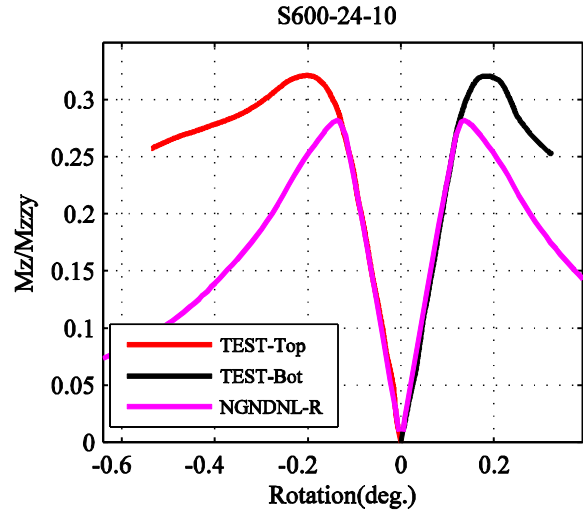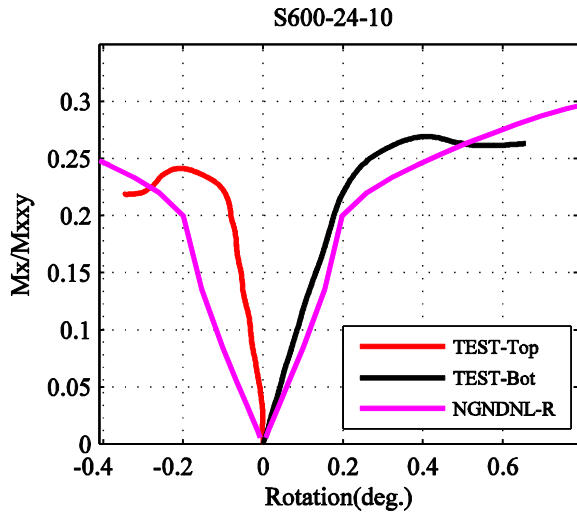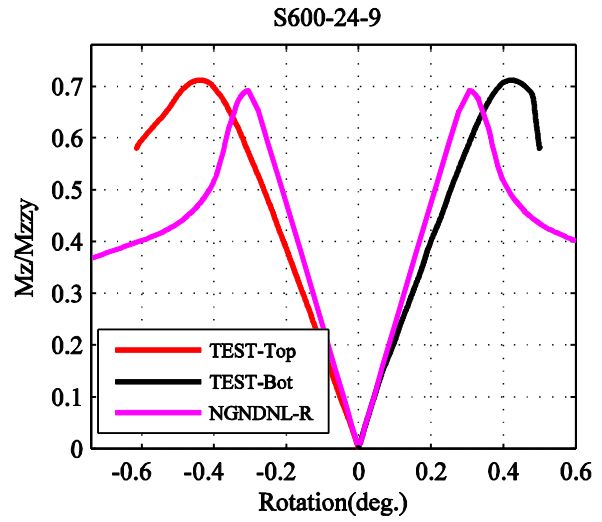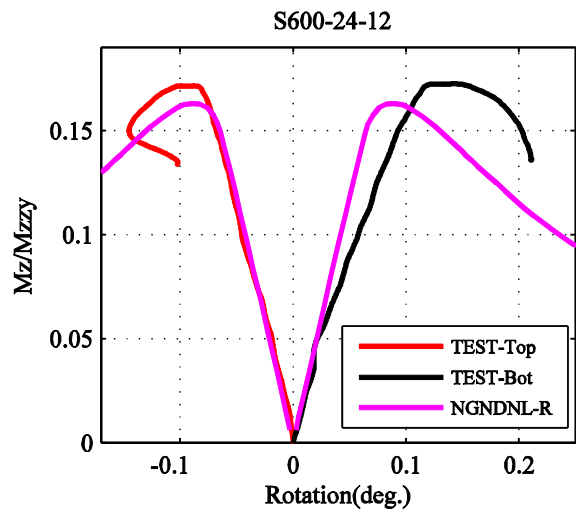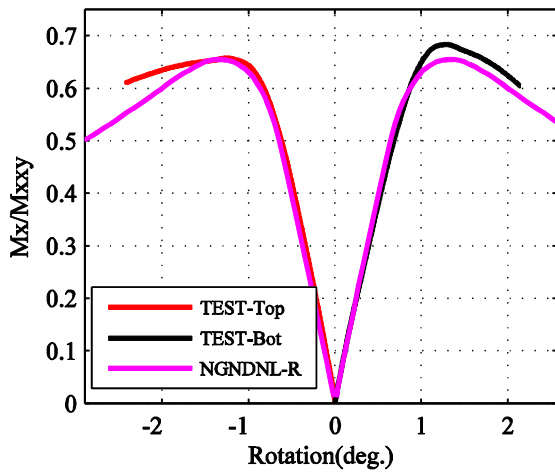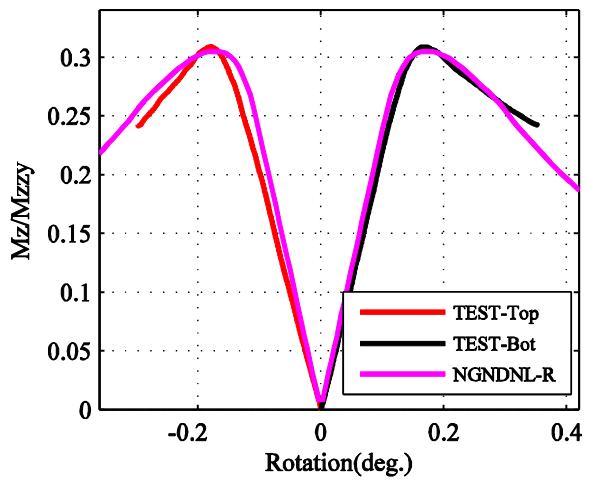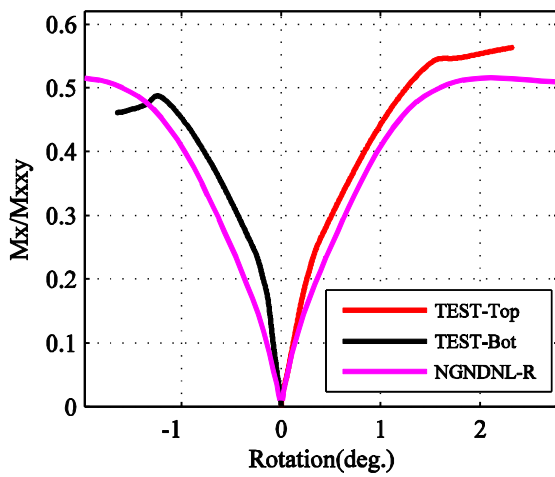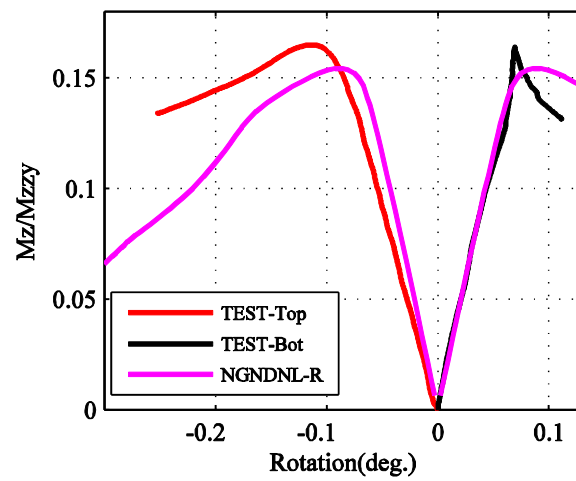
M$_x$-θ$_x$ (Minor axis)   **M$_z$-θ$_z$ (Major axis)**

S600-24-15

S600-24-15
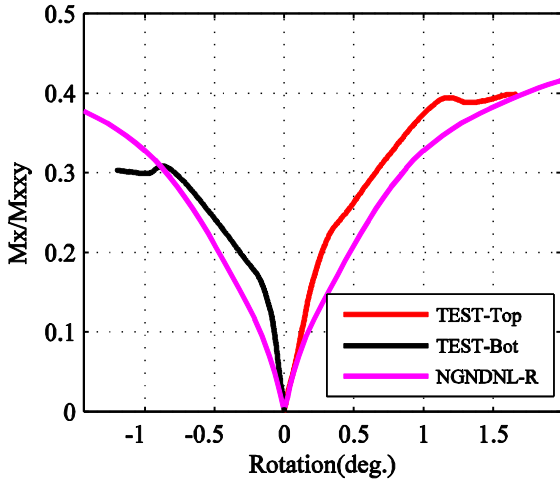
S600-24-16

S600-24-16
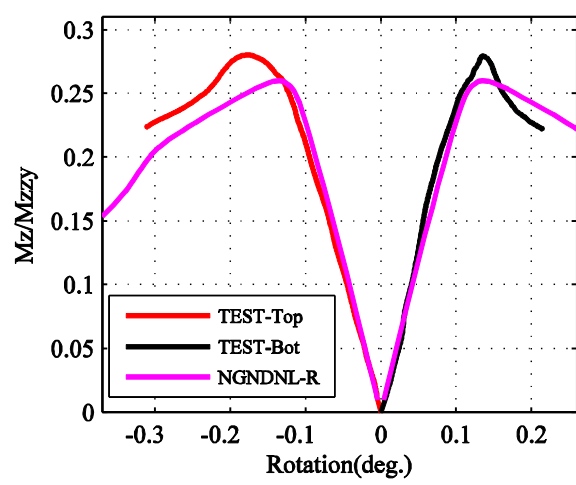
S600-24-17

S600-24-17

M$_x$-θ$_x$ (Minor axis)

M$_z$-θ$_z$ (Major axis)

S600-24-18

N/A
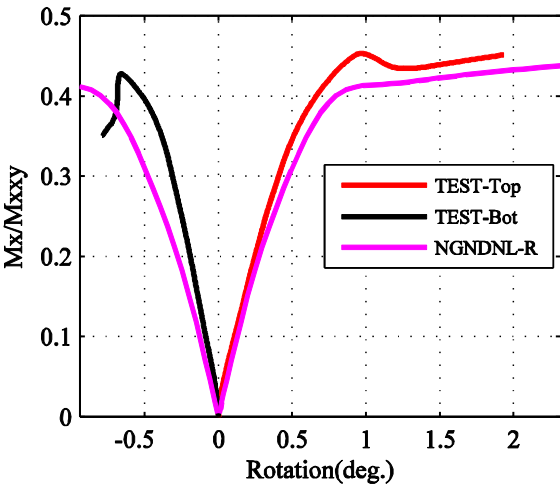
S600-24-19

S600-24-19

S600-24-20
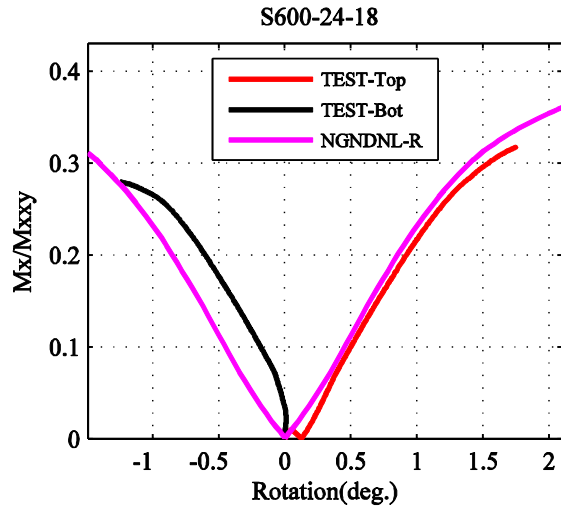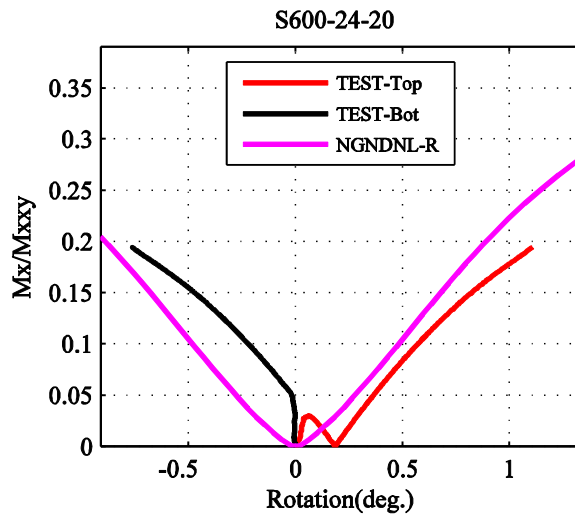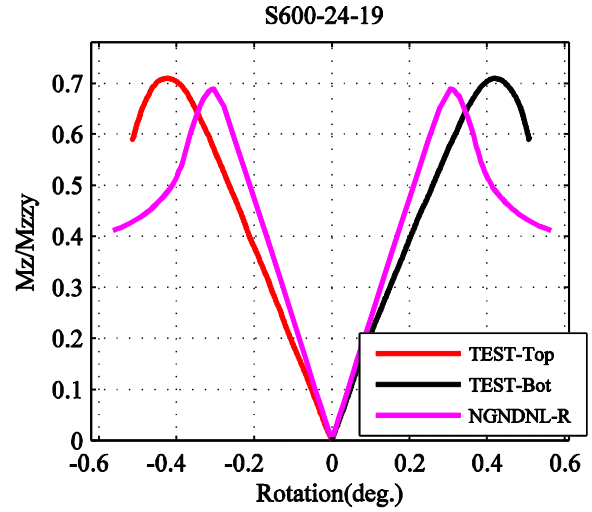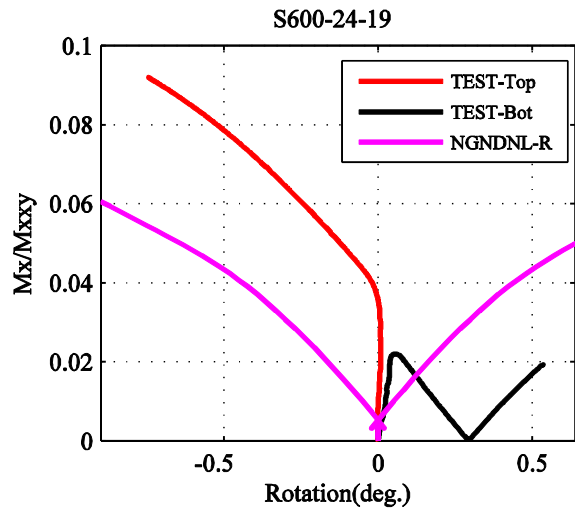
N/A

I.3 Moment-rotation curves: Long Specimens (S600-48)

The moment-rotation curves are calculated by using finite element models Option NGNDNL-C in the report: the model with nominal cross section; with negative global, local, and distortional buckling mode of imperfection; and with residual stress.

M_x-θ_x (Minor axis)

S600-48-1

M_z-θ_z (Major axis)

N/A

S600-48-2

N/A
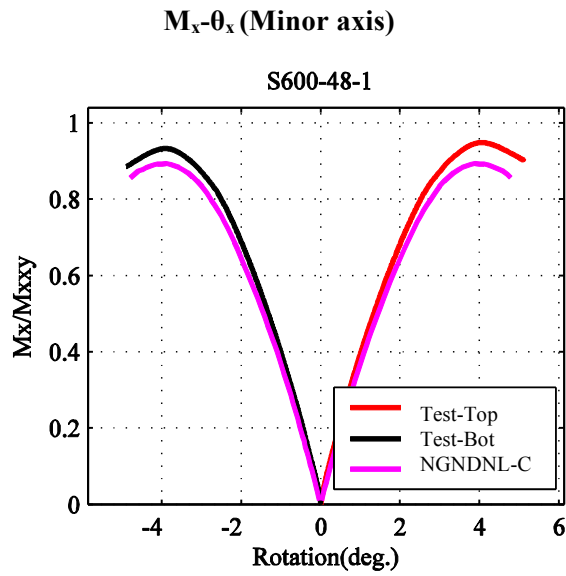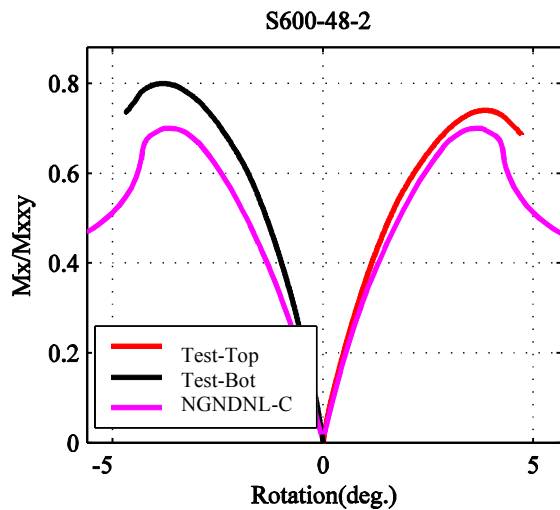
M$_x$-θ$_x$ (Minor axis)   **M$_z$-θ$_z$ (Major axis)**

S600-48-3

N/A

S600-48-4

N/A

S600-48-5

N/A
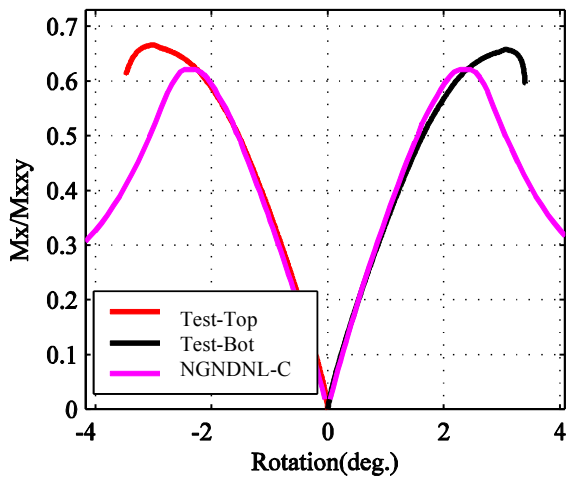
M_x-θ_x (Minor axis)   **M_z-θ_z (Major axis)**
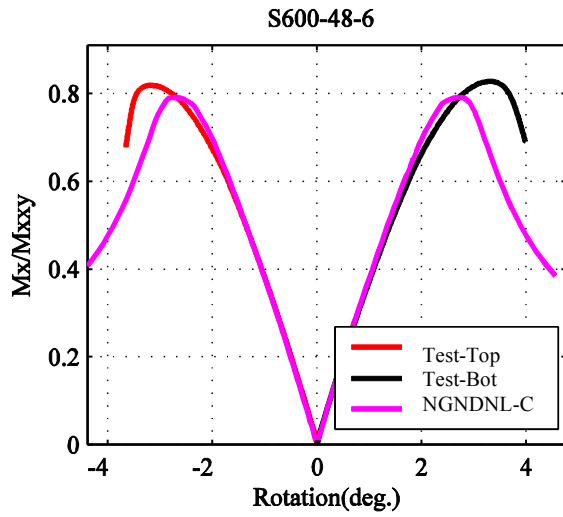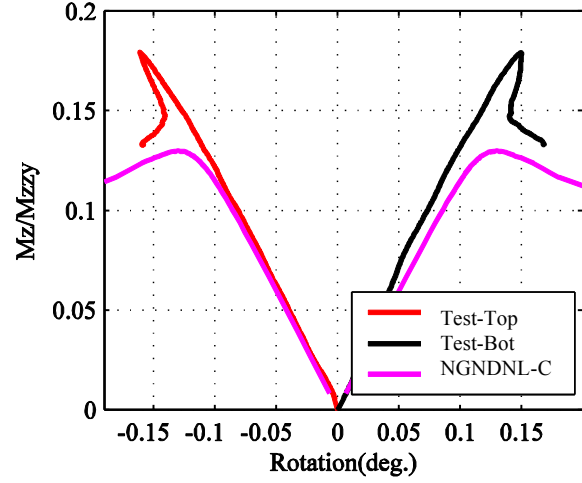

S600-48-6

N/A

S600-48-7

S600-48-7
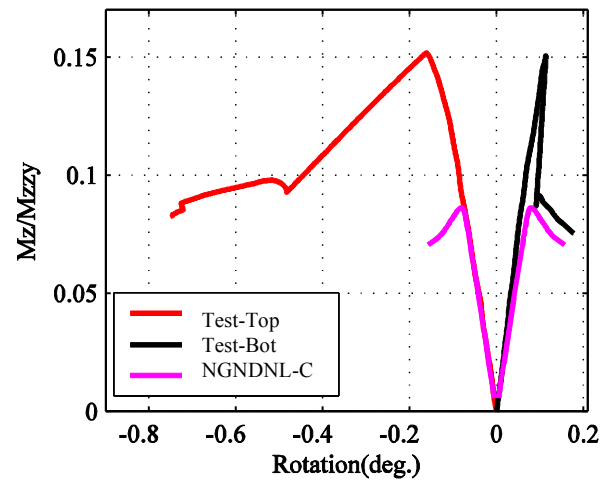
S600-48-8
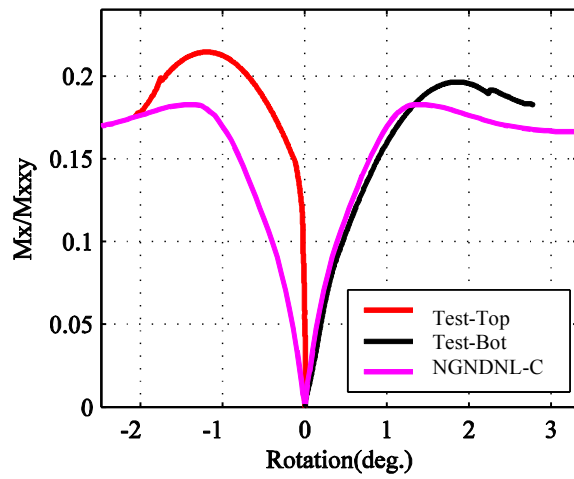
S600-48-8
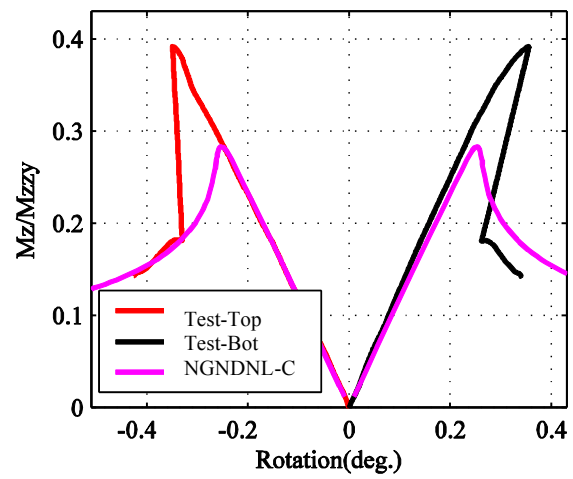
M_x-θ_x (Minor axis)
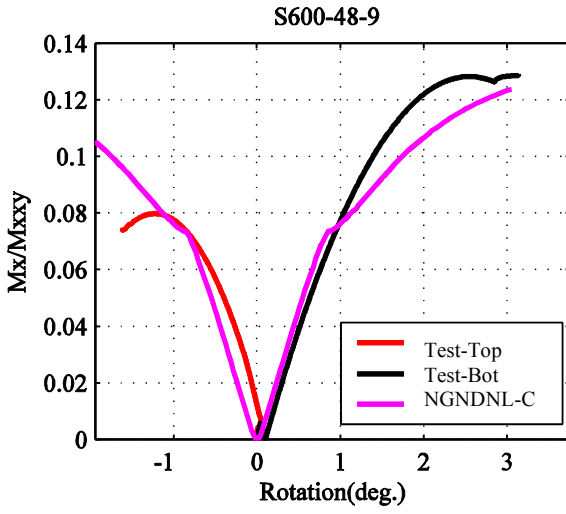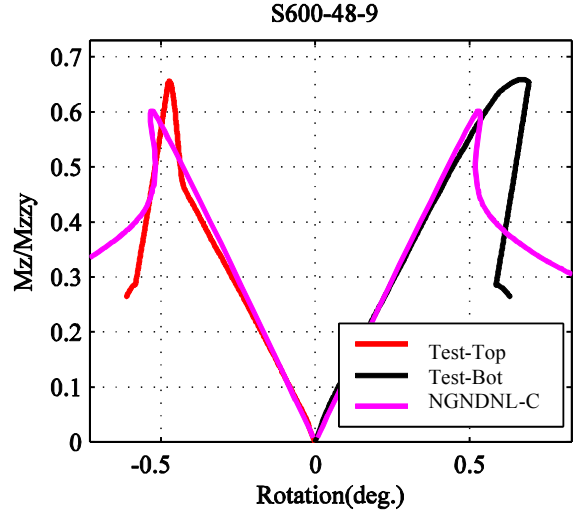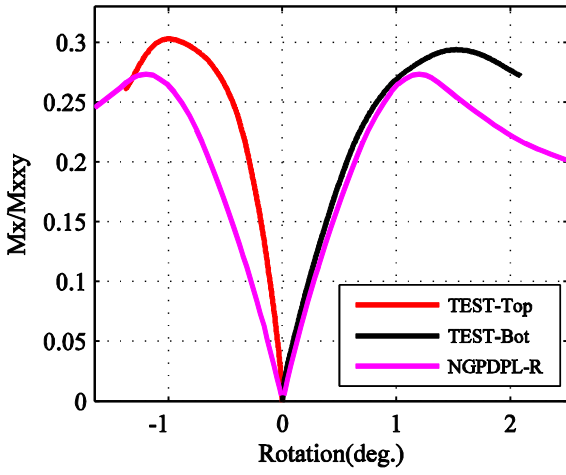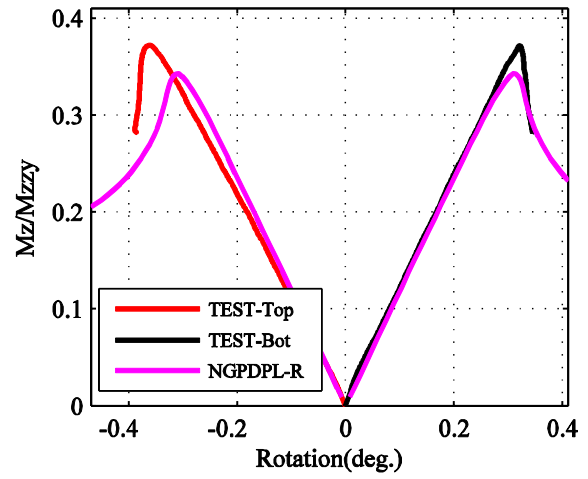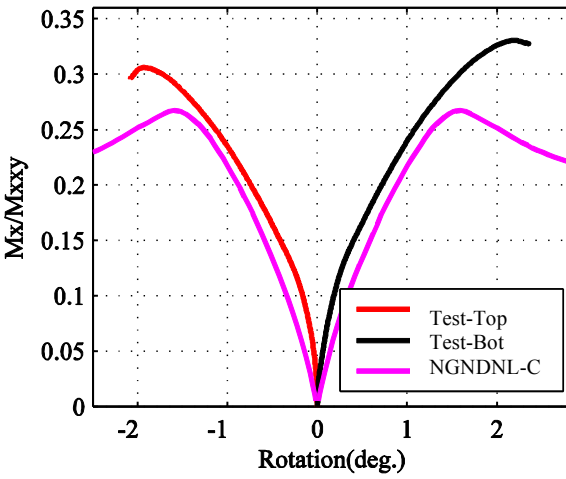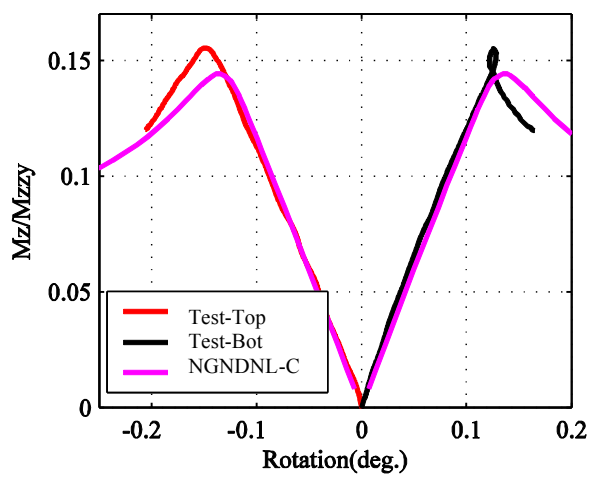
S600-48-9

S600-48-10

S600-48-11

M_z-θ_z (Major axis)

S600-48-9

S600-48-10

S600-48-11

417

M$_x$-θ$_x$ (Minor axis)   **M$_z$-θ$_z$ (Major axis)**

M$_x$-θ$_x$ (Minor axis)   **M$_z$-θ$_z$ (Major axis)**
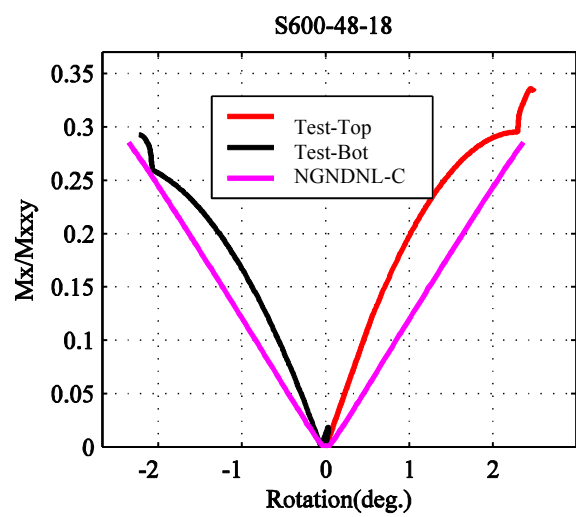

419
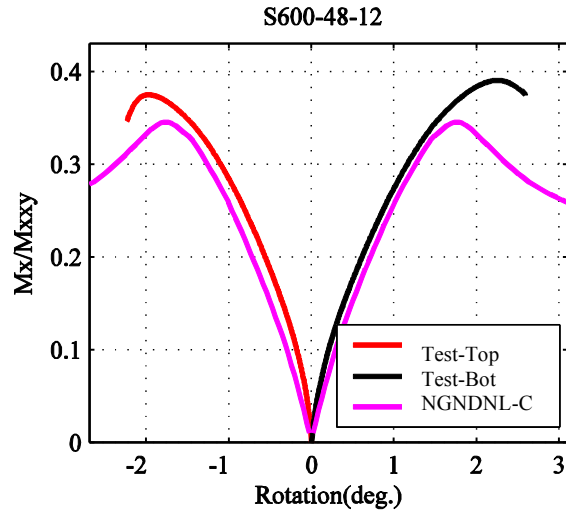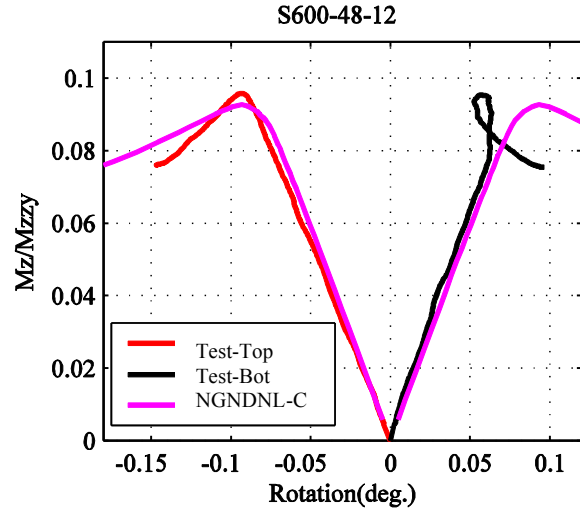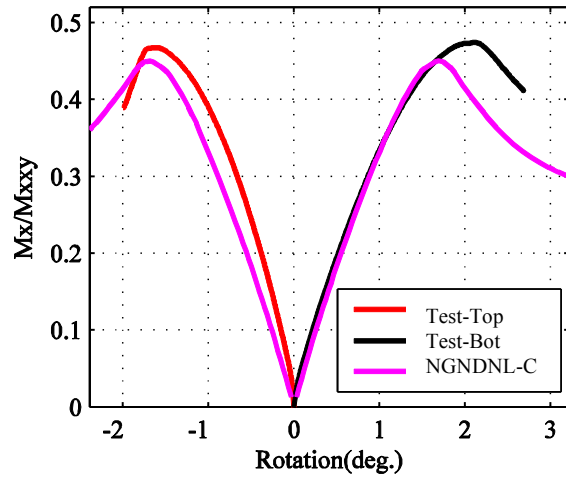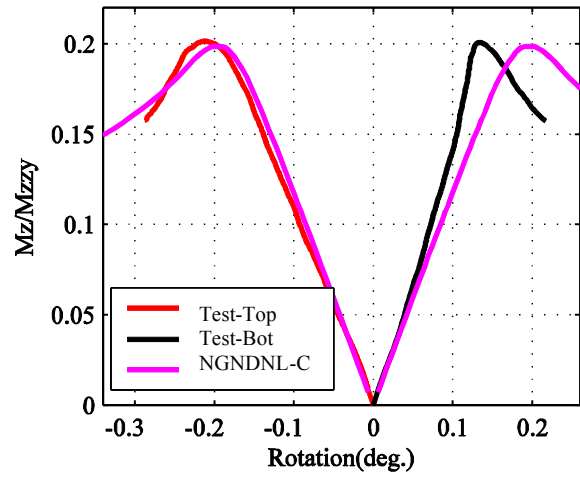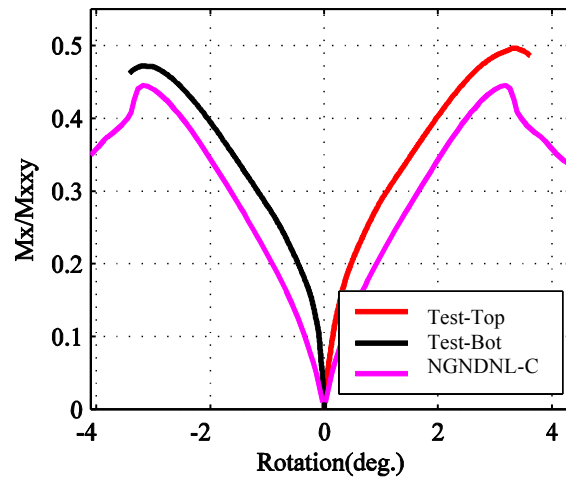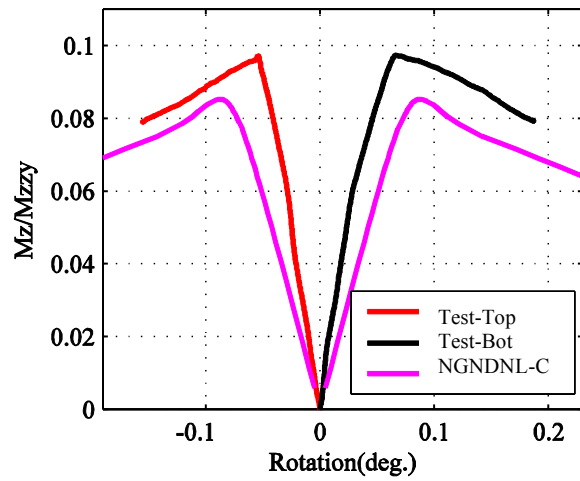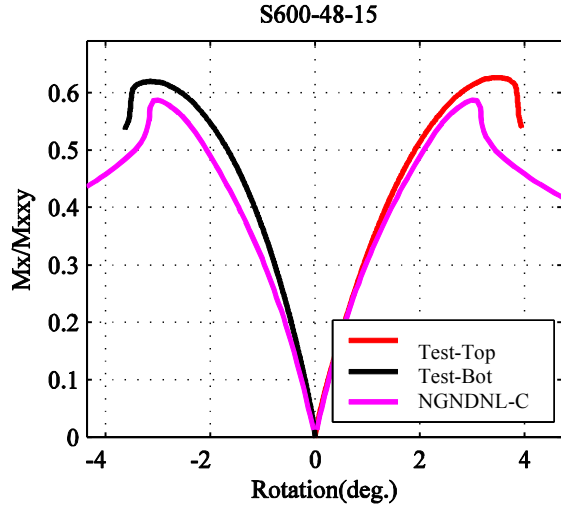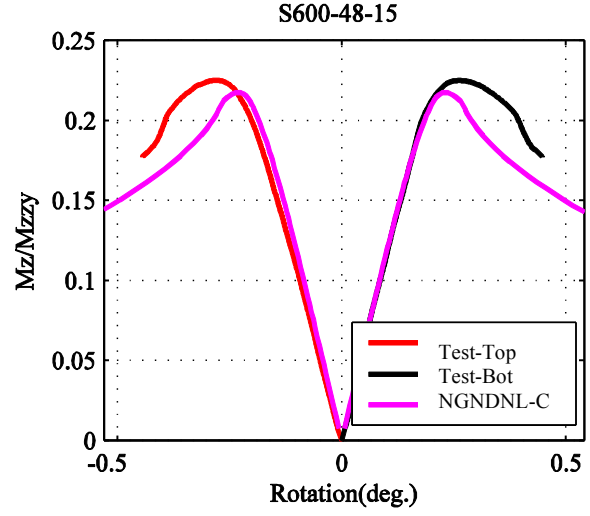
M_x-θ_x (Minor axis)

M_z-θ_z (Major axis)

S600-48-18
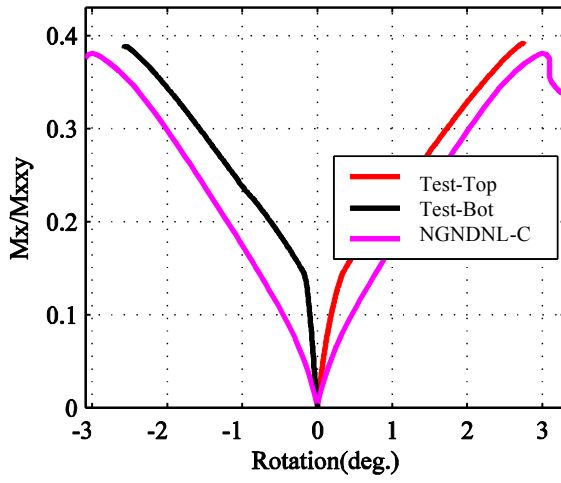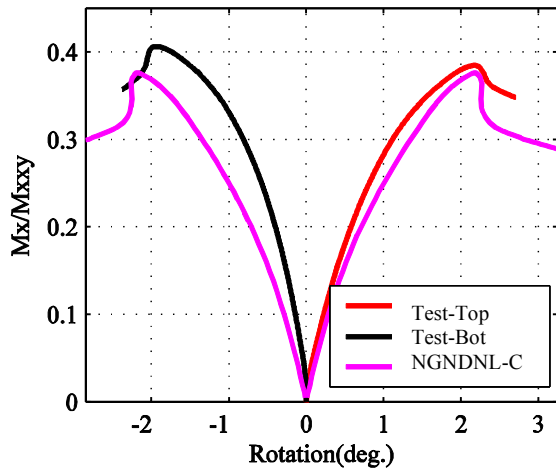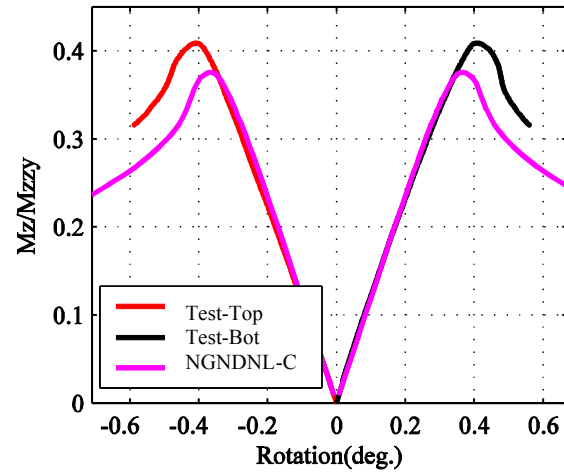
N/A

**American
Iron and Steel
Institute**

25 Massachusetts Avenue, NW
Suite 800
Washington, DC 20001
www.steel.org

The New Steel